

I.C. Göknaç  
L. Sevgi (Eds.)

# Complex Computing- Networks

Brain-like and  
Wave-oriented  
Electrodynamic  
Algorithms

**SPRINGER PROCEEDINGS IN PHYSICS 104**

---

## SPRINGER PROCEEDINGS IN PHYSICS

---

- 87 **Proceedings of the 25th International Conference on the Physics of Semiconductors**  
Editors: N. Miura and T. Ando
- 88 **Starburst Galaxies**  
Near and Far  
Editors: L. Tacconi and D. Lutz
- 89 **Computer Simulation Studies in Condensed-Matter Physics XIV**  
Editors: D.P. Landau, S.P. Lewis, and H.-B. Schüttler
- 90 **Computer Simulation Studies in Condensed-Matter Physics XV**  
Editors: D.P. Landau, S.P. Lewis, and H.-B. Schüttler
- 91 **The Dense Interstellar Medium in Galaxies**  
Editors: S. Pfalzner, C. Kramer, C. Straubmeier, and A. Heithausen
- 92 **Beyond the Standard Model 2003**  
Editor: H.V. Klapdor-Kleingrothaus
- 93 **ISSMGE**  
Experimental Studies  
Editor: T. Schanz
- 94 **ISSMGE**  
Numerical and Theoretical Approaches  
Editor: T. Schanz
- 95 **Computer Simulation Studies in Condensed-Matter Physics XVI**  
Editors: D.P. Landau, S.P. Lewis, and H.-B. Schüttler
- 96 **Electromagnetics in a Complex World**  
Editors: I.M. Pinto, V. Galdi, and L.B. Felsen
- 97 **Fields, Networks, Computational Methods and Systems in Modern Electrodynamics**  
A Tribute to Leopold B. Felsen  
Editors: P. Russer and M. Mongiardo
- 98 **Particle Physics and the Universe**  
Proceedings of the 9th Adriatic Meeting, Sept. 2003, Dubrovnik  
Editors: J. Trampetić and J. Wess
- 99 **Cosmic Explosions**  
On the 10th Anniversary of SN1993J (IAU Colloquium 192)  
Editors: J. M. Marcaide and K. W. Weiler
- 100 **Lasers in the Conservation of Artworks**  
LACONA V Proceedings, Osnabrück, Germany, Sept. 15–18, 2003  
Editors: K. Dickmann, C. Fotakis, and J.F. Asmus
- 101 **Progress in Turbulence**  
Editors: J. Peinke, A. Kittel, S. Barth, and M. Oberlack
- 102 **Adaptive Optics for Industry and Medicine**  
Proceedings of the 4th International Workshop  
Editor: U. Wittrock
- 103 **Computer Simulation Studies in Condensed-Matter Physics XVII**  
Editors: D.P. Landau, S.P. Lewis, and H.-B. Schüttler
- 104 **Complex Computing-Networks**  
Brain-like and Wave-oriented Electrodynamical Algorithms  
Editors: I.C. Gökner and L. Sevgi

---

Volumes 60–86 are listed at the end of the book.

I.C. Göknar L. Sevgi  
(Eds.)

# Complex Computing-Networks

Brain-like and Wave-oriented  
Electrodynamic Algorithms

With 223 Figures

 Springer

Izzet Cem Gökmar  
Levent Sevgi  
DOĞUŞ University  
Electronics and Communications Department  
Istanbul, Turkey  
E-mail: cgokmar@dogus.edu.tr, lsevgi@dogus.edu.tr

ISSN 0930-8989

ISBN-10 3-540-30635-8 Springer Berlin Heidelberg New York

ISBN-13 978-3-540-30635-1 Springer Berlin Heidelberg New York

Library of Congress Control Number: 2005936512

This work is subject to copyright. All rights are reserved, whether the whole or part of the material is concerned, specifically the rights of translation, reprinting, reuse of illustrations, recitation, broadcasting, reproduction on microfilm or in any other way, and storage in data banks. Duplication of this publication or parts thereof is permitted only under the provisions of the German Copyright Law of September 9, 1965, in its current version, and permission for use must always be obtained from Springer-Verlag. Violations are liable to prosecution under the German Copyright Law.

Springer is a part of Springer Science+Business Media.

springer.com

© Springer-Verlag Berlin Heidelberg 2006

Printed in The Netherlands

The use of general descriptive names, registered names, trademarks, etc. in this publication does not imply, even in the absence of a specific statement, that such names are exempt from the relevant protective laws and regulations and therefore free for general use.

Production: SPI Publisher Services

Cover concept: eStudio Calamar Steinen

Cover production: *design & production* GmbH, Heidelberg

Printed on acid-free paper      SPIN: 11412724      89/3100/SPI      5 4 3 2 1 0

## Preface

This book contains the ceremonials and the proceedings pertaining to the International Symposium CCN2005 on “Complex Computing-Networks: A Link between Brain-like and Wave-Oriented Electrodynamics Algorithms,” convened at Doğuş University of Istanbul, Turkey, on 13–14 June 2005, in connection with the bestowal of the honorary doctorate degrees on Professors Leopold B. Felsen and Leon O. Chua, for their extraordinary achievements in electromagnetics, and nonlinear systems, respectively. The symposium was co-organized by Cem Gökmar and Levent Sevgi, in consultation with Leopold B. Felsen and Leon O. Chua.

Istanbul is a city with wonderful natural and historical surroundings, a city not only interconnecting Asia and Europe but also Eastern and Western cultures. Therefore, CCN2005 was a memorable event not only in the lifetime of Drs. Felsen, Chua, and their families, but also for all the other participants who were there to congratulate the recipients and participate in the symposium.

CCN2005, together with the Bestowal Ceremony – unique in combining EM/APS and CAS disciplines – was an excellent opportunity for the colleagues, collaborators, students, and international scientists who gathered at Doğuş to disseminate and share the recent advances in the fields of electromagnetics, nonlinear systems and their computational aspects. The symposium attracted about 60 participants from several countries with 45 papers from academia and engineering institutes, which addressed diverse problems in both EM and CAS subject areas. The 2-day, parallel EM and CAS sessions ended with a joint session and a joint panel discussion on the problems and challenges of future electrical engineering education.

The degree-bestowal ceremony took place in the morning of 13 June 2005, together with the opening ceremony of CCN2005. After a short greeting by Prof. Talha Dinibütün, the Rector of Doğuş University, Prof. Sevgi, who had proposed Prof. Felsen’s nomination, delivered his introductory speech on Felsen’s achievements and personality. This was followed by the speech of Prof. Gökmar, who had proposed Prof. Chua’s nomination. The introduction of both nominees was followed by the bestowal of the degrees by Prof. Dinibütün. The ceremony continued with the acceptance replies of Profs. Felsen and Chua, and ended with their photographs being taken along with family, students, friends and colleagues. The gala dinner during the evening of 14 June 2005, was a special affair that took place at the Moda Sea Club, a wonderful place on the Asiatic seaside, in Kadıköy. After a short sunset cocktail party on the balcony, the guests enjoyed a selection of rich Turkish cuisine, a variety of unlimited drinks (wines and Turkish Raki) and music. The surprise of the evening came from Prof. Siddık Yarman, former rector of Işık University, who presented a short piano recital, from Turkish classical music to Argentinian tangos. The beat and emotions peaked when he played the well-known Jewish song, Havah Nagilah, for Leo Felsen.

## VI

The organizers are indebted to various individuals and organizations for their support of this event. Acknowledgement in particular goes to Dođuş University, TÜBİTAK – The Scientific and Technological Research Council of Turkey, TELSİM and IEEE Turkey Section. The editors express their sincere appreciation to all participants in the symposium and to the authors who contributed to this book. Special acknowledgement goes to the local committee members for their efforts during the workshop and to the editorial assistants Ç. Uluşık, M. Yıldız, T. Bekri and İ. Ergüler for their valuable collaboration.

**Unfortunately CCN2005 became the last event Leopold B. Felsen was able to attend, as his condition deteriorated upon his return to the States and he sadly passed away on 24 September 2005. We are honoured to have been able to offer him this last occasion to share his scientific knowledge and human values, both of which we hold in great esteem.**

İstanbul  
October 2005



İzzet Cem Gökner  
CCN Co-editor



Levent Sevgi  
CCN Co-editor

# Contents

---

## Part I Electromagnetic Theory

---

<b>Wave Models for Networks and Fields</b> C. Christopoulos, P. Sewell, and J. Paul .....	3
<b>Electromagnetic Field Interaction with a Transmission Line</b> J. Russer, A. Cangellaris, and P. Russer .....	13
<b>Scattering of a Plane-Wave by a Moving Half-Plane: A Full Relativistic Study</b> M. İdemem and A. Alkumru .....	27
<b>High-Frequency/Short-Pulse Wave Dynamics in Ray-Chaotic Scenarios: A Survey</b> V. Galdi, G. Castaldi, V. Fiumara, V. Pierro, I. M. Pinto, and L. B. Felsen .....	37
<b>Numerical Modeling and Simulation Studies of 2D Propagation over Non-flat Terrain and Through Inhomogeneous Atmosphere</b> Ç. Uluışık and L. Sevgi .....	45
<b>Fast Integral Equation Solutions: Application to Mixed Path Terrain Profiles and Comparisons with Parabolic Equation Method</b> C.A. Tunç, F. Akleman, V.B. Ertürk, A. Altıntaş and L. Sevgi.....	55
<b>A Pole Matching Method for the Analysis of Frequency Selective Surfaces</b> A. Cucini, M. Nannetti, F. Caminita and S. Maci .....	65
<b>About Complex Extensions and Their Application in Electromagnetics</b> M.J.G. Morales, C.D. Martinez and E.G.-Ribas .....	81
<b>Radiation of Sound from a Semi-Infinite Rigid Duct Inserted Axially into a Larger Infinite Tube with Wall Impedance Discontinuity</b> A. Büyükaksoy and A. Demir .....	87



VIII

<b>Scattering by a Perfect Conducting Elliptic Cylinder Immersed Halfway Between Two Half Spaces</b> A. Kamel and E. Niver .....	97
<b>Pattern Nulling of Offset Parabolic Reflector with Array Feed</b> B. Saka and A. Selçuk .....	105
<b>Tapered Dielectric Rod Antenna</b> E. Niver .....	113
<b>Design Alternatives of Spiral Antenna Arrays for Wireless Applications</b> G. Çakir and L. Sevgi .....	123
<b>Analysis of Multiple Vertical Strips in Planar Geometries via DCIM-MoM</b> T. Önal, N. Kinayman and M. İ. Aksun .....	133
<b>A Matlab-based Filter Design Tool Using the Analogy between Wave and Circuit Theories</b> G. Çakir, S. Gündüz and L. Sevgi .....	141
<b>A Generic Microstrip Structure with Broadband Bandstop and Bandpass Filter Characteristics</b> G. Çakir and L. Sevgi .....	149
<b>Analysis of Waveguide Structures by Combination of the Method of Lines and Finite Differences</b> R. Pregla .....	157
<b>Resonator Characterization by Microwave Active Circuits</b> C. Akyel .....	167
<b>Performance Evaluation in Optical Burst Switched Networks</b> S. Parlar and E. Topuz .....	177
<b>Nonlinearity and Multiscale Behaviour in Ocean Surface Dynamics: An Investigation Using HF and Microwave Radars</b> S. Anderson, C. Anderson and J. Morris .....	185
<b>Fine Tuning of Printed Triangular Monopole</b> C. Işık .....	197
<b>A Chiralic Circuit Element and Its Use in a Chiralic Circuit</b> T. Şengör .....	203

---

**Part II Circuit Theory**


---

<b>Dynamical Systems Analysis Using Differential Geometry</b> J.-M. Ginoux and B. Rossetto .....	213
<b>r-Neighbourhood Impact on the Behaviour of 2D Cellular Automata Model of Complex Interactions</b> A. Porebska .....	221
<b>Stability of CNN with Trapezoidal Activation Function</b> E. Bilgili, İ.C. Gökna, O.N. Uçan and M. Albora .....	225
<b>Applications of CNN with Trapezoidal Activation Function</b> E. Bilgili, İ.C. Gökna and O.N. Uçan .....	235
<b>A CNN-based Fingerprint Verification System</b> Q. Gao and G.S. Moschytz .....	243
<b>Hardware Architectures for the Evolution of Cellular Automata Functionality</b> M. Glesner, O. Soffke and P. Zipf .....	257
<b>Current Mode Double Threshold Neuron Activation Function</b> M. Yildiz, S. Minaei and İ. C. Gökna .....	267
<b>Gradient Networks for Clustering</b> H. Doğan and C. Güzeliş .....	275
<b>On a matrix inequality and its application to the synchronization in coupled chaotic systems</b> C.W. Wu .....	279
<b>Rigorous Study of Chua's Circuit in Terms of Periodic Orbits</b> Z. Galias .....	289
<b>Complex Behavior and its Analysis in Chaotic Circuits Networks with Intermittency</b> Y. Uwate, Y. Nishio and A. Ushida .....	297
<b>Bifurcations in Noisy Nonlinear Networks and Systems</b> W. Mathis .....	305
<b>When is a Linear Complementarity System Controllable?</b> M.K. Çamlıbel .....	315

X

<b>A Simple Artificial Neural Network Structure For Generating Chaos</b> N.S. Şengör.....	325
<b>Advanced Signal Processing Algorithms for Wireless Communications</b> E. Panayirci and H.A. Çirpan .....	333
<b>A Clock-controlled Stream Cipher with Dual Mode</b> İ. Ergüler and E. Anarim .....	343
<b>Modeling Controller Area Networks Using Discrete Event Simulation Technique</b> C. Bayılmış, İ. Ertürk, C. Çeken, and İ. Özçelik.....	353

---

**Part III**

---

<b>Laudation on Professor Leopold B. Felsen</b> L. Sevgi .....	361
<b>Laudation on Professor Leon O. Chua</b> İ. C. Gökmar .....	377
<b>Professor Felsen's Reply</b> L. B. Felsen .....	387
<b>Photo Gallery</b> .....	401
<b>Index</b> .....	411

---

---

Part I

Electromagnetic Theory

# Wave Models for Networks and Fields

C. Christopoulos, P. Sewell, and J. Paul

George Green Institute for Electromagnetics Research, University of Nottingham,  
Nottingham NG7 2RD, UK, [christos.christopoulos@nottingham.ac.uk](mailto:christos.christopoulos@nottingham.ac.uk),  
Fax: +44-115-951-5616, Tel.: +44-115-951-5557

## Abstract

The paper aims to illustrate the relationship and limits of applicability of the network and field paradigms as applied to the study of electromagnetic (EM) phenomena especially at high frequencies. A particular focus is the transmission-line modelling or matrix method (TLM) which is particularly suited to this discussion as it models EM phenomena by exploiting both paradigms. Particular attention is paid to the interpretation of TLM and the manner in which embedded subwavelength structures are modelled.

## Introduction

Advances in technology in recent years have led to the introduction of signal processing and transmission techniques in wire and/or wireless systems which are clocked at rates in the GHz range. Virtually all equipment connected to electrical supplies contains tightly packed controllers, microprocessors, sensors and actuators, communicating through multiple interconnects carrying high-speed digital signals. Wireless equipment is increasingly being introduced into both domestic and industrial environments. With several pieces of equipment in close proximity to each other, generating very high frequencies problems of interference, crosstalk, electromagnetic compatibility (EMC), and signal integrity (SI) increasingly become the dominant factors in design. Designers need access to efficient and accurate computer based tools to predict performance, optimise design, and reduce costs without incurring delays and re-engineering costs. The need for sophisticated numerical models becomes apparent as for the current highly integrated complex designs intuitive techniques based entirely on the skills of the designer are not adequate. It may be argued that with more powerful computers we can solve more complex problems using well established modelling methodologies. Although this is true up to a point, it fails to recognise that the complexity of the problems we need to solve grows faster than the technology available to us to search for solutions [1]. We need to not only make full use of modern computer

technology (including parallel and grid technologies) but also develop new and innovative approaches to modelling [2, 3]. These alone can offer a step increase in modelling and simulation capabilities and thus offer the scope for iterative design of complex practical systems. It is in this area of innovative modelling techniques that this paper aims to make a contribution.

At low frequencies the dominant paradigm is that of the network [4]. For electrically small circuits it is convenient to assume that electrical energy storage is concentrated (lumped together) in a component described as a capacitor. Similarly, magnetic energy is lumped in an inductor, losses in a resistor, etc. Under this assumption, the resulting circuit behaviour can be studied in its entirety by using topological concepts. The so-called lumped circuit theory is well developed and is the corner stone of the training of young engineers. It has many admirable attributes including simplicity, clarity, generality, and intellectual economy. One can envisage a lumped capacitor as the simplest “macromodel” embodying in a simple elegant formulation a rather complex physical process. As the frequency increases, the circuit can no longer be regarded as electrically small and the network paradigm fails. If “electrically small” assumption fails in only one dimension then, transmission line (TL) theory may be applied, based on distributed energy storage and loss. In the general case of a circuit which is electrically large in all three dimensions, the network paradigm must be replaced by the field paradigm. Here, transfer of action over distance between electrical charges is used to transfer energy and information. In addition to the topology of the circuit which is important when the network concept is used, we now also need to take account of the geometry of the circuit. This complicates matters significantly. In contrast to the network case where models and computer solvers are based on Kirchhoff’s laws, the physical laws representing interactions in this regime are expressed in Maxwell’s equations. It is pointed out that the fundamental concept is that of the field and that the network concept is a convenient simplification whose validity is subject to certain limitations.

In modern design at high-frequencies it is inevitable that field solutions are sought to Maxwell’s equations. However, the difficulties of solving these equations and the complexity of modern designs make for a combination which is very demanding. Computational electromagnetics (CEM) is the discipline which addresses the development of computer-based tools for solving electromagnetic problems in complex configurations. Several generic techniques exist for this task such as the method of moments, finite element method, finite difference time-domain method [3], and transmission-line modelling or matrix method (TLM) [2, 4]. We focus on the TLM method and its enhancements as it brings out more clearly the interplay between network and field concepts.

## The TLM Method

Ever since the advent of electricity as a scientific discipline efforts were made to relate its phenomenology to familiar mechanical concepts and to bring out

analogies between kinetic and potential energy and the concepts of lumped inductance and capacitance. High-frequency phenomena, e.g. wave propagation required a different way of thinking and the underlying mathematical modelling took a longer time to develop. The linkage between lumped component networks and fields were apparent for some time [5] but could not be exploited for the lack of powerful enough computational resources. However, in the 1970s work by Johns and colleagues [6] introduced the fundamentals of simulating EM field problems by analogy to networks. At the most basic level the analogy may be established by observing the isomorphism between equations describing one-dimensional wave propagation:

$$\frac{\partial^2 j}{\partial x^2} = \mu\epsilon \frac{\partial^2 j}{\partial t^2} + \mu\sigma \frac{\partial j}{\partial t} \quad (1)$$

and the equations for a lossy transmission line with series inductance  $L$ , shunt capacitance  $C$  and shunt resistance  $R$  for a segment  $\Delta x$  long:

$$\frac{\partial^2 i}{\partial x^2} = \frac{LC}{(\Delta x)^2} \frac{\partial^2 i}{\partial t^2} + \frac{L}{(\Delta x)^2} \frac{\partial i}{\partial t} R, \quad (2)$$

where  $j$  is the current density in the field problem and  $i$  is the current in the network problem. Inspection of (1) and (2) shows the desired analogy:

$$i \rightarrow j \quad \frac{L}{\Delta x} \rightarrow \epsilon \quad \frac{1}{R\Delta x} \rightarrow \sigma. \quad (3)$$

In effect, solution of the field problem may be reduced to the solution of a network problem consisting of a cascade of subnetworks each of size  $\Delta x$ . For accuracy, we must choose  $\Delta x \ll \lambda$  (typically  $10 \Delta x \sim \lambda$ ) to meet the criterion for using lumped component representations. We observe that using lumped components is tantamount to introducing a space discretization. This is the first step in solving a problem by computer as it allows a finite number of space sampling points and hence of memory allocations. The second step is the time discretization which allows a finite number of calculations to be performed and hence a finite run time. Time discretization is accomplished by replacing lumped components by transmission line segments (two-port link lines or one-port stubs). The finite propagation time  $\Delta t$  along these segments is effective the sampling time for the solution of the problem. In conclusion, in TLM, we construct a three-dimensional lattice or matrix of transmission lines consisting of the repetition of a basic cell or node of dimensions  $\Delta x \Delta y \Delta z \ll \lambda^3$  in which we map the geometrical, electrical, and materials details of the problem. Solution of this network yields the desired electric and magnetic field by analogy to the network voltages and currents. In this way the transitions from networks to fields is seamless offering great intellectual economy and all the advantages of the well developed and efficient network characterization and solving techniques. Basic nodes in TLM are available in two and three dimensions. As an example we show the 3D TLM symmetrical condensed node (SCN) in Fig. 1.

The basic computational scheme is based on the successive application of two procedures on all the nodes of the problem. These are the scattering of the 12 incident voltage pulses  $V^i$  to each node to produce 12 reflected pulses  $V^r$ :

$$V^r = [S]V^i \quad (4)$$

and the connection of the reflected voltage pulses to adjacent nodes to become the incident pulses at the next time step

$${}_{k+1}V^i = [C]_k V^r, \quad (5)$$

where  $[S]$  and  $[C]$  are appropriate scattering and connection matrices, respectively, [2].

Another way of looking at the TLM formulation is to reason that the network of transmission lines inside a node must be such that it presents an admittance to incoming voltage pulses that matches the admittance  $[Y]$  relating magnetic and electric fields. This effectively dictates that the incident and reflected voltage pulses are related as follows,

$$\{y_0[I] + [Y]\}V^r = \{y_0[I] - [Y]\}V^i, \quad (6)$$

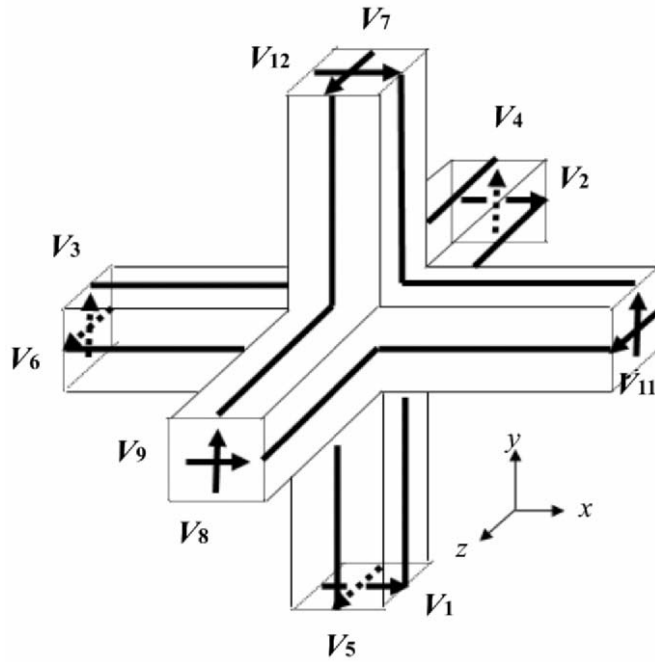


**Fig. 1.** The 3D TLM symmetrical condensed node (SCN)



where,  $[I]$  is the identity matrix and  $y_0$  is a scalar quantity. The best way to obtain the admittance matrix is to solve (6) as an eigenvalue problem. The resulting eigenvectors allow us to decompose the pulses  $V$  into their modal components  $X$ . Incident and reflected modal components are related by,

$$X_n^r = \frac{y_0 - \gamma_n}{y_0 + \gamma_n} X_n^i, \quad (7)$$

where  $\gamma_n$  is the eigenvalue for the  $n$ th mode. In 2D TLM schemes there are four degrees of freedom and hence four modes may be selected. The eigenvalues of  $[Y]$  are most easily identified from a cylindrical field expansion (for 2D) and manipulation of (7) then shows that modes experience a simple phase shift (delay) as they travel through the node [7]. In effect, the TLM node acts as an automatic analyser of incoming pulses into modes, shifts each mode accordingly and then recomposes the total voltage pulses for transmission to neighbouring nodes. Similar principles apply in 3D [8]. A field theoretical derivation of the TLM scheme directly from the method of moments has also been presented [9].

## Embedded Structures in TLM

We present here three examples of how the basic TLM scheme may be adapted to accommodate particular embedded objects such as thin wires, volumes of an unstructured mesh, and frequency dependent features.

A particular difficulty in dealing with practical problems is the description of thin wires (wire diameter smaller than nodal size) as part of a large problem space. The ideas explored in the previous section may be exploited here. At the surface of each node containing wire(s) the admittance matrix and its eigenvalues may be again derived (using cylindrical field expansions around long wires) so that incoming voltage pulses and their associated modal components are scattered accordingly taking account of the presence of the wire(s). Since even for 2D problems four modes are included, this is a superior scheme when compared to traditional approaches based on quasistatic approximations which include only (symmetrical) quasistatic solutions. The result is greater accuracy and better placement of individual wires of a wire bundle inside a node [10]. An example is shown in Fig. 2.

Arbitrarily placed subwavelength features may also be embedded into TLM modes using the procedures described in [11]. This is achieved by generalizing the modal approach of 6. A surface admittance operator can be identified that relates the tangential electric and magnetic field components on the boundaries of the TLM node by choosing a suitable set of local field equations that intrinsically satisfy the boundary conditions of the scattering object. The eigensolutions of this operator again yield the familiar scattering operation characteristic of TLM and embodied by (7). This process is perfectly general and promises to significantly extend the scope for accurate fine feature modelling within the TLM paradigm.

The approaches described above allow the introduction of wire-like features into a structured mesh. There are however applications where a greater flexibility in the structure of the mesh allows better models to be obtained, e.g. in avoiding staircase approximations of curved boundaries. Unstructured meshes based of triangular (in 2D) and tetrahedral (in 3D) nodes have also been developed based on modal techniques and the derivation whenever possible of network representations of each node. The latter, although not essential, is a very useful discipline in the derivation of these schemes as it ensures stability and passivity of the resulting schemes [12,13]. Of particular utility is the capability of formulating mixed structured and unstructured meshes of different spatial resolutions interfaced by triangular or tetrahedral elements [14].

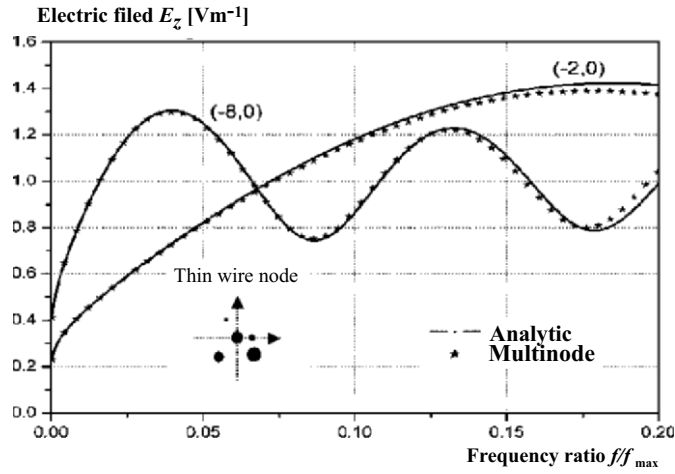


**Fig. 2.** Comparison of the fields in front of a wire bundle illuminated by a plane wave using the multiwire TLM-node. Observations are made both 2 and 8 nodes from the bundle. The wire diameters are in the range 1.4–10% of the node size

In these schemes, the use of significant volumes of structured meshes for large empty regions ensures that computational efficiency is maintained and moreover, the small quantity of unstructured mesh used to interface the structured regions are guaranteed an explicitly stable algorithm. An example of how this is done is shown in Fig. 3.

In many applications, where a time-domain solution is required, we have materials with frequency dependent properties and/or features which are fine compared with the prevailing spatial resolution and have frequency dependent properties (e.g. frequency selective surfaces, perforated screens, etc). In the latter case, one may envisage refining the mesh to the point where these features can be accurately mapped. However, the computational cost implications are very unfavourable and, in most cases, outside the reach of even the most powerful computers. An approach, which has been found advantageous, is to embed into the TLM algorithm

a digital filter procedure which mimics the behaviour of the embedded feature. The steps involved are to characterize the feature in the frequency-domain (by experimental, analytical, or numerical means), obtain the poles and zeros through the application of Prony's method, and to convert the resulting transfer function into a discrete time-domain procedure by applying the bilinear  $z$ -transform. This digital filter interface (DFI) is then embedded into the TLM time stepping procedure providing a very powerful and efficient technique.

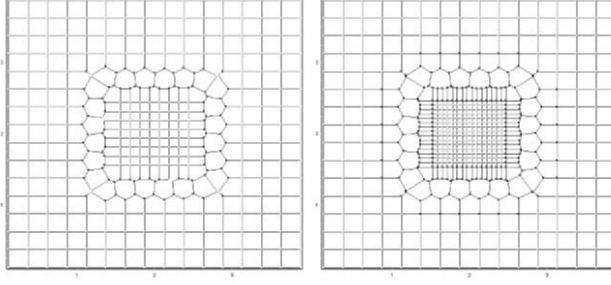


**Fig. 3.** Typical use of unstructured TLM nodes to interface structured Cartesian regions

Thin features, e.g. perforated screens and printed circuit boards may be introduced into a TLM mesh by modifying the procedure used to exchange information between adjacent cells. In the general case, the partial reflection and transmission caused by a feature is described by a scattering matrix, i.e.  $S(\omega)$

$$S_{=f}(\omega) = \begin{bmatrix} R(\omega) & T(\omega) \\ T(\omega) & R(\omega) \end{bmatrix}, \quad (8)$$

where the reflection and transmission coefficients  $R(\omega)$  and  $T(\omega)$  are frequency -dependent. A time-domain implementation is obtained by expressing  $R(\omega)$  and  $T(\omega)$  in the Padé form, e.g.

$$R(s) = \frac{\sum_{i=0}^{\text{NP}} b_i s^i}{\sum_{i=0}^{\text{NP}} a_i s^i} = \frac{b_0 + b_1 s + \dots + b_{\text{NP}} s^{\text{NP}}}{a_0 + a_1 s + \dots + s^{\text{NP}}}, \quad (9)$$

where  $s$  is the complex frequency, NP is the number of poles,  $a_i$  and  $b_i$  are real coefficients and  $a_{\text{NP}} = 1$ . The bilinear transform is

$$s = \frac{2}{\Delta t} \left( \frac{1 - z^{-1}}{1 + z^{-1}} \right), \quad (10)$$

where  $\Delta t$  is the time-step and  $z^{-1}$  represents a delay of one time-step. Using (10) in (9) yields directly the required discrete time algorithm [15].

A result for an equipment cabinet with a perforated wall containing a printed circuit board (PCB) as shown in Fig. 4. The PCB consisted of FR4 material with a copper backing having a total thickness of 1.6 mm. The relative permittivity of the FR4 material was taken as  $\epsilon_r = 4.55 - j0.080$ , independent of frequency. The copper backing on the PCB is electrically connected to the base of the cabinet. The digital filter approximations for the perforated screen had three poles and for the PCB had one pole. The measured and simulated results for the shielding effectiveness of this enclosure are shown in Fig. 5.

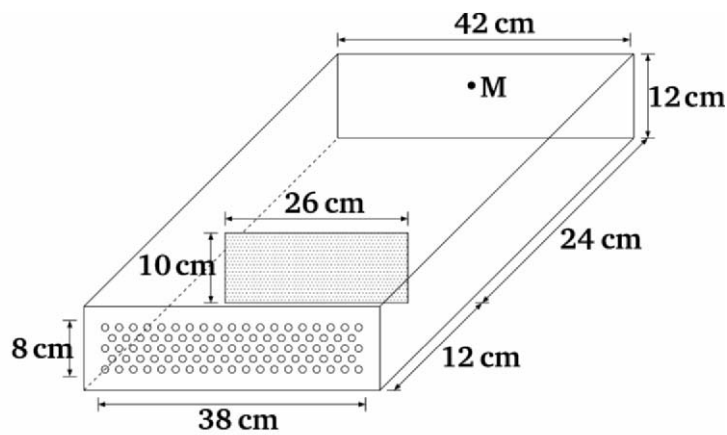


Fig. 4. Configuration of the PCB loaded cabinet with a perforated screen

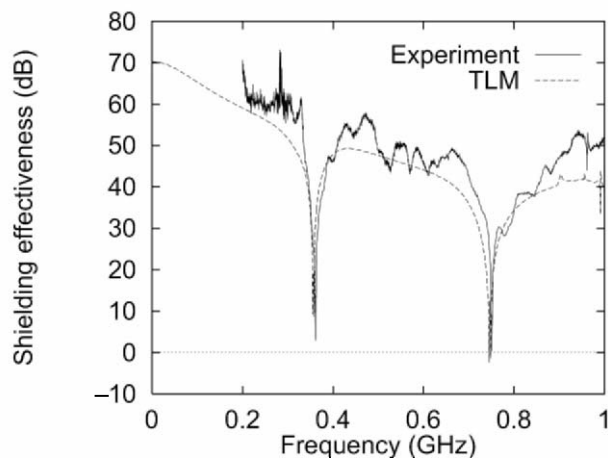


Fig. 5. Shielding effectiveness of a PCB loaded cabinet with a perforated screen

## Conclusions

The modelling of electromagnetic interactions in complex systems uses a variety of approaches based on the solution of Maxwell's equations by numerical means. We have shown how the synergies between network and field concepts may be profitably exploited in the TLM method to derive versatile solution algorithms of elegance, simplicity, and efficiency.

## References

- [1] D. Lowther, "Challenges in low frequency electromagnetic analysis and design", *Proc. IEE Conf. Comput. Electromagn.* Stratford on Avon, April 2004.
- [2] C. Christopoulos, *The Transmission-Line Modeling Method: TLM*, IEEE, Piscataway NJ 1995.
- [3] Taflovie and S.C. Hagness, *Computational Electrodynamics: The Finite-Difference Time-Domain Method*, 2nd ed. Norwell, MA: Artech House, 2000.
- [4] B.P. Russer, "The transmission line matrix method, in applied computational electromagnetics", *NATO ASI Series*, pp. 243–269, London: Springer Berlin Heidelberg New York, 2000.
- [5] G. Kron, "Numerical solution of ordinary and partial differential equations by means of equivalent circuits", *J. Appl. Phys.* 16, p. 172, 1945.
- [6] P.B. Johns and R.L. Beurle, "Numerical solution of two-dimensional scattering problems using a transmission-line matrix", *Proc. IEEE* 118, pp. 1203–1209, 1971.
- [7] T.K. Choong, P. Sewell, and C. Christopoulos, "Accurate modelling of an arbitrary placed thin wire in a coarse mesh", *IEEE Proc.-Sci. Meas. Technol.* 159(5), pp. 250–281, September 2002.
- [8] P. Sewell, Y.C. Choong, and C. Christopoulos, "An accurate thin-wire model for 3-D TLM simulations", *IEEE Trans. Electromagn. Compat.* 45(2), pp. 207–217, 2003.
- [9] M. Krumpholz and P. Russer, "A field theoretical derivation of TLM microwave theory and techniques", *IEEE Trans.* 42(9), pp. 1660–1668, Sept. 1994.
- [10] Y. Liu, P. Sewell, K. Biwojno, and C. Christopoulos, "A generalized node for embedding sub-wavelength objects into 3D transmission line models", *to appear IEEE Trans. Electromagn. Computability*.
- [11] P. Sewell, Y. Liu, and C. Christopoulos, "Electromagnetic modelling of fine features in photonic applications", *13th Workshop on optical waveguide theory and numerical modeling*, Grenoble, 8–9 April 2005.
- [12] P. Sewell et al., "Transmission-line modeling using unstructured triangular meshes", *IEEE Trans. Microwave Theory Tech.* 52(5), pp.1490–1497, 2004.

- [13] D.W.P. Thomas, A. Vukovic, and J.G. Wykes, “Transmission line modeling (TLM) based upon unstructured tetrahedral meshes. P. Sewell, T.M. Benson, C. Christopoulos, *IEEE Trans Microwave Theory Tech.* 53(6), pp. 1919–1928, June 2005.
- [14] P. Sewell et al, “Multi-grid interface in computational electromagnetics”, *Elec. Lett.* 40(3), pp. 162–163, 2004.
- [15] J. Paul, V. Podlozny, and C. Christopoulos, “The use of digital filters techniques for the simulation of fine features in EMC problems solved in the time-domain”, *IEEE Trans. Electromagn. Compatibility*, 45(2) pp. 238–244, May 2003.

# Electromagnetic Field Interaction with a Transmission Line

J. Russer, A. Cangelaris, and P. Russer

Department of Electrical and Computer Engineering, University of Illinois at Urbana-Champaign, 1406 W. Green St., Urbana, Illinois, 61801, USA

Institut für Hochfrequenztechnik, Technische Universität München, Arcisstr. 21, D-80333 Munich, Germany

## Abstract

The interaction of a two-wire transmission line with an incident electromagnetic field is investigated. It is shown that previous models, based on the reaction concept and the principle of reciprocity, can be extended to allow for the quantification of the induced currents and voltages at the transmission line terminations in the general case where the transmission line is unbalanced.

## Introduction

The influence of external fields on parallel wire structures configured as transmission-line circuits is an issue of concern in the design of noise-immune electronic systems. Traditionally, this topic has been addressed in the context of noise coupling to electronic wiring in large-scale platforms relevant to automotive and avionics EMC design. More recently, this topic has received significant attention in the context of noise-immune distribution of multi-GHz signals in performance-driven, integrated electronic systems. More specifically, the prediction and quantification through modeling of radiated emissions from and/or coupling to the printed circuit board that houses the components of an integrated electronic system is essential for ensuring system noise immunity and electromagnetic compliance.

When a set of parallel wires are configured to form a transmission line system, the following two requirements must be met for transmission line theory to provide for sufficiently accurate quantification of electromagnetic signal transmission on the system [1]. First, the cross-sectional dimensions of the wire and the distance between them should all be small compared to the wavelength for all frequencies in the operating bandwidth of the transmission line system. Second, the

transmission line system should be “balanced,” in the sense that at any cross section of the system on a plane perpendicular to the transmission-line axis the algebraic sum of the currents in all wires should be zero. Both of these conditions are, more often than not, violated in practice. The latter condition, in particular, is very difficult to satisfy in a printed circuit board environment, where the high density of component integration leads to unavoidable imbalances in wire lengths. Such imbalances are known to be the primary contributors to enhanced emissions from signal distribution networks [2]. However, violations of even the first requirement may occur in modern printed circuit board designs when a large number of wires are combined into a single bus. Consider, for example, an 8-conductor, planar (microstrip) interconnect bus used for a 10 Gbps signal transmission. At 5 GHz, assuming an effective permittivity of 4, the wavelength is 3 cm. If the conductor pitch in the bus is 0.2 cm the total lateral extent of the cross section of the bus is 1.5 cm, which amounts to an electrical length of half the wavelength at 5 GHz. Clearly, the validity of transmission line theory for the analysis of signal transmission for such a bus becomes questionable at the upper end of the transmitted signal bandwidth.

It is for these reasons that full-wave electromagnetic models are being employed for the quantification of signal transmission in high-speed interconnect structures. Given a set of driving (source) and receiving (termination) conditions, such models yield the currents in the conductors and the source and load circuits. Such modeling, while driven by the desire to assess the integrity of the transmitted signal, it also provides for the quantification of radiated emissions from the transmission-line structure. The reciprocal problem, namely, the quantification of signal coupling to the transmission line, requires the solution of yet another full-wave problem, where now the excitation is the incident electromagnetic field. However, if only the induced voltages and currents at the terminations are of interest, a simpler and computationally more efficient approach for their computation is possible. This approach is the main focus in this paper.

The literature of electromagnetic radiation from and coupling to transmission lines is very rich. Rather than providing a thorough review, we restrict ourselves to identifying the following three papers that are most relevant to the topic considered here [3–5]. The interested reader is referred to the additional references in the above papers for a more comprehensive review of the pertinent literature. The methodology we propose to use is closely related to the one discussed in [3]. However, the transmission line-related restrictions imposed in [3] are relaxed, thus extending the methodology to the calculation of electromagnetic field coupling to a set of parallel wires in a balanced or unbalanced transmission line configuration.

## Radiation from a Driven Transmission Line

Our presentation is for the case of the interaction of a time-harmonic electromagnetic field with the two-wire transmission line structure depicted in Fig. 1. It is assumed that the parallel longer sections of the two wires, taken to be along the



$x$  axis of the reference coordinate system, are of equal length. Thus, any imbalances in the system are introduced by the wire connections to the terminations. More specifically, assuming that the source and load are described in terms of lumped elements of negligible length compared to the wavelength of interest, their actual placement along the  $y$ -directed sections of the wires is taken as a variable in the definition of the geometry. Depending on their position, they split the  $y$ -directed sections of the wires into segments of different length. These segments, added to the length  $l$  of each one of the  $x$ -directed sections, result in the two wires having, in general, unequal lengths, thus leading to an unbalanced transmission line.

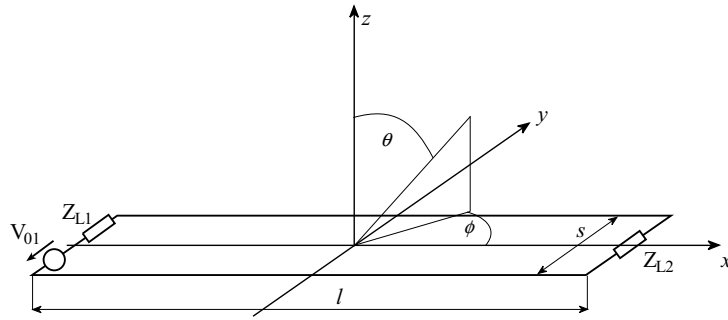


**Fig. 1.** A terminated two-wire transmission line

Assuming that the wire configuration of Fig. 1 is embedded in free space, its electromagnetic analysis can be performed using well-known, method-of-moments techniques for the solution of an integral equation statement of the pertinent electromagnetic problem [6]. Such an analysis yields the current distribution in the wires and provides for the subsequent computation of the radiated fields.

As an example, let us consider the case of a transmission line system of length  $l = 3.4$  m, wire axes separation  $s = 0.7$  m and circular wire cross section of diameter  $d = 1$  cm. The characteristic impedance,  $Z_0$ , is obtained from

$$Z_0 = \frac{Z_F}{\pi} \operatorname{arcosh} \left( \frac{s}{d} \right), \quad (1)$$

where  $Z_F$  is the free space wave impedance [7], to be 593 Ohm. The line is driven on the left by a voltage source of strength 1 V and input impedance  $Z_0$ . The termination impedance is chosen to be  $Z_0/3$  Ohm. The placement of both the load and the source is at a distance of 10.5 cm from the bottom wire. This results in an unbalanced system, where the top wire has a total length of 4.59 m, while the length of the bottom wire is 3.61 m.

The commercially-available software MiniNEC [8] was used for the full-wave solution of the problem. Depicted in Figs. 2 and 3 are the radiation patterns on the  $xy$  plane, at a frequency of 30 and 300 MHz, respectively. At these frequencies the difference in the wire lengths is approximately 0.1, and 1 wavelength. Three radiation patterns are depicted in each figure. Two of them are the radiation

pattern produced by the MiniNEC-computed currents in the wires for the unbalanced as well as for the balanced case (with source and load set at the center of the end sections, thus making the two wires equal in length). The third one is the radiation pattern produced by the currents obtained from a standard transmission-line theory based analysis of the structure. For this case, the current in the two  $y$ -directed end sections was taken to be constant along the wires, of value equal to the transmission-line theory result for the current through the voltage source for the left wire segment and the current through the load for the right wire segment. Once the current distribution in the wires are available, the resulting radiated fields can be readily computed in terms of electromagnetic potential integrals [7,9].

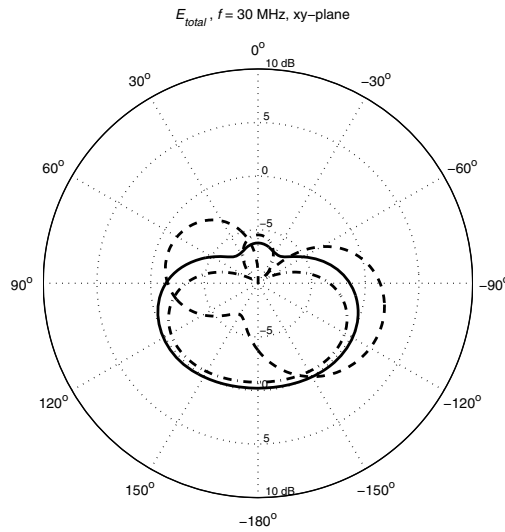


**Fig. 2.** Normalized radiation pattern for the two wire line in the  $xy$ -plane. Normalization is with respect to the average power density for each case.  $l = 3.4$  m,  $h = 0.7$  m,  $Z_{L1} = Z_0$ ,  $Z_{L2} = Z_0/3$ ,  $V_{01} = 1$  V,  $f = 30$  MHz. Solid line: Transmission-line current distributions with constant current at end wires ( $-22.1$  dBm). Dash-dot line: MoM solution for the balanced case ( $-22.2$  dBm, 1.2%). Dashed line: MoM solution for the unbalanced case ( $-19.2$  dBm, 2.4%). For each case the quantities in parentheses is the total radiated power and its percentage of the input power, i.e. the radiation efficiency

The radiation patterns make evident the impact of wire length differences and transmission line theory approximations on the accuracy of radiated emissions calculation from transmission-line systems. As anticipated, the accuracy of transmission line theory-based radiated emissions calculations worsens as the frequency increases and the electrical length of the end sections becomes an appreciable fraction of the wavelength. It is instructive to compare the current distributions in the wires for the three models. The magnitude and phase of the current distribution in the wires for the three cases and for the two frequencies of 30 and 300 MHz are depicted in Figs. 4–7. As anticipated, a significant discrepancy exists between the full-wave solution and the transmission-line solution

at 300 MHz. This discrepancy is attributed to the significant radiation from the two-wire system at this frequency, considering that the  $x$ -directed wire section are about three wavelengths long while the  $y$ -directed wires at the two ends are 0.7 wavelengths long. Furthermore, the impact of unequal wire lengths on the current distribution in the wires is also more pronounced at this higher frequency.

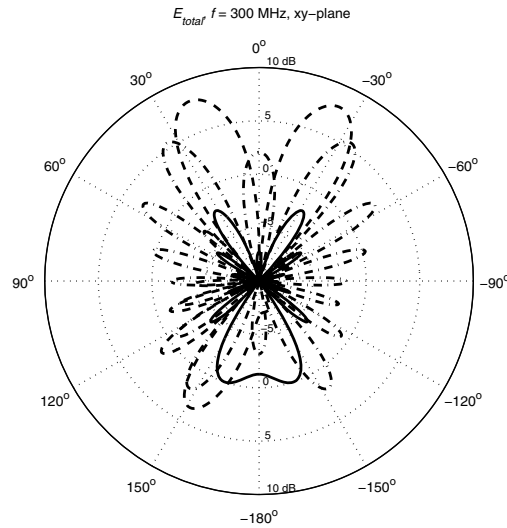


**Fig. 3.** Normalized radiation pattern for the two wire line in the  $xy$ -plane. Normalization is with respect to the average power density for each case.  $l = 3.4$  m,  $h = 0.7$  m,  $Z_{l1} = Z_0$ ,  $Z_{l2} = Z_0/3$ ,  $V_{01} = 1$  V,  $f = 300$  MHz. Solid line: Transmission-line current distributions with constant current at end wires ( $-4.3$  dBm). Dash-dot line: MoM solution for the balanced case ( $-8.3$  dBm, 28.5%). Dashed line: MoM solution for the unbalanced case ( $-8.5$  dBm, 25.4%). For each case the quantity in parentheses is the total radiated power and its percentage of the input power, i.e. the radiation efficiency

In summary, these computations make evident the impact that the electrical length of the wires and their separation as well as geometric imbalances in the transmission-line configuration can have on the accurate prediction of radiated emissions from transmission-line circuits. Thus, in view of the principle of reciprocity, one expects a similar discrepancy to be observed in the calculation of the coupling of electromagnetic fields to a two-wire, transmission line configuration under balanced and unbalanced conditions.

### Electromagnetic Coupling to a Transmission Line

The geometry depicted in Fig. 8 will be used for the development of a model for the prediction of the induced voltages and currents at the terminations of the two-wire transmission line configuration. The wires are assumed to be perfectly

conducting. The termination impedances  $Z_{L2}$  and  $Z_{L1}$  at  $x = \pm l/2$ , respectively, are assumed known. Both loads are assumed to be lumped; hence, their length is assumed to be negligible compared to the wavelength. Their actual position along the  $y$  coordinate is the parameter through which we control the balancing of the two-wire system.

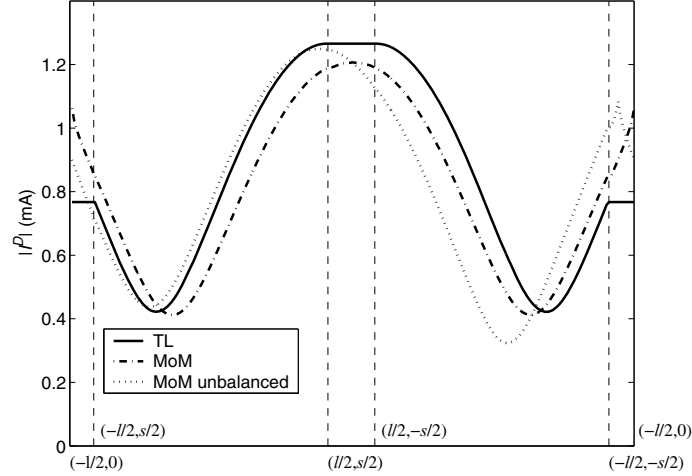


**Fig. 4.** Magnitude of the current distribution in the wires of the terminated two-conductor system of Fig. 1 at  $f = 30$  MHz

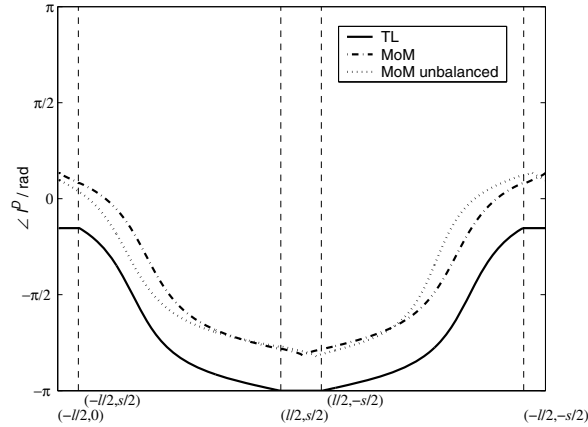


**Fig. 5.** Phase of the current distribution in the wires of the terminated two-conductor system of Fig. 1 at  $f = 30$  MHz

For the coupling problem the voltage source is set to zero. However, for the purposes of applying the concept of reaction and the associated reciprocity principle, we will also consider a driven problem where now the voltage source is nonzero.

Furthermore, the source and load impedances for the driven problem need not be the same with those of the coupling problem. Let  $I_t^D(x), I_b^D(x)$  be, respectively, the calculated currents along the top and bottom  $x$ -directed wires for the driven problem. Also, let  $I_l^D(y), I_r^D(y)$  be, respectively, the calculated currents along the left and right  $y$ -directed segments. Consider, next, the two cylindrical tubes formed by the surface of the two wires. These, together with the tubular surfaces enclosing the source and the load circuits define a closed surface  $S$  that encloses the two-wire configuration. In the volume  $V_e$  exterior to  $S$  the radiated fields  $(\mathbf{E}^r, \mathbf{H}^r)$  of the driven problem satisfy the source-free system of Maxwell's equations.

Consider, next, the coupling problem, where the terminated two-wire configuration is excited by an incident field. Without loss of generality, the incident field is taken to be a time-harmonic, uniform plane wave, defined by its direction of propagation and the polarization of its electric field. We define the incident field,  $(\mathbf{E}^i, \mathbf{H}^i)$ , as the field that would exist everywhere in space in the absence of the two-wire circuit. The interaction of the incident field with the wires results in a secondary field,  $(\mathbf{E}^s, \mathbf{H}^s)$ , radiated by the two-wire system.

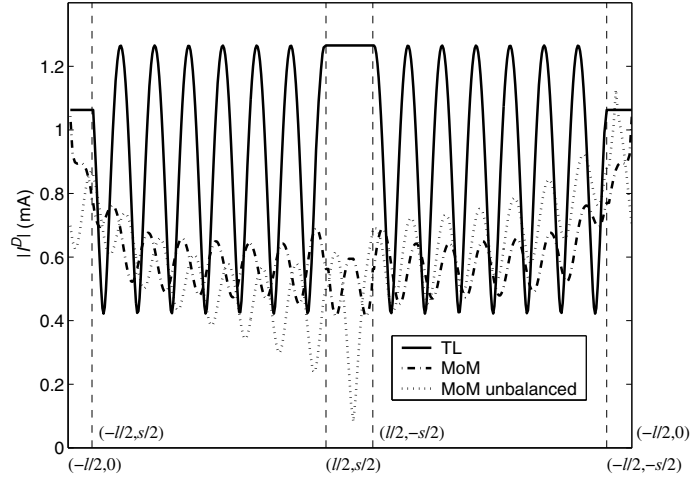


**Fig. 6.** Magnitude of the current distribution in the wires of the terminated two-conductor system of Fig. 1 at  $f = 300$  MHz

The resulting total field,  $(\mathbf{E}^t, \mathbf{H}^t)$ , is the superposition of the incident and secondary fields; hence, we write

$$\mathbf{E}^t = \mathbf{E}^i + \mathbf{E}^s, \quad \mathbf{H}^t = \mathbf{H}^i + \mathbf{H}^s. \quad (2)$$

In view of the linearity of the problem and the fact that the sources of the secondary field are the induced currents in the wires, it follows that the secondary field satisfies the source-free system of Maxwell's equations in  $V_e$ .

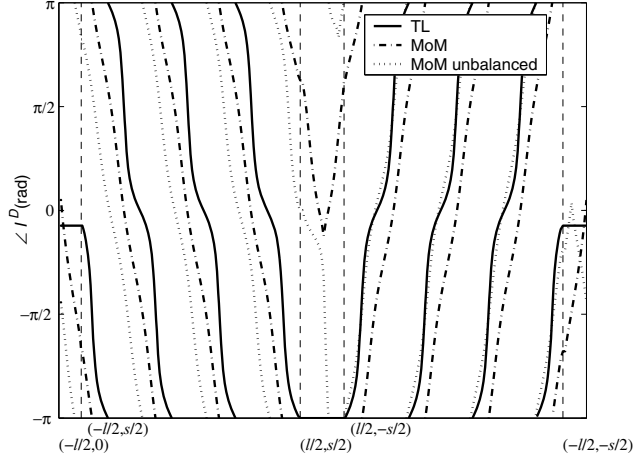


**Fig. 7.** Phase of the current distribution in the wires of the terminated two-conductor system of Fig. 1 at  $f = 300$  MHz

Use of the reciprocity theorem for the fields  $(\mathbf{E}^s, \mathbf{H}^s)$  and  $(\mathbf{E}^r, \mathbf{H}^r)$  in  $V_e$  yields

$$\int_S (\mathbf{E}^t \times \mathbf{H}^r - \mathbf{E}^r \times \mathbf{H}^t) \cdot \hat{n} ds = \int_S (\mathbf{E}^i \times \mathbf{H}^r - \mathbf{E}^r \times \mathbf{H}^i) \cdot \hat{n} ds, \quad (3)$$

where  $\hat{n}$  is the unit normal on  $S$ , taken to be pointing into  $V_e$ . In deriving the above equation use was made of (2). Since on the surface of the perfectly conducting wires it is  $\hat{n} \times \mathbf{E}^t = 0$  and  $\hat{n} \times \mathbf{E}^r = 0$ , (3) may be cast in the following form

$$\int_{S_{\text{gaps}}} (\mathbf{E}^t \times \mathbf{H}^r - \mathbf{E}^r \times \mathbf{H}^t) \cdot \hat{n} ds = \int_{S_x} (\mathbf{E}^i \times \mathbf{H}^r) \cdot \hat{n} ds + \int_{S_y} (\mathbf{E}^i \times \mathbf{H}^r) \cdot \hat{n} ds. \quad (4)$$

In the above equation  $S_{\text{gaps}} = S_{\text{source}} \cup S_{\text{load}}$  denotes the portions of the surface  $S$  enclosing the electrically small gaps at either end of the line associated with the source and load terminals, while  $S_x = S_x^t \cup S_x^b$  and  $S_y = S_y^t \cup S_y^b$ , are respectively, the portions of  $S$  associated with the  $x$ -directed ( $S_x^t$  for top and  $S_x^b$  for bottom) and the  $y$ -directed ( $S_y^t$  for top and  $S_y^b$  for bottom) sections of the two wires. The integral on the left-hand side of the above equation over  $S_{\text{gaps}}$  has been shown in [3] to be

$$\int_{S_{\text{gaps}}} (\mathbf{E}^t \times \mathbf{H}^r - \mathbf{E}^r \times \mathbf{H}^t) \cdot \hat{n} ds = (V_1^C I_1^D - V_1^D I_1^C) + (V_2^C I_2^D - V_2^D I_2^C), \quad (5)$$

where  $(V_1^C, I_1^C)$ ,  $(V_2^C, I_2^C)$  are the induced voltages and currents at the terminations due to the incident field, while  $(V_1^D, I_1^D)$ ,  $(V_2^D, I_2^D)$  are the voltages and currents at the source and load terminals for the driven problem.

Next we consider the remaining integrals on the right-hand side of (4). Since both integrals are of similar form, it suffices to consider only one of them. In par-

ticular, we choose to consider the integration over  $S_x^t$ . Let us introduce a local, right-handed, coordinate system on  $S_x^t$ , with  $\hat{n}$  and  $\hat{x}$  being two of the unit vectors. Clearly, the third unit vector  $\hat{t}$  is in the direction tangent to the contour of the cross-section of the wire. Let  $\hat{n} = \hat{n} \times \hat{x}$ . Making use of the vector identity

$$(\mathbf{a} \times \mathbf{b}) \cdot (\mathbf{c} \times \mathbf{d}) = (\mathbf{a} \cdot \mathbf{c})(\mathbf{b} \cdot \mathbf{d}) - (\mathbf{a} \cdot \mathbf{d})(\mathbf{b} \cdot \mathbf{c}) \quad (6)$$

we have

$$\int_{S_x^t} (\mathbf{E}^i \times \mathbf{H}^r) \cdot \hat{n} ds = \int_{S_x^t} (\mathbf{E}^i \cdot \hat{t})(\mathbf{H}^r \cdot \hat{x}) ds - \int_{S_x^t} (\mathbf{E}^i \cdot \hat{x})(\mathbf{H}^r \cdot \hat{t}) ds \quad (7)$$

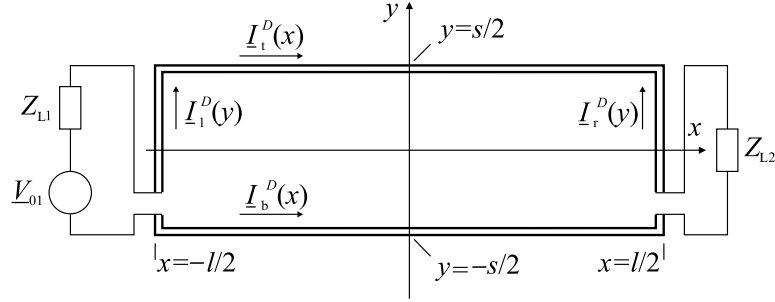


**Fig. 8.** Geometry of the terminated transmission line used for the calculation of the induced currents and voltages at the terminations due to an incident electromagnetic field

In considering further each one of the two terms on the right-hand side of (7) we will make the assumption that the cross-sectional dimension of the wires are much smaller than the wavelength. Thus, the variation of the incident electric and magnetic field vectors around the contour  $C_t(x)$  of the cross section of the top wire at position  $x$  will be assumed negligible and the field values on the contour will be taken to be equal to their values at the axis of the wire at the given position  $x$ . Consequently, the second integral on the right-hand side of (7) is written as follows

$$\int_{S_x^t} (\mathbf{E}^i \cdot \hat{x})(\mathbf{H}^r \cdot \hat{t}) ds = \int_{-l/2}^{l/2} \mathbf{E}_x^i(x, s/2, 0) \left( \int_{C_t(x)} (\mathbf{H}^r \cdot \hat{t}) dl \right) dx. \quad (8)$$

Recognizing the line integral of the tangential magnetic field  $\mathbf{H}^r \cdot \hat{t}$  along the contour  $C_t(x)$  as the axial current,  $I_t^D(x)$ , at position  $x$  in the top wire, the above integral may be cast in the following form

$$\int_{S_x^t} (\mathbf{E}^i \cdot \hat{x})(\mathbf{H}^r \cdot \hat{t}) ds = \int_{-l/2}^{l/2} \mathbf{E}_x^i(x, s/2, 0) I_t^D(x) dx. \quad (9)$$

Furthermore, in view of the fact that the wire cross sectional dimensions are assumed much smaller than the wire lengths, the axial component of the current on the wires is dominant, and any circulating component of the current can be assumed negligible; hence,  $\hat{x} \cdot \mathbf{H}^r \approx 0$  on  $S_x^t$  making the first term on the right-hand side of (7) approximately zero. Obviously, this approximation becomes exact for the case where the current flow on the two-wire system is taken to be consistent with the excitation of a transverse electric and magnetic (TEM) mode. Combining this result with (9), allows us to cast (7) in the form

$$\int_{S_x^t} (\mathbf{E}^i \times \mathbf{H}^r) \cdot \hat{n} ds = - \int_{-l/2}^{l/2} \mathbf{E}_x^i(x, s/2, 0) I_t^D(x) dx. \quad (10)$$

A similar development for the  $x$ -directed section of the bottom wire yields

$$\int_{S_x^b} (\mathbf{E}^i \times \mathbf{H}^r) \cdot \hat{n} ds = - \int_{-l/2}^{l/2} \mathbf{E}_x^i(x, -s/2, 0) I_b^D(x) dx. \quad (11)$$

Following an identical process as above it is straightforward to show that the remaining integral on the right-hand side of (4) may be cast in the form

$$- \int_{S_y} (\mathbf{E}^i \times \mathbf{H}^r) \cdot \hat{n} ds = \int_{-s/2}^{s/2} \mathbf{E}_y^i(-l/2, y, 0) I_1^D(y) dy + \int_{-s/2}^{s/2} \mathbf{E}_y^i(l/2, y, 0) I_r^D(y) dy. \quad (12)$$

Using (5), (10), (11), and (12) in (4) we obtain the following equation

$$(V_1^C I_1^D - V_1^D I_1^C) + (V_2^C I_2^D - V_2^D I_2^C) = F, \quad (13)$$

where, given the incident field and the current distribution along the wires obtained from the solution of the driven problem for a given set of source and load conditions, the right-hand side term  $F$  is computed as follows

$$\begin{aligned} F = & - \int_{-l/2}^{l/2} \mathbf{E}_x^i(x, s/2, 0) I_t^D(x) dx - \int_{-l/2}^{l/2} \mathbf{E}_x^i(x, -s/2, 0) I_b^D(x) dx \\ & - \int_{-s/2}^{s/2} \mathbf{E}_y^i(-l/2, y, 0) I_1^D(y) dy - \int_{-s/2}^{s/2} \mathbf{E}_y^i(l/2, y, 0) I_r^D(y) dy. \end{aligned} \quad (14)$$

Equation (13) contains the four unknown quantities of interest,  $V_1^C, I_1^C, V_2^C,$  and  $I_2^C$ . In view of the termination constraints

$$V_1^C = -Z_{L1} I_1^C, \quad V_2^C = -Z_{L2} I_2^C \quad (15)$$

only two of them are independent. Thus, two independent equations are required for their computation. These two equations can be obtained from (13) by using two independent sets of current distributions on the wires, obtained from the solution of the driven problem with two different sets of source and load conditions. It is important to emphasize that for the case of unbalanced transmission lines a full-wave electromagnetic field solver is used to calculate these ‘‘trial’’ sets of current distributions on the wires.



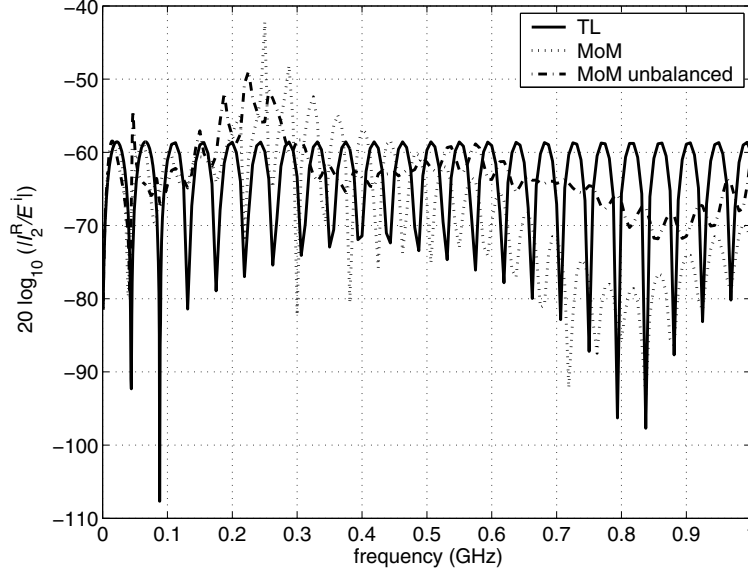


**Fig. 8.** Magnitude of induced load current due to an incident plane wave with a linearly-polarized,  $y$ -directed electric field, propagating in the  $+x$ -direction.  $E^i = E_y^i \hat{y}$ ,  $k = k_x \hat{x}$ ,  $Z_{L1} = 0$ ,  $Z_{L2} = Z_0$

### Numerical Examples

The response of the terminated transmission line excited by an incident electromagnetic field is obtained from (13–15). The line is terminated as shown in Fig. 1 with the source  $V_{01}$  shorted. The output of interest is the load current  $I_{L2}$  at the terminating impedance  $Z_{L2}$ , computed as a function of frequency for different polarizations and propagation directions of the incident field.

First we consider the case where the electric field of the incident wave is  $E^i = E_y^i \hat{y}$ , with propagation vector  $k = k_x \hat{x}$ . The line terminations are assigned the values  $Z_{L1} = 0$  and  $Z_{L2} = Z_0$ , where  $Z_0$  is the characteristic impedance of the transmission line. The calculated magnitude of the load current versus frequency is plotted in Fig. 9. The results from three models are depicted, namely, the transmission line-based model, the full-wave model for the balanced wire configuration, and the full-wave model for the unbalanced case. Once again, it is stressed that these models are the models used for the calculation of the trial currents used in (12) and (13) for the calculation of the voltages and currents at the loads.

For low frequencies the three models yield very similar results. This is to be expected since, as it is evident from (14), only the trial currents in the termination wires contribute to the source term and the transmission-line approximation of a constant current at the termination wires is reasonable at low frequencies.

Furthermore, at low frequencies any imbalances caused by differences in the lengths of the two wires have a minor impact on the current distributions. However, as the frequency increases and the wire separation becomes electrically large, the discrepancy between the current distributions along the wires for the balanced and unbalanced cases becomes more pronounced. Furthermore, for the transmission-line theory-based trial currents, the approximation of constant current at the end sections breaks down. Thus, for higher frequencies a significant difference is observed between the values of the induced load current predicted by the three models.

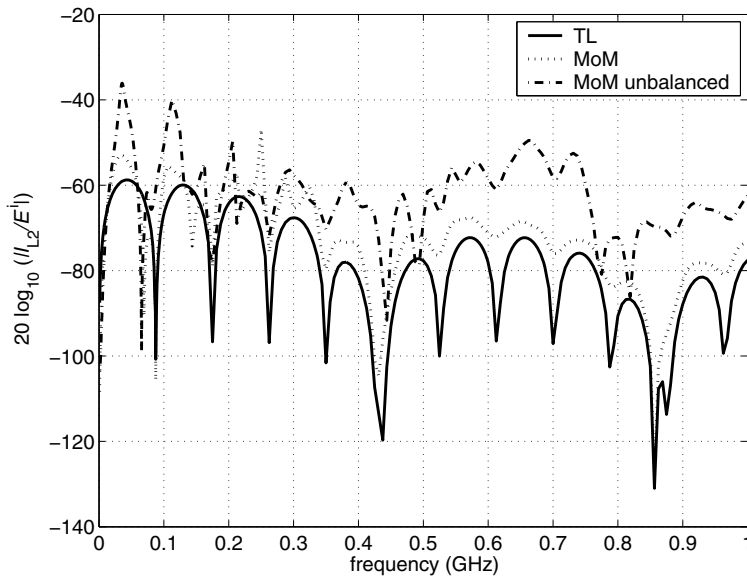


**Fig. 10.** Magnitude of the induced load current due to an incident plane wave with a linearly-polarized,  $x$ -directed electric field, propagating in  $+y$ -direction.  $\mathbf{E}^i = E_x^i \hat{x}$ ,  $\mathbf{k} = k_y \hat{y}$ ,  $Z_{L1} = Z_{L2} = Z_0$

As a second example we consider the case where the electric field of the incident wave is  $\mathbf{E}^i = E_x^i \hat{x}$ , with propagation vector  $\mathbf{k} = k_y \hat{y}$ . The line terminations are assigned the values  $Z_{L1} = Z_{L2} = Z_0$ , where  $Z_0$  is the characteristic impedance of the transmission line. The calculated magnitude of the load current versus frequency is plotted in Fig. 10. In this case the termination wires are normal to the incident electric field. Thus, the value of the source term  $F$  in (12) is impacted only by the interaction of the incident electric field with the  $x$ -directed wires. Thus, differences between the induced currents for the balanced and the unbalanced case are anticipated at all frequencies. This is indeed the case as illustrated in Fig. 10. With regards to the solution for the case of the balanced circuit,

obtained using the trial currents from the full-wave solution, and the solution obtained from using the transmission line currents as trial currents, we expect them to be in good agreement, overall, since the contribution of the end wires to the source term is zero. This good agreement is evident from the plot in Fig. 10. However, both Figs. 9 and 10 make apparent the importance of utilizing accurate “trail” currents, predicted from full-wave analysis in the system of (12–14) when the induced load voltages and currents are to be computed for the case of unbalanced transmission-line circuits and at frequencies for which the transmission-line configuration is electrically large

### Concluding Remarks

In summary, we have proposed and demonstrated a convenient mathematical formulation for the computation of electromagnetic coupling to the source and load ends of a two-wire system configured for use as a transmission line. The proposed methodology makes use of current distributions on the two-wire system, obtained with the system driven by a time-harmonic source and, thus, operated as an electromagnetic waveguide, in a reciprocity-based relationship between the fields of the coupling problem of interest and the driven problem, to yield a system of algebraic equations that can be solved readily for the induced currents or voltages at the terminations. Compared to past approaches, the proposed methodology allows for the induced voltages and currents to be calculated accurately even in the case of unbalanced wires.

As demonstrated through the numerical studies presented in the paper, the end sections of the wires, associated with the source and load connections, along with any imbalances in the system caused by these end connections, can have a significant impact on the induced currents and voltages, especially for those frequencies for which the electrical length of the end sections becomes appreciable. However, for such cases, the accuracy of the proposed methodology is strongly dependent on the accuracy with which the trial current distributions in the wires is calculated. More specifically, current distributions obtained from a full-wave analysis of the driven problem must be used as trial currents in the case of unbalanced transmission line configurations, as well as for frequencies for which the electrical size of the circuit and its end sections is appreciable.

### References

- [1] C.R. Paul, *Analysis of Multiconductor Transmission Lines*, John Wiley & Sons, Inc., New York, 1994
- [2] C.R. Paul, *Introduction to Electromagnetic Compatibility*, John Wiley & Sons, Inc., New York, 1992
- [3] D. Quak and R. Wiemans, “Analysis of the susceptibility of a two-wire transmission line to electromagnetic radiation”, *Proc. 1989 Int. Symp. Electromagn. Compat.* pp. 469–474, 1989

- [4] D. De Zutter and F. Olyslager, “High-frequency reciprocity-based circuit model for the incidence of electromagnetic waves on general waveguide structures”, *IEEE Trans. Microwave Theory Tech.* vol. 43, pp. 1826–1833, 1995
- [5] F. Olyslager, “High-frequency reciprocity based circuit model for the incidence of electromagnetic waves on general circuits in layered media”, *IEEE Trans. Microwave Theory Tech.* vol. 44, pp. 862–873, 1996
- [6] R.F. Harrington, *Field Computation by Moment Methods*, IEEE Press, San Francisco, 1968
- [7] P. Russer, *Electromagnetics, Microwave Circuit and Antenna Design for Communications Engineering*, Artech House, Boston, 2006
- [8] EM Scientific, Inc., MiniNEC, Carson City, Nevada, USA, <http://www.emsci.com>
- [9] R.F. Harrington, *Time Harmonic Electromagnetic Fields*, McGraw-Hill, New York, 1961

# Scattering of a Plane-Wave by a Moving Half-Plane: A Full Relativistic Study

M. İdemen<sup>1</sup> and A. Alkumru<sup>2</sup>

<sup>1</sup>Department of Mathematics,  
Yeditepe University, 26 Agustos Yerlesimi, 81120, Kayisdagi, Istanbul, Turkey,  
idemen@yeditepe.edu.tr

<sup>2</sup>Department of Electronics Engineering,  
Gebze Institute of Technology, 41400, Gebze, Kocaeli, Turkey,  
alkumru@gyte.edu.tr

## Abstract

The aim of the present work is to reveal the effect of the motion on the scattering by a moving edge. To this end one considers the edge of a half-plane, which moves with constant velocity. This *canonical problem* permits one to investigate the effect of both the velocity and the direction of motion on the reflection, shadowing, and edge-diffraction phenomena. In the present work the incident wave is supposed to be a monochromatic plane electromagnetic wave while the half-plane is perfectly conducting.

## Introduction

During more than one century which followed the foundation of Maxwell's theory, propagation and scattering of the electromagnetic wave have been investigated extensively by considering various kind of mediums and scatterers. A common property of a good deal of these investigations is that they concern the scatterers which are at rest with respect to the observer. But in some cases, which are of importance from both pure scientific and technical points of view, the scatterers are in motion. The communication satellites, guided missiles and modern swift vehicles such as air-planes, trains, and cars can be enumerated among this kind of scatterers. To have a correct and deep insight into moving objects one has to formulate and solve the related mathematical problems exactly through the concepts of the special theory of relativity [1]. In spite of its importance, the works devoted to this subject are rather few [2–11]. They are not interested, for example, in a detailed discussion of the shadowing and reflected waves individually. The aim of the present work consists of this task. To this end we consider the scattering

of a monochromatic plane wave by a moving half-plane and analyze the resulting problem through an exact full-relativistic approach. The results we will obtain from the solution of this *canonical problem* will permit us to reveal the effect of the motion on both the edge-diffraction and the shadowing and reflection phenomena. In order to reduce the mathematical difficulties inherent to both the half-plane configuration and the motion, we will consider only a particular case of motion which occurs with a constant velocity in a direction normal to the half-plane. Furthermore, the incident wave is assumed to be a plane wave propagating in an arbitrary direction which is normal to the edge.

The results we will obtain will show that the edge-excited wave is never time harmonic while the waves excited by the plane (i.e. the shadowing and reflected waves) are always time-harmonic. The frequency of these latter is sometimes equal to that of the incident wave but sometimes differs from it (Doppler's effect). It is also interesting that the apparent shadow and reflection boundaries are never parallel to the incident rays (aberrations). The physical explanations of various shifts are also different depending on the direction and numerical value of the velocity. One of the interesting issues we will obtain is that, depending on the values of the velocity and incidence angle, a shadow region appears in the apparently illuminated region while a lit region appears in the apparently shadow region. Furthermore, the moving sheet provides, sometimes, an energy to the reflected wave.

## Formulation of the Problem

Consider a cartesian coordinate system  $O'x'y'z'$  and assume that the half-plane  $\{x' \in (0, \infty), y' = 0, z' \in (-\infty, \infty)\}$  consists of a perfectly conducting sheet. In what follows this co-ordinate system and the conducting sheet will be denoted by  $K'$  and  $S$ , respectively. In the problem to be addressed in this work  $S$  (and  $K'$ ) makes a uniform rectilinear motion, in vacuum, with respect to another reference system  $K$  and is illuminated by a monochromatic plane wave. The problem consists then of the investigation of the influence of the motion on the scattered wave to be observed from the reference system  $K$ . This latter will be represented by a Cartesian coordinate system  $Oxyz$ . For the sake of simplicity, we will consider here only a particular case in which  $S$  moves parallel to the  $Oy$  axis (see Fig. 1).

Without loss of generality, the incidence angle  $\theta$  (observed in  $K$ ) may always be assumed as  $\theta \in (0, \pi)$  if two directions of motion are considered separately:  $\mathbf{v} = \pm v \mathbf{e}_y$ . Here  $v > 0$  denotes the velocity of  $S$  while  $\mathbf{e}_y$  stands for the usual unit coordinate vector. As to the polarization of the incident wave, it will be considered that the incident electric field is parallel to the edge, namely:

$$\mathbf{E}^i = \mathcal{R}\{E_0 \exp[ik(x \cos \theta + y \sin \theta - ct)]\} \mathbf{e}_z \quad (1)$$

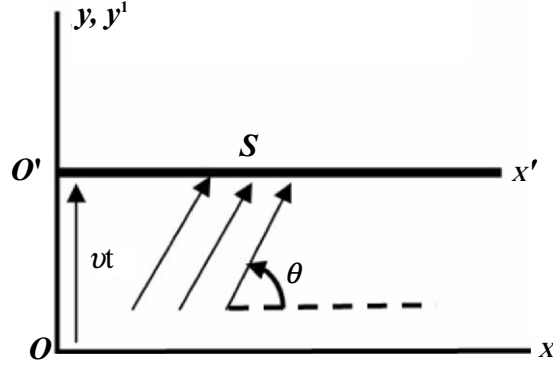


**Fig. 1.** Half-plane moving with velocity  $\mathbf{v} = v \mathbf{e}_y$

Here the super-indices (i) in  $E^i$  signifies the incident electric field,  $\Re\{\cdot\}$  stands for the real part while  $c$  is the velocity of the wave in vacuum. As to the constants  $k$  and  $E_0$ , they are the wave number and the complex amplitude of the incident electric field, respectively. It is worthwhile to notice that  $\omega = kc$  is the angular frequency.

## Solution of the Problem

To solve the problem mentioned above rigorously, we will transform first the expression of the incident wave, which is known in  $K$ , into the system  $K'$  and solve the problem in  $K'$ . Then the exact expression of the solution, obtained in  $K'$ , will be transformed into the system  $K$ . The above-mentioned transformations can be made through the Lorentz transformation formulae because they are quite exact expressions satisfying the Maxwell equations.

Let the clocks in  $K$  and  $K'$  be so adjusted that  $O \equiv O'$  when  $t = t' = 0$  (see Fig. 1). Here  $t$  and  $t'$  denote, as usual, the times measured in  $K$  and  $K'$ , respectively. Under this assumption one writes in  $K$  (for the sake of simplicity we will omit the operation  $\Re\{\cdot\}$  if it is not necessary)

$$\mathbf{E}^i = E_0 \exp[ik(x \cos \theta + y \sin \theta - ct)] \mathbf{e}_z \quad (2a)$$

and

$$\mathbf{H}^i = \left( \frac{E_0}{Z} \right) \exp[ik(x \cos \theta + y \sin \theta - ct)] (\sin \theta \mathbf{e}_x - \cos \theta \mathbf{e}_y), \quad (2b)$$

which are transformed into  $K'$  as

$$\mathbf{E}^i = \frac{E_0}{\sqrt{1-(v/c)^2}} \left( 1 - \frac{v}{c} \sin \theta \right) e^{ik'(x' \cos \theta' + y' \sin \theta') - i\omega' t'} \mathbf{e}_z \quad (3a)$$

$$\mathbf{H}^i = \frac{E_0}{Z \sqrt{1-(v/c)^2}} \left( 1 - \frac{v}{c} \sin \theta \right) e^{ik'(x' \cos \theta' + y' \sin \theta') - i\omega' t'} (\sin \theta' \mathbf{e}_x - \cos \theta' \mathbf{e}_y) \quad (3b)$$

with

$$k' = \frac{k}{\sqrt{1-(v/c)^2}} \left( 1 - \frac{v}{c} \sin \theta \right), \quad \omega' = k'c \quad (4a)$$

$$\sin \theta' = \frac{\sin \theta - v/c}{1 - (v/c) \sin \theta}, \quad \cos \theta' = \frac{\cos \theta}{1 - (v/c) \sin \theta} \sqrt{1 - (v/c)^2}. \quad (4b)$$

In (2b) and (3b)  $Z = \sqrt{\mu/\varepsilon}$  stands for the characteristic impedance of the space (i.e. the vacuum.  $\varepsilon$  = permittivity,  $\mu$  = permeability, and  $Z = 120\pi$ ). To reveal the expressions (3a) and (3b) one has to use the transform formulas [12]

$$x = x', \quad y = \frac{y' + vt'}{\sqrt{1-(v/c)^2}}, \quad t = \frac{t' + vy'/c^2}{\sqrt{1-(v/c)^2}}, \quad (5a)$$

$$E'_1 = \frac{E_1 + v\mu H_3}{\sqrt{1-(v/c)^2}}, \quad E'_2 = E_2, \quad E'_3 = \frac{E_3 - v\mu H_1}{\sqrt{1-(v/c)^2}} \quad (5b)$$

and

$$H'_1 = \frac{H_1 - v\varepsilon E_3}{\sqrt{1-(v/c)^2}}, \quad H'_2 = H_2, \quad H'_3 = \frac{H_3 + v\varepsilon E_1}{\sqrt{1-(v/c)^2}}. \quad (5c)$$

In (5b) and (5c) the subindices (1), (2), and (3) stand for the cartesian coordinates of vectors while  $k'$  and  $\theta'$  appearing in (3a) and (3b) are the wave-number and incidence angle observed in the system  $K'$ , respectively. It is worthwhile to remark that both  $\sin \theta'$  and  $\cos \theta'$  may have positive and negative values for  $\theta \in (0, \pi)$ . Hence the incidence direction to be observed in  $K'$  exhibits various interesting possibilities with  $\theta' \in (-\pi, \pi)$ .

Since the explicit expression of the incident wave is totally known in  $K'$  and the problem is already classical, by referring to some standard references (see for example [13]) one can directly write the expression of the scattered wave  $E_3^{rs}(x', y', t')$  as follows:



$$E_3^{rs}(x', y', t') = \frac{iE_0}{2\pi\sqrt{1-(v/c)^2}} \left(1 - \frac{v}{c} \sin \theta\right) \sqrt{k' + k' \cos \theta'} \int_L \frac{e^{i\alpha x' \pm \gamma(\alpha) y' - i\omega' t'}}{(\alpha - k' \cos \theta') \sqrt{\alpha + k'}} d\alpha, \quad (6)$$

where the integration line  $L$  denotes the real axis seen in Fig. 2 and  $\gamma(\alpha)$  is the square-root function  $\gamma(\alpha) = \sqrt{\alpha^2 - k'^2}$  defined in the complex-plane cut as shown in Fig. 2 with the condition  $\gamma(0) = -ik'$ . In (6) the sign ( $\pm$ ) stands for (+1) when  $y' < vt$  and (-1) when  $y' > vt$ .

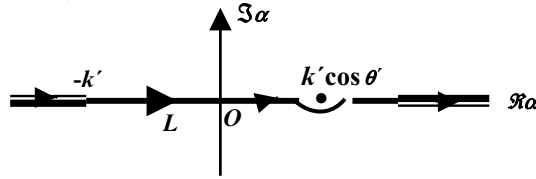


**Fig. 2.** The integration line  $L$  and the complex  $\alpha$ -plane

The expression of the scattered field  $E_3^s(x, y, t)$  which is valid in  $K$  can now be obtained by using the inverse Lorentz formulas [12]

$$x' = x, \quad y' = \frac{y - vt}{\sqrt{1-(v/c)^2}}, \quad t' = \frac{t - vy/c^2}{\sqrt{1-(v/c)^2}}, \quad (7a)$$

and

$$E_1^s = 0, \quad E_2^s = 0, \quad E_3^s = \frac{E_3^{rs} + v\mu H_1^{rs}}{\sqrt{1-(v/c)^2}} = \frac{1}{\sqrt{1-(v/c)^2}} \left[ E_3^{rs} - i \frac{v}{\omega'} \frac{\partial E_3^{rs}}{\partial y'} \right] \quad (7b)$$

From (6–7b) one gets

$$E_3^s(x, y, t) = \frac{iE_0 [1 - (v/c) \sin \theta]}{2\pi [1 - (v/c)^2]} \sqrt{k' + k' \cos \theta'} e^{-i\omega' \frac{(t - vy/c^2)}{\sqrt{1-(v/c)^2}}} \int_L \frac{[1 - (\pm) i v \gamma(\alpha) / \omega'] e^{i\alpha x \pm \gamma(\alpha) \frac{(y - vt)}{\sqrt{1-(v/c)^2}}}}{(\alpha - k' \cos \theta') \sqrt{\alpha + k'}} d\alpha \quad (8)$$

Now by making the substitutions

$$\alpha = k' \cos \beta, \quad \gamma(\alpha) = -ik' \sin \beta, \quad d\alpha = -k' \sin \beta \quad (9a)$$

and

$$x = R' \cos \phi', \quad \frac{y - vt}{\sqrt{1-(v/c)^2}} = -(\pm) R' \sin \phi', \quad \phi' \in (0, \pi) \quad (9b)$$

the resulting integral is transformed into a suitable form which can be evaluated by using the steepest-descent path method. Since  $\theta' \in (-\pi, \pi)$  this evaluation gives the following expression:

– When  $\theta' \in (0, \pi)$  or  $\sin \theta > v/c$  one has

$$E_3^s(x, y, t) = \begin{cases} -E_3^i(x, y, t)H(\theta' - \phi'), & y > vt \\ E_3^r(x, y, t)H(\theta' - \phi'), & y < vt \end{cases} + E_3^{ss}(x, y, t) \quad (10a)$$

– When  $\theta' \in (-\pi, 0)$  or  $\sin\theta < v/c$  one has

$$E_3^s(x, y, t) = \begin{cases} E_3^r(x, y, t)H(-\theta' - \phi'), & y > vt \\ -E_3^i(x, y, t)H(-\theta' - \phi'), & y < vt \end{cases} + E_3^{ss}(x, y, t). \quad (10b)$$

Here  $H(x)$  is the usual Heaviside unit step function while  $E_3^i(x, y, t)$  is the incident wave given through (2a).  $E_3^r(x, y, t)$  appearing in (10a and 10b) can be defined as the reflected wave by the moving conducting half plane and its explicit expression is given by

$$E_3^r(x, y, t) = -E_0 \frac{k''}{k} \exp[ik''(x \cos\theta'' + y \sin\theta'' - ct)], \quad (11a)$$

where

$$k'' = k \frac{[(1 - v/c)^2 + 2(v/c)(1 - \sin\theta)]}{1 - (v/c)^2} \quad (11b)$$

and

$$\cos\theta'' = \frac{k}{k''} \cos\theta, \quad \sin\theta'' = \frac{k}{k''} \frac{\{2(v/c) - [1 + (v/c)^2] \sin\theta\}}{[1 - (v/c)^2]} \quad (11c)$$

As to  $E_3^{ss}(x, y, t)$  appearing in (10a and 10b) it is the edge diffracted field which is expressed by

$$E_3^{ss}(x, y, t) = \frac{E_0}{\sqrt{2}} \frac{\left(1 - \frac{v}{c} \sin\theta\right)}{[1 - (v/c)^2]} \left(1 + \frac{v}{c} \sin\phi'\right) \sin\phi' \frac{\sqrt{k' + k' \cos\theta'}}{\sqrt{k' + k' \cos\phi'}} \\ \times \frac{F\left[\frac{1}{2} k'R'(\phi' - |\theta'|)^2\right]}{\cos\phi' - \cos\theta'} e^{-i\omega' \frac{(t - yv/c^2)}{\sqrt{1 - (v/c)^2}}} \frac{e^{ik'R'}}{\sqrt{k'R'}} \quad (12a)$$

with

$$\cos\phi' = \frac{x\sqrt{1 - v^2/c^2}}{\sqrt{x^2(1 - v^2/c^2) + (y - vt)^2}}, \quad \sin\phi' = \frac{|y - vt|}{\sqrt{x^2(1 - v^2/c^2) + (y - vt)^2}} \quad (12b)$$

and

$$R' = \sqrt{\frac{x^2(1 - v^2/c^2) + (y - vt)^2}{1 - v^2/c^2}}. \quad (12c)$$

In (12a) the function  $F(x)$  stands for

$$F(x) = \sqrt{x} e^{-ix} \operatorname{erfc}\left(e^{-ix/4} \sqrt{x}\right) \quad (13)$$

with  $\operatorname{erfc}(x)$  being the classical error function.

By considering (10a) together with (2a) and (11a), one concludes that when  $\sin\theta > v/c$  the incident wave is cancelled by  $(-E_3^i)$  in the region  $y > vt$  and  $\theta' > \phi'$  to create a shadow region. In the half-space  $y < vt$  a reflected wave of frequency  $\omega'' = k''c$ , which propagates in the direction determined by the angle  $\theta''$  is excited (see Fig. 3). The boundaries of the shadow and reflection regions are determined by the equation  $\tan\theta' = \tan\phi'$ , which is equivalent to

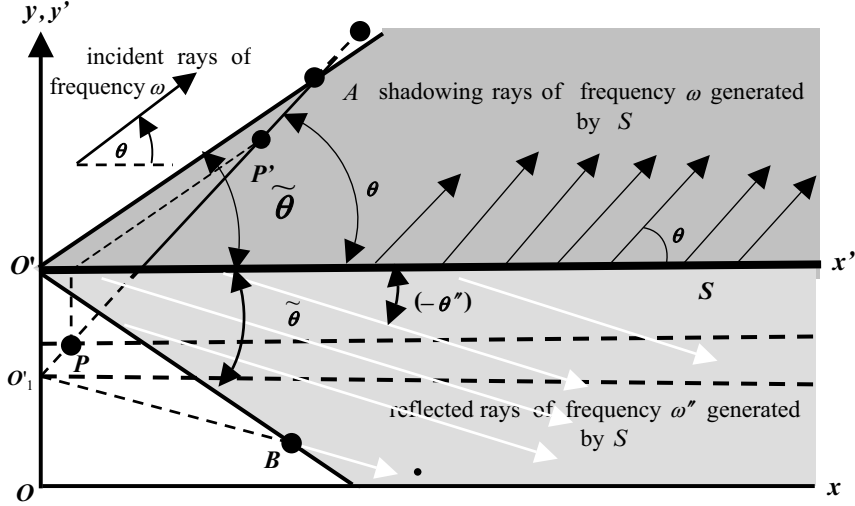


Fig. 3. Shadow and reflection boundaries when  $\theta \in (0, \pi/2)$  and  $\sin\theta > v/c$

$$y - vt = -(\pm)x \tan\tilde{\theta} \quad (14a)$$

with

$$\tan\tilde{\theta} = \frac{\sin\theta - v/c}{\cos\theta} = \frac{v/c - \sin\theta''}{\cos\theta''}. \quad (14b)$$

When  $\sin\theta < v/c$ , from (10b), (2a), and (11a), one concludes that the half-space located above the conducting sheet ( $y > vt$ ) is not shadowed. Indeed, in this half-space a monochromatic plane wave defined by (11a–11c) appears in the region where  $(-\theta') > \phi'$  (see Fig. 4). This interesting phenomenon can be easily explained by observing that in this case one always has  $\theta' \in (-\pi, 0)$ , which shows that the incident wave  $E_3^i$  seems to an observer lying in the reference system  $K'$  as a wave coming from the half-space  $y' > 0$  (i.e.  $y > vt$ ). Therefore, in  $K'$  it is reflected by the sheet into the region above it. The field defined by (11a) is nothing but this reflected wave observed by an observer lying in the reference system  $K$ .

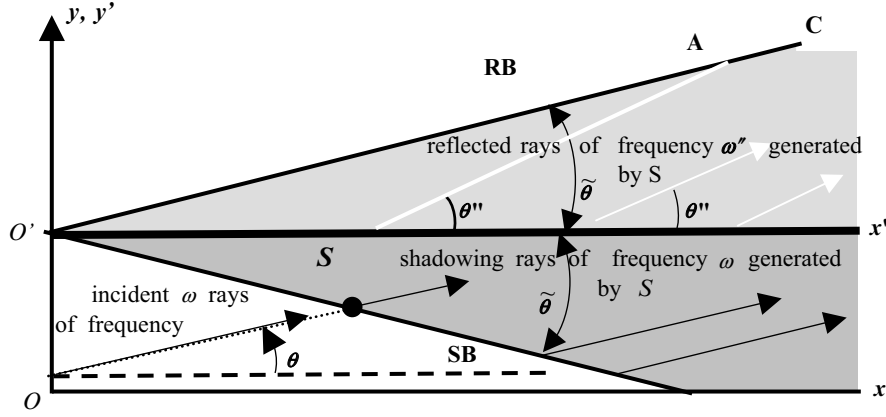


Fig. 4. Shadow and reflection boundaries when  $\theta \in (0, \pi/2)$  and  $\sin \theta < v/c$

It is also easily seen that in the half-space  $y < vt$  the incident wave is cancelled in the region defined by  $(-\theta') > \phi'$  to create a shadow region. For this case the reflection and shadow boundaries denoted by  $\tilde{\theta}$  can be determined by the equation  $\tan(-\theta') = \tan \phi'$ , namely:

$$\tan \tilde{\theta} = \frac{v/c - \sin \theta}{\cos \theta} = \frac{\sin \theta'' - v/c}{\cos \theta''}. \quad (15)$$

## Conclusions and Discussions

From the analysis made above one concludes that the scattering by a moving half-plane exhibits various interesting phenomena which are sometimes unexpected. For example, some terms excited by plane are not time-harmonic even if the incident wave is so. The time-harmonic terms are also divided into two groups. The frequency of the first group is quite identical to the frequency of the incident wave while that of the second group differs from it and depends also on the incidence angle and velocity. Another interesting issue due to the motion is that the reflections, as well as the shadow boundaries, are never parallel to the direction of the incident rays. Hence both the shadow and the reflection regions are sometimes smaller while sometimes larger than those pertinent to the motionless case.

What is much more interesting is that a shadow region is observed in seemingly illuminated region while a lit region (involving a wave of frequency equal to or different from the frequency of the incident wave!) is observed behind the half-plane (i.e., traditionally shadow region). These kind of unexpected phenomena are observed when the half-plane moves in a direction normal to itself.

## References

- [1] W. Pauli, *Theory of relativity*, Pergamon Press, New York, 1958.
- [2] A. Sommerfeld, *Optik*, 2nd ed., Akademische Verlagsgesellschaft, Leipzig, 1959.
- [3] C.T. Tai, "Two boundary-value problems involving moving media", *URSI meeting*, Washington D.C., 1965.
- [4] S.W. Lee and R. Mittra, "Scattering of electromagnetic waves by a moving cylinder in free space", *Canadian J. of Phys.* 1967.
- [5] D. Censor, "Scattering of electromagnetic waves by a cylinder moving along its axis", *Microwave Theory Tech.* vol. MTT-17, pp. 154–158, 1969.
- [6] M. Idemen and A. Alkumru, "Influence of the velocity on the energy patterns of moving scatterers", *J. Electromagn. waves Appl.* vol.18, pp. 3–22, 2004.
- [7] R.C. Restrick, "Electromagnetic scattering by a moving sphere", *Radio Sci.* vol. 3, pp. 1144–1154, 1968.
- [8] G.N. Tsandoulas, "Low-frequency diffraction by moving conducting strips", *J. Opt. Soc. Am.* vol. 59, pp. 1357–1360, 1969.
- [9] K.C. Lang, "Diffraction of electromagnetic waves by a moving impedance wedge", *Radio Sci.* vol. 6, pp. 655–663, 1971.
- [10] D. Censor, "Scattering in velocity-dependent systems", *Radio Sci.* vol. 7, pp. 331–337, 1972.
- [11] P. De Cupis, G. Gerosa, and G. Schettini, "Electromagnetic scattering by an object in relativistic translational motion", *J. Electromagn. waves Appl.* vol.14, pp. 1037–1062, 2000.
- [12] J.A. Kong, *Electromagnetic Wave Theory*, 2nd ed., Wiley-Interscience, New York, 1990.
- [13] B. Noble, *Methods based on the Wiener-Hopf techniques*, Chap. 2 Pergamon, Oxford: 1958.

# High-Frequency/Short-Pulse Wave Dynamics in Ray-Chaotic Scenarios: A Survey

V. Galdi<sup>1</sup>, G. Castaldi<sup>1</sup>, V. Fiumara<sup>2</sup>, V. Pierro<sup>1</sup>, I. M. Pinto<sup>1</sup>, and L. B. Felsen<sup>3</sup>

<sup>1</sup> Waves Group, Department of Engineering, University of Sannio, Corso Garibaldi 107, I-82100 Benevento, ITALY, [vgaldi@unisannio.it](mailto:vgaldi@unisannio.it), [castaldi@unisannio.it](mailto:castaldi@unisannio.it), [pierro@unisannio.it](mailto:pierro@unisannio.it), [pinto@sa.infn.it](mailto:pinto@sa.infn.it)

<sup>2</sup> DIIIIE, University of Salerno, Via Ponte Don Melillo, I-84084, Fisciano (SA), ITALY, [vfiumara@unisa.it](mailto:vfiumara@unisa.it)

<sup>3</sup> Department of Aerospace and Mechanical Engineering, Boston University, 110 Cummington St., Boston, MA 02215, USA (part-time). Also, University Professor Emeritus, Polytechnic University, Brooklyn, NY 11201, USA, [lfelsen@bu.edu](mailto:lfelsen@bu.edu)

## Abstract

*Ray chaos*, manifested by the eventual *exponential* divergence of nearby originating ray trajectories, is a peculiar phenomenon which can occur even in *linear* electromagnetic propagation environments with relatively *simple* geometry, as a consequence of the inherent nonlinearity of ray-tracing maps. This paper provides a compact review of known results on wave propagation in ray-chaotic scenarios, and their potential implications for electromagnetic engineering applications.

## Introduction

*Deterministic chaos* [1–3] is nowadays recognized as a pervasive natural phenomenon of relevance in many fields of applied science and engineering, including electromagnetics (EM) (see [4] for a compact review). Of special interest, under high-frequency (HF)/short-pulse (SP) conditions, are the theoretical aspects and implications of *ray chaos*, which is manifested by the *exponential separation* of nearby-originating ray trajectories launched into certain complex *deterministic* environments. Remarkably, such behavior, which could intuitively be expected in *very complex* and *cluttered* propagation scenarios (e.g., urban areas), can also be observed in *relatively simple* (but coordinate-nonseparable) structures that give rise to multiple reflections, focusing, and defocusing, such as homogeneously filled “billiard-shaped” enclosures [3, 5, 6], ( $n > 3$ )-disk “pinballs” [7, 8], or appropriately configured inhomogeneous refractive media with ray-trapping properties

[9]. At first glance, ray-chaos may appear as a mere artifact stemming from approximating a *linear wave* equation (which operates in the HF regime with arbitrarily small but *finite* wavelengths, and *does not* exhibit exponential sensitivity to initial conditions in deterministic environments) in terms of a *nonlinear ray* equation that is based on the *zero-wavelength* HF limit. Nevertheless, there is substantiated evidence that the dynamic behavior of ray-chaotically-inclined systems, when observed at short (but *finite*) wavelengths, exhibits anomalous features which differ considerably from those associated with “regular” (e.g., coordinate-separability-induced) ray characteristics. Therefore, in ray-chaotically-inclined configurations, the onset of ray chaos serves as a “footprint” in HF wave dynamics that implies a “transition” to observables which are no longer well-matched to the pre-chaotic wave physics (see [10–13] for a review of known results). Besides the inherent academic interest, ray chaos has been demonstrated to play an important role in a variety of engineering applications (see [14–21] and the references therein).

In an ongoing series of investigations [22–31], we have focused on the study of HF/SP EM wave dynamics in ray-chaotic scenarios. In this paper, we provide a compact overview of background theory (mainly within the framework of quantum physics) as well as selected results from our EM investigations.

## Summary of Known Results: “Ray-Chaotic Footprints”

Most available investigations on the HF wave dynamics in ray-chaotically-inclined configurations are set in a quantum physics framework (classical vs. quantum chaos, see [10–13] for a review). Nevertheless, the main results and conclusions are rather *general* and apply to all kinds of time-harmonic wave phenomena. In most studies, emphasis is placed on the analysis of high-order modes in ray-chaotic “billiard” resonators, both from a *numerical* [32–41] and *experimental* [42–53] viewpoint. Good agreement between theoretical conjectures, numerical simulations and measurements in 2-D and 3-D experiments has usually been observed for eigenvalue statistics [46, 51], and for eigenfunction morphology and spatial statistics [42, 44, 47].

What seems to emerge is the presence of *distinctive* features in the HF wave dynamics which distinguish ray-chaotic boundary value problems (BVPs) from those (e.g., coordinate-separable) exhibiting *regular* ray behavior. Remarkably, in most cases, such “ray-chaotic footprints” have *universal* properties. For instance, in internal BVPs, the (asymptotic) neighboring-eigenvalue spacing distribution for regular geometries is known to be *Poissonian* [54]. Conversely, for ray-chaotic geometries, theoretical [55], numerical [51, 56, 57], and experimental [46, 51] investigations have revealed a deep connection between the spectral (eigenvalue, eigenfunction) ensemble properties and certain classes of *random matrices* [58] which were first introduced in the 1960s by Wigner [59] and Dyson [60] to describe the spectra of *complex* quantum systems (e.g., atomic nuclei) whose Hamiltonians are not known in detail. More recent studies have shown other examples of

ray-chaotic footprints in internal BVPs, related to field nodal-domain [61] and impedance/scattering matrix [62, 63] statistics.

In *external* BVPs, ray-chaotic footprints have been observed in the random-like angular spectrum properties of the scattering matrix and cross-sections, with intriguing connections to the dwell-time distribution of the corresponding ray dynamics [7, 8].

Overall, with a few notable exceptions (see, e.g., [34]), the wave dynamics turns out to undergo a “transition” from a *regular* regime (with smooth dependence on parameter variations) to an *irregular* regime (with sensitive dependence on parameter variations, and ergodic random-like behavior), as the frequency of operation is increased. In such an irregular regime, the full-wave properties are most naturally described in statistical terms, and a well-established model is based on the assumption that the field at any point is a superposition of a large number of plane waves with fixed wavevector amplitude, and uniformly distributed arrival-directions and phases [64]. Under (generally fulfilled) additional ergodicity assumptions, this yields rather general consequences in the wavefield statistics: In an arbitrary spatial domain spanning several wavelengths (sufficiently large so as to yield meaningful statistics, and yet sufficiently small so as to reveal possible spatial variations), the wavefield samples constitute a zero-average Gaussian ensemble, with spatial field correlation exhibiting peculiar (universal) forms [64, 65] (e.g.,  $J_0$  Bessel function in the 2-D case). The random-plane-wave (RPW) model has been demonstrated to reproduce the statistical properties (both predicted [57] and measured [52]) of high-order HF wavefunctions of strongly chaotic billiards in the irregular ergodic regime, still in accord with the random-matrix theory [66]. Remarkably, similar RPW models have been developed and applied successfully to the study of complex radar signatures [19, 21] as well as narrowband EM reverberation enclosures [67]. The reader is also referred to [68–70], where examples of billiards with “mixed” dynamics are considered, and possible deviations from the RPW model are explored.

For SP excitation, the insofar complete analogy between quantum physics and EM is no longer generally applicable, since the equivalence between the wave equation and time-dependent Schrödinger equation holds only in particular approximated (e.g., paraxial) regimes. Therefore, application to the EM counterpart of known results from quantum physics concerning possible ray-chaotic footprints in the SP wave dynamics (see, e.g., [71, 72]) is not straightforward. However, intriguing results have recently been obtained in acoustics applications of ray-chaos-enhanced time-reversal focusing [16, 73–75], for which the EM analogy is rather straightforward. In these investigations, theoretical and experimental support is provided for the possibility, in ray-chaotic cavities, of achieving time-reversal focusing using a *single* transmitter/receiver, by trading off (in view of ergodicity) the conventional *spatial* sampling with *temporal* sampling. Further results for the SP case are discussed later (see also [31]).



## Summary of Our Recent Results

Our interest in ray-chaotic propagation scenarios originated with the study of *reverberating enclosures* (see [76] for a recent review of the subject). Besides their practical utility as tools for *narrowband* EM compatibility/interference testing, such structures constitute an intriguing paradigm of the deterministic/stochastic interactions in complex systems. In [22], we introduced a simple 2-D ray model of (mechanically) mode-stirred reverberating enclosures, which revealed the connection between the spatial field homogenization with Rayleigh-like field intensity distribution in time observed in reverberating enclosures [77] and the onset of chaos as the peak-to-peak displacement of the mode-stirring wall becomes comparable to the EM field wavelength. Remarkably, the simple model in [22] was found to reproduce experimentally observed features, thereby providing useful insight into the underlying physics, and suggesting conceptual foundations of the well known thermodynamic theory of reverberating enclosures [78], as well as performance assessment in terms of Lyapounov exponents [1–3]. This suggested a deeper investigation of the *general* properties of wave dynamics in ray-chaotically-inclined enclosures vs. enclosures with regular (nonchaotic) features. Our subsequent studies were accordingly structured along two main research lines:

1. *HF analysis* of novel classes of two-dimensional (2-D) ray-chaotic wave guiding/scattering configurations. In [24, 26, 27, 30], we explored a configuration consisting of dielectric stratifications with exponentially tapered refractive index profile bounded by a smooth perfectly-electric-conducting periodic undulating bottom surface. The main novel feature in this configuration, which constitutes the EM analog of the gravitational billiard in [9], is the absence of a top-layer boundary, thereby allowing internal-external coupling (via the undulating bottom) between refractively *spatially-confined* and *outgoing* (leaky) rays and modes. For this configuration, we performed a comprehensive *ray* analysis, which revealed the onset of typical chaotic behavior. For specially tailored synthetic test profiles, we also carried out a rigorous *full-wave* analysis that allowed for comprehensive parametric study of the associated wave dynamics, with estimates of accuracy. Results for the HF regime indicated trends toward irregularity and other anomalous characteristics (not observed in geometries with “regular” ray behavior) which can thus be interpreted as “ray-chaotic footprints”. In the irregular (random-like, ergodic) regime, the wave dynamics was found to be described effectively by random-wave statistical models similar to those in [10–13]. In order to gain further insight, in [28, 29] the above analysis was extended to a *cylindrical* version, whose transverse finite extent in free space allowed for characterization and assessment of (monostatic or bistatic) radar cross sections. The performance characteristics produced by these model environments might be of interest in radar countermeasures and smart microwave absorbers. Possible applications are currently under investigation.
2. *SP wavepacket* propagation in ray-chaotic (e.g., stadium-shaped) *enclosures*. These studies were initially aimed at the design of *pulsed* (wideband) reverber-

ating (multiechoing) enclosures, based on the speculation that, in *ray-chaotic* enclosures, under suitable conditions, an initially localized EM wave-packet would eventually generate a nearly-uniform and isotropic “pulse shower” illuminating an equipment under test in a fashion largely independent of the target location, orientation, shape, and electrical constitutive properties. In [23], a preliminary study in a stadium-shaped geometry, within the limits of a simple ray analysis, confirmed the viability of such approach. Rigorous *full-wave* numerical simulations of the same scenario were subsequently carried out in [25, 31], via finite-difference-time-domain (FDTD) method. While bouncing around the walls, along the ray path skeleton, the wavepacket was found to undergo focusing at the concave curved wall and natural spreading elsewhere (including straight-wall reflection), progressively losing its initial space-time localization, and eventually covering uniformly the entire enclosure. Statistical analysis of the late-time spatial field distributions revealed the presence of interesting *random-wave* signatures, in terms of Gaussian field distributions and *uniform* and *isotropic* spatial correlation (with correlation length on the order of the pulse length), which turn out to be consistent with those from random-wave models encountered in the time-harmonic case. The same statistical analysis performed for *regular* (e.g., rectangular and circular) geometries indicated more *regular* field distributions (even at late times), with significant deviations from Gaussian statistics and isotropic spatial correlation, and increased sensitivity to wavepacket initial conditions. This suggests *pulsed-reverberation* techniques with their space-filling randomized outcome as potential candidates for *wide-band* EM interference and/or EM compatibility testbeds.

## Conclusions and Perspectives

A compact overview of results pertaining to HF and SP wave dynamics in ray-chaotic scenarios, and their potential relevance to EM engineering applications, has been attempted here. In particular, several examples and paradigms of “ray-chaotic footprints” in the wave dynamics have been illustrated.

It is worth stressing that the summary here is far from exhaustive, and some of the relevant issues involved are *as yet unsettled* (see, e.g., [79]). The reader is encouraged to further explore this subject, which is not only appealing but may have potentially interesting applications.

## Acknowledgment

L.B. Felsen acknowledges partial support from Polytechnic University, Brooklyn, NY 11201, USA.

## References

- [1] A.J. Lichtenberg and M.A. Liebermann, *Regular and Stochastic Motion*, Springer Berlin Heidelberg New York, 1983.
- [2] L.O. Chua and S. Parker, *Proc. IEEE*, 75(8), 982, 1987.
- [3] E. Ott, *Chaos in Dynamical Systems*, Cambridge, Cambridge University Press, 1993.
- [4] I.M. Pinto, Proceedings of 8th International Conference on Electromagnetics in Advanced Applications (ICEAA '03), Torino, Italy, 511 September 8–12, 2003.
- [5] Ya. G. Sinai, *Russ. Math. Surveys*, 25(2), 137, 1970.
- [6] L.A. Bunimovich, *Chaos*, 1(2), 187, 1991.
- [7] A. Wirzba, *Phys. Rep.* 309(1–2), 1, 1999.
- [8] T. Kottos *et al.*, *Radio Sci.* 34(4), 747, 1999.
- [9] T. Harayama and P. Gaspard, *Phys. Rev. E*, 64(3), 036215, 2001.
- [10] M.V. Berry, *Proc. Roy. Soc. London*, A413, 183, 1987.
- [11] M. Tabor, *Chaos and Integrability in Nonlinear Dynamics*, New York, John Wiley & Sons, 1989.
- [12] M.C. Gutzwiller, *Chaos in Classical and Quantum Mechanics*, Springer Berlin Heidelberg New York, 1991.
- [13] F. Haake, *Quantum Signatures of Chaos*, Springer Berlin Heidelberg New York, 1991.
- [14] J.U. Nöckel *et al.*, *Optics Lett.* 19(21), 1693, 1994.
- [15] A. Mekis *et al.*, *Phys. Rev. Lett.* 75(14), 2682, 1995.
- [16] C. Draeger and M. Fink, *Phys. Rev. Lett.* 79(3), 407, 1997.
- [17] T. Fukushima *et al.*, *Opt. Exp.* 2(2), 21, 1998.
- [18] C. Gmachl *et al.*, *Science*, 280(5369), 1556, 1998.
- [19] A.J. Mackay, *IEE Proc. Radar Sonar Navig.* 164(6), 298, 1999.
- [20] P.B. Wilkinson *et al.*, *Phys. Rev. Lett.* 86(24), 5466, 2001.
- [21] A.J. Mackay, in *Ultra-Wideband, Short-Pulse Electromagnetics 5*, P.D. Smith and S.R. Cloude, Eds. New York, Kluwer/Academic Publishers, 723, 2002.
- [22] L. Cappetta *et al.*, *IEEE Trans. Electromagn. Compatibility*, 40(3), 185, 1998.
- [23] V. Fiumara *et al.*, Proceedings of 6th International Conference on Electromagnetics in Advanced Applications (ICEAA '99), Torino, Italy, September 15–17, 357, 1999.
- [24] V. Fiumara *et al.*, Proceedings of 2000 IEEE Antennas and Propagat. International Symposium and USNC/URSI Radio Science Meeting, Salt Lake City, UT, USA, July 16–21, 682, 2000.
- [25] V. Galdi *et al.*, Proceedings of 2003 IEEE Antennas and Propagat. International Symposium and USNC/URSI Radio Science Meeting, Columbus, OH, USA, June 22–27, 2003.
- [26] G. Castaldi *et al.*, Proceedings of 8th International Conference on Electromagnetics in Advanced Applications (ICEAA '03), Torino, Italy, September 8–12, 519, 2003.
- [27] G. Castaldi *et al.*, in *Electromagnetics in a Complex World: Challenges and Perspectives*, I.M. Pinto, V. Galdi, and L.B. Felsen, Eds. Springer-Verlag Berlin Heidelberg New York, 137, 2004.
- [28] G. Castaldi *et al.*, Proceedings of 2004 URSI International Symposium on Electromagnetic Theory, Pisa, Italy, May 23–27, 948, 2004.
- [29] G. Castaldi *et al.*, Proceedings of 2004 IEEE Antennas and Propagate International Symposium and USNC/URSI Radio Science Meeting, Monterey, CA, USA, June 20–26, 2004.
- [30] G. Castaldi *et al.*, *IEEE Trans. Antennas Propagat.* 53(2), 753, 2005.
- [31] V. Galdi *et al.*, *IEEE Antennas Propagat. Mag.* 47(1), 62, 2005.
- [32] R.J. Riddell, Jr., *J. Comp. Phys.* 31, 21, 1979.

- 
- [33] M.V. Berry, *Annals Phys.* 131(1), 163, 1981.
- [34] E.J. Heller, *Phys. Rev. Lett.* 53(16), 1515, 1984.
- [35] E.J. Heller, in *Chaos and Quantum Physics*, M.-J. Giannoni, A. Voros, and J. Zinn-Justin, Eds., London, Elsevier, 549, 1991.
- [36] E.B. Bogomolny, *Nonlinearity*, 5(4), 805, 1992.
- [37] E. Doron and U. Smilanski, *Nonlinearity*, 5(5), 1055, 1992.
- [38] E. Vergini and M. Saraceno, *Phys. Rev. E*, 52(3), 2204, 1995.
- [39] L. Kosztin and K. Schulten, *Int. J. Mod. Phys. C*, 8(2), 293, 1997.
- [40] B. Li et al., *Phys. Rev. E*, 57(4), 4095, 1998.
- [41] A.N. Kaufman et al., *Am. J. Phys.* 67(2), 133, 1999.
- [42] S. Sridhar, *Phys. Rev. Lett.* 67(7), 785, 1991.
- [43] H.-D. Gräf et al., *Phys. Rev. Lett.* 69(9), 1296, 1992.
- [44] J. Stein and H.-J. Stöckmann, *Phys. Rev. Lett.* 68(19), 2867, 1992.
- [45] H. Alt et al., *Phys. Rev. E*, 50(1), R1, 1994.
- [46] A. Kudrolli and S. Sridhar, *Phys. Rev. E*, 49(1), R11, 1994.
- [47] A. Kudrolli et al., *Phys. Rev. Lett.* 75(5), 822, 1995.
- [48] S. Deus et al., *Phys. Rev. E*, 52(1), 1146, 1995.
- [49] H. Alt et al., *Phys. Rev. Lett.* 74(1), 62, 1995.
- [50] H. Alt et al., *Phys. Rev. Lett.* 79(6), 1026, 1997.
- [51] H. Alt et al., *Phys. Rev. E*, 60(3), 2851, 1999.
- [52] H.-J. Stöckmann, *J. Mod. Opt.* 49(12), 2045, 2002.
- [53] V. Doya et al., *Phys. Rev. E*, 65(5), 056223, 2002.
- [54] M.V. Berry and M. Tabor, *Proc. Roy. Soc. London*, 356, 375, 1977.
- [55] P. Pechukas, *Phys. Rev. Lett.* 51(11), 943, 1983.
- [56] O. Bohigas et al., *Phys. Rev. Lett.* 52(1), 1, 1984.
- [57] S.W. McDonald and A.N. Kaufman, *Phys. Rev. A*, 37(8), 3067, 1988.
- [58] M.L. Mehta, *Random Matrices*, 2nd ed., San Diego, Academic Press, 1991.
- [59] E.P. Wigner, *SIAM Rev.* 9, 1, 1967.
- [60] F. Dyson, *J. Math. Phys.* 3, 140, 1962.
- [61] G. Blum et al., *Phys. Rev. Lett.* 88(11), 114101, 2002.
- [62] S. Hemmady et al., *Phys. Rev. Lett.* 94(1), 014102, 2005.
- [63] S. Hemmady et al., *Phys. Rev. E*, 71(5), 056215, 2005.
- [64] M.V. Berry, *J. Phys. A*, 10(12), 2083, 1977.
- [65] B. Eckhardt et al., *Europhys. Lett.* 46(2), 134, 1999.
- [66] F.M. Izrailev, *Phys. Lett. A*, 125(5), 250, 1987.
- [67] D.A. Hill, *IEEE Trans. Electromagn. Compatibility*, 40(3), 209, 1998.
- [68] M.V. Berry et al., *Proc. Roy. Soc. London*, A456, 1659, 2000.
- [69] A. Backer and R. Schubert, *J. Phys. A: Math. Gen.* 35(3), 539, 2002.
- [70] A. Backer et al., *Nonlinearity*, 15(5), 1417, 2002.
- [71] A. Peres, *Phys. Rev. A*, 30(4), 1610, 1984.
- [72] R.A. Jalabert and H.M. Pastawski, *Phys. Rev. Lett.* 86(12), 2490, 2001.
- [73] C. Draeger and M. Fink, *J. Acoust. Soc. Am.* 105(2), 611, 1999.
- [74] C. Draeger and M. Fink, *J. Acoust. Soc. Am.* 105(2), 618, 1999.
- [75] M. Fink and J. de Rosny, *Nonlinearity*, 15(1), R1, 2002.
- [76] P. Corona et al., *IEEE Trans. Electromagn. Compatibility*, 44(1), 87, 2002.
- [77] J.G. Kostas and B. Boverie, *IEEE Trans. Electromagn. Compatibility*, 33(4), 366, 1991.
- [78] P. Corona et al., *IEEE Trans. Electromagn. Compatibility*, 22(1), 2, 1980.
- [79] P. Seba, *Phys. Rev. Lett.* 64(16), 1855, 1990.

# Numerical Modeling and Simulation Studies of 2D Propagation over Nonflat Terrain and Through Inhomogeneous Atmosphere

Ç. Uluşık and L. Sevgi

Department of Electronics and Communication Engineering, Doğuş University, Acıbadem, 81010, Istanbul, Turkey, [culuisik@dogus.edu.tr](mailto:culuisik@dogus.edu.tr), [lsevgi@dogus.edu.tr](mailto:lsevgi@dogus.edu.tr)

## Abstract

This paper introduces Matlab-based two dimensional (2D) virtual propagation tools (VT) which can be used to investigate EM propagation over user-specified nonflat terrain through inhomogeneous atmosphere. The VTs can be used for both engineering (GSM coverage planning, digital site survey, etc.) and educational purposes (e.g., in EM Theory, Wireless Communication, Antennas and Propagation lectures).

## Introduction

The design of today's communication systems necessitates a good understanding of electromagnetic (EM) wave propagation in three-dimensional (3D) realistic environments [1–3].

The 3D EM wave equation in spherical coordinates, over nonflat lossy ground, above with nonhomogenous atmosphere has not been solved analytically, yet. However the 2D techniques have successfully been applied to simplified, but still realistic problems [1–16]. Historically, these techniques can be classified as:

1. Analytical approximate.
2. 2D Numerical.
3. Hybrid, which are combinations of 1 and 2.

Analytical solutions are based on ray/mode approaches (e.g., see [1, 2] for the details of early analytical approaches). The single and multiknife-edge analytical approximations of nonflat, nonpenetrable terrain profiles have also been introduced and are used if there are a few dominating hills between the transmitter and receiver [5, 6].

Numerical solutions are basically divided into two subgroups; the frequency-domain (FD) techniques, such as PE [9–12] and method of moments (MoM)

based propagators [7, 8], and the time-domain (TD) techniques that are based on finite-difference time domain (FDTD) [13] and transmission line matrix (TLM) [14] methods. Analytical solutions are limited only a number of idealized geometries and certain refractivity conditions, but they are easy to compute. On the other hand, numerical solutions are applicable to more general geometries with almost arbitrary refractivities, but they are computationally complex and time consuming. Therefore, it is wise to hybridize analytical–numerical methods intelligently to broaden their range of applicability and accuracy.

Standard atmosphere corresponds to atmospheric refractivity decreasing with height plus earth curvature, resulting an atmospheric refractivity increasing with height for normalized Cartesian coordinates. For bilinear type, there exists a surface duct (linearly decreasing atmospheric refractivity) up to a certain height given by the user and standard atmosphere over this height. Elevated duct (trilinear) type atmosphere means that there exists a duct between first and second heights also chosen by the user. The effect of atmosphere onto EM propagation can be observed by choosing the desired refractivity.

## Two-Dimensional Groundwave Propagators

A few Matlab-based 2D propagator VTs are designed and presented in this section (These VTs can be downloaded from <http://www3.dogus.edu.tr/lsevgi> or [culuisik](http://www3.dogus.edu.tr/culuisik)).

### Snell\_gui

A 2D propagation package Snell\_gui [4] is prepared using Matlab to visualize ray characteristics. The ray shooting algorithm is based on consecutive application of Snell's law. It shoots a number of rays through a propagation medium characterized by various linear vertical refractivity profiles, so the user may visualize various ducting and antiducting characteristics depending on the supplied parameters. The front-panel of the, Snell\_gui package is shown in Fig. 1.

### Knife\_gui

The package Knife\_gui is based on the mathematical formulation of the classical knife-edge problem [5, 6]. Diffraction occurs when the direct line-of-sight (LOS) propagation between the transmitter and the receiver is obstructed by an opaque obstacle whose dimensions are considerably larger than the signal wavelength, and the radio waves are scattered and additionally attenuated. The diffraction mechanism allows the reception of radio signals when the LOS conditions are not satisfied (NLOS case), whether in urban or rural environments.

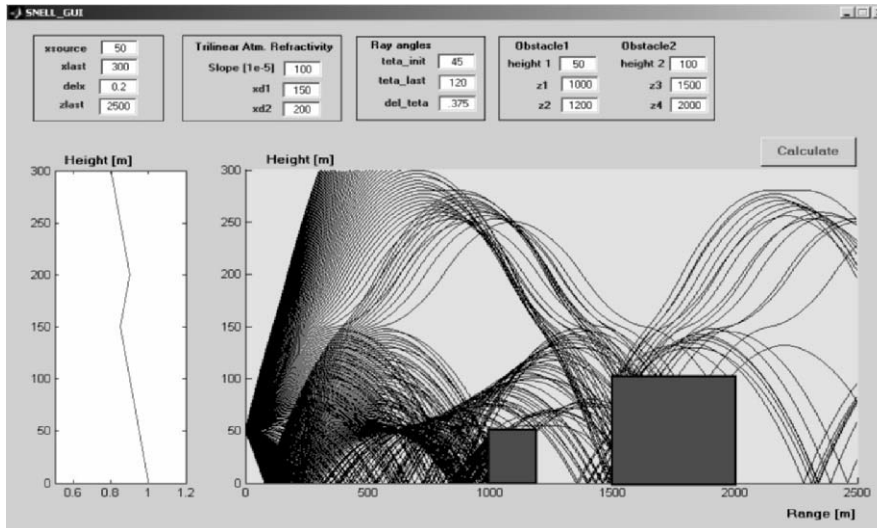


**Fig. 1.** The front panel of Snell\_gui (left) vertical refractivity profile (right) ray trajectories

The Matlab-based Knife\_gui VT is designed to account for the knife-edge diffraction effects. The front panel of this VT is shown in Fig. 2. First, the user specifies the boundary of the terrain by locating a number of points using the mouse. The rougher the terrain profile the higher the number of points that should be located. Then, the cubic-spline curve fitting algorithm is used to obtain the Z-dependent terrain function. Finally, the peak of the terrain is calculated automatically, and is replaced by a knife-edge obstacle with the same height at the same range.

Once, the user-specified parameters are supplied, propagation factor vs. range at a given height, and, propagation factor vs. height at the last range are calculated, and plotted at left and right, respectively (see Fig. 2).

The results of the 2-Ray model (i.e., the direct and ground-reflected rays) are also plotted in the figures, just to give an idea for the expected effects of the terrain.

The terrain profile may be recorded in a file for future usage. The name of the file may be supplied by the user. The created terrain files may also be called by the user. The buttons “save terrain” and “load terrain” are reserved for these purposes, respectively.

The creation of any type of a terrain profile is one of the most effective part of this tool, since one may often requires to rebuild an existing terrain and run his/her own propagation codes.

It should be noted that, Knife\_gui can be used for longitudinal terrain profiles with a dominating hill between the source and receiver that obscures the LOS path and the result may only represent the order of attenuation.

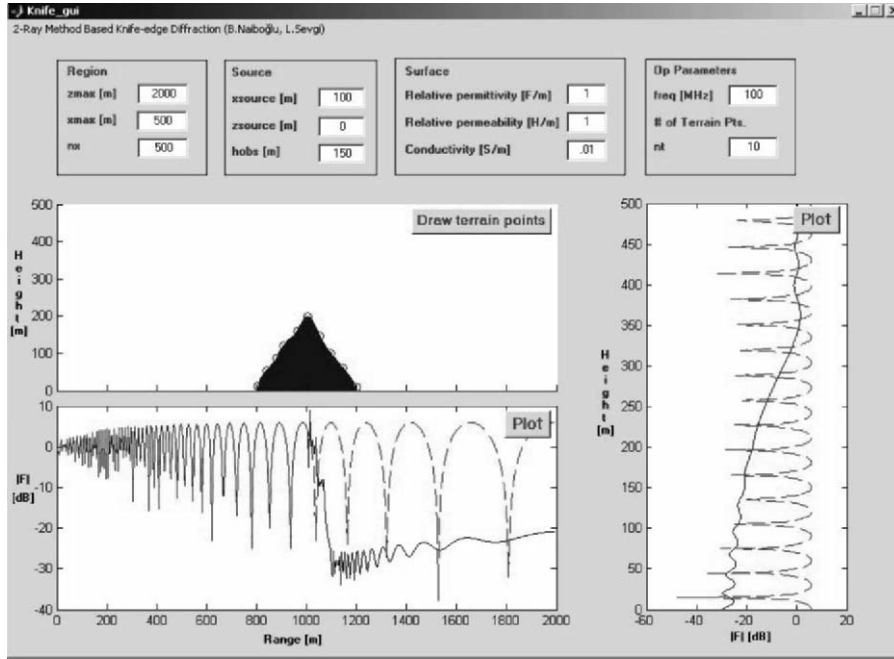


Fig. 2. The front panel of Knife\_gui

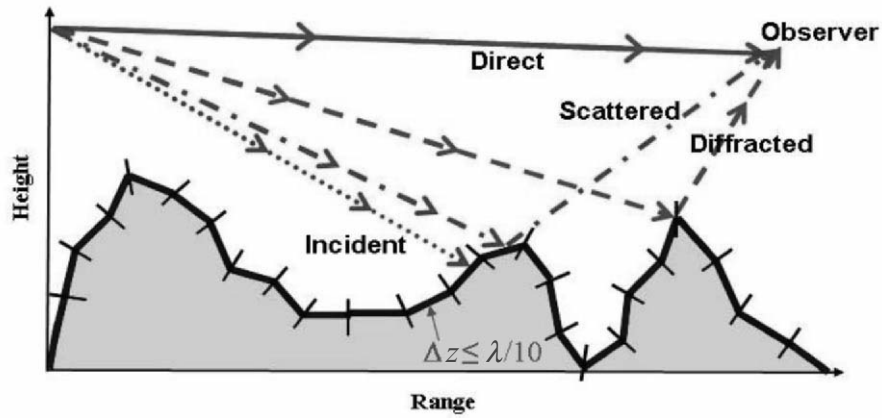


Fig. 3. Geometrical fundamentals of the Propmom\_gui



**Propmom\_gui**

The VT Propmom\_gui is based on the MoM and uses the 2D Green’s function. The surface length is approximated by  $N$  tilted straight segments of horizontal width  $\Delta z$  as shown in Fig. 3. Once, the digital longitudinal terrain segments are specified, segment currents, caused by the EM fields illuminating these segments, are calculated from  $N \times N$  matrix system  $[Z][I] = [V]$  where  $Z_{NN}$ ,  $I_N$ , and  $V_N$  are the surface impedance matrix of the segments, segment currents and incident voltages, respectively. Finally, the scattered fields caused by these segment currents at a chosen observation point are extrapolated by using the 2D– Green’s function propagators.

The front-panel of the Propmom\_gui VT is designed as shown in Fig. 4. Input parameters are given at the top of the interface. At the left side, terrain points are marked and terrain function is drawn on the top, and the diffraction loss vs. range at an observation height is drawn on the bottom. At right, the diffraction loss vs. height at maximum range is drawn.

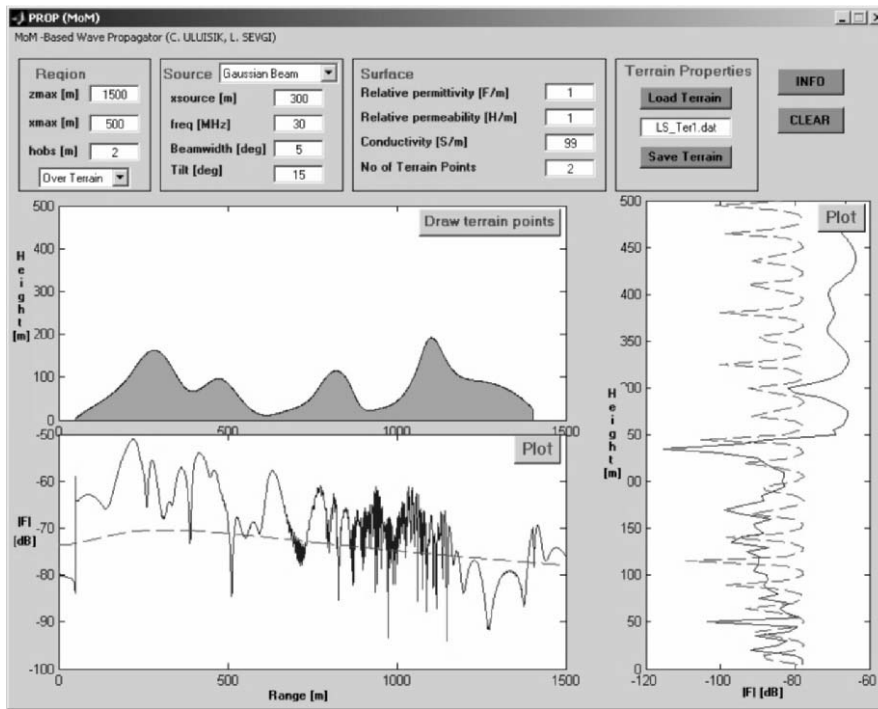


**Fig. 4.** The Propmom\_gui, dashed-lines represent flat earth 2D-Ray results. (top) user-built terrain profile (bottom) Signal vs. range at constant height, (right) Signal vs. height at constant range

### SSPE\_gui

The SSPE\_gui VT is based on step by step solution of a 2D parabolic (reduced from the 2D Helmholtz) equation based on discrete (fast) Fourier transformation (FFT), and models a one-way (forward) propagation problem [9].

PE is an initial value problem; an initial transverse field distribution is injected, and longitudinally propagated through a medium specified by its refractive index profile and the transverse field profile at the next range step is obtained. By sequential operations accessing the  $x$  and  $k_x$  domains via FFT and inverse FFT, respectively, one may obtain the transverse field profile at any range. In 2D rectangular coordinates, the earth's curvature is included by modifying the refractivity profile. Extra terms may also be added to model various super or sub-refraction propagation cases [1, 9].

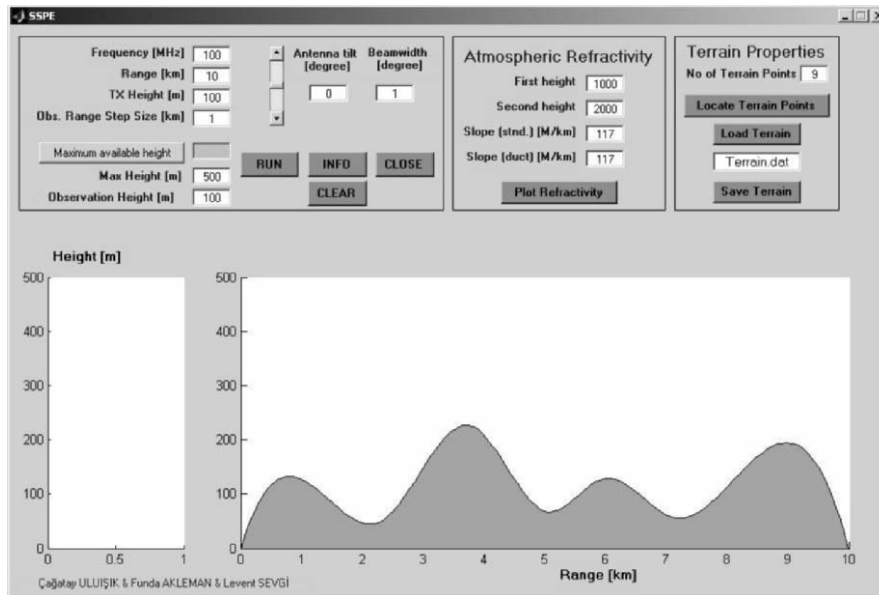


**Fig. 5.** The front panel of SSPE\_gui (left) signal vs. height (right) user-specified terrain and colored signal vs. range/height map

The front panel of the SSPE\_gui VT is shown in Fig. 5. The operational parameters are grouped into three: frequency and range/height are supplied at left; the transmit antenna parameters, such as the beamwidth and the tilt are supplied at the middle and refractivity profile is given at right. The two windows are reserved for height/range graphics. The field strength vs. range/height is plotted at the right window, together with the user-designed terrain profile. The refractivity and field vs. height are plotted inside the left window. Field vs. height at 10 different ranges between the transmitter and the receiver are plotted one by one at left, as the wave

propagates from left to the right. When maximum range is reached the 3D plot is given at right, where different colors correspond to different field strengths.

A few simulation scenarios are given in Figs. 6 and 7. In Fig. 6, a two-hill, relatively smooth terrain and its effect to the transmitted narrow beam at 100 MHz is shown. In Fig. 7, a rough surface and scattering of waves for a beam, tilted downwards at 60 MHz is given.

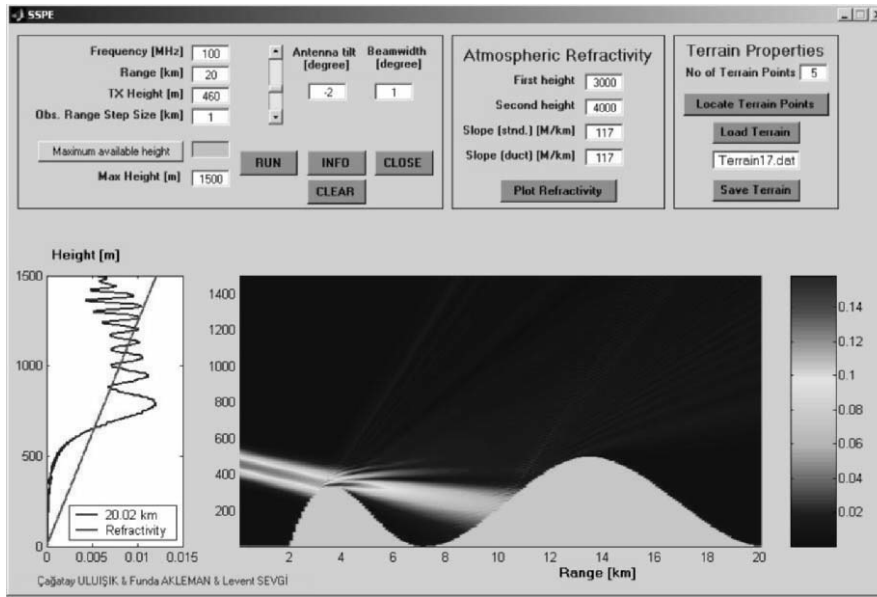


Fig. 6. SSPE\_gui VT and a typical 2-hill propagation scenario

## SSPE vs. MoM

The presented VTs in Sect. 2 work better under different, approximate conditions. The challenge is then to design a propagation scenario in which one can compare one VT against the other. Before doing this, they may be tested against each other under limiting cases. For example, Knife\_gui vs. Propmom\_gui comparison is possible if there is a “clear” single-knife-edge terrain between the Tr/Rx pair. Similarly, SSPE\_gui vs. Propmom\_gui comparison is possible for the flat-Earth case, where both can also be calibrated against analytical 2-Ray solution.

Beside these exceptional scenarios, one should be very careful while comparing one against the other. To illustrate this, a typical comparison is given in Fig. 8. Here SSPE\_gui is compared against Propmom\_gui. The field strength at a height of 100 m over the terrain is calculated using both methods. The magnitude of the

field strength calculated with the SSPE is about 5–10 dB less than the one calculated with MoM. The reason of this difference is that MoM does take into account not only the forward propagation and also the backward propagation where SSPE calculates only the forward propagation.

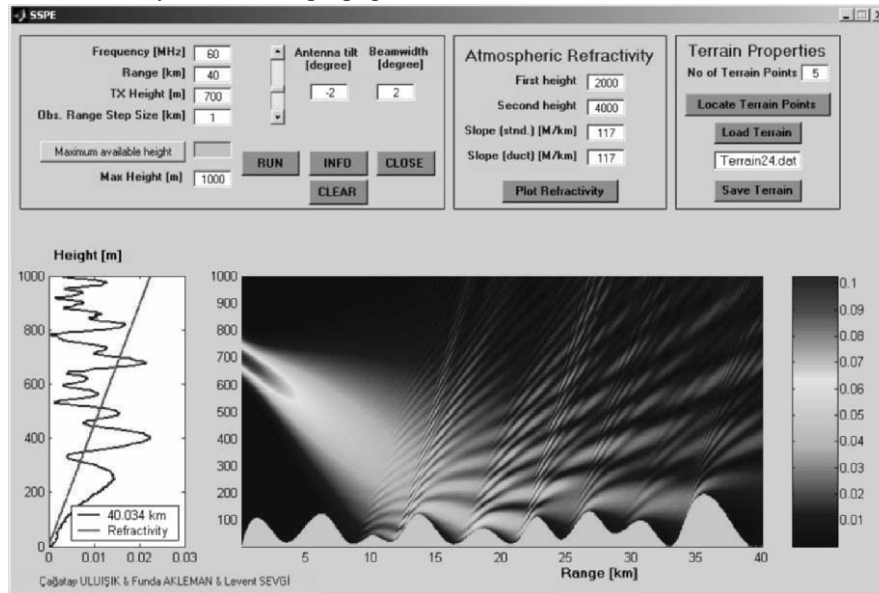


Fig. 7. Typical results for SSPE\_gui

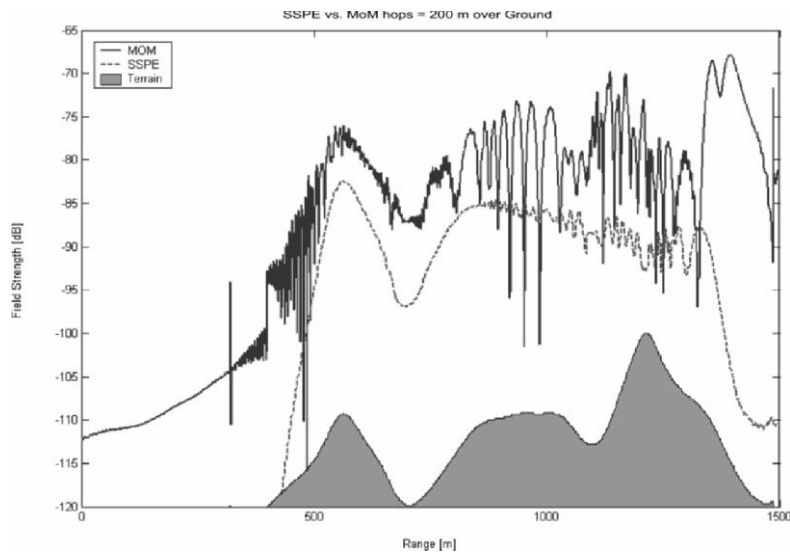


Fig. 8. SSPE vs. MoM: Signal vs. range at a height of 100 m over the terrain

## Conclusion

Different propagation VTs are presented in this paper. The aim is to discuss various challenging features of the 2D propagation simulations. These VTs may also be used as education tools in undergraduate and advanced level EM lectures.

## References

- [1] L. Sevgi, *Complex Electromagnetic Problems and Numerical Simulation approaches*, IEEE Press – John Wiley & Sons. NJ, June 2003
- [2] L. Sevgi, F. Akleman, L.B. Felsen, “Ground wave propagation modeling: problem-matched analytical formulations and direct numerical techniques”, *IEEE Antennas Propag. Mag.* Vol. 44, No.1, pp. 55–75, February 2002
- [3] L.B. Felsen, F. Akleman, L. Sevgi, “Wave propagation inside a two-dimensional perfectly conducting parallel plate waveguide: hybrid ray-mode techniques and their visualizations”, *IEEE Antennas Propag. Mag.* Vol. 46, No. 6, pp. 69–89, December 2004
- [4] L. Sevgi, “A ray shooting visualization matlab package for 2D ground wave propagation simulations”, *IEEE Antennas Propag. Mag.* Vol. 46, No. 4, pp. 140–145, October 2004
- [5] J.C. Schelleng, C.R. Burrows, E.B. Ferrel, “Ultra-short wave propagation”, *Proc. IRE*, Vol. 21, pp. 427–463, March 1933.
- [6] J. Deygout, “Multiple knife-edge diffraction of microwaves”, *IEEE Trans. Antennas Propag.* Vol. 51, No. 7, pp. 1679–1683, July 2000
- [7] C.A. Tunc, A. Altintas, V.B. Erturk “Examination of existent propagation models over large inhomogeneous terrain profiles using fast integral equation solution”, *IEEE Trans. Antennas Propag.* Vol. 53, No. 9, pp. 3080–3083, September 2005
- [8] J.T. Johnson, R.T. Shin, J.C. Eidson, L. Tsang, and J.A. Kong, “A method of moments model for VHF propagation”, *IEEE Trans. Antennas Propag.* Vol. 45, No. 1, pp. 115–125, January 1997
- [9] M. Levy, *Parabolic Equation Methods For Electromagnetic Wave Propagation*, IEE Institution of Electrical Engineers, 2000
- [10] A.E. Barrios, “A terrain parabolic equation model for propagation in the troposphere”, *IEEE Trans. Antennas Propag.* Vol. 42, pp. 90–98. 1994.
- [11] R. Janaswamy, “Path loss predictions in the presence of buildings on flat terrain: A 3-D vector parabolic equation approach”, *IEEE Trans. Antennas Propag.* Vol. 51, No. 8, pp. 1716–1728, August 2003
- [12] D.J. Donohue, J.R. Kuttler, “Propagation modeling over terrain using the parabolic wave equation”, *IEEE Trans. Antennas Propag.* Vol. 48, No. 2, pp. 260–277, February 2000
- [13] F. Akleman, L. Sevgi, “A novel time-domain wave propagator”, *IEEE Trans. Antennas Propag.* Vol. 48, No. 5, pp. 839–841, May 2000
- [14] M.O. Özyalçın, F. Akleman, L. Sevgi, “A novel TLM based time domain wave propagator”, *IEEE Trans. Antennas Propag.* Vol. 51, No. 7, pp. 1679–1683, July 2003

- [15] L. Sevgi, Ç. Uluşık, F. Akleman, “A matlab-based two-dimensional parabolic equation radiowave propagation package”, *IEEE Antennas Propag. Mag.* (to appear), 2005
- [16] Ç. Uluşık, L. Sevgi, “Modeling and simulation strategies in wireless propagation and coverage planning”, *Proc. EMC' 2005*, St. Petersburg, Russia, pp. 121–125, June 21–24, 2005

# Fast Integral Equation Solutions: Application to Mixed Path Terrain Profiles and Comparisons with Parabolic Equation Method

C.A. Tunç<sup>1</sup>, F. Akleman<sup>2</sup>, V.B. Ertürk<sup>1</sup>, A. Altıntaş<sup>1</sup> and L. Sevgi<sup>3</sup>

<sup>1</sup> Department of Electrical and Electronics Engineering, Bilkent University, Bilkent, Ankara, Turkey, celal@ee.bilkent.edu.tr, altintas@ee.bilkent.edu.tr

<sup>2</sup> Department of Telecommunication Engineering, Istanbul Technical University, Maslak, Istanbul, Turkey, funda@ehb.itu.edu.tr

<sup>3</sup> Department of Electronics and Communication Engineering, Doğuş University, Acıbadem 81010, Istanbul, Turkey, lsevgi@dogus.edu.tr

## Abstract

The numerical modeling and simulation of multimixed path surface wave propagation is discussed. Sea–land, sea–land–sea transitions are modeled via fast integral equation solutions and the results are compared against the parabolic equation method.

## Introduction

The calculation of propagation effects along ocean paths in the presence of different-sized islands has still been a challenging EM propagation problem. It requires analytical solution of three-dimensional (3D) wave equation with the specified boundary conditions in spherical coordinate system; this solution has not appeared yet. The efforts have been towards the solution along propagation paths between the transmitter and receiver in 2D simplified media. Analytical approximate solutions, based on either ray or mode, or their hybrid forms, mostly can tackle this problem in an approximate sense and when the propagation path heights are zero. Numerical simulators, such as fast integral equation (FIE) solutions and the split step parabolic equation method (SSPE) are promising techniques.

In real word systems, such as those exemplified above, the problem of determining the propagation characteristics between any two selected points can best be addressed via accurate and versatile simulation models. Such simulators are expected to accept the characteristics of the propagation environment as input (digitized map of the nonflat terrain, ground cover types, parameters of the troposphere,

etc.) and provide wave propagation characteristics as output, in a nearly real-time basis. Clearly such simulation tools would be indispensable to the decision-maker, service planner, site-engineer or the leader of a small military ground contingent, and it has therefore been a continuing challenge to develop simulators, which satisfy these requirements.

In this study, propagation along ocean paths including islands taking into consideration the electrical parameter differences between sea and land as well as island heights is investigated.

## Multiflat Mixed-Path Propagation Modeling

The multimixed path propagation problem that was first mentioned by Millington [1] is an interesting propagation problem at high frequencies (HF). The problem of excess propagation losses caused by the existing nonhomogeneous surface paths is taken into account and has been analyzed with different analytical approximate as well as numerical techniques in the frequency domain [1, –9]. Recently, promising time domain techniques have also been introduced [10, –11]. In fact, at 100 MHz and above, both land and sea surfaces act as a perfectly conducting (PEC) medium and mixed path effects are almost negligible. But for the lower frequencies, especially at HF (3–30 MHz) it is essential to analyze the propagation as a mixed path problem. Because of the higher penetration depth of the land the ground absorbs more energy than sea, since sea has a larger conductivity compared to land (typical electrical parameters – the conductivity and the relative permittivity – of the land and ocean are  $\epsilon_r = 15\text{--}20$ ,  $\sigma = 0.01 \text{ S m}^{-1}$  for land, and  $\epsilon_r = 70\text{--}80$ ,  $\sigma = 4\text{--}5 \text{ S m}^{-1}$  for ocean). If the path starts over Poor Ground (i.e.,  $\epsilon_r = 15$ ,  $\sigma = 0.001 \text{ S m}^{-1}$ ) and continues over the ocean, an increase of the signal at the transition between the two segments is expected; this is the well-known recovery effect, which has been observed experimentally by Millington [1]. The reverse is also true (i.e., if the path starts over the ocean and continues over the land a decrease of the signal at the transition between the two segments is expected). In early studies as well as recent numerical ones, only the electrical parameter variations of the surface are taken into account. The height differences along the propagation paths cannot be considered.

The Millington effect can be investigated analytically by using ray and/or mode methods. The ray (Norton) approach involves direct, ground-reflected, and surface waves on a spherical Earth, while the mode (Wait) approach involves surface waves in terms of Airy functions and based on the use of an equivalent earth-flattened linear atmosphere profile. The hybridization of these two extends the range of applicability of each; the HFMIX package has been introduced for this purpose [7]. Either by using ray-mode theories separately or by using HFMIX, one may deal with smooth-boundary phenomena, such as:

- Surface wave path loss or field strength variation with respect to range (especially beyond the horizon and when both transmitter and receiver are on the surface).



- Range and/or height propagation variations in interference regions (i.e., when transmitter and receiver are above the surface and within the line-of-sight, LOS).

It should be noted that ray-mode techniques cannot handle problems such as the propagation over rough surface terrain, or the propagation through surface and/or elevated ducts formed by inhomogeneous vertical as well as horizontal atmospheric conditions.

In Fig. 1, HF MIX computations of path loss calculations over multimixed path are shown for different propagation scenarios. In these plots, dashed and solid lines correspond to path loss over sea and mixed paths, respectively. It should be noted that altitude of land is taken as zero. The substantial sharp increase in the path loss is shown in Fig. 1a for a sea–land transition at 200 km away from the transmitter. In order to demonstrate effects of sea–land and land–sea transitions together a typical 50-km island, which is 200 km away from the transmitter, is chosen and path loss calculated for this scenario is plotted in Fig. 1b. The increase in the path loss and the recovery of the signal are clearly observed through sea–land and land–sea transitions, respectively. Finally, path loss variations through multipaths are given in Fig. 1c, d for eight and four islands between transmitter and receiver, respectively.

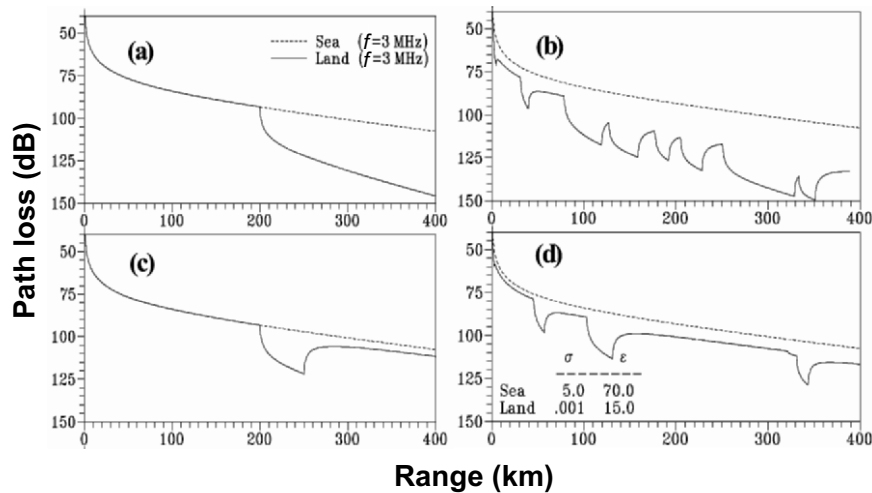


**Fig. 1.** Multipath loss versus range (a) sea–land transition at 200 km, (b) eight islands with lengths 4, 9, 41, 32, 15, 23, 78, and 18 km at radial distances 5, 42, 90, 139, 190, 218, 264, and 347 km, respectively, (c) a 50-km island at 200 km, (d) three islands with lengths 12, 28, and 13 km at distances 40, 98, and 331 km, respectively

It has been shown in many studies [2–9] that (a) having an island along the propagation path increases the path loss, (b) excess loss can be minimized by operating the radar at a lower frequency, (c) for the given example, excess loss caused by the islands is between 5 and 15 dB, (d) nearby islands cause more loss

than far islands, and (e) critical parameters for mixed-path losses are the radial lengths of the islands and the distance in between them.

## Multi-Nonflat Mixed-Path Propagation Modeling

The multi-sea–land transition contributions onto the surface wave path loss when the height of the land is nonzero can be handled – up to certain extent – numerically. The most promising numerical techniques for these types of problems are the SSPE [5–8] and the FIE [12–15].

### SSPE

A 2D groundwave propagation problem, which is described by the Helmholtz equation plus boundary conditions, can be reduced to a parabolic form under slow longitudinal variations (either in geometry or in medium refractivity). Transforming the boundary value problem into an initial-value problem makes the solution amenable to numerical implementation in terms of the discrete Fourier transform (DFT), as long as transverse boundary conditions are satisfied. A step-by-step longitudinal solution – the SSPE scheme – is given as

$$u(x, z) = \exp\left[j \frac{k_0}{2}(n^2 - 1)\Delta x\right] \times \text{FFT}^{-1}\left[\exp\left[-j \frac{k_z^2 \Delta x}{2k_0}\right] \text{FFT}\{u(x_0, z)\}\right], \quad (1)$$

where  $x$  and  $z$  are the longitudinal (range) and the vertical (height) coordinates, respectively, and  $u(x, z)$  is the wave function. The other parameters:  $\Delta x = x - x_0$ ,  $k_z$ ,  $k_0$ ,  $n$ , FFT and  $\text{FFT}^{-1}$  correspond to the range step size, transverse and free space wave numbers, the refractive index of the atmosphere, the fast and inverse fast Fourier transforms, respectively. The SSPE has been in use for more than three decades, first introduced for underwater acoustics and then for ground wave propagation modeling (see 6, 8 for a historical overview as well as analytical details).

The SSPE is a one-way scheme and can account for the forward scattered fields (i.e., backward scattered fields are neglected). It accounts for all types of boundary conditions as well as atmospheric effects that are included as the refractivity variations. Up to a certain extent, the SSPE can accommodate propagation over nonflat terrain paths. Modeling of nonflat terrain effects on the propagation of waves can be incorporated into the SSPE algorithm (a) by using piecewise linear (PL) approximations, (b) by conformal mapping (CM), and (c) by staircase discretization (SD).

### The Fast Integral Solutions: MoM with FBSA

Fast integral equation (FIE) methods have been used to calculate scattered field over an electrically large nonflat and/or rough terrain profile illuminated by an incident electromagnetic field (see [12–15] for the historical review, variety of applications, and related references). The method of moments (MoM) based propa-

gation models requires analytical derivation of the 3D Green's function. Moreover, the surface terrain profile function is also required. The electric field integral equation (EFIE) or the magnetic field integral equation (MFIE) can be used to represent the propagation of the TM- or TE-type polarized waves.

First, the propagation path (the longitudinal terrain profile) is replaced with a number of neighboring segments [12]. The segment lengths are specified according to the EM signal frequency. As a rough criterion, the length of each segment should be equal to or less than the wavelength over ten. Assuming that

- the incident field is of finite extent in space and illuminates only the propagation path portion between the transmitter and receiver
- current induced on each of the segment when illuminated by the source
- segment lengths and induced current on each segment are constant

one can apply the point-matching MoM technique and obtains the closed form matrix equation:

$$[V] = [\bar{Z}] \cdot [I], \quad (2)$$

where  $[I]$  contains the unknown coefficients of segment currents  $I_m$ ,  $[\bar{Z}]$  is the impedance matrix whose entries are given in [12], and  $[V]$  denotes the incident field evaluated at the matching points.

Direct solution of this matrix forms results in the segment currents from which the scattered fields at any specified observation point can be calculated using the Green's function propagator. Obviously, the solution of (2) is very time consuming as the number of segments increase (i.e., for the long-range propagation problems. For example, a 100 km propagation problem requires  $100,000 \times 100,000$  matrix inversion at 30 MHz (10 m wavelength). Instead of the direct solution of the system defined by (2), which requires  $O(N^3)$  operations, the forward-backward spectral acceleration (FBSA) with  $O(N)$  operations is used to find the unknown current coefficients for electrically very large terrains. For further details on FBSA, the reader is referred to [12–15]. It should be noted that FBSA can take into account the variations of the electrical parameters of the surface and uses impedance type boundary condition, therefore different combinations of land-sea transitions are possible. On the other hand, it cannot take the refractivity variations into account; only terrain effects can be investigated with this method.

## Numerical Results

The aim here is to show the advantages of using MoM-FBSA and the SSPE methods in the simulations of the mixed-path propagation problems. The main interest is to find out the effects of terrain heights along the propagation path at various signal frequencies. The atmosphere is assumed to be homogeneous. Because of the challenging nature of the problem only a limited number of studies exist in literature [4, 5, 9]. The strategy in the simulations is as follows

- specify a propagation scenario which focuses on the terrain height differences
- specify another scenario which focuses on the electrical parameters on the boundary

A typical scenario is pictured in Fig. 2. A 7-km long island of 100 m height is located 4 km away from the source, and the maximum range is 15 km. A 10 W, isotropically radiating transmitter, which is assumed as a horizontal electric dipole, is located  $0.9\lambda$  above the ocean and the height of receiver is taken as  $0.1\lambda$ .

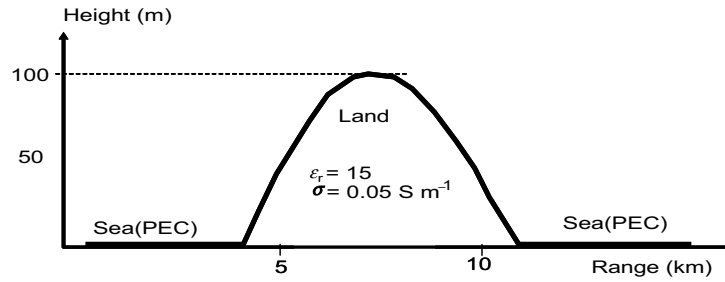


**Fig. 2.** A 15-km long scenario with a 7-km long, 100-m high island

The electric field calculated with the MoM-FBSA method in dB, along the propagation path shown in Fig. 2 at 30 MHz signal frequency is plotted in Fig. 3.

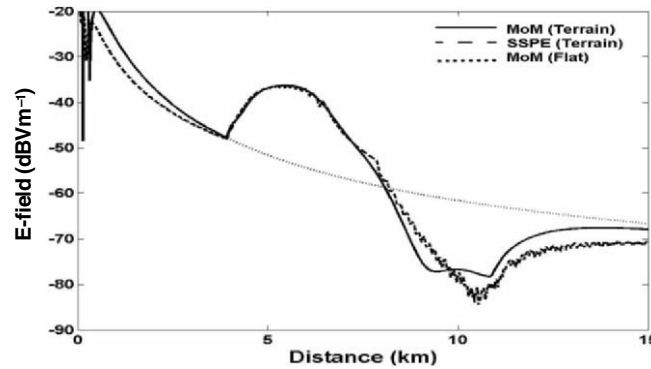


**Fig. 3.** Signal strength versus range over the scenario at 30 MHz is given in Fig. 2

In order to interpret the curves, first look at Fig. 1, the curves (a) and (b). The ocean – land transition causes a sharp decrease in the signal strength and the decrease is proportional with the signal frequency. Now, if we come back to Fig. 3, the smooth curve represents the results for the homogeneous, flat PEC path. The other two curves belong to nonflat PEC and lossy islands. Obviously, either PEC or lossy, the presence of the nonflat island strengthens the signal in front of, and weakens the signal behind the island. This is consistent with the result in [5] as shown in Fig. 4.

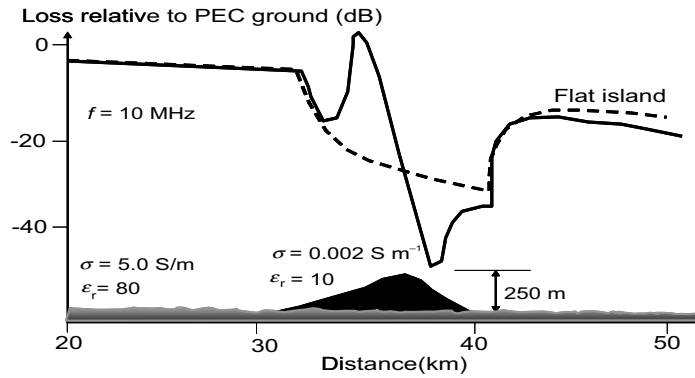


**Fig. 4.** Loss relative to a PEC ground versus range for an inhomogeneous path at 10 MHz. The propagation path includes a Gaussian-shaped, 10-km long, 250-m high island. Physical parameters, land:  $\sigma = 0.002 \text{ (S m}^{-1}\text{)}$ ,  $\epsilon_r = 10$ ; sea:  $\sigma = 5 \text{ (S m}^{-1}\text{)}$ ,  $\epsilon_r = 80$ . *Dashed:* island with zero-height [5]

To be able to see the signal level drop (Millington effect) at the sea–land interface simulated with the MoM-FBSA the plot in Fig. 3 is zoomed around that region. The result, shown in Fig. 5, clearly illustrates the Millington effect.

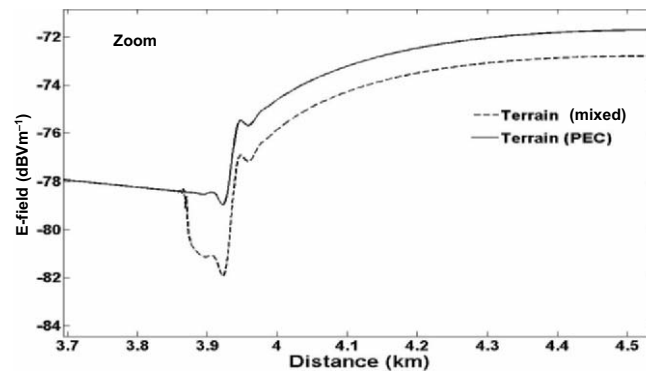


**Fig. 5.** Signal strength versus range over the scenario given in Fig. 2 (zoomed around sea–land junction at 4 km)

The last scenario is given in Fig. 6 for the path loss variations over PEC terrain, calculated by both MoM-FBSA and SSPE, for sea–land–sea transition where island height is 300 m and the frequency is 12 MHz. Here, transmitter and receiver heights are  $2.51\lambda$  and  $2.59\lambda$ , respectively. It should also be noted that indistinguishable results are obtained if the electrical parameters of the ground are taken into account together with irregular terrain.

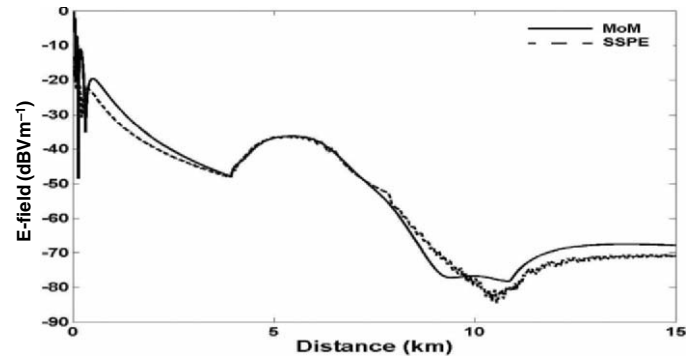


**Fig. 6.** MoM-FBSA versus SSPE for a typical propagation scenario (terrain height = 300 m,  $f = 12$  MHz). *Solid*: MoM with FBSA, *dashed*: SSPE

Extensive amount of numerical simulations are repeated for variety of propagation scenarios with different-sized islands at different operating frequencies and similar results are observed:

- The presence of an island along the ocean propagation paths causes sharp decreases in the signal strength and a recovery process occurs afterwards.
- The higher the frequency at HF band the deeper the signal loss at the ocean-land transition.
- The island height directly affects the signal strength both in front of the island and afterwards.
- The higher the island the stronger the signal strength in front of the island, and deeper the loss afterwards.

## Conclusions

Path loss simulations over multimixed paths through homogeneous atmosphere have been performed. The aim is to find out the contributions of island heights. Typical scenarios are designed and powerful propagators are compared. It is observed that if transmitter is a few wavelengths over ground, electrical changes of ground do not considerably affect the path loss variations, therefore the effect of height differences along the path dominates. However, both electrical parameters and irregular terrain should be considered when the transmitter is near to the surface of the ground.

---

## References

- [1] G. Millington, "Ground wave propagation over an inhomogeneous smooth earth", *Proc. IRE*, vol. 96, no. 39, 53–64, 1949
- [2] CCIR, "Ground wave propagation curves for frequencies between 10 kHz and 30 MHz", *CCIR Rec.*, 368–6, 1990
- [3] R.H. Ott and L.A. Berry, "An alternative integral equation for propagation over irregular terrain", *Radio Sci.*, vol. 5, 767–771, 1970
- [4] R.H. Ott and L.A. Berry, "An alternative integral equation for propagation over irregular terrain", 2, *Radio Sci.*, vol. 6, 429–435, 1971
- [5] N. Maslin, *HF Communications. A System Approach*, Pitman, Great Britain, 1987
- [6] M. Levy, *Parabolic Equation Methods for Electromagnetic Wave Propagation*, IEE Institution of Electrical Engineers, 2000
- [7] L. Sevgi and L.B. Felsen, "A new algorithm for ground wave propagation based on a hybrid ray-mode approach", *Int. J. Numerical Model.*, vol. 11, no. 2, 87–103, 1998
- [8] L. Sevgi, *Complex Electromagnetic Problems and Numerical Simulation Approaches*, IEEE Press Wiley, Berlin Hiedelberg New York, 2003
- [9] L. Sevgi, F. Akleman and L.B. Felsen, "Ground Wave Propagation Modeling: Problem-matched Analytical Formulations and Direct Numerical Techniques", *IEEE Antennas Propag. Mag.*, vol. 44, no. 1, 55–75, 2002
- [10] F. Akleman and L. Sevgi, "A Novel Finite Difference Time Domain Wave Propagator", *IEEE Trans. Antennas Propag.*, vol. 48, no. 5, 839–841, 2000
- [11] M. O. Özyalçın, F. Akleman, L. Sevgi, "A Novel TLM Based Time Domain Wave Propagator", *IEEE Trans. Antennas Propag.*, vol. 51, no. 7, 1679–1683, 2003
- [12] C.A. Tunc, "Application of spectral acceleration forward/backward method for propagation over terrain", *M. Sc. Dissertation*, Bilkent University, Ankara, 2003, <http://www.thesis.bilkent.edu.tr/0002378.pdf>
- [13] C.A. Tunc, A. Altintas, V.B. Ertürk, "Examination of existent propagation models over large inhomogeneous terrain profiles using fast integral equation solution", *IEEE Trans. Antennas Propag.*, vol. 53, no. 9, 3080–3083, 2005
- [14] H.-T. Chou and J.T. Johnson, "A novel acceleration for the computation of scattering from rough surfaces with the forward–backward method", *Radio Sci.*, vol. 33, 1277–1287, 1998
- [15] J.A. López, M.R. Pino, F. Obelleiro and J.L. Rodríguez, "Application of the spectral acceleration forward–backward method to coverage analysis over terrain profiles", *J. Electromagn. Waves Appl.*, vol. 15, 1049–1074, 2001

# A Pole Matching Method for the Analysis of Frequency Selective Surfaces

A. Cucini, M. Nannetti, F. Caminita and S. Maci

Department of Information Engineering, University of Siena, Siena 53100, Italy  
macis@ing.unisi.it

## Abstract

In this work, a pole matching method is presented for the analytical reconstruction, from full-wave data, of the scattering properties of frequency selective surfaces (FSS). This method allows one to synthesize the scattering response of an FSS from the identification of a few parameters, which exhibits a weak dependence with respect to the angle of incidence. This property implies that the full-wave analysis of the FSS can be performed for a limited set of incidence directions, from which the overall response can be obtained by a simple and numerically efficient algorithm. The final outcome is an analytical form for the scattering matrix which may be conveniently used in ray-tracing algorithms, based on local flat-surface approximations of curved FSS.

## Introduction

Frequency selective surfaces (FSS) [1, 2] are widely used for the realization of polarizers and dichroic reflectors. Due to the large dimensions of these structures, the analysis is usually performed by resorting to high-frequency techniques, such as Physical Optics (PO) or Geometrical Optics (GO), sometimes augmented by diffraction theories (PTD, UTD, ITD). In this framework, it would be desirable to have a simple and accurate surface impedance model of periodic surfaces, to be interfaced with existing high-frequency electromagnetic simulation tools.

Recently, a method has been introduced for the efficient synthesis of the FSS admittance (patch-type FSS) or impedance (aperture-type FSS) matrix, focused on the study of dispersion properties of FSS-based artificial surfaces [3–5]. This method is based on the application of the Foster's reactance theorem [6], which implies that FSS admittance functions of frequency satisfy the pole-zero analytical properties of the driving point LC admittance functions [7]. The identification of the poles and zeros of the FSS equivalent admittance allows a reconstruction of the surface response over a large frequency band. The FSS equivalent admit-



tance/impedance is derived directly from the method of moment (MoM) matrix, by a proper projection onto the Floquet modes.

In this work, the method is extended to the analysis and synthesis of FSS with losses. The method allows to synthesize the scattering response of an FSS, from the identification of a few parameters (poles and residues of the equivalent FSS admittance/impedance matrix) which exhibit a weak dependence on the angle of incidence. This property implies an MoM analysis of the FSS for a limited set of incidence angles. The overall response is then interpolated with a numerically efficient algorithm. Unlike the technique described in [7], here the analytical matching of pole and zeros is substituted with an analytical matching of poles and residues; this allows the generalization of the generalized Foster's properties to all the terms of the admittance (impedance) matrix in case of losses.

This chapter is organized as follows. Introduction provides a brief overview of the spectral domain Floquet waves (FW)-based MoM, for both patch-type and aperture-type FSS. In MoM Solution, a FW-based network and the relevant admittance/impedance matrix at the accessible modal ports are defined, with emphasis on the dominant mode two-ports admittance network. Accessible Mode Admittance Network presents some important properties of the two-ports FSS-network matrices and it indicates how they can be used in order to obtain an analytical approximation of the FSS-network matrix entries. In Properties of FSS-Network Matrix Entries an application-oriented algorithm is presented for the use of the method in conjunction with ray-tracing techniques. In Application Oriented Algorithm numerical results obtained from full-wave analysis and from the pole-residues analytical reconstruction are compared. Conclusions are drawn in Numerical Results.

## MoM Solution

Let us consider an infinite planar FSS consisting of patches printed on a multilayer dielectric slab. We will first describe the MoM analysis associated with patch-type FSS and next we will briefly present the results to aperture-type FSS obtained with a similar process. A rectangular  $(x, y, z)$  reference system is assumed with the  $z$  axis orthogonal to the FSS and the origin at the FSS level. The periodicities of the FSS are  $d_x$  and  $d_y$  along  $x$  and  $y$ , respectively. An incident, either transverse electric (TE) or transverse magnetic (TM), plane wave is assumed to illuminate the structure, with zero phase at the origin of the reference system. The incident plane wave imposes a phasing  $k_x$  and  $k_y$  in the principal directions, with  $k_x^2 + k_y^2 < \omega^2 / c^2$ .

The numerical computation of the equivalent currents at the interface of the planar periodic structure is performed via a numerical solution of the electric field integral equation (EFIE) by using a spectral periodic MoM approach. More than discussing the numerical implication of the MoM scheme, our objective here is to construct an appropriate form of the admittance matrix to characterize the FSS surface.

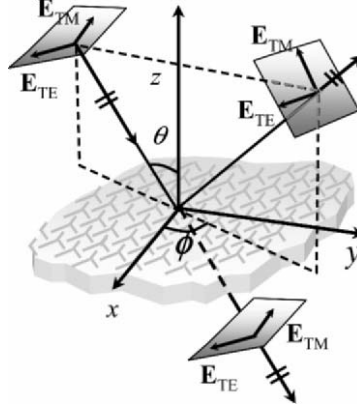


**Fig. 1.** A planar patch-type FSS and relevant plane wave excitation for TE and TM polarization

Due to the periodicity of the problem, the analysis can be reduced to that of a single periodic cell, with phase-shift boundary conditions applied to the ideal vertical walls. By applying the equivalence theorem (Fig. 2), an electric current distribution is assumed on the region of the metallic patches, radiating with the Green's function (GF) of the grounded slab. By imposing the boundary conditions on the surface of the metallic patches, the EFIE is derived, as follows:

$$\mathbf{E}_s(\mathbf{J}) + \mathbf{E}_{\text{imp}} = 0, \quad (1)$$

where  $\mathbf{E}_s$  is the field radiated by the currents  $\mathbf{J}$  induced on the dipoles, and  $\mathbf{E}_{\text{imp}} = \mathbf{E}_{\text{inc}} + \mathbf{E}_{\text{ref}}$  is the impressed field at the interface (in the absence of printed dipoles), which is given by the sum of the incident ( $\mathbf{E}_{\text{inc}}$ ) and reflected ( $\mathbf{E}_{\text{ref}}$ ) fields. From here on, the bold characters indicate vectors and the carets indicate unit vectors. As suggested by Tascone and Orta in [2], the equivalent currents  $\mathbf{J}$  are expressed in terms of basis functions,

$$\mathbf{J}(\mathbf{r}_t) = \sum_{n=1}^N I_n \mathbf{f}_n(\mathbf{r}_t), \quad (2)$$

where  $\mathbf{r}_t = x\hat{x} + y\hat{y}$  denotes the two-dimensional space vector. Figure 2 shows subdomain triangular basis functions, but entire domain basis functions can be used as well.

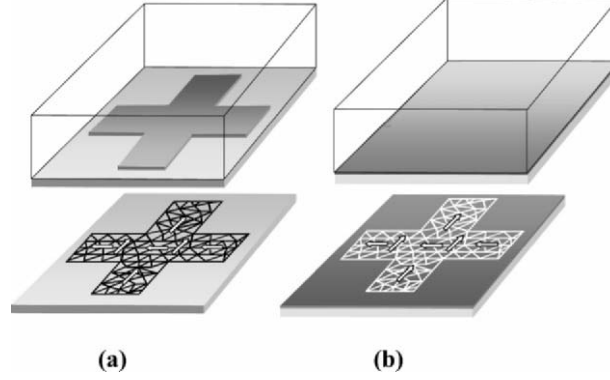


**Fig. 2.** Application of the equivalence principle to the basic cell of (a) patch-type FSS and (b) aperture-type FSS. Phase shift conditions are imposed on the vertical walls. A triangular mesh is shown, with subdomain basis functions used for the expansion of the electric

Let us denote by  $k_{xp'} = k_x + 2\pi p'/d_x$ ,  $k_{yq'} = k_y + 2\pi q'/d_y$  the FW wavenumbers in the  $x$  and  $y$  direction, respectively, and by  $\mathbf{k}_q = k_{xp'}\hat{x} + k_{yq'}\hat{y}$  the relevant vector form, where  $q$  denotes the two FW indices  $(p', q')$ . By denoting with  $\boldsymbol{\beta}_q$  the nodes of the reciprocal lattice,  $\boldsymbol{\beta}_q = \frac{2\pi p'}{d_x}\hat{x} + \frac{2\pi q'}{d_y}\hat{y}$ , and with  $\mathbf{k}$  the impressed vector wavenumber,  $\mathbf{k} = k_x\hat{x} + k_y\hat{y}$ , we obtain  $\mathbf{k}_q = \mathbf{k} + \boldsymbol{\beta}_q$ , with  $q = 0, 1, 2, \dots$  and  $\mathbf{k}_0 = \mathbf{k}$  by definition. It is also useful to introduce the normalized spectral vectors

$$\hat{\sigma}_q = \frac{\mathbf{k}_q}{\sqrt{\mathbf{k}_q \cdot \mathbf{k}_q}} ; \quad \hat{\alpha}_q = \hat{z} \times \hat{\sigma}_q \quad (3)$$

as a spectral basis to describe TM and TE field components, respectively. By using a Galerkin spectral MoM approach, (1) is reduced to the matrix equation

$$\bar{\bar{Z}}_{\text{MoM}} \bar{I} = \bar{V}, \quad (4)$$

where  $\bar{V} = \{V_m\}_{m=1, N}^T$  is the known column vector of the complex amplitude of the impressed field on the  $\mathbf{f}_n$  basis,  $\bar{I} = \{I_n\}_{n=1, N}^T$  is the column vector of the current expansion, and  $\bar{\bar{Z}}_{\text{MoM}} = \{Z_{mn}^{\text{MoM}}\}_{n, m=1, N}$  is the MoM impedance matrix, with entries given in an appropriate TE/TM form via

$$Z_{mn}^{\text{MoM}} = \sum_{q=0}^{M-1} \tilde{\mathbf{F}}_m^*(\mathbf{k}_q) \cdot [Z_{\text{GF}}^{\text{TM}}(\mathbf{k}_q) \hat{\sigma}_q \hat{\sigma}_q + Z_{\text{GF}}^{\text{TE}}(\mathbf{k}_q) \hat{\alpha}_q \hat{\alpha}_q] \cdot \tilde{\mathbf{F}}_n(\mathbf{k}_q). \quad (5)$$

In (5),  $\tilde{\mathbf{F}}_n(\mathbf{k})$  [ $\tilde{\mathbf{F}}_m(\mathbf{k})$ ] is the Fourier transform of the basis [test] function  $\mathbf{f}_n(\mathbf{r}_t)$  [ $\mathbf{f}_m(\mathbf{r}_t)$ ], sampled at the FW wavenumbers  $\mathbf{k}_q$ , and  $Z_{\text{GF}}^{\text{TM/TE}}(\mathbf{k})$  are the TM/TE components of the individual element spectral electric field GF, sampled at the

vector FW wavenumber  $\mathbf{k}_q$ . In (5), the modal FW expansion is truncated at the integer  $M-1$  with  $M$  larger than  $N$ ; this is an obvious consequence of the continuity of the FW on the entire periodicity cell, which implies the use of more FW modes than basis functions to describe the patch current. The GF impedances can be found by solving the pertinent transmission line problem representing the stratification for the TE and TM case. The MoM matrix can be expressed in the compact form as

$$\overline{\overline{Z}}_{\text{MoM}} = \overline{\overline{Q}} \overline{\overline{Z}}_{\text{GF}} \overline{\overline{Q}}, \quad (6)$$

where  $\overline{\overline{Z}}_{\text{GF}} = \text{diag}\{Z_{\text{GF}}^{\text{TM}}(\mathbf{k}_q), Z_{\text{GF}}^{\text{TE}}(\mathbf{k}_q)\}_{q=0, M-1}$  is a diagonal  $2M \times 2M$  matrix,  $\overline{\overline{Q}} = \{Q_{q,n}^{\text{TM}}, Q_{q,n}^{\text{TE}}\}_{\substack{q=0, M-1 \\ n=1, N}}$  is a  $2M \times N$  matrix and  $\overline{\overline{Q}}^H = \{Q_{m,q}^{\text{TM}*}, Q_{m,q}^{\text{TE}*}\}_{\substack{m=1, N \\ q=0, M-1}}^T$  is an  $N \times 2M$  matrix, the superscript  $H$  denoting transpose conjugate. The entries of the  $Q$  matrices are given by  $Q_{i,q}^{\text{TM}} = \tilde{\mathbf{F}}_i(\mathbf{k}_q) \cdot \hat{\sigma}_q$ ,  $Q_{i,q}^{\text{TE}} = \tilde{\mathbf{F}}_i(\mathbf{k}_q) \cdot \hat{\alpha}_q$  ( $i=n, m$ ).

For an aperture-type FSS, the FSS is substituted by a continuous, infinitely thin PEC screen with magnetic current distribution on both sides; these currents have equal amplitude and opposite signs on the two different sides to ensure the continuity of the electric field through the aperture. The integral equation which imposes the continuity of the magnetic field is  $\mathbf{H}_s^+(\mathbf{M}) + \mathbf{H}_{\text{imp}} = \mathbf{H}_s^-(-\mathbf{M})$ , where the superscript  $+$  and  $-$  refer to the Green's function of the upper and lower region, respectively. The magnetic current is expanded in terms of basis functions

$$\mathbf{M}(\mathbf{r}_t) = \sum_{n=1}^N V_n \mathbf{g}_n(\mathbf{r}_t) \times \hat{z}. \quad (7)$$

Imposing the continuity of the magnetic field leads to the following representation

$$\overline{\overline{Y}}_{\text{MoM}} \overline{\overline{V}} = \overline{\overline{I}}, \quad (8)$$

where  $\overline{\overline{V}} = \{V_n\}_{n=1, N}^T$  is the unknown column vector,  $\overline{\overline{I}} = \{I_m\}_{m=1, N}^T$ ,  $I_m = -\tilde{\mathbf{G}}_m^*(\mathbf{k}) \cdot \mathbf{H}_{\text{imp}}(\mathbf{k})$  is the known column vector of the impressed magnetic field on the MoM basis. The MoM matrix may be expressed in the compact form

$$\overline{\overline{Y}}_{\text{MoM}} = \overline{\overline{P}} \overline{\overline{Y}}_{\text{GF}} \overline{\overline{P}}, \quad (9)$$

where  $\overline{\overline{Y}}_{\text{GF}} = \text{diag}\{Y_{\text{GF}}^{\text{TM}}(\mathbf{k}_q), Y_{\text{GF}}^{\text{TE}}(\mathbf{k}_q)\}_{q=1, M} = \overline{\overline{Z}}_{\text{GF}}^{-1}$  is a diagonal  $2M \times 2M$  matrix, obtained by solving the GF  $z$ -transmission line for each FW wavevector,  $\overline{\overline{P}}^H = \{P_{m,q}^{\text{TM}*}, P_{m,q}^{\text{TE}*}\}_{\substack{m=1, N \\ q=0, M-1}}^T$  is an  $N \times 2M$  matrix, and  $\overline{\overline{P}} = \{P_{q,n}^{\text{TM}}, P_{q,n}^{\text{TE}}\}_{\substack{q=0, M-1 \\ n=1, N}}$  is a  $2M \times N$  matrix, whose components are given by  $P_{i,q}^{\text{TM}} = \tilde{\mathbf{G}}_i(\mathbf{k}_q) \cdot \hat{\sigma}_q$ ,  $P_{i,q}^{\text{TE}} = \tilde{\mathbf{G}}_i(\mathbf{k}_q) \cdot \hat{\alpha}_q$  ( $i = n, m$ ), being  $\tilde{\mathbf{G}}_i(\mathbf{k})$  the Fourier transform of  $\mathbf{g}_i(\mathbf{r}_t)$ .

## Accessible Mode Admittance Network

Let us assume that we are observing the field at a certain distance  $z$  from the FSS. In this case, the FW modes that are completely attenuated do not contribute to the field at  $z$ . In a multimode network description, this implies that the relevant modal ports can be considered as not “accessible” to the observer, and therefore neglected. This concept was introduced by Rozzi [8] for waveguide problems and is commonly used to calculate the coupling between FSSs located at different levels [2]. When we are dealing with the scattering from an FSS, the only accessible mode is the propagating one. On the other hand, when dealing with the FSS interaction with a proximity located antenna or array, accessible modes also include higher order evanescent modes that have a nonnegligible amplitude at the antenna/array level. Denoted by  $2M_A$  the number of accessible TE-TM ports, consider the  $2M_A$ -port network in Fig. 3, where each port is associated to an FW mode of TE or TM type. This network consists of a multiport “FSS network” loaded in parallel at each port by a modal TE or TM transmission line representing the unprinted multilayer dielectric slab. The FSS-network is conveniently characterized by  $2M_A \times 2M_A$  admittance (impedance) matrices

$$\bar{I}_{\text{FW}}^{\text{FSS}} = \bar{Y}_{\text{FSS}} \bar{V}_{\text{FW}} \quad (10)$$

for patch-type FSS

$$\bar{V}_{\text{FW}} = \bar{Z}_{\text{FSS}} \bar{I}_{\text{FW}}^{\text{FSS}} \quad (11)$$

for aperture-type FSS, where  $\bar{I}_{\text{FW}}^{\text{FSS}} = [I_{\text{FW},q}^{\text{TM}}, I_{\text{FW},q}^{\text{TE}}]_{q=0, M_A-1}^T$  ( $\bar{V}_{\text{FW}} = [V_{\text{FW},q}^{\text{TM}}, V_{\text{FW},q}^{\text{TE}}]_{q=0, M_A-1}^T$ ), is the vector of the FW amplitudes of the magnetic (electric) field expansion at the FSS level and denotes the FW electric current flowing into the FSS network (the FW voltage at the ports).

The FSS-network matrices are given as a function of  $\bar{Z}_{\text{MoM}}$  matrix as

$$\bar{Y}_{\text{FSS}}(k_x, k_y; \omega) = \bar{q} \left( \bar{Z}_{\text{MoM}} \right)^{-1} \bar{q} \left[ \bar{Y}_{\text{GF}} - \bar{q} \left( \bar{Z}_{\text{MoM}} \right)^{-1} \bar{q} \right]^{-1} \bar{Y}_{\text{GF}} \quad (12)$$

for patch-type FSS, and

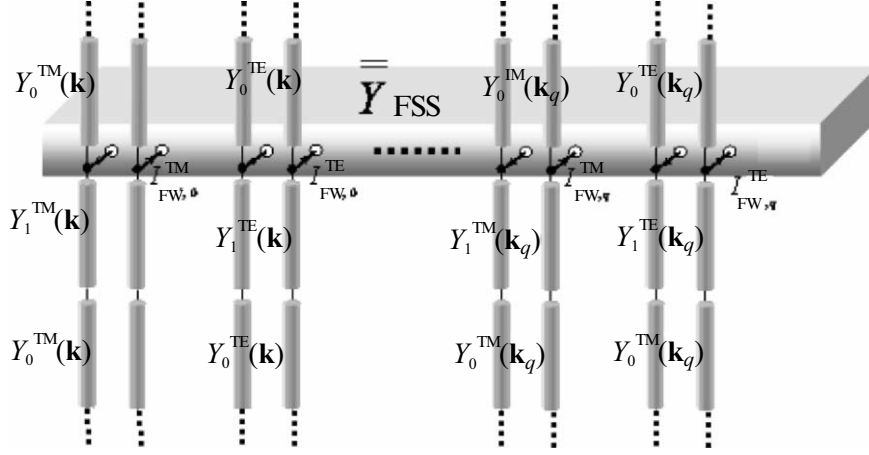


**Fig. 3.** Multiport accessible FW-mode network and relevant transmission-line parameter  $Y_0^{TM}(\mathbf{k}) = \frac{\omega \mathcal{E}_0}{k_z}$ ,  $Y_0^{TE}(\mathbf{k}) = \frac{k_z}{\omega \mu_0}$ ;  $Y_1^{TE}(\mathbf{k}) = \frac{k_{z1}}{\omega \mu_0}$ ,  $Y_1^{TM}(\mathbf{k}) = \frac{\omega \mathcal{E}_r \mathcal{E}_0}{k_{z1}}$  are the modal  $z$ -transmission line TE-TM characteristic admittances relevant to the free-space (subscript 0) and the dielectric regions (subscript 1), respectively, and  $k_z = \sqrt{k^2 - k_x^2 - k_y^2}$  and  $k_{z1} = \sqrt{\epsilon_r k^2 - k_x^2 - k_y^2}$

$$\bar{Z}_{FSS}(k_x, k_y; \omega) = \bar{p} \left( \bar{Y}_{MoM} \right)^{-1} \bar{p} \left[ \bar{Z}_{GF} - \bar{p} \left( \bar{Y}_{MoM} \right)^{-1} \bar{p} \right]^{-1} \bar{Z}_{GF} \quad (13)$$

for aperture-type FSS. In (12) and (13), the dependence on the frequency and on the impressed wave vector has been emphasized, and  $\bar{q} = \{Q_{q,n}^{TM}, Q_{q,n}^{TE}\}_{q=0, M_A-1, n=1, N}$ ,  $\bar{p} = \{P_{q,n}^{TM}, P_{q,n}^{TE}\}_{q=0, M_A-1, n=1, N}$ , are matrices of size  $2M_A \times N$  which project the MoM basis onto the FW basis (and vice versa for their transpose conjugate  $\bar{q}^H$  and  $\bar{p}^H$ ).

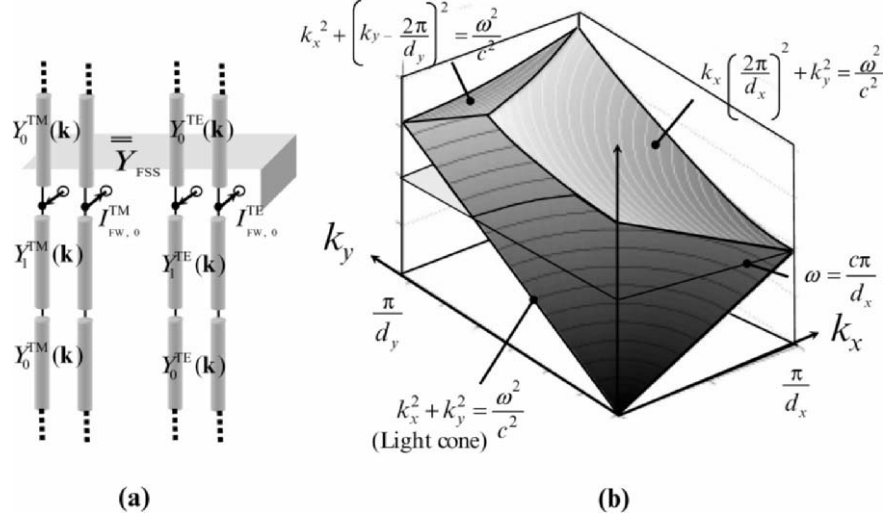


**Fig. 4.** (a) Two-port modal network relevant to propagating the TE and TM FW-mode. (b) Diagram  $(k_x, k_y) - \omega$  (the figures refer to a case  $d_x > d_y$ ). Below the two portions of the upper conical surfaces, the higher order FW modes are cutoff. This region identifies the validity of the FSS-network in (a). The free-space speed of light is denoted by  $c$ . The “light cone” is also depicted, and its surface identifies the cutoff of the dominant propagating mode

### Dominant-Mode Two-Port Admittance Network

Let us assume that only one pair of TE-TM propagating FW modes are accessible for a given  $z$  level ( $M_A = 1$ ). As a special case of (10) (capacitive FSS) and (11) (inductive FSS), the FSS is modeled by the two-port network shown in Fig. 4a. The utilization of a two-port network is subject to the existence of an observation level  $z$  where the dominant TE and TM FW-modes are the *only* accessible modes. This implies that all the higher-order FW-modes must be cutoff. The cut-off condition of the higher-order FW-modes implies a limitation to the observable dispersion diagram. Figure 4b shows a dispersion diagram with angular frequency  $\omega$  on the vertical axis and the wavenumbers  $k_x$  and  $k_y$  on the horizontal axes. Due to the periodicity of the FW spectrum, the observation may be restricted to the Brillouin region  $(-\pi/d_x < k_x < \pi/d_x, -\pi/d_y < k_y < \pi/d_y)$ , with a further (due to the symmetry of the structure) restriction to positive values of  $k_x$  and  $k_y$ . The cut-off region for higher-order modes is imposed by the conditions  $k_{\xi\eta}^2 + k_{\eta\eta}^2 > \omega^2/c^2$  for  $(\xi, \eta) \neq (0, 0)$ . As a consequence, within the observed wavenumber plane, the cut-off region is delimited by portions of two cones whose vertices are at the FW wavenumbers closest to the origin (details are shown in Fig. 4b). A third cone is depicted in the same figure; its surface  $k_x^2 + k_y^2 = \omega^2/c^2$  defines the cut-off of the dominant mode. Although this

cone is not essential for the validity of the two-port model, it bounds the slow-wave region and is important for the study of the dispersion properties. Intersections of this cone with the vertical planes  $\omega-k_x$  and  $\omega-k_y$  identify the well-known “light lines” in these two planes. Figure 4b also shows the horizontal plane  $\omega = \omega_M = c\pi/\max(d_x, d_y)$ , which is the minimum frequency at which the higher-order FW modes are attenuated for *any* wavenumber.

## Properties of FSS-Network Matrix Entries

Here we describe the properties of the two-port FSS matrix entries in order to establish a convenient analytical form. For the sake of convenience, let us consider each element of the matrix as a function dependent on  $\theta$  and  $\phi$ , where  $k_x = k_0 \sin\theta \cos\phi$  and  $k_y = k_0 \sin\theta \sin\phi$ . In this case, the cut-off region shown in Fig. 4 can be expressed as a function of  $\theta$  and  $\phi$ , obtaining the surfaces presented in Fig. 5.

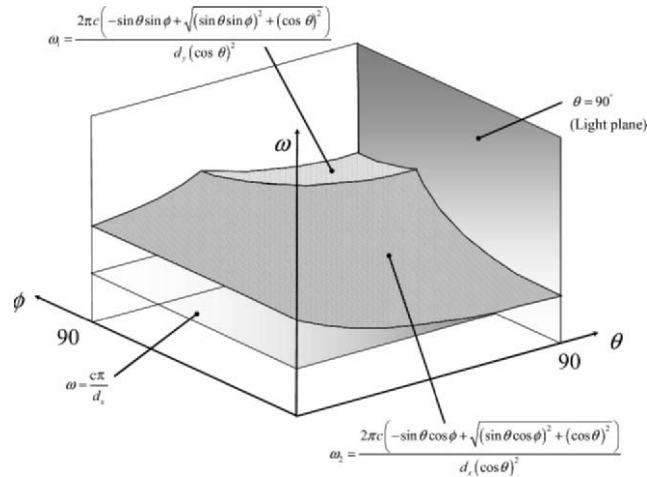


**Fig. 5.** Monomodal propagation region for the fundamental FW  $(\theta, \phi) - \omega$  (the figures refer to a case  $d_x > d_y$ ). Below the two portions of the upper surfaces  $\omega_1(\theta, \phi)$  and  $\omega_2(\theta, \phi)$ , the higher order FW modes are cut off. This region identifies the validity of the FSS-network in Fig. 4a. The free-space speed of light is denoted by  $c$ . The “light plane” is also depicted, and its surface identifies the cut-off of the dominant propagating mode

## Absence of Losses

Consider for simplicity the patch-type FSS and denote by  $Y_{\text{FSS}}^{ij}(\theta, \phi, \omega)$  the entries of the two-port dominant mode admittance matrix. In the absence of losses, the



equivalent FSS admittance is purely reactive for every  $\omega$ . Note that this is valid within the cut-off region of the higher-order FW-modes described in Fig. 4; indeed, for frequency where another pair of TE-TM modes is propagating, the two-port FSS matrix loses its properties to be purely reactive. The imaginary part of the (purely imaginary) entries, seen as a function of frequency, possesses the same pole structure of a passive LC admittance matrix, with capacitive behavior at low frequency. Moreover, from network theory, it can be demonstrated that all the entries of the FSS-network matrix have the same poles [9]. Thus, the properties of the FSS matrix entries are:

1. all the entries  $Y_{\text{FSS}}^{ij}(\theta, \phi, \omega)$  possess the same poles
2. the poles lie on the real  $\omega$ -axis and are simple
3. a zero must be in  $\omega = 0$
4. the poles are symmetrically displaced with respect to the origin

An important consequence of these properties is that the admittance frequency function can be approximated by the following limited-bandwidth expression

$$Y_{\text{FSS}}^{ij}(\theta, \phi, \omega) = \sum_{n=1}^N \frac{-2ja_n^{ij}(\theta, \phi)\omega}{\omega^2 - \beta_n^2(\theta, \phi)} + ja_0^{ij}(\theta, \phi)\omega. \quad (14)$$

In (14) the following properties hold

5.  $a_n^{ij}(\theta, \phi)$  represents the ( $\omega$ -independent) residue associated to the  $n$ th pole in the  $\omega$ -plane and it is a real function of the incident angle. For the diagonal entries  $a_n^{ii}(\theta, \phi)$  is real and positive

### Small Losses

In the case of small losses, each FSS network matrix entry can be approximated as

$$Y_{\text{FSS}}^{ij}(\theta, \phi, \omega) = \sum_{n=1}^N \frac{-2ja_n^{ij}(\theta, \phi)\omega}{\omega^2 - \beta_n^2(\theta, \phi) - j\omega\gamma_n(\theta, \phi)} + ja_0^{ij}(\theta, \phi)\omega, \quad (15)$$

the same expression can be written for  $Z_{\text{FSS}}^{ij}(\theta, \phi, \omega)$  entries for aperture-type FSS.

In (15) small losses have been assumed, i.e.,  $\beta_n(\theta, \phi) \gg \gamma_n(\theta, \phi)$ , so that  $-\gamma_n(\theta, \phi)/2$  and  $\beta_n(\theta, \phi)$  are the real and imaginary part of the pole, respectively. Under the small losses assumption the poles are very close to the real  $\omega$ -axis and their position in the complex  $\omega$  plane can be evaluated from the real axis frequency variation of the imaginary part of the matrix entries. The following properties are verified:

1.  $a_n^{ij}(\theta, \phi)$  represents the  $\omega$ -independent residue associated to the  $n$ th pole and in the  $\omega$  plane it is a real function of the incidence angle. For diagonal entries  $a_n^{ii}(\theta, \phi)$  real and positive

2. The quantities  $a_0^{ij}(\theta, \phi), a_\infty^{ij}(\theta, \phi)$  are independent on  $\omega$  and represent the quasistatic capacitance (inductance) of the patch-type (aperture type) FSS. Their dependence on  $(\theta, \phi)$  is found to be very weak and thus very easy to approximate;

Equation (15) allows an analytical definition of the admittance (impedance), over a broad frequency range, on the basis of the determination of the aspect-dependent poles and residues. As will be discussed later on, they can be calculated for a few values of the incidence angles, and can then be approximated.

We note that the numerical calculation of  $\overline{Y}_{\text{FSS}}$  in (15) is accurate at those angles where  $Y_{\text{FSS}}^{ij}$  exhibits poles or zeros, because the MoM matrix is well-conditioned there.

### **Approximation of Poles and Residue**

From the approximation (15), the analytical representation of the FSS in a broad frequency range can be derived from the following functions

$$a_n^{ij}(\theta, \phi), \beta_n(\theta, \phi), \gamma_n(\theta, \phi), a_0^{ij}(\theta, \phi). \quad (16)$$

In many practical cases, the poles that should be considered are very few. As a practical rule the approximation is very good if one includes the poles within the frequency range of interest plus the closer one outside the same range. Since in many cases the properties of the FSS are used at low frequency regime or close to the first resonance, the inclusion of one or two poles is satisfactory in most of the cases.

All the functions in (16) show a very weak variation against the incidence angles and are easy to approximate from the data related to a few angular samples by a simple trigonometric polynomial form

$$\tilde{\Psi}_n^{ij}(\theta, \phi) = \sum_{n_1=0}^{N_1} \sum_{n_2=0}^{N_2} \left[ \delta_{n_1 n_2} \cos(n_2 \phi) \cos(2n_1 \theta) + \eta_{n_1 n_2} \sin(n_2 \phi) \sin(2n_1 \theta) \right], \quad (17)$$

where  $\delta_{n_1 n_2}$  and  $\eta_{n_1 n_2}$  are coefficients calculated on the basis of a least mean square approximation. In many practical cases,  $N_1$  and  $N_2$  are very small integer numbers. As an illustrative example, Fig. 6 presents the approximated curves for the ring-dipole FSS shown in the inset.

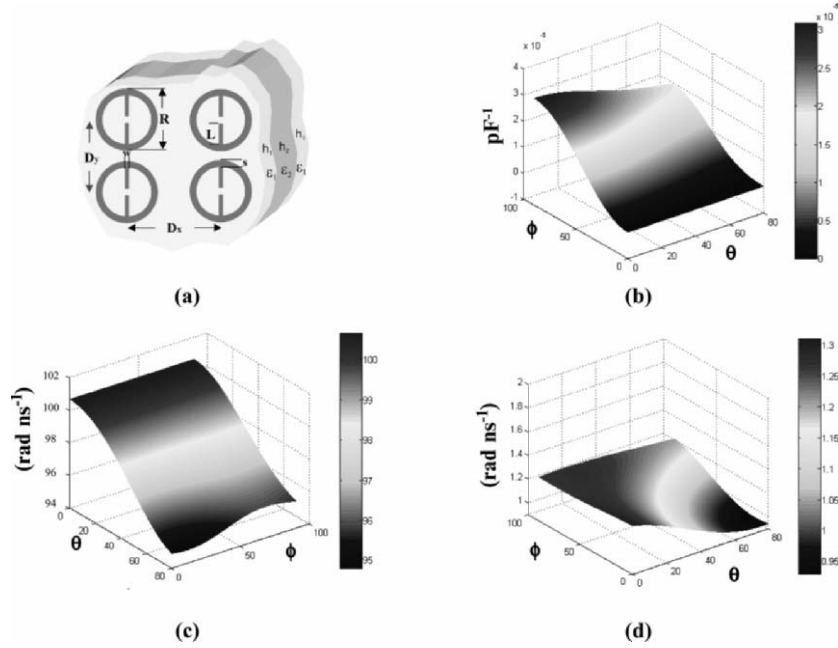


**Fig. 6.** Approximated poles and residue surfaces for a ring-dipole FSS. (a) Structure layout;  $D_x = 8.5$  mm,  $D_y = 6.5$  mm,  $L = 1.9$  mm,  $w = 0.4$  mm,  $R = 5.57$  mm,  $s = 1.18$  mm,  $h_1 = 0.75$  mm,  $\epsilon_{r1} = 4.4 - j0.0704$ ,  $h_2 = 2.7$  mm,  $\epsilon_{r2} = 1.13 - j0.00565$ . (b) Approximated surfaces for a residue  $a_2^{11}(\theta, \phi)$ . (c) An example of an approximated surfaces for the real part of one pole  $\beta_2^{11}(\theta, \phi)$  and (d) for the imaginary part of one pole  $\gamma_2^{11}(\theta, \phi)$ . For all this function the approximated surfaces have been evaluated with  $N_1 = 2$  and  $N_2 = 1$

## Application-Oriented Algorithm

The analysis of curved FSS reflectors or frequency selective radomes, which are large in terms of a wavelength, are often based on the flat surface approximation of the local curved structure and on the decomposition of the illuminating wave in terms of local rays or beams. These schemes use local reflection and transmission coefficients to calculate local currents or scattered fields, thus requiring the calculation of the scattering matrix for a large number of incident aspects and frequencies. The pole-residue method described here allows an agile transmission of data from a EM solver for the analysis of FSS and a EM solver based on high-frequency (HF) method (e.g., Physical Optics, Geometric Optics, etc.). The present polo-residue matching scheme, thanks to the capability to reconstruct an analytical form of the admittance matrix, with the use of few parameters, establishes a link from the FSS solver and the HF solver by exchanging data relevant to the few interpolation coefficients. The logical scheme of this data exchange is

shown in Fig. 7. Data, relevant to an angular under sampling of the FSS matrix entries, feed a “Data Compressor” which calculates the coefficients of the least mean square approximation of poles and residues. The coefficients  $\delta_{n_1 n_2}$  and  $\eta_{n_1 n_2}$  are thus transmitted to the HF solver which is provided by a “Decoder Module”. This module constructs the analytical form of  $\bar{Y}_{\text{FSS}}(\theta, \phi, \omega)$  over continuous angles and frequencies. From this latter matrix, the scattering matrix is obtained from simple algebraic manipulations. This scheme does not alter the internal architecture of the solvers and implies a preprocessing time which is negligible with respect to the overall calculation time.

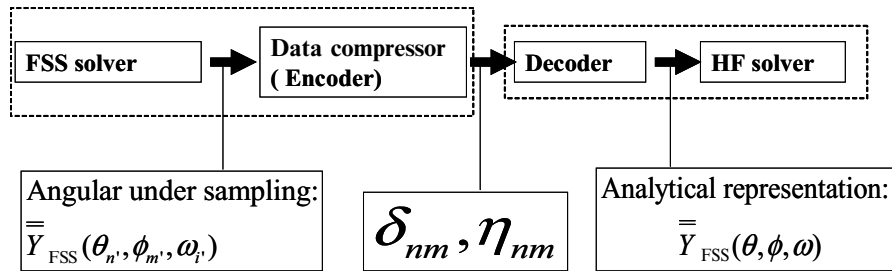
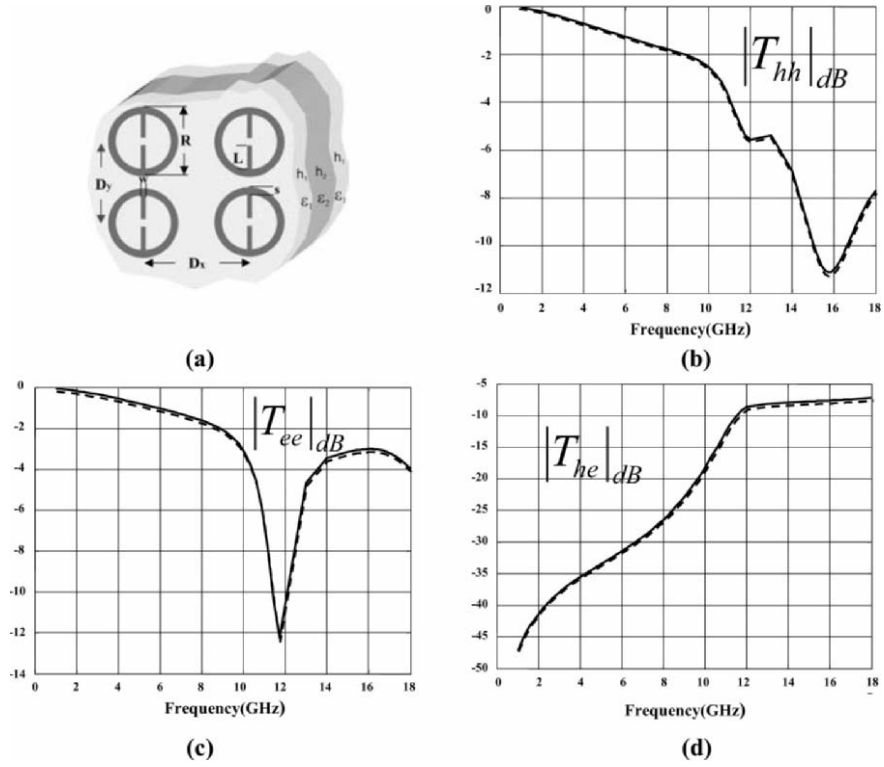


Fig. 7. Logical structure of the data compression algorithm

## Numerical Results

The analytical closed form of the  $Y_{\text{FSS}}^{ij}(\theta, \phi, \omega)$  have been used to reconstruct the scattering parameters of the entire structures shown in the inset of the Figs. 8 and 9. Both the figures show the transmission coefficients for an incidence plane wave. The continuous lines are the full-wave analysis results while the dotted ones are the reconstructed solutions via the present method. A good agreement between the two solutions is found for all the components of the scattering parameters



**Fig. 8** Transmission coefficients for an incidence plane wave impinging from  $\theta=25$  and  $\phi=57$ . (a) FSS layout (the geometry is the same of that in Fig.6 (a)). Continuous lines refer to full-wave analysis results obtained by the spectral domain method of moment; dotted lines refer to analytical solution reconstructed via pole-residue method. (b) TE-polarized incident wave and TE-polarized transmitted wave, (c) TM-polarized incident wave and TM-polarized transmitted wave, (d) TE-polarized incident wave and TM-polarized transmitted wave.

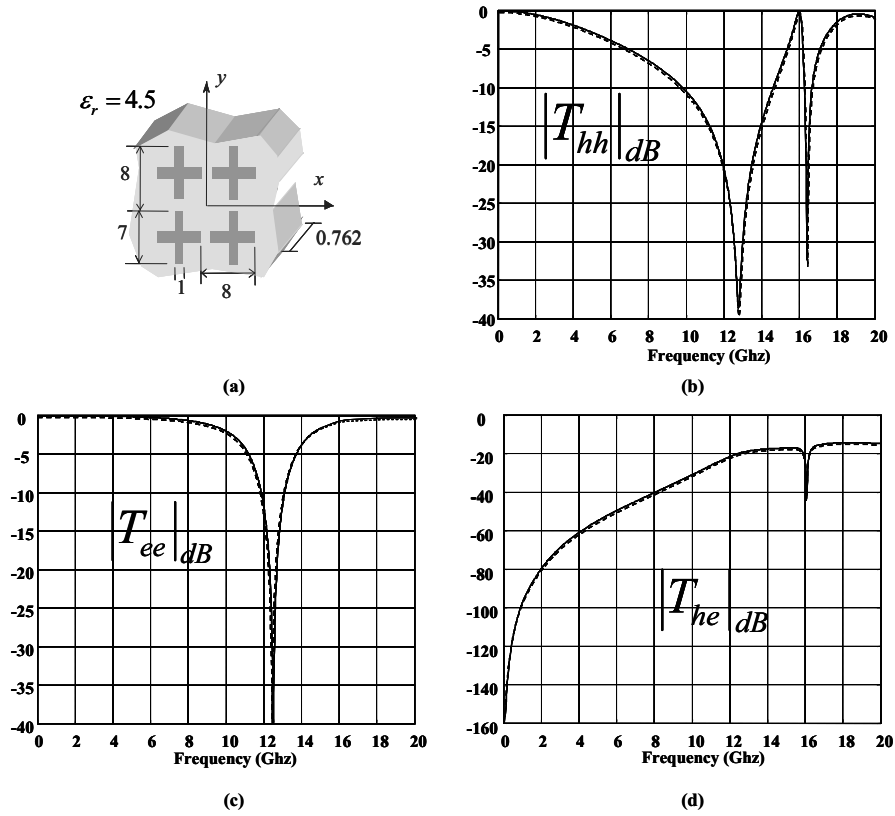


**Fig. 9.** Transmission coefficients for an incident plane wave impinging from  $\theta=60$  and  $\phi=30$ . (a) FSS layout. Continuous lines refer to full-wave analysis results obtained by the spectral domain method of moment; dotted lines refer to analytical solution reconstructed via pole-residue method. (a) TE-polarized incident wave and TE-polarized transmitted wave, (b) TM-polarized incident wave and TM-polarized transmitted wave, (c) TE-polarized incident wave and TM-polarized transmitted wave.

## Conclusions

In this paper, a method for obtaining the analytical solution of the admittance (scattering) matrix of FSSs is presented. This method has been illustrated here with reference to a patch-type FSS or aperture-type FSS. On the basis of a spectral MoM solution, an equivalent network-matrix is defined with the ports corresponding to the accessible TE and TM FW of the exact Floquet expansion. The admittance matrix is then characterized by poles and residues associated to the matrix entries for a few values of the incidence angles. The identification of a set of sur-

faces associated with the poles and residue of the FSS and their regularity allows the interpolations of these surfaces by low-order polynomials. Network theory properties allow the approximation of the entries in terms of summation of rational functions. The consequent closed form expression is applied to evaluate the generalized scattering matrix as a function of the angle and polarization of incidence plane wave.

It is worth remarking that the full-wave analysis for each incident aspect  $(\theta, \phi)$  is very efficient, since it implies the inversion of a moderate size MoM matrix; however, obtaining accurate information on the continuous  $(\theta, \phi)$  domain requires a large amount of computational time. The main peculiarity of the method presented here is concerned with the possibility of reconstructing an analytical closed form the generalized scattering matrix in the continuous  $(\theta, \phi)$  domain over a large frequency range, starting from the response of the structure at a few samples. This is particularly useful to establish a link between an FSS solver and an HF solver for the analysis of large FSS curved structure or frequency selective radome no matter about the internal code solver structure. The general process described here can be applied for the synthetic description of different wave phenomena, like those relevant to surface wave propagation and electromagnetic band-gap description, near-field interaction (Green's function) and wave diffraction involving periodic surfaces.

## References

- [1] B.A. Munk, *Frequency Selective Surfaces: Theory and Design*, Wiley, Berlin Hiedelberg New York, 2000
- [2] J.C. Vardaxoglou, *Frequency Selective Surfaces*, Research Studies Press Ltd, Taunton, England, 1997
- [3] P.-S. Kildal, "Artificially soft and hard surfaces in electromagnetics," *IEEE Trans. Antennas Propag.* 38, 1537–1544, (1990)
- [4] S. Maci and P.-S. Kildal, "Hard and soft gangbuster surfaces," *Proceedings of the URSI International Symposium on Electromagnetic Theory*, Pisa, Italy, May 23–27, 2004, URSI, Pisa, 2004, Vol. 2, pp. 290–292
- [5] M. Bozzi, S. Germani, L. Minelli, L. Perregini, and P. deMaagt, "Efficient calculation of the dispersion diagram of planar electromagnetic band-gap structures by the MoM/BI-RME method," *IEEE Trans. Antennas Propag.*, Special Issue on Artificial Magnetic Conductors, Soft/Hard Surfaces, and Other Complex Surfaces 53, 29–35, (2005)
- [6] R.E. Collin, *Foundations for Microwave Engineering*, McGraw Hill, New York 1992
- [7] S. Maci, M. Caiazzo, A. Cucini, and M. Casaletti, "A pole-zero matching method for EBG surfaces composed of a dipole FSS printed on a grounded dielectric slab," *IEEE Trans. Antennas Propag.*, Special Issue on Artificial Magnetic Conductors, Soft/Hard Surfaces, and Other Complex Surfaces 53, 70–81, (2005)
- [8] T.E. Rozzi, "Network analysis of strongly coupled transverse apertures in waveguide," *Int. J. Circuit Theory Appl.* 1, 161–178, (1973)
- [9] E.A. Guillemin, *Synthesis of Passive Networks*, Robert E. Krieger, New York, 1977

# About Complex Extensions and Their Application in Electromagnetics

M.J.G. Morales<sup>1</sup>, C.D. Martinez<sup>1</sup> and E.G.-Ribas<sup>2</sup>

<sup>1</sup> Department Teoría de la Señal y Comunicaciones e I. T, Universidad de Valladolid,  
Campus Miguel Delibes, s/n. 47011 Valladolid, Spain,  
gonmor@tel.uva.es, cardeh@rest.tel.uva.es

<sup>2</sup> Área de Teoría de la Señal y Comunicaciones.  
Department IEECS, Universidad de Oviedo, Ant. Edificio de Ingenieros,  
Campus de Viesques, s/n. 33204 Gijón, Spain, egr@tsc.uniovi.es

## Abstract

This work is concerned with the analysis of the possibilities to perform complex transformations from solutions to wave equations which depend on a real variable into a complex-coordinates space. In first place, the solutions resulting from adding a constant imaginary term to the initial real coordinates have been explored in detail. A more general analysis concerning the possibilities to obtain valid complex transformations is next explored. The work itself frames into a “coming back to basics” procedure involving what we have named as Complex Signal Theory, necessary to fully understand the physical insight under the complex analysis of wave propagation problems.

## Introduction

The so-called *analytical continuation* of functions from real to complex variable has been extensively used from the 1970s as an analytical tool for solving electromagnetic problems, mainly those concerned with the radiation and scattering of Gaussian beams (refer, for instance, to [1, 2]). This kind of analysis has presented powerful possibilities from the practical point of view. That complex extension implies certain transformations from physical real quantities to nonphysical complex ones (the distance between two real positions becomes a complex distance between nonreal points, real angles become complex ones); new complex reflection and diffraction laws arise, together with physical descriptions in terms of complex rays, etc. Besides the practical uses of such an approach, we find both interesting and important to understand its physical insight and meaning and its possible interpretation.



For that purpose, the present authors have devoted some papers [3–6] to the analysis and interpretation of those complex quantities, along with the suitable parameterizations of the complex spaces arising thereof, and the corresponding real propagation space. Based on these results, the procedure is currently being extended to the analysis of scattering problems, obtaining also well-defined parameterizations for the induced currents [7] as well as the analysis of scattering fields and physical reflection–diffraction laws currently under investigation.

These results together with our initial aims suggested a *general scheme* of how the problem should be tackled, leading to a very important *coming back to basics* procedure involving what we have denominated as *Complex Signal Theory* [8]. This scheme involves (a) the revision and extension of a set of important theoretical concepts, and (b) the practical application of these theoretical analyses into Electromagnetics. The present work, framed in (a), is concerned with a reconsideration and possible extension of the idea of generating new or more general solutions of the (scalar) wave equation by a complex continuation of real points or coordinates in a previous solution. This work will summarize the results and conclusions obtained up to date regarding these questions by considering two successive phases.

In the first phase, introduced in *Complex Extensions*, the *complex extension* of a function, obtained by adding a constant imaginary part to the real coordinates, is considered. The aim here is to analyze the possibilities and restrictions of this technique when applied to problems which are described by a differential equation with its own boundary conditions, and in particular, to the 2D and 3D electromagnetic radiation and scattering problems. The second phase deals with a more general treatment of the complex extension, *general complex transformations* in *General Complex Transformations*, in which a real coordinate is converted into a complex function of the real coordinates of the position. The conditions to be imposed on the transformation to provide with valid solutions to the original real problem lead to a set of general equations; their analysis will provide with important conclusions about the possibilities of this kind of generalization.

## Complex Extensions

The starting point is a given function of real coordinates,  $G(\vec{r})$  which is a valid solution to a certain problem (wave equation plus boundary conditions), for instance, the Green's function of a particular EM problem. The possibilities of the complex extension will be explored by adding an imaginary displacement to the real argument of the function,  $\vec{r} \rightarrow \vec{r} = \vec{r} + i\vec{b}$  [4, 7] (usually represented by the original coordinates in which the problem was defined), and understanding and translating the meaning of such a function into the real space.<sup>1</sup> The underlying ideas of this

---

<sup>1</sup> For instance, the 2D radiated field by an infinite line current source in free space is proportional to  $H_0^{(1)}(k_0 |\vec{r} - \vec{r}_s|)$ . The usual complex transformation consists on adding an

analysis are directly related to answer questions like (a) is this an analytic continuation or, in fact, is a nonanalytic complex transformation? (b) is the same to complexify source locations than observation points? (c) is this procedure valid in any coordinates system?

The analytical study concerning this problem was based on the fact that the new set of solutions had to continue being valid solutions of the original wave equation; thus, the new associated problems arising from the complexification procedure (problems for which the new functions might be valid solutions) have been studied in detail for the complex extensions which leads to the transformation from homogeneous plane waves to inhomogeneous plane waves, from cylindrical waves to complex beams, and from spherical waves to complex revolution symmetry beams. As a particular application, the analysis of the complex radiation condition has been also studied in detail, as well as the relation between the original real coordinates space and the space of complex coordinates. The details of this analysis may be found in [9].

The main conclusions regarding these analyses may be summarized as follows (a) this type of complex transformation is not an analytical continuation from the real space into the complex one. This means that the nice properties associated to holomorphic functions do not hold in these problems; (b) only those coordinates that do not appear as metric coefficients in the wave equation are susceptible to be extended into a complex variable with the new solution continuing being a valid solution to the original wave equation<sup>2</sup>; (c) as a consequence, this kind of transformation will be only valid to represent inhomogeneous plane waves, complex beams, and 3D complex axis-symmetric beams from their corresponding real solutions, that is, plane waves, cylindrical waves and 3D spherical waves; (d) for the point source (3D) or line source (2D) problems in free space, the complex displacement of observation points is equivalent to the displacement of the source points; in the absence of sources, only the displacement of the observation points makes sense.

## General Complex Transformations

Let  $G(\zeta)$  be a given function of a real variable, any of the coordinates of a suitable 2D- or 3D-coordinate system, which is a valid solution to a certain 2D- or

---

imaginary constant term to the source coordinates,  $x_s = x_s - ib \cos \vartheta$ ,  $z_s = z_s - ib \sin \vartheta$  leading to  $H_0^{(1)}(k_0 |r - \mathbf{r}_s|)$

<sup>2</sup> For instance, the real angular variable  $\varphi$  may be extended into a complex variable  $\varphi = \varphi - i\nu$  in the polar description of a 2D free source problem,

$$\frac{1}{\rho} \frac{\partial}{\partial \rho} \left( \rho \frac{\partial G}{\partial \rho} \right) + \frac{1}{\rho^2} \frac{\partial^2 G}{\partial \varphi^2} + k^2 G = 0; \quad (1)$$

in this case, the metric coefficients  $1/\rho$  and  $1/\rho^2$  do not depend on variable  $\varphi$ . This extension, when applied to a homogeneous plane wave, provides with a valid description for the nonhomogeneous plane wave solution

3D-problem (wave equation plus boundary conditions). Next, the possibilities of a complex extension will be explored by considering the transformation from the real variable,  $\zeta$ , to a complex variable,  $\mathbf{w}$ , defined as an arbitrary function of position,  $\zeta \rightarrow \mathbf{w}(\vec{r}) = u(\vec{r}) + iv(\vec{r})$ . Note that the position might be expressed in a coordinate system at will. Obviously,  $G(\mathbf{w})$  satisfies the same wave equation in  $\mathbf{w}$  as  $G(\zeta)$  did respect to  $\zeta$ . For that,  $G(\mathbf{w})$  must be analytic in a certain domain of the complex  $\mathbf{w}$ -plane in order to guarantee the existence of derivatives of  $G(\mathbf{w})$ . The allowed transformations are those for which the new function  $g(\vec{r}) := G[\mathbf{w}(\vec{r})]$  is also a valid solution of the 2D- or 3D-wave equation. The underlying ideas to this problem are related to questions like (a) is the constant imaginary extension described in Sect. 2 the only valid transformation to obtain new descriptions of the solutions of a wave problem? (b) which are the conditions for the general transformation  $\mathbf{w}$  to provide with valid solutions to the wave equation? The cases for 2D plane waves, 2D cylindrical waves and 3D spherical waves with spherical symmetry have been carefully analyzed [8] leading to a number of interesting and important results that will be next summarized.

The extension  $x \rightarrow \mathbf{w}(x, y)$  in the 2D plane wave problem will be valid if the condition

$$\frac{\partial G}{\partial \mathbf{w}} \left( \frac{\partial^2 \mathbf{w}}{\partial x^2} + \frac{\partial^2 \mathbf{w}}{\partial y^2} \right) + k^2 G \left[ 1 - \left( \frac{\partial \mathbf{w}}{\partial x} \right)^2 - \left( \frac{\partial \mathbf{w}}{\partial y} \right)^2 \right] = 0 \quad (2)$$

is fulfilled. Arguing that  $G$  and  $dG/d\mathbf{w}$  are linearly independent, this condition leads to the following pair of equations,

$$\frac{\partial^2 \mathbf{w}}{\partial x^2} + \frac{\partial^2 \mathbf{w}}{\partial y^2} = 0 \text{ and } \left( \frac{\partial \mathbf{w}}{\partial x} \right)^2 + \left( \frac{\partial \mathbf{w}}{\partial y} \right)^2 = 1 \quad (3)$$

with the transformations  $\mathbf{w}$  being independent of  $k$ . By making the substitution  $\mathbf{w} = u(x, y) + iv(x, y)$  in the last equations, one concludes that  $\mathbf{w}(x, y)$  is not a holomorphic function. On the other hand, by differentiating the first equation (3) respect to  $x$  and  $y$  and using the second equation, one easily arrives to the conclusion that the only valid transformations are the linear ones, i.e.,  $\mathbf{w} = ax + by + c$  with  $a, b, c \in C$ , and  $a^2 + b^2 = 1$  (as it is the case in *Complex Extensions*).

The extension<sup>3</sup>  $\rho \rightarrow \mathbf{w}(\rho, \varphi) = \mathbf{w}(x, y)$  in the 2D cylindrical wave problem leads to the following condition on  $\mathbf{w}$ ,

$$\frac{\partial G}{\partial \mathbf{w}} \left( \frac{\partial^2 \mathbf{w}}{\partial x^2} + \frac{\partial^2 \mathbf{w}}{\partial y^2} - \frac{1}{\mathbf{w}} \left[ \left( \frac{\partial \mathbf{w}}{\partial x} \right)^2 + \left( \frac{\partial \mathbf{w}}{\partial y} \right)^2 \right] \right) + k^2 G \left[ 1 - \left( \frac{\partial \mathbf{w}}{\partial x} \right)^2 - \left( \frac{\partial \mathbf{w}}{\partial y} \right)^2 \right] = 0, \quad (4)$$

which can be split, on the same argument as before, in the pair of equations

<sup>3</sup> The problem is much more simple-stated and solved by using cartesian coordinates. That is the reason why we rewrite the transformation as  $\rho \rightarrow \mathbf{w}(x, y)$

$$\frac{\partial^2 \mathbf{w}}{\partial x^2} + \frac{\partial^2 \mathbf{w}}{\partial y^2} - \frac{1}{\mathbf{w}} = 0 \text{ and } \left( \frac{\partial \mathbf{w}}{\partial x} \right)^2 + \left( \frac{\partial \mathbf{w}}{\partial y} \right)^2 = 1. \quad (5)$$

By defining  $\mathbf{s}(x, y) = \mathbf{w}^2(x, y)$ , the new equations for  $\mathbf{s}$  can be easily solved, with the final result that the most general valid transformation is  $w = \sqrt{(x + a_1)^2 + (y + b_1)^2}$  with  $a_1, b_1 \in \mathbb{C}$  (as is the case in *Complex Extensions*).

Finally, the extension  $r \rightarrow \mathbf{w}(r, \vartheta, \varphi) = \mathbf{w}(x, y, z)$  in the 3D spherical wave problem (with spherical symmetry) leads to

$$\begin{aligned} \frac{\partial G}{\partial \mathbf{w}} \left( \frac{\partial^2 \mathbf{w}}{\partial x^2} + \frac{\partial^2 \mathbf{w}}{\partial y^2} + \frac{\partial^2 \mathbf{w}}{\partial z^2} - \frac{2}{\mathbf{w}} \left[ \left( \frac{\partial \mathbf{w}}{\partial x} \right)^2 + \left( \frac{\partial \mathbf{w}}{\partial y} \right)^2 + \left( \frac{\partial \mathbf{w}}{\partial z} \right)^2 \right] \right) + \\ k^2 G \left[ 1 - \left( \frac{\partial \mathbf{w}}{\partial x} \right)^2 - \left( \frac{\partial \mathbf{w}}{\partial y} \right)^2 - \left( \frac{\partial \mathbf{w}}{\partial z} \right)^2 \right] = 0. \end{aligned} \quad (6)$$

As before, this condition can be written as a pair of equations in  $(x, y, z)$  that may be rewritten in terms of the auxiliary variable  $\mathbf{s}(x, y, z) = \mathbf{w}^2(x, y, z)$ ; the new equations for  $\mathbf{s}$  may be written as

$$\frac{\partial^2 \mathbf{s}}{\partial x^2} + \frac{\partial^2 \mathbf{s}}{\partial y^2} + \frac{\partial^2 \mathbf{s}}{\partial z^2} = 6 \text{ and } \left( \frac{\partial \mathbf{s}}{\partial x} \right)^2 + \left( \frac{\partial \mathbf{s}}{\partial y} \right)^2 + \left( \frac{\partial \mathbf{s}}{\partial z} \right)^2 = 4\mathbf{s}. \quad (7)$$

The analyses of these equations result much more complicated than in the 2D cylindrical wave problem. At this point, it has been demonstrated that the usual extension in *Complex Extensions* is a valid solution to this equation; by the way, the possibility of a more general solution is currently under analysis.

## Conclusions

In this paper, we have studied the possibilities offered by a complex extension of the real coordinates in solutions to the scalar wave equation for generating more general classes of solutions. Two instances of that extension have been considered. The first one consists in a mere constant imaginary translation in any coordinates that do not appear in the metric coefficients of the corresponding coordinate system, such as  $x, y$  and  $z$  in a cartesian system, and  $\varphi$  in cylindrical or spherical ones. In particular, inhomogeneous plane or cylindrical waves are obtained as generalizations of homogeneous ones, and axis-symmetrical spherical waves are related to waves with spherical symmetry. In a second step, we have defined a more general complex extension in which any real coordinate is transformed into a complex variable, function of the position coordinates. For the two-dimensional problems considered, the valid transformations are not holomorphic and the only class of solutions obtained always reduce to the simple translations previously considered. In three dimensional problems the situation is very involved, and it is the object of current analysis. The detailed analyses concerning those studies have

provided also with new ideas about generalizing complex transformations that will be tackled in future works.

## Acknowledgment

This work has been supported by the Spanish Education Ministry under grant TIC2002-03121 (30% internal founding, 70% FEDER founding).

## References

- [1] G. Deschamps, "Gaussian Beam as a Bundle of Complex Rays," *Electronic Letters*, vol. 7, pp. 684–685, 1971
- [2] L. Felsen, "Complex Rays," Philips Research Reports 30, pp. 187–195, 1975
- [3] E. Gago-Ribas, M.J. González Morales, C.D. Martínez, "Analytical Parametrization of a 2D Real Propagation Space in Terms of Complex Electromagnetic Beams," *Special Issue on Electromagnetic Theory – Scattering and Diffraction, IEICE Trans. on Electronics*, vol. E80-C, no. 11, pp. 1434–1439, Japan, November 1997
- [4] E. Heyman and L.B. Felsen, "Gaussian Beam and Pulsed-Beam Dynamics: Complex-Source and Complex-Spectrum Formulations Within and Beyond Paraxial Asymptotics," *J. Opt. Soc. Am. A*, vol. 18, no. 7, pp. 1588–1611, 2001
- [5] E. Gago-Ribas, M.J. González Morales, "2D Complex Point Source Radiation Problem. I. Complex Distances and Complex Angles," *Special Issue on Electromagnetic Problems and Numerical Simulation Techniques: Current Status – Future Trends. Turkish Journal of Electric Engineering and Computer Sciences*, vol. 10, no. 2, pp. 317–343, 2002
- [6] M.J. González Morales, E. Gago-Ribas, "Complex Point Source Radiation Problem. II. Complex Beams," *Special Issue on Electromagnetic Problems and Numerical Simulation Techniques: Current Status – Future Trends. Turkish Journal of Electric Engineering and Computer Sciences*, vol. 10, no. 2, pp. 345–369, 2002
- [7] M.J. González Morales, E. Gago-Ribas, C. Dehesa Martínez, "A First Approach to Complex Analysis in EM: PO Currents under Complex Beam Incidence," *IEEE Transactions on Antennas and Propagation*. In reviewing process (Ref.: AP0505-0370)
- [8] E. Gago-Ribas, M.J. González Morales, C.D. Martínez. "Challenges and Perspectives of Complex Spaces and Complex Signal Theory Analysis in Electromagnetics: First Steps," *Electromagnetics in a Complex World: Challenges and Perspectives. Springer Proceedings in Physics*, vol. 96. Springer, Berlin Heidelberg New York, Ed.: I.M. Pinto, V. Galdi, L.B. Felsen. pp. 175–188. 2003. ISBN 3-540-20235-8
- [9] C.D. Martínez, M.J. González-Morales, E. Gago-Ribas. "About Complex Extensions to the Solution of Waves Equations in Electromagnetics," *Informe de Investigación. Spanish Ministry of Science and Technology. Project TIC2002-03121*. 2005

# Radiation of Sound from a Semi-Infinite Rigid Duct Inserted Axially into a Larger Infinite Tube with Wall Impedance Discontinuity

A. Büyükaksoy and A. Demir

Department of Mathematics, Gebze Institute of Technology,  
P.O. Box 141, Gebze 41400, Kocaeli, Turkey  
alinur@gyte.edu.tr, ademir@gyte.edu.tr

## Abstract

In the present work the radiation of sound from a bifurcated circular waveguide formed by a semi-infinite rigid duct inserted axially into a larger infinite tube with discontinuous wall impedance is analyzed. The formulation of the boundary-value problem in terms of Fourier integrals leads to a matrix Wiener–Hopf equation which is uncoupled by the introduction of infinite sum of poles. The exact solution is then obtained in terms of the coefficients of the poles, where these coefficients are shown to satisfy infinite system of linear algebraic equations. This system is solved numerically and the influence of the parameters such as the outer cylinder radius and the discontinuity of the surface impedances on the radiation phenomenon is shown graphically.

## Introduction

In the present work the radiation of sound from a bifurcated circular waveguide formed by a semi-infinite rigid duct inserted axially into a larger infinite tube with discontinuous wall impedance is analyzed. This problem is a generalization of a previous work by A.D. Rawlins [1] who considered the same geometry in the case where the infinite cylindrical casing surrounding the semi-infinite rigid tube is lined uniformly with an acoustically absorbing material. The generalization consisting of assuming that the lining of the outer cylinder is discontinuous (two-part) is not straightforward, since the resulting boundary-value problem leads to a matrix Wiener–Hopf equation in stead of a scalar one. We will assume that the mouth of the inner cylinder is separated from the rim of impedance discontinuity occurring on the outer cylinder by a length  $l$ :

To the best of authors' knowledge, the mixed boundary value problem which we will solve in this article, has not been previously treated and may serve as a reference problem for combined analytical–numerical techniques. In its original form,

the matrix Wiener–Hopf equation encountered in this work does not seem to be solvable by applying the known factorization methods. However, for  $l \leq 0$ , it is shown that the premultiplication by a suitable entire matrix, reduces the matrix Wiener–Hopf equation into a form for which the weak factorization method is applicable (see for example [1–3]). The solution contains two infinite sets of unknown coefficients satisfying two infinite systems of linear algebraic equations. These systems are solved numerically and the influence of the surface impedances of the two-part outer cylinder on the diffraction phenomenon is shown graphically.

## Analysis

Consider the radiation problem depicted in Fig. 1. A time harmonic plane sound wave mode with time factor  $\exp(-i\omega t)$ , propagates out of the open end of a semi-infinite circular cylindrical duct defined by  $\{\rho = a, \phi \in [0, 2\pi), z < 0\}$  where  $(\rho, \phi, z)$  denote the usual cylindrical polar coordinates. This semi-infinite tube is inserted axially into a larger infinite waveguide of radius  $\rho = b$ . The part  $\{\rho = b, \phi \in [0, 2\pi), z < l \leq 0\}$  of the outer duct is lined with an acoustically absorbent material having a surface admittance  $\eta_1$ , while the part  $\{\rho = b, \phi \in [0, 2\pi), z > l\}$  is coated by another acoustically absorbent material which is characterized by a surface admittance  $\eta_2$ . From the symmetry of the geometry of the problem and of the incident field, the acoustic field everywhere will be independent of  $\phi$ . We shall therefore introduce a scalar potential  $u(\rho, z)$  which defines the acoustic pressure and velocity by  $p = i\omega\sigma_0 u$  and  $\mathbf{v} = \text{grad } u$ , respectively, where  $\sigma_0$  is the density of the undisturbed medium.

The incident field is taken to be

$$u^i = \exp(ikz), \quad (1)$$

where  $k = \omega/c$  denotes the wave number of the space. For the sake of analytical convenience we will assume that the surrounding medium is slightly lossy and  $k$  has a small positive imaginary part. The lossless case will be obtained by letting  $\text{Im } k \rightarrow 0$  at the end of the analysis.

For analysis purposes it is convenient to express the total field  $u^T(\rho, z)$  as follows

$$u^T(\rho, z) = \begin{cases} u_1(\rho, z) + u^i(z); & \rho < a, z \in (-\infty, \infty) \\ u_2(\rho, z) & ; \quad \rho \in (a, b), z \in (-\infty, \infty) \end{cases} \quad (2)$$

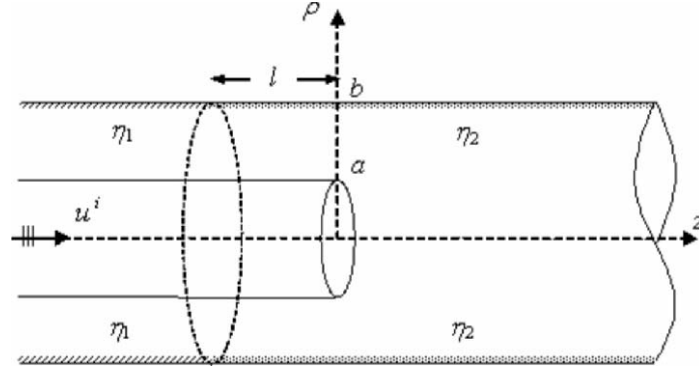


Fig. 1. Geometry of the problem

### Derivation of the Wiener–Hopf system

For the unknown fields  $u_1(\rho, z)$  and  $u_2(\rho, z)$  which satisfy the Helmholtz equation

$$\left[ \frac{1}{\rho} \frac{\partial}{\partial \rho} \left( \rho \frac{\partial}{\partial \rho} \right) + \frac{\partial^2}{\partial z^2} + k^2 \right] u_j(\rho, z) = 0, \quad j = 1, 2 \quad (3)$$

it is appropriate to use the following Fourier integral representations

$$u_1(\rho, z) = \int_L A(\alpha) J_0(K\rho) e^{-i\alpha z} d\alpha \quad (4a)$$

and

$$u_2(x, y) = \int_L [B(\alpha) J_0(K\rho) + C(\alpha) Y_0(K\rho)] e^{-i\alpha z} d\alpha \quad (4b)$$

with  $J_0(K\rho)$  and  $Y_0(K\rho)$  being the Bessel and Neumann functions of zeroth order and

$$K(\alpha) = \sqrt{k^2 - \alpha^2}. \quad (4c)$$

The square-root function is defined in the complex  $\alpha$ -plane, cut along  $\alpha = k$  to  $\alpha = k + i\infty$  and  $\alpha = -k$  to  $\alpha = -k - i\infty$ , such that  $K(0) = k$ .

The unknown spectral coefficients  $A(\alpha)$ ,  $B(\alpha)$  and  $C(\alpha)$  are to be determined with the aid of the following boundary and continuity relations:



$$\frac{\partial}{\partial \rho} u_1(a, z) = 0, \quad z < 0 \quad (5a)$$

$$\frac{\partial}{\partial \rho} u_1(a, z) - \frac{\partial}{\partial \rho} u_2(a, z) = 0, \quad z \in (-\infty, \infty) \quad (5b)$$

$$e^{ikz} + u_1(a, z) = u_2(a, z), \quad z > 0 \quad (5c)$$

$$\eta_2 u_2(b, z) - \frac{1}{ik} \frac{\partial}{\partial \rho} u_2(b, z) = 0, \quad z < l \quad (5d)$$

$$\eta_2 u_2(b, z) - \frac{1}{ik} \frac{\partial}{\partial \rho} u_2(b, z) = 0, \quad z > l \quad (5e)$$

Inserting (4a) and (4b) into (5a–e) and inverting the resulting integral equations we obtain after some straightforward manipulations, the following matrix Wiener–Hopf equation:

$$\begin{bmatrix} \frac{2i}{\pi kb} (\eta_1 - \eta_2) & K(\alpha) M_1(\eta_2, \alpha) e^{i\alpha l} \\ \frac{2i}{\pi kb} \frac{(\eta_1 - \eta_2) J_0(Ka)}{K(\alpha) J_1(Ka)} & M_0(\eta_2, \alpha) e^{i\alpha l} \end{bmatrix} \begin{bmatrix} \Phi_1^+(\alpha) \\ \Phi_2^+(\alpha) \end{bmatrix} - \begin{bmatrix} 0 & K(\alpha) M_1(\eta_1, \alpha) e^{i\alpha l} \\ \frac{2i}{\pi kb} (\eta_1 - \eta_2) & M_0(\eta_1, \alpha) e^{i\alpha l} \end{bmatrix} \begin{bmatrix} \Phi_1^-(\alpha) \\ \Phi_2^-(\alpha) \end{bmatrix} = \begin{bmatrix} 0 \\ -1 \end{bmatrix} \frac{2i}{\pi kb} \frac{(\eta_1 - \eta_2)}{2\pi i(\alpha + l)} \quad (6)$$

In the above equation  $\Phi_{1,2}^+(\alpha)$  and  $\Phi_{1,2}^-(\alpha)$  are defined by

$$\Phi_1^+(\alpha) = \frac{1}{2\pi} \int_0^\infty \frac{\partial}{\partial \rho} u_1(a, z) e^{i\alpha z} dz \quad (7a)$$

$$\Phi_1^-(\alpha) = \frac{1}{2\pi} \int_{-\infty}^0 [u_1(a, z) - u_2(a, z)] e^{i\alpha z} dz \quad (7b)$$

$$\Phi_2^+(\alpha) = \frac{1}{2\pi} \int_l^\infty \left[ \eta_2 u_2(b, z) - \frac{1}{ik} \frac{\partial}{\partial \rho} u_2(b, z) \right] e^{i\alpha(z-l)} dz \quad (7c)$$

$$\Phi_2^-(\alpha) = \frac{1}{2\pi} \int_{-\infty}^l \left[ \eta_2 u_2(b, z) - \frac{1}{ik} \frac{\partial}{\partial \rho} u_2(b, z) \right] e^{i\alpha(z-l)} dz \quad (7d)$$

Since,  $u_j(\rho, z) = \mathcal{O}(e^{ik|z|})$  as  $|z| \rightarrow \infty$  owing to the analytical properties of Fourier integrals we can show that  $\Phi_{1,2}^+(\alpha)$  and  $\Phi_{1,2}^-(\alpha)$  are regular in the upper ( $\text{Im } \alpha > \text{Im}(-k)$ ) and lower ( $\text{Im } \alpha < \text{Im } k$ ) halves of the complex  $\alpha$ -plane.

Here  $J(n_j, \alpha)$ ,  $Y(n_j, \alpha)$  and  $M_p(n_j, \alpha)$  stand for

$$\mathcal{J}(\eta_j, \alpha) = \eta_j J_0(Kb) + \frac{K(\alpha)}{ik} J_1(Kb) \quad (8a)$$

$$\mathcal{Y}(\eta_j, \alpha) = \eta_j Y_0(Kb) + \frac{K(\alpha)}{ik} Y_1(Kb) \quad (8b)$$

and

$$M_p(\eta_j, \alpha) = \left[ J_p(Ka) \mathcal{Y}(\eta_j, \alpha) - Y_p(Ka) \mathcal{J}(\eta_j, \alpha) \right], \quad p = 0, 1; j = 1, 2. \quad (8c)$$

Notice that  $M_0(n_j, \alpha)$  and  $K(\alpha)M_1(n_j, \alpha)$  are entire functions of  $\alpha$ .

### Solution of the Coupled System of Wiener–Hopf Equations

In order to solve the matrix Wiener–Hopf equations given in (6) it is convenient first to multiply it on the left by the following entire matrix

$$\begin{bmatrix} 1 & 0 \\ M_0(\eta_2, \alpha) & -K(\alpha)M_1(\eta_2, \alpha) \end{bmatrix},$$

to get

$$\frac{2i}{\pi kb}(\eta_1 - \eta_2) \frac{\Phi_1^+(\alpha) e^{-i\alpha l}}{K(\alpha)M_1(\eta_1, \alpha)} + N(\alpha) \Phi_2^+(\alpha) = \Phi_2^-(\alpha) \quad (9a)$$

$$\frac{2}{\pi a} \frac{\Phi_1^+(\alpha) L(\alpha)}{K^2(\alpha)} - \frac{2}{\pi a} \frac{\Phi_2^-(\alpha) e^{i\alpha l}}{K(\alpha)M_1(\eta_2, \alpha)} = \Phi_1^-(\alpha) + \frac{1}{2\pi i} \frac{1}{(\alpha + k)}, \quad (9b)$$

with

$$N(\alpha) = \frac{M_1(\eta_2, \alpha)}{M_1(\eta_1, \alpha)}, \quad (9c)$$

$$L(\alpha) = \frac{\mathcal{J}(\eta_2, \alpha)}{J_1(Ka)M_1(\eta_2, \alpha)} \quad (9d)$$

Consider first the Wiener–Hopf equation in (9a) and rearrange it in the following form

$$\frac{2i}{\pi kb}(\eta_1 - \eta_2) \frac{N^+(\alpha) \Phi_1^+(\alpha) e^{-i\alpha l}}{K(\alpha)M_1(\eta_2, \alpha)} + \Phi_2^+(\alpha) N^+(\alpha) = \frac{\Phi_2^-(\alpha)}{N^-(\alpha)} \quad (10)$$

Here,  $N^+(\alpha)$  and  $N^-(\alpha)$  are the split functions regular and free of zeros in the upper and lower half planes, respectively, resulting from the Wiener–Hopf factorization of  $N(\alpha)$  as

$$N(\alpha) = N^+(\alpha)N^-(\alpha) \quad (11a)$$

Their explicit expressions can easily be obtained as

$$N^+(\alpha) = [i\eta_1 J_0(kb) + J_1(kb)]^{1/2} [i\eta_2 J_0(kb) + J_1(kb)]^{-1/2} \prod_{m=1}^{\infty} \frac{1 + \alpha/\alpha_m}{1 + \alpha/\beta_m}, \quad (11b)$$

where  $\alpha = \pm \alpha_m$ 's are symmetrical zeros of the function  $K(\alpha) M_1(n_1, \alpha)$  while  $\alpha = \pm \beta_m$ 's are symmetrical zeros of  $K(\alpha) M_1(n_2, \alpha)$ .

The left-hand side of (12) is an upper function except for the poles of the first term resulting from the zeros of  $K(\alpha) M_1(n_2, \alpha)$  lying in the upper half-plane, namely at  $\alpha = \beta_m$  with

$$K(\pm \beta_m) M_1(n_2, \pm \beta_m) = 0, \quad \text{Im} \beta_m > \text{Im} k. \quad (12)$$

If the infinite system of poles is subtracted from both sides of (10), we obtain

$$\frac{2i}{\pi kb} (\eta_1 - \eta_2) \frac{\Phi_1^+(\alpha) N^+(\alpha) e^{-i\alpha l}}{K(\alpha) M_1(\eta_2, \alpha)} - \sum_{m=0}^{\infty} \frac{c_m}{\alpha - \beta_m} + \Phi_2^+(\alpha) N^+(\alpha) = \frac{\Phi_2^-(\alpha)}{N^-(\alpha)} - \sum_{m=0}^{\infty} \frac{c_m}{\alpha - \beta_m}, \quad (13a)$$

with

$$c_m = 2i \frac{(\eta_1 - \eta_2) \Phi_1^+(\beta_m) N^+(\beta_m) e^{-i\beta_m l}}{\pi kb K(\beta_m) M_1'(\eta_2, \beta_m)}. \quad (13b)$$

Here the prime (') stands for the derivation with respect to  $\alpha$ : The application of the analytical continuation principle together with the Liouville's theorem yields

$$\frac{\Phi_2^-(\alpha)}{N^-(\alpha)} = \sum_{m=0}^{\infty} \frac{c_m}{\alpha - \beta_m}, \quad (14a)$$

$$\Phi_2^+(\alpha) N^+(\alpha) = \sum_{m=0}^{\infty} \frac{c_m}{\alpha - \beta_m} - 2i \frac{(\eta_1 - \eta_2) \Phi_1^+(\alpha) N^+(\alpha) e^{-i\alpha l}}{\pi kb K(\alpha) M_1(\eta_2, \alpha)}. \quad (14b)$$

Consider now the Wiener–Hopf equation in (9b) and write the scalar kernel  $L(\alpha)$  as a product of two functions  $L^+(\alpha)$ ,  $L^-(\alpha)$ ; where  $L^+(\alpha)$  is regular and free of

zeros in the upper half plane  $\text{Im } \alpha > -\text{Im } k$  and  $L^-(\alpha)$  is regular and free of zeros in the lower region  $\text{Im } \alpha < \text{Im } k$ . By following the method described in [?], this product split can easily be accomplished to give

$$L^+(\alpha) = \left\{ \frac{\mathcal{J}(\eta_2, 0)}{J_1(ka)[J_1(ka)\mathcal{Y}(\eta_2, 0) - Y_1(Ka)\mathcal{J}(\eta_2, 0)]} \right\}^{1/2} e^{-\alpha T} \times \prod_{m=1}^{\infty} \frac{(1 + \alpha / \xi_m)}{(1 + \alpha / \chi_m)(1 + \alpha / \beta_m)}, \quad (15a)$$

$$L^-(\alpha) = L^+(-\alpha), \quad (15b)$$

where  $T$  stands for

$$T = \frac{i}{\pi} [b \ln b - a \ln a - (b - a) \ln(b - a)] \quad (15c)$$

and  $\xi_m$  and  $\chi_m$  are the roots of the following equations:

$$\sqrt{k^2 - (\chi_m)^2} J_1\left(a\sqrt{k^2 - (\chi_m)^2}\right) = 0, \quad (16a)$$

$$ik\eta_2 J_0\left(b\sqrt{k^2 - (\xi_m)^2} + \sqrt{k^2 - (\xi_m)^2} J_1\left(b\sqrt{k^2 - (\xi_m)^2}\right) = 0\right). \quad (16b)$$

Now, (9b) can be rewritten as

$$-\frac{2}{\pi ka} \frac{\Phi_1^+(\alpha)}{(k + \alpha)} L^+(\alpha) = \frac{2}{\pi a} \frac{(k - \alpha)\Phi_2^-(\alpha)e^{i\alpha l}}{K(\alpha)M_1(\eta_2, \alpha)L^-(\alpha)} + \frac{\Phi_1^-(\alpha)}{L^-(\alpha)}(k - \alpha) + \frac{(k - \alpha)}{2\pi i L^-(\alpha)(k + \alpha)}. \quad (17)$$

By proceeding similarly, its solution reads

$$\frac{\Phi_1^+(\alpha)}{(k + \alpha)} L^+(\alpha) = \frac{\pi a^\infty}{2_{m=1}} \frac{d_m}{\alpha + \beta_m} - \frac{ka}{2i(k + \alpha)L^+(k)}, \quad (18a)$$

$$\frac{\Phi_1^-(\alpha)}{L^-(\alpha)}(k - \alpha) = -\frac{2}{\pi a} \frac{\Phi_2^-(\alpha)(k - \alpha)e^{i\alpha l}}{K(\alpha)M_1(\eta_2, \alpha)L^-(\alpha)} + \prod_{m=1}^{\infty} \frac{d_m}{\alpha + \beta_m} - \frac{1}{2\pi i(k + \alpha)} \left[ \frac{(k - \alpha)}{L^-(\alpha)} - \frac{2k}{L^+(k)} \right], \quad (18b)$$

with

$$d_m = \frac{2}{\pi a} \frac{(k + \beta_m) \Phi_2^-(-\beta_m) e^{-i\beta_m l}}{K(\beta_m) M_1'(\eta_2, -\beta_m) L^+(\beta_m)}. \quad (18c)$$

The solution of the simultaneous Wiener–Hopf equations has now been obtained in terms of infinite series of constants  $c_m$  and  $d_m$ . By using (13b), (18a), (18c) and (14a) we can show that these constants are to be solved through the solution of the following two infinite sets of linear algebraic equations

$$\frac{2}{\pi a} \frac{N^+(\beta_r)(k + \beta_r) e^{-i\beta_r l}}{K(\beta_r) M_1'(\eta_2, -\beta_r) L^+(\beta_r)} \sum_{m=1}^{\infty} \frac{c_m}{\beta_r + \beta_m} + d_r = 0, \quad (19a)$$

$$\frac{\pi k b}{(\eta_1 - \eta_2)} \frac{K(\beta_r) M_1'(\eta_2, \beta_r) e^{i\beta_r l}}{N^+(\beta_r)} c_r + i\pi a \frac{(k + \beta_r)}{L^+(\beta_r)} \sum_{m=1}^{\infty} \frac{d_m}{\beta_r + \beta_m} = -\frac{ka}{L^+(\beta_r) L^+(k)}. \quad (19b)$$

These coupled systems of algebraic equations will be solved numerically. All the numerical results were derived by truncating the infinite series and the infinite systems of linear algebraic equations after the first  $N$  terms. It is checked that the amplitude of the diffracted field becomes insensitive to the increase of the truncation number after  $N = 5$ .

## Scattered Field and Computational Results

The scattered field in the region  $\rho < a$ , can be obtained by evaluating the following integral

$$u_1(\rho, z) = - \int_{\mathcal{L}} \Phi_1^+(\alpha) \frac{J_0(K\rho)}{K(\alpha) J_1(Ka)} e^{-i\alpha z} d\alpha \quad (20)$$

with where  $\mathcal{L}$  is a straight line parallel to the real  $\alpha$ -axis, lying in the strip  $\text{Im}(-k) < \text{Im}(\alpha) < \text{Im}(k)$ . Replacing  $\Phi_1^+(\alpha)$  in the above integral by its expression given in (18a) we get, for  $z > 0$ ,

$$u_1(\rho, z) = -2\pi i \sum_{n=1}^{\infty} \left[ \frac{\pi a}{2} (k - \xi_n) \sum_{m=1}^{\infty} \frac{d_m}{-\xi_n + \beta_m} + \frac{ka}{2iL^+(k)} \right] \frac{L^+(\xi_n) M(\eta_2, -\xi_n)}{K(\xi_n) \mathcal{J}'(\eta_2, -\xi_n)} J_0[K(\xi_n)\rho] e^{i\xi_n z}. \quad (21)$$

The transmission coefficient  $\mathcal{T}$  of the fundamental mode is defined as the complex coefficient multiplying the travelling wave term  $\exp(i\xi_1 z)$  and is computed from the contribution of the first pole at  $\alpha = -\xi_1$ . The result is

$$\begin{aligned}
 T = -\pi \left[ i\pi a (k - \xi_1) \prod_{m=1}^{\infty} \frac{d_m}{-\xi_1 + \beta_m} + \frac{ka}{L^+(k)} \right] \\
 \times \frac{L^+(\xi_1) J_1(K(\xi_1)a) \mathcal{Y}(\eta_2 - \xi_1)}{\left[ -\eta_2 \xi_1 b J_1(K(\xi_1)b) + K(\xi_1) \xi_1 b \frac{J_0(K(\xi_1)b)}{ik} \right]} \quad (22)
 \end{aligned}$$

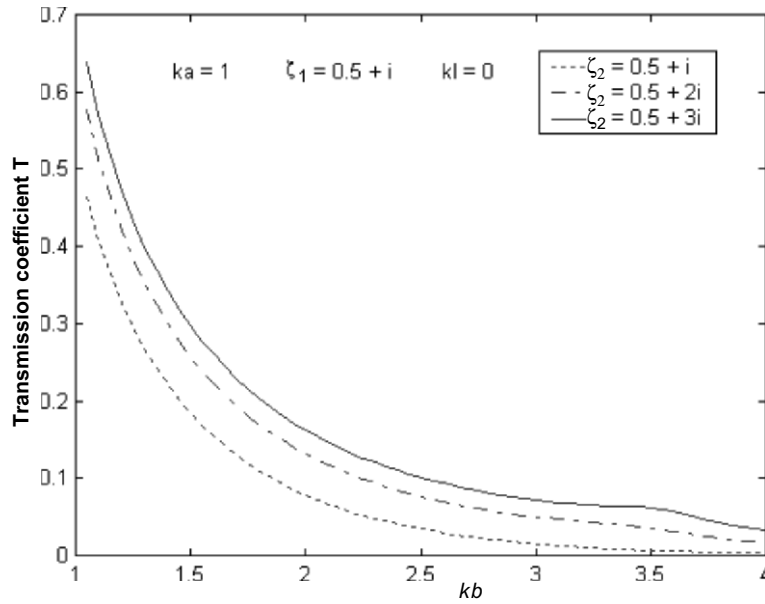


**Fig. 2.** Transmission coefficient versus the radius  $kb$  of the external waveguide for different values of  $\xi_2$

Figure 2 shows the variation of the transmission coefficient versus the radius of the outer cylinder in the case where  $l = 0$ , for different values of the acoustic impedance contrast. We increased the imaginary part of  $\xi_2 = 1/\eta_2$ , while the impedance  $\xi_1 = 1/\eta_1$  is kept constant. It is observed that the amplitude of the transmitted field increases when the contrast  $|\xi_2 - \xi_1|$  increases, as expected.

## References

- [1] A.D. Rawlins, "A bifurcated circular waveguide problem", *IMA J. Appl. Math.*, vol. 54, pp. 59–81, 1995
- [2] M. Idemen, "A new method to obtain exact solutions of vector Wiener-Hopf equations", *ZAMM*, vol. 59, pp. 656–658, 1979
- [3] I. D. Abrahams, "Scattering of sound by two parallel semi-infinite screens", *Wave Motion*, vol. 9, pp. 289–300, 1987

# Scattering by a Perfect Conducting Elliptic Cylinder Immersed Halfway Between Two Half Spaces

A. Kamel<sup>1</sup> and E. Niver<sup>2</sup>

<sup>1</sup>Heliopolis Center, P.O. Box 433, 11757 Cairo, Egypt, alaa@ureach.com

<sup>2</sup>Electrical and Computer Engineering, New Jersey Institute of Technology, Newark, NJ 07102, USA, niver@njit.edu

## Abstract

Scattering of electromagnetic waves by an elliptic cylinder immersed halfway between two half spaces of different properties has been studied. A discrete index radial Mathieu function transform is derived and used to obtain scattered fields in both half spaces.

## Introduction

To investigate the features of various media by means of electromagnetic radiation, it is necessary to know the field scattered by inhomogeneities of these media. The problem under consideration has also acquired practical relevance in fields such as the study of contaminated surfaces as well as detection of defects. Additionally the solution of canonical problems such as the one under consideration is important in the sense of scattering and diffraction theories. The aim of this article is to present solutions, in terms of new discrete index of the radial Mathieu function transform, to the problem of the scattering of electromagnetic waves by a perfect conducting elliptic cylinder immersed halfway between two half spaces of different properties. The problem of scattering by an elliptic metal cylinder at the interface between isorefractive half-spaces had been dealt with in the literature [1]. The configuration under consideration and the formulation presented in this article, to the best of the authors' knowledge, has not been considered before.

## Formulation

We consider the problem of scattering of harmonic electromagnetic waves by an infinite cylinder of elliptic cross-section embedded halfway between two semi-infinite media of different properties. Let  $u, \phi, z$  be elliptic coordinates with the axis of the elliptic cylinder along the  $z$  axis on the interface between the two half

spaces and the normal to the interface at  $\phi = \pm\pi/2$ . We take the surface of the elliptic cylinder as  $u = a$  and the distance between the foci as  $2w$ . Medium one occupies the half space  $R_1 = \{a < u < \infty, 0 \leq \phi \leq \pi, -\infty < z < \infty\}$  while medium two occupies the half space  $R_2 = \{a < u < \infty, 0 \geq \phi \geq -\pi, -\infty < z < \infty\}$ .

The time dependence is  $\exp(-i\omega t)$  whose factor will be suppressed throughout.

$k_1, \epsilon_1$  and  $\mu_1$  are, respectively, the wave number, permittivity, and permeability in  $R_1$ .  $k_2, \epsilon_2$  and  $\mu_2$  are corresponding quantities in  $R_2$ . A Dirichlet condition is imposed on the surface of the elliptic cylinder. It should be noted that the treatment of the problem with the Neumann boundary condition is imposed on the surface of the elliptic cylinder goes on lines similar to those discussed in this article. In what follows field excitation is provided by an impressed line source located at  $(u_0, \phi_0)$  in medium one.

By using the symmetry of the problem structure with respect to the planes  $\phi = \pm\pi/2$ , we split the problem into two independent subproblems. The boundary conditions on the symmetry planes correspond to either an electric wall or a magnetic wall. Without loss of generality, we confine our attention to the case of an electric wall. Under the above conditions the field components are derived from a Green's function  $G = E_z / i\omega\mu$ , where  $E_z$  is the longitudinal electric field. The transverse field components are obtained from  $E_z$  as

$$H_u = \frac{-i\omega\epsilon}{k^2 h} \frac{\partial E_z}{\partial \phi}, \quad (1a)$$

$$H_\phi = \frac{i\omega\epsilon}{k^2 h} \frac{\partial E_z}{\partial u}. \quad (1b)$$

$G$  satisfies the inhomogeneous Helmholtz equation

$$(\nabla_t^2 + k_1^2)G_1(u, \phi) = -\frac{\delta(u - u_0)\delta(\phi - \phi_0)}{h^2}, \quad (2a)$$

where  $k_1 = \omega/c_1$ ,  $c_1 = 1/\sqrt{\mu_1\epsilon_1}$  is the speed in  $R_1$ ,  $h^2 = w^2(\cosh^2 u - \cos^2 \phi)$  is the Jacobian of the transformation from the  $(x, y)$  coordinate system to the  $(u, \phi)$  coordinate system.

In  $R_2$ ,  $G_2(u, \phi)$  satisfies the homogeneous Helmholtz equation

$$(\nabla_t^2 + k_2^2)G_2(u, \phi) = 0, \quad (2b)$$



where  $k_1 = \omega/c_1$ ,  $c_2 = 1/\sqrt{\mu_2 \epsilon_2}$  is the speed in  $R_2$ .  $\nabla_t^2$  stands for the transverse (with respect to  $z$ ) Laplacian

$$\nabla_t^2 = \frac{1}{h^2} \left[ \frac{\partial^2}{\partial u^2} + \frac{\partial^2}{\partial \phi^2} \right] \quad (3)$$

Tangential field components are continuous across the interface between the two media

$$E_{z_1}(u, \phi = 0) = E_{z_2}(u, \phi = 0), \quad (4a)$$

$$H_{u_1}(u, \phi = 0) = H_{u_2}(u, \phi = 0). \quad (4b)$$

Equation (4b) reduces on account of (1a) to

$$\frac{1}{\mu_1} \frac{\partial}{\partial \phi} E_{z_1}(u, \phi = 0) = \frac{1}{\mu_2} \frac{\partial}{\partial \phi} E_{z_2}(u, \phi = 0) \quad (4b')$$

and radiation condition is to be satisfied as  $u \rightarrow \infty$ .

A Dirichlet boundary condition is imposed on the surface of the elliptic cylinder requiring

$$E_{z_{1,2}}(u = a, \phi) = 0. \quad (4c)$$

We propose to solve the above boundary value problem by means of a discrete index of radial Mathieu function transform.

Applying the index transform

$$G_{1,2}(u, \phi) = \sum_p g_{1,2}(v_{1,2p}, \phi) \Phi_{1,2p}(k_{1,2}w, u) \quad (5)$$

to (2a) and (2b) and making use of orthogonality relation in (A10), we obtain the ordinary differential equations (ODEs)

$$\left[ \frac{d^2}{d\phi^2} + (v_{1p}^2 - k_1^2 w^2 \cos^2 \phi) \right] g_1(v_{1p}, \phi) = -\Phi_{1p}(k_1 w, u_0) \delta(\phi - \phi_0), \quad (6a)$$

$$\left[ \frac{d^2}{d\phi^2} + (v_{2p}^2 - k_2^2 w^2 \cos^2 \phi) \right] g_2(v_{2p}, \phi) = 0 \quad (6b)$$

whose solutions are in terms of angular Mathieu functions [3].

We represent  $g_1(v_{1p}, \phi)$  as

$$g_1(v_{1p}, \phi) = g_1^{(0)}(v_{1p}, \phi) + g_1^{(1)}(v_{1p}, \phi) \quad (7)$$

$g_1^{(0)}(v_{1p}, \phi)$  satisfies the source conditions:

1.  $g_1^{(0)}(v_{1p}, \phi)$  is continuous across  $\phi = \phi_0$

$$g_1^{(0)}(v_{1p}, \phi_0 - 0) = g_1^{(0)}(v_{1p}, \phi_0 + 0) \quad (8a)$$

2.  $\frac{d}{d\phi} g_1^{(0)}(v_{1p}, \phi)$  is discontinuous across  $\phi = \phi_0$  with

$$\frac{d}{d\phi} g_1^{(0)}(v_{1p}, \phi) \Big|_{\phi_0+0} - \frac{d}{d\phi} g_1^{(0)}(v_{1p}, \phi) \Big|_{\phi_0-0} = -\Phi_{1p}(k_1, u_0) \quad (8b)$$

and both  $g_1^{(0)}(v_{1p}, \phi)$  and  $g_1^{(1)}(v_{1p}, \phi)$  satisfy the electric wall boundary condition at  $\phi = \pi/2$ , namely

$$g_1^{(0)}(v_{1p}, \pi/2) = g_1^{(1)}(v_{1p}, \pi/2) = 0. \quad (9)$$

In what follows, we choose for the ODEs in (6a) and (6b) solutions of the form

$$S_{v_{1,2p}}(k_{1,2}w, \phi) = \sum a_{1,2n} \sin[(v_{1,2p} + 2n)\phi], \quad (10a)$$

$$C_{v_{1,2p}}(k_{1,2}w, \phi) = \sum b_{1,2n} \cos[(v_{1,2p} + 2n)\phi]. \quad (10b)$$

Hence,

$$g_1^{(0)}(v_{1p}, \phi) = \frac{f_{v_{1p}}(k_1w, \phi_>)C_{v_{1p}}(k_1w, \phi_<)}{W_p} \Phi_{1p}(k_1w, u_0) \quad (11a)$$

where  $\phi_> | \phi_<$  is the lesser | greater of  $\phi$  and  $\phi_0$ ,

$$f_{v_{1p}}(k_1w, \phi) = C_{v_{1p}}(k_1w, \pi/2)S_{v_{1p}}(k_1w, \phi) - S_{v_{1p}}(k_1w, \pi/2)C_{v_{1p}}(k_1w, \phi) \quad (11a1)$$

$$W_p = C_{v_{1p}}(k_1w, \pi/2)S_{v_{1p}}'(k_1w, 0)C_{v_{1p}}(k_1w, 0) \quad (11a2)$$

with the prime indicating differentiation with respect to  $\phi$ , and

$$g_1^{(1)}(v_{1p}, \phi) = A_1(v_{1p})f_{v_{1p}}(k_1w, \phi) \quad (11b)$$

In  $R_2$ ,  $g_2(v_{2p}, \phi)$  satisfies the electric wall boundary condition at  $\phi = -\pi/2$ . Hence

$$g_2^{(1)}(v_{2p}, \phi) = A_2(v_{2p})f_{v_{2p}}(k_2w, \phi), \quad (12)$$

where

$$f_{v_{2p}}(k_2w, \phi) = C_{v_{2p}}(k_2w, -\pi/2)S_{v_{2p}}(k_2w, \phi) - S_{v_{2p}}(k_2w, -\pi/2)C_{v_{2p}}(k_2w, \phi). \quad (13)$$

$A_1(v_{1p})$  and  $A_2(v_{2p})$  are transform spectra to be determined from the boundary conditions on the interface between the  $R_1$  and  $R_2$  as per (4a) and (4b<sup>1</sup>)

*Remark.* The Dirichlet boundary condition on the surface of the elliptic cylinder, given in (4c), is built in the eigen functions  $\Phi_{1,2p}(k_{1,2}w, u)$ . This is one advantage of using the discrete index of radial Mathieu function transform for problems with boundaries along  $u = \text{constant}$ .

$$G_1(u, \phi) = G_1^{(0)}(u, \phi) + G_1^{(1)}(u, \phi), \quad (14a)$$

where

$$G_1^{(0)}(u, \phi) = \sum_p \frac{f_{v_{1p}}(k_1w, \phi_>)C_{v_{1p}}(k_1w, \phi_<)}{W_p} \Phi_p(k_1w, u_0) \Phi_p(k_1w, u), \quad (14b)$$

$$G_1^{(1)}(u, \phi) = \sum_p A_1(v_{1p})f_{v_{1p}}(k_1w, \phi) \Phi_{1p}(k_1w, u), \quad (14c)$$

$$G_2(r, \phi) = \sum_p A_2(v_{2p})f_{v_{2p}}(k_2w, \phi) \Phi_{2p}(k_2w, u). \quad (15)$$

Applying the boundary conditions in (4a) and (4b<sup>1</sup>) we obtain

$$\tau \sum_p \left\{ \frac{f_{v_{1p}}(k_1w, \phi_0)}{S'_{v_{1p}}(k_1w, 0)C_{v_{1p}}(k_1w, \pi/2)} \Phi_{1p}(k_1w, u_0) - A_1(v_{1p})S_{v_{1p}}(k_1w, \pi/2)C_{v_{1p}}(k_1w, 0) \right\} \times$$

$$\Phi_{1p}(k_1w, u) = - \sum_p A_2(v_{2p})S_{v_{2p}}(k_2w, -\pi/2)C_{v_{2p}}(k_2w, 0) \Phi_{2p}(k_2w, u) \quad (16a)$$

$$\sum_p A_1(v_{1p})C_{v_{1p}}(k_1w, \pi/2)S'_{v_{1p}}(k_1w, 0) \Phi_{1p}(k_1w, u) =$$

$$\sum_p A_2(v_{2p})C_{v_{2p}}(k_2w, -\pi/2)S'_{v_{2p}}(k_2w, 0) \Phi_p(k_2w, u) \quad (16b)$$

with  $\tau = \mu_1 / \mu_2$ .

## Linear System Derivation

We multiply (16a) and (16b) by  $\Phi_{1q}(k_1 w, u)$  and integrate on  $u$  from  $a$  to  $\infty$  utilizing the orthonormality relation of (A10) to reach

$$\tau \left\{ \frac{f_{v_{1q}}(k_1 w, \phi_0)}{S'_{v_{1q}}(k_1 w, 0) C_{v_{1q}}(k_1 w, \pi/2)} \Phi_{1q}(k_1 w, u_0) - A_1(v_{1q}) S_{v_{1p}}(k_1 w, \pi/2) C_{v_{1p}}(k_1 w, 0) \right\} = - \sum_p A_2(v_{2p}) S_{v_{2p}}(k_2 w, -\pi/2) C_{v_{2p}}(k_2 w, 0) C_{qp} \quad \forall q, \quad (17a)$$

$$A_1(v_{1q}) C_{v_{1q}}(k_1 w, \pi/2) S'_{v_{1q}}(k_1 w, 0) = \sum_p A_2(v_{2p}) C_{v_{2p}}(k_2 w, -\pi/2) S'_{v_{2p}}(k_2 w, 0) C_{qp} \quad \forall q, \quad (17b)$$

where

$$C_{qp} = \int_a \Phi_{1q}(k_1 w, u) \Phi_{2p}(k_2 w, u) du. \quad (18)$$

We cast the linear system as

$$\mathbf{s} + \mathbf{D}_1 [-\tau S_{v_{1p}}(k_1 w, \pi/2) C_{v_{1p}}(k_1 w, 0)] \mathbf{A}_1 = \mathbf{C} \mathbf{D}_2 [-S_{v_{2p}}(k_2 w, -\pi/2) C_{v_{2p}}(k_2 w, 0)] \mathbf{A}_2, \quad (19a)$$

$$\mathbf{D}_3 [C_{v_{1q}}(k_1 w, \pi/2) S'_{v_{1q}}(k_1 w, 0)] \mathbf{A}_1 = \mathbf{C} \mathbf{D}_4 [C_{v_{2p}}(k_2 w, -\pi/2) S'_{v_{2p}}(k_2 w, 0)] \mathbf{A}_2, \quad (19b)$$

where  $\mathbf{s}$  is the vector

$$\mathbf{s} = \left\{ \frac{\tau f_{v_{1q}}(k_1 w, \phi_0)}{S'_{v_{1q}}(k_1 w, 0) C_{v_{1q}}(k_1 w, \pi/2)} \Phi_{1q}(k_1 w, u_0) \right\}. \quad (20)$$

$\mathbf{D}_i[\cdot]$ ,  $i=1:4$  are diagonal matrices with diagonal elements  $[\cdot]$  and  $\mathbf{A}_{1,2}$  are the vectors of spectral amplitudes.

From the above we derive

$$\mathbf{A}_1 = \mathbf{M}_1^{-1} \mathbf{s}, \quad (21a)$$

$$\mathbf{A}_2 = \mathbf{M}_2^{-1} \mathbf{s}, \quad (21b)$$

where

$$\mathbf{M}_1 = \mathbf{C} \mathbf{D}_4^{-1} (\mathbf{D}_2 \mathbf{C}^{-1} \mathbf{D}_3 - \mathbf{D}_4 \mathbf{C}^{-1} \mathbf{D}_1), \quad (21c)$$

$$\mathbf{M}_2 = \mathbf{D}_3 \mathbf{C} \mathbf{D}_2 - \mathbf{D}_1 \mathbf{C} \mathbf{D}_4. \quad (21d)$$

*Remark.* Had we used expansions on the angular periodic Mathieu functions instead of the discrete index of radial Mathieu functions transform, the lack of an

orthogonality relation for the radial Mathieu functions of integer order would have resulted in the appearance of dense matrices in the linear system. This is another advantage of using the discrete index of radial Mathieu function transform for problems with boundaries along  $\phi = \text{constant}$ .

## Conclusions

The problem of scattering of electromagnetic waves by an elliptic cylinder with a Dirichlet condition on its surface and buried halfway between two half spaces has been formulated in terms of a new index of the radial Mathieu function transform. Expressions for the total field have been derived. It is concluded that the index of the radial Mathieu function transform formulation suits naturally expressing the fields in domains bounded by both radial and angular boundaries. It also allows for expressing the electromagnetic field for arbitrary refractive indices in the two half spaces. The approach of this paper is applicable for 2D and 3D problems of thermal conductivity, acoustics and elastodynamics. It applies as well, with the appropriate index transform, to right circular cylindrical and spherical configurations.

## References

- [1] D. Erricolo and P.L.E. Uslenghi, "Exact Radiation and Scattering for an Elliptic Metal Cylinder at the Interface Between Isorefractive Half-Spaces", *IEEE-AP*, 52, 9, 2004, pp. 2214–2225
- [2] N.L.B. Felsen and N. Marcuvitz, *Radiation and Scattering of Waves*, Prentice Hall Inc., New Jersey, USA, 1973
- [3] D.M. Abramowitz and I. Stegun, *Handbook of Mathematical Functions*, Dover Publications, New York, USA, 1970

# Pattern Nulling of Offset Parabolic Reflector with Array Feed

B. Saka and A. Selçuk

Department of Electrical and Electronics Engineering,  
Hacettepe University, 06800 Beytepe, Ankara, birsen@hacettepe.edu.tr

## Abstract

This paper presents nulling in offset parabolic reflector with cluster array feed employing a genetic algorithm (GA). Unlike the conventional GA which uses random initial phase and amplitude settings, initial settings of one of the individuals is chosen as binary representation of conjugate field matching vector. We consider the pattern nulling problem in circularly polarized case which is widely used in most satellite and other terrestrial communication systems.

## Introduction

The study of array-feed parabolic reflector is largely concentrated on pattern shaping, beam scanning, and compensation of surface distortions. The main goal of these investigations is the desired beam pattern with low side lobe levels. Low sidelobes do not guarantee adequate reception of a desired signal in the presence of jamming or interference sources. It then becomes necessary to insert deep null to reject the jamming sources [1, 2].

Widely used search based techniques for electromagnetic applications are conjugate gradient, random search, and genetic algorithms. Conjugate gradient and random search methods have the disadvantage of getting stuck in local minima. The global optimization methods such as genetic algorithm (GA), overcomes getting trapped in local minima. The comparison between the GA and other search based techniques is well documented in the literature [3–7]. GA offers a very attractive solution for beamforming and pattern nulling problem of the parabolic reflector with array feed [8, 9]. In this study, we implement the GA for pattern nulling problem of the offset parabolic reflector with array feed.

## Focal Region Fields of Offset Parabolic Reflector

The offset parabolic reflector with array feed geometry is shown in Fig. 1. The diameter and the focal length of the reflector are  $D_{\text{off}}$  and  $f$ , respectively. The cluster array feed with interelement spacing  $d$  is located on the focal plane of the reflector and the aperture angle with respect to the  $z$ -axis is denoted by  $\theta_{\text{off}}$ . A uniformly polarized incident plane wave induces electric currents on the reflector surface, which in turn produces the scattered fields on the focal plane. Using the PWS-FFT approach of Nagamune and Pathak [10], scattering fields from axially symmetric parabolic reflector to the focal plane, when incident plane wave comes from the  $\theta_i$  direction can be written as:

$$E(x, y; \theta_i) = \int_{-\infty}^{\infty} \int_{-\infty}^{\infty} V(k'_x, k'_y; \theta_i) e^{-jk'_x x} e^{-jk'_y y} e^{-jk'_z z} dk'_x dk'_y, \quad (1)$$

where the scattered field  $V(k'_x, k'_y; \theta_i)$  characterizes the axially symmetric parabolic antenna. For our offset parabola geometry, the above formula must be modified in order to calculate the focal region fields on the  $(x_f, y_f)$  plane. We can introduce new coordinates  $(x_f, y_f, z_f)$  by rotating the  $y$  axis through  $\theta_{\text{off}}$  and by introducing a coordinate transformation between  $(x, z)$  and  $(x_f, z_f)$  in terms of  $\theta_{\text{off}}$ . Equation (1) then becomes

$$E(x, y) = \int_{-\infty}^{\infty} \int_{-\infty}^{\infty} V(k'_x, k'_y) e^{-jk'_x \cos \theta_{\text{off}} x_f} e^{-jk'_y y_f} e^{-jk'_z \sin \theta_{\text{off}} x_f} dk'_x dk'_y. \quad (2)$$

We now define  $k'_\alpha = k'_x \cos \theta_{\text{off}} + k'_z \sin \theta_{\text{off}}$ , so that

$$E(x, y) = \int_{-\infty}^{\infty} \int_{-\infty}^{\infty} V(k'_x, k'_y) e^{-jk'_\alpha x_f} e^{-jk'_y y_f} e^{-jk'_z f} dk'_x dk'_y. \quad (3)$$

After some manipulations, the integral in (3) can be defined in terms of  $k'_\alpha$  and  $k'_y$  for the case of the offset parabolic antenna, where the array feed is on  $(x_f, y_f)$  plane and the scattered field becomes [11]

$$E(x_f, y_f; \theta_i) = \int_{-\infty}^{\infty} \int_{-\infty}^{\infty} \mathfrak{S}(k'_\alpha, k'_y) e^{-jk'_\alpha x_f} e^{-jk'_y y_f} e^{-jk'_z f} dk'_\alpha dk'_y, \quad (4)$$

where

$$\mathfrak{S}(k'_\alpha, k'_y) = \frac{V(k'_x, k'_y)}{\cos \theta_{\text{off}} - (k'_x / k'_y) \sin \theta_{\text{off}}} \quad (5)$$

and

$$k'_x = k'_\alpha \cos \theta_{\text{off}} - \sin \theta_{\text{off}} \sqrt{k^2 - k_y'^2 - k_\alpha'^2}. \quad (6)$$

Equation (4) gives us the possibility of calculating the focal region field of the offset parabolic reflector via Fourier transform techniques.

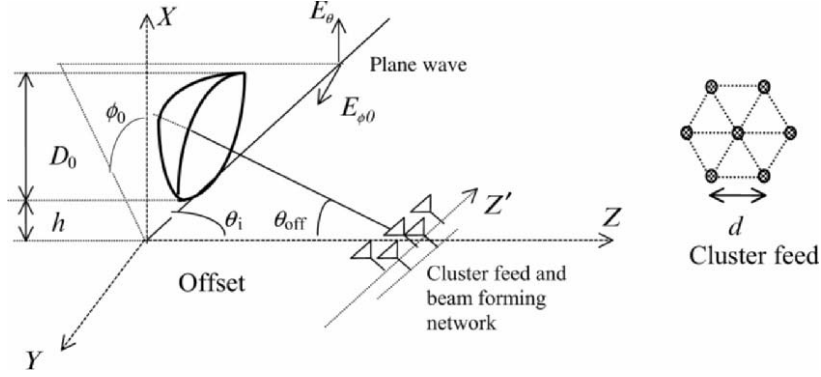


Fig. 1. Geometry of offset parabolic reflector with cluster feed

## Pattern Nulling Formulation

Our goal is to define the cost function which meets our requirements such as low-side lobes, pattern nulls for jamming sources and main beam for the desired direction. The cost function of the GA to be employed in this paper is based on a typical beam forming problem defined as [12, 13]:

$$\begin{aligned} & \min w^H R w \\ & \text{subject to } w^H (\bar{E}(\theta_i, \phi_{\text{const}}) \cdot \hat{\rho}_a) = f_i \quad i = 1, \dots, L, \end{aligned} \quad (7)$$

where  $L$  is the number of the constraints which defines the peak and the nulls of the pattern.  $f_i$  takes the values of 1 or 0, depending on whether the constraint defines a peak or a null, respectively. The other parameters in (7) can be defined with regard to the array-feed reflector beamforming problem shown in Fig. 1.  $\hat{\rho}_a$  is the polarization vector of the array antenna. For simplicity, we choose the array feed antenna pattern to be unity in all directions.  $w$  is the weight vector whose elements,  $w_m = a_m e^{j\delta_m}$  represent complex array weights of feed element  $m$ .  $\bar{E}(\theta_i, \phi_{\text{const}})$  is the electric field on the array elements when the incident plane wave is coming from the  $(\theta_i, \phi_{\text{const}})$  direction.  $R = \bar{E}(\theta_i, \phi_{\text{const}}) \cdot \bar{E}^H(\theta_i, \phi_{\text{const}})$  is a matrix describing the coupling between secondary scattering electric fields from the reflector reaching the field elements.

The optimization problem given in (7) is known as linearly constraint beam former or Capon's beam former. Capon's beam former attempts to minimize the power contributed by signals coming from directions other than  $\theta_i (i = 1, \dots, L)$ , while maintaining a fixed gain in the directions  $\theta_i (i = 1, \dots, L)$ . A closed-form solution to this problem is available, but it requires matrix inversion. For array-feed



parabolic reflector applications, the matrix is ill conditioned (the ratio of the matrix elements are very high because of the high gain and narrow beam properties of the parabolic reflector) and evaluation of the matrix inversion requires special treatment.

Our aim is to find the optimum weight vector due to cost or fitness function given below, using a GA

$$F(w_1, \dots, w_M) = \min \left\{ w^H R w + \alpha \left| w^H \left( \bar{E}(\theta_{peak}) \cdot \hat{\rho}_a \right) - 1 \right| + \beta \sum_{i=1}^{L-1} \left| w^H \left( \bar{E}(\theta_{nulli}) \cdot \hat{\rho}_a \right) \right| \right\}, \quad (8)$$

where  $M$  is the number of array elements.  $L$  is the number of constraints, which defines the nulls of the pattern.  $\alpha$  and  $\beta$  are positive numbers which weight the relative importance of the nulls and the peak, respectively. Fig. 2 shows a flow-chart of the implemented GA. In this study, GA iteration begins with an initial population including the conjugate field matching (CFM) weight vector [14]. CFM weight vector is calculated by  $w_0 = \gamma \bar{E}^*(\theta_{peak}) \cdot \hat{\rho}_a$ , where  $\gamma$  is some constant.

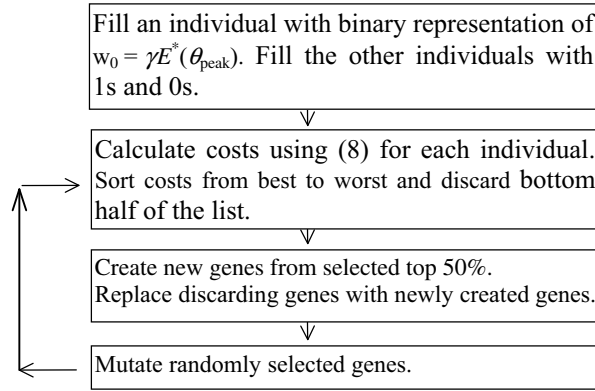


Fig. 2. Flow chart of the genetic algorithm

## Results and Conclusion

In the numerical calculations we choose an offset parabolic reflector with seven element cluster feed. Cluster feed is located on the focal plane of the offset reflector as shown in Fig. 1. The offset reflector antenna parameters are taken as  $D_0 = 108\lambda$ ,  $f = 94.87\lambda$ ,  $h = 16.87\lambda$ , and  $\theta_{off} = 38.11^\circ$ . The interelement spacing of the cluster array feed is chosen to be  $d = \lambda$ .

We selected two chromosomes representing the phase ( $\delta_m$ ) and the amplitude ( $a_m$ ) of the array element weights. Twenty individuals are used for each chromosome. Each chromosome consists of  $M=7$  genes, and each gene is represented by 5 bits. This implies that the amplitude and phase of the coefficients are multiples of  $0.0323^\circ$  and  $11.6129^\circ$ , respectively.

In the calculations, we tested the algorithm with two jammer signals which have the same power as the desired signal. In the results to be presented, the GA is carried out through 70 iterations. Typically achieved cost values as a function of the GA iterations are shown in Fig. 3. Here  $\text{cost1} = w^H R w$ ,  $\text{cost2} = \alpha \left| w^H \left( \bar{E}(\theta_{\text{peak}}) \cdot \hat{\rho}_a \right) - 1 \right|$ ,  $\text{cost3} = \beta \left| w^H \left( \bar{E}(\theta_{\text{null1}}) \cdot \hat{\rho}_a \right) \right|$ , and  $\text{cost4} = \beta \left| w^H \left( \bar{E}(\theta_{\text{null1}}) \cdot \hat{\rho}_a \right) \right|$  refer to the individual terms in (7). Furthermore, each term is normalized with respect to its maximum value for illustration purposes. It is evident from Fig. 3 that convergence is achieved after about 60 iterations.

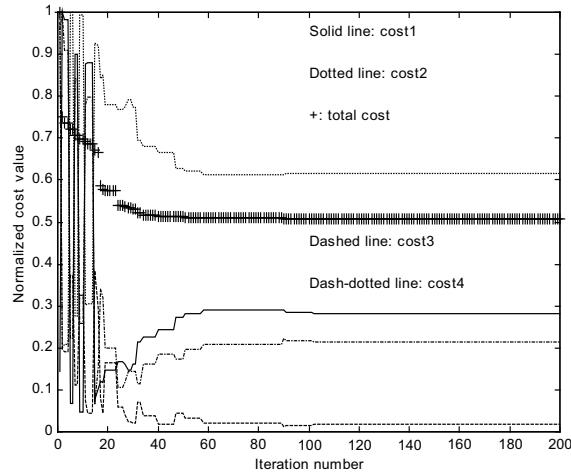


**Fig. 3.** Convergence of the implemented genetic algorithm

The optimization procedure is carried out when the desired and jamming signals are on the same constant  $\phi$  plane. For the determination of optimized weight vector performances other than the optimization plane, the results are given both in  $u-v$  and  $\theta-\phi$  graphs. The  $u-v$  graph represents the projection of the incident field on the  $xy$ -plane. In the  $u-v$  graphs, vertical and horizontal axis are  $v = \sin \theta \sin \phi$ , and  $u = \sin \theta \cos \phi$ , respectively. Thus, the polar and azimuthal angle dependences are presented.

We tested the algorithm for various scenarios when the incident plane wave and array feed are circularly polarized. In the first example given in Fig. 4, the desired

signal and jamming sources are at  $\theta_{\text{peak}} = 0^\circ$ ,  $\theta_{\text{null1}} = 0.5^\circ$ , and  $\theta_{\text{null2}} = -0.6^\circ$  on the  $\phi_{\text{const}} = 60^\circ$  plane. The desired nulls are in the region of the main beam. The achieved null depth is 20 dB. In Fig. 5, the desired signal and jamming sources are at  $\theta_{\text{peak}} = -0.6^\circ$ ,  $\theta_{\text{null1}} = 0^\circ$ , and  $\theta_{\text{null2}} = 0.4^\circ$  on the  $\phi_{\text{const}} = 30^\circ$  plane. In this example, one of the desired null corresponds to the natural main beam of the paraboloid. This causes the main beam to split into two parts. The null depth is calculated to be approximately 40 dB.

In the examples we have investigated, the sidelobe and jamming signal suppressions achieved are more than 20 dB and 40 dB, respectively. We have shown the applicability of the GA on the nulling problem of the offset feed parabolic reflector. The robust global optimization properties of the GA make it useful in analyzing such problems with easy implementation.

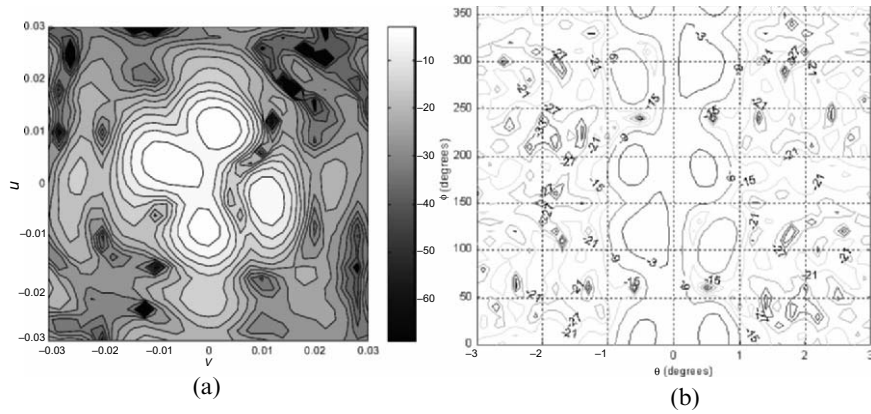


**Fig. 4.** Optimized pattern of offset reflector with array feed for circular polarization:  $\phi_{\text{const}}=60^\circ$ ,  $\theta_{\text{peak}}=0^\circ$ ,  $\theta_{\text{null1}}=0.5^\circ$ ,  $\theta_{\text{null2}}=-0.6^\circ$ , (a)  $u-v$  graph, (b)  $\theta-\phi$  graph

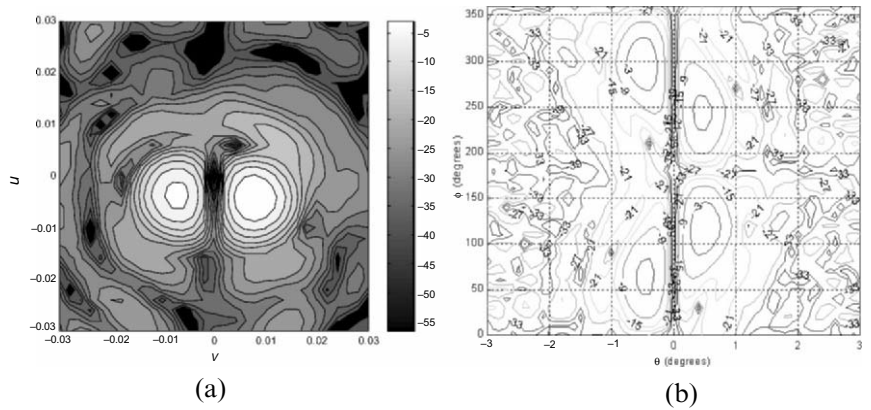


**Fig. 5.** Optimized pattern of offset reflector with array feed for circular polarization:  $\phi_{\text{const}}=30^\circ$ ,  $\theta_{\text{peak}}=-0.6^\circ$ ,  $\theta_{\text{null1}}=0^\circ$ ,  $\theta_{\text{null2}}=0.4^\circ$ , (a)  $u-v$  graph, (b)  $\theta-\phi$  graph

---

## References

- [1] R.A. Shore, "Adaptive nulling in hybrid reflector antennas", *Electromagnetics*, vol. 15, pp. 93–121, January/February 1995.
- [2] K.S. Rao, G.A. Morin, M.Q. Tang, S. Richard, and K.K. Chan, "Development of a 45 GHz multiple-beam antenna for military satellite communications", *IEEE Trans. Antennas Propag.*, vol. 43, pp. 1036–1047, October 1995.
- [3] R.L. Haupt, "Phase-only adaptive nulling with a genetic algorithm", *IEEE Trans. Antennas Propag.*, vol. 45, pp. 1009–1015, June 1997.
- [4] R.L. Haupt, "An introduction to genetic algorithms for electromagnetics", *IEEE Antennas Propag. Mag.*, vol. 37, pp. 7–15, April 1995.
- [5] K.S. Tang, K.F. Man, S. Kwong, and Q. He, "Genetic algorithms and their applications", *IEEE Signal Process. Mag.*, pp. 22–37, November 1996.
- [6] J.M. Johnson and Y. Rahmat-Samii, "Genetic algorithms in engineering electromagnetics", *IEEE Antennas Propag. Mag.*, vol. 39, pp. 7–25, August 1997.
- [7] K. Yan and Y. Lu, "Sidelobe reduction in array-pattern synthesis using genetic algorithm", *IEEE Trans. Antennas Propag.*, vol. 45, pp. 1117–1122, July 1997.
- [8] B. Saka, "Genetic algorithm implementation for array-feed parabolic reflector", *J. Electromagn. Waves Appl.*, vol. 13, no. 11, pp. 1511–1521, 1999.
- [9] S.L. Avila, W.P. Carpes, and J.A. Vasconcelos, "Optimization of an offset reflector antenna using genetic algorithms", *IEEE Trans. Magn.*, vol. 40 (2 II), pp. 1256–1259, March 2004.
- [10] A. Nagamune and P.H. Pathak, "An efficient plane wave spectral analysis to predict the focal region fields of parabolic reflector antennas for small and wide angle scanning", *IEEE Trans. Antennas Propag.*, vol. 38, pp. 1746–1756, November 1990.
- [11] B. Saka, E. Afacan, and E. Yazgan, "Beam steering antenna design for low altitude radar systems", *J. Electromagn. Waves Appl.*, vol. 11, pp. 215–224, February 1997.
- [12] H. Krim and M. Vilberg, "Two decades of array signal processing research", *IEEE Signal Process. Mag.*, pp. 67–94, July 1996.
- [13] C.-Y. Tseng and L.J. Griffiths, "A simple algorithm to achieve desired patterns for arbitrary arrays", *IEEE Trans. Signal Process.*, vol. 40, pp. 2737–2746, November 1992.
- [14] B. Saka and E. Yazgan, "Pattern optimization of a reflector antenna with planar array feeds and cluster feeds," *IEEE Trans. Antennas Propag.*, vol. 45, pp. 93–97, January 1997.

# Tapered Dielectric Rod Antenna

E. Niver

Department of Electrical and Computer Engineering, New Jersey Institute of Technology, Newark, NJ 07102, USA, niver@njit.edu

## Abstract

The numerical results of a theoretical model for a tapered rod excited by the dominant  $HE_{11}$  mode are compared to experimental measurements. The theoretical model is based upon the combination of the exact modal field solutions for a step profile cylindrical dielectric rod waveguide, *local mode theory*, and the *equivalence principle* for the determination of equivalent current densities. The far-zone radiation field is considered to be the summation of the two radiating components in the dielectric rod/cone structure. The “aperture” of the uniform dielectric rod at the transition plane (rod/cone interface) and the dielectric taper itself. In the former case, the field is obtained from the equivalent surface current densities on the aperture surface, whereas in the latter case, the field is obtained from the equivalent volume polarization current density induced in the conical structure. Mode converter was constructed to excite the proper mode in experimental measurements to compare the proposed theoretical model. Satisfactory agreement was achieved in comparing theory to experimental measurements. This paper aims to look at certain class of complex electromagnetic problems that are currently under investigation, and/or, that need to be addressed; and a tutorial introduction into modeling and numerical simulation approaches.

## Introduction

The dielectric rod antenna consists of a dielectric cylinder excited by a hollow waveguide. It was observed that by shaping the radiating end of the dielectric rod, the radiation characteristics improved considerably giving better directivity and beamwidth. However, these studies were conducted on a dielectric rod excited with the  $TE_{11}$  mode from a hollow waveguide [1]. The fundamental propagating mode in a cylindrical dielectric structure is the  $HE_{11}$  mode which has no cut-off frequency.

Yaghjian and Kornhauser [2] studied the problem of a circular semi-infinite dielectric rod antenna excited by the hybrid  $HE_{11}$  mode from a hollow waveguide. Based on the postulation that the tapering of the radiating end would match the impedance of the dielectric rod to that of free space, Georghiades [3] and Hoydal

[4] predicted the radiation patterns of the dielectric tapered rod antenna excited by the  $HE_{11}$  mode. They made use of the *local mode theory* in conjunction with equivalent surface and volume current distributions. Previous studies indicate that the local mode theory is quite useful in applications involving tapered geometries [5]. The results of the methods used in are compared here with the experimentally measured radiation patterns of the tapered dielectric rod antenna. The observation of a main lobe along the axis of the dielectric cone, in the case of the  $HE_{11}$  mode, supports the assumptions made of an adiabatic tapering of the dielectric. The conical structure is approximated by a series of thin concentric cylinders. The radiation field is then synthesized as the superposition of the fields from the dielectric-rod and from the conical taper. The tapering must be sufficiently slow to avoid higher-order coupling effects.

### Formulation of the Problem

Consider the combined dielectric rod/cone geometry depicted in Fig. 1. It consists of a uniform dielectric rod with core radius  $a$  and refractive index  $n_1$  immersed in an infinite medium of refractive index  $n_2$ . At  $z = 0$  the dielectric rod begins to taper linearly into a cone. In order to consider only the guided modes in the rod, the condition  $n_1 > n_2$  must be satisfied. In general, the waveguide can support multiple modes depending on the media parameters  $n_1$ ,  $n_2$ , the free-space wavelength  $\lambda$  and the rod radius  $a$ . The  $HE_{11}$  mode is called the fundamental mode of a cylindrical dielectric waveguide because it is the only mode without a cutoff condition.

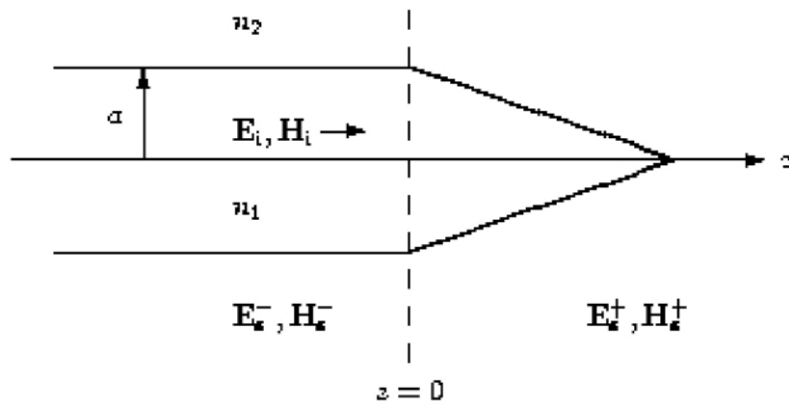


Fig. 1. Tapered uniform cylindrical dielectric rod/cone geometry

Let  $\mathbf{E}_i, \mathbf{H}_i$  represent the incident vector fields of a possible mode propagating in the  $+z$  direction. As this incident surface wave propagates into the tapered region, a fraction of the field is reflected back in the  $-z$  direction while the rest is considered to be transmitted further and will be referred to as scattered fields. The

scattered fields are represented by  $\mathbf{E}_s^-, \mathbf{H}_s^-$  in the  $z < 0$  region and  $\mathbf{E}_s^+, \mathbf{H}_s^+$  in the  $z > 0$  region. Hence, the total fields for  $z < 0$  can be written as:

$$\mathbf{E}_t^- = \mathbf{E}_i + \mathbf{E}_s^-, \quad \mathbf{H}_t^- = \mathbf{H}_i + \mathbf{H}_s^- \quad (1)$$

and for  $z > 0$

$$\mathbf{E}_t^+ = \mathbf{E}_i + \mathbf{E}_s^+, \quad \mathbf{H}_t^+ = \mathbf{H}_i + \mathbf{H}_s^+ \quad (2)$$

The far field consists mainly of the scattered fields  $\mathbf{E}_s, \mathbf{H}_s$  since the incident fields  $\mathbf{E}_i, \mathbf{H}_i$  do not contribute to the far field radiation. Hence, the far field radiation can be determined by finding the total scattered fields due to the rod/cone geometry.

These fields are evaluated by decomposing the rod/cone structure into two separate regions as shown in Fig. 2, and then using fictitious equivalent surface and volume currents as sources to account for the scattered fields in the  $z < 0$  region, as shown in Fig. 2(a), as

$$\mathbf{E}_a^- = \mathbf{E}_i, \quad \mathbf{H}_a^- = \mathbf{H}_i \quad (3)$$

and in Fig. 2(b) for  $z > 0$  as

$$\mathbf{E}_a^+ = \mathbf{0}, \quad \mathbf{H}_a^+ = \mathbf{0}. \quad (4)$$

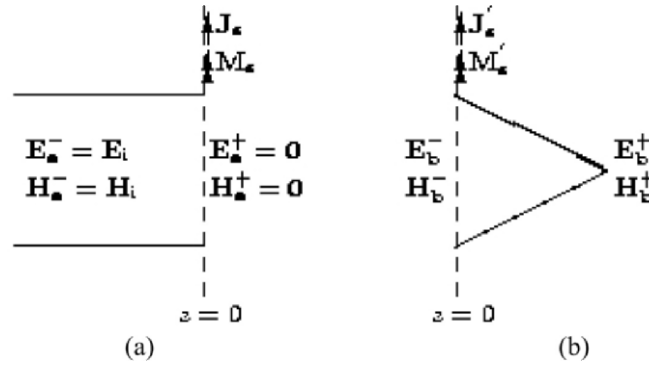


**Fig. 2.** Decomposition of the dielectric rod/cone structure: (a) The dielectric rod in the  $z < 0$  region. (b) The tapered dielectric in the  $z > 0$  region

To support these fields the *surface equivalence theorem*, introduced by Schelkunoff, states that there may exist fictitious electric and magnetic *surface current densities*  $\mathbf{J}_s$  and  $\mathbf{M}_s$  on the  $z=0$  plane such that:

$$\mathbf{J}_s = \hat{\mathbf{n}} \times (\mathbf{H}_a^+ - \mathbf{H}_a^-) = -\hat{\mathbf{z}} \times \mathbf{H}_i. \quad (5)$$

$$\mathbf{M}_s = -\hat{\mathbf{n}} \times (\mathbf{E}_a^+ - \mathbf{E}_a^-) = \hat{\mathbf{z}} \times \mathbf{E}_i. \quad (6)$$

The total fields must equal the superposition of the fields in Fig. 2a and b. Therefore, the fields in Fig. 2b are given by:

$$\mathbf{E}_b^- = \mathbf{E}_t^- - \mathbf{E}_i = \mathbf{E}_s^-, \quad \mathbf{H}_b^- = \mathbf{H}_t^- - \mathbf{H}_i = \mathbf{H}_s^- \quad (7)$$

for  $z < 0$ , and

$$\mathbf{E}_b^+ = \mathbf{E}_t^+ - \mathbf{0} = \mathbf{E}_s^+ + \mathbf{E}_i, \quad \mathbf{H}_b^+ = \mathbf{H}_t^+ - \mathbf{0} = \mathbf{H}_s^+ + \mathbf{H}_i, \quad (8)$$

for  $z > 0$ . Again according to the *surface equivalence* theorem, these fields yield fictitious surface current densities  $\mathbf{J}'_s$  and  $\mathbf{M}'_s$  in the  $z=0$  plane. The superposition of the fictitious surface currents in Fig. 2a and b must produce a null field. Hence,

$$\mathbf{J}_s^t = \mathbf{J}_s + \mathbf{J}'_s = \mathbf{0} \Rightarrow \mathbf{J}'_s = -\mathbf{J}_s \quad (9)$$

$$\mathbf{M}_s^t = \mathbf{M}_s + \mathbf{M}'_s = \mathbf{0} \Rightarrow \mathbf{M}'_s = -\mathbf{M}_s \quad (10)$$

Thus for Fig. 2b the equivalent surface currents are

$$\mathbf{J}'_s = \hat{\mathbf{z}} \times \mathbf{H}_i, \quad \mathbf{M}'_s = -\hat{\mathbf{z}} \times \mathbf{E}_i \quad (11)$$

and are known. From  $\mathbf{J}'_s$  and  $\mathbf{M}'_s$ , the unknown fields  $\mathbf{E}_s$  and  $\mathbf{H}_s$  can be evaluated. The equivalent surface currents  $\mathbf{J}'_s$  and  $\mathbf{M}'_s$  account for only a part of the total scattered field. The remaining scattered field is due to the unknown field  $\mathbf{E}_c$  in the cone as depicted in Fig. 3a. This scattered field can now be found by introducing an equivalent electric *volume current density* as seen in Fig. 3b.

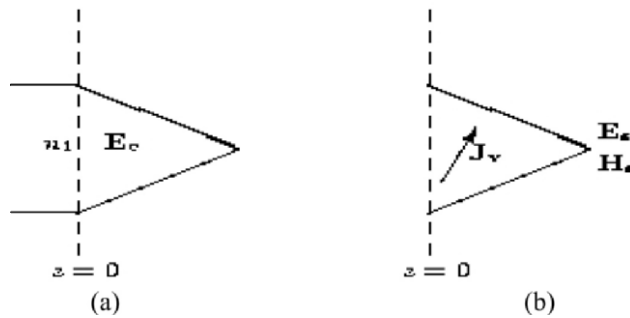


**Fig. 3.** The dielectric cone: (a) actual problem, (b) volume equivalence model



The equivalent volume current  $\mathbf{J}_v$  exists only within the space previously occupied by the dielectric cone where it radiates into a free-space environment. By manipulating, Maxwell's equations, valid within the dielectric cone, it can be shown that

$$\nabla \times \mathbf{E}_s = -j\omega\mu_2 \mathbf{H}_s, \quad (12)$$

$$\nabla \times \mathbf{H}_s = \mathbf{J}_v + j\omega\epsilon_2 \mathbf{E}_s, \quad (13)$$

where

$$\mathbf{J}_v = j\omega\epsilon_2(n_1^2 - 1)\mathbf{E}_c \quad (14)$$

and where  $\mathbf{E}_c$  is the unknown E-field within the dielectric cone. However,  $\mathbf{E}_c$  which is dependant on the radius of the cone, can be determined using the *local mode theory* and the principle of *power conservation*.

## The Dielectric Taper

In the case of a slow change in the profile of the dielectric rod, it is possible to evaluate approximately the modal field solutions of Maxwell's equations within local regions [2]. These *local modes* are governed by the local field solutions and the principle of conservation of power. Since such a solution assumes a negligible change in the power of the local mode, it is often called the *adiabatic approximation*. The local mode field solutions are constructed by approximating the dielectric cone by a series of cylindrical sections as shown in Fig. 4. The profile is independent of  $z$  within each section and is defined at the center  $z=z_c$ . The local mode field solutions within each *finite* section are approximated by the modal fields of an *infinitely* long rod having radius  $a(z)$  equal to the radius at the center of the section.

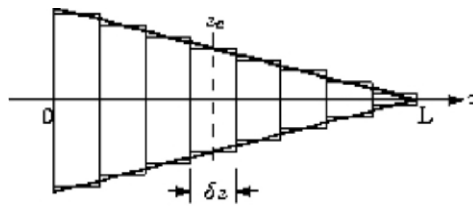


Fig. 4. The approximate model for the dielectric cone

Assuming that the length of the section  $\delta z$  is large compared to the length scale of the fields within  $\delta z$ , such an approximation is fairly accurate.

As a local mode propagates, its phase increases across each section by the product of  $\beta(z_c)$  and the section length  $\delta z$ . Consequently, the phase at an arbitrary position along the nonuniform dielectric rod is the sum of such products.

However, the slow variation of the dielectric rod means that the propagation constant  $\beta(z_c)$  varies only slightly between adjacent sections. Hence the sum of the phase contributions from each section can be approximated [2] by

$$\sum_{i=1}^n \beta(z_c) \delta z = \int_0^z \beta(\xi) d\xi. \quad (15)$$

## Power Conversation

The local mode fields are very accurate approximations to Maxwell's equations in *slowly* varying waveguides. However since they do not represent an exact solution, the local mode will suffer some loss of power as it propagates along the conical region. This loss of power can be attributed to coupling to radiation modes and higher order local modes. Even though the radius  $a(z)$  varies from section to section, the power of the local mode must be conserved along the dielectric rod/cone structure. This principle of power conservation can be expressed as

$$P_{z<0} = P_{z>0}, \quad (16)$$

where  $P_{z<0}$  is the total average power carried by the mode in the uniform cylindrical dielectric waveguide for the  $\text{HE}_{11}$  mode [5] is:

$$P_{z>0} = \frac{\pi}{4} E_{\text{rod}}^2(z) \left\{ \frac{1}{u^2(z)} \left[ C_1(z) a^2(z) J_0^2(\gamma a) + (C_1(z) a^2(z) - C_2(z)) J_1^2(\gamma a) \right] + \left[ \frac{J_1(\gamma a)}{w(z) K_1(\zeta_a)} \right]^2 \left[ (C_3(z) a^2(z) + C_4(z)) K_1^2(\zeta_a) - C_3(z) a^2(z) K_0^2(\zeta_a) \right] \right\} \quad (17)$$

where  $\gamma_a = u(z)a(z)$  and  $\zeta_a = w(z)a(z)$ , while the parameters  $u$ ,  $w$ ,  $C_1$ ,  $C_2$ ,  $C_3$  and  $C_4$  are also shown to be functions of  $z$  since they all change as the profile changes. From above one can obtain

$$|E_{\text{rod}}(z)| = |E_{\text{rod}}| \sqrt{\frac{P_0}{P_0(z)}}, \quad |H_{\text{rod}}(z)| = |H_{\text{rod}}| \sqrt{\frac{P_0}{P_0(z)}}, \quad (18)$$

where  $|E_{\text{rod}}|$  and  $|H_{\text{rod}}|$  are the constant field amplitudes in the dielectric rod. In order to simplify further calculations, the unknown excitation coefficients are chosen so as to normalize the directive gain to unity (0 dB) at the maximum of the main radiation lobe.

## Numerical and Experimental Results

The theoretical predictions of the previous sections were compared with the far field radiation pattern generated by dielectric cones excited with the fundamental  $HE_{11}$  mode. The experimental set-up consisted of a signal generator that excited the fields inside a waveguide of rectangular cross-section. This cross-section was gradually converted into a circular cross-section, thereby forming an open-ended circular waveguide. A mode converter was then attached to the circular waveguide. Finally, a cylindrical dielectric rod with tapered ends was inserted into the mode converter. Figure 5 shows the antenna assembly used in the experiment.

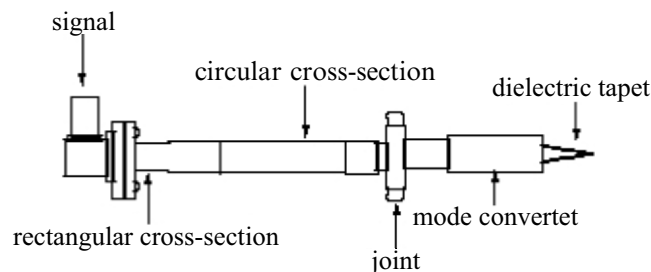


**Fig. 5.** Experimental antenna assembly

A mode converter is attached to the section of waveguide described above. The  $TE_{11}$  field in the circular waveguide is thus converted to a propagating  $HE_{11}$  mode. The mode converter used in this experiment was designed by Pietrangelo [8]. Again, the radiation pattern emitted by the open-ended mode converter was compared against the theoretical radiation pattern for the  $HE_{11}$  mode as predicted by Thomas [9]. The theoretical results are plotted along with the experimentally observed radiation patterns in Fig. 6a. There is a good agreement between the two sets of data indicating a satisfactory conversion of the  $TE_{11}$  mode into the  $HE_{11}$  mode. The far field radiation patterns from a tapered dielectric cone excited by the

$HE_{11}$  mode was determined previously by Hoydal [5]. For this purpose, a set of three taper lengths were used with two different materials, Teflon,  $n = 1.449$  and plexiglass  $n = 1.6$ . The taper lengths under study were 2.8, 1.9 and 1.5 long. Figure 6b shows the typical far field pattern for the dielectric cone.

## Conclusions

The use of the local mode theory and the principles of power conservation to model the linear tapering of a cylindrical dielectric rod has produced satisfactory results when theory is compared with experimental measurements.

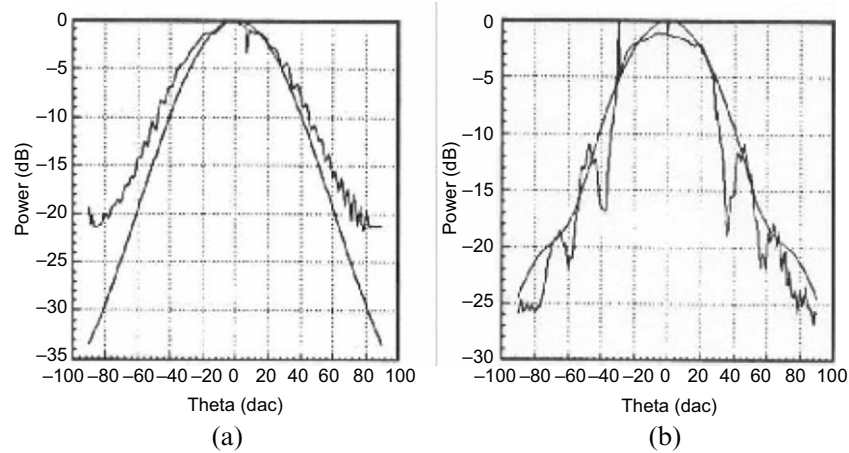


**Fig. 6.** (a)  $HE_{11}$  mode far field radiation pattern from an open-ended mode converter with guide radius= 7.5 mm at 18 GHz. The straight line (*lower curve*) is a theoretical result and the upper line is an experimental result, (b)  $HE_{11}$  mode far field radiation pattern for teflon tapered rod of  $L=2.8$  cm,  $n=1.449$ ,  $a = 7.5$  mm in the far field of  $r=1$  m,  $\varphi = 0^\circ$  at 18 GHz. The straight line (*upper curve*) is a theoretical result and the lower curve is an experimental result

## Acknowledgment

The author would like to thank to his former graduate students Nicholas Georghiades, Tor-Odd Hoydal and Anil Prabhakar. Greg Pietrangelo is acknowledged for design and construction of the mode converter. Special acknowledgments are to Dr. Felix Schwering for suggesting the formulation of the problem. Professor Gerald Whitman deserves thanks for fruitful discussions.

## References

- [1] A.A. Kishk and L. Shafai, "Radiation Characteristics of the Short Dielectric Rod Antenna: A Numerical Solution," *IEEE Transactions on Antennas and Propagation*, vol. AP-35, No. 2, pp. 139–146, February 1987
- [2] A.W. Snyder and J.D. Love, *Optical Waveguide Theory*, Chapman and Hall Ltd., London, 1983
- [3] A.D. Yaghjian and Kornhauser, "A Modal Analysis of the Dielectric-rod Antenna Excited by the  $HE_{11}$  Mode," *IEEE Transactions on Antennas and Propagation*, vol. AP-20, pp. 122–128, 1972
- [4] N.I. Georghiades, "The Tapered Dielectric Rod-Conical Antenna," M.Sc. Thesis, New Jersey Institute of Technology, 1988.

- 
- [5] Tor-Odd Hoydal, "Radiation from the Cylindrical Dielectric Taper," M.Sc. Thesis, New Jersey Institute of Technology, 1991
  - [6] G.M. Whitman, F.Schwering, W.Y Chen, A.Triolo and J.Junnart, *The Integrated Dielectric Slab Waveguide-Wedge Antenna*, in Directions For the Next Generation of MMIC Devices and Systems, N.K.Das and H.Bertoni, editors, Plenum Press, New York, pp. 181–195, 1997
  - [7] A. Prabhakar, "Radiation from the Tapered Dielectric Rod Antenna," M.Sc. Thesis, New Jersey Institute of Technology, 1993
  - [8] G. Pietrangelo, "Design of a  $HE_{11}$  to  $TE_{11}$  Mode Convertor," Senior Project, New Jersey Institute of Technology, 1989.and J. D. Love, *Optical Waveguide Theory*, Chapman and Hall Ltd., London, 1983
  - [9] B. MacA. Thomas, "Theoretical Performance of Prime-Focus Paraboloids using Cylindrical Hybrid-Mode Feeds," *Proceedings IEEE* , vol. 118, pp. 1539–1549, November 1971

# Design Alternatives of Spiral Antenna Arrays for Wireless Applications

G. Çakir<sup>1</sup> and L. Sevgi<sup>2</sup>

<sup>1</sup>Department of Electronics and Communication Engineering,  
Kocaeli University, Kocaeli, Turkey, gonca@kou.edu.tr

<sup>2</sup>Department of Electronics and Communication Engineering,  
Doğuş University, Acıbadem, 81010 Istanbul, Turkey, lsevgi@dogus.edu.tr

## Abstract

Design alternatives of low-cost, small-size, and high-performance spiral antenna arrays for wireless applications are presented. Polarization and radiation characteristics, beam forming, and pattern nulling capabilities are investigated numerically via the finite-difference time-domain (FDTD) and numerical electromagnetic code (NEC-2) simulators.

## Introduction

Spiral antennas are circularly polarized and almost frequency independent, and can be used for broadband and/or multiband multipurpose applications, such as in mobile communication, early warning, and direction finding systems, bluetooth applications, etc. [1–13]. They have been analyzed under various conditions; spirals in free space [5, 11, 12], spirals on planar reflectors [3–13], spirals in cavities [5] and spirals on dielectric substrates [5–10]. The shape of a spiral radiator can be equiangular [1], Archimedean [2, 5, 6, 8–13] or logarithmic, etc.

The consumer wants to use PC laptops in different applications, for example, listen to the FM radio, watch TV channels, to access easily to all kinds of wireless connections via three-band GSM systems and Bluetooth devices. On the other hand, the producer wants to have a single broadband antenna to cope with all these requirements. One solution is to design (almost) frequency-independent arrays of spiral elements with beam forming and pattern nulling capabilities [14]. The purpose here is to discuss design alternatives for both PC laptops and Bluetooth trans-receivers.

## Archimedean Spiral Antenna Optimized for 2.5 GHz

Archimedean spirals have mostly circular and/or rectangular shapes, and are fabricated either on microstrips or wire-elements forms [4]. The upper and lower frequencies of the radiation are determined by the feed point distance and diameter of the spiral antenna. Radiation patterns of Archimedean spirals are typically bi-directional, but can be backed by conducting plates (less than quarter-wavelength in distance) or cavities to eliminate the back lobes [3]. They are mostly two-arm, but multiarm types are also used to improve pattern symmetry, and direction finding performance.

Spiral antennas are balanced structures so they require balanced feed. Input impedance of the spiral antennas are in the order of  $140\text{--}200\Omega$ . Normally, they are connected to unbalanced  $50\Omega$ - coax cables [3], therefore a *balun* must be included with the feed design.

The radiation field can be decomposed into right and left hand circular polarized (RHCP and LHCP) components by using  $E_\theta$  and  $E_\phi$  as  $E_R = E_\theta + j E_\phi$  and  $E_L = E_\theta - j E_\phi$ . The axial ratio AR (defined as  $AR = (|E_R| + |E_L|) / (|E_R| - |E_L|)$ ) is a parameter that describes the degree of CP, depends on the number of antenna turns (nt), and is approximately given by  $AR = (2nt + 1) / 2nt$  for large number of turns. Figure 1 shows the Archimedean spiral antenna element designed and optimized for Bluetooth applications.

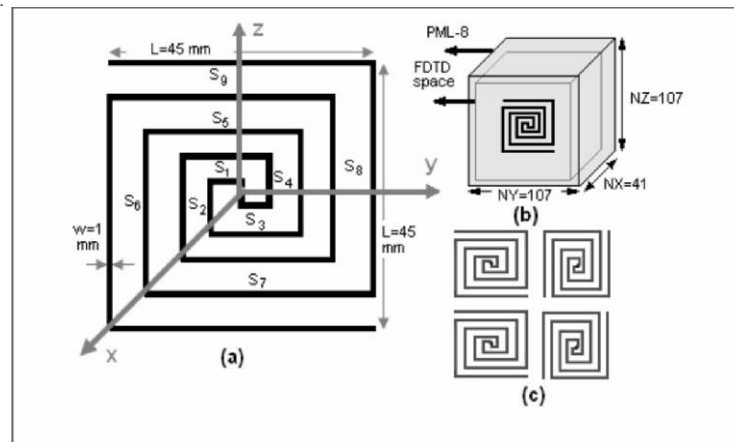


**Fig. 1.** (a) Configuration Archimedean spiral antenna, (b) FDTD computation space, (c)  $2 \times 2$  hybrid HV spiral array antenna

As will be shown, this antenna may be used from VHF frequencies up to a few GHz. The antenna which is optimized for the frequencies around 2.5 GHz is composed of two arms inside of a  $45\text{ mm} \times 45\text{ mm}$  aperture. The antenna arms are made of a wire of 1mm-radius, and are symmetrically wound with respect to the

feed point and each arm has  $K$  filaments ( $K=9$ ) whose lengths are  $x_0, x_0, 2x_0, 2x_0, 3x_0, 3x_0, \dots, Kx_0, Kx_0$ . The shortest and longest filaments are  $x_0=10$  mm and  $9x_0=45$  mm, respectively. The incremental increase of filaments is 10 mm. The antenna is located on the  $yz$ -plane as shown in the figure. The FDTD computation space and discretization values are also given in the figure (see Fig. 1b), together with a  $2 \times 2$  array composed of these Archimedean elements (see Fig. 1c). It should be noted that, the outer-most filament of this spiral are horizontal at left, but vertical at right, which are named as H-arm and V-arm elements, respectively. This is important, since it determines the domination of vertical ( $E_\theta$ ) and horizontal ( $E_\phi$ ) polarized components of the radiated fields.

## Design Alternatives and Simulations

Different planar arrays of this Archimedean spirals are designed and array performances are investigated numerically by using in-house prepared FDTD package [15] and the public-domain NEC-2 code [16] comparatively. Characteristic parameters such as input impedance and AR are calculated and it is found that the input impedance of the Archimedean spiral is around  $200 \Omega$  (and real), and AR is much less than 3 dB around 2.5 GHz, as expected and well documented elsewhere [6–9]. Therefore, the emphasis has placed on radiation characteristics and beam forming capabilities in this section.

### *The FDTD and NEC-2 parameterizations*

The performances of the Archimedean spiral antenna and various arrays of these elements are simulated via the FDTD and NEC-2 codes, therefore electromagnetic radiation characteristics are obtained in both time and frequency domains. The NEC-2 yields radiation patterns directly, but off-line frequency transformation is required for the FDTD-based patterns. The FDTD was first used in [5] to investigate various performance parameters of the spirals.

The discretization parameters of NEC-2 simulations are as follows:

- Each arm is divided into 80 segments (with 5 mm segment length that corresponds to more than wavelength over 20 at 2.5 GHz) therefore, 160 segments are used to represent a single Archimedean antenna.
- A  $7.5 \text{ cm} \times 7.5 \text{ cm}$  PEC planar plane at 1 cm back of each antenna is modeled as a square mesh with the sizes of  $5 \text{ mm} \times 5 \text{ mm}$ ; this means 450 segments are used for each antenna.
- Less than a minute is enough to calculate radiation characteristics of a single antenna (610 seg.), around 7 min for  $2 \times 2$  (2440 seg.) and 25 min for  $2 \times 3$  (3,660 seg.) arrays with PEC at back with NEC in a 512 MB RAM memory PC with 1 GHz CPU speed.
- On the other hand, an array of  $2 \times 5$  requires total of 6,100 segments and typical calculations with NEC in the same PC is more than 150 min.



Similarly, FDTD discretization parameters are:

- A  $41 \times 107 \times 107$  computation volume is required for the same single Archimedean antenna in FDTD ( $\Delta x = \Delta y = \Delta z = 1$  mm)
- On the other hand, the volume reaches up to  $41 \times 395 \times 155$  for  $2 \times 5$  array
- The number of simulation time step is 3000 which is enough for the transient time analysis ( $\Delta t = 1.92$  ps)
- The volume is terminated by 8-cell Berenger's PML
- Far fields are extrapolated via the TD near-to-far field transformation (NTTF)
- FDTD analysis of the spiral with  $7.5$  cm  $\times$   $7.5$  cm PEC plate lasts nearly 15 min (nearly 98% of this time is used for 180-point NTTF transformation)
- The computation time for the  $2 \times 5$  array reaches up to 9 h

It should be noted that, NEC-2 simulates single frequency radiation characteristics. On the other hand broadband characteristics can be obtained via single FDTD simulation by exciting the antenna with a voltage pulse. Then, off-line frequency transformation is applied at a number of desired frequencies to the time domain recorded data and radiation patterns are obtained.

### **Single Archimedean Spiral**

First, single Archimedean elements are investigated numerically and results are shown in Figs. 2 and 3.

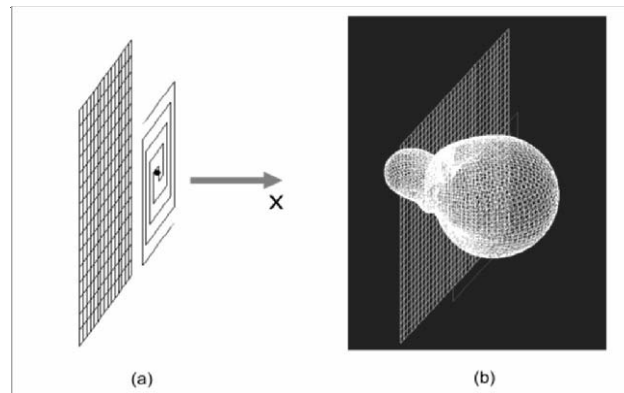


**Fig. 2.** The discrete NEC-2 model of the Archimedean spiral backed by a conducting plate and its 3D radiation pattern at 2.5 GHz (directivity gain is 9.4 dB)

Archimedean spirals are planar and typically bi-directional. The bi-directional characteristic can be changed to unidirectional by backing the spiral element with a conducting plane. A few numerical tests have been done with both packages to optimize the plate sizes and distance from the antenna. It is found that backing the antenna element (1 cm behind) with a conducting plate (1.5 times larger than the antenna) yields nearly 20 dB front-to-back-ratio (FBR), and directivity gain of 9.4 dB.

In Fig. 2, the Archimedean spiral with a conducting plate behind, modeled in NEC-2, and its three-dimensional (3D) radiation pattern are plotted. Horizontal ( $xy$ -plane) radiation patterns of both electric field components are plotted in Fig. 3.

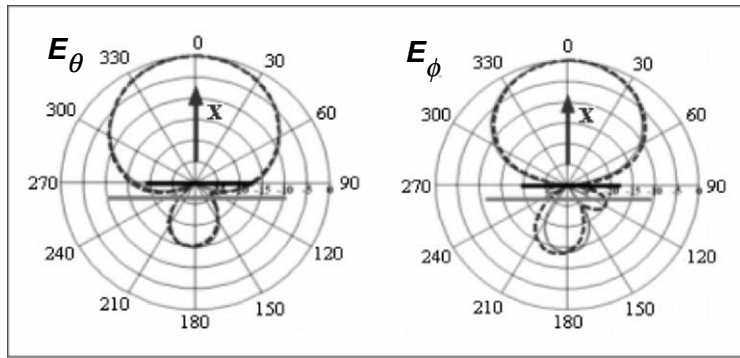


**Fig. 3.** Horizontal radiation patterns of the Archimedean spiral backed with a conducting plate (1 cm behind) at 2.5 GHz (directivity gain is 9.4 dB); *Solid*: FDTD, *Dashed*: NEC-2

### Archimedean Spiral Arrays

In addition to the broadband characteristics, multiple Archimedean spirals may also be used to form phased arrays, so that adoptive beam forming and interference nulling capabilities can be satisfied [14]. Various arrays of  $2 \times 2$ ,  $2 \times 3$ , and  $2 \times 5$  are designed and investigated numerically with both FDTD and NEC-2 packages. These tests showed that an array of  $2 \times 5$  (ten element Archimedean spirals) meet optimum design requirements (i.e., low-size, beam forming capability of nearly  $60\text{--}90^\circ$  and beam steering capability up to  $\pm 30^\circ$ ) when interelement distance is taken as 8 cm. Figures 4 and 5, show two examples.

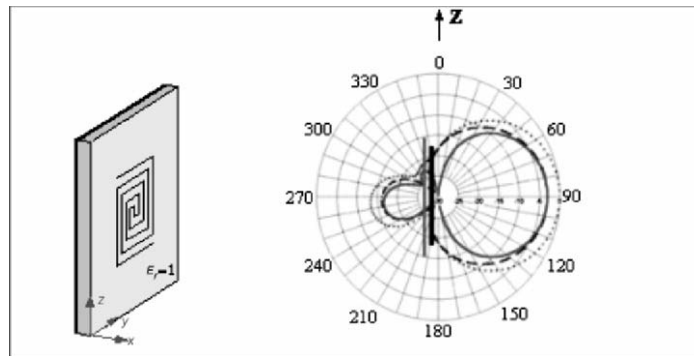


**Fig. 4.** Vertical radiation pattern of the two-arm Archimedean spiral antenna at 2.5 GHz with directivity gain of 9.4 dB, *Solid*:  $E_\theta$ , *Dashed*:  $E_\phi$ , *Dotted*: Total field

In Fig. 4, the vertical radiation pattern (at 2.5 GHz operating frequency) of the single Archimedean spiral antenna is given. In Fig. 5, the pattern of the  $2 \times 5$  Archimedean array is plotted. The directivity gains of the single and array Archimedean are calculated to be 9.4 and 18.2 dB, respectively. It should be noted that, both  $E_\theta$  and  $E_\phi$  components of the radiated fields have almost equal amplitudes as shown in the figures, which results in a pure CP at this frequency.

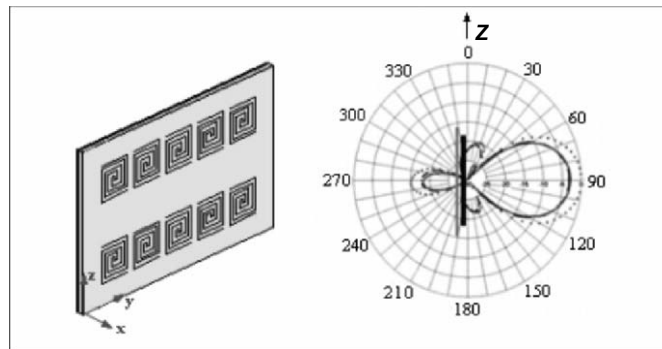


**Fig. 5.** Vertical ( $xz$ -plane) radiation pattern of the  $2 \times 5$  array at 2.5 GHz with directivity gain of 18.2 dB, Solid:  $E_\theta$ , Dashed:  $E_\phi$ , Dotted: Total field

Beam steering capabilities of the  $2 \times 5$  Archimedean array are given in Figs. 6 and 7, for the beam angles of  $0^\circ$  and  $30^\circ$ , respectively. It should be noted that elements are excited phase shifted, equal amplitude voltage sources in NEC-2, but with equal amplitude, time delayed voltage pulses in FDTD to point main beam of the array along a desired direction. The NEC-2 and FDTD results agree very well.

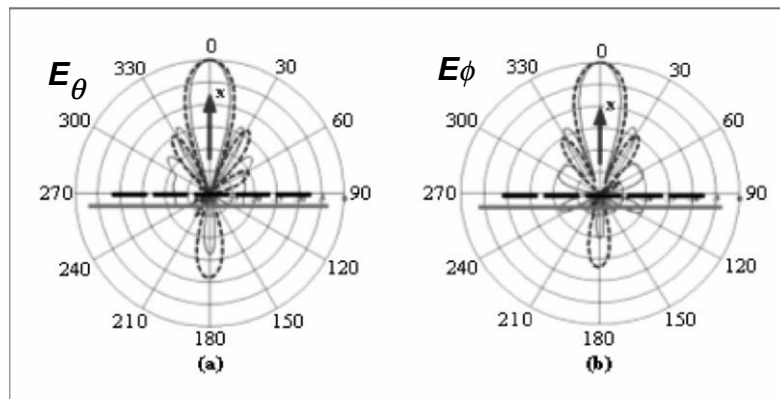


**Fig. 6.** Horizontal ( $xy$ -plane) radiation pattern of the  $2 \times 5$  Archimedean spiral array at 2.5 GHz operating frequency; Solid: FDTD, Dashed: NEC-2 (directivity gain is 18.2 dB). All elements are equally fed (no phasing in NEC-2, no delay in FDTD)

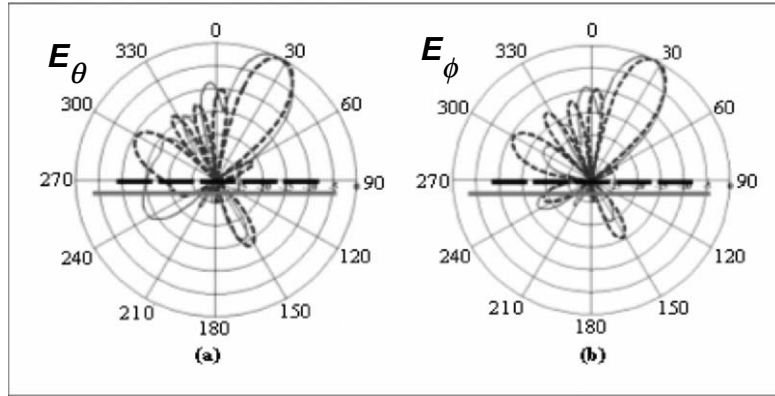


**Fig. 7.** Horizontal ( $xy$ -plane) radiation patter of the  $2 \times 5$  Archimedean spiral array at 2.5 GHz operating frequency; *Solid*: FDTD, *Dashed*: NEC-2 (directivity gain is 18.2 dB). Beam angle is  $30^\circ$  from boresight (elements are phase shifted in NEC-2 and delayed in FDTD)

The last examples belong to the FDTD simulations of a single spiral element, and an array of Archimedean spirals, both of which are designed on microstrip structures. The results are presented in Figs. 8 and 9, respectively.

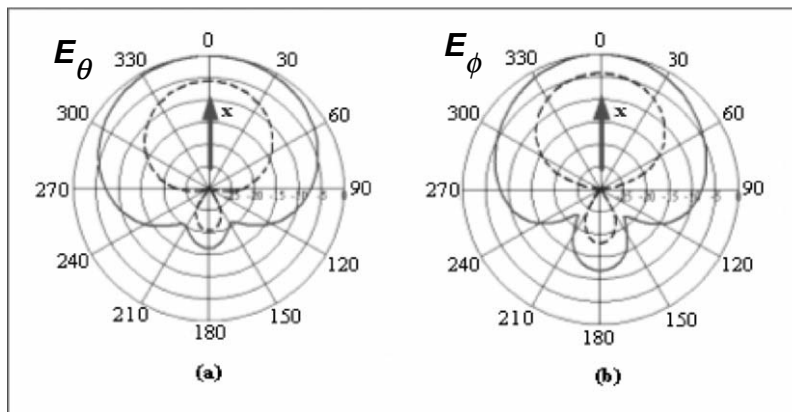


**Fig. 8.** Beams of the single microstrip Archimedean spiral at 2.5 GHz; *Solid*:  $\epsilon_r = 9.6$ , *Dashed*:  $\epsilon_r = 1.0$

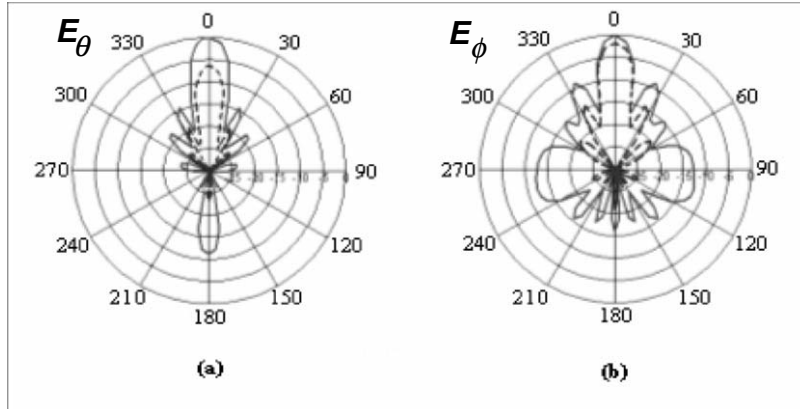


**Fig. 9.** Beams of the  $2 \times 5$  microstrip Archimedean spiral array at 2.5 GHz; *Solid:*  $\epsilon_r = 9.6$ , *Dashed:*  $\epsilon_r = 1.0$

## Conclusion

Design alternatives of low-cost, small-size broadband Archimedean spiral arrays for wireless applications are discussed. The dimensions are specified according to optimum CP performance around 2.5 GHz. Their beam forming and beam steering capabilities are investigated. Numerical simulations showed that this structure may be used to cover all radio/TV broadcast up to several GHz frequencies. Electronically and/or mechanically switched sub arrays of  $2 \times 3$  or  $2 \times 4$  can also be used without severe degradation in broadband nature and beam forming performances if space/dimension is a critical design parameter.

## References

- [1] R. Sivan-Sussman, "Various modes of the equiangular spiral antenna", *IEEE Trans. Antennas and Propag.*, vol. 11, pp. 533–539, September 1963
- [2] J.A. Kaiser, "The Archimedean two-wire spiral antenna", *IRE Trans. Antennas Propag.*, AP-8, pp. 312–323, May 1960
- [3] H. Nakano, K. Nogami, S. Arai, H. Mimaki and J. Yamauchi, "A spiral antenna backed by a conducting plane reflector", *IEEE Trans. Antennas Propag.*, vol. 34, No. 6, pp. 791–796, 1986
- [4] W.L. Stutzman, G.A. Thiele, *Antenna Theory and Design*, second ed., Wiley NY, USA, 1998

- 
- [5] C.W. Penney, R.J. Luebbers, "Input impedance, radiation pattern and radar cross section of spiral antennas using FDTD", *IEEE Trans. Antennas Propag.*, vol. 42, No. 9, pp. 1328–1332, 1994
  - [6] K. Nakayama, H. Nakano, "Radiation characteristics of a conformal spiral antenna", *Electron. and Commun. in Jpn*, Part 1, vol. 83, no. 5, pp. 107–114, 2000
  - [7] H. Nakano, J. Eto, Y. Okobe, J. Yamauchi, "Tilted- and axial-beam formation by a single-arm rectangular spiral antenna with compact substrate and conductive plane", *IEEE Trans. Antennas Propag.*, vol. 50, no. 1, pp. 17–23, 2002
  - [8] H. Nakano, H. Yasui and J. Yamauchi, "Numerical analysis of two-arm spiral antennas printed on a finite-size dielectric substrate", *IEEE Trans. Antennas Propag.*, vol. 50, no. 3, pp. 362–370, 2002
  - [9] H. Nakano, M. Ikeda, K. Hitosugi and J. Yamauchi, "A spiral antenna sandwiched by dielectric layers", *IEEE Trans. Antennas Propag.*, vol. 52, no. 6, pp. 1417–1423, 2004
  - [10] J.M. Bell, M.F. Iskander, "A low-profile Archimedean spiral antenna using a EBG ground plane", *IEEE Antennas Wireless Propag. Lett.* vol. 3, pp. 223–226, 2004
  - [11] M.N. Afsar, Y. Wang, R. Cheung, "Analysis and measurement of a broadband spiral antenna", *IEEE Antennas Propagation Magazine*, vol. 46, no. 1, pp. 59–64, 2004
  - [12] T. Cencich, J.A. Huffman, "The analysis of wideband spiral antennas using modal decomposition", *IEEE Antennas Propag. Mag.*, vol. 46, no. 4, pp. 20–26, 2004
  - [13] H. Nakano, K. Hitosugi, N. Tatsuzawa, D. Togashi, H. Mimaki, J. Yamauchi, "Effects on the radiation characteristics of using a corrugated reflector with a helical antenna and an electromagnetic band-gap reflector with a spiral antenna", *IEEE Trans. Antennas Propag.*, vol. 53, no. 1, pp. 191–199, 2005
  - [14] L. Sevgi, G. Çakir, "A broadband array of archimedean spiral antennas for wireless applications", *Microwave Opt. Technol. Lett.*, January 20, 2006
  - [15] L. Sevgi, *Complex EM Problems and Numerical Simulation Approaches*, IEEE Press and Wiley, NY, USA, 2003
  - [16] G.J. Burke, A.J. Poggio, Numerical electromagnetic code-Method of Moments, part I: Program description, theory, Technical Document, 116, Naval Electronics System Command (ELEX 3041), July (1977)

# Analysis of Multiple Vertical Strips in Planar Geometries via DCIM-MoM

T. Önal<sup>1</sup>, N. Kinayman<sup>2</sup> and M. İ. Aksun<sup>1</sup>

<sup>1</sup>Department of Electrical and Electronics Engineering, Koç University, Sariyer, Istanbul, 34450, Turkey e-mails: tonal@ku.edu.tr; iaksun@ku.edu.tr

<sup>2</sup>M/A-COM, Corporate RD, 1011 Pawtucket Blvd. M/S 261, Lowell, MA 01853 USA e-mail: kinayman@tycoelectronics.com

## Abstract

Vertical metallizations in planar geometry, like via holes in MMICs, shorting strips, and probe feeds in microstrip antennas, have become the integral parts of high-frequency circuits and/or multifunction antennas. Therefore, an efficient full-wave electromagnetic simulation algorithm needs to be developed for the analysis of planar geometries with multiple vertical metallizations. In this study, it is demonstrated that using the method of moments (MoM) in conjunction with the discrete complex image method (DCIM) for the analysis of printed structures with multiple vertical strips results in a robust and efficient full-wave analysis tool. The use of DCIM together with MoM has already proved to be very efficient for printed geometries, where efficiency implies the overall computational performance. However, the approach proposed here is not only efficient in this sense but also extremely efficient to handle multiple vertical metallization.

## Introduction

Spatial-domain method of moments (MoM) is one of the most popular techniques for the solution of mixed-potential integral equation (MPIE) for printed geometries in multilayer planar media [1]. Introduction of the closed-form Green's functions with the help of discrete complex image method (DCIM) [2], their robust and efficient derivation using the two level approach [3,4] and analytical evaluation of the corresponding matrix entries [5] have improved the efficiency of this method considerably. However, this efficiency was only achievable in the case of horizontal-only planar conductors and several problems arise in the implementation of the vertical metallizations mainly due to the implementation of DCIM to get spatial-domain Green's functions. The problems related to the implementation of DCIM-MoM for the analysis of printed geometries with vertical metallization

were discussed and their remedies were proposed and implemented in [6]. In this work, the method proposed and implemented in [6] for the analysis of vertical metallization is extended to facilitate the analysis of printed structures with multiple vertical metallization with almost no additional computational cost to the cost of the same horizontal geometry with one vertical metallization.

## Formulation of the Problem

For the sake of illustration, a typical 3D microstrip structure is shown in Fig. 1, where there are multiple planar layers with infinite extent in transverse directions, i.e.,  $xy$ -plane, and two vertical strips.

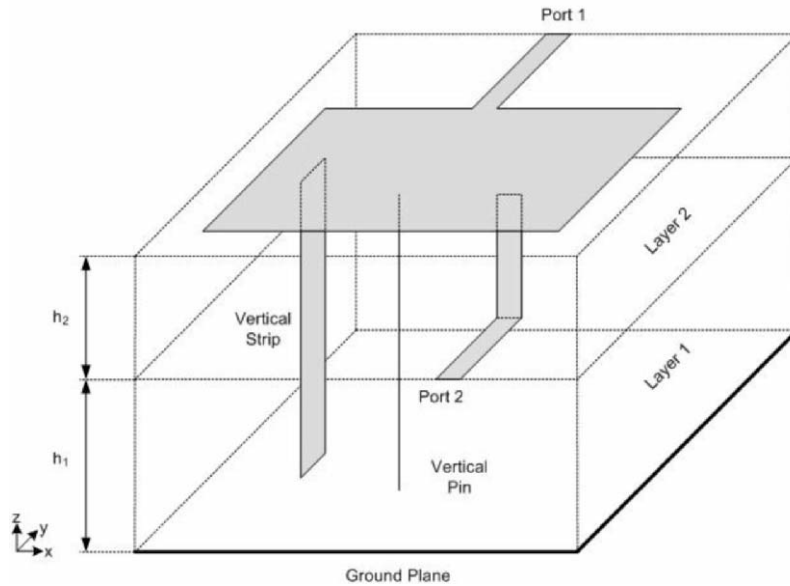


**Fig. 1.** A general 3D microstrip structure

The analysis of such structures via DCIM-MoM requires writing MPIE first: the tangential components of the electric field on the conductor surfaces are written in terms of the surface current density  $\mathbf{J}$  and the associated Green's functions of vector and scalar potentials, which result in the following MPIEs:

$$E_i = -j\omega G_{ii}^A * J_i + \frac{1}{j\omega} \frac{\partial}{\partial i} (G^q * \nabla \cdot \mathbf{J}) \quad \text{for } i = x, y, \quad (1)$$



$$E_z = -j\omega G_{zx}^A * J_x - j\omega G_{zy}^A * J_y - j\omega G_{zz}^A * J_z + \frac{1}{j\omega} \frac{\partial}{\partial z} (G^q * \nabla \cdot \mathbf{J}), \quad (2)$$

where  $G_{xx}^A = G_{yy}^A$ , the term  $G_{ij}^A$  and  $G^q$  represent the  $i$ -directed vector potential at  $\mathbf{r}$  due to a  $j$ -directed electric dipole of unit strength located at  $\mathbf{r}'$  and the scalar potential of a unit point charge associated with an electric dipole, respectively. As the integral equations are obtained in the spatial domain, the Green's functions – the kernels of integral equations – need to be obtained in the spatial domain as well, where DCIM is employed to transfer the spectral-domain Green's functions (known analytically in planar layered media) to the spatial domain analytically [4]. Once the spatial-domain Green's functions are obtained in closed-forms, the only unknown, the current density in the integral equations, can be solved for by using the MoM, which transfers the integral equation to a set of linear equations. In the implementation of the MoM, the unknown function, the surface current density  $\mathbf{J}$  in this case, is expanded in terms of known basis functions with unknown coefficients, as  $J_i(x, y, z) = \sum_m I_i^{(m)} B_i^m(x, y, z)$ , where  $i$  can be  $x$ ,  $y$  or  $z$ ,  $B_i^m$  is the basis function with unknown coefficient  $I_i^{(m)}$  defined at  $m$ th, position on the subdivided conductor. After substituting the expanded current densities into the integral equations (1) and (2), the boundary conditions are applied in the integral sense through the well-known testing procedure of the MoM, where the field expressions are multiplied by known testing functions  $T_i^{m'}$  for  $i = x, y, \text{ or } z$  and integrated on the conductors and set to zero. As a result of all these steps, a matrix equation for the unknown amplitudes of the basis functions is obtained as  $[\mathbf{Z}][\mathbf{I}] = [\mathbf{V}]$ , where  $\mathbf{Z}$  is the impedance,  $\mathbf{V}$  is the excitation, and  $\mathbf{I}$  is the unknown current amplitude matrices. Note that the impedance matrix is composed of sub-matrices,  $Z_{xx}, Z_{xy}, Z_{yx}$ , and  $Z_{yy}$ , corresponding to matrix entries due to horizontal conductors, and  $Z_{xz}, Z_{zx}, Z_{yz}, Z_{zy}$ , and  $Z_{zz}$ , corresponding to matrix entries due to vertical conductors and to interactions of vertical conductors with horizontal conductors, all of which were already given in [6]. In the evaluation of the matrix entries corresponding to vertical conductors, the main difficulty arises from the implementation of DCIM to get the spatial-domain closed-form Green's functions, which require the use of constant  $z$  and  $z'$  values during the exponential approximation of the spectral-domain Green's functions via the generalized pencil-of-function method. In other words, employed closed-form Green's functions are only valid for those fixed values of  $z$  and  $z'$ . However, since MoM matrix entries associated with the vertical conductors require the convolution and inner-product integrals to be performed over  $z$  and/or  $z'$  variables, such an approximation with fixed values of  $z$  and  $z'$  results in a Green's function for the fixed values of  $z$  and  $z'$ , but cannot be used to calculate the convolution and inner-product integrals. As a result, MoM matrix entries involving  $z$  and/or  $z'$

integrations need a special treatment, which was proposed in [6] and is demonstrated on the following inner-product term:

$$\left\langle \frac{\partial}{\partial z} T_z(y, z), G_x^q * \frac{\partial}{\partial x} B_x(x, y) \right\rangle = \int dy T_z(y) \iint dx' dy' \frac{\partial}{\partial x'} B_x(x', y') \cdot \int dz \frac{\partial}{\partial z} T_z(z) G_x^q(x-x', y-y', z, z' = \text{cons}). \quad (3)$$

Note that the integration over  $z$  in (3) is the source of the problem since the closed-form spatial-domain Green's function  $G_x^q$  is already evaluated at constant  $z$ . So to be able to employ it in the above integration, it has to be evaluated at sufficiently enough points along the  $z$ -direction. However, if the spatial-domain Green's function  $G_x^q$  is written in terms of its spectral-domain representation  $\tilde{G}_x^q$ , the innermost integral in the above expression becomes

$$F_x^q \stackrel{\text{def}}{=} \int dz \frac{\partial}{\partial z} T_z(z) \frac{1}{4\pi} \int_{SIP} dk_\rho k_\rho H_0^{(2)}(k_\rho |\rho - \rho'|) \tilde{G}_x^q(k_\rho, z, z' = \text{cons}) \equiv \frac{1}{4\pi} \int_{SIP} dk_\rho k_\rho H_0^{(2)}(k_\rho |\rho - \rho'|) \cdot \text{GPOF} \left\{ \int dz \frac{\partial}{\partial z} T_z(z) \tilde{G}_x^q(k_\rho, z, z' = \text{cons}) \right\}, \quad (4)$$

where  $\text{GPOF} \{ \}$  represents the approximation process with complex exponentials by using the GPOF method. The integration over  $z$  can be evaluated analytically once the spatial-domain Green's function in the inner-product expression (3) is written in terms of the inverse transform of its spectral-domain representation. Then, the exponential approximation procedure using the GPOF method is invoked for the resulting spectral-domain function. Therefore, the need for evaluation of the spatial-domain Green's function at different  $z$ -points is eliminated by obtaining this auxiliary function. When  $F_x^q$  is substituted into (3), the following expression is obtained:

$$\left\langle \frac{\partial T_z}{\partial z}, G_x^q * \frac{\partial B_x}{\partial x} \right\rangle = \iint du dv F_x^q(u, v, z' = \text{cons}) \cdot \int dy T_z(y) \frac{\partial}{\partial u} B_x(x-u, y-v), \quad (5)$$

where  $x-x'=u$ ,  $y-y'=v$ , and  $x=x_{sp}$ , i.e., the  $x$ -coordinate of the vertical metalization which is constant for this case. Note that the evaluation of the auxiliary function  $F_x^q(u, v)$  does not depend on the lateral directions, and they are explicit functions of  $u = x - x'$  and  $v = y - y'$ . Therefore, as long as the basis functions used to represent the current densities along the vertical conductors have identical  $z$ -dependencies, the same auxiliary functions can be used to find the matrix entries corresponding to another vertical strip. In other words, the auxiliary functions corresponding to the basis and/or testing functions on a vertical conductor are obtained as explicit functions of  $x$  and  $y$ , as long as the domains of  $z$  and  $z'$

integrations are the same. This is not a severe restriction because it only requires the use of the same basis and testing functions for all vertical conductors, and no restriction on the meshing of horizontal conductors.

## Results and Discussions

In this part of the study, the formulation described above is applied to a microstrip line with four vertical  $y$ -spanning strips, as shown in Fig. 2, to assess the computational efficiency of the method. Note that the word “efficiency” used here is in the sense of MoM matrix fill-in time required for every additional vertical conductor. The dielectric constant of the medium is  $\epsilon_r = 4.0$ , the length and width of the line is 18.0 and 0.1 cm, respectively. The thickness of the substrate is 0.4 cm, the frequency of operation is 2 GHz. To validate the method, the current distribution along the microstrip line is obtained by the method proposed in this paper, and compared to that from a commercially available EM simulation software *em* by Sonnet. An excellent agreement is observed, slight differences in the amplitude can be attributed to the inherent models of the approaches: *em* by Sonnet solves the problem in shielded environment while the method proposed here solves it in open environment, which inevitable causes some differences on the resonant frequencies for the structures.

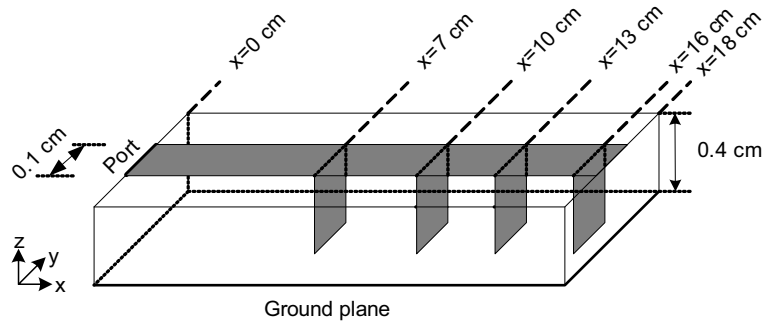


**Fig. 2.** Microstrip line with shorting strips:  $f = 2.0$  GHz,  $\epsilon_r = 4.0$

Once the validation is complete, the computational efficiency of the proposed method is assessed in terms of the CPU (central processing unit) time obtained from a 1.5 GHz Centrino CPU. Considering that the basic unit of the whole method is the GPOF method, and that it is repeatedly used to get the closed-form Green’s functions and the auxiliary functions, Table 1 provides the information on the total number of GPOF implementation and the total CPU times corresponding to Green’s functions with fixed  $z$  and  $z'$  values (for a 3D structure, only  $G_{xx}^A = G_{yy}^A$  and  $G_x^q$  are in this category), and corresponding to different types of

auxiliary functions. Note that these counts are based on assuming two basis functions along the vertical conductors, and two counts of GPOF for each Green's function and three counts of GPOF for each auxiliary functions. As the thickness of the substrate is uniform, which is usually the case for most of antenna and microwave applications, two basis functions are used over every vertical strip, and naturally they have the same  $z$  and  $z'$  dependencies, satisfying the only criterion for the efficiency of the method for multiple vertical strips.

After having noted the fundamental contributor to the fill-in time, and its counts, the microstrip line in Fig. 2 is first analyzed with one vertical strip (at  $x = 7.0$  cm), and then the number of vertical strips is increased to four by one-by-one.

As the ultimate measure for the efficient handling of multiple vertical metallization, in addition to the first one, the percentage increase in the matrix fill time for additional vertical strips are listed in Table 2. It is observed that adding new vertical strips to the existing ones has almost no effect on the computational complexity of the whole method. This can be stated with numbers that adding new vertical strips to the microstrip line with one vertical strip costs about 1.2 percent of the cost of adding the first vertical strip. In Table 2, the CPU time to fill the MoM matrix entries of the first vertical strip is normalized to 100, excluding already filled in  $Z_{xx}$  entries, and the CPU times to fill the additional MoM matrix entries corresponding to 2nd, 3rd and 4th vertical strips are found to be less than 1.3 s each.

**Table 1.** Gpof count and corresponding cpu times

Green's or Auxiliary functions involving	Number of GPOF applied	CPU time (s)
no $z$ or $z'$ integrations	4	1.078
only $z$ or $z'$ integrations	18	2.000
both $z$ and $z'$ integrations	24	3.500

**Table 2.** Percentage increase in matrix fill time

Number of vertical strips	Percentage increases in Matrix fill time (%)
1	100
2	1.207
3	1.234
4	1.272

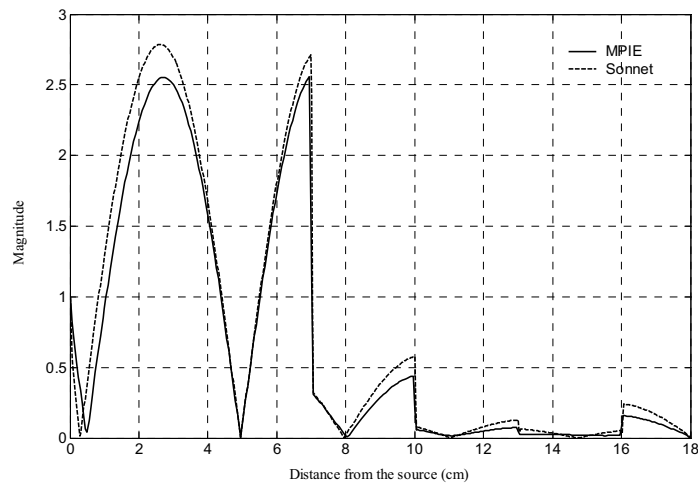


**Fig. 3.** Magnitudes of the current distribution obtained by using the proposed method (designated by MPIE) and by *em* from Sonnet

## Conclusion

As vertical conductors have become the indispensable parts of microwave and antenna circuits, there has been demand for EM-based simulation tools that would efficiently handle printed structures with multiple vertical metallization. In this paper, this issue has been addressed with a proposed method and its validation. Since the efficiency of the DCIM-MoM for horizontal only structures has already been proven, this method has recently been tailored for printed structures with multiple vertical conductors. In the case of vertical conductors, the efficiency of the method, DCIM-MoM, has been hindered by the difficulties arising during the use and derivation of spatial-domain Green's functions. After having addressed these difficulties with a suitable solution, its extension to multiple vertical metallizations has been explained. It has been shown mathematically and numerically that as long as the vertical dependencies of the basis or testing functions are chosen to be the same, the inclusion of additional vertical metallizations is extremely efficient. Therefore, this approach seems to be a good candidate to use in conjunction with an optimization algorithm in a CAD tool.

## References

- [1] J.R. Mosig, "Arbitrarily shaped microstrip structures and their analysis with a mixed potential integral equation", *IEEE Trans. on Microwave Theory Technol.*, vol. MTT-36, no. 2, pp. 314–323, February 1988
- [2] Y.L. Chow, J.J. Yang, D.G. Fang, G.E. Howard, "A closed-form spatial Green's function for the thick microstrip substrate", *IEEE Trans. Microwave Theory Technol.*, vol. 39, pp. 588–592, March 1991
- [3] G. Dural, M.I. Aksun, "Closed-form Green's functions for general sources and stratified media", *IEEE Trans. Microwave Theory Technol.*, vol. 43, pp. 1545–1552, July 1995
- [4] M.I. Aksun, "A robust approach for the derivation of closed-form Green's functions", *IEEE Trans. Microwave Theory Technol.*, vol. 44, no. 5, pp. 651–658, May 1996
- [5] L. Alatan, M.I. Aksun, K. Mahadevan, M.T. Birand, "Analytical evaluation of the MoM matrix elements", *IEEE Trans. on Microwave Theory Technol.*, vol. 44, pp. 519–525, April 1996
- [6] N. Kinayman, M.I. Aksun, "Efficient use of closed-form Green's functions for the analysis of planar geometries with vertical connections", *IEEE Trans. Microwave Theory Technol.*, vol. 45, pp. 593–603, May 1997

# A Matlab-based Filter Design Tool Using the Analogy between Wave and Circuit Theories

G. Çakir<sup>1</sup>, S. Gündüz<sup>1</sup> and L. Sevgi<sup>2</sup>

<sup>1</sup> Department of Electronics and Communication Engineering, Kocaeli University  
Kocaeli, Turkey, gonca@kou.edu.tr, sibel@kou.edu.tr

<sup>2</sup> Department of Electronics and Communication Engineering,  
Doğuş University, Acıbadem, 81010, Istanbul, Turkey, lsevgi@dogus.edu.tr

## Abstract

A Matlab-based lumped (LC) and scattered (microstrip line) filter design tool is designed. Based on the analogy between wave and circuit (transmission line) theories a broadband filter prototype is introduced for all types of lowpass, highpass, bandpass, and bandstop filters. The designed microstrip filters are also validated via the finite-difference time-domain method. The tool can be used as teaching, learning, and design purposes.

## Introduction

Lumped element filter theory has already reached in its mature stage and design principles and steps are mostly given in undergraduate lecture notes (see, for example, [1] for classical approaches and examples). On the other hand, the design of microwave filters based on waveguides, cavities, and microstrip circuits has been subject of many articles, and still remains of great importance in the development of microwave networks (see, for example, [2, 3]). Basically, there are two different microstrip filter design approaches; to start with full wave electromagnetic equations, or to use the analogy between wave and circuit (transmission line) theories [4].

In this paper, a Matlab-based filter design tool, FILTER\_GUI, is introduced. The user first selects the filter type (one out of four) and then specifies filter parameters – frequency band, center frequency, attenuation, etc. Then, the order of the filter is calculated and the lumped (LC) element filter prototype is designed. A generic microstrip line filter is used for all types of filters, and once the LC prototype is ready the tool calculates microstripline filter dimensions based on the analogy between wave and circuit (transmission line) theories. The full-wave finite-difference time-domain simulator M-PATCH [3] is also used for data verification.

## Analog (Lumped Element) Filter Theory

Analog filter theory deals with the design of lumped (LC) element filters. There are various mathematical methods in analog filter theory. Two of them are widely used (see Fig. 1);

- Butterworth filters which satisfy the desired amplitude response without ripples inside the passband
- Chebyshev filters which yields steeper initial descent into the stopband, and the payoff is the undesired ripples in the passband.

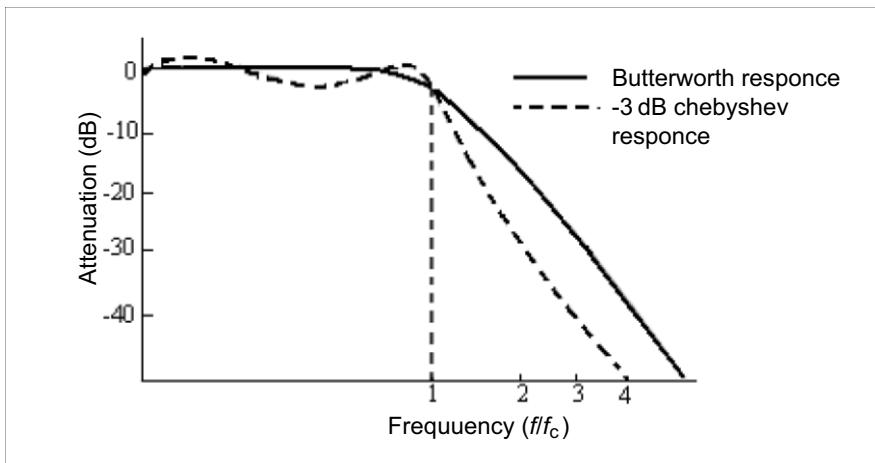


**Fig. 1.** The Butterworth and Chebyshev filter responses

In a two port circuit, each of the  $L$  and  $C$  elements and their combinations has different frequency characteristics at microwaves. For example, a capacitor (inductor) connected parallel (serial) between the input and output ports, behaves like a low-pass filter. On the other hand, they behave like highpass filters if connected serially between the input and output. Cascading multiple of these elements results in broadband filters as depicted in Fig. 2. Here, Chebyshev type filter is used.

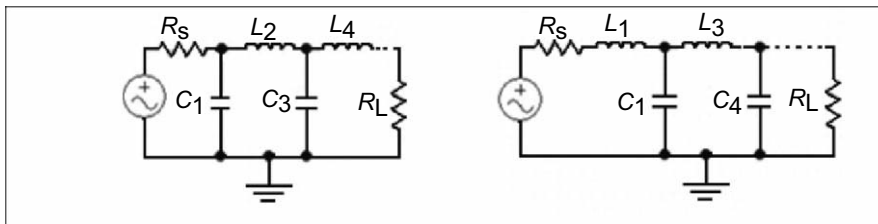


**Fig. 2.** Two typical lowpass filter prototypes



The design parameters for the Chebyshev filters are the maximum permissible ripple in the passband  $R_{dB}$  and the attenuation at a given frequency beyond the passband,  $A_{dB}$ . The order of the filter is specified from these two parameters. The actual design procedure is nothing but supplying these two filter characteristics. The first step is to guess the order of the lowpass prototype. The lowpass prototype has a source impedance of  $R_s=1 \Omega$  and a cutoff frequency of  $\omega_c=1$ . By using the frequency and impedance scaling lowpass prototype can be converted into a highpass, bandpass, or bandstop prototype (Fig. 3).

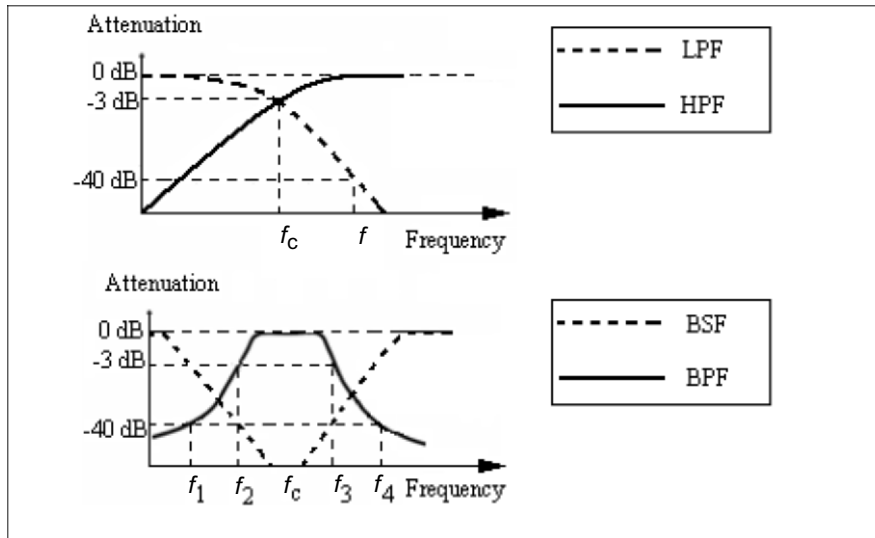


Fig. 3. Lowpass, highpass, bandpass, and bandstop filter characteristics

## Microstrip Filter Design

Lumped (LC) element filters mostly work at low frequencies. Circuit elements such as inductors and capacitors are available only for a limited range of values and are difficult to implement at microwaves. Also electrical effects of element seals, connection wires, jumper lengths, etc., are no longer negligible at microwave frequencies. Therefore, scattered parameters approach (i.e., transmission line theory) is used in filter design at microwaves.

Microwave filters are mostly integrated on a printed board with other system circuits and elements, therefore microstrip lines are the basic filter elements at microwaves. One design approach is to use Richard's transformations coupled with Kuroda's four identities [2], which allows realization of the lumped element filter prototypes in terms of open or short-circuited transmission line stubs [4] (see

Fig. 4) (Note that  $N$  is the degree of a filter). Richard's transformations convert series inductors to series stubs, and shunt capacitors to shunt stubs. Since microstrip-line implementation of the series stubs is extremely difficult. Kuroda identities are used to convert these to shunt stubs (see Fig. 5).

Richard's transformation is used in the implementation of lowpass filter prototype at microwaves. With this transformation a lowpass filter prototype can be transformed into its transmission line equivalent lowpass prototype. According to Richard's transformation a capacitor can be replaced with an open-circuited stub, and an inductor can be replaced with a short-circuited stub (see Fig. 6). The lengths of these stubs should be  $\lambda/8$  at the cutoff frequency. Note that  $N$  is the degree of a filter.

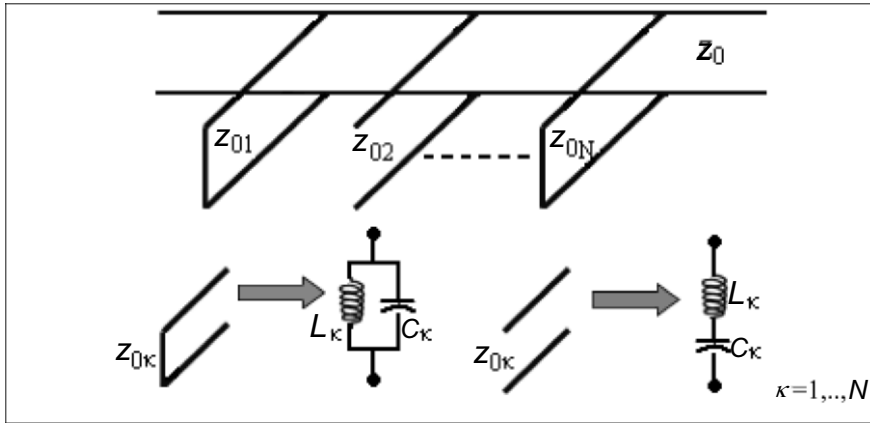


Fig. 4. Open- and short-circuited transmission line stubs and their equivalent circuits

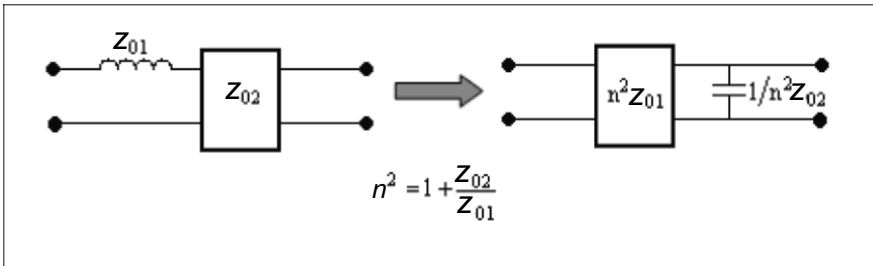
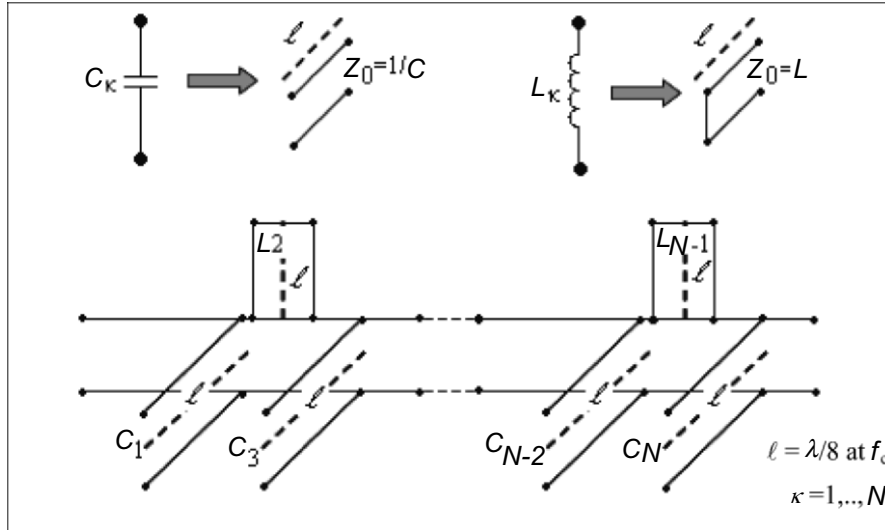
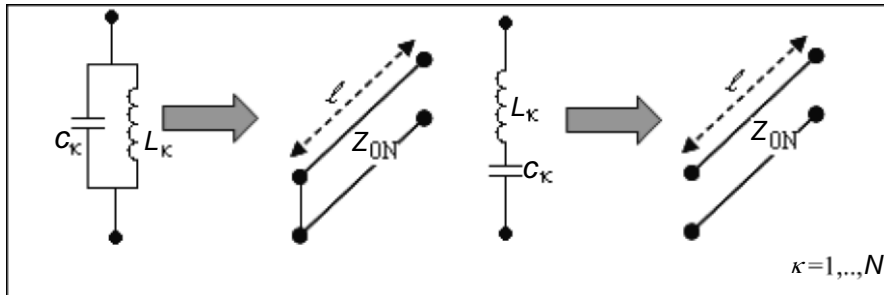


Fig. 5. Series to parallel stub using Kuroda identities



**Fig. 6.** Lumped (LC) element to transmission line lowpass filter transformation

At microwaves, bandpass, and bandstop filters require elements which behave as series or parallel resonant circuits. Therefore, bandpass and bandstop filter prototypes can be realized using quarter-wavelength-long transmission line resonators. A parallel resonator circuit of lumped element filter prototype can be replaced with a short-circuited stub [3] (see Fig.7). On the other hand, a series resonator in bandstop filter prototype can be replaced with an open-circuited stub at microwave frequencies.



**Fig. 7.** Filter sections used in bandpass and bandstop filter at microwave frequencies

### The Matlab Filter Design Package

The MATLAB tool FILTER.GUI has been prepared for both LC and microstrip circuit filter design [4]. The front panel of the tool is shown in Fig. 8. A pop-up menu at top-right is reserved for the selection of any of lowpass, highpass, band-pass and bandstop filter types. Once the user specifies a filter type the filter frequency characteristic, its LC prototype, and the microstripline prototype appear at top-left. Filter characteristics and microstripline substrate specifications (dielectric thickness and relative permittivity) are supplied by the user either from the data boxes or by using the sliding bars. The output data of the designed filter is given at bottom-left. Here, the order of the filter, values of LC elements, and the dimensions of the microstripline prototype filter are given at this section. The graph at bottom-right is for the frequency response of the designed filter. The transfer function vs. frequency (either in linear or in logarithmic scale) is given at this window. Lowpass filter is used as the default type in the front panel.

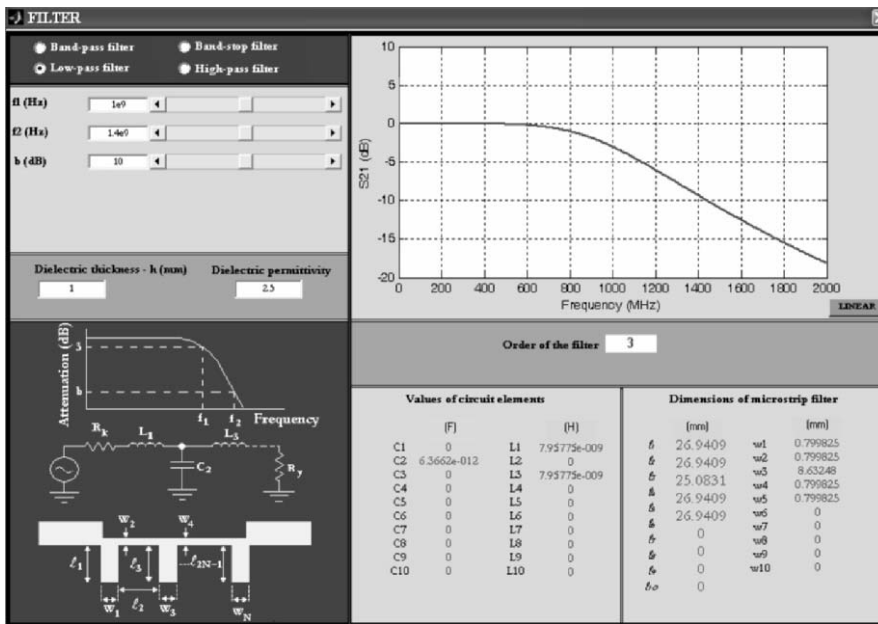
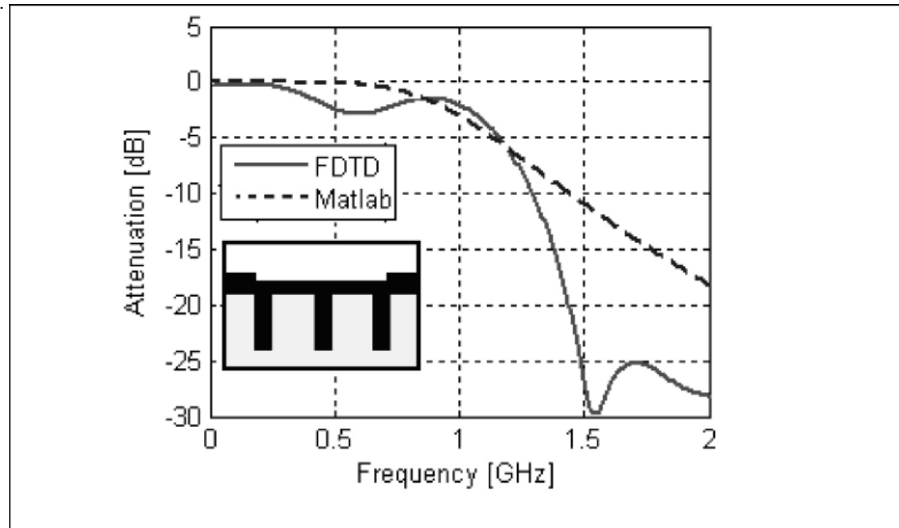


Fig. 8. The front panel of the FILTER\_GUI tool with a third-order lowpass filter design

An example of a lowpass filter design is presented in Fig. 9. Here, the user specifies the 3 dB filter cutoff frequency as 1 GHz, and 10 dB attenuation at 1.4 GHz. With these specifications the order of the filter is found to be 3. The values of the LC elements of the third-order lowpass filter and microstrip filter dimensions are calculated accordingly. Insertion loss vs. frequency obtained with both the Matlab filter tool and M-PATCH package are also given in Fig. 10. As observed, filter characteristics are in good agreement.



**Fig. 9.** The filter responses obtained via both Matlab tool and the M-PATCH package

The next example belongs to a bandpass filter design. A 1 GHz passband around the center frequency of 2 GHz is requested. The outof passband attenuation is requested to be 20 dB at 3 GHz. Figure 9 shows frequency responses of this filter. Again, the specifications are observed to be satisfied.

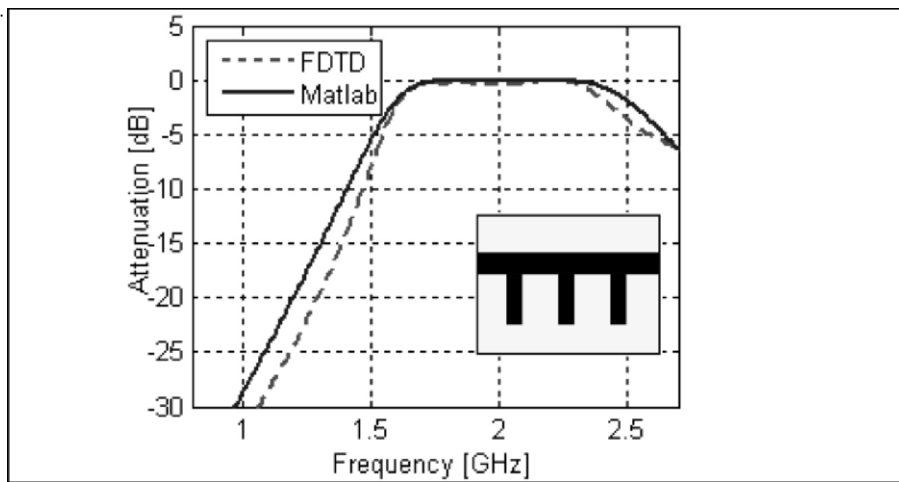


**Fig. 10.** A third-order bandpass filter design; Insertion loss vs. frequency obtained via the tool and M-PATCH package

## Conclusion

The analogy between lumped and scattered parameter representations can be used in filter design. A Matlab filter tool that can be used for both engineering and educational purposes is designed. Any type of a filter with the desired band and attenuation characteristics is chosen first. The tool designs the filter with LC elements and then converts it into a microstrip line filter. The same microstrip circuit is used for all types of filters and the desired characteristics are satisfied by only adjusting the widths and lengths of main line and the stubs.

## References

- [1] C. Bowick, *Circuit Design*, NewNess, Boston, 1982
- [2] M.D. Pozar, *Microwave Engineering*, Addison-Wesley, Menlo Park, 1990
- [3] L. Sevgi, *Complex Electromagnetic Problems and Numerical Simulation Approaches*, IEEE Press, Piscataway, NJ, 2003
- [4] S. Gündüz, "Broadband microstrip filter design", M.S.E.E Thesis, University of Koçaeli, 2005

# A Generic Microstrip Structure with Broadband Bandstop and Bandpass Filter Characteristics

G. Çakir<sup>1</sup> and L. Sevgi<sup>2</sup>

<sup>1</sup>Department of Electronics and Communication Engineering,  
Kocaeli University, Kocaeli, Turkey, gonca@kou.edu.tr

<sup>2</sup>Department of Electronics and Communication Engineering,  
Doğuş University, Acıbadem, 81010 Istanbul, Turkey, lsevgi@dogus.edu.tr

## Abstract

Novel, generic double-arm microstrip structures which can be used as both electromagnetic bandstop and bandpass filters are introduced. The design steps, numerical simulations, practical realization, and experimentations are briefly discussed. Examples of microstrip electromagnetic bandstop and bandpass filters are presented.

## Introduction

Microstrip planar electromagnetic (EM) bandstop (BS) and bandpass (BP) structures have been widely used in microwave and millimeter wave wireless systems and MMIC applications [1, 2], for example, to improve radiation and beam steering characteristics of antennas [3], to achieve high performance filters, to act as an artificial magnetic conductor [4], to form frequency-selective surfaces, and to design power dividers, couplers, etc. These structures have attracted significant interest especially because of the simplicity in manufacturing and ease in monolithically integration with other circuits.

Novel, generic microstrip double-arm structures are introduced to design compact EM BS and BP filters. One of the structures was first introduced in [5] for the realization of EM bandgap filters. Then, the double-arm structure has been modified also to obtain EM BP filters [6]. In this paper, first, analog filter design principles are summarized briefly to give a clue for the construction of the generic structure. Then, characteristics of the EM BS and BP filters are analyzed with an FDTD-based M-PATCH package [7, 8]. The dimensions are optimized after a series of numerical simulations. Finally, the filters are fabricated, the scattering parameters are measured, and the results are presented as insertion loss vs. frequency.

## Classical Chebychev-Type Broadband Filters

Broadband filters may be designed by using serial/parallel combinations of multi-inductor ( $L$ ) and capacitor ( $C$ ) elements. The theory of analog filter design is in its mature stage and variety of filter analysis and synthesis methods can be found in classical books. One of the different types is the Chebychev filter, which is used when steeper descent (attenuation) beyond the passband is required at a cost of a permissible ripple (see, [9] for brief information and various applications). The design parameters of the Chebychev filter are the maximum permissible ripple inside the band, and the attenuation at a given frequency outside, that determines the descent rate; from which the order of the filter can be extracted. Figure 1 illustrates frequency characteristics of EM BS and BP filters.

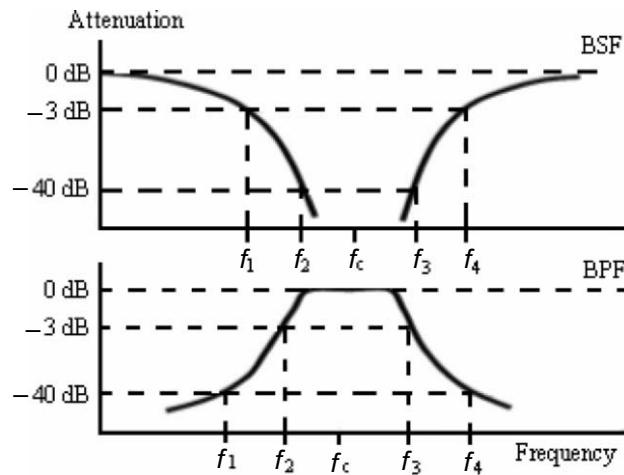


**Fig. 1.** EM BS (top) and BP (bottom) filter design characteristics

The standard design prototype is the lowpass filter (LP), and the other prototypes – highpass (HP), BP and BS filters – can be derived from this LP design. A generic third-order LP filter that can be used to design BP and BS filters is shown in Fig. 2 together with LP to BP, and LP to BS filter transformations. As shown in Fig. 2, serial  $LC$  resonant circuits inserted parallel, and parallel resonant circuits inserted serially between input and output behaves as a BS filter. Alternatively, a parallel  $LC$  resonant circuit inserted parallel, and series resonant circuit inserted serially between input and output behaves as a BP filter. In other words, replacing serial and parallel resonant pairs in the circuit results in a transformation from BS to BP filter, and this forms the initiative of the design of the generic double-arm microstrip structure.



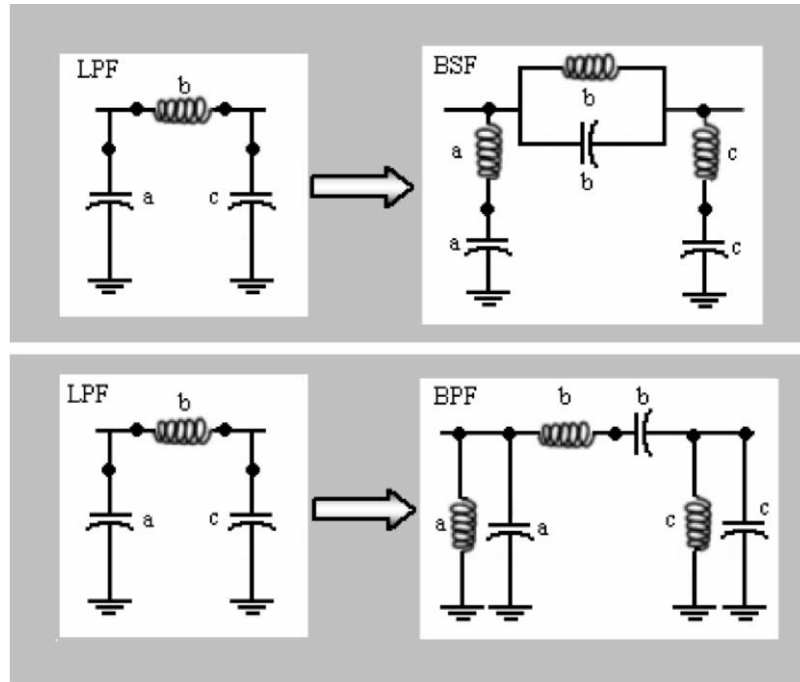


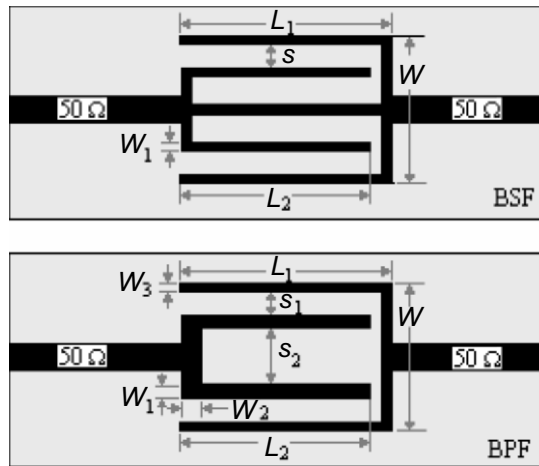
**Fig. 2.** Classical analogy between LP and BS (top), and BP (bottom) filters. Actual values are obtained via well-known transformation equations [9]

## The Generic Double-Arm Microstrip Structures

Lossless open- or short-circuited (i.e., OC or SC) short stubs act as pure inductors or capacitors, depending on the signal wavelength [7], and they are widely used in microstrip circuits, such as impedance matchers, couplers, filters, etc. Similarly, OC and/or SC stubs may be used as serial or parallel resonant pairs when bend and coupled to the main line in microstrip circuits.

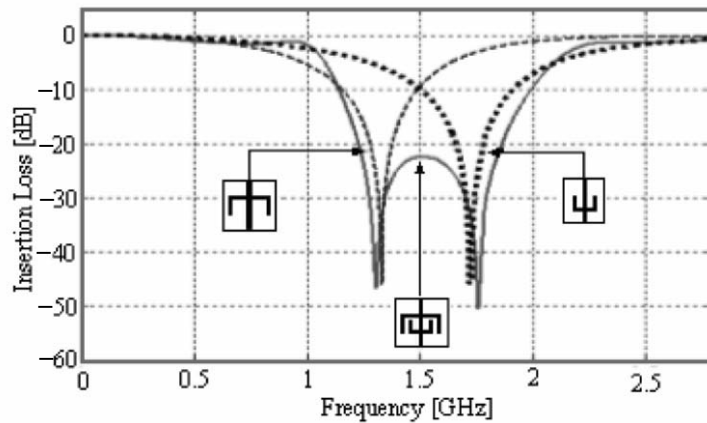
The proposed structures are given in Fig. 3, and are composed of two slot-etched (L-shaped) stubs one coupled to the other on the rectangular patch. The two L-shaped stubs, one in the vicinity of the other, on both sides of the main line (top figure) act as two parallel  $LC$  circuits with two different resonance frequencies, and are capacitively coupled each other so as to obtain broad and clean stopband characteristics. Once the main line is removed and sizes are optimally selected (bottom figure) the structure behaves like a BP filter. These generic structures are investigated numerically as well as experimentally (and found that it is almost equivalent to the third-order BS and BP structures given in Fig. 2). First, the dimensions are optimized according to the design requirements by performing

several simulation trials via the FDTD package M-PATCH [7]. Then, the structure is fabricated with optimum dimensions and its  $S$ -parameters are measured with Agilent-8714 ES network analyzer.



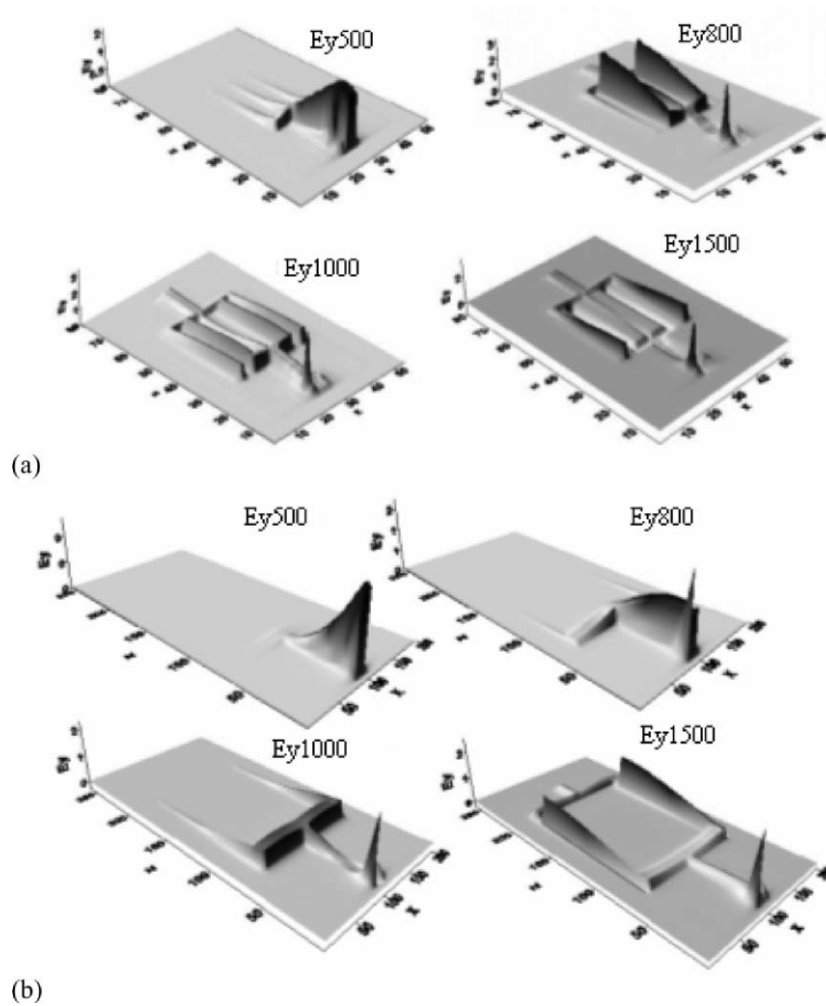
**Fig. 3.** Proposed microstrip generic structure for EM BS (a), and BP (b) filters

Figure 4 explains the analogy of the proposed structure for the BS filter design. Here, the structure in Fig. 3a is used and the parameters are chosen as follows: Center frequency: 1.5 GHz, bandwidth: 500 MHz, attenuation: 40 dB, input/output loads:  $50 \Omega$ , substrate  $\epsilon_r = 2.4$ , thickness:  $h = 1$  mm,  $W = 25$  mm,  $L_1 = 30$  mm,  $L_2 = 27$  mm,  $s = 5$  mm.



**Fig. 4.** Design principles of the proposed structure and individual and collective effects of the L-shaped arms (insertion loss vs. frequency)

As seen, the L-shaped stubs individually act as single resonant pairs and result in attenuation in narrow bands (the shorter and longer stubs resonate at higher and lower frequencies, respectively). The transient responses of both structures are investigated via the FDTD method and typical examples are given in Fig. 5.



**Fig. 5.** Transient EM behaviors in the substrate, beneath the microstrip structures (a) BS, (b) BP filters

The simulated transient responses at different time instants are shown for the visualization of broadband EM scattering along the structures, where one can trace the propagation along the line, wave coupling to the stubs and multireflections, back and forth that eliminates/strengthens signal transmission inside a certain

band. From these time domain responses broadband frequency responses are calculated via off-line discrete Fourier transformation (DFT).

The transfer characteristics of the BS filter with the parameters given for Fig. 4, obtained numerically and experimentally, are plotted in Fig. 6. The simulated and measured results agree very well. Variety of simulation tests are performed to analyze effects of some of the geometrical parameters, such as the slot width ( $s$ ) and the patch length ( $L_1$ ). These tests show that the width of the stopband decreases as the slot width increases, and center frequency of the filter is inversely proportional with the length  $L_1$ .

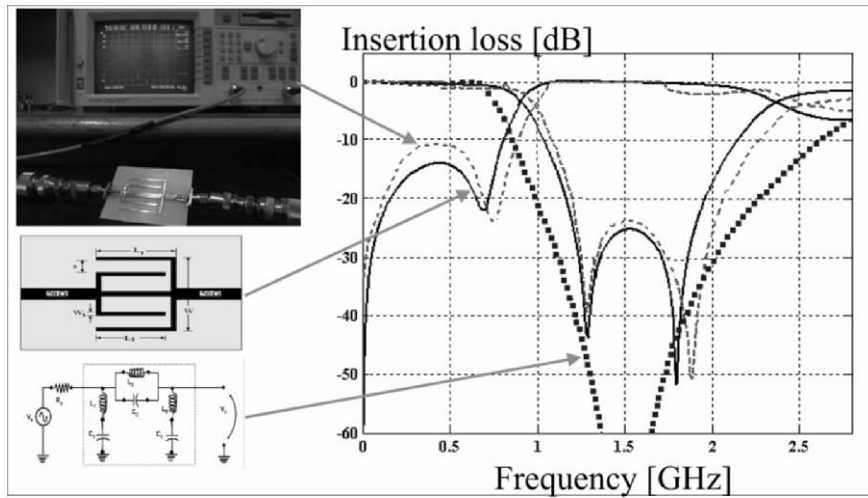


**Fig. 6.** Insertion loss vs. frequency of the proposed EM BS filter

The characteristics of the third-order Chebychev BS filter as shown in Fig. 2 (top) is also plotted in Fig. 6, with the actual element values of  $C_1=5.933$  pF,  $L_1=1.897$  nH,  $C_2=1.100$  pF,  $L_2=10.186$  nH, and  $C_3=5.837$  pF,  $L_3=1928$  nH for  $50 \Omega$  source and load impedances.

The same generic structure may also be used to obtain EM BP filter. In order to do that the main line between the two L-shaped arms is removed, and DC blockage and BP characteristics are satisfied by the capacitive coupling between the arms. An example is given in Fig. 7, which is obtained after a series of FDTD parameter optimization simulations. The parameters of this 1.5 GHz filter with 500 MHz bandwidth on a microstrip with  $\epsilon_r=2.4$  and  $h=1$  mm, are found to be  $W=46$  mm,  $L_1=43$  mm,  $L_2=27$  mm,  $W_1=1$  mm,  $W_2=5.9$  mm,  $W_3=0.3$  mm,  $s_1=0.3$  mm,  $s_2=42.8$  mm. Again, good agreement between the simulation results and the measurement data is obtained, as clearly observed in the figure. It should be noted that the width of the passband of the filter may be extended by (1) moving the center frequency toward the higher frequency region, (2) by using dielectric substrate with higher permittivity values [10].

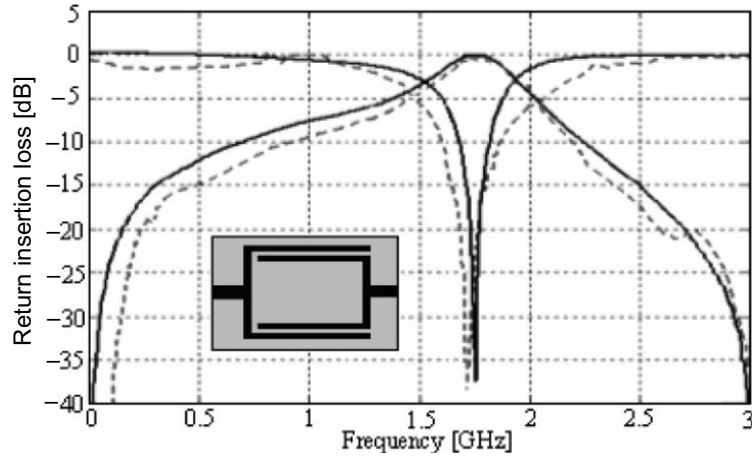


**Fig. 7.** Insertion loss vs. frequency of the BP filter; *Solid*, FDTD; *dashed*, Measurement

EM BP filters may also be realized with the first EM BS structure (in Fig. 3a) by using SC pins. An example is given in Fig. 8. Here, the center frequency of the BP filter is around 4.5 GHz, and the width of the passband is nearly 2 GHz.

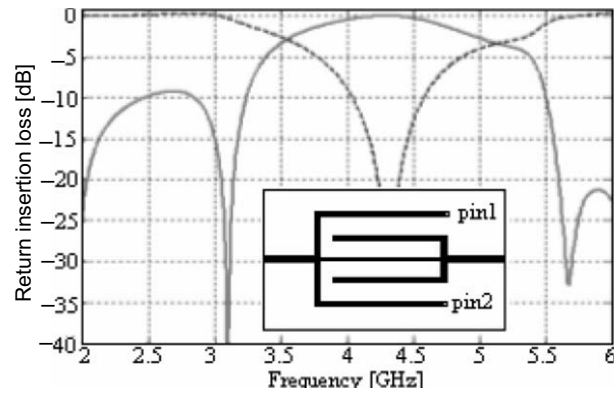


**Fig. 8.** BP filter characteristics of the first structure with SC pins at the end of the longer L-shaped arm

## Conclusion

Novel double-arm generic microstrip structures that can be used both as EM bandpass and bandstop filters are proposed. Classical filter approaches are used initially for the analogy and to create the shape of the structure first, and optimized via a full-capable FDTD simulator. The structures are also fabricated and measured for the validation purposes. It is demonstrated that the bandstop and bandpass characteristics can flexibly be controlled by tuning the lengths and interdistance of the stubs and/or by using short circuit pins. The filter performances may also be improved by using multigeneric elements between input and output of the circuit.

## References

- [1] Y. Rahmat-Samii and H. Mosallaei, "Electromagnetic band-gap structures: Classification, characterization and applications", *Proc. IEEE-ICAP Symp.*, pp. 560–564, 2001
- [2] S. -G. Mao, and M.-Y. Chen, "A novel periodic electromagnetic bandgap structure for finite-width conductor-backed coplanar waveguides", *IEEE Microwave Wireless Components Lett.*, no. 11, pp. 261–263, 2001
- [3] L. Yang, M. Fan, F. Chen, J. She and Z. Feng, "A novel compact electromagnetic band-gap (EBG) structure and its application for microwave circuits", *IEEE Trans. MTT*, vol. 53, no. 1, pp. 183–190, 2005
- [4] A. Erentok, P.L. Lulyak and R.W. Ziolkowski, "Characterization of a volumetric metamaterial realization of an artificial magnetic conductor for antenna applications", *IEEE Trans. Antennas Propag.*, vol. 53, no. 1, pp. 160–172, 2005
- [5] G. Çakır and L. Sevgi, "Design of a novel microstrip electromagnetic bandgap (EBG) structure", *Microwave Opt. Technol. Lett.*, vol. 46, no. 4, pp. 399–401
- [6] G. Çakır and L. Sevgi, "A double-arm generic microstrip electromagnetic bandgap structure with bandpass and bandstop characteristics", *Proceedings of the fifth International Conference on Antenna Theory and Techniques*, pp. 464–466, Ukraine, May 2005
- [7] L. Sevgi, *Complex Electromagnetic Problems and Numerical Simulation Approaches*, IEEE Press, Piscataway, NJ, USA, 2003
- [8] G. Çakır, "Beam scanning microstrip array antenna design for mobile communication systems: Analytical calculations, computer simulations and measurements", Doctorate Thesis, University of Kocaeli, 2004
- [9] C. Bowick, *RF Circuit Design*, NewNess, Boston, 1982
- [10] S. Gündüz, Broadband microstrip filter design, M.S.E.E Thesis, (in Turkish) University of Kocaeli, 2005

# Analysis of Waveguide Structures by Combination of the Method of the Lines and Finite Differences

R. Pregla

University of Hagen, 58084 Hagen, Germany, r.pregla@fernuni-hagen.de *Dedicated to Professor Dr. Leopold Felsen*

## Abstract

Based on generalized transmission line equations a novel impedance/admittance transformation algorithm with finite differences is proposed and substantiated. This algorithm is of second-order accuracy. The algorithm is combined with the method of lines. The algorithm is suitable for eigenmode calculations and for the analysis of waveguide structures with anisotropic materials.

## Introduction

Generalized transmission line (GTL) equations in matrix notation were developed some years ago for developing efficient analysis algorithms based on the method of lines [1–3]. They can be written for arbitrary orthogonal coordinate systems where one of the coordinates is the direction of propagation (or direction of solution) and for general anisotropic materials [3]. These GTL equations are coupled, first-order differential equations for the transversal electric and magnetic fields with respect to the propagation (or solution) direction. Especially, in Cartesian coordinates these GTL equations can be combined to wave equations for the transversal electric or magnetic fields and can be solved analytically. However, this combination and solution is not possible in cases where the coupling matrices depend on the desired coordinate for the solution. In Fig. 1 examples of cylindrical waveguides with inhomogeneous layers are given. To obtain the eigenmodes of these waveguides we assume wave propagation according to  $\exp(-j\beta z)$  in longitudinal or  $z$ -direction. In the cross-section we discretize in azimuthal direction and solve the equations for homogeneous layers in radial direction by the general procedure described in [4]. In case of inhomogeneous layers in azimuthal direction an analytical solution in radial direction cannot be given. For such cases we have developed an impedance/admittance transformation with finite differences analog to

the analytical case [3, 5–8]. The algorithm is analog to the construction of difference operators presented in [9] and is therefore of second-order accuracy. Most of the given formulation is quite general and can be used with other FD methods as well. This is a numerically stable algorithm. It can also be used for concatenating various waveguide sections in complex devices in analogous way. The algorithm will be substantiated by numerical results.

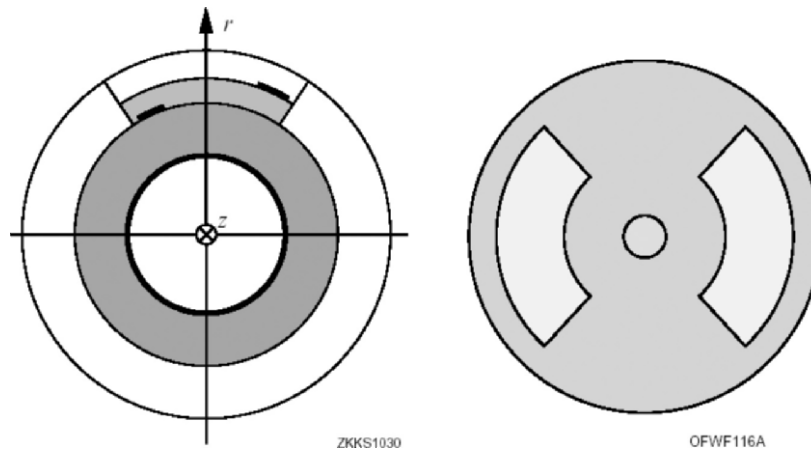


Fig. 1. Cross-sections of cylindrical waveguides with inhomogeneous layers

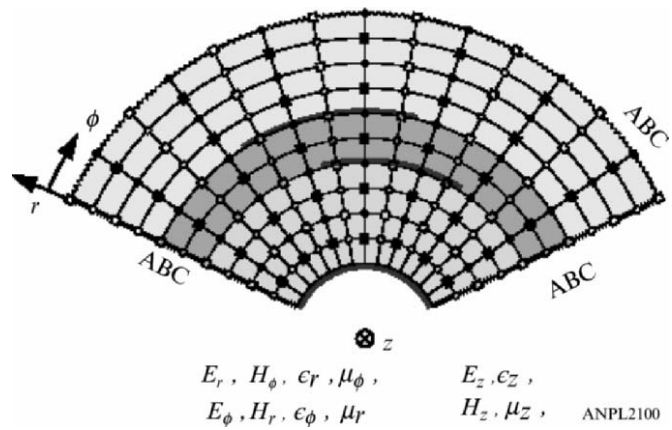


Fig. 2. Discretized circular cross-sections as example



## Basic Theory

### GTL Equations in Matrix Notation

The algorithm to be developed is based on GTL equations which are analogous to the well-known equations for coupled multiconductor transmission lines. GTL equations can be derived in arbitrary orthogonal coordinate systems [3]. The material can be arbitrary anisotropic and inhomogeneous. The device or waveguide under study is divided into homogeneous sections or layers in the direction  $x_3$  of special solution (analytical or by FD). Hence, the material parameters in the cross-sections (layers) are functions of  $x_1$  and  $x_2$  (in layers one of these coordinates) only. By using the following definitions

$$\hat{\mathbf{E}} = [E_{x_1}, E_{x_2}]^t, \quad \hat{\mathbf{H}} = [\tilde{H}_{x_2}, -\tilde{H}_{x_1}]^t, \quad (1)$$

the GTL equations in matrix notation are given by [3]

$$\frac{\partial}{\partial \bar{x}_3} \hat{\mathbf{E}} = -j [R_H^{x_3}] \hat{\mathbf{H}} - [S_E^{x_3}] \hat{\mathbf{E}}, \quad \frac{\partial}{\partial \bar{x}_3} \hat{\mathbf{H}} = -j [R_E^{x_3}] \hat{\mathbf{E}} - [S_H^{x_3}] \hat{\mathbf{H}}, \quad (2)$$

where  $\bar{x}_1, \bar{x}_2, \bar{x}_3$  are the coordinates of orthogonal coordinate system, normalized with the free space wave number. The magnetic field components are normalized with the free space wave impedance  $\eta_0$ , symbolized by a tilde ( $\tilde{\cdot}$ ). The propagation or the special solution takes place in  $\bar{x}_3$ -direction. The matrices  $[R_{E,H}^{x_3}]$  and  $[S_{E,H}^{x_3}]$  contain the differential operators in transversal direction and the material parameters normalized with the metric factors. The superscript symbolise the direction  $x_3$ . For details see [3]. We give here also the formulas for cylindrical coordinates  $r, \phi, z$  and for solution in  $r$ -direction for the special anisotropic case where the matrices  $[S_{E,H}^r]$  are zero. By using the definitions

$$[\hat{\mathbf{E}}^r] = [\bar{r}E_\phi, E_z]^t, \quad [\hat{\mathbf{H}}^r] = [\tilde{H}_z, -\bar{r}\tilde{H}_\phi]^t, \quad (3)$$

we obtain the GTL equations in more detail

$$\bar{r} \frac{\partial}{\partial \bar{r}} [\hat{\mathbf{H}}^r] = -j [R_E^{rc}] [\hat{\mathbf{E}}^r], \quad \bar{r} \frac{\partial}{\partial \bar{r}} [\hat{\mathbf{E}}^r] = -j [R_H^{rc}] [\hat{\mathbf{H}}^r]. \quad (4)$$

In case of eigenmode calculation we assume propagation in  $z$ -direction according to  $\exp(-j\sqrt{\epsilon_{re}}\bar{z})$  and replace  $D_{\bar{z}}$  by  $-j\sqrt{\epsilon_{re}}$ . We write the GTL equations (4) according to

$$\bar{r} \frac{d}{d\bar{r}} [\hat{H}^{re}] = -[R_E^{re}] [\hat{E}^{re}], \quad \bar{r} \frac{d}{d\bar{r}} [\hat{E}^{re}] = -[R_H^{re}] [\hat{H}^{re}], \quad (5)$$

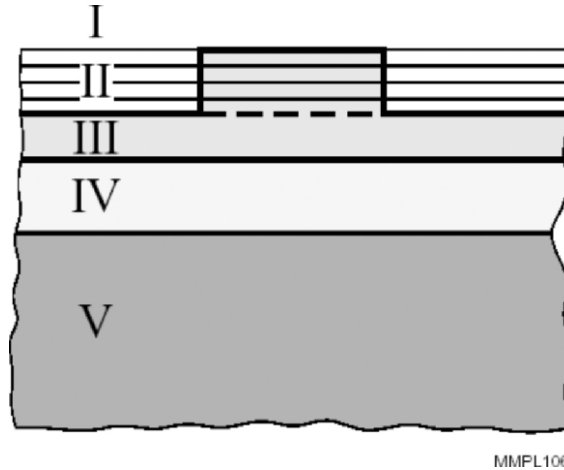
where the superscript “e” symbolises the eigenmode problem. We redefined the field vectors according to

$$[\hat{E}^{re}] = [\bar{r}E_\phi, -jE_z]^t, \quad [\hat{H}^{re}] = [j\tilde{H}_z, \bar{r}\tilde{H}_\phi]^t. \quad (6)$$

Especially in case of inhomogeneous layers the GTL equations in (5) cannot be solved analytically.

### Impedance transformation with finite differences

**Discretization.** The fields and the field equations are discretized in the cross-section. Figure 3 shows as example a cross-section of a microstrip waveguide on a cylindrical body with two-dimensional discretization of adequate discretization points. The one-dimensional discretization is given by radial lines connecting the  $\square$  and  $\bullet$  points, respectively. The type of boundary conditions depends on the special problem. The field components are collected in column vectors and writing in



MMPL1061

Fig. 3. Cross-section of a rib waveguide with subdivision of the rib layer

boldface letters. In the one-dimensional case the collection is performed in  $\phi$ -direction e.g., starting at the left boundary. In the two-dimensional case the collection is made in radial direction and from left to right. The material parameters are collected in diagonal matrices. In what follows, matrices are written with boldface italic letters. For details see [2, 3]. In discretized form (2) reads:

$$\frac{d}{d\bar{u}} \hat{\mathbf{H}} = -j\hat{\mathbf{R}}_E \hat{\mathbf{E}} - \hat{\mathbf{S}}_H \hat{\mathbf{H}}, \quad \frac{d}{d\bar{u}} \hat{\mathbf{E}} = -j\hat{\mathbf{R}}_H \hat{\mathbf{H}} - \hat{\mathbf{S}}_E \hat{\mathbf{E}}. \quad (7)$$

We have withdrawn the superscripts and introduced the general coordinate  $\bar{u}$  for  $\bar{x}_3$ . The combined GTL equation is a first-order differential equation

$$\frac{d}{d\bar{u}} \hat{\mathbf{F}} = \hat{\mathbf{Q}} \hat{\mathbf{F}}, \quad \hat{\mathbf{F}} = [\mathbf{E}^t, \mathbf{H}^t]^t. \quad (8)$$

$$\hat{\mathbf{Q}} = - \begin{bmatrix} \mathbf{S}_E & j\mathbf{R}_H \\ j\mathbf{R}_E & \mathbf{S}_H \end{bmatrix} \quad \text{or} \quad \hat{\mathbf{Q}} = -\bar{u}^{-1} \begin{bmatrix} 0 & \mathbf{R}_H^{re} \\ \mathbf{R}_E^{re} & 0 \end{bmatrix}. \quad (9)$$

$u$  is the coordinate for which we would like to solve the equation. The matrix  $\hat{\mathbf{Q}}$  in (9) on the left side is given in the general form; on the right side it is given for the eigenmode problem according to (5). In many cases, e.g., for isotropic materials the submatrices  $\mathbf{S}_{E,H}$  are equal to zero. In many cases the matrix  $\hat{\mathbf{Q}}$  depends on  $u$ . In the eigenmode problem of Fig. 1 e.g., an analytical solution in the inhomogeneous layers is impossible. (The solution for the homogeneous layers is described in [4].) Therefore, we describe solutions with the help of finite differences in the next sections. Especially the solution with quadratic field interpolation is adequate in these problems.

**Linear field interpolation.** We divide the section or the layer in as many subsections or sublayers as necessary (see layer II in Fig. 3) of length or thickness  $\Delta\bar{u}$ , respectively. For small distances  $\Delta\bar{u}$  between the subports A and B we obtain by using finite differences and linear field interpolation between the sub-ports A and B:

$$\hat{\mathbf{F}}_B - \hat{\mathbf{F}}_A = \hat{\mathbf{Q}} (\hat{\mathbf{F}}_B + \hat{\mathbf{F}}_A), \quad \hat{\mathbf{Q}} = 0.5\Delta\bar{u}\hat{\mathbf{Q}}(\bar{u}^m), \quad \bar{u}^m = 0.5(\bar{u}_A + \bar{u}_B). \quad (10)$$

On the left side we used, as usual, central differences and on the right side arithmetic mean values. Equation (10) results in

$$\hat{\mathbf{F}}_A = (\hat{\mathbf{I}} + \hat{\mathbf{Q}})^{-1} (\hat{\mathbf{I}} - \hat{\mathbf{Q}}) \hat{\mathbf{F}}_B = \mathbf{V}_{AB} \hat{\mathbf{F}}_B. \quad (11)$$

Equation (11) may be transformed to

$$\begin{bmatrix} \mathbf{E}_A \\ \mathbf{E}_B \end{bmatrix} = \begin{bmatrix} z_{11} & z_{12} \\ z_{21} & z_{22} \end{bmatrix} \begin{bmatrix} \mathbf{H}_A \\ -\mathbf{H}_B \end{bmatrix}, \quad \begin{bmatrix} \mathbf{H}_A \\ -\mathbf{H}_B \end{bmatrix} = \begin{bmatrix} y_{11} & y_{12} \\ y_{21} & y_{22} \end{bmatrix} \begin{bmatrix} \mathbf{E}_A \\ \mathbf{E}_B \end{bmatrix}. \quad (12)$$

Now, the impedance and admittance transformation formulas between the ports A and B are analogous to the well-known cases. By defining impedances and admittances according to  $\mathbf{E}_{A,B} = \hat{\mathbf{Z}}_{A,B} \mathbf{H}_{A,B}$  and  $\mathbf{H}_{A,B} = \hat{\mathbf{Y}}_{A,B} \mathbf{E}_{A,B}$ , we have in detail

$$\hat{\mathbf{Y}}_A = \hat{y}_{11} - \hat{y}_{12}(\hat{y}_{22} + \hat{\mathbf{Y}}_B)^{-1} \hat{y}_{21}, \quad \hat{\mathbf{Z}}_A = \hat{z}_{11} - \hat{z}_{12}(\hat{z}_{22} + \hat{\mathbf{Z}}_B)^{-1} \hat{z}_{21} \quad (13)$$

As in the analytic algorithm the field and impedance/admittance transformation can also be performed in the opposite direction in analogous manner.

**Quadratic field interpolation.** For approximating the left side of (8) we used central differences. It is well known that the result is of second order accuracy in the center between the supports A and B [9]. Now, we would also like to have second-order accuracy on the right side of (8). In (10) we have used arithmetic mean values between the supports A and B with first-order accuracy. To obtain second-order accuracy we need three supports. Figure 4 illustrates the quadratic interpolation for a single function  $f(x)$ . The following interpolation with

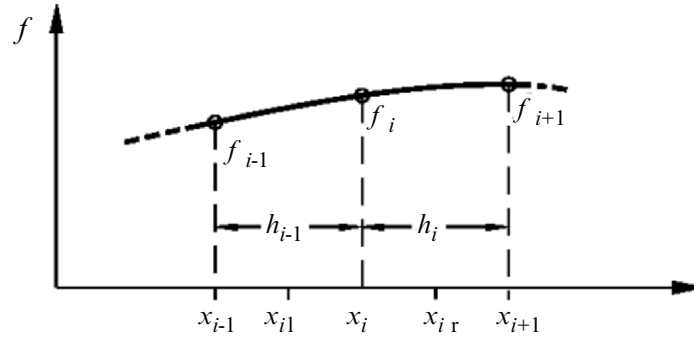


**Fig. 4.** Quadratic interpolation between two points by using three neighbouring points

quadratic accuracy holds for the places  $x = x_{i1} = x_i - h_{i-1}/2$  and  $x = x_{ir} = x_i + h_i/2$  on the left and right sides of  $x_i$ :

$$f(x_{i1}) = f_{i-1} \frac{h_i + h_{i-1}/2}{2(h_{i-1} + h_i)} + f_i \frac{h_i + h_{i-1}/2}{2h_i} + f_{i+1} \frac{-h_{i-1}h_i}{4h_i(h_{i-1} + h_i)}, \quad (14)$$

$$f(x_{ir}) = f_{i-1} \frac{-h_i h_i}{4h_{i-1}(h_{i-1} + h_i)} + f_i \frac{h_{i-1} + h_i/2}{2h_i - 1} + f_{i+1} \frac{h_{i-1} + h_i/2}{2(h_{i-1} + h_i)}, \quad (15)$$

Using equidistant discretization ( $h_{i-1} = h_i$ ) we obtain

$$f(x_{i1}) = \frac{3}{8}f_{i-1} + \frac{3}{4}f_i - \frac{1}{8}f_{i+1}, \quad f(x_{ix}) = \frac{3}{4}f_i + \frac{3}{8}f_{i+1} - \frac{1}{8}f_{i-1}. \quad (16)$$

We will now use the results with equidistant discretization for the field vector  $\mathbf{F}$ . The nonequidistant case is analogous:

$$\mathbf{F}(\bar{u}^m) = -\frac{1}{8}\mathbf{F}_O + \frac{3}{4}\mathbf{F}_A + \frac{3}{8}\mathbf{F}_B, \quad \mathbf{F}(\bar{u}^m) = \frac{3}{8}\mathbf{F}_A + \frac{3}{4}\mathbf{F}_B - \frac{1}{8}\mathbf{F}_C. \quad (17)$$

$\mathbf{F}_{O,C}$  is  $\mathbf{F}$  at  $\bar{u}_O = \bar{u}_A - \Delta\bar{u}$  and  $\bar{u}_C = \bar{u}_B + \Delta\bar{u}$ , respectively. The point O is on the left side of A and the point C is on the right side of B. Both formulas are for the same point  $\bar{u}^m$  (see (10)).

Now we would like to use these two different formulas for (16) at two different points, actually  $\bar{u}_1^m = 0.5(\bar{u}_1 + \bar{u}_2)$  and  $\bar{u}_2^m = 0.5(\bar{u}_2 + \bar{u}_3)$ . We obtain

$$\mathbf{F}_2 - \mathbf{F}_1 = \hat{\mathbf{Q}} \left( \frac{3}{8}\mathbf{F}_1 = \frac{3}{4}\mathbf{F}_2 = \frac{1}{8}\mathbf{F}_3 \right), \quad \hat{\mathbf{Q}}_1 = \Delta\bar{u}\hat{\mathbf{Q}}(\bar{u}_1^m). \quad (18)$$

$$\mathbf{F}_3 - \mathbf{F}_2 = \hat{\mathbf{Q}}_2 \left( \frac{3}{4}\mathbf{F}_2 + \frac{3}{8}\mathbf{F}_3 - \frac{1}{8}\mathbf{F}_1 \right), \quad \hat{\mathbf{Q}}_2 = \Delta\bar{u}\hat{\mathbf{Q}}(\bar{u}_2^m). \quad (19)$$

For linear change of the field i.e., for  $\mathbf{F}_3 = \mathbf{F}_2 + (\mathbf{F}_2 - \mathbf{F}_1)$  in the first equation and  $\mathbf{F}_1 = \mathbf{F}_2 - (\mathbf{F}_3 - \mathbf{F}_2)$  in the second equation, we obtain again the result as arithmetic mean value. This procedure can be continued with further steps  $\Delta\bar{u}$  until the upper side of the layer or the end of the section. Knowing, e.g., the field at plane (or cross-section) 1 (or A) we can now determine the fields at planes (cross-sections) 2 (or B) and 3 (or C) by the equation system

$$\begin{bmatrix} \mathbf{I} - \frac{3}{4}\hat{\mathbf{Q}}_1 & \frac{1}{8}\hat{\mathbf{Q}}_1 \\ \mathbf{I} + \frac{3}{4}\hat{\mathbf{Q}}_2 & \frac{3}{8}\hat{\mathbf{Q}}_2 - \mathbf{I} \end{bmatrix} \begin{bmatrix} \mathbf{F}_2 \\ \mathbf{F}_3 \end{bmatrix} = \begin{bmatrix} \mathbf{I} + \frac{3}{8}\hat{\mathbf{Q}}_1 \\ \frac{1}{8}\hat{\mathbf{Q}}_2 \end{bmatrix} \mathbf{F}_1. \quad (20)$$

The field at plane (or cross-section) 2 is given from this equation system by

$$\mathbf{F}_2 = \hat{\mathbf{V}}_1\mathbf{F}_1 \quad (21)$$

Where

$$\hat{V}_1 = \left[ \left( \mathbf{I} - \frac{3}{4} \hat{\mathbf{Q}}_1 \right) + \frac{1}{8} \hat{\mathbf{Q}}_1 \left( \mathbf{I} - \frac{3}{8} \hat{\mathbf{Q}}_2 \right)^{-1} \left( \mathbf{I} + \frac{3}{4} \hat{\mathbf{Q}}_2 \right) \right]^{-1} \times \left[ \left( \mathbf{I} - \frac{3}{8} \hat{\mathbf{Q}}_1 \right) + \frac{1}{64} \hat{\mathbf{Q}}_1 \left( \mathbf{I} - \frac{3}{8} \hat{\mathbf{Q}}_2 \right)^{-1} \hat{\mathbf{Q}}_2 \right] \quad (22)$$

The fields at plane (or cross-section)  $k + 1$  at  $\bar{u}_{k+1} = \bar{u}_k + \Delta\bar{u}$  with  $k \geq 2$  are given from (19) by

$$\left( \mathbf{I} - \frac{3}{8} \hat{\mathbf{Q}}_2 \right) \mathbf{F}_3 = \left( \mathbf{I} + \frac{3}{4} \hat{\mathbf{Q}}_2 \right) \mathbf{F}_2 - \frac{1}{8} \hat{\mathbf{Q}}_2 \mathbf{F}_1, \quad (23)$$

$$\left( \mathbf{I} - \frac{3}{8} \hat{\mathbf{Q}}_k \right) \mathbf{F}_{k+1} = \left( \mathbf{I} + \frac{3}{4} \hat{\mathbf{Q}}_k \right) \mathbf{F}_k - \frac{1}{8} \hat{\mathbf{Q}}_k \mathbf{F}_{k-1}, \quad (24)$$

$$\mathbf{F}_{k+1} = \hat{V}_k \mathbf{F}_k, \hat{V}_k = \left( \mathbf{I} - \frac{3}{8} \hat{\mathbf{Q}}_k \right)^{-1} \left( \mathbf{I} + \frac{3}{4} \hat{\mathbf{Q}}_k - \frac{1}{8} \hat{\mathbf{Q}}_k \hat{V}_{k-1}^{-1} \right), \quad (25)$$

where  $k \geq 2$  and

$$\hat{\mathbf{Q}}_k = \Delta\bar{u} \hat{\mathbf{Q}}(\bar{u}_k^m), \bar{u}_k^m = 0.5(\bar{u}_k + \bar{u}_{k+1}), \bar{u}_1 = \bar{u}_A. \quad (26)$$

For  $k = 1$  see (21). The short-circuit admittance and open-circuit impedance matrices in the sublayer  $k$  for impedance/admittance transformation are calculated from (11) by using  $\hat{V}_k$ . The impedance or admittance transformation is performed analogously as before in case of linear field interpolation. The impedance/admittance transformation in opposite direction is analogous. These field transformation formulas can also be used for beam propagation methods (BPM).

## Numerical Results

The rib waveguide cross-section (see Fig. 3) is suitable to check the accuracy of the algorithm because we can transform the impedances in all layers I–V in one step with analytical formulas. To test the impedance/admittance transformation formulas we first calculated the value  $n_{\text{eff}} = \sqrt{\epsilon_{\text{eff}}}$  for the HE<sub>00</sub>-mode of the structure in the conventional way. In the second case we use the proposed impedance/admittance transformation with finite differences, e.g., in the rib layer (layer II) between the horizontal interfaces of the sub-layers. The rib layer was divided into sublayers according to Fig. 3. Only for the rib layer we used the FD formulas.

The results for the frequency range  $k_0d = 5$  to  $k_0d = 6$  are shown in Fig. 5a. Parameter is the number of sublayers. The results approach the analytical values from the lower (upper) side in the linear (quadratic) case. Figure 5b shows the difference of the values obtained at  $k_0d = 6$  with the FD impedance/admittance transformation and the analytical result as function of the chosen number of sublayers (1/number). We can see that with increasing number of the sublayers the value  $n_{\text{eff}}$  converges to the value with analytical impedance/admittance transformation. The error for the linear field approximation is nearly three times larger than the error for quadratic field approximation.

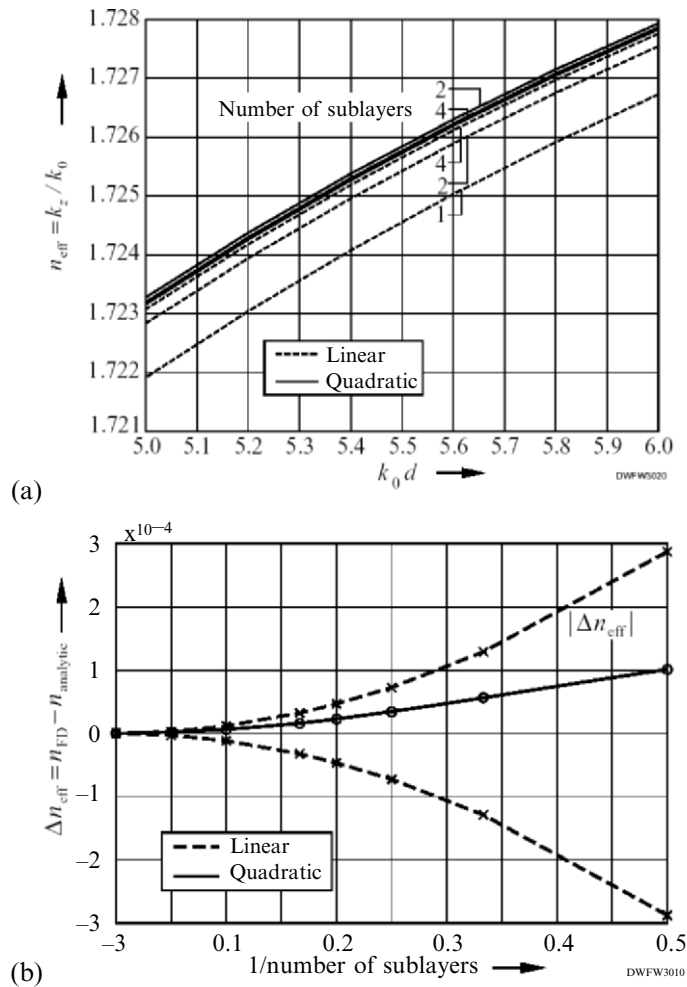


**Fig. 5.** Results for the  $\text{HE}_{00}$ -mode of the structure in Fig. 2 using linear and quadratic FD impedance/admittance transformation formulas in the rib layer: (a) dispersion (b) convergence of the  $n_{\text{eff}}$  value at  $k_0d = 6$

## References

- [1] R. Pregla and W. Pascher, "The method of lines", in: T. Itoh, (ed.), *Numerical Techniques for Microwave and Millimeter Wave Passive Structures*, Wiley, New York, 1989, pp. 381–446
- [2] R. Pregla, "Efficient and accurate modeling of planar anisotropic structures by the method of lines", *IEEE MTT-S 2002*, Vol. 50, June 2002, pp. 1469–1479
- [3] R. Pregla, "Modeling of optical waveguide structures with general anisotropy in arbitrary orthogonal coordinate systems", *IEEE J. Sel. Top. Quantum Electron.*, Vol. 8, No. 6, pp. 1217–1224
- [4] R. Pregla, "General formulas for the method of lines in cylindrical coordinates", *IEEE Trans. Microwave Theory Technol.*, Vol. 43, No. 7, 1995, pp. 1617–1620
- [5] R. Pregla, "The impedance/admittance transformation – an efficient concept for the analysis of optical waveguide structures", *Integrated Photonics Research Topical Meeting*, July 1999, Santa Barbara, USA, pp. 40–42
- [6] R. Pregla, "Novel algorithms for the analysis of optical fiber structures with anisotropic materials", *International Conference on Transparent Optical Networks*, June 1999, Kielce, Poland, pp. 49–52
- [7] R. Pregla, "Efficient modeling of conformal antennas", *Millenium Conference on Antennas and Propagation*, Davos, Switzerland, April 2000, paper 0682
- [8] R. Pregla, "The method of lines as generalized transmission line technique for the analysis of multilayered structures", *AEUe Int. J. Electron. Commun.*, Vol. 50, No. 5, September. 1996, pp. 293–300
- [9] L.A. Greda and R. Pregla, "Hybrid analysis of three-dimensional structures by the method of lines using novel nonequidistant discretization", *IEEE MTT-S IMS Dig.*, Seattle/USA, June 2002, pp. 1877–1880



# Resonator Characterization by Microwave Active Circuits

C. Akyel

Ecole Polytechnique de Montréal, Canada, cevdet.akyel@polymtl.ca

## Abstract

Permittivity measurements using resonant cavity techniques have been the subject of numerous studies over past 40 years. Conventional cavity perturbation measurements normally use a transmission cavity, sweeper, power detector, and an oscilloscope or other instrument to record the resonance curve and thereby provide the necessary information on the  $Q$ -factor to calculate the permittivity of a sample material placed within the cavity.

Some recent measurement methods referred to as “active” make use of oscillating loop containing the test cavity such that the frequency of oscillation is close to the resonant frequency of the cavity with its test sample. An appropriate algorithm adjusts components in the resonant loop such that the oscillating frequency is made exactly equal to the resonant frequency of the test cavity.

The  $Q$ -factor of the cavity is found by modulating a phase shifter within the loop, such as to produce a frequency shift in the oscillating frequency, proportional to the cavity  $Q$ -factor. The absolute value of the  $Q$ -factor is then found by relating the relative  $Q$ -factor measurement of the test cavity to the measurement made on a reference cavity containing a sample material of known permittivity.

## Introduction

The measurement of the resonant frequency ( $f_{0s}$ ) and the  $Q$ -factor ( $Q_{LS}$ ) of a perturbed microwave cavity has been of increasing interest in the measurement of the dielectric properties of materials [1, 2]. In addition, such measurements are also used for nondestructive on line measurements of physical and chemical parameters that have to be monitored in various industrial processes. In this latter application, open cavity rather than closed-cavity resonators must be used. More recently, automatic tracking techniques have also been used for measuring passive-cavity parameters in dynamic processes. Similar tracking systems were used to measure the permittivity of materials. The technique now presented measures of both the resonant frequency shift and the  $Q$ -factor by means of a phase-locked microwave loop circuit generating a number of microwave frequency signals. The active signals are measured with an automatic microwave frequency counter. The pro-

posed technique of measurement is entirely digital; therefore, it is very accurate and reliable. In addition, the rate of measurement is limited largely by the count rate of the automatic frequency counter such that the required time of measurement for the cavity  $Q$ -factor and the resonant frequency can be less than 12 s.

## Method and Theory of Measurement

The closed-loop circuit for measuring the passive frequency shift of microwave cavity resonances by active frequency techniques was described in previous papers [3, 4]. The block diagram in Fig. 1 illustrates how changes in the loaded  $Q$ -factor of the microwave cavity may be measured simultaneously with the frequency shift by the use of the same automatic microwave frequency counter. An electronic phase shifter introduces a periodic phase shift inside the closed-loop circuit. The corresponding frequency shift of the oscillating system is measured with the frequency counter. A microprocessor then adjust the mechanical phase shifter in the closed loop such as to minimize the amplitude of the measured frequency shifts. At this setting of the closed-loop system the average active frequency ( $f_0$ ) corresponds to the passive resonant frequency of the cavity, and the active frequency shift  $\Delta f_0$  can then be used to calculate the loaded  $Q$ -factor of the cavity as below (see Figs. 1 and 2). A human being recognizes external environment by using variety of sensor information. The scenario given in Fig. 2 possesses majority of challenging EM problems, from communication to control, system management to cooperation, etc. Some problems may be listed as follows:

### **Frequency Generated by a Step Phase Modulation Inside the Reentrant Loop**

Under steady-state conditions it can be shown that the system in Fig. 1 will oscillate when the total phase shift in the reentrant loop is equal to an integral number  $N$  of a  $2\pi$  radian and the total gain is greater than unity. The above phase condition can be written, with no perturbation of the cavity as follows:

$$\omega T + \Phi_C(\omega, \omega_0, Q_L) + \Phi_{M0} + \Phi_A + \Phi_e = 2\pi N, \quad (1)$$

$$\omega' T + \Phi_C(\omega', \omega_0, Q_L) + \Phi_{M0} + \Phi_A + \Phi_e' = 2\pi N, \quad (2)$$

where

$\Phi_e$  = the value of the electronic phase shifter at the minimum value of the stepwise phase modulation,

$\Phi_e'$  = the value of the electronic phase shifter at the maximum value of the stepwise phase modulation. The peak to peak value  $\Delta \Phi = \Phi_e' - \Phi_e$  is kept constant throughout the experiment.

$\omega$  = the radian oscillation frequency when the value of the electronic phase shifter is  $\Phi_e$ ,

$\omega'$  = the radian oscillation frequency when the value of the electronic phase shifter is  $\Phi_e'$ ,

$\Phi_{M0}$  = the value of the mechanical phase shift without a sample in the cavity. This value is adjusted to some value between  $0^\circ$  and  $360^\circ$  such that the oscillation conditions of (1) and (2) are satisfied and the frequency difference  $\omega - \omega'$  is its minimum value, as shown in Fig. 2,

$\Phi_A$  = the total phase shift of the amplifiers and the other components used in the closed loop shown in Fig. 1. This value can be considered to be constant within the operating range,

$\omega_0$  = the passive resonant frequency of the unperturbed cavity,

$Q_L$  = the loaded cavity  $Q$ -factor of the unperturbed cavity,

$\Phi_C(\omega, \omega_0, Q_L)$  = the respective phase shifts introduced by the cavity at the oscillation frequency  $\omega$ ,

$\Phi_C(\omega', \omega_0, Q_L)$  = the respective phase shifts introduced by the cavity at the oscillation frequency  $\omega'$ ,

$T$  = the time required by the signal to travel around the closed loop (see Fig. 3).

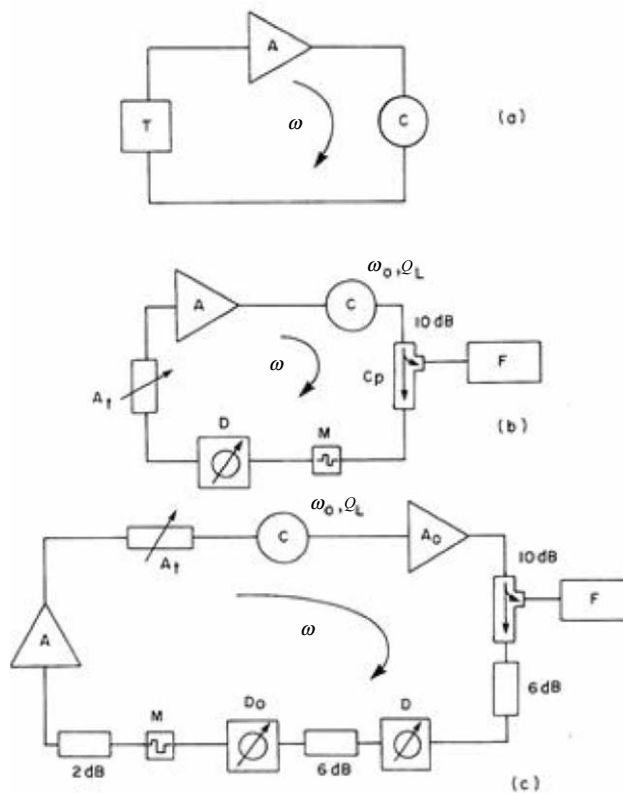
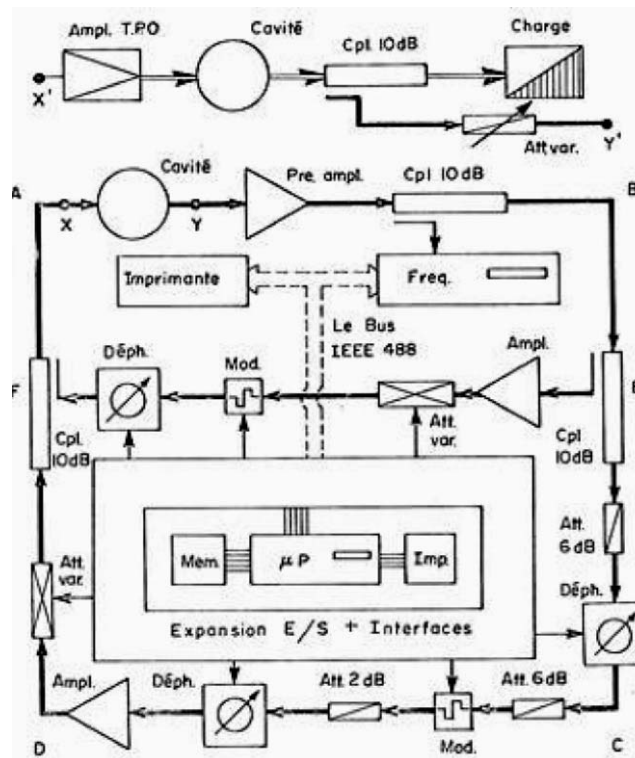


Fig. 1. Active resonating loop at microwave frequencies

The system in Fig. 1 will also oscillate at different frequencies when the cavity resonant frequency and the cavity  $Q$ -factor are perturbed from  $f_0$  and  $Q_L$  to  $f_{0S}$  and  $Q_{LS}$ . The new frequencies ( $\omega_s, \omega_s'$ ) generated by the perturbed cavity are given by the following expressions:

$$\omega_s T + \Phi_C(\omega_s, \omega_{0S}, Q_{LS}) + \Phi_{M0S} + \Phi_A + \Phi_e = 2\pi N, \quad (3)$$

$$\omega_s' T + \Phi_C(\omega_s', \omega_{0S}, Q_{LS}) + \Phi_{M0S} + \Phi_A + \Phi_e' = 2\pi N. \quad (4)$$



**Fig. 2.** Schematic arrangement for an active circuit of high power real-time permittivity measurements

In previous equations,  $\Phi_{M0}$  is the value of the mechanical phase shift when a sample is introduced into the cavity such that the oscillation conditions of (3) and (4) are satisfied and the frequency difference ( $\omega_s - \omega_s'$ ) is at its minimum value.

In (1–4) the value of  $N$  is constant such as to avoid frequency mode jumps in the generated signals. In practice, it was found that a frequency shift of up to 60 MHz at an operating frequency of 2,450 MHz could be tolerated without observing frequency mode jumps, provided the length of the reentrant loop was

minimized. The values of  $\Phi_C(\omega_S, \omega_{0S}, Q_{LS})$  and  $\Phi_C(\omega_S', \omega_{0S}, Q_{LS})$  correspond to the phase shift introduced by the perturbed cavity at frequencies  $\omega_S$  and  $\omega_S'$ .

**Relation Between the Cavity Resonance Perturbation ( $f_0 - f_{0S}$ ) and the active radian Frequency Shift ( $\omega_S - \omega$ )**

The relation between the active frequencies of the perturbed and unperturbed cavity, with no phase modulation inside the reentrant loop, has been given as follows:

$$\omega_S - \omega = 2\pi\Delta f_0/F, \quad (5)$$

where

$$F = 1 + \frac{\omega T}{Q_0} + \frac{\omega T Q_e}{Q_0^2} \quad (6)$$

and

$Q_0$  = the unloaded cavity factor,

$Q_e$  = the external cavity  $Q$ -factor,

$T$  = the time required for an electric signal to travel around the loop,

$\Delta f_0$  = the passive resonant frequency shift of the cavity equal to  $(f_0 - f_{0S})$ .

The value of  $T$  was obtained by a phase shift versus frequency shift measurements with a network analyzer, and it was found to be 7 ns. The value of  $Q_0$  (also measured with the analyzer and a counter) was in the order of 6,000 for the cavity designed in Fig. 1. At an operating frequency of 2,450 MHz, the value of  $\omega T/Q_0$  therefore, is, much less unity. Similarly, it can be shown that the value of  $\omega T Q_e/Q_0^2$  is negligible, and (6) is therefore reduced to the following simple equation:

$$\omega_S - \omega = 2\pi(f_{0S} - f_0) \quad (7)$$

Equation (7) indicates that the difference in the active frequencies ( $f_S - f$ ) is equal to the difference ( $f_{0S} - f_0$ ) in the passive resonant frequency of the test cavity.

Passive resonant frequency shifts of a test cavity therefore can be measured directly with an automatic frequency counter, as shown in Fig. 2.

**Relation between the Normalized Cavity Q-Factors ( $Q_{LS}/Q_L$ ) and the Active Frequencies**

The loaded test cavity in Fig. 1 will produce a phase shift  $\Phi_C(\omega_S, \omega_{0S}, Q_{LS})$  at the radian oscillation frequency  $\omega_S$  for a cavity resonance  $\omega_{0S}$  as follows:

$$\Phi_C(\omega_S, \omega_{0S}, Q_{LS}) = \tan^{-1} \left[ 2Q_{LS} \frac{(\omega_S - \omega_{0S})}{\omega_{0S}} \right], \quad (8)$$

where  $Q_{LS}$  is the loaded cavity  $Q$  with a sample and  $\omega_{0S}$  is the resonant frequency, with a sample, expressed in radians.

For small values of  $\Phi_C(\omega_S, \omega_{0S}, Q_{LS})$ , less than  $15^\circ$ , we can write:

$$\Phi_C(\omega_S, \omega_{0S}, Q_{LS}) = 2Q_{LS}(\omega_S - \omega_{0S}) / \omega_{0S}. \quad (9)$$

In a similar manner we can also write:

$$\Phi_C(\omega, \omega_0, Q_L) = 2Q_L(\omega - \omega_0) / \omega_0, \quad (10)$$

$$\Phi_C(\omega', \omega_0, Q_L) = 2Q_L(\omega' - \omega_0) / \omega_0, \quad (11)$$

$$\Phi_C(\omega_S', \omega_{0S}, Q_{LS}) = 2Q_{LS}(\omega_S' - \omega_{0S}) / \omega_{0S}. \quad (12)$$

For the preceding equations we find that:

$$\frac{\omega_S - \omega_S'}{\omega - \omega'} = \frac{Q_L}{Q_{LS}} \frac{\omega_{0S}}{\omega_0} \frac{\left[ 1 + \frac{\omega_0 T}{2Q_L} \right]}{\left[ 1 + \frac{\omega_{0S} T}{2Q_{LS}} \right]}. \quad (13)$$

For the value of  $T = 7$  ns and  $\omega_0 = 2\pi \times 2,450$  MHz the value of  $\omega_0 T / 2Q_{LS} < 1$  whenever  $Q_{LS} > 50$ . Hence  $\omega_0 T / 2Q_{LS} \ll 1$  when  $Q_{LS} \gg 500$ ; (13) may then be simplified as follows:

$$\frac{Q_{LS}}{Q_L} = \frac{\omega_{0S}}{\omega_0} \frac{(\omega - \omega')}{(\omega_S - \omega_S')}. \quad (14)$$

However, the  $\omega$  value can easily be made equal to  $\omega_0$ , by a proper choice of the phase value  $\Phi_M$ , as already shown in Fig. 2. Hence, from (7) and (14), we can write the normalized loaded cavity  $Q$ -factor ( $Q_{LS}/Q_L$ ) when  $\omega_S$  is also set equal to  $\omega_{0S}$  by varying  $\Phi_M$  in the same manner:

$$\frac{Q_{LS}}{Q_L} = \frac{\omega_S}{\omega} \frac{(\omega - \omega')}{(\omega_S - \omega_S')}. \quad (15)$$

We, therefore, have shown in (7) and (15) that the passive cavity perturbation parameters  $(f_0 - f_{0s})$  and  $(Q_L/Q_{LS})$  can be obtained from active frequency measurements when the initial loaded cavity  $Q$ -factor ( $Q_L$ ) is known.

## Permittivity Measurements

When a small sample is introduced in a cavity, it causes a frequency shift. If the sample has losses, the complex frequency shift is given by:

$$\frac{\omega - \omega_0}{\omega} = - \frac{\iiint (\Delta \epsilon E \cdot E_0^* + \Delta \mu H \cdot H_0^*) dV}{\iiint (\epsilon_0 E \cdot E_0^* + \mu_0 H \cdot H_0^*) dV}, \quad (16)$$

where  $E_0, H_0$  and  $E, H$  represent the field in the original and perturbed cavity, respectively, and  $\omega_0$  and  $\omega$  are the corresponding resonant frequencies. In addition,  $\Delta \epsilon$  and  $\Delta \mu$  are the changes in the permittivity and permeability of the medium of cavity, respectively, due to the introduction of the sample. Also, the  $dV$  is the elemental volume. A small change in permittivity at a point of zero electric field or a small change of permeability at the position of zero magnetic field does not vary the resonant frequency.

For a small nonmagnetic sample ( $\mu_r = 1$ ) placed at the electric field maximum, the electric field applied to the sample can be assumed uniform, and (16) can be simplified as:

$$\frac{\omega - \omega_0}{\omega} = - \frac{\int_{V_s} \Delta \epsilon E \cdot E_0^* dV}{2\epsilon_0 \int_{V_0} |E_0|^2 dV}. \quad (17)$$

In the previous equation,  $\Delta \epsilon = \bar{\epsilon} - \epsilon_0$  and  $\bar{\epsilon} = \bar{\epsilon}_r \cdot \epsilon_0$ . But  $\bar{\epsilon}_r = \epsilon_r' - j\epsilon_r''$ . Thus (17) becomes:

$$\frac{\omega - \omega_0}{\omega} = - \frac{\int_{V_s} (\bar{\epsilon}_r - 1) E \cdot E_0^* dV}{2\epsilon_0 \int_{V_0} |E_0|^2 dV}. \quad (18)$$

The change of the complex eigenfrequency can be related to the changes in the resonance frequency  $f = \text{Re}(f)$  and the  $Q$ -factor of the cavity through the relation (14), or in a simplified form as follows:

$$\frac{\omega - \omega_0}{\omega} = \left( \frac{f_s - f_0}{f_0} \right) + \frac{j}{2} \left( \frac{1}{Q_s} - \frac{1}{Q_0} \right). \quad (19)$$

In previous equation,  $Q_s$  and  $Q_0$  are the quality factors of the cavity with and without sample in the cavity, and  $f_s$  and  $f_0$  are the resonant frequencies of the cavity with or without the sample in the sample holder.

Comparing (18) with (19), we have:

$$\left(\frac{f_s - f_0}{f_0}\right) + \frac{j}{2} \left(\frac{1}{Q_s} - \frac{1}{Q_0}\right) = -\left(\frac{\epsilon_r - 1}{2}\right) \frac{\int_{V_s} E \cdot E_0^* dV}{2 \int_{V_0} |E_0|^2 dV} \quad (20)$$

Finally, the real part and the imaginary parts of permittivity are:

$$(\epsilon_r' - 1) = \frac{1}{2C_0} \left(\frac{f_0 - f_s}{f_0}\right), \quad (21)$$

$$\epsilon_r'' = \frac{1}{C_0} \left(\frac{1}{Q_s} - \frac{1}{Q_0}\right), \quad (22)$$

where

$$C_0 = -\frac{\int_{V_s} E \cdot E_0^* dV}{2 \int_{V_0} |E_0|^2 dV}. \quad (23)$$

In (21) and (22), the parameter  $C_0$  is generally assumed to be a constant, which depends of the geometry and the location of the sample and resonant mode of the cavity, but approximately independent of the permittivity of samples. When the resonant mode is a higher order mode, it is very complicated to calculate  $C_0$  using classical electromagnetic analytical methods. Thus,  $C_0$  is usually obtained by a calibration method using a known permittivity sample as a standard. It should be pointed out that the standard sample should be as small as possible and should have a similar geometry with the samples to be measured so as to improve the measurement accuracy.



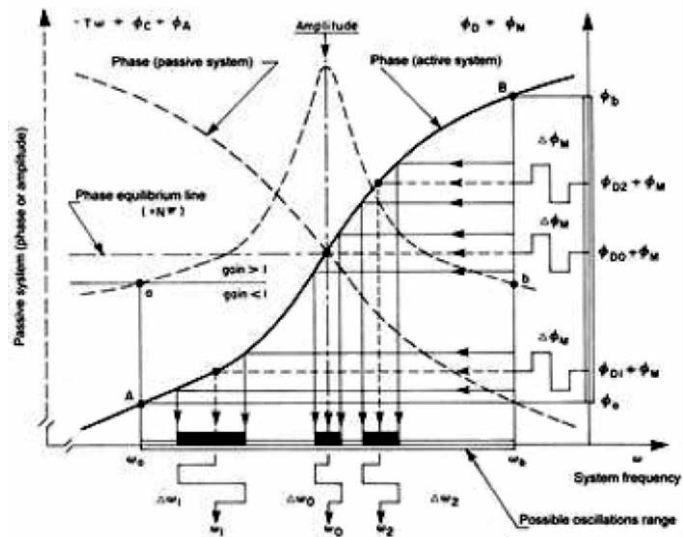


Fig. 3. Measurement principle; phase relation-based active system algorithm

### References

- [1] G. Birnbaum and J. Franeau, "Measurements of dielectric constant and loss of solids and liquids by a cavity perturbation method", *J. Appl. Phys.*, Vol. 20, pp. 817–818, 1949
- [2] S.K. Chatterjee, "Microwave cavity resonators, some perturbation effects and their application", *J. Brit Inst. Radio Eng.*, Vol. 13, pp. 481–488, 1953
- [3] C. Akyel, R.G. Bosisio and G.E. April, "An active frequency technique for precise measurements on dynamic microwave cavity perturbation", *IEEE Trans. Instrum. Meas.*, Vol. TM-27, No. 4, pp. 364–368, 1978
- [4] C. Akyel, "Techniques actives pour caractérisation micro-ondes de matériaux en cavité résonante", *J. Wave – Mater. Interact.*, Vols. 5 & 6, No. 4, October 1991

# Performance Evaluation in Optical Burst Switched Networks

S. Parlar and E. Topuz

Electronics and Communication Engineering Department, Istanbul Technical University, Maslak, 34469 Istanbul, Turkey, selin@cscrs.itu.edu.tr, topuz@ehb.itu.edu.tr

## Abstract

The accelerating demand for higher network capacities has driven the need for backbone wavelength division multiplexed (WDM) all-optical networks (AON) capable of dynamically routing several millions even billions of packets that are in transit. At the present state of technological development optical burst switching (OBS) appears to be the most promising switching technique for meeting transparency and bandwidth on demand requirements in such ultra high capacity networks. Several protocols have been proposed for OBS networks. In this work, we consider a version of the Just-In-Time (JIT) protocol and investigate its burst drop probability (BDP) performance utilizing a Monte-Carlo simulation approach.

## Introduction

As a result of the sharp increase in the Internet traffic in recent years, service providers are facing an accelerating demand for greater bandwidths in backbone terrestrial networks. Optical networks (ON) present an attractive solution for meeting this demand due to their capability of providing great amount of raw bandwidth along fiber links and the higher switching capacities of optical cross-connects (OXC) in comparison to existing electronic routers. However, the effective usage of bandwidth capacity of fiber links could only be realized after the introduction of wavelength division multiplexed (WDM) technology. So far, several switching techniques have been proposed to transmit data over WDM networks, and current research is focused on all optical networks (AONs) wherein the data is kept in the optical domain throughout the network without undergoing optic/electronic/optic (OEO) conversion at intermediate nodes. Switching techniques proposed for AONs can be classified under the following main types: optical circuit switching (OCS), optical packet switching (OPS), and optical burst switching (OBS). OCS technology, though well matured and widely deployed, is rather inefficient in meeting bandwidth on demand requirement. On the other hand, the implementation

of OPS may still be a decade away, awaiting some major technological advancements. OBS has been proposed as an intermediate solution for eliminating the major disadvantages of OCS and OPS.

## Optical Burst Switching

OBS makes better use of network resources when compared to OCS, and it can readily be implemented on AONs, utilizing off-the-shelf hardware. In OBS, data packets which need to be routed to the same destination are aggregated into super packets called bursts before they are injected to the network. A burst has only one control packet which is sent in a separate signaling channel with an offset time, and unlike OCS, the burst is sent after this offset time without waiting for the acknowledgement of successful end-to-end reservation. Control packets undergo OEO conversion at the intermediate nodes, and offset time is determined in such a way as to account for the total processing delay encountered by the control packet along its route. As a result, the switching fabric can be configured dynamically for the requested resource.

Since wavelength ( $\lambda$ ) channels are not engaged on a continuous basis in serving the traffic demand between a pair of nodes, their idle periods can be utilized in serving different transmission requests. Hence, at the present state of technological developments, among the switching techniques mentioned above, OBS seems to be the most suitable approach for improving the bandwidth utilization efficiency in an existing or to be deployed AON.

The following three main protocols have been proposed for OBS: just-in-time (JIT), horizon, and just-enough-time (JET) [1]. In this paper, we consider the simulation of an OBS network utilising a variation of JIT protocol developed by the JumpStart Group in the USA. [2] which utilizes on-the-fly path unicast signaling, explicit setup and estimated release and does not require a global time synchronization in the network. This feature of the JIT protocol is essential for the applicability of the Monte Carlo technique for modeling and simulation of OBS networks.

## Simulation Approach

In order to analyze the performance of OBS, we utilize the simulation approach proposed in [3] which is based on the Monte Carlo Technique (MCT) [4]. The network is assumed to have reached steady-state conditions and that all processes have stationary distributions. Each transmission attempt of a set of bursts constitutes a random MC experiment resulting in burst transmission/drop events. In a single execution of the simulation, this experiment is repeated in a sufficiently large number of times,  $N_s$ , so as to determine an estimator  $B\hat{D}P$  for the performance parameter burst drop probability (BDP), together with an associated confidence

interval. Confidence interval is attached to a certain MC run size,  $N_S$ , by running the simulation several times and calculating the variance of the samples for  $B\hat{D}P$  obtained at each step.

Our model may be divided into two subparts: burst injection and contention control. Burst injection is governed by the current traffic offered to the network as described by the burst arrival process and the internodal weights, as well as by the  $\lambda$  assignment scheme and the protocol. Contention control, on the other hand, involves identification of burst collision events on the intermediate nodes and determination whether or not they can be avoided utilizing provided contention resolution techniques.

There are two major difficulties in evaluating the overall BDP performance in an OBS network. First, it presents a computational extensive task which rapidly grows to become untractable as the network complexity is increased [5]. Second, no workable definition has so far been reported in the literature for the concept of load in an OBS network, which would be necessary for a single parameter quantification BDP performance of the network. In this paper we use the two-parameter quantification approach proposed in [3], wherein the simulation results are represented as functions of both the average accepted number,  $N_A$ , of bursts by the network at a simulation run of size,  $N_S$ , as well as of the channel occupation ratio,  $U$ , defined as,

$$U = 1 / (1 + T_{\text{idle}}/T_{\text{busy}}) \quad (1)$$

where,  $T_{\text{busy}}$  is determined by summing burst duration with a route dependent off-set time and  $T_{\text{idle}}$  by the burst arrival process.

## Network Topology and Simulation Results

The studied network model is the 16-node NSFNET topology (Fig. 1). There are 25 bidirectional fiber links each of supporting 64  $\lambda$ -channels in one direction. All nodes are treated as edge nodes, and it is assumed that full wavelength conversion capability may be provided to all or to a subset of the nodes for contention resolution purposes. We consider a fixed routing scheme and use Dijkstra's shortest path algorithm for route computation in the network by determining the weights of the links simply by their physical lengths. Moreover, for convenience, we introduced following simplifying assumptions: constant burst length; *fixed routing* along shortest paths; uniform traffic matrix; *exponentially distributed* interarrivals.

For all calculations presented in this paper, the MCS run size  $N_S = 120$  has been used. We have verified independently that this run size yields a confidence interval for the numerical results obtained for  $B\hat{D}P$  sufficient to ensure two digit precision. A typical set of results for the variation of  $B\hat{D}P$  with  $N_A$  and  $U$  is given in Fig. 2. The estimators for BDP presented in Fig. 2 correspond to the average values taken over 120 MCSs, for each  $(N_A, U)$ .

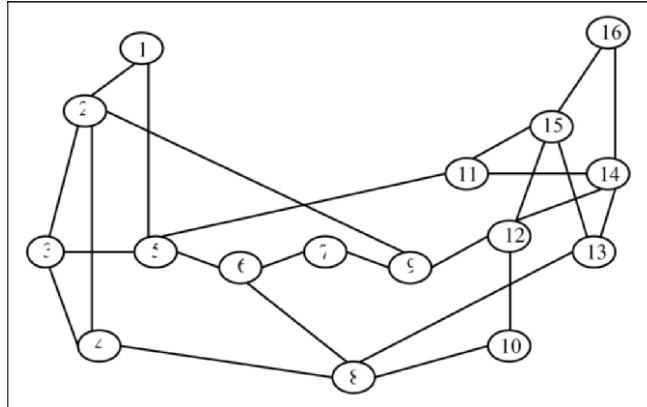


Fig. 1. 16-node NSFNET topology

**Burst Contention**

Figure 2 shows that for constant  $U$  burst dropping probability increases with  $N_A$ . This is to be expected, since more traffic requests result in more  $\lambda$ -channel reservations on the links; hence, burst contention probability rises. However, burst contention is not only a function of the number of accepted burst at the instant corresponding to a MC experiment but also of a local time window around the burst as determined by the burst arrival process and quantified by the channel utilization ratio  $U$ .

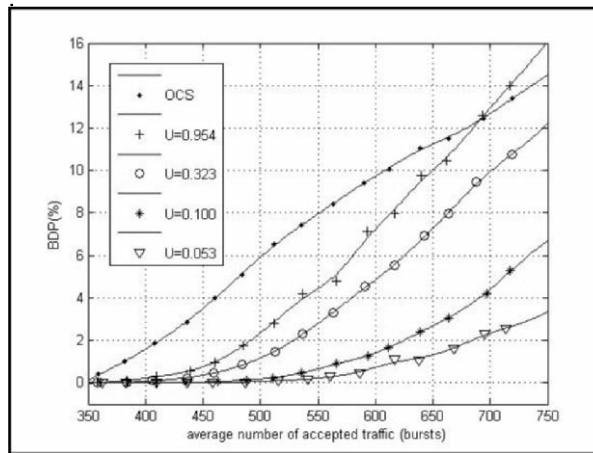


Fig. 2.  $B\hat{D}P$  vs.  $N_A$  for various values of  $U$

The significance of this latter effect is clearly observable in Fig. 2 by noting the differences between  $B\hat{D}P$  values corresponding to different  $U$  values for the same number of accepted bursts. This can be explained by the fact that as  $U$  increases,

the possibility for interposition of bursts decreases. This is better demonstrated by the sample output given in Table 1 for  $N_A \cong 500$ .

**Table 1.** Average number of interposed bursts for increasing  $U$  at  $N_A = 511$

$N_A = 511$	
$U$	Average number of interposed bursts
0.053	77
0.100	57
0.323	21
0.954	0

As seen from this table the number of interposed bursts rapidly increases at lower  $U$  values resulting in a lower burst contention probability and, hence in a lower Table 1, average number of interposed bursts for increasing  $U$  at  $N_A = 511$  for given  $N_A$ . In other words, for the same value of Table 1, average number of interposed bursts for increasing  $U$  at  $N_A = 511$ ,  $N_A$  increases with decreasing  $U$  due to the cumulative effect of interposition and  $\lambda$ -conversion, which can be clearly seen from the representative example given in Table 2.

**Table 2.**  $\hat{BDP}$  vs.  $N_A$  for various values of  $U$

	$U = 0.954$	$U = 0.100$
$\hat{BDP}$ (%)	0.951	0.938
$N_A$	460	566
average number of directly transmitted bursts	237	293
average number of only $\lambda$ -converted bursts	218	93
average number of only interposed bursts	0	62
average number of both interposed and converted bursts	0	113

As a result of these observations, we can conclude that OBS would significantly improve the performance of an OCS network when the overall network traffic load decreases as a result of decrease in either  $N_A$  or in  $U$ . For comparison purposes, we have also plotted in Fig. 2 the variation of connection blocking probability with  $N_A$  in an OCS network with the same topology. It should be noted that in Fig. 2 there is substantial difference between the curves marked with OCS and  $U = 0.954$ , although one would expect that for  $U$  values approaching 1, i.e., full channel utilization, burst blocking probability in an OBS network would approach to the connection blocking probability an OCS network. However, this difference can easily be understood by noting that in the present implementation of JIT protocol the definition of  $N_A$  excludes bursts which fail to get acknowledgement for the presence of a free difference  $\lambda$ -channel at the source node, whereas

corresponding connection requests are counted as blocked connections in the case of OCS.

**Table 3.** A comparison of successfully delivered network traffic at  $N_A = 511$  for various values of  $U$

	$U = 0.954$	$U = 0.323$	$U = 0.100$	$U = 0.053$
average number of directly transmitted bursts	263	264	265	266
average number of only $\lambda$ -converted bursts	237	158	87	66
average number of only interposed bursts	0	21	57	71
average number of both interposed and converted bursts	0	63	100	106
average number of bursts lost	11	5	2	2

One of the interesting results that is obtained via simulation is that the number of directly transmitted bursts does not change with  $U$ , whereas the number of interposed and  $\lambda$ -converted ones are strongly dependent on  $U$ . A sample comparison is given in Table 3, and it can again be seen that the interposition dominates the various factors effecting  $B\hat{D}P$  in OBS networks.

### Contention Resolution

In the previous examples it was assumed that all of the nodes in the reference network topology are equipped with full wavelength conversion capability. By observing the number of conversion at each node, we are able to determine the bottlenecks in the network, i.e., the overloaded nodes/links. The average number of  $\lambda$ -conversions made on each node of the network for contention resolution purposes is shown in Fig. 3 for constant  $U$  and  $N_A$ .

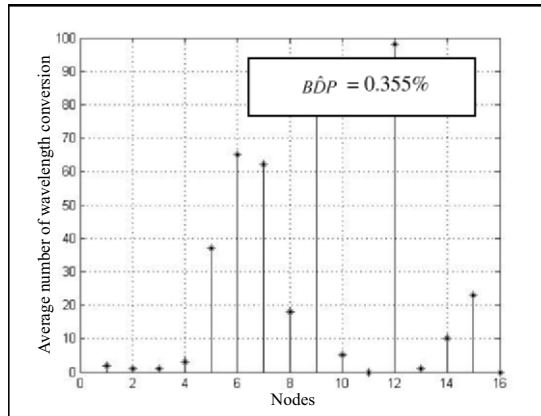


**Fig. 3.** Number of  $\lambda$ -conversions at  $N_A = 511$  and  $U = 0.100$  for full  $\lambda$ -conversion capability at each node

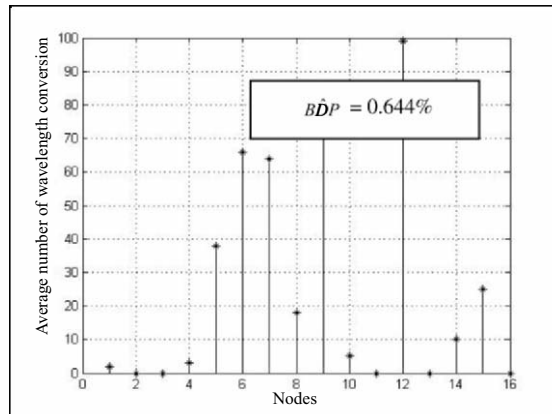


**Fig. 4.** Number of  $\lambda$ -conversions at  $N_A = 511$  and  $U = 0.100$  for no  $\lambda$ -conversion capability at nodes 2, 3, 11, 13, and 16

From Fig. 3, it is seen that nodes 6, 7, 9, and 12 are the most crowded ones in the considered topology. In other words, under the uniform traffic matrix and fixed routing assumptions considered here, these nodes are shared by many routes. Indeed, given the above-mentioned constraints this could be anticipated by simply looking at the network topology given in Fig. 1, that the links between these centrally placed nodes would get overloaded at increased traffic loads.

On the other hand, one observes from Fig. 3 it seems that very little  $\lambda$ -conversions occur at nodes 1, 2, 3, 4, and 13, and almost no  $\lambda$ -conversion is needed at nodes 11 and 16. Therefore, we expect that this it would have little effect on the  $BDP$  performance of the network, if  $\lambda$ -conversion capability would be provided not to all nodes in the network but rather to a suitably chosen subset of these nodes. This is demonstrated in Fig. 4 which corresponds to the case wherein no  $\lambda$ -conversion capability is provided at 5 of the 16 nodes in the network. It should be noted that, as expected, in this case  $BDP$  increases only slightly from 0.355 to 0.644% and the numbers of  $\lambda$ -conversions made in the other nodes of the network remain essentially unchanged.

## Conclusion

We have demonstrated the feasibility of a Monte-Carlo type simulation approach for evaluation of the overall  $BDP$  performance in an OBS network under fairly realistic conditions. The applicability of our approach is restricted to protocols which do not require a global synchronization and to networks which have reached steady-state conditions characterized by stationary distributions of all processes. Utilizing a version of the JIT protocol as an example, we have been able to investigate the effects of the various factors effecting the  $BDP$  in an OBS network. Although, in the presentation, some additional restrictions were in-



roduced in relation to traffic and to routing and wavelength assignment (RWA) algorithms, it should be noted that these latter are introduced solely for the purposes of simplifying the discussion and the proposed method can be used with equal ease and efficiency under different traffic and RWA assumptions.

## References

- [1] J. Teng, "A study of optical burst switched networks with the jumpstart just in time signaling protocol", Ph.D. Thesis, Graduate Faculty of North Carolina State University, USA, 2004
- [2] I. Baldine, G.N. Rouskas, et.al., "JumpStart: A just-in-time signaling architecture for WDM burst-switched networks", *IEEE Communications Magazine*, vol. 40, no. 2, 82–89, 2002
- [3] S. Parlar, "Determination of blocking probabilities in optical burst switched networks with monte carlo simulation", MSc Thesis, Institute of Science and Technology of Istanbul Technical University, Turkey, 2005
- [4] W.H. Tranter, et.al., *Principles of Communication Systems Simulation with Wireless Applications*, New Jersey: Prentice Hall, 2004
- [5] A. Bragg and H. Peros, "Modeling and analysis of ultra-high capacity optical networks, advanced simulation techniques", *Conference (ASTC) 2004*, Virginia, April 18–22, 2004

# Nonlinearity and Multiscale Behaviour in Ocean Surface Dynamics: An Investigation Using HF and Microwave Radars

S. Anderson, C. Anderson and J. Morris

Defence Science and Technology Organisation,  
Edinburgh, SA 5111, Australia, [stuart.anderson@dsto.defence.gov.au](mailto:stuart.anderson@dsto.defence.gov.au)

## Abstract

This paper addresses the problem of identifying the nonlinear hydrodynamic processes which contribute to the time-varying geometry of the sea surface via their radar signatures. Progress is illustrated with results from a broad research program based on a suite of radars, from HF to millimetre wave, and also make use of information derived from passive electromagnetic sensors in the visible and infrared bands.

## Introduction

The ocean surface boundary layer can be modelled as a dynamical system subject to forces acting over an extraordinary range of spatial and temporal scales. At the global scale, the oceanic response can be represented in terms of familiar phenomena such as tides, Rossby waves, Kelvin waves, and tsunamis, while at progressively shorter length scales we observe infragravity waves, gravity waves, capillary waves, and eventually thermal fluctuations. From a practical point of view, though, the range which is most relevant to human affairs and characterised by variability requiring measurement extends from length scales of  $\sim 10^4$  m to  $\sim 10^{-2}$  m.

The equations which describe the evolution of the state of the sea surface are essentially nonlinear – formally they describe the class of volume preserving diffeomorphisms in  $R^3$  – but, over a wide range of conditions, a linearised hydrodynamic approximation yields an satisfactory solution, accurate to a relative precision of typically  $10^{-2} - 10^{-3}$ . While this approach serves many practical needs well, it breaks down under some of the most interesting conditions, such as high sea states and wave breaking. Further, when air–sea fluxes integrated over one scale determine stresses and dynamical response at another scale, nonlinear effects can emerge as the dominant factors. And furthermore, when the remote sensing signatures of linear phenomena saturate, it is only through the signatures

of the nonlinear effects that we can measure the oceanographic and meteorological parameters of interest.

In order to investigate these phenomena, the researcher's tool of choice is usually electromagnetic radiation. The reasons for this are clear – the vector nature of the field supplies multiple degrees of freedom for the coupling to the surface, the electrical properties of sea water are known and well behaved, electromagnetic stress is negligible, the boundary value problem formulated from Maxwell's equations is linear in the field variables so simultaneous sensing with multiple electromagnetic sensors is feasible, both active and passive sensing technologies are widely available, achievable spatial and temporal sampling resolutions are consistent with the phenomena of interest, and so on. Thus the central task which presents itself is the design and interpretation of radar remote sensing measurements which reveal the nonlinear dynamics of the surface boundary layer over a wide range of spatial and temporal scales – an inverse problem.

In practice the solution of Maxwell's equations relies on introducing a number of assumptions and approximations, each of which has its own domain of validity. Typical examples of such simplifications of the electromagnetic aspects of the problem are (1) adopting the Rayleigh hypothesis, (2) replacing the vector wave equation with the Helmholtz equation and solving for temporal variability via the quasistationary approximation, and (3) modelling the sea water as a perfectly electrically conducting fluid. Clearly the solution of the inverse problem relies on the correct formulation of the direct problem. Hence not only must we characterise the dynamical system under investigation, we must ensure the fidelity of the mapping which embodies the relation between the incident and scattered electromagnetic field for the corresponding class of boundary conditions.

This paper reports on part of an integrated research program – RIOBL (Radio-physical Investigation of the Oceanic Boundary Layer) – which is addressing some aspects of the ocean remote sensing problem with the aid of a suite of radar and other electromagnetic sensors. In the following section, the way in which nonlinearity manifests itself in radar signatures is formalised as a departure from linear state evolution. Next, the individual radar sensors contributing to RIOBL are briefly described and representative measurement capabilities illustrated with results from recent trials. The signatures of some specific nonlinear processes are modelled and compared with sensor measurements. Here we focus attention on wave–wave interactions in the gravity wave regime, studied both in the spatial domain and in  $k$ -space, modulational instability of wave trains arising from nonlinearity and (possibly) locally nonuniform wind stress, and the presence of impenetrable bodies in the flow. Finally, some related activities of the RIOBL program are reviewed.

## **Evolution of the Oceanic Boundary Layer Geometry**

Viewed as a dynamical system, the ocean boundary layer geometry can be described by a Hamiltonian which generates the equations of motion and hence defines the

temporal evolution of the geometry which constitutes the boundary condition for the Maxwell equations. As a simple illustration, consider the ‘oceanographic’ spectral model of the sea surface, that is, a superposition of weakly interacting primary waves, whose directional power density (the directional wave spectrum) is governed by an appropriate radiative transport equation,

$$\frac{\partial N(\vec{k})}{\partial t} = S_{\text{in}} + S_{\text{nl}} + S_{\text{dis}} + \dots,$$

where  $S_{\text{in}}$  is the source term for wave generation by wind or other causes,  $S_{\text{nl}}$  is the source term for nonlinear wave–wave interactions, and  $S_{\text{dis}}$  represents dissipation processes. Numerous parametric models for  $N(k)$  have been proposed, based on a wide variety of experimental data. The nonlinearity associated with wave–wave interactions is particularly relevant to HF radar where gravity waves are the primary entities which contribute to the scattering process. For the moment we assume a low sea state so the surface is single valued and take the water body to be simply connected, that is, we ignore spray.

One effect of nonlinear interactions is to modify the instantaneous surface geometry, as with the Stokes expansion, for example, resulting in sharpened crests and flattened troughs. This may be amenable to static (instantaneous) measurement; for instance, accurate measurement of surface slope or the statistical distribution of surface slope provides a partial window onto this aspect of nonlinearity, as will be discussed later. Another class of consequences can be seen in the dynamics, manifested as temporal coherence structure associated with phase coupling and exchange of energy between normal modes.

In field theoretic notation, we can write the Hamiltonian of the gravity wave field as a sum over orders of wave interaction [1],

$$\begin{aligned} H &= \sum_k \omega_k a_k^+ a_k + \sum_{k,j} V_{k,j} a_k^+ a_j a_{k-j} + \sum_{j,k,l} \Gamma_{j,k,l} a_k^+ a_l^+ a_j a_{k+l-j} + \dots \\ &\equiv H_2 + H_3 + H_4 + \dots, \end{aligned}$$

where  $a_k^+$  and  $a_k$  are the creation and annihilation operators for the normal modes  $\psi_k = e^{i(kx - \omega_k t)}$ . The time evolution of the surface, represented here by state vector  $\Psi(t)$ , is then given by

$$\Psi(t) = e^{iH(t-t_0)} \Psi(t_0)$$

If we adopt the approximation  $H=H_0$  then the surface is predicted to evolve as

$$\Psi_{\text{lin}}(t) = e^{iH_0(t-t_0)} \Psi(t_0) = e^{iH_0(t-t_0)} \sum_k c_k \psi_k(t_0) = \sum_k c_k e^{iH_0(t-t_0)} e^{i(kx - \omega_k t_0)},$$

which becomes

$$\Psi_{\text{lin}}(t) = \sum_k c_k e^{-i\omega_k(t-t_0)} e^{i(kx-\omega_k t_0)} = \sum_k c_k e^{i(kx-\omega_k t)} = \sum_k c_k \Psi_k(t),$$

which is the state resulting from independent propagation of the normal modes, as expected. The precision with which we can measure the nonlinear dynamics of a system initially in state  $\Psi(t_0)$  depends on the ability of the sensor scattering kernel to discriminate between the state space trajectory  $\Psi(t_0) \xrightarrow{H_0} \Psi_{\text{lin}}(t)$  and the trajectory  $\Psi(t_0) \xrightarrow{H} \Psi_{\text{obs}}(t)$ . How this difference manifests itself in a given radar signature will depend on the choice of signal processing and influence the selection of optimum radar parameters.

## Radar Sensors for Oceanic Boundary Layer Studies

The frequency bands which have been employed for active coherent radar sensing of the sea surface range from MF ( $\sim 10^6$  Hz) to W-band ( $\sim 10^{11}$  Hz), while lidar and other optical sensors operate up to  $\sim 10^{15}$  Hz. The present operational radar capability in the RIOBL program fall within the range  $3 \times 10^6$ – $3 \times 10^{10}$  Hz, as detailed later. It is apparent that some established technologies are not yet represented in our inventory, notably VHF radar and synthetic aperture radars in any band, but there is still considerable scope for multiscale measurements of ocean surface geometry.

### HF Radar

At the low end of the frequency scale, RIOBL makes use of four HF radars. Three of these are state-of-the-art skywave radars [2] while one, SECAR, is an advanced HF surface wave radar [3]. The skywave radars operate from 5 to 30 MHz, the surface wave radar from 4 to 16 MHz. The transmit and receive facilities of the Australian Jindalee skywave radar are shown in Fig. 1.



**Fig. 1.** Transmit and receive facilities of the Jindalee skywave radar

HF skywave radars achieve vast coverage at the expense of subjecting the signals to the fluctuations of the ionospheric magnetoplasma, so the quality of the data is dependent on the prevailing space weather. Nevertheless, a sea surface geometry description in terms of a spectrum of gravity waves can be extracted from the Doppler spectrum of the radar echoes. The contributions arising from nonlinear wave–wave interactions are generally localised in Doppler and hence can be separated under favourable propagation conditions.



**Fig. 2.** Receive array of the SECAR HF surface wave radar

HF surface wave radars avoid the problems of the ionosphere and hence yield superior quality information, though with some unique complications arising from the subtleties of surface wave propagation. Nominal sampling parameters of all the HF radar sensors are listed in Table 1.

### ***Microwave Radar***

The microwave facilities supporting RIOBL consist of two van-mounted radars, both fully polarimetric [4]. Figure 2 shows the vans deployed during a recent measurement campaign. One system operates from 8 to 18 GHz [4], the other from 0.1 to 18 GHz. Wide-angle bistatic operation is supported. These radars can achieve range resolutions down to 0.15 m, but beamwidth is limited to  $\sim 3^\circ$  at 10 GHz, so crossrange resolution is the main limitation in practice. Principal sampling parameters are listed in Table 1.



**Fig. 3.** DSTO's dual microwave radars (a) and millimetre wave radar (b)

### Millimetre Wave Radar

A fully polarimetric mm-wave radar operating at 35 GHz has been built to provide a capability for studying capillary waves, spray, and spume, and surfactant effects. At present this radar is not integrated into a mobile facility. Principal sampling parameters are included in Table 1.

**Table 1.** Principal sampling parameters of radars involved in the RIOBL program

	HF skywave	HF surface	microwave (2 radars)	mm-wave
frequency band (GHz)	0.005 – 0.030	0.004 – 0.016	(i) 8–18 (ii) 0.1–18	35
maximum range (km)	3,000	300	(i) 6 (ii) 10	6
range resolution (m)	5,000	3,000	(i) 0.15–150 (ii) 0.15–150	0.15–150
beamwidth at mid-band (deg.)	0.5–1	2–4	(i) 3 (ii) 3	3
pulse repetition frequency (Hz)	3–60	2–60	(i) $10-10^5$ (ii) $10-10^5$	$10-10^5$
coherent integration (s)	1–60	1–150	(i) 0.02–10 (ii) 0.02–10	0.01–10
bistatic mode	Y	Y	(i) Y (ii) N	N
polarimetric	N	N (VV only)	(i) Y (ii) Y	Y

## Radar Signatures of Nonlinear Processes

### Wave Shape

The wave shape asymmetries engendered by nonlinearity and the corresponding slope distributions are amenable to direct measurement by various radar and lidar sounding techniques, depending on the scattering geometry. Polarimetric radar is well suited to the measurement of large-scale surface slopes when the characteristic length scale  $l$  of large-scale slope variability satisfies  $l \gg \lambda$  and when small scale roughness is present so as to provide a Bragg scattering surface texture with its distinctive scattering matrix [5]. For X-band radar, where  $\lambda \sim 0.03$  m, the extended Bragg scattering kernel domain of validity corresponds to a minimum

length scale of  $\sim 1$  m, which is adequate for resolving surface gravity waves in the frequency band below  $\sim 0.5$  Hz.

From the present perspective, the key issue is whether polarimetric radar can measure the spatial slope distribution with precision sufficient to identify the presence of nonlinear contributions and to determine their spatial and spectral properties. We have chosen to address this question by examining the ‘known’ surface geometry of ship wakes.

Adopting the two-scale surface model with extended Bragg scattering from capillary waves, we have modelled the polarimetric response of a representative wake as computed by two ship wake modelling codes – one linearised [6], one fully nonlinear [7]. The nonlinearity arises both at the free surface, where the kinematic and dynamic boundary conditions apply, and in the approximations used to model the rigid body condition. Figure 4 shows the elevation distribution in the wake of a uniformly translating submerged spheroid as computed by the two codes.

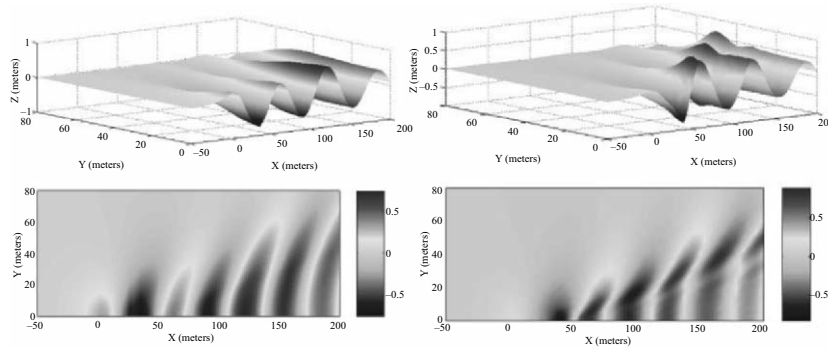


**Fig. 4.** Surface displacement for the Kelvin wake produced by a submerged spheroid computed by (a) linear hydrodynamics, and (b) fully nonlinear hydrodynamics

Figure 5 shows the predicted polarimetric radar response from the wake computed according to linearised hydrodynamics [8]; it is evident that the crosspolar response in the linear polarisation basis provides far greater sensitivity and ability to map the wake slope pattern than the copolar responses. The conditions under which the crosspolar response or an alternative polarimetric analysis can achieve the requisite accuracy are the subject of on-going research.



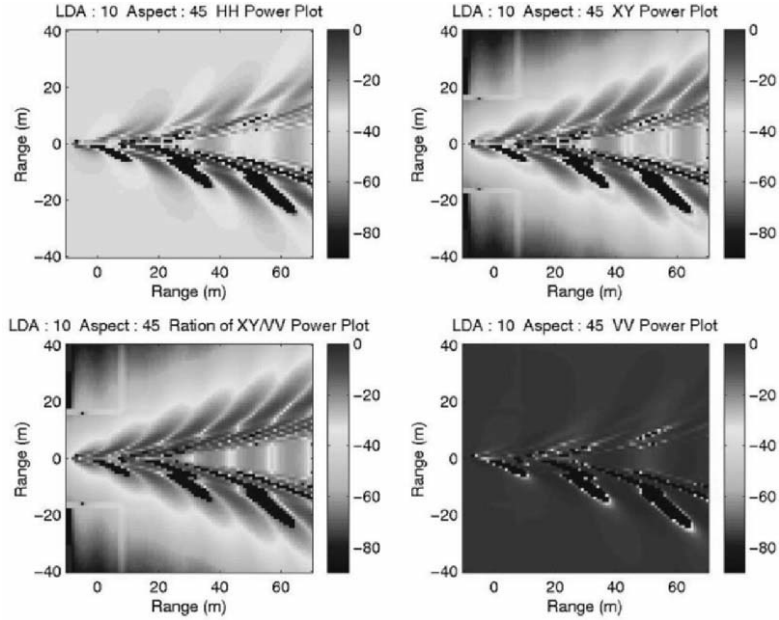


Fig. 5. Simulated wake power scattering matrix elements, ( $XY \leftrightarrow HV, VH$ )

### Wave Harmonics and Intermodulation Products

Another signature related to wave shape is the direct measurement of phase-locked harmonics and intermodulation products arising from weak nonlinear interactions of primary modes as described by  $H_3$ ,  $H_4$ , etc., in accordance with the predictions of Stokes [9], Zakharov [10], Hasselmann [11] and others. Quasilocality of the interaction in  $k$ -space supports a direct interpretation of features in the HF radar Doppler spectrum in terms of a weighted integral function of the actual Hamiltonian  $H_3$ . This is illustrated in Fig. 6 which compares (1) a sea clutter Doppler spectrum recorded with a skywave radar, with (2) a theoretical spectrum calculated for the prevailing sea conditions as determined by an in situ wavebuoy but assuming linear wave theory, and (3) a theoretical spectrum allowing for nonlinear wave triad interactions. The contributions of nonlinearity are obvious in this example. By collecting data at multiple frequencies, and for bistatic geometries, it is possible to derive additional information about  $H_3$ . The extent to which higher order nonlinearities can be observed in HF Doppler spectra is the subject of ongoing research, especially as the action and energy fluxes associated with on-shell resonances may obscure the geometrical signature.

**Wave Instabilities**

Weak interaction theory appears to provide a satisfactory description of some classes of nonlinear behaviour but the theory fails to predict local nonlinearities such as the Benjamin–Feir instability. This modulational sideband instability occurs when  $kh > 1.36$  and is thus expected to be present in developing seas where a strong narrow-band wave spectrum is observed.

Data was acquired under conditions expected to favour the Benjamin–Feir instability during an experiment in the Timor Sea with the SECAR HF surface wave radar [3]. Figure 7 presents a continuous-wavelet transform of the clutter data and compares it with the predictions of a simplified clutter model based on linear wave evolution. The measurements give the impression of a low frequency modulation of the linear spectrum with a period in the vicinity of 100 s. Theoretical analysis is underway to assess the likelihood that this effect is the signature of recurrence as predicted by Lake et al. [12].

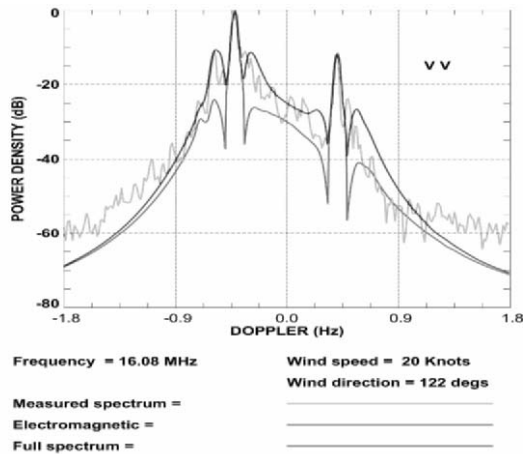


**Fig. 6.** Simulated HF Doppler spectra with and without hydrodynamic nonlinearity compared with a measured spectrum obtained with skywave radar

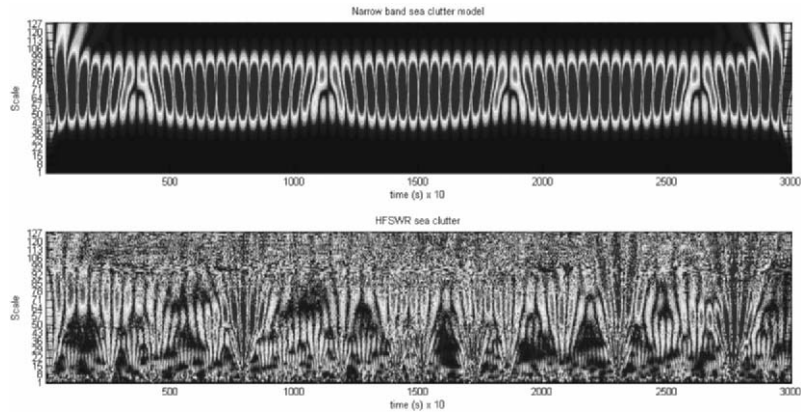


**Fig. 7.** Continuous wavelet transform of a simple narrow-band clutter model (top) with that of experimental HF surface wave clutter data

Another example of spatiotemporal modulation of the gravity wave field is presented in Fig. 8, obtained with an HF surface wave radar. Here the ratio of scattering contributions from specific linear wave components to those from nonlinear wave components is plotted against range. Superimposed on the figure is the received power, showing that the signal-to-noise ratio is high out to range cell 90 or so. The distinctive feature of the nonlinear-to-linear ratio (NLR) is the strong periodic modulation on a length scale of  $\sim 10$  range cells. In this measurement the range cell depth was  $\sim 1.5$  km, so the ‘wavelength’ of the modulation was  $\sim 15$  km. This is perhaps more consistent with coupling to atmospheric gravity waves, but purely hydrodynamic explanations may exist. Again, detailed analysis is underway to resolve the issue.

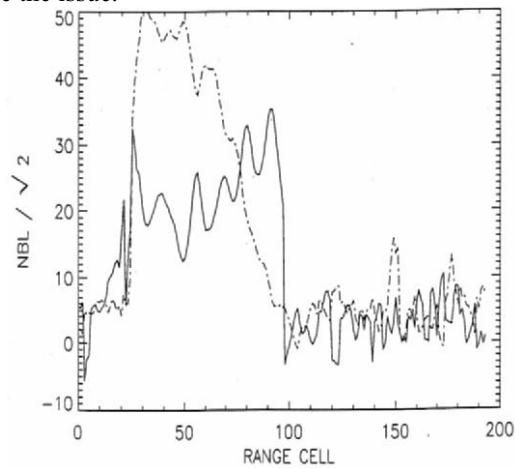


**Fig. 8.** Range variation of a parameter which measures one particular nonlinear-to-linear wave ratio, showing periodic modulation, not yet explained

### **Breaking Waves**

Breaking waves are an extreme case of nonlinear behaviour and hitherto have been studied mainly in terms of their configuration space geometry. Interest in their radar signatures has, until recently, concentrated on time domain signatures and their statistical characterisation – the well-known ‘sea spike’ clutter phenomenon. Physics-based modelling of the radar signatures of breaking waves has tended to focus on (1) specular point trajectories, and (2) integral formulations such as moment methods applied to simple one-dimensional evolving wave profiles.

We have studied wave breaking via the Cloude–Pottier decomposition of the coherency matrix and obtained good agreement with theory; details can be found in [13] and [14].

### **Conclusions**

Nonlinear processes are active over a wide range of spatial scales in the oceanic boundary layer. While complicating the behaviour and mathematical description of the boundary layer, these processes can provide means for determining important geophysical parameters which are poorly resolved by sensor response predicated on linearised physics.

In this paper we have illustrated some representative studies from our multisensor research program aimed at elucidating the mechanisms of hydrodynamic nonlinearity in the oceanic boundary layer. HF radars have been used to measure nonlinear wave interactions in  $k$ -space, while polarimetric microwave radar techniques have been developed and applied to the equivalent problem of ocean wave shape measurement in configuration space, after validation on deterministic wake patterns. Electromagnetic scattering from breaking waves has been modelled and compared with experiment through the agency of the Cloude–Pottier decomposition of the coherency matrix. Measurements of foam and spray generation have been conducted, though these are not reported here. Other electromagnetic sensing techniques such as sunglint inversion, previously based on linear wave theory, are being extended to address the nonlinear reality.

Forthcoming experiments will involve multiple sensor measurements of a common sea patch to crossvalidate techniques and guide the development of matched signal processing.

## References

- [1] J.F. Willemsen, “Universal aspects of nonlinear gravity wave interactions”, in: *‘Nonlinear Dynamics of Ocean Waves’*, A. Brandt, S.E. Ramberg and M.F. Shlesinger (Eds.), World Scientific, Singapore, 1992
- [2] S.J. Anderson, “Mapping Australia’s oceans with over-the-horizon radar”, *Presented at the Australian Institute of Physics Congress*, Canberra, 2005
- [3] S.J. Anderson, P.J. Edwards, P. Marrone and Y.I. Abramovich, “Investigations with SECAR – a bistatic HF surface wave radar”, *Proc. RADAR 2003*, Adelaide, 2003
- [4] W.C. Anderson, P.Dansie, R. Hawkes and A. Mahoney, “The MRD high resolution radar facility and its application to target signature analysis”, *Proc. Radarcon 90*, Adelaide, 1990
- [5] D.L. Schuler, J.S. Lee, D. Kasilingam, and E. Pottier, “Measurement of ocean surface slopes and wave spectra using polarimetric SAR image data”, *Remote Sensing Environ.*, 98, 198–211, 2004
- [6] E.O. Tuck and D.C. Scullen, *‘Sea Wave Pattern Evaluation : SWPE 7.0 Simplified Users Guide’*, Scullen and Tuck Pty Ltd, Adelaide, 2003
- [7] D.C. Scullen and E.O. Tuck, *‘Nonlinear Free-surface Flow solver: Users’ Guide’*, The University of Adelaide, 2002
- [8] S.J. Anderson and J.Morris, “Validation of computational models of ship wakes by means of polarimetric radar signature analysis”, *Proceedings of the International Congress on Industrial and Applied Mathematics*, Sydney, July 2003
- [9] G.G. Stokes, “On the theory of oscillatory waves”, *Trans. Camb. Philos. Soc.* 8, 441–455, 1847
- [10] V.E. Zakharov, “Stability of periodic waves of finite amplitude on the surface of a deep fluid”, *J. Appl. Mech. Technol. Phys.* 9, 190–194, 1968
- [11] K. Hasselmann, “On the non-linear energy transfer in a gravity-wave spectrum, part 1 : general theory”, *J. Fluid Mech.* 12, 481, 1962
- [12] H.C. Yuen and B.M. Lake, “Nonlinear deep water waves : Theory and experiments”, *Phys. Fluids*, 18(8), 956–960, 1982
- [13] J.T. Morris, S.J. Anderson, and S.R. Cloude, “A study of the X-band entropy of breaking ocean waves”, *Proceedings IGARSS 2003*, Toulouse, 711–713, 2003
- [14] J.T. Morris, “Polarimetric properties of radar echoes from features on the ocean surface”, Ph.D. Thesis, Department of Electrical and Electronic Engineering, University of Adelaide, September 2004

# Fine Tuning of Printed Triangular Monopole

C. Işık

Department of Electronics and Communication Engineering, Istanbul Technical University, Maslak, 34469 Istanbul, Turkey, isikcev@ehb.itu.edu.tr

## Abstract

A simple design for fine tuning of the monopole which involves a tuning strip placed as a part of the monopole at the feed point of the antenna is presented. Utilizing the strip, the maximum return loss was increased in the order of 15 dB and the fine tuning range of the centre frequency is about  $\pm 150$  MHz for the return loss  $> 30$  dB.

## Introduction

Recently, much effort to overcome the technical difficulties in the ultra-wideband system has been expended by researchers and industry that delivered the regulation of spectrum mask and mitigated the interferences with other communication systems. There are general factors determining the antenna performance of the wideband system. Those are input matching representing VSWR and antenna efficiency, radiation pattern, frequency-independent main lobe, gain flatness and so on [1–6]. Conventional designs of printed monopoles on a dielectric substrate for improving the operating bandwidth and reducing the length of monopole are usually achieved by suitably adjusting the flare angle of the triangular monopole [1–3]. In this letter, I present a simple design for ultimate impedance matching of the monopole which involves a tuning strip placed as a part of the monopole at the feed point of the antenna (Fig. 1). By adjusting the length and width of the strip, better impedance matching and fine tuning of the centre frequency of the antenna can easily be realized without significantly reducing antenna bandwidth. The proposed structure has been implemented utilizing several strip lengths and widths and it was demonstrated that the return loss of microstrip-fed printed triangular monopole antennas can be substantially increased without adversely affecting their bandwidth. Details of the experimental results are presented and discussed.

## Antenna Design and Experimental Results

Figure 1 shows the geometry of the microstrip-fed printed monopole antenna and the feeding line. Triangular part of the monopole has a length  $\ell$  of  $0.136\lambda_0$  and a width  $d$  of  $0.073\lambda_0$ . As a result, the flare angle is  $30^\circ$  and for the antenna without the strip the centre frequency is 1.82 GHz. The feeding line is a  $50\ \Omega$  microstrip line with  $w=0.8$  mm and  $g=0.12\lambda_0$  where  $\lambda_0=164.8$  mm is the free-space wavelength for the centre frequency 1.82 GHz (see Fig. 1). The structure is realized on an aluminate substrate ( $\epsilon_r=9.8$ ,  $120\text{ mm} \times 100\text{ mm}$ ,  $h=0.76$  mm).

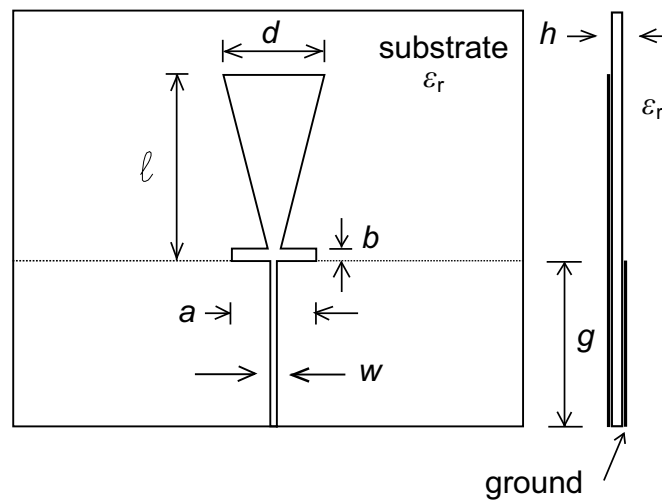
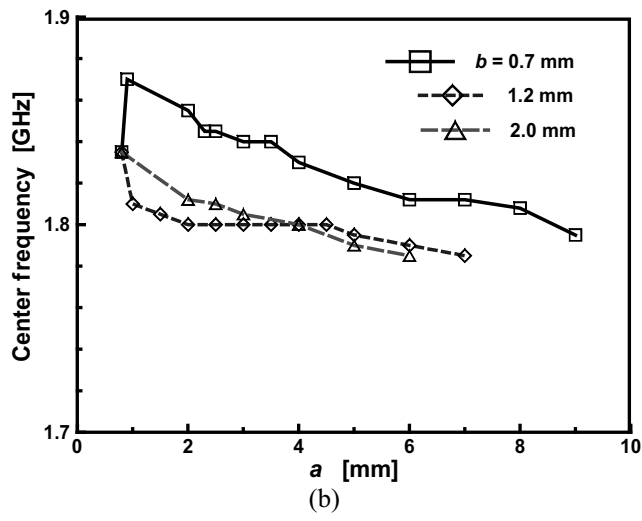
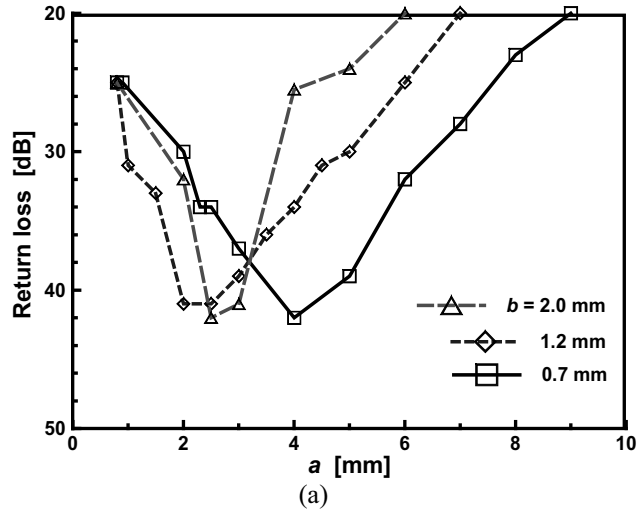


**Fig. 1.** Geometry of microstrip-fed printed triangular monopole with the tuning strip

The microstrip-fed triangular antennas with various strip length ( $a$ ) and width ( $b$ ) are built and tested. Measured values of bandwidth, centre frequency and maximum return loss values of the antenna structures investigated are shown in Fig. 2 as a function of the strip length ( $a$ ), for the strip width ( $b$ ) parameter values of 2.0, 1.2 and 0.7 mm. The values of other parameters of the antenna geometry related to the figures are  $\epsilon_r=9.8$ ,  $w=0.8$  mm,  $h=0.76$  mm,  $g=20$  mm,  $\ell=22.5$  mm,  $d=12$  mm. The common starting point of the curves in Fig. 2 corresponds to the monopole without the strip.

As seen in Fig. 2a, the return loss at the centre frequency can be increased from 25 dB to 42 dB by adjusting the values of the strip parameters  $a$ ,  $b$ . While increasing the return loss, the bandwidth ( $\Delta f$ ) and centre frequency ( $f_0$ ) also undergo some changes. It can be deduced from the results in Fig. 2b, that only the narrow strip ( $b=0.7$  mm) case provides fine tuning around the centre frequency of the monopole without the strip, which is defined as the frequency which yields maximum return loss. The bandwidth values depicted in Fig. 2c are all determined from the return loss value of 30 dB, for comparison purposes. The results are

summarized in Table 1, to enable a comparison between the antennas with different strip dimensions.





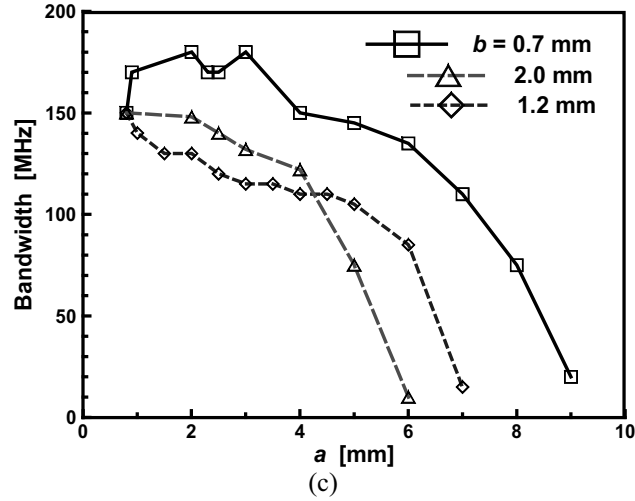


**Fig. 2.** (a) Measured return loss characteristics of the monopole versus the strip length for different strip widths, (b) measured centre frequency characteristics of the monopole versus the strip length for different strip widths, (c) measured bandwidth characteristics of the monopole versus the strip length for different strip widths

$a$ (mm)	4.0	2.0	3.0	–
$b$ (mm)	0.7	1.2	2.0	–
$L_r$ (dB)	42	42	42	25
$f_0$ (GHz)	1.83	1.80	1.81	1.83
$\Delta f$ (MHz)	150	130	140	–
$\Delta a$ (mm)	4.2	3.7	1.8	–

**Table 1.** Comparison between monopoles with different strip dimensions for the maximum return loss

In this table  $a$  and  $f_0$  correspond to the values which yield maximum return loss value ( $L_r$ ) for the corresponding strip width  $b$ . The bandwidth  $\Delta f$  around  $f_0$  is measured for 30 dB return loss, in all cases.  $\Delta a$  values given in the table which correspond to total permissible variation of the strip length  $a$ , under the condition that the return loss exceeds 30 dB provide a measure of the tuning sensitivity of the proposed design. The last column in Table 1 shows the  $f_0$  and  $L_r$  values of the conventional antenna without the strip. It is clearly seen from Table 1 that the narrow strip ( $b=0.7$  mm) provides match without altering the centre frequency of the antenna. Note also, since  $\Delta a$  is largest for the narrow strip, it will be easier to fine tune the structure to achieve stated bandwidth return loss performance.

Figure 3 shows the curves of the measured return loss versus frequency for the antennas with the three sets of strip dimensions shown in Table 1. For comparison

purposes, the measured return loss of the triangular monopole without the strip is also shown on the same figure. In all cases the utilization of the strip provides excellent matching with residual return losses of about 40 dB, and relatively bandwidth of about 20% for  $L_r > 10$  dB. On the other hand, it can also be seen from this figure that for the conventional antenna without the strip, the relative bandwidth determined for  $L_r > 10$  dB is 24%. This result is in good agreement with that reported in [1] for similar conventional antenna structure when the flare angle  $30^\circ$ . It can, therefore, be concluded that the utilization of a tuning strip as proposed in this letter, will significantly improve the matching of triangular monopoles without appreciably affecting their bandwidth.

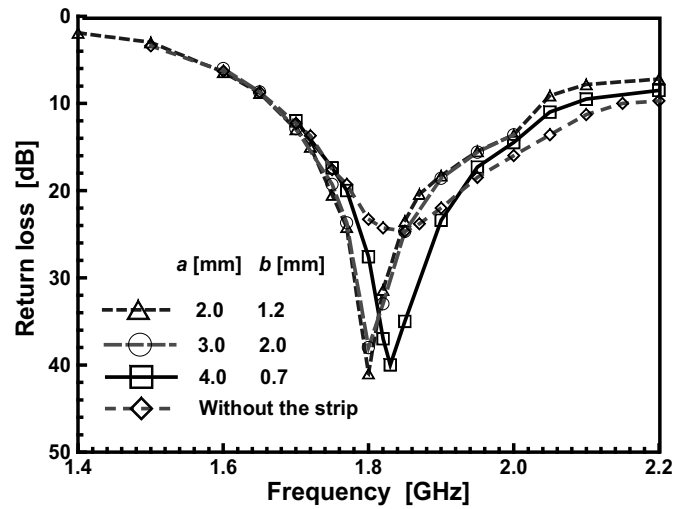


**Fig. 3.** Measured return loss of the monopole versus frequency for different optimum strip width and length

## Conclusions

A novel design which is simple to implement, and which provides ultimate match for the microstrip-fed triangular monopole antenna has been described and discussed. It has been experimentally shown that for different strip widths and lengths, the return loss which was 25 dB without the strip can be increased to about 40 dB with the proposed structure. Moreover, the proposed design does not appreciably affect the attainable bandwidths, and easily allows for finely adjustment of the bandwidth, centre frequency and the return loss of such antennas required different applications in mobile and telecom communications.

## References

- [1] K.L. Wong, Y.F. Lin, “Strip line-fed printed triangular monopole”, *Electron. Lett.*, 33 (17) pp. 1428–1429, 1997
- [2] J.J. Johnson, Y. Rahmat-Samii, “The tab monopole”, *IEEE Trans. Antennas Propag.*, 45 (1), pp. 187–188, 1997
- [3] Y.D. Lin, S.N. Tsai, “Coplanar wave guide-fed unipolar bow-tie antenna”, *IEEE Trans. Antennas Propag.*, 45 (2), pp. 305–306, 1997
- [4] Z.N. Chen, “Impedance characteristics of planar bow-tie like monopole antennas”, *Electron. Lett.*, 36 (13), pp. 1100–1101, 2000
- [5] M.J. Ammann, Z.N. Chen, “A wide-band shorted planar monopole with bevel”, *IEEE Trans. Antennas Propag.*, 51 (4), pp. 901–903, 2003
- [6] J.W. Lee, C.S. Cho, J. Kim, “A new vertical half disc-loaded ultra-wideband monopole antenna (VHDM) with a horizontally top-loaded small disc”, *IEEE Antennas Wireless Propag. Lett.*, 4, pp. 198–201, 2005

# A Chiralic Circuit Element and Its Use in a Chiralic Circuit

T. Şengör

Department of Electronics and Communication Engineering, Yildiz Technical University, Beşiktaş, 34349 Istanbul, Turkey, sengor@yildiz.edu.tr

## Abstract

A chiral material is modeled by a circuit element approach in this paper. The definition of a suitable circuit element, which we call chiralic circuit element, is given by this approach. We defined chiralic circuits, which use chiralic circuit element. A chiralic circuit is a device designed by using chiralic materials.

## Introduction

The chiralic materials have some interesting properties: propagation velocity of waves in chiral media is an example. A chiral media split a wave into two counterparts both of them propagates with different velocities. Does this character may be useful to design some specific circuits, devices, or systems? Most of biological systems, phantom materials are chiral media, basically. So, the interaction mechanism of electromagnetic waves and signals with living bodies are related to the characters of chiral materials. This interaction gives an idea to consider some suitable circuit modelization of biological materials. Considering a chiral medium as a circuit-like element does this modelization. We make specific arrangements to do this and derive a suitable definition usable for such circuit-like elements. We call chiralic circuit element.

We consider the simple case. The constitutive relations are follower for an isotropic, nondispersive chiral medium where  $\epsilon$ ,  $\mu$ , and  $\chi$  are permittivity, permeability, and chirality, respectively [1]:

$$\mathbf{B} = \mu\mathbf{H} + \chi \frac{\partial \mathbf{E}}{\partial t}, \quad (1a)$$

$$\mathbf{D} = \epsilon\mathbf{E} - \chi \frac{\partial \mathbf{H}}{\partial t}, \quad (1b)$$

The use of Laplace's transform [2] is convenient as a result of some certain analytical restrictions: We consider  $\mathbf{B}$  is summable over all finite intervals and there is a constant  $c$  for which

$$\int_0^{\infty} |\mathbf{B}| e^{-ct} dt < \infty, \quad (2a)$$

then

$$\underline{\mathbf{B}}^{\Delta} = \mathcal{L}\{\mathbf{B}; p\} = \int_0^{\infty} \mathbf{B} e^{-pt} dt, \quad \text{Re } p > 0, \quad (2b)$$

is exist when  $p = \sigma + i\tau$  is such that  $\sigma \geq c$ . The Laplace's transforms of (1a) and (1b) are:

$$\underline{\mathbf{B}} = \underline{\mu}\underline{\mathbf{H}} + \chi p \underline{\mathbf{E}} - \chi \mathbf{E}_0, \quad (3a)$$

$$\underline{\mathbf{D}} = \varepsilon \underline{\mathbf{E}} - \chi p \underline{\mathbf{H}} + \chi \mathbf{H}_0, \quad (3b)$$

where  $\mathbf{E}_0$  and  $\mathbf{H}_0$  are initial values.

Let us consider a regular surface  $S$ .  $\mathbf{E}$  and  $\mathbf{H}$  have continuous derivatives on  $S$ . The integration of (3a) and (3b) on  $S$  gives

$$\underline{\phi}^b = \underline{\mu}\underline{\phi}^h + p\chi\underline{\phi}^e - \chi\phi_0^e, \quad (4a)$$

$$\underline{\phi}^d = \varepsilon\underline{\phi}^e - p\chi\underline{\phi}^h + \chi\phi_0^h, \quad (4b)$$

where we use definitions below:

$$\begin{bmatrix} \underline{\phi}^b \\ \underline{\phi}^d \end{bmatrix} = \int_S \begin{bmatrix} \underline{\mathbf{B}} & \underline{\mathbf{H}} \\ \underline{\mathbf{D}} & \underline{\mathbf{E}} \end{bmatrix} \cdot d\mathbf{S}, \quad (5a)$$

$$\begin{bmatrix} \phi_0^e \\ \phi_0^h \end{bmatrix} = \int_S \begin{bmatrix} \mathbf{E}_0 & \mathbf{H}_0 \end{bmatrix} \cdot d\mathbf{S}. \quad (5b)$$

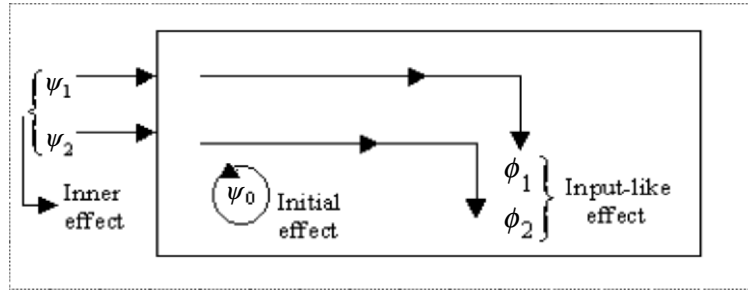


Fig. 1. A suitable schematic interpretation of chiralic circuit element

### Chiralic Circuit Element

The specific functions included in (3a) and (3b) have some characteristics suitable to determine new concepts in circuit and system theories. Let us rearrange (3a) and (3b) as

$$\underline{\Phi} = \begin{bmatrix} p\chi & \mu \\ \varepsilon & -p\chi \end{bmatrix} \underline{\Psi} + \chi \begin{bmatrix} -1 & 0 \\ 0 & 1 \end{bmatrix} \psi_0, \tag{6}$$

to illustrate these concepts, where  $\Psi_0$  is the initial value matrix; i.e.,  $t=0$ . Here we put definitions below:

$$\underline{\Phi} \stackrel{\Delta}{=} [\underline{\phi}^b \quad \underline{\phi}^d]^T, \tag{7a}$$

$$\underline{\Psi} \stackrel{\Delta}{=} [\underline{\phi}^e \quad \underline{\phi}^h]^T, \tag{7b}$$

$$\Psi_0 \stackrel{\Delta}{=} [\phi_0^e \quad \phi_0^h]^T. \tag{7c}$$

Now, let us think of the chiral material using the approaches in circuit and system techniques [3]. The functions  $\underline{\Phi}$  and  $\underline{\Psi}$  in (6) are like the output and input concepts in circuit and system theory, respectively. The role of  $\Psi_0$  is the same as the initial value of input. We can consider a circuit element corresponding to (6) if we put following concepts: the  $\underline{\Phi}_{[2 \times 1]}$  and  $\underline{\Psi}_{[2 \times 1]}$  are suitable to consider as the input-like effect and the inner effect, respectively (Fig. 1). The uses of these two effect functions give the equations similar to circuit-system equations. We call these equations chiralic circuit equations.

A chiralic circuit element is defined in Laplace transform domain with parameter  $p$  by (6). The chiralic circuit element is a circuit-like device (Fig. 1).

## Chiralic Circuits

Let us consider the Laplace's transformation of Maxwell's equations from (2b). We write:

$$\text{rot}\underline{\mathbf{E}} + p\underline{\mathbf{B}} - \underline{\mathbf{B}}_0 = -\underline{\mathbf{J}}^m, \quad (8a)$$

$$\text{rot}\underline{\mathbf{H}} - p\underline{\mathbf{D}} + \underline{\mathbf{D}}_0 = \underline{\mathbf{J}}^e, \quad (8b)$$

$$\text{div}\underline{\mathbf{D}} = \underline{\rho}^e, \quad (8c)$$

$$\text{div}\underline{\mathbf{B}} = \underline{\rho}^m. \quad (8d)$$

Let us consider a closed volume  $V$ . Let  $S$  be a regular surface in  $V$  and  $C$  be the boundary of  $S$ . We accept  $\underline{\mathbf{E}}$  and  $\underline{\mathbf{H}}$  have partial derivatives with respect to the space coordinates on  $S$  and  $C$  up to the first order. We accept  $\underline{\mathbf{D}}$  and  $\underline{\mathbf{B}}$  have first order partial derivatives with respect to the space coordinates in  $V$ . The surface integrals of (8a) and (8b) and volume integrals of (8c) and (8d) give follower, where dot ( $\dot{\phantom{x}}$ ) over  $\phi$  illustrates the first-order derivative with respect to time, respectively:

$$\underline{\mathbf{V}}^e + p\underline{\mu}\underline{\phi}^h + p^2\underline{\chi}\underline{\phi}^e = p\underline{\chi}\underline{\phi}_0^e + \underline{\mu}\underline{\phi}_0^h + \underline{\chi}\dot{\underline{\phi}}_0^e - \underline{\mathbf{I}}^m, \quad (9a)$$

$$\underline{\mathbf{U}}^m - p\underline{\varepsilon}\underline{\phi}^e + p^2\underline{\chi}\underline{\phi}^h = p\underline{\chi}\underline{\phi}_0^h - \underline{\varepsilon}\underline{\phi}_0^e + \underline{\chi}\dot{\underline{\phi}}_0^h - \underline{\mathbf{I}}^e, \quad (9b)$$

$$\underline{\varepsilon}\underline{\phi}^e - p\underline{\chi}\underline{\phi}^h = -\underline{\chi}\underline{\phi}_0^h + \underline{\mathbf{q}}^e, \quad (9c)$$

$$\underline{\mu}\underline{\phi}^h + p\underline{\chi}\underline{\phi}^e = \underline{\chi}\underline{\phi}_0^e + \underline{\mathbf{q}}^m. \quad (9d)$$

Here we put following definitions, where T illustrates the matrix transposition:

$$\underline{\mathbf{V}}^T = \begin{bmatrix} \underline{\mathbf{V}}^e & \underline{\mathbf{U}}^m \end{bmatrix} \stackrel{\Delta}{=} \oint_C \begin{bmatrix} \underline{\mathbf{E}} & \underline{\mathbf{H}} \end{bmatrix} \cdot d\mathbf{C}, \quad (10a)$$

$$\underline{I}^T = \left[ \underline{I}^m \quad \underline{I}^e \right] \stackrel{\Delta}{=} \int_{\mathcal{S}} \left[ \underline{J}^m \quad \underline{J}^e \right] \cdot d\mathbf{S}, \quad (10b)$$

$$\underline{Q}^T = \left[ \underline{q}^e \quad \underline{q}^m \right] \stackrel{\Delta}{=} \int_V \left[ \rho^e \quad \rho^m \right] dV. \quad (10c)$$

Using three  $4 \times 1$  vectors puts the (9a–9d) to following matrix form by:

$$\begin{aligned} \begin{bmatrix} 1 & 0 & p^2 \chi & p\mu \\ 0 & 1 & -p\varepsilon & p^2 \chi \\ 0 & 0 & \varepsilon & -p\chi \\ 0 & 0 & p\chi & \mu \end{bmatrix} \times \begin{bmatrix} \underline{V}^e \\ \underline{U}^m \\ \underline{\phi}^e \\ \underline{\phi}^h \end{bmatrix} &= \begin{bmatrix} p\chi & \mu & \chi & 0 \\ -\varepsilon & p\chi & 0 & \chi \\ 0 & -\chi & 0 & 0 \\ \chi & 0 & 0 & 0 \end{bmatrix} \times \begin{bmatrix} \underline{\phi}_0^e \\ \underline{\phi}_0^h \\ \dot{\underline{\phi}}_0^e \\ \dot{\underline{\phi}}_0^h \end{bmatrix} \\ &+ \begin{bmatrix} -1 & 0 & 0 & 0 \\ 0 & 1 & 0 & 0 \\ 0 & 0 & 1 & 0 \\ 0 & 0 & 0 & 1 \end{bmatrix} \times \begin{bmatrix} \underline{I}^m \\ \underline{I}^e \\ \underline{q}^e \\ \underline{q}^m \end{bmatrix}. \end{aligned} \quad (11)$$

A specific partitioning of matrix (11) gives following two matrix equations, which are suitable to consider as equations of a convenient circuit:

$$\mathbf{U} \underline{V} + p \begin{bmatrix} p\chi & \mu \\ \varepsilon & p\chi \end{bmatrix} \underline{\Psi} = \begin{bmatrix} p\chi & \mu \\ \varepsilon & p\chi \end{bmatrix} \psi_0 + \chi \mathbf{U} \psi'_0 + \begin{bmatrix} -1 & 0 \\ 0 & 1 \end{bmatrix} \underline{I}, \quad (12a)$$

$$\begin{bmatrix} \varepsilon & -p\chi \\ p\chi & \mu \end{bmatrix} \underline{\Psi} = \chi \begin{bmatrix} 0 & -1 \\ 1 & 0 \end{bmatrix} \psi_0 + \mathbf{U} \underline{Q}. \quad (12b)$$

$\mathbf{U}_{[2 \times 1]}$  is unit matrix ( $2 \times 2$ ),  $V_{[2 \times 1]}$  is the output-like effect,  $I_{[2 \times 1]}$  is the source defined by total amount of current,  $Q_{[2 \times 1]}$  is the source defined by total amount of charge distribution: i.e.,

$$\underline{I} \stackrel{\Delta}{=} \begin{bmatrix} I^m & I^e \end{bmatrix}^T, \quad (13a)$$

$$\underline{Q} \stackrel{\Delta}{=} \begin{bmatrix} q^e & q^m \end{bmatrix}^T. \quad (13b)$$



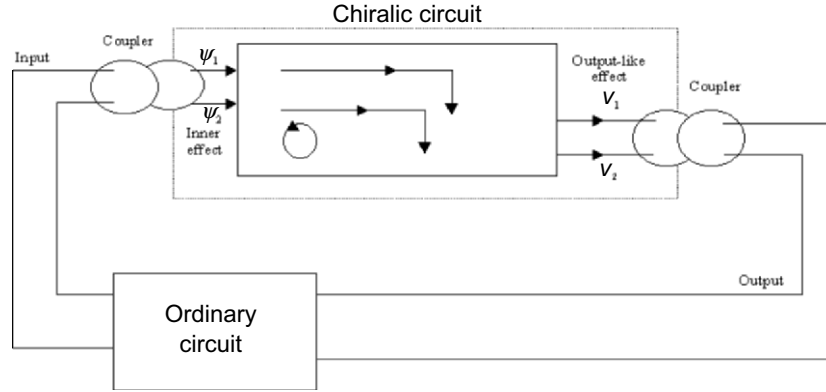


**Fig. 2.** A suitable schematic interpretation of chiralic circuit involving a chiralic circuit element

The  $\underline{V}$  and  $\underline{\Psi}$  like output voltage and output current, respectively, in circuit theory. Similarly, the  $\underline{\Psi}_0$  and  $\underline{\dot{\Psi}}_0$  like initial conditions and  $\underline{I}$  and  $\underline{Q}$  like the source. We call  $\underline{\Psi}_{0[2 \times 1]}$  and  $\underline{\dot{\Psi}}_{0[2 \times 1]}$  initial effects. Equations (12a) and (12b) may be considered as a circuit-like equation and a circuit-like element definition, respectively. So, (12a) and (12b) may be solved by circuit techniques. We call chiralic circuit equations (12a) and (12b). These equations are suitable to use designing circuits including chiralic materials. We call chiralic circuits such devices. The chiralic circuit is a device designed by using a chiralic circuit element (Fig. 2). The summary of the analogy explained above between the concept of chiralic circuits and the concept of circuits and systems theory is given in Table 1.

### Examples

We take (12a) and (12b) and investigate the influences of the variations of various parameters on the chiralic circuit variables (see Table 1). The chirality was changed among 0.001, 0.1, 10, and 100 and conclusions in below are considered: the first element of output-like effect; i.e.,  $\underline{V}_1$  grows 0.01 V up for  $\chi=1$ . The second element of output-like effect; i.e.,  $\underline{V}_2$  grows 100 A up.  $\underline{V}_1$  grows from 100 V to 200 V up.  $\underline{V}_2$  grows from 0.01 A to 10 A up. If the first element of inner effect; i.e.,  $\underline{\psi}_1$  grows then the output-like effect grows. If  $\underline{\psi}_1$  drops down then the output-like effect decreases. If  $10^{-3} < \chi < 10$  then the output-like effect is almost the same. The variation of chirality between  $10^{-3}$  and 10 does not make change in output-like effect. The variations of output-like effect versus inner effect for smaller values of chirality less than  $4\pi \times 10^{-7}$  give the result below: the first and second elements of output-like effects grow 200 V and 100 A up, respectively. If  $\chi$  decreases to  $10^{-20}$  from  $10^{-7}$ , then the first element of inner effect decreases a value less than 1. If  $\chi < 10^{-30}$  then the inner effect is almost zero.

**Table 1.** Analogy between the concept of chiralic circuit and the concept of systems

chiralic circuit variables	systems variables
$\underline{V} = \left[ \begin{matrix} \underline{V}^e & \underline{U}^m \end{matrix} \right]^T$ output-like effect	output (voltage)
$\underline{I} = \left[ \begin{matrix} \underline{I}^m & \underline{I}^e \end{matrix} \right]^T$ source effect	input (current)
$\underline{Q} = \left[ \begin{matrix} \underline{q}^e & \underline{q}^m \end{matrix} \right]^T$ source effect	source
$\underline{\Phi} = \left[ \begin{matrix} \underline{\phi}^b & \underline{\phi}^d \end{matrix} \right]^T$ input-like effect	output
$\underline{\Psi} = \left[ \begin{matrix} \underline{\phi}^e & \underline{\phi}^h \end{matrix} \right]^T$ inner effect	output
$\underline{\Psi}_0 = \left[ \begin{matrix} \phi_0^e & \phi_0^h \end{matrix} \right]^T$ initial effect	initial condition
$\underline{\dot{\Psi}}_0 = \left[ \begin{matrix} \dot{\phi}_0^e & \dot{\phi}_0^h \end{matrix} \right]^T$ initial effect	initial condition
Equation (6): chiralic circuit element	description equation
Equation (12a): circuit-like equation	either loop and node equations or tableau equation or state equation [3, p. 728]
Equation (12b): circuit-like element description	description equation

### Conclusions and Discussions

The chiralic circuit element is defined. The essentials of a circuit-like device are given. The design of chiralic circuits is considered and chiralic circuit equations are given. Some properties of chiralic circuits are discussed. The method is very useful for calculations in very complicated systems working at all frequencies.

### References

[1] J.A. Kong, *Electromagnetic Wave Theory*, EMW Publishing, Cambridge, MA, 2000  
 [2] I.N. Sneddon, *The Use of Integral Transforms*, McGraw-Hill, New York, 1972  
 [3] L.D. Chua, C.A. Desoer, E.S. Kuh, *Linear and Nonlinear Circuits*, Series in Electrical Engineering, McGraw-Hill, New York, 1987

---

---

## Part II

### Circuit Theory

# Dynamical Systems Analysis Using Differential Geometry

J.-M. Ginoux and B. Rossetto

Laboratoire P.R.O.T.E.E., équipe EBMA/ISO  
Université du Sud Toulon-Var, B.P. 20132, 83957, La Garde,  
ginoux@univ-tln.fr, rossetto@univ-tln.fr

## Abstract

This paper aims to analyze trajectories behavior and attractor structure of chaotic dynamical systems with the Differential Geometry and Mechanics formalism. Applied to slow-fast autonomous dynamical systems (S-FADS), this approach provides: on the one hand a kinematics interpretation of the trajectories motion, and on the other hand, a direct determination of the slow manifold equation. The attractivity of this manifold established with a new criterion makes it possible to ensure attractors stability. Then, a qualitative description of the geometrical structure of the attractor is presented. It consists in considering it as the deployment in the space phase of a special submanifold that is called singular manifold. The attractor can be obtained by integration of initial conditions taken on this singular manifold. Applications of this method are made for the following models: cubic-Chua, and Volterra-Gause.

## Introduction

In the *Mechanics* formalism the solution of a dynamical system is considered as the co-ordinates of a moving point M at the instant  $t$ . Then, three kinematics variables are attached to this point which represents the “trajectory curve”:

$\vec{X}(t)$ : parametric representation of chaotic orbit

$\vec{V}(t)$ : instantaneous velocity vector

$\vec{\gamma}(t)$ : instantaneous acceleration vector.

The Differential Geometry allows to use the Frénet frame [2] which is moving with the “trajectory curve” and directed towards its motion, consists in, a unit tangent vector to the “trajectory curve”, a unit normal vector, directed towards the

interior of the concavity of the curve and a unit binormal vector to the trajectory curve so that the trihedron  $(\vec{\tau}, \vec{\beta}, \vec{v})$  is direct (cf. Fig. 1).

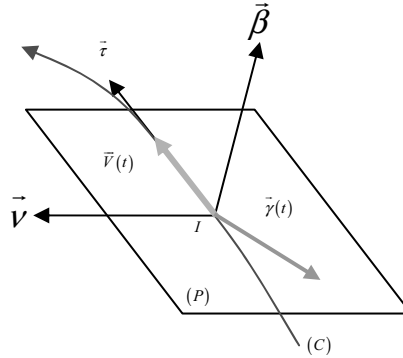


**Fig. 1.** Frénet frame and osculating plane

In this moving frame the instantaneous acceleration vector may be decomposed in a tangential and normal component both depending on instantaneous velocity and acceleration vectors directions

$$\begin{aligned} \gamma_t &= \frac{\vec{\gamma} \cdot \vec{V}}{\|\vec{V}\|}, \\ \gamma_n &= \frac{\|\vec{\gamma} \wedge \vec{V}\|}{\|\vec{V}\|}. \end{aligned} \quad (1)$$

The osculating plane [7] to the “trajectory curve” presented in Fig. 1. is the plane passing through a fixed point I and spanned by the instantaneous velocity and acceleration vectors. Its equation may be provided by the coplanarity condition (2).

$$\forall M \in (P) \Leftrightarrow \exists (\mu, \eta) \in \mathbb{R}^2 / \vec{IM} = \mu \vec{V} + \eta \vec{\gamma}.$$

This coplanarity condition may be written:

$$\vec{IM} \cdot (\vec{V} \wedge \vec{\gamma}) = 0. \quad (2)$$

In this formalism, trajectory presents two “metric properties”:

- curvature which expresses the rate of change of the tangent when moving along the “trajectory curve”.  $\mathfrak{R}$  represents the radius of curvature.
- torsion which measures, roughly speaking, the magnitude and sense of deviation of the “trajectory curve” from the osculating plane, or, in other words, the rate of change of the osculating plane.  $\mathfrak{S}$  represents the radius of torsion

$$\frac{1}{\mathfrak{R}} = \frac{\|\vec{\gamma} \wedge \vec{V}\|}{\|\vec{V}\|^3} = \frac{\gamma_v}{\|\vec{V}\|^2}, \quad (3)$$

$$\frac{1}{\mathfrak{S}} = -\frac{\vec{\gamma} \cdot (\vec{\gamma} \wedge \vec{V})}{\|\vec{\gamma} \wedge \vec{V}\|^2}.$$

Then, the use of the instantaneous acceleration vector makes it possible to delimit the *slow* and *fast* domains of the phase space.

### **Definition**

The domain of the phase space in which the tangential component of the instantaneous acceleration vector is negative, i.e., the domain in which the system is decelerating is called *slow* domain. The domain of the phase space in which the tangential component of the instantaneous acceleration vector is positive, i.e., the domain in which the system is accelerating is called *fast* domain.

## **New Method of Determination of the Slow Manifold Equation**

Applying both formalisms, recalled in the previous section, to slow-fast autonomous dynamical systems (S-FADS) or to autonomous dynamical systems which can be considered as slow-fast (CAS-FADS), i.e., systems whose functional Jacobian matrix has a “fast eigenvalue” which is a real, negative and dominant on a large domain of the phase space [6], a new method of determination of the slow manifold equation is proposed.

### **Proposition 1**

The equation of the osculating plane (P) passing through a fixed point I of a dynamical system (S-FADS or CAS-SFADS) and spanned by the instantaneous, velocity vector  $\vec{V}$  and acceleration vector  $\vec{\gamma}$ , is the slow manifold equation associated to this system.

In order to specify the attractivity of this manifold a new criterion based on the envelope theory is also proposed [4].

**Proposition 2**

The attractivity of the slow manifold is given by the sign of the torsion which constitutes the envelope of the slow manifold defined by the osculating plane.

It can be shown [4] that the total differential with respect to time of the osculating plane equation defined by the coplanarity condition (2) corresponds to the torsion. Thus, the location of the points where the torsion vanishes corresponds to the location of the points where the osculating plane is stationary.

Then, a qualitative description of the attractor structure is presented with the introduction of a submanifold called singular manifold.

**Proposition 3**

The singular manifold is defined like the location of the points belonging to the slow manifold and for which the tangential component of the instantaneous acceleration vector vanishes. This leads to the following equations:

$$\begin{cases} \phi = 0, \\ \gamma_r = 0. \end{cases} \quad (4)$$

This one-dimensional manifold is a submanifold of the slow manifold.

Let us consider the location of the points obtained by integration in a given time of initial conditions taken on this manifold. Each point being iterated to the antecedent point. They constitute a submanifold which also belongs to the attractor. The whole of these manifolds corresponds to different points of integration making it possible to reconstitute the attractor by redeployment of the singular manifold.

## Applications and Numerical Simulations

Applications of this new method are made for the following models: cubic-Chua and Volterra–Gause.

### **Cubic-Chua's circuit**

Let us first recall the cubic Chua's circuit [1] which is a (S-FADS). Parameters used are

$$\varepsilon = 0.05, \mu = 2,$$

$$\vec{V} = \begin{pmatrix} \frac{dx}{dt} \\ \frac{dy}{dt} \\ \frac{dz}{dt} \end{pmatrix} = \begin{pmatrix} \frac{1}{\varepsilon} \left( z - \frac{44}{3}x^3 - \frac{41}{2}x^2 - \mu x \right) \\ -z \\ -0.7x + y + 0.24z \end{pmatrix}. \quad (5)$$

In Fig. 2 is plotted the slow manifold equation associated to the cubic-Chua's circuit.

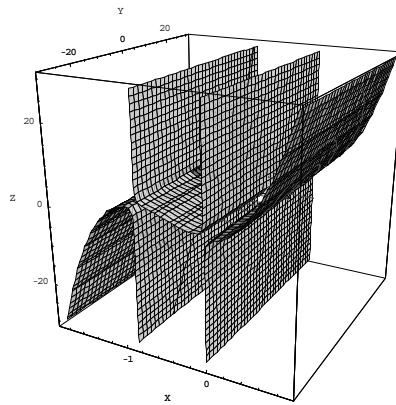


**Fig. 2.** Slow manifold equation associated to the cubic-Chua's circuit defined by the osculating plane method

In Fig. 3 is plotted the location of the point where the torsion associated to the cubic-Chua's circuit vanishes.



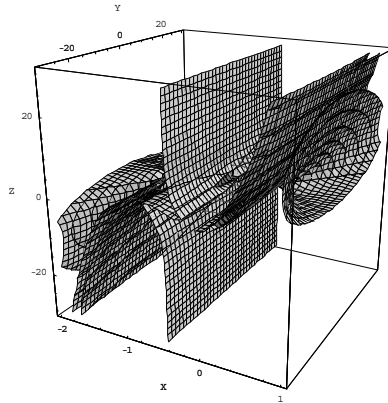


**Fig. 3.** Location of the point where the torsion associated to the cubic-Chua's circuit vanishes, i.e., where the osculating plane is stationary

### ***Volterra–Gause model***

In order to illustrate the concept of deployment let us apply it on a three-dimensional predator–prey model elaborated by Ginoux et al. [3]. This model consisted of a prey, a predator and top-predator has been named Volterra–Gause because it combines the original model of Volterra (1926) incorporating a logistic limitation of Verhulst (1838) type on the growth of the prey and a limitation of Gause (1935) type on the intensity of the predation of the predator on the prey and of top-predator on the predator

$$\vec{V} = \begin{pmatrix} \frac{dx}{dt} \\ \frac{dy}{dt} \\ \frac{dz}{dt} \end{pmatrix} = \vec{F} \begin{pmatrix} f(x, y, z) \\ g(x, y, z) \\ h(x, y, z) \end{pmatrix} = \begin{pmatrix} \frac{1}{\xi} \left( x(1-x) - x^{\frac{1}{2}}y \right) \\ -\delta_1 y + x^{\frac{1}{2}}y - y^{\frac{1}{2}}z \\ \varepsilon z \left( y^{\frac{1}{2}} - \delta_2 \right) \end{pmatrix}. \quad (6)$$

Parameters used are

$$\xi = 0.866, \quad \varepsilon = 1.428, \quad \delta_1 = 0.577, \quad \delta_2 = 0.376.$$

This model exhibits a chaotic attractor in the snail shell shape presented in Fig. 4. The use of the algorithm developed by Wolf et al. [8] made it possible to compute what can be regarded as its Lyapunov exponents: (+0.035, 0.000, -0.628).

Then, the Kaplan–Yorke [5] conjecture provided the following Lyapunov dimension: 2.06. So, the fractal dimension of this chaotic attractor is close to that of a surface and it is thus possible to consider a deployment of a singular manifold. Taking some points on the slow manifold for which the tangential component of the instantaneous acceleration vector vanishes, and joining these points, a “line” or more generally, a “curve” is formed. Then, using numerical integration, this “curve” (respectively, “line”) is deployed through the phase space and its deployment reconstitutes to the attractor shape. The result is plotted in Fig. 4.

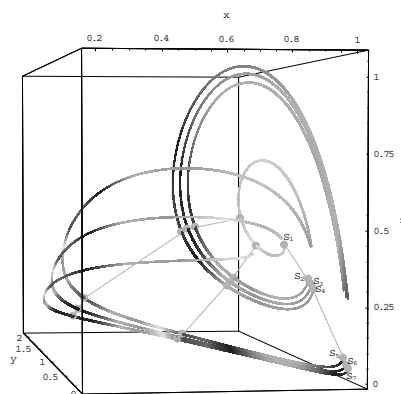


**Fig. 4.** Deployment of the singular manifolds  $(S_1, S_2)$  joining the singular points J and K of the system (6)

## Conclusions and Discussions

The use of *Mechanics* and *Differential Geometry* formalism provided on one hand, a kinematics interpretation of the nature of the motion of chaotic trajectories, and on the other hand, a direct determination of the slow manifold equation associated to (S-FADS) or to (CAS-FADS). It is obvious that on the slow manifold, provided by the osculating plane method, the “trajectory curve” is decelerating.

Moreover, the introduction of the singular manifold which can reconstitute the attractor by successive integrations of points taken on this submanifold, i.e., by re-deployment, provides a qualitative description of its structure.

The *Mechanics* formalism and more precisely the radius of curvature and the torsion could be useful to go further in the geometrical description and thus in the understanding of the attractor structure.

## References

- [1] L.O. Chua, M. Komuro & T. Matsumoto, “The Double Scroll Family,” *IEEE Trans. Circuits Syst.*, 33, vol. 11, 1072–1097, 1986
- [2] F. Frenet, “Sur les courbes à double courbure.” Ph-D, Abstract in *J. de Math.* 17, 1852
- [3] J.M. Ginoux, B. Rossetto & J.L. Jamet, “Chaos in a Three-dimensional Volterra–Gause Model of Predator–prey type,” *Int. J. Bifurcations and Chaos*, 5, vol. 15, 1689–1708, 2005
- [4] J.M. Ginoux & B. Rossetto, “Dynamical Systems Stability and Attractor Structure using Acceleration,” *Int. J. Bifurcat. Chaos*, (in press), 2005
- [5] J. Kaplan & J.A. Yorke, “Chaotic behavior of multidimensional difference equations, in functional differential equations and approximation of fixed points,” *Lect. Notes Mathe.*, 730, 204–227, 1979
- [6] S. Ramdani, B. Rossetto, L.O. Chua & R. Lozi, “Slow Manifold of Some Chaotic Systems—Laser Systems Applications,” *Int. J. Bifurcat. Chaos*, 10, vol. 12, 2729–2744, 2000
- [7] D.J. Struik, *Lectures on Classical Differential Geometry*, Addison-Wesley, Reading (1961), reed. Dover, 1988
- [8] A. Wolf, J.B. Swift, H.L. Swinney & J.A. Vastano, “Determining Lyapunov Exponents from a Time Series,” *Physica D*, vol. 16, 285–317, 1985

# **$r$ -Neighbourhood Impact on the Behaviour of 2D Cellular Automata Model of Complex Interactions**

A. Porebska

Department of Electrical Engineering, AGH University of Science and Technology,  
al. Mickiewicza 30, 30-059 Krakow, Poland, porebska@uci.agh.edu.pl

## **Abstract**

This paper presents results of the research of the complex interactions' model, which is based on the  $r$ -neighbourhood 2D cellular automaton. The automaton rule was formulated due to the social impact theory, proposed by Latane and Nowak. We tested how the size of neighbourhood influenced the behaviour of the automaton and for which minimum  $r$  value, the process of system interactions is reflected in the proper way.

## **The $r$ -Neighbourhood 2D Cellular Automaton**

The 2D cellular automata (CA) is the net of cells. The interactions are described on elements, which belong to the  $r$ -neighbourhood, that is these elements positioned in the distance, which not exceed  $r$  from the  $ij$ th cell (Fig. 1).

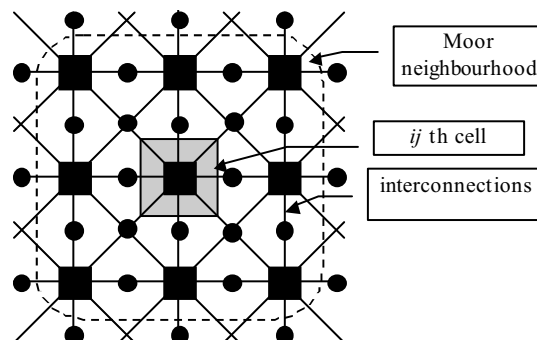


**Fig. 1.** 9-Element Moore neighbourhood of the  $ij$  th cell for  $r=1$ , marked by the dotted line contour.

We consider two types of neighbourhoods: Von Neumann – it includes cells positioned in south, north, west and east direction from the  $ij$  th cell, Moore – it includes cells positioned in south, north, west, east, south-east, south-west, north-east and north-west direction from the  $ij$  th cell.

Elementary cells can take only two values  $\sigma_{i,j}(t) \in \{-1, 1\}$  and their next state depends on the states of neighbouring cells, according to the rule. The rule, which reflects the complex interactions among elements of a whole system due to the social impact theory (formulated by Latane [1]) was proposed by Nowak [2]. If we assume that in the  $r$ -neighbourhood the impact of each  $kl$  th cell is directly proportional to the so called strength parameter  $f_{kl}$  and inversely proportional to the square of distance  $d_{ijkl}$  from the  $ij$  th cell, the rule function is [3]

$$\sigma_{ij}(t+1) = \text{sign} \left( \sum_{\substack{k=i-r, \dots, i+r \\ l=j-r, \dots, j+r \\ kl \neq ij}} \frac{f_{kl}}{d_{ijkl}^2} \sigma_{kl}(t) + \beta f_{ij} \sigma_{ij}(t) \right), \quad (1)$$

where the distance is

$$d_{ijkl} = \max(|i-k|, |j-l|). \quad (2)$$

The value of the distance variable is between 1 and the neighbourhood radius  $r$ .

## Impact of the Radius of the Neighbourhood on the Automata Behaviour

We assumed the same value of strength parameters  $f$  and  $\beta$  in order to simplify the model of interactions and test only the impact of the increase of the  $r$  value on the final state of the automaton. Thus, nearest neighbours take the main role in the creation of the next state. But their impact can be minimised by more distant cells if only their number is big enough. From this point of view the  $r$  radius should be bigger to reflect the impact of a large set of cells. On the other hand, in real systems, individuals change their preferences by the contact with rather small group of other elements, which are placed not far from the individual in the system space. Because of that radius  $r$  can be decreased.

For the  $r \geq 1$ , we made a series of experiments to observe how the different  $r$  values influence the final state of the automaton. In each case, the cells taking the minority state do not touch borders of the net, in order not to disturb the process of the final state creation by the boundary conditions.

The program for the CA simulation was written in Turbo Pascal and run on AMD Duron personal computer.

### The input sets

We tested six categories of input sets for which cells in "1" state created characteristics patterns: IN1 – a single convex figure, IN2 – a few convex figures of different size, IN3 – a concave figure, IN4 – the figure containing irregular opposite state regions inside, IN5 – separate points and groups of maximum 4 points, IN6 – the crossing segments.

**The stabilisation of the automaton for various  $r$  value**

The radius of the neighbourhood was changed from 1 to the maximum dimension of the biggest input figure (21). We tested how many steps  $K$  were necessary to receive the final state and what kind of stabilisation would be observed (majority states only or various states). This same experiment was made for both Von Neumann and Moore types of neighbourhood. The results are shown in Figs. 2 and 3. The rule function (1) is the weighted majority function. In the case of  $r = 1$  it is not possible that the separate minority states survive. The same occurs for other value of  $r$ . Bigger islands (more then four cells) of minority states remain stable for Von Neumann type of neighbourhood for every  $r$ .

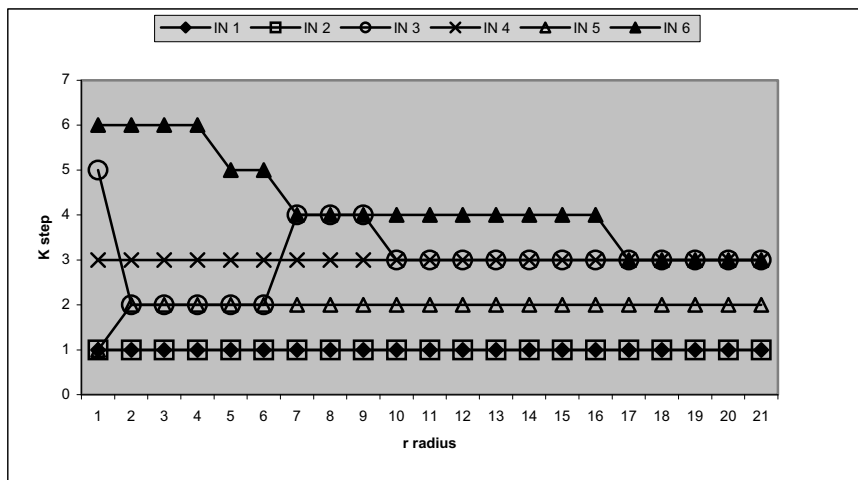


**Fig. 2.** The relation between the radius  $r$  and the step  $K$  for Von Neumann type neighbourhood

In Fig. 2 we can see that for majority of inputs, the number of steps  $K$  is the same for different  $r$ . The input patterns were not change. Only for IN5 and IN6 we observed removing the input pattern, faster for bigger  $r$  in the second case.

For the Moore type of neighbourhood the graphs have the peak points (see Fig. 3). Starting with the  $r$  value of the peak point the automaton stabilises in one majority state only. Below this value some of the minority states survive.

For the convex input figures, the  $r$  in the peak is bigger then for concave ones. After the peak,  $K$  does not change together with increasing  $r$  in some intervals.

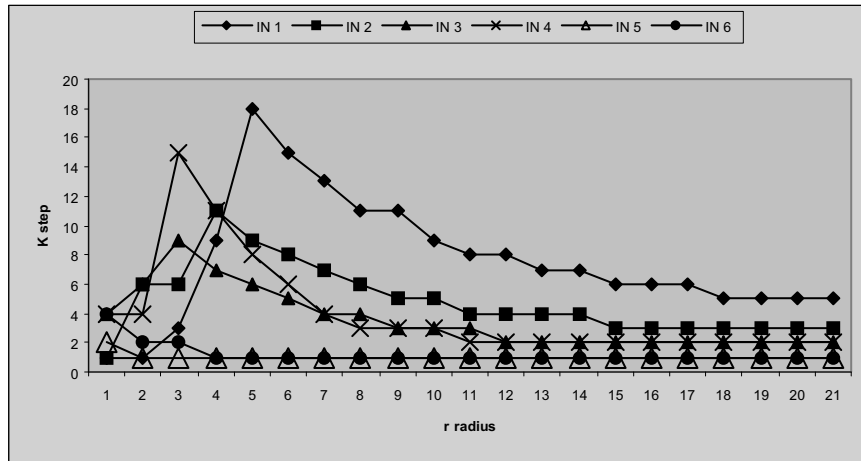


Fig. 3. The relation between the radius  $r$  and the step  $K$  for Moore type of neighbourhood

## Conclusions

Together with the extension of the Moore type neighbourhood above some level we lose the information about the local behaviour of the CA cells. As the result, only the global process of minority states' death can be observed. In the case of the Von Neumann type neighbourhood, the behaviour of the automaton is the same for various radiuses. Thus, the increase of  $r$  does not result in more precise model of the system. Moreover, more time for the automaton processing is demanded.

## Acknowledgements

This work has been supported by the research grant of the AGH University of Science and Technology, Krakow, Poland.

## References

- [1] B. Latane, "The psychology of social impact", *American Psychology*, 36, 343, 1981
- [2] A. Nowak, J. Szamrej, B. Latane, "From private attitude to public opinion: A dynamic theory of social impact", *Psychological Review*, vol. 97 No 3, pp. 362–376, 1990
- [3] A. Porebska, "The Model of Complex Interactions in 2D Cellular Automata", *Proceedings of ECCTD '03*, Cracow, Poland, pp. 109–112, 2003

# Stability of CNN with Trapezoidal Activation Function

E. Bilgili<sup>1</sup>, I.C. Gökner<sup>2</sup>, O.N. Uçan<sup>3</sup> and M. Albora<sup>4</sup>

<sup>1</sup> TUBITAK-MAM, Gebze, Kocaeli, erdem.bilgili@mam.gov.tr

<sup>2</sup> Department of Electronics and Communication Engineering Doğuş University, Acıbadem, 81010, Istanbul, cgoknar@dogus.edu.tr

<sup>3</sup> Department of Electrical and Electronic Engineering İstanbul University, Avcılar, İstanbul, uosman@istanbul.edu.tr

<sup>4</sup> Department of Jeophysics Engineering İstanbul University, Avcılar, İstanbul, muhittin@istanbul.edu.tr

## Abstract

This paper presents the stability conditions of cellular neural network (CNN) scheme employing a new nonlinear activation function, called trapezoidal activation function (TAF). The new CNN structure can classify linearly nonseparable data points and realize Boolean operations (including XOR) by using only a single-layer CNN. In order to simplify the stability analysis, a feedback matrix  $W$  is defined as a function of the feedback template  $A$  and 2D equations are converted to 1D equations. The stability conditions of CNN with TAF are investigated and a sufficient condition for the existence of a unique equilibrium and global asymptotic stability is derived.

## Introduction

Cellular neural networks (CNNs) are widely used in image processing and pattern recognition fields [1–5]. CNN is a large-scale nonlinear processing array consisting of, unlike most other neural networks, only locally interconnected cells; this facilitates its analysis, design and implementation with VLSI circuits. In image processing applications, each cell in CNN represents a pixel in the image. Stability issues of CNN are investigated in many papers. Some of these are: (1) that CNN is stable if the templates are symmetrical is proven in [4,5], (2) the focus is on the dynamic behavior of two-cell CNN in [6], (3) stability conditions of generalized cellular neural networks are given in [7], (4) in [4–7], CNN stability is analyzed for the standard activation function as in [4,5], and (5) global exponential stability conditions of CNN via a new Lyapunov function are stated in [8]. It is well-known



that the standard uncoupled CNN single-layer structures, extremely useful for realizing Boolean functions, are not capable of classifying linearly nonseparable data. Uncoupled CNN can only classify linearly separable data, that is can only separate the input space with hyper-planes [9]. Recently, a single perceptron-like cell with: (1) double threshold, (2) implemented using only five MOS transistors, (3) capable of classifying data, which are not linearly separable has been reported in [10].

In this paper, the definition of standard CNN with PWL (CNNwPWL) is briefly reviewed, then the proposed trapezoidal activation function (TAF) and CNN with TAF (CNNwTAF), which is a generalization of CNN with double threshold, are introduced. Then, stability analysis of CNNwTAF is achieved: *first* by converting the 2-D template description of the CNNwTAF into a system of vector ordinary differential equations (VODE), and *finally* by applying the Lyapunov stability criterion to extract a sufficient condition for global asymptotic stability.

## CNN with Sigmoid PWL Activation Function

CNN as defined by Chua and Yang is described by a set of differential equations:

$$\frac{dX}{dt} = -X + A * Y + B * U + I \quad (1)$$

with the operation  $*$  in conventional form meaning

$$\frac{dx_{ij}(t)}{dt} = -x_{ij}(t) + \sum_{k=1}^{2r+1} \sum_{l=1}^{2r+1} A_{kl} y_{i+k-r-1, j+l-r-1}(t) + \sum_{k=1}^{2r+1} \sum_{l=1}^{2r+1} B_{kl} u_{i+k-r-1, j+l-r-1}(t) + I$$

for  $i=1, 2, \dots, m, j=1, 2, \dots, n,$  (2)

where  $m$  and  $n$  represent the number of rows and columns of the cellular neural network and  $u_{ij}, x_{ij}, y_{ij}$  denote the input state and output of the cell  $C(i, j)$ , respectively. The templates  $A, B$  composed of the weights  $A_{ij}$  and  $B_{ij}$  denote the feedback and feed-forward templates, respectively. The term  $I$ , called the offset (bias), is a constant for each cell. For a CNN with  $r$ -neighborhood, it is clear that  $A$  and  $B$  have size  $(2r+1) \times (2r+1)$ .

In standard CNN literature, the relation between the output and the state of the cell is defined by a sigmoid activation function [4,5], its standard Piecewise-Linear (PWL) version, which is defined by (3), is illustrated in Fig. 1a.

$$y_{ij}(t) = \frac{1}{2} \left( \left| x_{ij}(t) + 1 \right| - \left| x_{ij}(t) - 1 \right| \right). \quad (3)$$

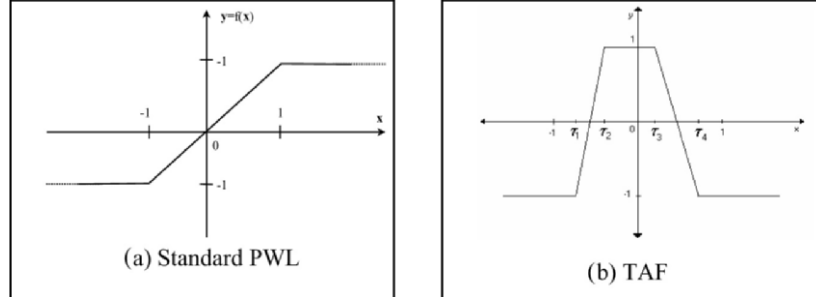


**Fig. 1.** Activation functions; (a) Standard PWL activation function, (b) Trapezoidal activation function (TAF)

### CNN with Trapezoidal Activation Function (TAF)

Recently an activation function with double threshold has been introduced and implemented with five MOS transistors in [10]; the finite slope version of this activation function, which will be used in this paper, is shown in Fig. 1b, and its representation in (4). Note that the standard PWL activation function shown in Fig. 1a is recovered and if the slopes  $m_1$ ,  $m_2$  tend to infinity the double threshold activation function in [10] is obtained

$$y = f(x) = \begin{cases} -1, & x < \tau_1, \\ m_1 x - n_1, & \tau_1 \leq x \leq \tau_2, \\ 1, & \tau_2 \leq x \leq \tau_3, \\ m_2 x - n_2, & \tau_3 \leq x \leq \tau_4, \\ -1, & x > \tau_4, \end{cases} \quad (4)$$

such that  $-1 \leq \tau_1 < \tau_2 < \tau_3 < \tau_4 \leq 1$ ,  $m_1 = \frac{2}{\tau_2 - \tau_1}$ ,  $n_1 = \frac{\tau_1 + \tau_2}{\tau_2 - \tau_1}$ , and  $m_2 = \frac{2}{\tau_3 - \tau_4}$ ,

$$n_2 = \frac{\tau_3 + \tau_4}{\tau_3 - \tau_4}.$$

### Stability of CNN with TAF

In the case of arbitrary  $r$ -neighborhood,  $1 \leq r \leq \min\{m, n\}$ , where  $m, n$  represent number of rows and columns of the cellular neural network, (2) can be rewritten as

$$\frac{dx_{ij}(t)}{dt} = -x_{ij}(t) + \sum_{k=1}^{2r+1} \sum_{l=1}^{2r+1} A_{kl} f(x_{i+k-r-1, j+l-r-1}(t)) + s_{ij}, \quad (5a)$$

where

$$s_{ij} = \sum_{k=1}^{2r+1} \sum_{l=1}^{2r+1} B_{kl} u_{i+k-r-1, j+l-r-1}(t) + I_{ij}. \quad (5b)$$

The term  $s_{ij}$  is a different constant value for each cell, as the inputs  $u_{ij}$  are constant, similarly the terms  $B_{kl}$  and  $I_{ij} = I$  are constant. The activation function  $f$  used in (5) is the trapezoidal activation function defined by (4). As there are  $m \times n$  cells in a CNN, there are  $m \times n$  states in total. For the purpose of describing the behaviour of the CNN by a system of vector ordinary differential equations (VODE) as in [9,12], a map, which transforms the description of the cells in a 2-D space into a 1-D space is given with

$$\begin{bmatrix} C_{11} & C_{12} & \dots & C_{1n} \\ C_{21} & C_{22} & \dots & C_{2n} \\ \vdots & \vdots & C_{ij} & \vdots \\ C_{m1} & C_{m2} & \dots & C_{mn} \end{bmatrix} \longrightarrow [C_{11} \ C_{12} \ \dots \ C_{1n} \ \dots \ C_{ij} \ \dots \ C_{m1} \ C_{m2} \ \dots \ C_{mn}]' = C. \quad (6a)$$

The elements of the vector  $C$  can be represented as  $C_p$  where  $p = j + (i - 1)n$ . The inverse relation is given by following expression:

$$i(p) = \left\lfloor \frac{p}{n} \right\rfloor, \quad j(p) = p \bmod(n) \quad (6b)$$

where  $\lfloor \bullet \rfloor$  means that  $i(p)$  is the quotient of the division  $p/n$ .

In the sequel (5) will be rewritten in the following form using (6):

$$\frac{d}{dt} x_p(t) = -x_p(t) + \sum_{q=1}^{mn} w_{pq} f(x_q(t)) + s_p, \quad p = 1, 2, \dots, mn \quad (7)$$

Comparing (5) and (7), a relation between coefficients  $w_{pq}$  and the elements  $A_{kl}$  of the template matrix will be established. An extremely sparse matrix  $W$  as in (8a) can be constructed:

$$W_{pq} = \begin{cases} A_{i(q)-i(p)+r+1, j(q)-j(p)+r+1}, & 1 < i(q) - i(p) + r + 1 < 2r + 1 \\ & 1 < j(q) - j(p) + r + 1 < 2r + 1 \\ 0, & \text{else} \end{cases} \quad (8a)$$

Note that  $W$  has the symmetry property described in (8b)

$$W_{pq} = W_{mn+1-q, mn+1-p}. \quad (8b)$$

Equation (9) is obtained, considering expressions (7) and (8) then defining  $x_{ij}(t) = x_p(t)$  and  $s_{ij} = s_p$  for  $p = j + (i - 1)n$

$$-x_{ij}(t) + \sum_{k=1}^{2r+1} \sum_{l=1}^{2r+1} A_{kl} f(x_{i+k-r-1, j+l-r-1}(t)) = -x_p(t) + \sum_{q=1}^{mn} w_{pq} f(x_q(t)). \quad (9)$$

Finally (7) can be rewritten in the more compact form as

$$\frac{d}{dt} X = -X + W \cdot f(X) + S \quad (10)$$

with  $X = [x_1(t), x_2(t), \dots, x_p(t)]'$ ,  $S = [s_1, s_2, \dots, s_p]'$ ,  $p = mn$  and  $W$  is a weight matrix with the dimension  $(mn \times mn)$ .

At an equilibrium state, the following condition holds for each cell  $\frac{d}{dt} x_p(t) = \dot{x}_p(t) = \dot{x}_{pe} = 0$ , which used in (7) gives:

$$x_{pe}(t) = \sum_{q=1}^{mn} w_{pq} f(x_{qe}(t)) + s_p \quad \text{for } p = 1, 2, \dots, mn. \quad (11)$$

Therefore in order to find the equilibrium states one has to investigate the solutions of the algebraic equation (12) for a given set of constant inputs

$$X = W \cdot f(X) + S, \quad \text{where } X = [x_1, x_2, \dots, x_i]', \quad i = mn. \quad (12)$$

If we define a function  $G$ , such that

$$G(X) = W \cdot f(X) + S. \quad (13)$$

Substituting (13) for the right-hand side of (12), (14) is obtained

$$X = G(X), \quad (14)$$

which means that the equilibrium state  $X_e$  is a fixed point of the function  $G: \mathfrak{R}^{mn} \rightarrow \mathfrak{R}^{mn}$ . Since  $G$  is continuous and bounded, according to Brouwer fixed-point theorem [11], there is at least one fixed point of (14).

## Lyapunov Stability

It is clear that there is at least one equilibrium point of (7) according to Brouwer fixed point theorem. Now, Lyapunov stability criterion will be applied to check the stability of this point. If  $X_e = [x_{1e}, x_{2e}, \dots, x_{ie}]'$ ,  $i = mn$ , is an equilibrium point, then the deviation  $e_i$  for a single cell at a given time  $t$  is

$$e_i(t) = x_i(t) - x_{ie}, \quad i = 1, 2, \dots, mn, \quad (15)$$

where,  $x_i(t)$  is the state of the cell  $i$  and  $x_{ie}$  is the equilibrium point of the same cell. Rate of change in the deviation of each cell will then be

$$\dot{e}_i(t) = \dot{x}_i(t). \quad (16)$$

Substitution of the right-hand side of (7) for  $\dot{x}_i(t)$  yields

$$\dot{e}_i(t) = \dot{x}_i(t) = -x_i(t) + \sum_{q=1}^{mn} w_{iq} f(x_q(t)) + s_i. \tag{17}$$

By rearranging (17)

$$x_i(t) = e_i(t) + x_{ie} \tag{18}$$

then comparing (11), (17), (18):

$$\dot{e}_i(t) = -e_i(t) + \sum_{q=1}^{mn} w_{iq} [f(e_q(t) + x_{qe}) - f(x_{qe})] \tag{19}$$

is obtained.

An equilibrium point of (19) is  $e_e = [0, 0, \dots, 0]'$  to prove the global asymptotic stability of CNNs described by (7), it is sufficient to prove the global asymptotic stability of the trivial solution of (19) as TAF  $f(\bullet)$  satisfies the Lipschitz condition [8,11].

Let the positive function defined by (20) be selected as a Lyapunov function candidate

$$P(x) = \frac{1}{2} \sum_{i=1}^{m \cdot n} c_i (x_i - x_{ie})^2, \quad c_i > 0 \quad \text{for } i=1, 2, \dots, mn. \tag{20}$$

Differentiation of this function with respect to  $t$  along trajectories yields

$$\frac{dP}{dt} = \sum_{i=1}^{mn} c_i \cdot e_i(t) \left\{ -e_i(t) + \sum_{q=1}^{mn} w_{iq} [f(e_q(t) + x_{qe}) - f(x_{qe})] \right\}. \tag{21}$$

The trapezoidal activation function given in (4) satisfies the Lipschitz condition

$$|f(x) - f(y)| \leq \mu |x - y|, \quad \mu > 0 \tag{22}$$

with

$$\mu \geq \max \{m_1, -m_2\} = \max \left\{ \frac{2}{\tau_2 - \tau_1}, \frac{2}{\tau_4 - \tau_3} \right\}. \tag{23}$$

Rearranging (21) by using inequality (22) the following inequalities can be written as:

$$\frac{dP}{dt} \leq \sum_{i=1}^{mn} \left[ -c_i e_i^2(t) + c_i \sum_{q=1}^{mn} |w_{iq}| |e_i(t)| \mu |e_q(t)| \right], \tag{24}$$

$$\frac{dP}{dt} \leq \sum_{i=1}^{mn} \left[ -c_i e_i^2(t) + \frac{1}{2} \sum_{q=1}^{mn} |w_{iq}| \left( e_i^2(t) + (c_i \mu e_q(t))^2 \right) \right], \tag{25}$$

$$\frac{dP}{dt} \leq \sum_{i=1}^{mn} \left[ -c_i e_i^2(t) + \frac{1}{2} \sum_{q=1}^{mn} |w_{iq}| e_i^2(t) + \frac{1}{2} \sum_{q=1}^{mn} |w_{iq}| (c_i \mu e_q(t))^2 \right], \tag{26}$$

$$\frac{dP}{dt} \leq -\sum_{i=1}^{mn} \left[ c_i - \frac{1}{2} \sum_{q=1}^{mn} |w_{iq}| - \frac{1}{2} \sum_{q=1}^{mn} |w_{qi}| c_q \mu^2 \right] e_i^2(t). \tag{27}$$

Then it is sufficient that the following inequality be satisfied to ensure stability:

$$\left[ c_i - \frac{1}{2} \sum_{q=1}^{mn} |w_{iq}| - \frac{1}{2} \sum_{q=1}^{mn} |w_{qi}| c_q \mu^2 \right] > 0. \tag{28}$$

From (11a) (11b) one can see that the matrix  $W$  has the property

$$\sum_{q=1}^{m \ n} w_{iq} = \sum_{q=1}^{m \ n} w_{qi} \leq \sum_{k=1}^{2r+1} \sum_{l=1}^{2r+1} A_{kl}. \quad (29)$$

Rearranging inequality (28) as

$$c_i - \frac{1}{2} \sum_{q=1}^{m \ n} |w_{iq}| - \frac{1}{2} \mu^2 \sum_{q=1}^{m \ n} c_q^2 |w_{qi}| > 0, \quad (30)$$

then selecting all the constants  $c_i$  to have the same value  $c$  and considering the relation between the template  $A$  and the matrix  $W$  in (29)  $c_i = c$ ,  $c > 0$ ,  $i = 1, 2, \dots, mn$

$$c - \left( \frac{1 + c^2 \mu^2}{2} \right) \sum_{q=1}^{m \ n} |w_{iq}| > 0, \quad (31)$$

$$\sum_{q=1}^{m \ n} |w_{iq}| < \frac{2c}{c^2 \mu^2 + 1}, \quad (32)$$

and finally the inequality

$$\sum_{k=1}^{2r+1} \sum_{l=1}^{2r+1} |A_{kl}| < \frac{2}{c^2 \mu^2 + 1} c \quad (33)$$

is reached which, represents a sufficient condition for the stability of the system. It shows how the stability of CNNwTAF depends on the elements of the template  $A$  and the maximum absolute slope of the activation function. In order to extend the stability range, the best value of the parameter  $c$  used in Lyapunov function can be investigated. If the right-hand side of inequality (43) is set as large as possible, the elements of the template  $A$  will take their values in a wider range. Therefore,  $c$  has been set to  $1/\mu$  which value makes the right-hand side of inequality maximum. If inequality (43) is rearranged using  $c = 1/\mu$

$$\sum_{k=1}^{2r+1} \sum_{l=1}^{2r+1} |A_{kl}| < \frac{1}{\mu} \quad (34)$$

is obtained as a sufficient stability condition. To summarize it has been shown that:

**Theorem:** For fixed constant inputs if the template element values of CNNwTAF described by state equations (1) satisfy inequality (33) then the state trajectory converges asymptotically to a unique equilibrium state; moreover the optimal bound for inequality (33) is obtained as  $c = 1/\mu$ .

Condition (34) re-evaluated for CNNwPWL, yields the stability criterion

$$\sum_{k=1}^{2r+1} \sum_{l=1}^{2r+1} |A_{kl}| < 1, \quad (35)$$

since there is only one slope  $\mu$  equal to 1 in PWL activation function, as shown in Fig. 1a.

## Conclusion

In this paper, CNN with a new kind of nonlinearity, namely trapezoidal activation function (CNNwTAF) has been introduced; CNNwTAF is a generalization of the single perceptron-like cell with double threshold which was presented in [10]. Sufficient stability criterion has been obtained for CNNwTAF by transforming the 2-D state equations of CNNwTAF into regular 1-D state equations then using fixed-point and Lyapunov stability theorems; that this stability criterion can also be applied to CNN with PWL activation function has also been shown. Another improvement on the stability criterion is that, stable templates can be designed without possessing the symmetry property. In particular, stable non-symmetrical templates will be very useful in texture classification and pattern recognition fields. Another advantage provided by CNNwTAF is the extra design flexibility made possible by the availability of tunable parameters of the activation function which can be adjusted jointly with or disjoint from the template parameters.

## References

- [1] T. Sziranyi, M. Csapodi, "Texture Classification and Segmentation by Cellular Neural Network using Genetic Learning", Research Report, Analogical and Neural Computing Systems Research Lab., Computer and Automation Institute of Hungarian Academy of Sciences (MTA-SZTAKI), Budapest, Hungary, Nov. 1, 1994
- [2] L. Wang, J. Pineda de Gyvez, ES. Sinencio, "Time Multiplexed Color Image Processing Based on a CNN with Cell-State Outputs", *IEEE Trans. VLSI Syst.* 1998; 6(2): 314–322
- [3] CW. Chen, L. Chen, "Cellular Neural Network Architecture for Gibbs Random Field Based Image Segmentation", *J. Electron. Imag.* 1998; 7(1): 45–51
- [4] L.O. Chua, L. Yang, "Cellular Neural Networks: Theory". *IEEE Trans. Circuit Syst.* 1988; 35(10): 1257–1272
- [5] L.O. Chua, L. Yang, "Cellular Neural Networks: Applications", *IEEE Trans. Circuit Syst.* 1988; 35(10): 1273–1288
- [6] P.P. Civalleri, M. Gilli, "On the Dynamic Behavior of Two-Cell Cellular Neural Networks", *Int. J. Circuit Theory Applic.* 1993; 21(5): 451–471
- [7] C. Güzelis, L.O. Chua, "Stability Analysis of Generalized Cellular Neural Networks", *Int. J. Circuit Theory Applic.* 1993; 21(1): 1–33
- [8] D.M. Zhou, L.M. Zhang, "Global Exponential Stability of Cellular Neural Networks", ICONIP 2001, 8. *Proceedings of International Conference on Neural Information Processing*, Shangai, China, November 14–18, 2001
- [9] S. Majorana, L.O. Chua, "A Unified Framework for Multilayer High Order CNN", *International Journal of Circuit Theory and Applications* 1998; 26(6): 567–592
- [10] Y.D. Aksin, S. Aras, I.C. Goknar, "CMOS Realization of User Programmable, Single-Level, Double-Threshold Generalized Perceptron", *Proceedings of Turkish Artificial Intelligence and Neural Networks Conference*, TAINN-2000, Izmir, Turkey, June 2000

- [11] M. Vidyasagar, *Nonlinear System Analysis*; Electrical Engineering Series, Prentice Hall: New Jersey, 1978
- [12] L. Chua, T. Roska, *Cellular Neural Networks and Visual Computing*, Cambridge University Press, Cambridge, 2002



# Applications of CNN with Trapezoidal Activation Function

E. Bilgili<sup>1</sup>, İ.C. Gökner<sup>2</sup> and O.N. Uçan<sup>3</sup>

<sup>1</sup> TUBITAK-MAM, Gebze, Kocaeli, erdem.bilgili@mam.gov.tr

<sup>2</sup> Department of Electronics and Communication Engineering, Doğuş University, Acıbadem, 81010, Istanbul, cgoknar@dogus.edu.tr

<sup>3</sup> Department of Electrical and Electronic Engineering, İstanbul University, Avcılar, İstanbul, uosman@istanbul.edu.tr

## Abstract

This paper presents some applications of cellular neural network (CNN) scheme employing a new nonlinear activation function, called trapezoidal activation function (TAF). The new CNN structure can classify linearly nonseparable data points and realize Boolean operations (including XOR) by using only a single-layer CNN.

## Introduction

Cellular neural networks (CNNs) are widely used in image processing and pattern recognition fields [1–4]. CNN is a large-scale non-linear processing array consisting of, unlike most other neural networks, only locally interconnected cells; this facilitates its analysis, design and implementation with VLSI circuits. In image processing applications, each cell in CNN represents a pixel in the image. It is well-known that the standard uncoupled CNN single-layer structures, extremely useful for realizing Boolean functions, are not capable of classifying linearly non-separable data. The parity is a binary function of the inputs, which returns a high output if the number of inputs set to 1 is odd and a low output if that number is even. Therefore, for  $n$  inputs, the parity problem consists of being able to divide the  $n$ -dimensional input space into disjoint decision regions such that all input patterns in the same region yield the same output and, thus is linearly non-separable. Uncoupled CNN can only classify linearly separable data, that is can only separate the input space with hyper-planes [4]. Recently a single perceptron-like cell with: (1) double threshold, (2) implemented using only five MOS transistors, (3) capable of classifying data which are not linearly separable has been reported in [5,6].

In Sect. 1 of this paper, the definition of standard CNN with PWL (CNNwPWL) is briefly reviewed, then the proposed trapezoidal activation function (TAF) and CNN with TAF (CNNwTAF), which is a generalization of CNN with double threshold, are introduced and sufficient stability criterion of CNNwTAF is given. In Sect. 2, it is shown that a single-layer CNNwTAF can be used for performing non-separable tasks such as eXclusive OR (XOR) and parity problems.

### CNN with Sigmoid PWL Activation Function

CNN as defined by Chua and Yang is described by a set of differential equations:

$$\frac{dX}{dt} = -X + A * Y + B * U + I \quad (1)$$

with the operation \* in conventional form meaning:

$$\frac{dx_{ij}(t)}{dt} = -x_{ij}(t) + \sum_{k=1}^{2r+1} \sum_{l=1}^{2r+1} A_{kl} y_{i+k-r-1, j+l-r-1}(t) + \sum_{k=1}^{2r+1} \sum_{l=1}^{2r+1} B_{kl} u_{i+k-r-1, j+l-r-1}(t) + I$$

for  $i=1, 2, \dots, m, j=1, 2, \dots, n$  (2)

where  $m$  and  $n$  represent the number of rows and columns of the cellular neural network, and  $u_{ij}, x_{ij}, y_{ij}$  denote the input state and output of the cell  $C(i, j)$ , respectively. The templates  $A, B$  composed of the weights  $A_{ij}$  and  $B_{ij}$  denote the feedback and feed-forward templates, respectively. These templates have equal size, which depends on the predefined neighborhood radius of the cellular neural network. The term  $I$ , called the offset (bias), is a constant for each cell.

In standard CNN literature, the relation between the output and the state of the cell is defined by a sigmoid activation function [2,3], its standard Piecewise-Linear (PWL) version, which is defined by (3), is illustrated in Fig. 1a

$$y_{ij}(t) = \frac{1}{2} \left( \left| x_{ij}(t) + 1 \right| - \left| x_{ij}(t) - 1 \right| \right) \quad (3)$$

### CNN with Trapezoidal Activation Function (TAF)

Recently an activation function with double threshold has been introduced and implemented with five MOS transistors in [5,6]; the finite slope version of this ac-

tivation function, which will be used in this paper, is shown in Fig. 1b, and its representation in (4).

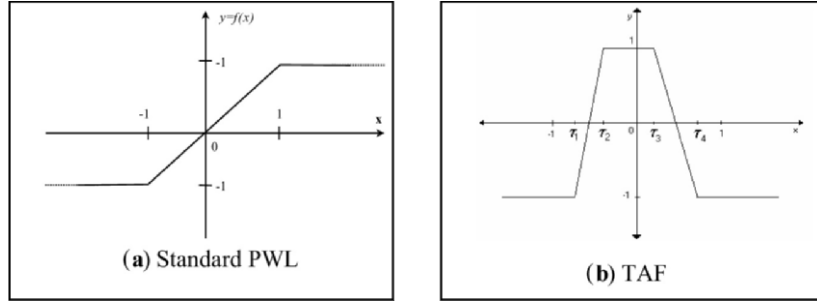


**Fig. 1.** Activation functions: (a) Standard PWL activation function, (b) Trapezoidal activation function (TAF)

$$y = f(x) = \begin{cases} -1, & x < \tau_1, \\ m_1x - n_1, & \tau_1 \leq x \leq \tau_2, \\ 1, & \tau_2 \leq x \leq \tau_3, \\ m_2x - n_2, & \tau_3 \leq x \leq \tau_4, \\ -1, & x > \tau_4, \end{cases} \text{ such that } -1 \leq \tau_1 < \tau_2 < \tau_3 < \tau_4 \leq 1, \quad (4)$$

$$\text{where } m_1 = \frac{2}{\tau_2 - \tau_1}, n_1 = \frac{\tau_1 + \tau_2}{\tau_2 - \tau_1} \text{ and } m_2 = \frac{2}{\tau_3 - \tau_4}, n_2 = \frac{\tau_3 + \tau_4}{\tau_3 - \tau_4}.$$

### **Sufficient Stability Condition of CNNwTAF**

Sufficient stability condition of CNNwTAF is given in [7] as

$$\sum_{k=1}^{2r+1} \sum_{l=1}^{2r+1} |A_{kl}| < \frac{1}{\mu}, \quad (5)$$

where  $r$  is the neighborhood,  $\mu$  the maximum absolute value of the slopes of activation function, and  $A_{kl}$  is the element of the template  $A$ . To summarize it has been shown that:

**Theorem:** For fixed constant inputs if the template element values of CNNwTAF described by state equations (1) satisfy inequality (5) then the state trajectory converges asymptotically to a unique equilibrium state.

Condition (5) re-evaluated for CNNwPWL, yields the stability criterion

$$\sum_{k=1}^{2r+1} \sum_{q=1}^{2r+1} |A_{kl}| < 1, \quad (6)$$

since there is only one slope  $\mu$  equal to 1 in PWL activation function, as shown in Fig. 1.

## Linearly Nonseparable Applications

As mentioned in sect. 1, the single-layer uncoupled standard CNN is very useful for realizing Boolean functions, but is not capable of performing the XOR operation which consists of linearly non-separable data. The XOR-type classification to date has been achieved with multi-layer structures [4,8]. In the sequel, CNNwTAF will be used for performing the XOR operation with a single-layer structure as introduced in [5,6].

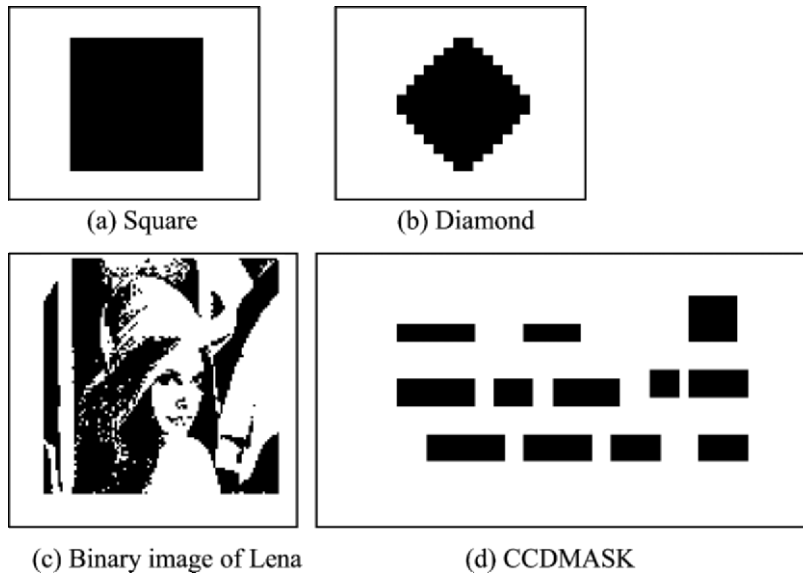


Fig. 2. Original image which used for XOR applications

### Parity 2

This kind of CNN performs the eXclusive OR (XOR) on adjacent pixels of a line. “Given the four possible combination of two adjacent pixels, the output will be white only if these adjacent pixels are not of the same kind, otherwise the output is

black.” This task is linearly non-separable and cannot be realized with a single layer standard uncoupled CNN. The templates and the activation function parameters are

$$A = \begin{bmatrix} 0 & 0 & 0 \\ 0 & 0.125 & 0 \\ 0 & 0 & 0 \end{bmatrix}, \quad B = \begin{bmatrix} 0 & 0 & 0 \\ 0 & 0.25 & 0.1 \\ 0 & 0 & 0 \end{bmatrix}, \quad I = -0.075 \quad (7)$$

$$[\tau_1, \tau_2, \tau_3, \tau_4] = [-0.2, -0.1, 0.0, 0.1]$$

Four input images, which have been used in these applications of the paper, are illustrated in Fig. 2. Using these templates the outputs of CNNwTAF corresponding to these special input images are shown in Fig. 3. Using the transpose of template  $B$ , everything else remaining the same, XOR on adjacent pixels of a vertical line is performed. The outputs for this task are shown in Fig. 4.

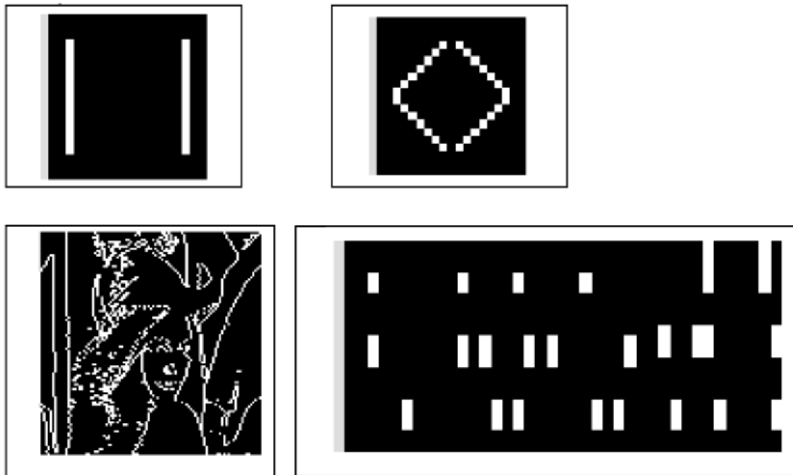


Fig. 3. CNN outputs for horizontal parity 2 applications

### **Parity 2 on three adjacent pixels**

This kind of CNN performs the XOR operation on adjacent three pixels of a line according to “given the three adjacent pixels of a line, the output will be white if the pixel at the center and at least one of the neighboring pixels is not of the same kind; otherwise, if all three pixels are of the same kind, the output is black”. This task is also linearly non-separable; choosing the templates and the activation function parameters as in (8), the outputs to the same test input set are shown in Fig. 5.

$$A = \begin{bmatrix} 0 & 0 & 0 \\ 0 & 0.125 & 0 \\ 0 & 0 & 0 \end{bmatrix}, \quad B = \begin{bmatrix} 0 & 0 & 0 \\ 0.1 & 0.25 & 0.1 \\ 0 & 0 & 0 \end{bmatrix}, \quad I = -0.075, \quad (8)$$

$$[\tau_1, \tau_2, \tau_3, \tau_4] = [-0.3, -0.2, 0.1, 0.2].$$

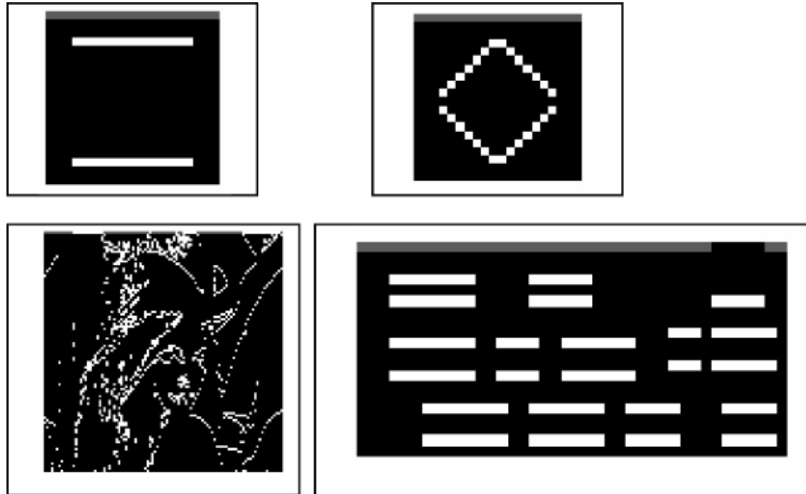


Fig. 4. CNN outputs for vertical-2 applications

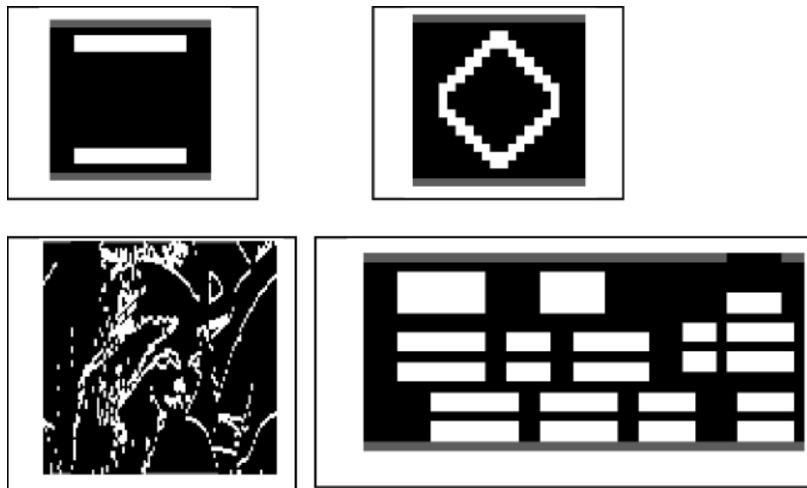


Fig. 5. CNN outputs for parity 2 over 3-pixels in the same vertical line

If the template  $B$  is transposed, one can use this templates and same activation function for performing same function on the vertical lines.

## Conclusion

In this paper, CNN with a new kind of nonlinearity, namely Trapezoidal Activation Function (CNNwTAF) has been introduced. CNNwTAF is a generalization of the single perceptron-like cell with double threshold which was presented in [5,6]. The theoretical sufficient stability results have been tested on various well-known examples. Another improvement on the stability criterion is that, stable templates can be designed without possessing the symmetry property. In particular, stable non-symmetrical templates will be very useful in texture classification and pattern recognition fields. Another advantage provided by CNNwTAF is the extra design flexibility made possible by the availability of tunable parameters of the activation function which can be adjusted jointly with or disjoint from the template parameters. Finally, the advantage of CNNwTAF in providing a single layer CNN capable of performing linearly non-separable tasks such as eXclusive OR and parity problems has been demonstrated with several examples but needs further elaboration and application to real-life problems such as anomaly detection in geophysics, early epileptic seizure warning in medicine.

## References

- [1] L. Wang, J. Pineda de Gyvez, E.S. Sinencio, "Time Multiplexed Color Image Processing Based on a CNN with Cell-State Outputs", *IEEE Transactions of VLSI Systems*, 1998; 6(2): 314–322
- [2] L.O. Chua, L. Yang, "Cellular Neural Networks: Theory", *IEEE Transactions on Circuit and Systems* 1988; 35(10): 1257–1272
- [3] L.O. Chua, L. Yang, "Cellular Neural Networks: Applications", *IEEE Transactions on Circuit and Systems*, 1988; 35(10): 1273–1288
- [4] S. Majorana, L.O. Chua, "A Unified Framework for Multilayer High Order CNN", *International Journal of Circuit Theory and Applications* 1998; 26(6): 567–592
- [5] Y.D. Aksin, S. Aras, I.C. Gökner, "CMOS Realization of User Programmable, Single-Level, Double-Threshold Generalized Perceptron", *Proceedings of Turkish Artificial Intelligence and Neural Networks Conference, TAINN-2000*, Izmir, Turkey, June 2000
- [6] Y.D. Aksin, S. Aras, I.C. Gökner, "Realization and Extensions of User Programmable, Single-Level, Double-Threshold Generalized Perceptron", *Istanbul University Journal of Electrical & Electronics Engineering (IU-JEEE)* 2001; 1(1): 123–129

- [7] E. Bilgili, I.C. Gökner , O.N. Uçan , M. Albora, “Stability of CNN with Trapezoidal Activation Function”, *Complex Computing-Networks: A Link Between Brain-Like And Wave-Oriented Electrodynamical Algorithms – ECE*, İstanbul,Turkey, 13–14 June 2005
- [8] L. Chua, T. Roska , *Cellular Neural Networks and Visual Computing*, Cambridge University Cambridge, 2002



# A CNN-based Fingerprint Verification System

Q. Gao<sup>1</sup> and G.S. Moschytz<sup>2</sup>

<sup>1</sup> Swiss Federal Laboratories for Materials Testing and Research (EMPA),  
Switzerland

<sup>2</sup> Bar Ilan University, Israel

## Abstract

In this paper, a CNN-based fingerprint verification system is realized. It consists of three main processing stages, Image Preprocessing, Feature Extraction, and Feature Matching, as well as a system database.

In the Image-Preprocessing stage, the quality of an original gray-scale noisy fingerprint image is enhanced. As a result, a binary thinned fingerprint is obtained. In the Feature-Extraction stage, distinguishable real features (ridge endings and ridge bifurcations) in the thinned fingerprint as well as their feature attributes are extracted. False features are eliminated based on a distance criterion. In the subsequent Feature-Matching stage, a similarity comparison scheme which is tailor-made for CNNs is presented. For the final decision, a combination of two simple criteria with an adjustable parameter is proposed.

By using a real fingerprint test database, the simulation results show that the system is able to distinguish between two fingerprints which belong to two different people. It can achieve zero False Acceptance Rate for any possible user in the test database, if the adjustable parameter is suitably chosen. Under the requirement of zero False Acceptance Rate, the system can achieve a relatively good False Rejection Rate for almost half of the users in the test database.

## Motivation

Personal identification can be encountered almost everywhere in our society. Recently, with the increasing demand on high security, *positive person identification* has become more and more important in our everyday life. The term positive person identification means identification of a person with high certainty. The traditional identification methods are based on “*something that you possess*” and “*something that you know*” such as key, user-ID, password, PIN, etc. [1]. Another family of identification methods makes use of the physical characteristics of a person, e.g., fingerprints, hands, voice, iris, signature, etc. These characteristics are called *biometrics* [1]. Among all biometrics, the fingerprint is the oldest and the most prevalent one.

Thanks to the increasing power of computers and to the substantial progress in fingerprint capture devices, the use of fingerprint for computer-aided personal

identification in civilian applications, such as banking security and physical access control, is becoming increasingly attractive. In particular, fingerprint based positive personal identification in portable applications is of great significance. For the purpose of commercialization, such a system has to take the following four crucial factors into consideration: *processing speed*, *recognition rate*, *power consumption*, and *size*.

Cellular Neural Networks (CNNs) [2,3], proposed by Chua and Yang in 1988, are able to execute complex nonlinear signal processing operations completely in parallel and simultaneously with low power consumption, because each *cell* itself is a relatively simple analog circuit “processor.” Moreover, each cell is locally interconnected with its neighboring cells within some predefined neighborhood. This *local connectivity* property makes CNNs very suitable for VLSI implementation, resulting in CNN chips which are tailor-made for real-time image and signal processing. Furthermore, thanks to the advanced techniques in fingerprint sensors [4,5] and CNN hardware implementation [6,7], it is very likely in the not-too distant future to incorporate a capacitive fingerprint sensor on a CNN chip. Thus, CNNs have the potential to *realize a fingerprint-based recognition system on one chip*.

Until now, CNNs have shown their superiority among others in image processing, pattern recognition and generation, as well as nonlinear signal processing in general [8,9]. In this paper, we examine the potential of CNNs for fingerprint-based personal verification with the view of realizing the resulting system on one CNN chip.

## CNN-based Fingerprint Verification System

The main problem in fingerprint verification is to decide how similar two fingerprints are, the one to be verified and the one stored in the database.

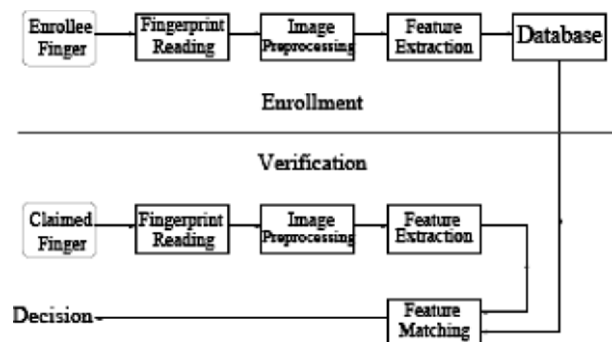


Fig. 1. Block diagram of a CNN-based fingerprint verification system

A CNN-based fingerprint verification system is illustrated in Fig. 1. The system works in two distinct modes: enrollment and verification. The purpose of the enrollment mode is to create a database. During this mode, the fingerprint of an enrollee finger is first captured and then processed in the subsequent two stages: Image Preprocessing and Feature Extraction. Image-Preprocessing is aimed at enhancing the quality of the captured fingerprint image which is very noisy in nature, thus facilitating the subsequent stage, Feature Extraction. After the Feature Extraction stage, a set of representative features of the enrollee fingerprint, *the minutia template*, is stored in the database. During the verification mode, a claimed finger undergoes the same three processing steps as in the enrollment mode. The result, *a test minutia template*, is compared with a minutia template from the database in the Feature Matching stage. A matching score which measures the similarity between the two minutia templates is calculated. Higher values indicate higher confidence in a match. In practice, the matching score is compared with a threshold which is predefined by the user for the final decision, *Yes* or *No*.

## CNN Fingerprint Image Preprocessing

Normally, the images captured in the Fingerprint Reading stage are gray-scale and subject to noise. Their quality is therefore not satisfactory for accurate processing. For this reason, Image Preprocessing is a crucial part of a fingerprint-based verification system. It aims at reducing noise, enhancing the quality of the captured fingerprint image, and facilitating the subsequent processing steps.

### Algorithm overview

The proposed CNN fingerprint image preprocessing algorithm consists of three successive operation units: Fingerprint Sharpening, Fingerprint Ridge Enhancement, and Fingerprint Thinning, see Fig. 2. The detailed description of this algorithm and some examples can be found in [10].

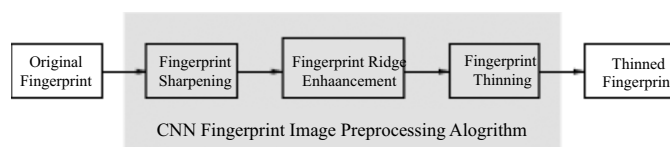


**Fig. 2.** Block diagram of Fingerprint Image Preprocessing

The goal of Fingerprint Sharpening is to increase the contrast of an original fingerprint, and to sharpen ridges and reduce the noise in the original fingerprint. Fingerprint Ridge Enhancement removes white holes within fingerprint ridges, and transforms the gray-scale input image into a black/white output image. Fin-

gerprint Thinning reduces the width of ridges to one pixel. This step will facilitate the extraction of characteristic features in the Feature-Extraction stage.

**Fingerprint sharpening algorithm**

In this stage, two CNN operations – CNN High-boost and CNN Lowpass – are applied to the original gray-scale fingerprint image. Its block diagram is shown in Fig. 3.

An original gray-scale fingerprint first goes through a CNN High-boost operation. A key point distinguishing this operation from a normal CNN High-boost operation is that the bias  $I$  is not constant but an image of the same size as the original fingerprint. Usually, in an original gray-scale fingerprint, some regions are brighter and some are darker, which makes it advantageous to have a spatially variant bias. The algorithm to generate this bias image  $I$  is composed of three operations: Heat Diffusion, Contrast Stretching, and Gray-Scale Inversion. The CNN High-boost is then followed by a CNN Lowpass filter which suppresses the high frequency noise. The resulting image is shown in Fig. 5b.

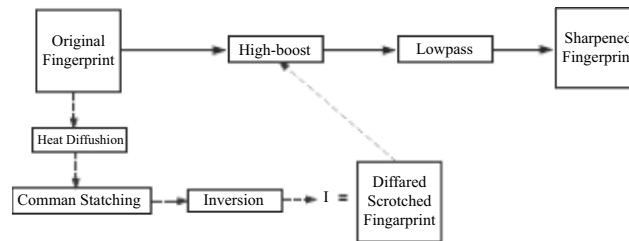


Fig. 3. Block diagram of Fingerprint Sharpening

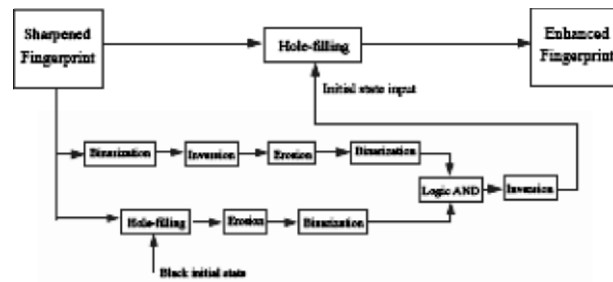


Fig. 4. Block diagram of Fingerprint Ridge Enhancement

### ***Fingerprint ridge enhancement algorithm***

In this stage, a CNN Hole-filling template [11] is used to further improve the quality of the fingerprint obtained in the Fingerprint Sharpening unit. In a normal CNN Hole-filling operation, the input image is binary and the states are initialized as black but with a white boundary. During this operation, all white areas surrounded by black pixels in an image are filled with black pixels. But in fingerprints, we wish to fill up with dark pixels only the bright areas surrounded by dark pixels *within* ridges, thus enhancing ridges, while outside the ridges all bright areas surrounded by dark pixels have to remain bright. To attain this goal, we have to find an appropriate initial-state image for the Hole-filling operation.

Fig. 4 presents the block diagram of the Fingerprint Ridge Enhancement Algorithm. The algorithm used for creating an appropriate initial state is emphasized by a darker mask. It consists of two parallel stages. The goal of the upper stage is to obtain a “binarized” fingerprint directly from the gray-scale sharpened fingerprint, in which ridges are thinner than their corresponding gray-scale counterpart valleys. The lower stage is aimed at marking those valleys in the sharpened fingerprint by *black* which are completely surrounded by ridges. The outputs of the two parallel stages pass together through the Logic AND operation. Finally, this output fingerprint is inverted. *This is the appropriate initial state image we were looking for.*

Now, the sharpened fingerprint goes through the main CNN Hole-filling operation together with the above obtained initial state image. This CNN Hole-filling operation fills up with black pixels only the white holes within ridges, keeps open all valleys completely surrounded by ridges, and at the same time transforms the gray-scale input fingerprint into a black/white fingerprint. The final result is shown in Fig. 5c.

### ***Fingerprint thinning algorithm***

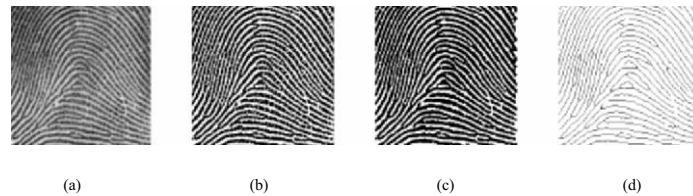
Fingerprint Thinning peels black pixels from ridges until the ridges are only one pixel wide. For this purpose, a CNN Thinning template set [11] has been employed. This set is composed of eight different templates. It peels black pixels on ridges from eight different directions – northwest, north, northeast, east, southeast, south, southwest, and west.

Fig. 5d is the result of the Thinning operation. This thinned fingerprint maintains almost all characteristics of the original fingerprint of Fig. 5a. From this thinned fingerprint, fingerprint features can be more easily extracted, as will be discussed in the forthcoming section, *CNN Fingerprint Feature Extraction*.

## CNN Fingerprint Feature Extraction

The goal of the Feature-Extraction unit is to extract distinguishable features in fingerprints, as well as their attributes, in order to guarantee the subsequent unit: Feature Matching.

One distinguishes two main features in a fingerprint image: ridge endings and ridge bifurcations [1,12]. An ending is a feature where a ridge terminates. A bifurcation is a feature where a ridge splits from a single path to two paths at a Y-junction. Due to noisy original images and artifacts produced in the Image-Preprocessing stage, spurious minutiae will always be present. Thus, after the minutiae are extracted, the spurious minutiae must be eliminated.



**Fig. 5.** Image preprocessing: (a) original fingerprint (b) Sharpened fingerprint (c) Enhanced fingerprint (d) Thinned fingerprint

### Algorithm overview

The proposed CNN Feature-Extraction algorithm consists of four main processing units – *Ending Detection*, *Bifurcation Detection*, *False Feature Elimination*, and *Direction Detection* – in addition to several simple CNN operations, see Fig. 6. The detailed description of this algorithm can be found in [13].

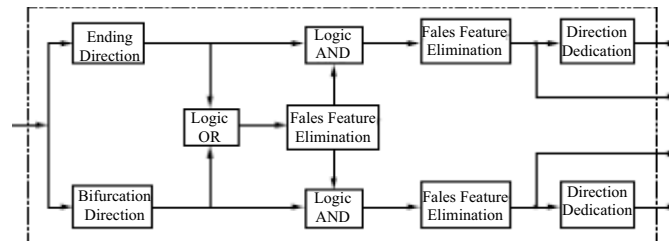


**Fig. 6.** Block diagram of fingerprint feature extraction

First, the endings and bifurcations are extracted in parallel from the thinned fingerprint image in the *Ending-Detection* and *Bifurcation-Detection* units. The resulting two images are added together in the *Logic OR* operation [11], and the output fed to the *False Feature-Elimination* unit. Here, false feature sets consisting of at least one ending and one bifurcation can be deleted. With the subsequent *Logic AND* [11] we obtain a new ending/bifurcation image. In the following two *False Feature-Elimination* operations, the remaining false endings and false bifur-

cations are eliminated separately. The resulting endings and bifurcations are then regarded as real features and result in an *ending feature image* and a *bifurcation feature image*. Finally, the direction of ridges leaving endings and bifurcations is extracted separately in the *Direction-Detection* units.

### Ending-Detection algorithm

In a thinned fingerprint image, a ridge ending has only one black neighbour in its nearest  $3 \times 3$  neighbourhood. Thus, we can find these points by first eliminating all isolated black points, and then finding all black points that have at most one black neighbour, see Fig. 7.

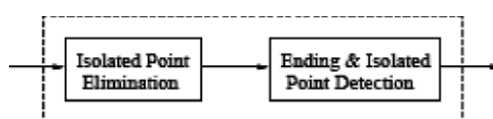


Fig. 7. Block diagram of the Ending-Detection algorithm

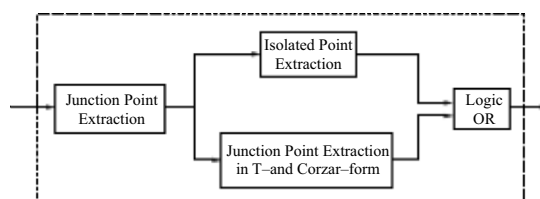


Fig. 8. Block diagram of the Bifurcation-Detection Algorithm

### Bifurcation-Detection algorithm

In a thinned fingerprint image, a bifurcation has exactly three black neighbours in its nearest  $3 \times 3$  neighbourhood. But not all points which have exactly three black neighbours are bifurcations. This is taken into account by our algorithm, as shown in Fig. 8.

In “Junction Point Extraction”, the black pixels which have at least three black neighbours in their nearest neighbourhood are extracted. However, this still leaves T- and Corner-forms from which we have to extract real bifurcations. To this end, two different operations are applied in parallel: Isolated Point Extraction [11] and Junction Point Extraction in T- and Corner-form. The first extracts black pixels which are alone in an input image, the second retains only black pixels which have at least two black neighbours among their north, east, south, and west neighbours. Finally, the resulting two images are added in *Logic OR* [11] to obtain only the bifurcations.

### False Feature-Elimination algorithm

As mentioned earlier, false minutiae – endings and bifurcations – are not always avoidable after *Ending Detection* and *Bifurcation Detection* and must be eliminated.

Experience shows that two false minutiae – two false endings, or two false bifurcations, or one false ending and one false bifurcation – are normally close to each other [12]. Based on this fact, we have developed a CNN False Feature-Elimination algorithm that can eliminate two black points with a distance smaller than or equal to  $n$  pixels. Here distance means the number of white pixels separating two black pixels. Our algorithm is shown in Fig. 9.

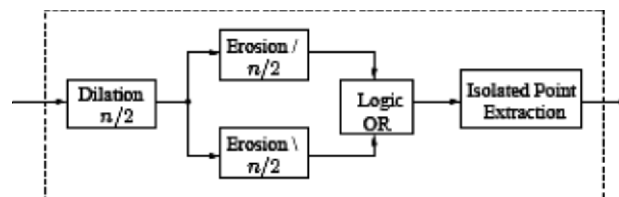


**Fig. 9.** Block diagram of the False Feature-Elimination Algorithm (for distance  $\leq n$ -pixels,  $n$  is even)

Assuming that  $n$  is given, the input first goes through the Dilation operation  $n/2$  times. As a result, two black points whose distance was equal to or smaller than  $n$  will be connected together and form an ensemble. This ensemble then goes through two different Erosion operations in parallel, *Erosion/* and *Erosion/*,  $n/2$  times each. *Erosion/* works as follows: black pixels whose northeast and southwest neighbours are both black remain black, all other pixels become or remain white. A similar principle holds for *Erosion/*. After this, the two resulting images are added together in the Logic OR operation, and finally the Isolated Point Extraction operation is applied.

### Direction-Detection algorithm

In *digital* fingerprint-based verification systems, the direction of ridges leaving endings and bifurcations is represented by a vector parallel to the ridges leaving minutiae. In a planar CNN system, this cannot be done, because the output of the system is an image.

In order to extract the direction of ridges leaving endings and bifurcations, we use the CNN operation *Figure Reconstruction* [11]. With this operation, we can reconstruct one or several figures from an input image by using a suitable initial state.



## CNN Fingerprint Feature Matching

The goal of the Fingerprint Feature-Matching unit is to decide whether the fingerprint to be verified ( $\mathfrak{F}^r$ ) is the same as one ( $\mathfrak{F}^d$ ) in the system database under some conditions. To attain this goal, a similarity function needs to be defined first, then a decision criterion, e.g., a distance threshold. The final decision:  $\mathfrak{F}^r = \mathfrak{F}^d$  is made, when the distance between  $\mathfrak{F}^r$  and  $\mathfrak{F}^d$  is smaller than or equal to the predefined threshold. Otherwise, one decides that  $\mathfrak{F}^r \neq \mathfrak{F}^d$ .

It should be noted that the features extracted in the Fingerprint Feature-Extraction unit are sensitive to translation displacement and rotation. We have integrated *Translation* into our Feature-Matching algorithm and taken *Rotation* into account in the System Database. We store not only the ending and bifurcation feature images of the user's fingerprint, but also their rotated versions in the system database. This spares rotation operations normally needed in a minutia-based feature matching.

### Feature matching overview

The proposed CNN Fingerprint Feature-Matching algorithm consists of two main processing units: *Similarity Comparison* and *Decision Making*, as illustrated in Fig. 10. The detailed description of this algorithm can be found in [14].

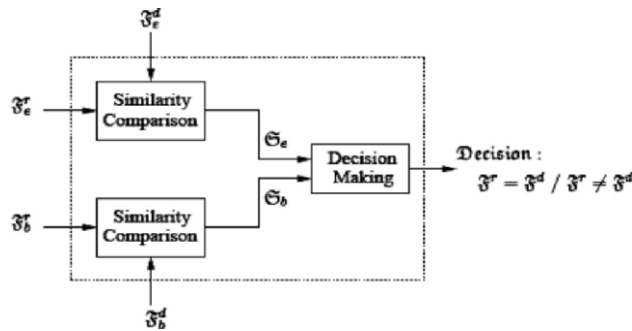


Fig. 10. Block diagram of fingerprint feature matching

In the upper *Similarity Comparison* unit, the ending feature image  $\mathfrak{F}_e^r$  of  $\mathfrak{F}^r$  is compared with the ending feature image  $\mathfrak{F}_e^d$  of  $\mathfrak{F}^d$ . The lower *Similarity Comparison* unit works similarly. As a result, so-called similarity degrees  $\mathfrak{S}_e$  and  $\mathfrak{S}_b$  are determined. Finally, depending on the values of  $\mathfrak{S}_e$  and  $\mathfrak{S}_b$ , a decision is made in *Decision Making* whether  $\mathfrak{F}^r$  is to be considered as identical with or different from  $\mathfrak{F}^d$ .

**Similarity comparison**

The Similarity Comparison unit is aimed at determining the similarity degree of two images. Fig. 11 shows its block diagram for the ending feature images. It looks similar for the bifurcation feature images.

As shown in Fig. 11, the ending feature image  $\mathcal{F}_e^r$  is shifted to predetermined positions  $(k, l)$  in *Translation* and the result is denoted by  $\mathcal{F}_e^r(k, l)$ . Then,  $\mathcal{F}_e^r(k, l)$  is compared with  $\mathcal{F}_e^d$  in *Point Pattern Comparison*. At each position  $(k, l)$ , we obtain a comparison score  $S_e(k, l) \in [0, 1]$  which describes the similarity between  $\mathcal{F}_e^r(k, l)$  and  $\mathcal{F}_e^d$ . The smaller  $S_e(k, l)$ , the more similar  $\mathcal{F}_e^r(k, l)$  and  $\mathcal{F}_e^d$ .

Let  $S_{e_{min}}$  be the minimum of  $S_e(k, l)$  over all considered positions  $(k, l)$ , and denote by  $(k_e, l_e)$  (one of) the position(s) at which the minimum is taken. We then define the similarity degree between  $\mathcal{F}_e^r$  and  $\mathcal{F}_e^d$  as

$$\mathfrak{S}_e = ( S_{e_{min}}, k_e, l_e ).$$

The same is done for the bifurcation feature images and  $k_b, l_b, S_{b_{min}}, \mathfrak{S}_b$  are defined accordingly.  $\mathfrak{S}_e$  and  $\mathfrak{S}_b$  together describe the similarity between  $\mathcal{F}^r$  and  $\mathcal{F}^d$ . Based on  $\mathfrak{S}_e$  and  $\mathfrak{S}_b$ , a decision will be made in *Decision Making* whether  $\mathcal{F}^r = \mathcal{F}^d$  or  $\mathcal{F}^r \neq \mathcal{F}^d$ .

For the detailed description of Point Pattern Comparison and Translation, we refer to [14].

**Decision making**

*Decision Making* is the last stage in the Feature-Matching unit. It is shown in Fig. 12. The decision  $\mathcal{F}^r = \mathcal{F}^d$  is made if  $\mathfrak{S}_e$  and  $\mathfrak{S}_b$  satisfy both criteria, *Position* and *Average*. Otherwise, the decision  $\mathcal{F}^r \neq \mathcal{F}^d$  is taken.

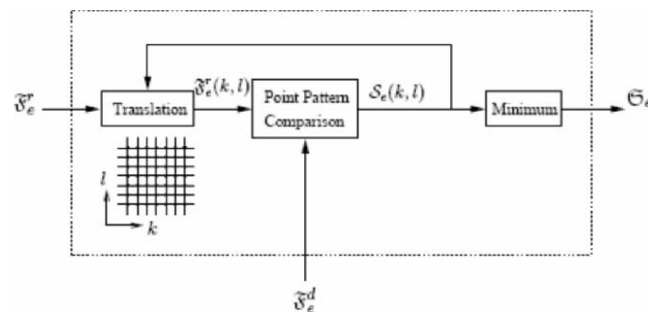


**Fig. 11.** Similarity comparison for ending feature image

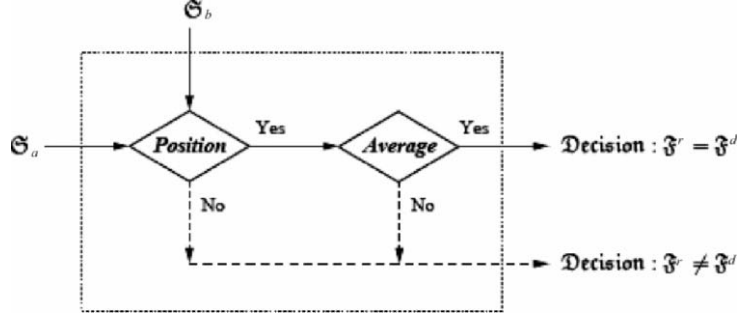


Fig. 12. Decision making

(1) *Position*. The Position criterion is satisfied if the position  $(k_c, l_c)$  is within the  $3 \times 3$  neighborhood of the position  $(k_b, l_b)$  in the Translation Grid. This can be written as

$$\max\left(\frac{|k_c - k_b|}{T_{\text{step}}}, \frac{|l_c - l_b|}{T_{\text{step}}}\right) \in \{0, 1\}, \quad (1)$$

where  $T_{\text{step}}$  is the step size between two adjacent positions, see [14].

Note that in the *Position* criterion, we do not require  $(k_c, l_c) = (k_b, l_b)$  exactly. The reason is that the distortion in fingerprints caused by translation, rotation and some other noise may result in the loss of fingerprint features. All this can impair the reliability of the similarity degree  $S_e$  and  $S_b$  obtained in the *Similarity Comparison* unit. Thus, the proposed  $3 \times 3$  neighborhood in the Translation Grid in the *Position* criterion can increase the tolerance of the Feature-Matching algorithm to all possible distortions inherent in fingerprints.

(2) *Average*. As mentioned earlier, the smaller  $S_{e \min}$  and  $S_{b \min}$ , the more we consider  $S^r$  and  $S^d$  to be identical. Among the many possible criteria, we propose to consider both fingerprints,  $S^r$  and  $S^d$ , to be identical only if

$$\frac{S_{e \min} + S_{b \min}}{2} < \theta_{\text{ms}}, \quad (2)$$

for some  $\theta_{\text{ms}} \in [0, 1]$ .

The parameter  $\theta_{\text{ms}}$  needs to be adjusted depending on applications. A smaller  $\theta_{\text{ms}}$  specifies a tighter *Average* criterion, which may result in a higher possibility with which  $S^r$  will be rejected. In very high security applications, we prefer a very low False Acceptance Rate (FAR) which requires a small  $\theta_{\text{ms}}$ . On the contrary, in forensic applications, we prefer a low False Rejection Rate (FRR) which requires a large  $\theta_{\text{ms}}$ . In practice, for a specific application, these two factors trade off against one other.

The performance of the system was evaluated by two different rates, the False Acceptance Rate and the False Rejection Rate. As the name implies, the FAR describes the ability of the system to differentiate between unequal fingerprints, while the FRR describes the ability of the system to identify fingerprints which belong to the same finger. To this end, a real fingerprint database was used. It contains 168 fingerprints belonging to 21 different people and each person has eight different scans of the same finger.

Simulations were performed as follows: one fingerprint version of person  $i$  is stored in the system database, while the other 20 people are regarded as imposters who try to enter the system without permission. Hence, out of 168 fingerprints, 160 fingerprints, belonging to the other 20 people, are used to determine  $FAR(i)$  and the eight fingerprints of person  $i$  are used to determine  $FRR(i)$ . Moreover, in the decision criteria, we chose  $\Theta_{ms} = 0.5$ .

Fig. 13 illustrates the resulting FAR and FRR. As can be seen from Fig. 13(a), we obtain a zero FAR for any possible user in the test database. This means that no matter which person is stored in the system database, any fingerprint from the other 20 people will be correctly rejected.

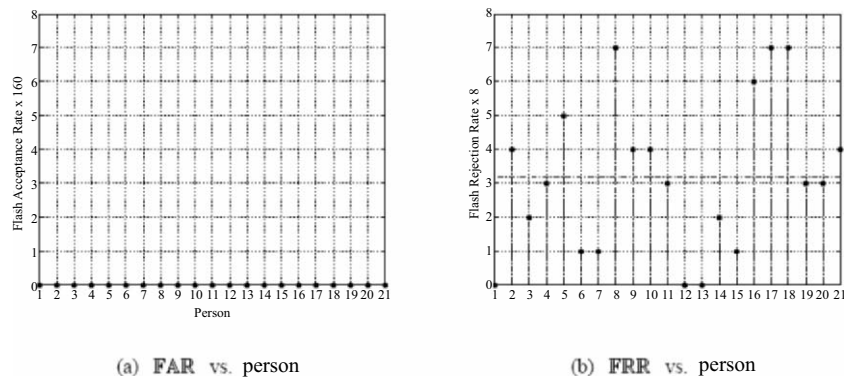


**Fig. 13.** System performance

Figure 13b shows the strong dependency of the FRR on the person stored in the system database. For person 1, 12, and 13, we obtain  $FRR = 0$ . This means that for each of them all 8 fingerprint versions are correctly verified. For person 8, 17, and 18, we obtain the worst possible  $FRR = 7/8$  which means that none of the other seven fingerprint versions of the same person is allowed to access the system, except the fingerprint version stored in the system database itself. Taking an average over all people, we get  $\overline{FRR} = \frac{67}{21} = 0,399$ . This means that for the test data-

base on average a system user will be falsely rejected slightly more than three times every eight attempts. The unsatisfying FRR for some people can be explained by the largely varying quality between different fingerprint versions of the same person.

## Conclusions

A fingerprint verification system has been fully designed and realized by using CNNs. It consists of three processing stages, Image Preprocessing, Feature Extraction, and Feature Matching, as well as of a system database.

The proposed CNN Image-Preprocessing algorithm can improve the contrast of an original gray-scale fingerprint, reduce the high frequency noise in the original fingerprint, recover the destroyed connectivity in the ridges thus enhancing the fingerprint ridges, and finally turn the original fingerprint image into a binary image. The resulting black lines all have unit width while containing essentially all the necessary characteristics of the original fingerprint image.

The proposed CNN Feature-Extraction algorithm is able to extract almost all genuine endings and bifurcations as well as their corresponding direction attributes, and to eliminate the spurious endings and bifurcations which may result from the noisy original fingerprint and the previous processing operations.

The proposed CNN Feature-Matching algorithm is simple and effective. It compares  $\mathcal{S}^r$  and  $\mathcal{S}^d$  by determining the similarity degree between their ending feature images and that between their bifurcation feature images, and reaches a decision by applying the combination of two simple criteria. It is able to tackle translation as well as rotation distortions. It is able to recognize that  $\mathcal{S}^r = \mathcal{S}^d$ , if  $\mathcal{S}^r$  is only a translated and/or rotated version of  $\mathcal{S}^d$ .

## References

- [1] A. Jain, R. Bolle, and S. Pankanti, *Biometrics: Personal Identification in Networked Society*. Kluwer Dordrecht, 1999
- [2] L.O. Chua and L. Yang, "Cellular Neural Networks: Theory," *IEEE Transactions on Circuits and Systems – I*, vol. 35, no. 10, pp. 1257–1272, October 1988
- [3] —, "Cellular Neural Networks: Applications," *IEEE Transactions on Circuits and Systems–I*, vol. 35, no. 10, pp. 1273–1290, October 1988
- [4] S. Jung, R. Thewes, T. Scheiter, K.F. Gosser, and W. Weber, "A Low-Power and High-Performance CMOS Fingerprint Sensing and Encoding Architecture," *IEEE Journal of Solid State Circuits*, vol. 34, no. 7, pp. 978–984, July 1999
- [5] S. Shigematsu, H. Morimura, Y. Tanabe, T. Adachi, and K. Machida, "A Single-Chip Fingerprint Sensor and Identifier," *IEEE Journal of Solid State Circuits*, vol. 34, no. 12, pp. 1852–1859, December 1999
- [6] T. Roska, "Analogic CNN Computing: Architectural, Implementation, and Algorithmic Advances – a Review," in *IEEE International Workshop on Cellular Neural Networks and their Applications*, V. Tavsanoğlu, Ed., London, April 1998, pp. 3–9
- [7] G. Linan, A. Rodriguez-Vazquez, S. Espejo, and R. Domínguez-Castro, "ACE16K: A 128×128 Focal Plane Analog Processor with Digital I/O," in *IEEE International Workshop on Cellular Neural Networks and their Applications*, Frankfurt, July 2002, pp. 132–139

- [8] K.R. Crouse and L.O. Chua, "Methods for Image Processing and Pattern Formation in Cellular Neural Networks: A Tutorial," *IEEE Transactions on Circuits and Systems – I*, vol. 42, no. 10, pp. 583–601, October 1995
- [9] M.H. ter Brugge, J.A.G. Nijhuis, and L. Spaanenburg, "A Practical CNN System for Toll Driving," in *European Conference on Circuit Theory and Design*, vol. 2, Stresa, Italy, August 1999, pp. 1003–1006
- [10] Q. Gao, P. Förster, K.R. Möbus, and G.S. Moschytz, "Fingerprint Recognition Using CNNs: Fingerprint Preprocessing," in *Proceedings of the IEEE International Symposium On Circuits and Systems*, vol. 3, Sydney, Australia, May 2001, pp. 433–436
- [11] T. Roska et al., "CNN Software Library (templates and algorithms), vers. 7.3," Analogical & Neural Computing Laboratory, Computer and Automation Research Institute, Hungarian Academy of Sciences, Technical Report DNS-CADET-15, 1999
- [12] L.C. Jain et al., *Intelligent Biometric Techniques in Fingerprint and Face Recognition*. CRC Press, 1999
- [13] Q. Gao and G.S. Moschytz, "Fingerprint Feature Extraction Using CNNs," in *European Conference on Circuit Theory and Design*, vol. 1, Espoo, Finland, August 2001, pp. 97–100
- [14] —, "Fingerprint Feature Matching Using CNNs," in *Proceedings of the IEEE International Symposium On Circuits and Systems*, vol. 3, Vancouver, Canada, May 2004, pp. 73–76

# Hardware Architectures for the Evolution of Cellular Automata Functionality

M. Glesner, O. Soffke and P. Zipf

Institute of Microelectronic Systems, Department of Electrical Engineering and Information Technology, Darmstadt University of Technology, D-64283 Darmstadt, zipf@mes.tu-darmstadt.de

## Abstract

Cellular automata are basic computational structures of interacting units which are capable of exposing self-organization and emergent behavior. To investigate this behavior we implemented a distributed hardware/software environment covering a genetic algorithm and attached hardware accelerators for a fast specimen evaluation in a hardware-in-the-loop fashion. To keep the accelerator flexible enough to support a fast adaptation of the cell interconnect structure our hardware is realized on FPGA hardware. We describe the software of the genetic algorithm and then concentrate on the architecture optimizations necessary for a flexible, yet reasonably small implementation of the cellular automata hardware. The resulting area/time trade-off is discussed. In addition, an architecture for runtime reconfiguration of the cellular automaton is proposed.

## Introduction

Cellular automata (CA) have a long history going back to von Neumann. They describe basic massively parallel calculations in a decentralized computing system in an idealized way in terms of a lattice of identical cells which communicate in a next-neighbor style. For overviews on CA history, background and applications, see [1,6,7]. CAs are highly regular structures supporting a cell-based design style which becomes necessary with shrinking technology nodes and the advent of nanoelectronic circuits [8,9]. Circuits based on the principles of cellular automata are a promising approach towards meeting optimization criteria like low power consumption, high performance and small circuit size. Such arrangements expose interesting properties, including adaptiveness [10] or the emergence of complex system behavior from the very simple individual cell settings (see, e.g. [2,11]).

Emergence here means the appearance of higher-level qualities of such a system arising from the lower-level qualities of its components. CAs are one of the most simple and general arrangements for that kind of interaction. The investigation

of emergent behavior is not limited to regular lattice structures as they are found in traditional CAs, but can be extended to more nature-like systems [3]. In fact, a specific model of interconnect networks was found to be extremely well suited to model and analyze nature-inspired systems, the small-world networks [4,5]. Small-world graphs exhibit a certain degree of irregularity, though embedded in an otherwise regular lattice structure. Figure 1 shows an example of a regular lattice graph and a small-world graph.

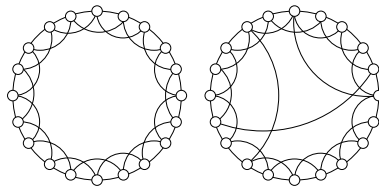


**Fig. 1.** Principle of a regular (*left*) and a small-world (*right*) connected lattice with 20 nodes, following [4]. For the small-world graph, only a few connections are irregular, which might result in different node grades

Such a structure can be created by randomly displacing individual edges while walking once through all the nodes. For larger graphs, some basic graph properties like the average path length  $L$  or the local clustering coefficient  $C$  of nodes depend very sensitive on the probability chosen for the random displacements. In a specific range of displaced edges lies the small-world region which is, basically, characterized by a small  $L$  combined with a still large  $C$ , thus well supporting closely connected local interaction and short global paths.

The effect of randomly replacing a growing number of local connections by arbitrary (potentially global) connections is shown in Fig. 2. It can be seen that a few number of displacements in a completely regular lattice graph already result in a greatly reduced characteristic path length. At the same time, the local clustering remains high for a long time. Finally, the graph adopts the characteristics of a random graph. A small path length should support global communication much better than found in regular lattice structures. A high local clustering, at the same time, should provide (almost) the same capability for local information interchange as possible in a regular lattice.

## Overview

For further investigations of CAs based on different interconnect models, a fast method to evaluate the behavior of a large number of specific CA specimen must be available. A genetic algorithm (GA) can be used to evolve CA behavior in the form of a transition function (TF) table. Assuming a regular lattice structure, the



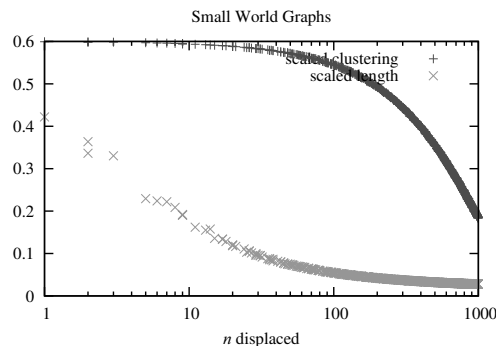


**Fig. 2.** Characteristic path length and local clustering coefficient for a series of displaced graph structures (averaged over 10 runs). The small-world region is found between highly ordered (small  $n$ ) and random graphs (large  $n$ ).

TF table completely defines the individual automaton and its behavior. The high number of different individuals produced by the GA will result in a large base of samples for a comparison of different models. For the GA process, the fitness of each individual of each generation must be evaluated by applying sample patterns (a set of initial cell states, IC) and inspecting the output patterns (final cell states) after a certain number of steps. To accelerate the GA beyond a simple distribution of the workload to several hosts, a dedicated hardware directly performing the CA computations can be used.

In this paper a software implementation of the GA is discussed likewise a hardware architecture for fast CA evaluation with hardwired cell connections and a communication interface for TF and IC down- and output pattern uploading. A method is discussed which allows to trade speed for area. Finally, an architecture is presented which allows to program the cell interconnection pattern at runtime via the network interface.

### Client/Server Implementation of the Genetic Algorithm

The GA software is implemented as a distributed Java program using a client/server architecture. The GA is running as a client process. Its task is the generation of an initial and any new generation of CA individuals. A stub server process is used to encapsulate the hardware accelerator which performs the execution of individual CAs. The individuals are completely represented by their transition function (TF) tables (their genetic code), which are evolved by the GA. For an automaton execution, the automaton input is a bit pattern defining the initial state for each cell. The output is the actual state vector after a specific number of transi-

tion steps. To start a simulation, a set of TF tables and a set of test vectors must be transferred from the client to a server process. The test vectors are then applied to each individual by the dedicated hardware accelerator and the resulting outputs are sent back to the client.

### **Genetic algorithm implementation**

For each new generation the operations selection, cross-over and mutation are applied to the current individuals to form the next generation. In addition, one can work with elitism, ensuring that the fittest individuals of each generation survive into the next one without being changed. The algorithm given in Fig. 3 shows the cycle of the GA in pseudocode (the variables correspond to sets of data vectors and are denoted with square brackets). The fitness of the individuals is needed for the selection and elitism processes and is calculated by evaluating each individual of `this_gen` using a set of 100 sample input vectors. For this purpose, the TF tables and a set of sample data are sent to the servers for CA simulations before. The fitness rating inside the `rate_all` function is performed based on the performance data delivered by the server processes.

```

func genetic algorithm
  begin
    this_gen[] ← generate-initial-population();
    for number_of_generations do
      send(this_gen[], samples[]);
      receive(performance[]);
      fitness[] ← rate_all(this_gen[], performance[]);
      elite[] ← elitism(this_gen[], fitness[]);
      selected[] ← select(this_gen[], fitness[]);
      selected[] ← crossover(selected[]);
      mutate(selected[]);
      next_gen[] ← selected[] ∪ elite[];
      this_gen[] ← next_gen[];
    od
  end

```

**Fig. 3.** Pseudocode of GA cycle

The answers are collected and the fitness of individuals  $i$  is calculated based on its performance on the sample input vectors

$$fitness_i = \frac{\sum_{\forall k \in samples} c_{i,k}}{|samples|}$$

where  $c_{i,k} = 1$  if sample  $k$  was classified correctly and  $c_{i,k} = 0$  otherwise and `samples` is the set of input sample vectors. The individuals of the last generation of the GA represent the result of the evolution process.

### **Server processes**

The main purpose of the server processes is the evaluation of individuals, i.e., to get performance data for each individual in terms of how good it can solve the sample problems represented by the sample input vectors. This functionality is encapsulated in the server process. After receiving a set of TF tables and a set of test vectors, it produces a byte stream which is sent to the FPGA via a network connection. It then immediately switches to receive mode and collects the result data produced by the FPGA. This byte stream is converted to the external data format, an array of Boolean vectors, and sent back to the server.

### **Integration of the hardware model**

The cellular automaton is embedded into an testbed architecture which enables the communication with the server process encapsulating the hardware-implemented CA via a serial link. Actually, this serial connection can be bridged to an TCP/IP connection using an RJ45 socket sized device which is known as XPORT.

The overall architecture is depicted in Fig. 4. The architecture allows to first download all test input patterns and all individuals (represented by their TF table) via a serial link or a TCP/IP connection, respectively. These data are stored in two RAMs implemented with the block RAMs of the FPGA. When the RAMs are completely initialized, the state registers of the automaton cells can initially be loaded from the *input pattern RAM* with a certain input pattern and a certain number of CA cycles can be performed for a certain individual the TF table of which is provided by the *function table RAM*. The results are finally located in the state registers and are transferred to a parallel loadable shift register. The serial controller starts to transmit the data while the CA continues to process the next input pattern. If a transmission is still in progress when the CA has completely processed the current pattern/individual combination (which usually is the case), the CA is stopped until the transmitter is ready to be loaded with the current result. This approach allows to continuously upstream the calculation results with maximal link speed. The testbed automatically performs the above described operations for all possible pattern/individual pairs in a predefined order and is finally ready to receive new configuration data from the serial link.

## **The Cellular Automata Model**

The straight forward CA realization for cells with one bit wide input and output ports consists of a Boolean function  $f$  which maps the current state and the inputs of a cell to its next state stored at the rising edge of the clock in the cell's state register. Thus, each cell can be considered as a finite state machine (FSM) with two

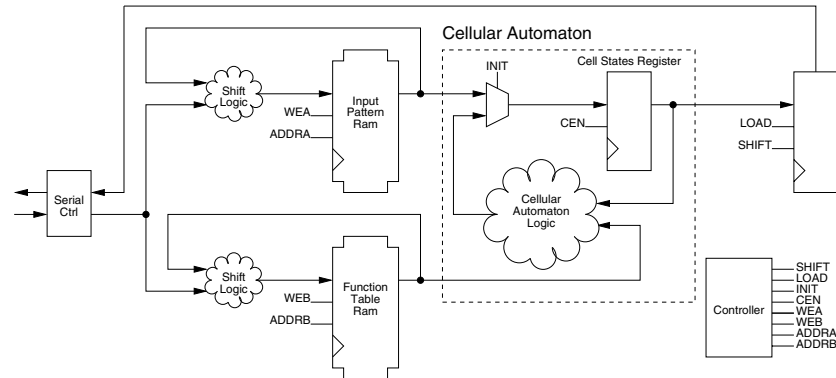


**Fig. 4.** Architecture of the CA testbed. The TF tables and the input patterns of the CA are stored in embedded Block RAM (BRAM) of the FPGA. The interfacing to the server process is realized by a serial link

states. Therefore the overall automaton consists of  $N$  interacting FSMs. The state of a certain FSM serves as its output, i.e., each cell forms a special case of a Moore-machine. The inputs of each FSM are the outputs of  $M$  other FSMs according to the adjacency matrix. Having this in mind, it is obvious, that the overall CA has  $2^N$  distinguishable states. The input to the automaton is an  $N$  bit IC pattern forming the initial state. The automaton then performs a certain number of cycles updating its state in each cell. Afterwards, the result of the operation performed by the CA is its final state. As mentioned earlier, the main task of the hardware acceleration is to evaluate a large number of individuals using a large number of ICs as fast as possible. In order to perform this task, it is necessary to have the (Boolean) function  $f$  programmable. Therefore, it is realized by a Look-up Table (LUT) as shown in Fig. 5a. Figure 5b shows the CA cell internals. A number of LUTs and the initial patterns are downloaded from a host computer via the interface described in the previous section. A controller ensures that the automaton performs a certain number of cycles for all possible LUT/input combinations and finally the generated output patterns are uploaded to the host computer for further evaluation.

### **Approach for a time/area trade-off**

The parallel access to the transition table results in huge input multiplexers for each cell, accounting for large area requirements. The mutliplexer size can be reduced by sequencing the table accesses. Figure 6a shows the adapted cell for the sequential scheme, using four sequential accesses. In four consecutive cycles, the four quarters of the transition table are connected to the cell inputs and the table access is partially decoded using five of the seven address bits. The four remaining

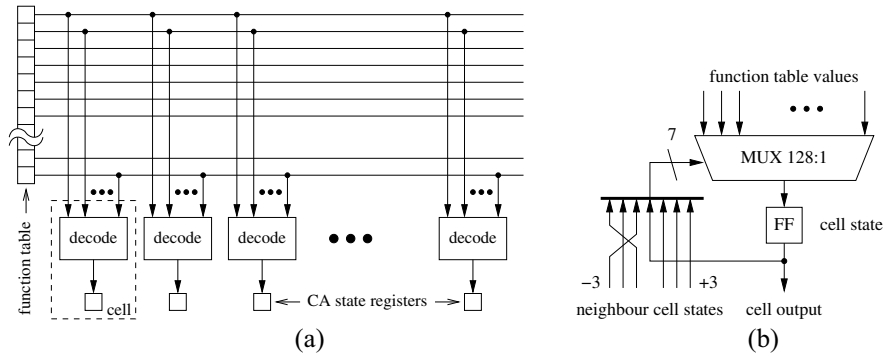


**Fig. 5.** (a) Hardware realization of an RLCA with  $M = 6$  inputs. The inputs of all multiplexers are the same for all cells and are defined by a global table. (b): Hardware realization of a single cell with  $M = 6$  inputs. The selection signal for the multiplexer is a binary number formed by the current state of the corresponding cell and the  $M$  states of the cell's inputs. The output of each multiplexer defines the next state of the corresponding cell

possible bit values are shifted into four flip-flops and one is selected (using the remaining two address bits) and stored into the state flip-flop in a fifth cycle. This shift/select scheme can be used for any  $r$ -splittings of the transition table into  $2^r$  sections, resulting in a  $2^r$ -bit shift chain and  $2^r + 1$  clock cycles for one CA step, thus enabling a time/area trade-off. This is especially true for FPGA-based designs, where a large number of flip-flops is available but the logic resources are limited. In this case, unused registers can directly be traded for multiplexer area: The input size of the main multiplexer of each cell is reduced to  $1/2^r$ th which means an area reduction by a factor of  $2^r$ . In the case of  $r = 2$ , the 4-split reduces the number of inputs from 128 to 32, along with the number of global wires to each cell, which is a tremendous improvement. For the table splitting on the other hand, we need an additional sequencer for the  $2^r$  cycles and  $128/2^r$  ( $32$  for  $r = 2$ )  $2^r:1$  multiplexers, finalizing the trade-off.

**Reconfigurable interconnect architecture**

A similar architecture which allows to *program* an arbitrary connection between individual cells is depicted in Fig. 6b. We use a mixed parallel/sequential method similar to the scheme already explained in the earlier section. All cell outputs can be routed to any input of any of the other cells. The states of all cells are sequentially transferred to all other cells using a  $2^p$  bit wide bus. This transfer is performed in  $2^q$  consecutive clock cycles. A run-time programmable  $p+q$  bit wide register holds the index of the neighbor whose state is needed. Thus,  $M$  such slices are needed within one cell. If the number of cells is less than  $2^{p+q}$ , the additional

bits in the last transfer cycle are ignored by setting the bits in the index register properly. For example, if  $p = 6$  and  $q = 2$ , the 256 possible states are transferred in four clock cycles using a 64 bit bus. Five clock cycles are needed in total in order to have the state of the neighboring cell available at the slice's output.

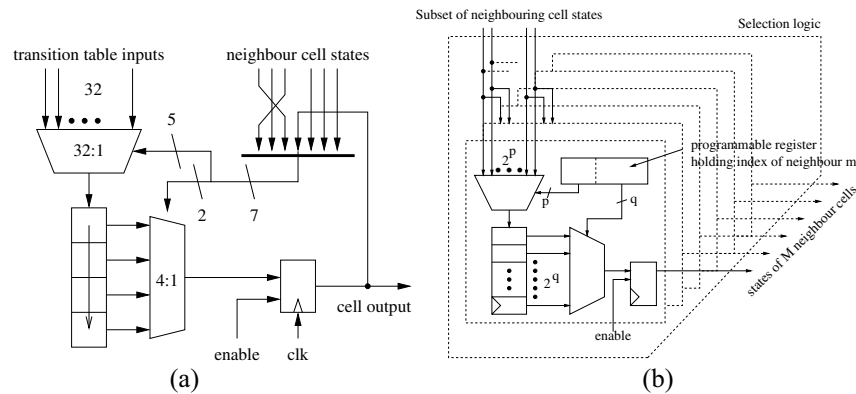


**Fig. 6.** (a) Internal structure of a cell for the area improved CA. Besides the main cell flip-flop, four additional flip-flops are used to collect the four possible next-state bits. An additional multiplexer selects the right one after four clock cycles. The whole cell requires five clock cycles for one CA step. (b) Reconfigurable communication backplane: The  $N$  (with  $N \leq 2^{p+q}$ ) current states of the cells are sequentially transmitted in  $2^p$  consecutive clock cycles using blocks of  $2^q$  bits.  $M$  registers hold the indices of the cells which are connected to the cell under consideration. Each index is encoded by  $p+q$  bits, where  $p$  bits are used to address the bit number within a block and  $q$  bits represent the block's address

## Conclusion

A hardware-in-the-loop approach is used for the hardware accelerated evaluation of cellular automata evolved by a genetic algorithm which is implemented in software. Based on a basic parallel hardware implementation of the CA, an area/time trade-off is developed and a flexible solution feasible for the fast evaluation of different connection structures in the small-world domain, a run-time programmable architecture, is presented.

## References

- [1] M. Mitchell, "Computation in cellular automata: A selected review," in *Non-Standard Computation: molecular computation, cellular automata, evolutionary algorithms, quantum computers*, T. Grams, S. Bornholdt, M. Gross, M. Mitchell, and T. Pellizzari, Eds. New York: Wiley-VCH, 1998
- [2] R. Dogaru, "Universality and Emergent Computation in Cellular Neural Networks", *World Scientific Publishing Company*, March 2003, World Scientific Series on Nonlinear Science, Series A, vol. 43

- [3] A.-L. Barabási, *Linked: The New Science of Networks*, 1st ed. Perseus Books Group, May 2002
- [4] D.J. Watts and S.H. Strogatz, "Collective dynamics of 'small-world' networks," *Nature*, vol. 393, pp. 440–442, June 1998
- [5] D.J. Watts, *Small Worlds: The Dynamics of Networks between Order and Randomness*, Princeton and Oxford: Princeton University Press, 1999
- [6] S. Wolfram, "Universality and complexity in cellular automata," *Physica D*, vol. 10, no. 3–35, 1984
- [7] P. Sarkar, "A brief history of cellular automata," *ACM Computing Surveys (CSUR)*, vol. 32, no. 1, pp. 80–107, March 2000
- [8] S. Borkar, T. Karnik, and V. De, "Design and reliability challenges in nanometer technologies," in *Proceedings of the 41st Design Automation Conference*, 7–11 June 2004, p. 75
- [9] F. Peper, J. Lee, F. Abo, T. Isokawa, S. Adachu, N. Matsui, and S. Mashiko, "Fault-tolerance in nanocomputers: A cellular array approach," *IEEE Transactions on Nanotechnology*, vol. 3, no. 1, pp. 187–201, March 2004
- [10] R. Dogaru and L.O. Chua, "Mutations of the game of life: a generalized cellular automata perspective of complex adaptive systems," *International Journal of Bifurcation and Chaos*, vol. 10, no. 8, pp. 1821–1866, 2000
- [11] R. Dogaru, A. Iftime, D. Darloman, and M. Glesner, "An exhaustive analysis of emergent behaviors in recurrent cellular computing systems with outertotalistic cells," in *International Semiconductor Conference (CAS 2003)*, vol. 2, 28 September–2 October 2003, pp. 391–394

# Current Mode Double Threshold Neuron Activation Function

M. Yildiz, S. Minaei and İ. C. Gökmar

Department of Electronics and Communication Engineering  
Doğuş University, Acıbadem, 81010, Istanbul, myildiz@dogus.edu.tr,  
sminaei@dogus.edu.tr, cgokmar@dogus.edu.tr

## Abstract

CMOS implementation of a neuron activation function. Proposed current mode circuit can classify data separable with more complex decision boundaries than hyperplanes. SPICE simulation results are included to verify the expected outcomes.

## Introduction

The basic building block of a Feed-forward Artificial Neural Network (FANN) is a simple processing element called neuron. The response of each neuron in a FANN is the output of a block with nonlinear transfer characteristic, called activation function, in the shape of a sigmoid which is monotonically nondecreasing and is bounded by finite upper and lower limits. Typical activation functions are: the hard limiter characterized by the signum function, the piecewise linearized version of the hard limiter, or the continuously differentiable version expressed with the exponential function [1]. A popular choice for neuron activation function (NAF) can be defined as

$$f(x) = \frac{2}{1 + e^{-kx}} - 1, \quad (1)$$
$$f(x) = \begin{cases} +1, & x > 0, \\ -1, & x < 0, \end{cases}$$

where  $k > 0$  is proportional to the neuron gain determining the steepness of the continuous function  $f(x)$ . The continuous function is shown in Fig. 1. for  $k=7$ .



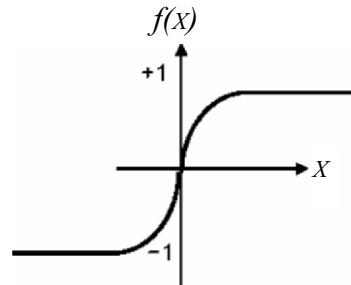


**Fig. 1.** Neuron activation function

The kind of data that the perceptron classifies can be linearly separable by a hyperplane as shown in Fig. 2a and not of the type as shown in Fig. 2b which necessitates an activation function with double threshold; its piecewise linear version is called the Trapezoidal Activation Function (TAF). The stability properties of NN with TAF have been investigated in [3]; a switched capacitor CMOS implementation of a cell with TAF was proposed in [4].

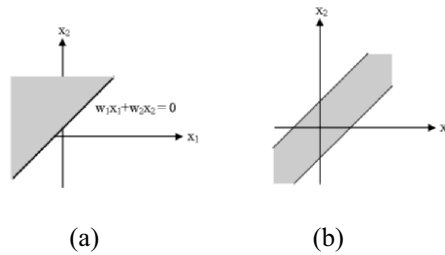


**Fig. 2.** (a) Linearly separable (b) double threshold decision regions

In this paper an analog circuit realization of a neuron activation function is proposed to classify data of the two hyper-planes. The circuit makes use of two CMOS-only current follower circuits operating in current mode; one follower has a transfer characteristic which is shaped like a sigmoid and the other shaped like a sigmoid rotated around the  $y$ -axis, together providing a TAF hence, a decision region like in Fig. 2b. Moreover, it is shown that by mismatching the bias currents of the followers more interesting decision regions can be obtained.

## Current Followers

The Current Follower (CF), with its symbol shown in Fig. 3, is an active multi-terminal element defined with the following matrix equality:

$$\begin{bmatrix} I_Y \\ V_X \end{bmatrix} = \begin{bmatrix} \pm K & 0 \\ 0 & 0 \end{bmatrix} \begin{bmatrix} I_X \\ V_Y \end{bmatrix}, \quad (2)$$

where the plus and minus signs of the current transfer ratio refer to a CF+ and CF-, respectively;  $K$  is the current gain of the current follower.

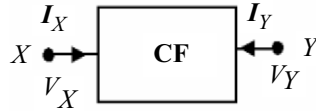


Fig. 3. Symbol of the current follower

Current followers have been widely used to synthesize various analog signal processing circuits, such as analog filtering circuits [5]. Similarly using CFs to develop a double threshold classifier seems to be promising.

Current mirrors are used to construct current followers. A class AB CMOS realization of a CF+ is given in Fig. 4 and its DC transfer characteristic is shown in Fig. 5; this characteristic can be used to build the desired activation function of neural network structures. CF- is obtained by adding cross-coupled current-mirrors to the implementation of CF+.

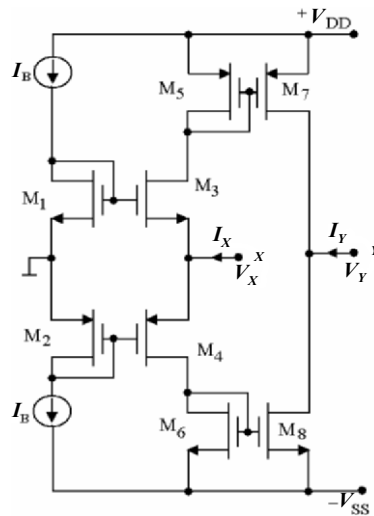


Fig. 4. Class AB implementation of CF+

The desired new configuration for realizing a double threshold classifier can be obtained by using a shifted CF+ and a shifted CF- in the implementation.

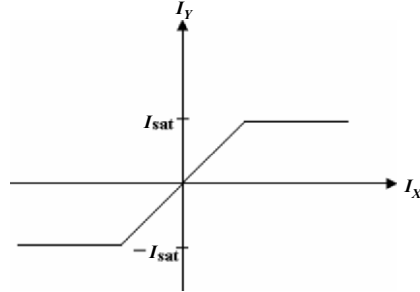


Fig. 5. DC transfer characteristics of a CF+

### Block Diagram Description

The block diagram of the proposed circuit, consisting of two current follower blocks with transfer characteristics shown in the boxes and expressed as in (3), is given in Fig. 6. In (3)  $K$  is the current follower circuit's current gain and the other symbols are as shown in the block diagram of Fig. 6; it should be observed that the current sources at the input ports provide the  $x$ -axis intercept of the current followers. The adder blocks shown in Fig. 6 need to be implemented simply with single nodes as the circuit operates in current mode

$$I_{o1} = \begin{cases} -I & \text{for } I_{i1} > c, \\ KI_{i1} & \text{for } d < I_{i1} < c, \\ I & \text{for } I_{i1} < d, \end{cases} \quad (3)$$

$$I_{o2} = \begin{cases} I & \text{for } I_{i2} > b, \\ KI_{i2} & \text{for } a < I_{i2} < b, \\ -I & \text{for } I_{i2} < a. \end{cases}$$

In order to achieve the appropriate trapezoidal current transfer characteristic shape as shown in Fig. 6 the following constraints must be satisfied:

$$d \geq b \text{ and } I_{i1} = I_{i2} = I_{in}. \quad (4)$$

However, as will be shown in the sequel, much more interesting decision regions can be obtained if the equality constraint in (4) is not fulfilled.

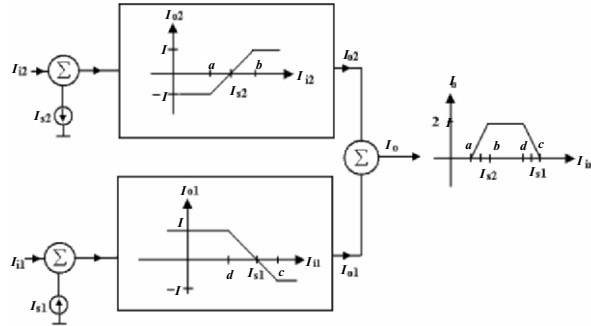


Fig. 6. Activation function circuit block diagram

### MOS Circuit

The proposed activation function circuit's schematic which consists of two current followers, is shown in Fig. 7. The transistors  $M_1$  and  $M_2$  in the figure are for providing the bias, transistors  $M_3, M_4, M_5$  and  $M_6$  constitute the input stage of the negative current follower, transistors  $M_7, M_8, M_9$  and  $M_{10}$  constitute the input stages of the positive current follower. Current sources  $I_{s1}$  and  $I_{s2}$  are used to shift the input currents of the current follower, consequently of the  $x$ -axis intercepts of TAF. This shift of the intercept points by adjusting the starting and ending boundaries of the specified decision region makes the device custom tunable. It should be observed that in the circuit all the transistors are working in saturation. In the sequel PSPICE simulation results using TSMC MOSIS 0.35  $\mu\text{m}$  CMOS process model will be given.

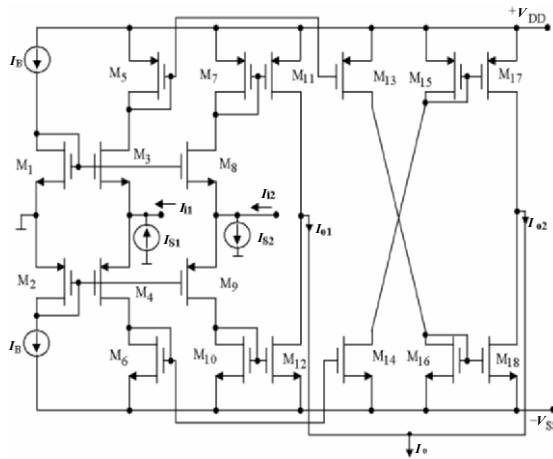


Fig. 7. The schematic of the circuit

## Simulation Results

The voltage supply used in the proposed circuit is  $\pm 2.5$  V, the current  $I_B$  is chosen as  $200 \mu\text{A}$  and the total power dissipation of the circuit is  $19.3 \text{ mW}$ . The dimensions of the transistors are given in Table 1. Following a SPICE simulation,  $I_{o1}-I_{i1}$  and  $I_{o2}-I_{i2}$  characteristics of the circuit are shown in Fig. 8a and b, respectively. Taking  $I_{i1}=I_{i2}=I_{in}$ ,  $I_{s1}=50 \text{ mA}$  and  $I_{s2}=20 \text{ mA}$ , results in the  $I_o-I_{in}$  characteristic of the circuit shown in Fig. 9.

MOSFET	$W (\mu\text{m})$	$L (\mu\text{m})$
$M_1, M_2, M_3, M_4$	10	0.7
$M_5, M_6, M_9, M_{10}, M_{11},$ $M_{12}, M_{13}, M_{14}, M_{15}, M_{16}, M_{18}$	7	0.7
$M_7, M_{17}$	9	0.7
$M_8$	8	0.7

**Table 1.** Dimensions of the transistors

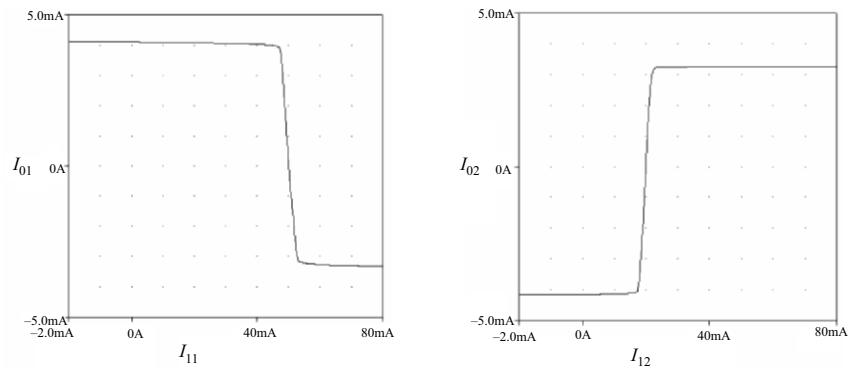


**Fig. 8.** (a)  $I_{o1}-I_{i1}$  characteristics of the circuit. (b)  $I_{o2}-I_{i2}$  characteristic of the circuit

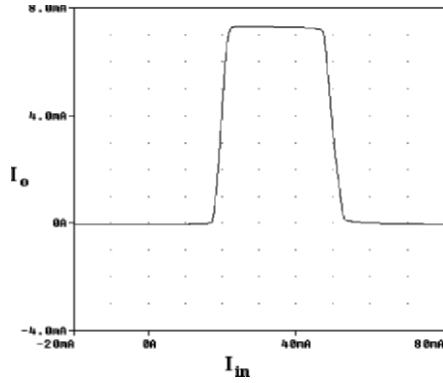


Fig. 9.  $I_o$ - $I_{in}$  characteristic of the circuit

The 3-D surface graphics of the circuit for  $I_{i1}=I_{i2}=I_{in}$  is shown in Fig. 10 which exhibits the desired behavior of an FANN cell with TAF.

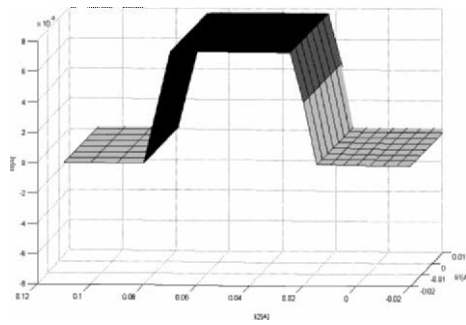


Fig. 10. Surface graphic of FANN cell with TAF

The surface graphics of the circuit for unequal input currents  $I_{i1}$  and  $I_{i2}$  (equality in (4) not satisfied) is shown in Fig. 11. The interesting feature of this surface graphic is the presence of three different decision regions.

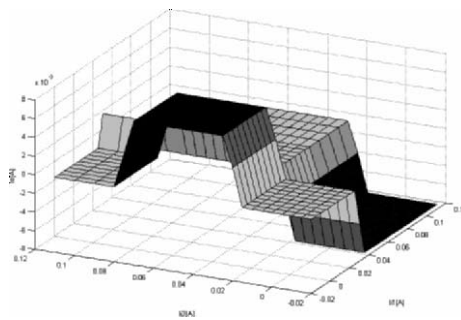


Fig. 11. Surface graphic of FANN cell

## Conclusion

In this paper, a current mode CMOS-only neuron activation function circuit has been proposed. This neuron classifies linearly nonseparable data, subject to some boundary conditions. Violation of boundary conditions yields more complex decision regions which need to be identified.

For further research, the main issue that remains to be addressed is the exact class of data which can be identified with such a circuit topology.

## References

- [1] C. Fausto and V. Maurizio, "A Mixed Mode Perceptron Cell for VLSI Neural Networks", *ICECS*, pp. 377–380, 2001
- [2] A.K. Gupta and N. Bhat, "Asymmetric Cross-Coupled Differential Pair Configuration to realize Neuron Activation Function and its Derivative", *IEEE Trans. Circuit Syst.*, vol. 52, pp.10–13, 2005
- [3] E. Bilgili., İ.C. Gökner and O.N. Uçan "Cellular Neural Networks with Trapezoidal Activation Function," resubmitted to *Int. J. Circuit Theory Applic.*
- [4] D.Y. Aksın, S. Aras, İ.C. Gökner, "CMOS Realization of User Programmable, Single-Level, Double-Threshold Generalized Perceptron," *Proceedings of Turkish Artificial Intelligence and Neural Networks Conference, TAINN-2000*, İzmir, Turkey, June 2000
- [5] S.I. Lio, J.J. Chen, H.W. Tsao and J.H. Tsay, "Design of biquad filters with a single current follower", *IEE Proceedings*, Part G, vol. 140, No. 3, 1993

# Gradient Networks for Clustering

H. Dođan and C. Güzeliş

Department of Electrical & Electronics, Dokuz Eylül University Kaynaklar Campus, 35160 Buca, Izmir, Turkey  
hatice.dogan@eee.deu.edu.tr,  
cuneyt.guzelis@deu.edu.tr  
Tel. +90-232-4127164 Fax: +90-232-4534279

## Abstract

In this paper, two different optimization formulations for clustering problem are considered. The first one is the common mixed-integer optimization formulation and the second one is the binary integer optimization formulation which was proposed by the authors. The costs of the optimization problems were minimized by two different gradient dynamical networks. The performances of the networks were compared with each other on the image compression applications.

## Introduction

Clustering is the partition of the data into  $k$  groups in such a way that data in a given group are more similar to each other according to a chosen similarity measure than the rest [1, 2]. Each group is called cluster. In a former work of the authors, a new mixed-integer optimization formulation for the clustering problem was proposed which is quite different from the ones available in the literature and transformed into a binary integer optimization formulation [3]. In this paper, the performances of the max coupled gradient network which was proposed for the minimization of the common optimization formulation [4] and the gradient network which was proposed for the minimization of the binary integer optimization formulation are compared with each other. The paper is organized as follows: the max coupled gradient network is reviewed in Sect. 2, the gradient network is explained in Sect. 3, applications and results are presented in Sect. 4 and conclusions are given in Sect. 5.



## Max Coupled Gradient Network

A common optimization formulation of the clustering can be given as the following optimization problem:

$$\begin{aligned} \min \quad & E(\mathbf{C}, \mathbf{M}) = \sum_{i=1}^k \sum_{j=1}^L m_{ij} \|\mathbf{x}_j - \mathbf{c}_i\|^2 \\ \text{subject to (s.t.) } & \mathbf{M} \in \mathbb{S} = \left\{ \mathbf{M} \in \{0,1\}^{k \times L} \mid \sum_{i=1}^k m_{ij} = 1 \right\}, \end{aligned} \quad (1)$$

where  $\mathbf{x}_j$ ,  $j = 1, \dots, L$ ;  $\mathbf{x}_j \in R^n$  a finite set of sample data vectors,  $k$  is the number of clusters,  $\mathbf{C}_{n \times k} = (\mathbf{c}_1, \dots, \mathbf{c}_k)$ ;  $\mathbf{c}_i \in R^n$ , is the center matrix which consists of  $k$ ,  $n$  dimensional center vectors,  $\mathbf{M}_{k \times L} = (\mathbf{m}_1, \dots, \mathbf{m}_L)$  with  $\mathbf{m} \in \{0,1\}^k$ , is an indicator matrix whose elements represent the memberships of data to certain clusters and  $\|\cdot\|$  is the Euclidean norm. Constraints provide that no data vector can be assigned to more than one cluster.

A coupled gradient network which consists of two coupled interacting networks C-network and M-network was proposed for the minimization of (1) in [4]. C-network is a dynamical network which is associated to continuous variables, i.e. centers. M-network is an algebraic network which is associated to discrete variables, i.e., cluster indicators. The network operates in a similar way to  $k$ -means clustering but centers and partitions are updated in a different manner. The output of the C-network is given as an input of the M-network without waiting the settlement of the C-network. The convergence analysis of this network can be found in [4]. The C-network consists of  $n \times k$  neurons which has linear activation functions and has the following linear dynamics:

$$\frac{d\mathbf{c}_i}{dt} = -\nabla_{\mathbf{c}_i} E(\mathbf{C}, \mathbf{M}) = 2 \sum_{j=1}^L m_{ij} (\mathbf{x}_j - \mathbf{c}_i), \quad (2)$$

$m_{ij}$ 's in (2) are the outputs of algebraic M-network (maxnet) which consists of  $k \times L$  neurons whose inputs are equal to  $-\|\mathbf{x}_j - \mathbf{c}_i\|^2$ .  $m_{ij}$ 's can be calculated by using (3)

$$m_{ij} = \begin{cases} 1 & \text{if } -\|\mathbf{x}_j - \mathbf{c}_i\|^2 \geq -\|\mathbf{x}_j - \mathbf{c}_i\|^2 \quad \forall t \neq i, \\ 0 & \text{otherwise.} \end{cases} \quad (3)$$

If  $m_{ij} = 1$  for more than one  $i$  for the same  $j$  index, the smallest  $i$  should be chosen to satisfy the constraint  $\sum_{i=1}^k m_{ij} = 1$ .

The forward Euler numerical integration was used for the computer simulation. The initial centers were chosen among the sample data in a random way. The time step in the numerical integration was set to 0.005.

## Gradient Network

The binary integer optimization formulation of clustering was proposed in [3]

$$\begin{aligned} \max \quad E(\mathbf{M}) &= \sum_{i=1}^k \frac{1}{\sum_{j=1}^L m_{ij}} \|\mathbf{X}\mathbf{m}_i^T\|^2 \\ \text{s.t.} \quad \mathbf{M} &\in \mathbb{S}, \end{aligned} \quad (4)$$

where  $\mathbf{m}_i$  is the  $i$ th row of the matrix  $\mathbf{M}$ . In the last equation, objective function is the sum of maximum of different discrete equations. Each equation is coupled to each other via  $\sum_{i=1}^k m_{ij} = 1$ .

A Gradient network which consists of  $k \times L$  neurons was proposed for the minimization of (4) in [3]. The columns of the network represent the data vectors that are to be classified and the rows of the network represent the given classes.  $m_{ij}$ 's are the outputs of the neurons. The winner-take-all rule was adopted to the outputs of the neurons that are in the same column for the satisfaction of the constraints. The dynamics of this network is given as

$$U_{m_{ij}}^{z+1} = -\frac{\sum_{j=1}^L \sum_{r=1}^L \mathbf{x}_j^T \mathbf{x}_r m_{ij}^z m_{ir}^z}{\left(\sum_{j=1}^L m_{ij}^z\right)^2} + 2 \frac{\sum_{r=1}^L \mathbf{x}_j^T \mathbf{x}_r m_{ir}^z}{\sum_{j=1}^L m_{ij}^z}, \quad (5)$$

$$m_{ij}^{z+1} = \begin{cases} 1 & \text{if } U_{m_{ij}}^{z+1} = \max \{ U_{m_{1j}}^{z+1}, \dots, U_{m_{kj}}^{z+1} \}, \\ 0 & \text{otherwise.} \end{cases} \quad (6)$$

where  $z$  is the simulation step. To prevent the network for being trapped in early local minima noise is introduced into the system. During the optimization process the additive noise should approach zero in time so that the network itself will become deterministic prior to reaching the final solution.

## Applications

The networks are tested on image compression applications. To compress an image, the whole image is divided into  $L$  blocks (a block represents a data vector  $\mathbf{x}_j$  which occupies  $l \times l$  pixels) and mapped onto the networks as network parameters. The data vectors were extracted from  $128 \times 128$  images. The images were divided into  $4 \times 4$  blocks to generate none-overlapping 16 dimensional vectors. The  $k$  was chosen as 128. Algorithms were tested with 20 different random initial conditions. If an empty cluster occurs during the simulation,  $E(\mathbf{M})$  becomes infinite, because the number of elements in one cluster is in the denominator. To avoid this situation (6) is modified as follows:

$$m_{ij}^{z+1} = \begin{cases} 1 + 10^{-6} & \text{if } U_{m_{ij}}^{z+1} = \max \{ U_{m_{1j}}^{z+1}, \dots, U_{m_{kj}}^{z+1} \}, \\ 10^{-6} & \text{otherwise.} \end{cases} \quad (7)$$

The peak signal-to-noise ratio (PSNR) which is defined for an  $N \times N$  image as

$$\text{PSNR} = 10 \log_{10} \frac{255 \times 255}{\frac{1}{N^2} \sum_{r=1}^N \sum_{r=1}^N (f_{tr} - \hat{f}_{tr})^2}$$

where  $f_{tr}$  and  $\hat{f}_{tr}$  are the pixel gray levels from the original and the reconstructed images and 255 is the peak gray level [5]. The PSNR results are shown in Table 1.

**Table 1.** Average PSNRs of the reconstructed images

Images	Max Coupled GN	Gradient Network
bird	32.43	33.08
Lena	27.57	27.86
cameraman	24.57	25.79

## Conclusions

In this paper two different optimization formulations and two different gradient networks are considered. According to the simulation results the performance of the gradient network is better than the max coupled gradient network. Also the gradient network has two major advantages:

- (1) optimization is done according to the one variable which indicates the membership of the data vector and
- (2) contrary to the first formulation, the second formulation does not contain the distance term so the computation time needed for the gradient network is much less than the max coupled gradient network.

## References

- [1] A.K. Jain, R.C. Dubes, *Algorithms for Clustering Data*, New Jersey, Prentice Hall (1988)
- [2] R.O. Duda, P.E. Hart, D.G. Stork, *Pattern Classification*, 2nd ed. New York, Wiley-Interscience (2000)
- [3] H. Doğan, C. Güzeliş, "A gradient network for vector quantization and its image compression applications", *Lecture Notes in Computer Science*, 2714 (2003) 554–561
- [4] H. Doğan, C. Güzeliş, "K-means clustering with max coupled gradient network", Submitted to *IEEE Transactions on Circuits and Systems*
- [5] A. Gerscho, R.M. Gray, *Vector Quantization and Signal Compression*, Dordrecht Kluwer Academic Publishers (1992)

# On a Matrix Inequality and Its Application to the Synchronization in Coupled Chaotic Systems

C.W. Wu

IBM T. J. Watson Research Center, P.O. Box 218,  
Yorktown Heights, NY 10598, USA

## Abstract

We study a matrix inequality problem which was found to be useful in deriving sufficient conditions for the synchronization in networks of coupled chaotic systems. We consider classes of matrices for which this problem has an exact solution and solve the general case by solving sequentially a series of semidefinite programming problems.

## Introduction

Recently, synchronization in networks of coupled chaotic systems has received considerable attention [1–4]. In [1,5–7], sufficient conditions for synchronization were obtained by means of a Lyapunov function and under certain assumptions the synchronization condition is reduced to a condition that depends on properties of the coupling matrix. For instance, in [8] the synchronization condition depends on the smallest nonzero eigenvalue of the symmetric part of the coupling matrix. On the other hand, for coupled linear systems the synchronization condition depends on the eigenvalues of the coupling matrix. Since the eigenvalues of a matrix can differ significantly from the eigenvalues of its symmetric part, the question is whether we can bridge the gap between these two sets of conditions. We show that this question can be studied by solving an optimization problem with nonlinear semidefinite constraints. In particular, we solve this problem by solving a sequence of linear semidefinite programming problems.

We say a real matrix  $G$  is positive (semi-)definite if its symmetric part  $\frac{1}{2}(G + G^T)$  is positive (semi-)definite, i.e.,  $x^T(G + G^T)x > 0 (> 0) \forall x \neq 0$ . We denote this by  $G \succ 0$  ( $G \succeq 0$ ). This is equivalent to saying that the eigenvalues of  $G + G^T$  are positive (nonnegative).

## Synchronization in a Coupled Network of Chaotic Systems

**Definition 1.**  $\mathcal{W}$  is the set of real matrices with zero row sums and nonpositive off-diagonal elements.  $\mathcal{W}_s$  is the set of irreducible symmetric matrices in  $\mathcal{W}$ .

**Definition 2.** A function  $f(y, t)$  is  $P$ -uniformly decreasing if  $(y-z)^T P (f(y, t) - f(z, t)) \leq -c \|y-z\|^2$  for some  $c > 0$  and all  $y, z, t$ .

It is easy to show that matrices in  $\mathcal{W}_s$  have a simple zero eigenvalue [1]. We begin with a version of the synchronization result in [1,8]:

**Theorem 1.** A coupled network of  $n$  identical chaotic systems described by the state equation

$$\dot{x} = (f(x_1, t), \dots, f(x_n, t))^T + (G \otimes D(t))x, \quad (1)$$

where  $x = (x_1, \dots, x_n)^T$  synchronizes in the sense that  $\|x_i - x_j\| \rightarrow 0$  as  $t \rightarrow \infty$  if there exists a symmetric  $P \succ 0$  and a matrix  $U \in \mathcal{W}_s$  such that:

- The function  $f(y, t) + \alpha D(t)y$  is  $P$ -uniformly decreasing
- For all  $t$ ,  $U(G - \alpha I) \otimes PD(t) \preceq 0$ .

In (1), the matrix  $G$  describes the static coupling topology between systems whereas the matrix  $D(t)$  describes the time-varying coupling term between two systems. The term  $\alpha D(t)y$  is the amount of feedback needed to stabilize  $\dot{y} = f(y, t)$ . Theorem 1 motivates us to define the following quantity.

**Definition 3.** Let  $\mu(G)$  be the supremum of the set of real numbers  $\mu$  such that  $U(G - \mu I) \succeq 0$  for some  $U \in \mathcal{W}_s$ .

Using this definition, it follows that the network in (1) synchronizes if there exists a symmetric matrix  $P \succ 0$  such that  $f(y, t) + \mu(G)D(t)y$  is  $P$ -uniformly decreasing and  $PD(t) = D(t)^T P \preceq 0$  for all  $t$  [5]. This suggests that  $\mu(G)$  is a measure of how well the topology of the coupled network is amenable to synchronization. The larger  $\mu(G)$  is, the smaller  $D(t)$  needs to be and the easier it is to synchronize the network.

Theorem 1 is obtained via Lyapunov's direct method and can be a global result. There exists another class of synchronization criteria based on the computation of Lyapunov exponents. These results are local in nature and are mathematically less rigorous. In these criteria, the nonzero eigenvalue of  $G$  with the smallest real part is important. Under certain conditions, by Corollary 3 this eigenvalue is larger than the

smallest nonzero eigenvalue of the symmetric part of  $G$ . Studying  $\mu(G)$  allows us to find out what the gap is between the applicability of these two classes of methods.<sup>1</sup>

### Properties of $\mu(G)$

Since matrices in  $W_s$  are positive semidefinite, the set of real numbers such that  $U(G - \mu I) \succeq 0$  for some  $U \in W_s$  is an interval, i.e., if  $U(G - \mu I) \succeq 0$  for some  $U \in W_s$ , then  $U(G - \lambda I) \succeq 0$  for all  $\lambda \leq \mu$ .

**Lemma 1 [1].** If  $A \in W_s$  and either  $AX \succeq 0$  or  $AX \preceq 0$ , then  $X$  is a matrix with constant row sums.

Lemma 1 implies that  $\mu(G)$  is only defined when the matrix  $G$  has constant row sums. A matrix with constant row sums can be converted into a matrix with zero row sums by adding a multiple of the identity matrix. Thus for the purpose of finding  $\mu(G)$  we can assume without loss of generality that  $G$  has zero row sums. In other words, adding  $\alpha I$  to  $G$  shifts  $\mu(G)$  by  $\alpha$ . Therefore we focus on the set of zero row sums matrices. For a matrix with zero row sums, 0 is an eigenvalue with eigenvector  $e = (1, \dots, 1)^T$ . The next theorem shows that the quantity  $\mu(G)$  exists for zero row sum matrices and gives a lower bound.

**Theorem 2.** If  $G$  has zero row sums, then  $\mu(G)$  exists, i.e. there is a real number  $\mu$  and a matrix  $U \in W_s$  such that  $U(G - \mu I) \preceq 0$ . Furthermore,

$$\mu(G) \geq \beta(G) \geq \lambda_{\min} \left( \frac{1}{2} (G + G^T) \right),$$

where  $\beta$  is defined as  $\beta(G) = \min_{x \perp e, \|x\|=1} x^T G x$

*Proof.* Let  $J$  be the  $n$  by  $n$  matrix of all 1s and let  $Q = I - \frac{1}{n} J$ . It is clear that  $Q \in W_s$ . Let  $U = Q$ . Define the symmetric matrix  $H = \frac{1}{2} (U(G - \mu I) + (U(G - \mu I))^T) = \frac{1}{2} (G + G^T) - \mu Q - \frac{1}{2n} (JG + G^T J)$ . Since  $Je = ne$  and  $Ge = Qe = 0$ , it follows that  $He = 0$ . Let  $x \perp e$  with  $\|x\| = 1$ . This means that  $Qx = x$ . Then  $x^T H x = \frac{1}{2} x^T (G + G^T) x - \mu x^T x - \frac{1}{2n} x^T (JG + G^T J) x$ . Since  $x \perp e$ , this implies

---

<sup>1</sup> See [5] for further discussion between these two classes of results

$Jx = 0$  and thus  $x^T Hx = \frac{1}{2} x^T (G + G^T)x - \mu$  which means that  $H \succeq 0$  if,  $\mu \leq \frac{1}{2} x^T (G + G^T)x$ . This implies  $\mu(G) \geq \beta(G)$ . The proof is then complete by noting that  $\beta(G) \geq \min_{\|x\|=1} x^T Gx = \lambda_{\min} (1/2 (G + G^T))$ .

Note that  $\beta(G) = \min_{\|Kx\|=1} x^T K^T G K x = \lambda_{\min} (\frac{1}{2} K^T (G + G^T) K)$ , where  $K$  is an  $n$  by  $n-1$  matrix whose columns form an orthonormal basis of  $e^\perp$ , the orthogonal complement of  $e$ . Furthermore, by the Courant–Fischer min–max theorem,  $\beta(G) \leq \lambda_2 (\frac{1}{2} (G + G^T))$ , the second smallest eigenvalue of  $\frac{1}{2} (G + G^T)$ .

**Definition 4.** For a matrix  $G$  with zero row sums, let  $L(G)$  denote the eigenvalues of  $G$  that do not correspond to the eigenvector  $e$ .

**Corollary 1.** If  $G$  is a real matrix with zero row sums and zero column sums, then  $\mu(G) \geq \lambda_2^s(G)$  where  $\lambda_2^s(G)$  is the smallest eigenvalue in  $L(\frac{1}{2} (G + G^T))$ .

*Proof.* Since  $e$  is an eigenvector of  $\frac{1}{2} (G + G^T)$ , we have  $\lambda_2^s(G) = \beta(G)$ . The result then follows from Theorem 2.

**Corollary 2.** If  $G \in W$  and has zero column sums, then  $\mu(G) \geq \beta(G) \geq 0$ . If in addition  $G + G^T$  is irreducible, then  $\mu(G) \geq \beta(G) > 0$ .

*Proof.* For a symmetric matrix  $X \in W$ ,  $\lambda_2(X) \geq 0$ . For a matrix  $X \in W_s$ ,  $\lambda_2(X) > 0$ . This is a consequence of Perron–Frobenius theory (see e.g., [1]). The theorem then follows from Theorem 2 and the fact that  $G + G^T \in W$ .

Next we show an upper bound for  $\mu(G)$ .

**Definition 5.** For a real matrix  $G$  with zero row sums, define  $\mu_2(G)$  as  $\mu_2(G) = \min_{\lambda \in L(G)} \operatorname{Re}(\lambda)$ , where  $\operatorname{Re}(\lambda)$  is the real part of  $\lambda$ .

**Theorem 3.** If  $G$  is a real matrix with zero row sums, then  $\mu(G) \leq \mu_2(G)$ .

*Proof.* This is a generalization of Theorem 3 in [5] and the proof is similar. Let  $\lambda \in L(G)$  with corresponding eigenvector  $v$ . Let  $U \in W_s$  be such that  $U(G - \mu I) \succeq 0$  for some real number  $\mu$ . The kernel of  $U$  is spanned by  $e$ . By definition of  $L(G)$ ,  $v$  is not in the kernel of  $U$ . Since

$(G - \mu I)v = (\lambda - \mu)v$ , this implies that  $v^*U(G - \mu I)v = (\lambda - \mu)v^*Uv$ . Positive semidefiniteness of  $U(G - \mu I)$  implies that  $\text{Re}(v^*U(G - \mu I)v) \geq 0$ . Since  $U$  is symmetric positive semidefinite and  $v$  is not in the kernel of  $U$ ,  $v^*Uv > 0$ . This implies that  $\text{Re}(\lambda) - \mu > 0$ .  $\square$

The following result may be of independent interest.

**Corollary 3.** If  $G$  is a real matrix with zero row sums, then

$$\lambda_{\min}(1/2(G + G^T)) \leq \beta(G) \leq \mu_2(G).$$

*Proof.* Follows from Theorems 2 and 3.  $\square$

Theorems 2 and 3 show that  $\beta(G) \leq \mu(G) \leq \mu_2(G)$ . Next we present two classes of matrices for which there is a closed form expression for  $\mu(G)$ .

**Theorem 4.** If  $G$  is a real normal matrix with zero row sums, then  $\beta(G) = \mu(G) = \mu_2(G)$ .

*Proof.* First note that by normality  $G$  has zero column sums (see for example [1]). Furthermore, for a real normal matrix, the eigenvalues of  $(1/2)(G + G^T)$  are just the real parts of the eigenvalues of  $G$  [9]. This implies that  $\mu_2(G) = \lambda_2^s(G)$ . The result then follows from Corollary 1 and Theorem 3.  $\square$

**Theorem 5** [5]. If  $G$  is a triangular zero row sums matrix, then  $\mu(G) = \mu_2(G)$ .

In the following section, we study via computer simulations matrices in  $\mathcal{W}$  whose values of  $\mu(G)$  are close to  $\mu_2(G)$ .

### Computing $\mu(G)$ via Semidefinite Programming

In this section, we show how  $\mu(G)$  can be computed by solving a sequence of semidefinite programming (SDP) problems.

First we note that by Theorems 2 and 3,  $\mu(G)$  can be bounded in the interval  $[\beta, \mu_2]$ . Next we show that for a fixed  $\mu$ , finding  $U \in \mathcal{W}_s$  such that  $U(G - \mu I) \succeq 0$  is a feasibility SDP problem. Clearly  $U(G - \mu I) \succeq 0$  is a linear matrix inequality. A matrix  $U$  is in  $\mathcal{W}_s$  if and only if:

1.  $U$  is symmetric
2. all off-diagonal elements of  $U$  are nonpositive
3. each row of  $U$  sums to zero
4. zero eigenvalue of  $U$  has multiplicity 1, i.e.,  $0 \notin L(G)$ .

The first three requirements can clearly be cast as matrix constraints for an SDP problem. As for the fourth requirement, it is easy to show that it is equivalent to



the linear matrix inequality  $K^T U K \succ 0$  where  $K$  is as defined in Sect. 3. To ensure that we do not get a very small  $U$ , we use the constraint  $K^T U K \succeq I$  instead. It is clear that this does not affect the value of  $\mu(G)$ . Thus the feasibility SDP problem we need to solve is

$$\begin{aligned} &\text{Find } U = U^T \text{ such that} \\ &U(G - \mu I) \succeq 0, \quad U_{cc} = 0, \quad U_{ij} \leq 0 \quad \forall i \neq j \quad \text{and} \quad -K^T U K \succeq I. \end{aligned} \quad (2)$$

Since the set of values of  $\mu$  such that  $U(G - \mu I) \succeq 0$  for some  $U \in \mathcal{W}_s$  is an interval, we can compute  $\mu(G)$  by using the bisection method to successively refine  $\mu$  and then solving the corresponding SDP problem (2). This is shown in Algorithm 1 where  $ub$  is initially set to  $\mu_2(G)$  and  $lb$  is initially set to  $\beta(G)$ .

---

**Algorithm 1** Compute  $\mu(G)$

---

```

 $\mu \leftarrow ub$ 
if Problem (2) is infeasible then
  while  $|ub - lb| > \varepsilon$  do
     $\mu \leftarrow 1/2(ub + lb)$ 
    if Problem (2) is infeasible then
       $ub \leftarrow \mu$ 
    else
       $lb \leftarrow \mu,$ 
    end if
  end while
end if
 $\mu(G) \leftarrow \mu$ 

```

---

There exists many public domain and commercial programs that can solve SDP problems. The reader is referred to [http://www-user.tu-chemnitz.de/~helmberg/sdp\\_software.html](http://www-user.tu-chemnitz.de/~helmberg/sdp_software.html) for a list. We have elected to use CSDP 4.7 [10] with the YALMIP 3 MATLAB interface (<http://control.ee.ethz.ch/~joloef/yalmip.msql>) to solve the SDP problem.

### Zero row sums matrices

Our computer results are summarized in Table 1. Zero row sums matrices of small order are generated and their values of  $\mu(G)$  are computed. For each order  $n$ , 5,000 zero row sums matrices are chosen by generating the off-diagonal elements independently from a uniform distribution in the interval  $[-1/2, 1/2]$ . The matrices are categorized into two groups depending on whether all their eigenvalues are real or

not. For each group, the mean and the standard deviation of the quantities

$$0 \leq i(G) = \frac{\mu(G) - \beta(G)}{\mu_2(G) - \beta(G)} \leq 1 \text{ and } r(G) = \frac{\mu(G)}{\mu_2(G)} \text{ are listed.}$$

order	only real eigenvalues				real and complex eigenvalues			
	$i(G)$		$r(G)$		$i(G)$		$r(G)$	
	mean	std	mean	std	mean	std	mean	std
3	0.9862	0.0621	1.0166	1.2065	0.8672	0.1724	2.1340	34.0588
4	0.9766	0.0777	1.0227	0.9181	0.5251	0.4002	0.2362	56.8556
5	0.9715	0.0809	1.0113	0.0589	0.3191	0.3353	3.0385	133.0064
10	0.9731	0.0894	1.0060	0.0214	0.1451	0.1095	-2.8780	424.5138

**Table 1.** Statistics of  $i(G) = \frac{\mu(G) - \beta(G)}{\mu_2(G) - \beta(G)}$  and  $r(G) = \frac{\mu(G)}{\mu_2(G)}$  for zero row sum matrices.

We observe quite a difference between the behavior of  $i(G)$  and  $r(G)$  for matrices with only real eigenvalues and for matrices with complex eigenvalues. In particular, we see that  $i(G)$  is close to 1 for matrices with only real eigenvalues which implies that  $\mu(G)$  is close to  $\mu_2(G)$  in this case. On the other hand, for matrices with complex eigenvalues, the statistics of  $i(G)$  show that  $\mu(G)$  is usually significantly less than  $\mu_2(G)$ .

**Matrices in  $W$**

Our computer results for matrices in  $W$  are summarized in Table 2. For each order  $n$ , 5,000 zero row sums matrices are chosen by generating the off-diagonal elements independently from a uniform distribution in the interval  $[-1,0]$ . The matrices are categorized into two groups depending on whether all their eigenvalues are real or not. For each group, the mean and the standard deviation of the quantities  $i(G)$  and  $r(G)$  are listed.

**Table 2.** Statistics of  $i(G) = \frac{\mu(G) - \beta(G)}{\mu_2(G) - \beta(G)}$  and  $r(G) = \frac{\mu(G)}{\mu_2(G)}$  matrices in  $W$ .

order	only real eigenvalues				real and complx eigenvalues			
	$i(G)$		$r(G)$		$i(G)$		$r(G)$	
	mean	std	mean	std	mean	std	mean	std
3	0.9862	0.0612	0.9984	0.0084	0.8663	0.1698	0.9777	0.0337
4	0.9816	0.0658	0.9977	0.0095	0.9196	0.1389	0.9875	0.0246
5	0.9758	0.0770	0.9971	0.0112	0.9307	0.1292	0.9901	0.0211
10	0.9818	0.0260	0.9987	0.0020	0.9333	0.1097	0.9936	0.0123

In contrast to general zero row sums matrices, the behaviors of  $\mu(G)$  for matrices in  $W$  with only real eigenvalues and for matrices in  $W$  with complex eigenvalues are similar. Furthermore,  $\mu(G)$  is very close to  $\mu_2(G)$ , especially for matrices with only real eigenvalues. It remains to be seen whether the small discrepancy between  $\mu(G)$  and  $\mu_2(G)$  is real or an artifact of the numerical algorithm.

## Conclusions

We study a quantity  $\mu(G)$  of a matrix  $G$  which characterizes the coupling topology in networks of coupled chaotic systems. This quantity is useful in determining a synchronization criterion for the network. We derive upper and lower bounds for  $M(G)$ , give closed form expressions of  $\mu(G)$  for some classes of matrices and present an algorithm for determining  $\mu(G)$  using semidefinite programming. The computer results suggest that  $\mu(G)$  is close to the upper bound  $\mu_2(G)$  when

1.  $G \in W$  or
2.  $G$  is a zero row sums matrix with only real eigenvalues.

An interesting question for further investigation is what are the (non-normal) matrices for which  $\beta = \mu_2$ ?

Finally, we would like to point out that for the case of dynamic coupling topology ( $G = G(t)$  is a matrix that changes with time), the quantity  $\beta(G(t))$  is useful in characterizing the synchronization properties [11].

## References

- [1] C.W. Wu, L.O. Chua, "Synchronization in an array of linearly coupled dynamical systems", *IEEE Trans. Circ. and Syst.-I* 42 (1995) 430–447
- [2] L. Pecora, T. Carroll, G. Johnson, D. Mar, K.S. Fink, "Synchronization stability in coupled oscillator arrays: solution for arbitrary configurations", *Int. J. of Bifurcat. Chaos* 10 (2000) 273–290
- [3] C.W. Wu, "Synchronization in coupled chaotic circuits and systems", *World Scientific* (2002)
- [4] X.F. Wang, G. Chen, "Synchronization in small-world dynamical networks", *Int. J. Bifurcat. and Chaos* 12 (2002) 187–192
- [5] C.W. Wu, "Synchronization in coupled arrays of chaotic oscillators with nonreciprocal coupling", *IEEE Trans. Circuit and Syst.-I* 50 (2003) 294–297
- [6] C.W. Wu, "Synchronization in networks of nonlinear dynamical systems coupled via a directed graph", *Nonlinearity* 18 (2005) 1057–1064
- [7] C.W. Wu, "Synchronization in arrays of coupled nonlinear systems with delay and nonreciprocal time-varying coupling", *IEEE Trans. Circuit Syst.-II* 53 (2005) 282–286
- [8] C.W. Wu, "Perturbation of coupling matrices and its effect on the synchronizability in arrays of coupled chaotic circuits", *Physics Letters A* 319 (2003) 495–503
- [9] R.A. Horn, C.R. Johnson, *Matrix analysis*, Cambridge University Press (1985)

- [10] B. Borchers, CSDP: a C library for semidefinite programming. *Optimal Methods and Software* 11 (1999) 613–623 (<http://www.nmt.edu/~borchers/csdp.html>)
- [11] C.W. Wu, “Algebraic connectivity of directed graphs”, *Linear and Multilinear Algebra* 53 (2005) 203–223

# Rigorous Study of Chua's Circuit in Terms of Periodic Orbits

Z. Galias

AGH — University of Science and Technology, al. Mickiewicza 30, 30-059  
Krakow, Poland, galias@agh.edu.pl, <http://zet.agh.edu.pl/~galias>

## Abstract

In this work, we carry out a rigorous analysis of Chua's circuit in terms of short periodic orbits. The circuit is considered with parameter values for which the Roessler type attractor is observed. A very narrow enclosure of the set enclosing the attractor is found and all short periodic orbits embedded within the numerically observed attractor are located. A comparison with nonrigorous technique for detection of periodic orbits using the method of close returns is also presented.

## Introduction

The existence and exact positions of periodic orbits are key properties in analysis of nonlinear systems and in many applications. In this work, we describe and compare two methods for detection of periodic orbits in chaotic systems. The first one is a nonrigorous method based on the search for pseudoperiodic points, while the second one is an interval arithmetic method allowing to rigorously find all short cycles.

In Sect. 3 results of finding periodic orbits using a combination of the method of close returns and the Newton method are presented. In Sect. 4 we describe a rigorous method for finding all low-period cycles and its application for the Chua's circuit. We also compare the results obtained with these two methods.

## Chua's Circuit

The Chua's circuit [1] is a simple third-order piecewise linear electronic circuit exhibiting very complex trajectories. It is defined by the set of equations

$$\begin{aligned}
 C_1 \dot{x}_1 &= (x_2 - x_1) / R - g(x_1), \\
 C_2 \dot{x}_2 &= (x_2 - x_1) / R + x_3, \\
 L \dot{x}_3 &= -x_2 - R_0 x_3,
 \end{aligned}
 \tag{1}$$

where  $g(z) = G_b z + 0.5(G_a - G_b)(|z+1| - |z-1|)$  is a three segment piecewise linear characteristics. The circuit is studied with the following parameter values (after parameter rescaling)  $C_1 = 1$ ,  $C_2 = 7.65$ ,  $G_a = -3.4429$ ,  $G_b = -2.1849$ ,  $L = 0.06913$ ,  $R = 0.33065$ ,  $R_0 = 0.00036$ , for which the Roessler-type attractor is observed in computer simulations (compare Fig. 1a).

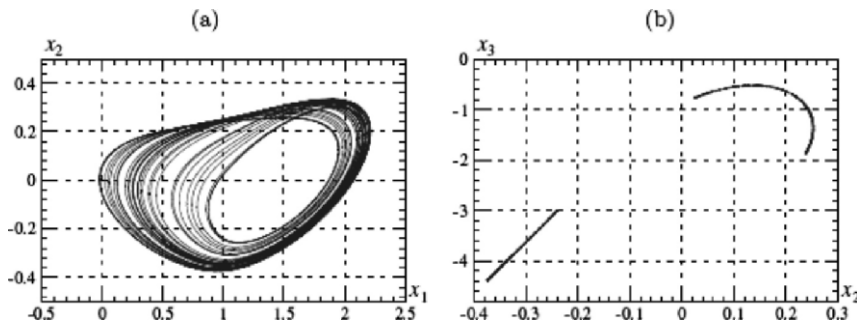


**Fig. 1.** Computer simulations of Chua’s circuit, (a) Roessler-type attractor, (b) trajectory of the Poincaré map defined by the hyperplane  $\Sigma_2 = \{x: x_1 = 1\}$

The state space  $\mathfrak{R}^3$  can be divided into three open regions  $U_1 = \{x \in \mathfrak{R}^3 : x_1 < -1\}$ ,  $U_2 = \{x : |x_1| < 1\}$ , and  $U_3 = \{x : x_1 > 1\}$  separated by planes  $\Sigma_1 = \{x: x_1 = -1\}$  and  $\Sigma_2 = \{x: x_1 = 1\}$ . In the regions  $U_i$ , the system is linear, the state equation can be written as:  $\dot{x} = A_i(x - p_i)$  where  $A_i \in \mathfrak{R}^{3 \times 3}$ ,  $p_i \in \mathfrak{R}^3$  and the solution has the form

$$\varphi(t, x) = e^{A_i t}(x - p_i) + p_i .$$

In the analysis of the Chua’s circuit we use the technique of the Poincaré map. We study the Poincaré map  $P: \Sigma_2 \mapsto \Sigma_2$  defined as:

$$P(x) = \varphi(\tau(x), x) ,
 \tag{2}$$

where  $\varphi(t, x)$  is the trajectory of the system based at  $x$ , and  $\tau(x)$  is the time needed for the trajectory  $\varphi(t, x)$  to reach  $\Sigma_2$ . An example trajectory of  $P$  is shown in Fig. 1b.

For piecewise linear systems the planes separating linear regions are the most natural choice for the hyperplanes defining the Poincaré map. For the parameter values considered the Poincaré map is continuous on the attractor, which makes it possible to rigorously find all short period cycles.

## Detection of Short Periodic Orbits

As the first method for detection of periodic orbits we use a combination of the method of close returns and the Newton method. Periodic orbits of  $P$  are three extracted using the *method of close returns* [2]. We monitor a trajectory  $(y_i)$  and look for  $\delta$ -pseudoperiodic orbits, i.e., for points  $y_i$  such that  $\|y_{i+p} - y_i\| \leq \delta$ , where  $\delta$  is a small positive real number.

The performance of the method of close returns used for finding all low-period cycles depends on the way we treat pseudoperiodic orbits that are close to each other. A criterion to distinguish different orbits is based on the computation of distance between two pseudoperiodic orbits

$$\text{dist} \left( (x_i)_{i=0}^{p-1}, (y_i)_{i=0}^{p-1} \right) = \min_{0 \leq i < p} \max_{0 \leq j < p} \|x_{(i+j) \bmod p} - y_j\| .$$

If we find a new pseudoperiodic orbit  $(x_0, x_1, \dots, x_{p-1})$  of length  $p$  we compute its distance from all pseudoperiodic orbits of the same length already found. If the minimum distance is smaller than  $\varepsilon$ , where  $\varepsilon$  is a fixed positive real number, we skip the new pseudoperiodic orbit.

The method of close returns is a very good technique for detection of periodic orbits from experimental data. The quality of pseudoperiodic orbits obtained using this method is however low, i.e.,  $\delta$  is usually large. In theory we could choose arbitrarily small value of  $\delta$  to locate all periodic orbits embedded within a chaotic attractor. The main drawback of using very small  $\delta$  is that we would have to wait very long to find any pseudoperiodic orbit.

In case we have access to the equations defining the dynamical system we can use this information to improve approximation of the periodic orbit. One of the options is to use the Newton method. The Newton method is an iterative method for finding zeros of an  $n$ -dimensional function  $f: \mathfrak{R}^n \mapsto \mathfrak{R}^n$ . Starting from the initial point  $x_0$  we compute successive approximations using the formula:

$$x_{k+1} = x_k - f'(x_k)^{-1} f(x_k) ,$$

where  $f'(x_k)$  is the Jacobian matrix of  $f$  evaluated at  $x_k$ . The Newton method has a quadratic convergence provided that the initial point is chosen close enough to the zero of  $f$ .

The Newton method can be used for finding period- $p$  orbits of  $f$  by applying the Newton operator to the map  $F: \mathfrak{R}^{np} \mapsto \mathfrak{R}^{np}$  defined by

$$[F(z)]_k = x_{(k+1) \bmod p} - f(x_k) \quad \text{for } 0 \leq k < p$$

where  $z = (x_0, \dots, x_{p-1})$ .  $F(z) = 0$  if and only if  $x_0$  is a fixed point of  $f^p$ . This approach gives better results than searching for zeros of the map  $\text{id} - f^p$ .

The method for detection of periodic orbits of  $P$  up to length  $m$  consists of the following steps. For successive iterations  $y_i$  of  $P$ , we compute the distance between  $y_i$  and the previous iterations  $y_{i-p}$  for  $p = 1, 2, \dots, m$ . If for a given  $p$  the distance  $\|y_i - y_{i-p}\|$  is smaller than  $\delta$  we use the Newton method to improve approximation

of the position of the periodic orbit starting from  $(x_j)_{j=0}^{p-1}$ , where  $x_j = y_{i-p+j}$  for  $j = 0, \dots, p - 1$ . If the Newton method does not converge the pseudoperiodic orbit is skipped. Next we compute the distance between this periodic orbit and periodic orbits of the same length found before. If the minimum distance is smaller than  $\varepsilon$  the pseudoperiodic orbit is skipped. The orbit is also skipped if we suspect that  $p$  is not the minimum period, i.e., if

$$\min_{0 \leq l < k} \max_{0 \leq i < p} \|x_{(i+l) \bmod p} - x_{i \bmod k}\| < \varepsilon,$$

for some  $k$  such that  $p \mid k$ . Otherwise, we record the periodic orbit as a new one. This technique has been applied for search of periodic orbits of length  $p \leq 30$  of the Poincaré map  $P$  associated with the Chua's circuit. In the search process we have used  $\delta = 0.03$  for detection of pseudoperiodic orbits and  $\varepsilon = 0.001$  for elimination of close orbits. The trajectory of the Poincaré map composed of 10,000 points was generated. 38013  $\delta$ -pseudoperiodic orbits were found. The last orbit was found for the iteration  $i = 5024$ . For the remaining iterations no new periodic orbits were found. This indicates that probability of locating all periodic orbits with period  $p \leq 30$  is high.

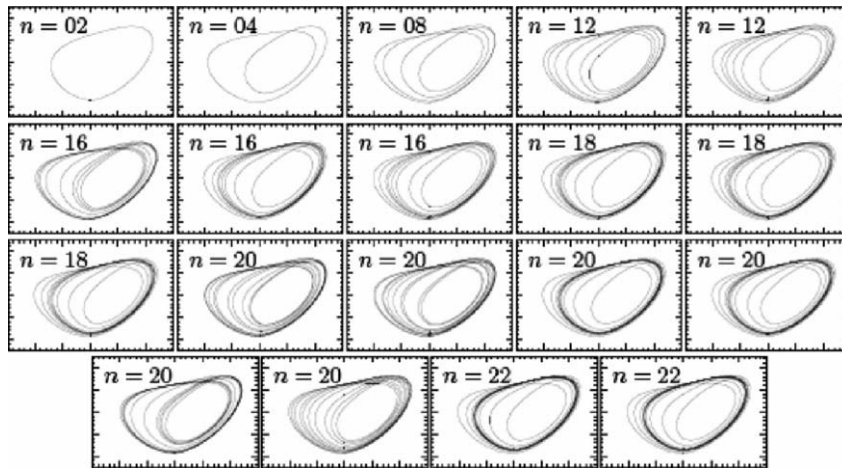


Fig. 2. Short periodic orbits of the Chua's circuit

Periodic orbits with length  $n \leq 22$  are shown in Fig. 2. The results are collected in Table 1. We report the starting point  $x_0$ , the maximum distance

$$\delta' = \max_{0 \leq i < tn} |P(x_{(i+1) \bmod n}) - x_i|$$

after improving the approximation using the Newton method, the distance  $d$  to the closest orbit found before and number  $s$  of periodic orbits that were skipped in the search process as they were located close to a given orbit. This parameter tells us how frequently trajectories visit the neighborhood of a given orbit.

A periodic orbit may be not found if either it is located in the part of the attractor which is visited very rarely or what is more likely the orbit is located close to



another orbit, i.e., we have chosen too large  $\varepsilon$ . On the other hand decreasing  $\varepsilon$  may produce many spurious orbits. For example, when  $\varepsilon = 10^{-5}$  was used the procedure found two period-2 orbits, and two period-4 orbits, while we know from the results obtained in the next section that there is only one period-2 and one period-4 orbit.

We cannot say whether all orbits found are true different periodic orbits. For example it is likely that the second of the period-18 orbits found corresponds in fact to the same orbit as the first one. In the next section we verify the results obtained here with the results of rigorous computations. We confirm that for  $p \leq 16$  all orbits are found correctly, and no spurious orbits are detected. It however remains unknown whether the results obtained for  $p > 16$  are correct.

**Table 1.** Periodic orbits of the Poincaré map found using the method of close returns combined with the Newton method,  $Q_p$  — the number of period- $p$  cycles found, see explanations in the text

$p$	$Q_p$	$x_0$	$\delta'$	$s$	$d$
2	1	(1, -0.3461301, -4.091637)	$5.333 \cdot 10^{-15}$	1643	
4	1	(1, -0.3687684, -4.309752)	$3.783 \cdot 10^{-15}$	2215	
8	1	(1, -0.3717717, -4.348158)	$5.344 \cdot 10^{-15}$	1363	
12	2	(1, -0.373035, -4.355357)	$4.910 \cdot 10^{-15}$	1441	
		(1, -0.3733681, -4.363451)	$7.116 \cdot 10^{-15}$	1088	0.239
16	3	(1, -0.3691527, -4.322555)	$5.333 \cdot 10^{-15}$	730	
		(1, -0.3598914, -4.230372)	$4.475 \cdot 10^{-15}$	943	0.625
		(1, -0.3496305, -4.110303)	$6.222 \cdot 10^{-15}$	1087	0.163
18	3	(1, -0.3746798, -4.374072)	$1.248 \cdot 10^{-14}$	1599	
		(1, -0.35243, -4.1553221)	$7.572 \cdot 10^{-15}$	1	0.00198
		(1, -0.3745622, -4.374266)	$1.603 \cdot 10^{-14}$	1403	0.0688
20	6	(1, -0.3663728, -4.295061)	$7.119 \cdot 10^{-15}$	409	
		(1, -0.3677206, -4.308418)	$1.868 \cdot 10^{-14}$	515	0.273
		(1, -0.3528742, -4.159789)	$1.246 \cdot 10^{-14}$	551	0.606
		(1, -0.3735302, -4.364973)	$5.352 \cdot 10^{-15}$	429	0.335
		(1, -0.3738581, -4.364436)	$7.167 \cdot 10^{-15}$	527	0.195
		(1, -0.3450963, -4.081265)	$1.068 \cdot 10^{-14}$	577	0.131
22	2	(1, -0.3526614, -4.157643)	$1.158 \cdot 10^{-14}$	482	
		(1, -0.3744092, -4.372982)	$1.022 \cdot 10^{-14}$	526	0.101
24	9				
26	7				
28	18				
30	12				

## Study of Periodic Orbits with Interval Methods

Here, we validate the results obtained in the previous section using the interval methods. For rigorous evaluation of  $P$  and its Jacobian we use analytical formulas for solutions of linear systems (see [3] for details).

We start the rigorous analysis by finding a positively invariant set  $A$  (i.e., a set such that  $P(x) \in A$  for all  $x \in A$ ) containing the numerically observed attractor. We have proved that the set  $A$  shown in Fig. 3 is positively invariant. This was done by covering the region  $A$  by a number of boxes, computing image of each box, and checking that all images are enclosed in  $A$ .

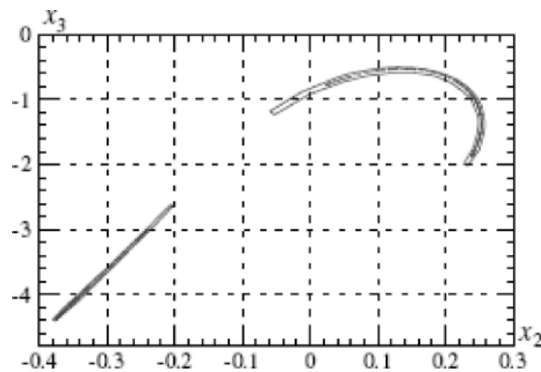


**Fig. 3.** A positively invariant set enclosing the numerically observed attractor

In the second step, we find the graph representation of the dynamics of the system in the trapping region (see also [4]). The trapping region is covered by  $\varepsilon$ -boxes, i.e., sets of the form  $v = [k_1 \varepsilon_1, (k_1+1) \varepsilon_1] \times [k_2 \varepsilon_2, (k_2+1) \varepsilon_2]$ , where  $k_i$  are integer numbers,  $\varepsilon_i$  are fixed positive real numbers, and  $\varepsilon = (\varepsilon_1, \varepsilon_2)$ . In the following computations we use the covering of  $A$  composed of 11891  $\varepsilon$ -boxes with  $\varepsilon = (0.000125, 0, 0003125)$ .

Next, the set  $E = \{(v_i, v_j) : P(v_i) \cap v_j \neq \emptyset\}$  of nonforbidden transitions between these boxes is found. It was checked that for the covering considered  $\#E = 67485$ .

Using the graph representation we can find all low-period cycles of the Poincaré map (see [5] for details). We start by finding all period- $p$  cycles in the graph. In order to study the existence of periodic orbits corresponding to this cycle we use the Hansen–Sengupta operator  $H$ , which is a standard interval tool for proving the existence of zeros of nonlinear maps (compare [6]). We evaluate the interval operator  $H$  on the interval vector  $z$ , corresponding to the cycle under study. If  $z \cap H(z) = \emptyset$  then there is no period- $n$  orbits in  $z$ . If  $H(z) \subset z$  then there is exactly one period- $n$  orbit inside  $z$ .

Using the procedure described earlier we have found all periodic orbits of  $P$  with period  $p \leq 16$ . The results are collected in Table 2. One should notice that there are no periodic orbits with period 6, 10, and 14.

**Table 2.** Number of periodic orbits of the Poincaré map found using interval methods,  $Q_p$  is the number of period- $p$  cycles

$p$	2	4	6	8	10	12	14	16
$Q_p$	1	1	0	1	0	2	0	3

These results confirm that the nonrigorous method discussed in the first part of this paper correctly detects all periodic orbits up to period 16. We were however not able to check the results obtained for longer periods due to very long computation time needed to complete the full search for periodic orbits in the trapping region.

## Conclusions

In this paper we have described two methods for detection of periodic orbits in chaotic systems. As an example, we have used these methods for finding short periodic orbits for the Chua's circuit.

We have shown that the method of close returns combined with the Newton method is capable of detecting all low-period cycles. Its main advantage is that it is an easy to implement general method, which can be used for a broad class of nonlinear systems.

We have also described a rigorous method for studying the existence of periodic orbits in piecewise linear systems. The main assumptions for the method to work is that the Poincaré map is continuous in the region containing the numerically observed attractor. With this assumption it is possible to find all low-period cycles for the system.

For the Chua's circuit, we have found a trapping region for the Poincaré map and all periodic orbits with period  $n \leq 16$  enclosed in the trapping region. These results have been used to validate the results obtained by the first method.

## Acknowledgments

This work was sponsored in part by KBN, grant no. 2P03A 041 24, and by the AGH University of Science and Technology, grant no. 10.10.120.133.

## References

- [1] L. Chua, G. Lin, “Canonical realisation of Chua’s circuit family”, *IEEE Trans. Circ. Syst. CAS-37* (1990) 885–902
- [2] D. Lathrop, E. Kostelich, “Characterisation of an experimental strange attractor by periodic orbits”, *Phys. Rev. A* 40 (1989) 4028–4031
- [3] Z. Galias, “Positive topological entropy of Chua’s circuit: A computer assisted proof”, *Int. J. Bifurcation and Chaos* 7 (1997) 331–349
- [4] M. Dellnitz, A. Hohmann, “A subdivision algorithm for the computation of unstable manifolds and global attractors”, *Numerische Mathematik* 75 (1997) 293–317
- [5] Z. Galias, “Counting low-period cycles for flows”, accepted for publication in *Int. J. Bifurcation and Chaos* (2005)
- [6] A. Neumaier, *Interval Methods for Systems of Equations*, Cambridge University Press, New York (1990)

# Complex Behavior and its Analysis in Chaotic Circuits Networks with Intermittency

Y. Uwate<sup>1</sup>, Y. Nishio<sup>1</sup> and A. Ushida<sup>2</sup>

<sup>1</sup>Department of Electrical and Electronic Engineering, Tokushima University, Tokushima 770-8506 Japan.

<sup>2</sup>Department of Mechanical–Electronic Engineering, Tokushima Bunri University, Sanuki 769-2193 Japan.

## Abstract

In this study, a complex behavior in a ring of chaotic circuits related with intermittency is investigated. When each chaotic circuit generates three-periodic solution, various different types of synchronization states are observed. However, if a control parameter of each chaotic circuit is varied to generate intermittency chaos near the three-periodic window, intermittency bursts interrupt the synchronizations and different synchronizations reappear after the bursts settle down.

## Introduction

Synchronization and the related bifurcation of coupled chaotic networks are good models to describe various higher-dimensional nonlinear phenomena in the field of natural science. In particular, the breakdown of chaos synchronization has attracted many researchers' attentions and their mechanisms have been gradually made clear [1–5]. However, a lot of phenomena around chaos synchronization are still veiled as well as other nonlinear problems. Hence, in order to understand and exploit such phenomena, it is important to discover them, to model them, and to investigate them.

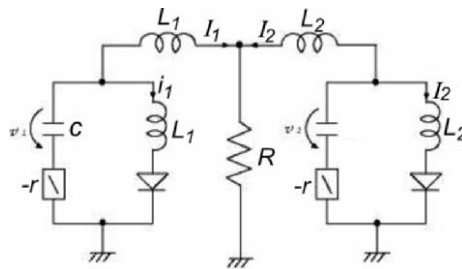
On the other hand, intermittency chaos [6] is deeply related to the edge of chaos [7] and many people suggest that such a behavior between order and chaos gains better performance for various kinds of information processing than fully developed chaos. Therefore, we consider that unveiling various roles of the intermittency chaos is important to exploit it for future engineering applications.

In this study, a complex behavior in a ring of chaotic circuits related with intermittency is investigated. At first, we analyze behavior in a basic system of two coupled chaotic circuits. Next, we observe more complex behavior when the two coupled chaotic circuits are expanded to a ring of chaotic circuits. In that case, we observe various different types of synchronization states when each chaotic

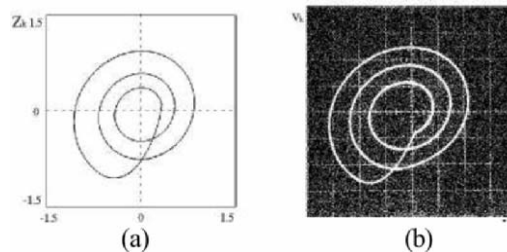
circuit generates three-periodic solution. And, we vary a control parameter of each chaotic circuit to generate intermittency chaos near the three-periodic window. So, we can observe a complex behavior of the various synchronization states. Namely, intermittency bursts interrupt the synchronizations and different synchronizations reappear after the bursts settle down.

## Basic Coupled Circuit

Figure 1 shows the basic coupled circuit. Each subcircuit is three-dimensional autonomous one and consists of three memory elements, one linear negative resistor and one diode. We can regard the diodes as pure resistive elements, because operation frequency is not too high. Figure 2 shows three-periodic attractor observed from each subcircuit.



**Fig. 1.** Basic coupled circuit



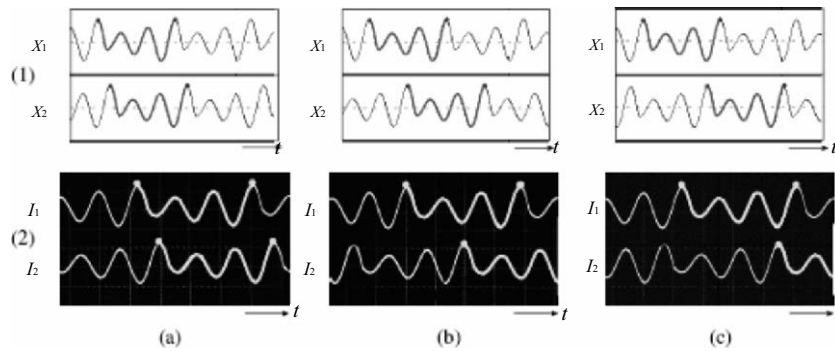
**Fig. 2.** Three-periodic attractor observed from each subcircuit. **(a)** Computer calculated result.  $x_k$  vs.  $z_k$ .  $\alpha = 7.0$ ,  $\beta = 0.152$ ,  $\gamma = 0.0$ , and  $\delta = 100.0$ . **(b)** Circuit experimental result  $I_k$  vs.  $v_k$ .  $L_1 = 300$  mH,  $L_2 = 10$  mH,  $C = 33$  nF,  $r = 740$   $\Omega$  and  $R = 0.0$   $\Omega$

Figure 3(1) shows that three different types of synchronization states, when the two circuits generating the three-periodic attractors are coupled. These three synchronization states can be obtained by giving different initial conditions. As we can see from the figures, the two circuits tend to be synchronized in antiphase. This is because the states minimizing the energy consumed by the coupling resistor  $R$  correspond to stable synchronization states. For three-periodic solutions

there exist three different peaks in the waveform. Hence, three different synchronization states can coexist as shown in Fig. 3 (1).

We also confirm the generation of the three different synchronization states in circuit experiments as shown in Fig. 3(2).

Next, we vary a control parameter of each subcircuit to generate intermittency chaos near the three-periodic window as shown in Fig. 4.



**Fig. 3.** Time waveforms of three synchronization states. (1) Computer calculated results.  $\alpha = 7.0, \beta = 0.152, \gamma = 0.005$  and  $\delta = 100.0$ . (2) Circuit experimental results.  $L_1 = 300$  mH,  $L_2 = 10$  mH,  $C = 33$  nF,  $r = 740 \Omega$  and  $R = 40.0 \Omega$ . (a) State  $T_1$ . (b) State  $T_2$ . (c) State  $T_3$ .

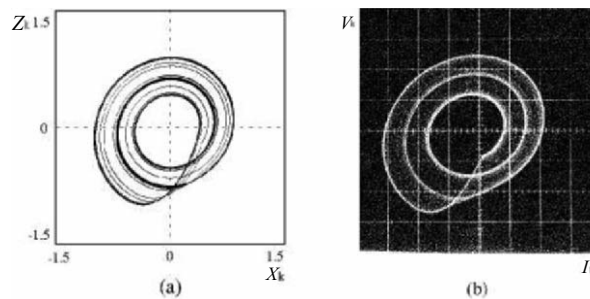


**Fig. 4.** Intermittency chaos near the three-periodic window. (a) Computer calculated result.  $x_k$  vs.  $z_k$ .  $\alpha = 7.0, \beta = 0.133682, \gamma = 0.0$  and  $\delta = 100.0$ . (b) Circuit experimental result.  $I_k$  vs.  $v_k$ .  $L_1 = 300$  mH,  $L_2 = 10$  mH,  $C = 33$  nF,  $r = 735 \Omega$  and  $R = 0.0 \Omega$ .

If we couple the two chaotic circuits when the intermittency chaos appear, we can observe a complex behavior of the three synchronization states. Namely, intermittency bursts disturb the synchronizations and different synchronizations appear and disappear in a chaotic way.

In order to investigate the complex phenomenon, we define the Poincaré section as  $z_1 = 0$  and  $x_1 < 0$ . The data of  $x_1$  on the Poincaré map is denoted as  $\hat{x}_1$ .

Further we plot the discrete data of  $\hat{x}_2$  on the Poincaré map when  $\hat{x}_1$  is smaller than  $-1.2$ . This threshold is introduced in order to extract only the data when  $\hat{x}_1$  takes the largest peak (bullets in the waveform in Fig. 3). Figure 5(a) shows the discrete data of  $\hat{x}_2$  obtained by the above-mentioned method. We can see that the synchronization states are interrupted by the intermittent bursts and different synchronization states reappear after the bursts settle down. Although the results can not be shown in the same manner, we also confirmed the same phenomenon in the circuit experiments. The changing of the synchronization states can be shown in a picture as Fig. 5b.

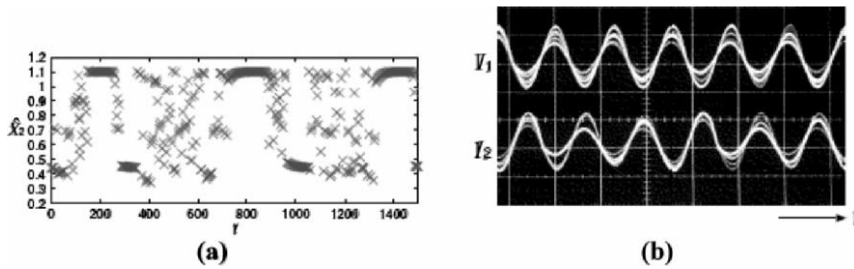


**Fig. 5.** Time series of synchronization states disturbed by intermittency chaos. (a) Computer calculated results.  $\alpha = 7.0$ ,  $\beta = 0.133682$ ,  $\gamma = 0.005$  and  $\delta = 100.0$ . (b) Circuit experimental results.  $L_1=300$  mH,  $L_2=10$  mH,  $C=33$  nF,  $r=735$   $\Omega$  and  $R = 40.0$   $\Omega$

### Ring of Chaotic Circuits

In this section, we consider a ring of the circuits as shown in Fig. 6. In this circuit adjacent two subcircuits are coupled by one resistor  $R$ . Because such coupling systems tend to minimize the energy consumed by the coupling resistors, every two adjacent subcircuits tend to synchronize with antiphase.

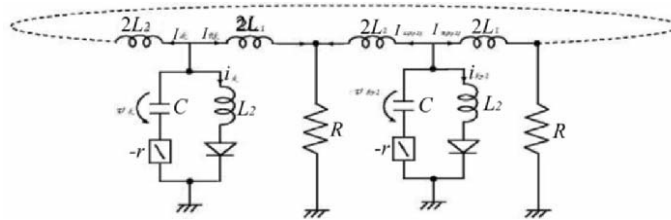


**Fig. 6.** Ring of chaotic circuits



At first, the  $i$ - $v$  characteristics of the diodes are approximated by two-segment piecewise-linear functions as

$$v_d(i_k) = 0.5(r_d i_k + E - |r_d i_d - E|). \quad (1)$$

By changing the variables and parameters:

$$\begin{aligned} I_{Rk} &= \sqrt{\frac{C}{L_1}} E x_{Rk} \quad I_{Lk} = \sqrt{\frac{C}{L_1}} E x_{Lk} \quad i_k = \sqrt{\frac{C}{L_1}} E y_k \quad v_k = E z_k, \\ t &= \sqrt{L_1 C} \tau \quad \alpha = \frac{L_1}{L_2} \beta = r \sqrt{\frac{C}{L_1}} \quad \gamma = R \sqrt{\frac{C}{L_1}} \quad \delta = r_d \sqrt{\frac{C}{L_1}}, \end{aligned} \quad (2)$$

the normalized circuit equations are given as:

$$\left\{ \begin{aligned} \frac{dx_{Rk}}{d\tau} &= \frac{1}{2} \left\{ \beta(x_{Rk} + x_{Lk} + y_k) - z_k - \gamma(x_{Rk} + x_{L(k+1)}) \right\}, \\ \frac{dx_{Lk}}{d\tau} &= \frac{1}{2} \left\{ \beta(x_{Rk} + x_{Lk} + y_k) - z_k - \gamma(x_{Lk} + x_{R(k+1)}) \right\}, \\ \frac{dy_k}{d\tau} &= \alpha \left\{ \beta(x_{Rk} + x_{Lk} + y_k) - z_k - f(y_k) \right\}, \\ \frac{dz_k}{d\tau} &= x_{Rk} + x_{Lk} + y_k, \end{aligned} \right. \quad (k = 1, 2, 3, \dots, N), \quad (3)$$

where

$$f(y_k) = 0.5(\delta y_k + 1 - |\delta y_k - 1|) \quad (4)$$

and

$$x_{LN} = x_{L1}, \quad x_{R0} = x_{RN} \quad (5)$$

Note that when the coupling parameter  $\gamma$ , which is in proportion to  $R$ , is equal to zero, the coupling term in (3) vanishes. For all of computer calculations, the fourth-order Runge–Kutta method is used with step size  $h = 0.005$ .

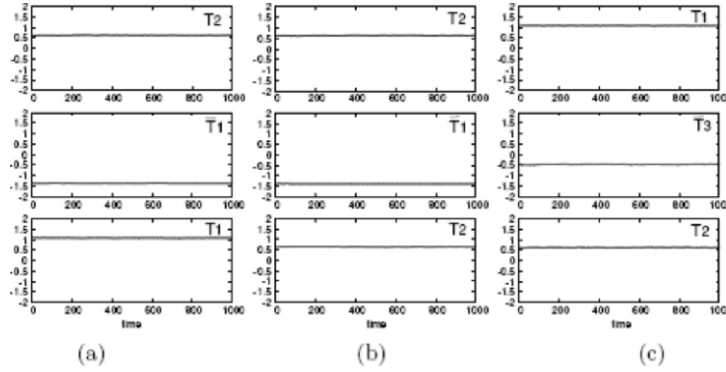


**Fig. 7.** Various different types of synchronization states (computer calculated results).  $\alpha=7.0$ ,  $\beta=0.16$ ,  $\gamma=0.005$  and  $\delta=50.0$ .

Upper figures:  $\hat{x}_{R2} + \hat{x}_{L2}$  Middle figures:  $\hat{x}_{R3} + \hat{x}_{L3}$ . Lower figures:  $\hat{x}_{R4} + \hat{x}_{L4}$

At first, we carried out computer simulations for the case of  $N = 4$ . When each chaotic circuit generates three-periodic solution, we observed various different types of synchronization states by changing initial values. Figure 7 shows three examples of the synchronization states. In the figure, the upper figures show the data of  $\hat{x}_{R2} + \hat{x}_{L2}$ , when  $\hat{x}_{R1} + \hat{x}_{L1}$  is smaller than  $-1.2$ . The middle and the lower figures are  $\hat{x}_{R3} + \hat{x}_{L3}$  and  $\hat{x}_{R4} + \hat{x}_{L4}$ , respectively. Namely, each figure shows the synchronization state of the circuits, when  $\hat{x}_{R1} + \hat{x}_{L1}$  is defined as the reference signal. As shown in Fig. 3, the two coupled circuits have three different synchronization states ( $T_1$ ,  $T_2$ , and  $T_3$ ). Because this feature remains in the case of the ring, we can confirm the generation of various different synchronization patterns characterized by combinations of  $T_1$ ,  $T_2$ , and  $T_3$ . For example, the upper figure in Fig. 7a shows that the synchronization state between the reference circuit and the second circuit is  $T_2$  (see Fig. 3b). Note that the synchronization state between the reference circuit and the third circuit is inverted, because this type of coupling makes the adjacent circuits to be synchronized at antiphase. In the case of  $N = 4$ , we can say that there exist  $3^{4-1} = 27$  synchronization patterns in the ring.

Next, we vary a control parameter of each chaotic circuit to generate intermittency chaos near the three-periodic window. We can observe a complex behavior of the various synchronization state in a ring of chaotic circuits when the intermittency chaos appear. Figure 8 shows that the frozen synchronization patterns in Fig. 7 are disturbed by intermittency chaos and different patterns appear and reappear in a chaotic way.

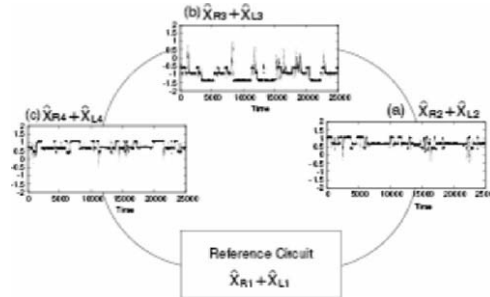


**Fig. 8.** Time series of synchronization states disturbed by intermittency chaos for  $N = 4$ .  $\alpha = 7.0$ ,  $\beta = 0.152$ ,  $\gamma = 0.005$  and  $\delta = 50.0$ . (a)  $\hat{x}_{R2} + \hat{x}_{L2}$ . (b)  $\hat{x}_{R3} + \hat{x}_{L3}$ . (c)  $\hat{x}_{R4} + \hat{x}_{L4}$ .

Next, we consider the case of  $N = 8$ . In this case,  $3^{8-1} = 2,187$  different synchronization patterns coexist, when each chaotic circuit generates three-periodic window. We can confirm that the complex phenomena changing a large number of synchronization patterns are generated in the ring (see Fig. 9).

This feature would be expanded to the ring with  $N$  chaotic circuits for any even  $N$ . In that case, we could observe the complex phenomena changing  $3^{(N-1)}$  different synchronization patterns.

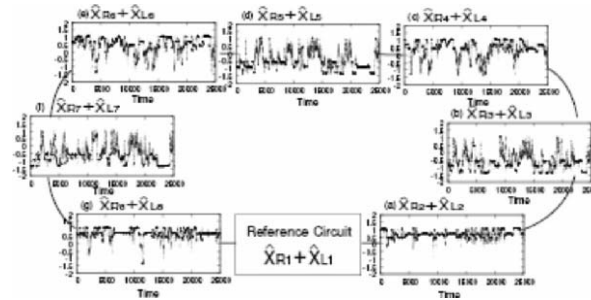


**Fig. 9.** Time series of synchronization states disturbed by intermittency chaos for  $N = 8$ .  $\alpha = 7.0$ ,  $\beta = 0.152$ ,  $\gamma = 0.005$  and  $\delta = 50.0$ . (a)  $\hat{x}_{R2} + \hat{x}_{L2}$ . (b)  $\hat{x}_{R3} + \hat{x}_{L3}$ . (c)  $\hat{x}_{R4} + \hat{x}_{L4}$ . (d)  $\hat{x}_{R5} + \hat{x}_{L5}$ . (e)  $\hat{x}_{R6} + \hat{x}_{L6}$ . (f)  $\hat{x}_{R7} + \hat{x}_{L7}$ . (g)  $\hat{x}_{R8} + \hat{x}_{L8}$

### Conclusions

In this study, we investigated a complex behavior in a ring of coupled chaotic circuits related with intermittency chaos near the three periodic window. We confirmed that the intermittency bursts interrupt the synchronization states and different synchronization patterns reappear after the bursts settle down.

## Remark

We have proposed the modeling of the complex behavior in the two coupled chaotic circuits related with intermittency using a first-order Markov chain with four states. By computer simulations, we have confirmed the results obtained from the Markov chain model agree very well [8]. Furthermore, we consider that the switchings of the synchronization states in the complex behavior are caused by intermittency bursts of each chaotic circuit. Hence, we modeled the complex behavior by using one-dimensional map derived from the subcircuit and occurrence probabilities of different synchronization states [9].

## References

- [1] N. Platt, E.A. Spiegel and C. Tresser, "On-Off Intermittency: A Mechanism for Bursting," *Phys. Rev. Lett.*, vol. 70, no. 3, pp. 279–282, 1993
- [2] E. Ott and J.C. Sommerer, "Blowout Bifurcations: the Occurrence of Riddled Basins and On-Off Intermittency," *Phys. Lett.* vol. A, 188, pp. 39–47, 1994
- [3] P. Ashwin, J. Buescu and I. Stewart, "Bubbling of Attractors and Synchronisation of Chaotic Oscillators," *Phys. Lett.* vol. A, 193, pp. 126–139, 1994
- [4] T. Kapitaniak and L.O. Chua, "Locally-Intermingled Basins of Attraction in Coupled Chua's Circuits," *Int. J. Bifurcation & Chaos*, vol. 6, no. 2, pp. 357–366, 1996
- [5] M. Wada, Y. Nishio and A. Ushida, "Analysis of Bifurcation Phenomena on Two Chaotic Circuits Coupled by an Inductor," *IEICE Trans. Fundamentals*, vol. E80-A, no. 5, pp. 869–875, May 1997
- [6] Y. Pomeau and P. Manneville, "Intermittent Transition to Turbulence in Dissipative Dynamical Systems," *Comm. Math. Phys.*, vol. 74, pp. 189–197, 1980
- [7] C.G. Langton, "Computation at the Edge of Chaos: Phase Transitions and Emergent Computation," *Physica D*, vol. 42, pp. 12–37, 1990
- [8] Y. Uwate and Y. Nishio, "Complex Behavior in Coupled Chaotic Circuits Related with Intermittency", *Proceedings of International Symposium on Nonlinear Theory and its Applications (NOLTA'04)*, pp. 589–592, Nov. 2004
- [9] Y. Uwate and Y. Nishio, "Modeling Using 1-D Map of Complex Behavior in Coupled Chaotic Circuits with Intermittency", *Proceedings of European Conference on Circuit Theory and Design (ECCTD'05)*, August 2005

# Bifurcations in Noisy Nonlinear Networks and Systems

W. Mathis

TET, Department of Electrical Engineering and Computer Science, University of Hannover, 30167 Hannover, Germany, mathis@tet.uni-hannover.de

## Abstract

In this paper, we discuss the analysis of noisy nonlinear systems and circuits. Especially we consider circuits with an oscillatory behavior and limit cycles, respectively. Moreover, we study the Andronov–Hopf bifurcation in sinusoidal electrical oscillators under noisy disturbance. For this purpose the deterministic description of oscillators must be generalized using the concept of probability functions as well as invariant measures. It turns out that these two bifurcation approaches are not equivalent in general. We illustrate these noisy bifurcation concepts by means of a Meissner oscillator including a transistor.

## Introduction

Although noise is of interest in all classes of nonlinear circuit this subject was studied during the last few years very intensively in the case of oscillator circuits. It is known that oscillators belong to the earliest electronic circuits. In 1913, Meissner developed a first tube oscillator for radio transmitter applications; see Mathis [20] for details of the history of electrical oscillators. Of course, tubes are replaced in almost all modern oscillator circuits by transistors but the functionality of these circuits does not change in principles. Especially the oscillatory behavior of these circuits can only be obtained if nonlinearity is included. This leads to nonlinear differential equations for the deterministic description of this class of circuits and it became a big obstacle for a successful circuit analysis. It follows that a complete and systematic design process for the class of oscillatory circuits including nonlinearities is missing until now although some progress was made during the last two decades. Recent efforts are related to the development of design approaches using computer algebra systems where the nonlinear describing equations can be solved at least in the case of polynomial nonlinearity models. These approaches apply nonlinear transformation and equivalence principles (see

e.g., [22]) as well as perturbation series (averaging [19–23], Volterra series [9], polynomial series [7]) and the Andronov–Hopf bifurcation theorem ([1, 12, 16, 17, 25]) in order to deal with nonlinearities. Although the main ideas of these concepts are well-known, further research is needed in order to develop a reliable CAD system for oscillators which is useful for designers of oscillator circuits.

Whereas deterministic analysis approaches proceed the problem of noise in oscillator circuits came in the focus of research during the last few years. Since electronic oscillator circuits based on nonlinear devices we have to consider noise in nonlinear circuits. Some interesting results about noisy nonlinear circuits were published by Weiss and Mathis [31] as well as Wyatt and Coram [33] but their physical descriptions are restricted in essential to thermal noise in nonlinear circuits and we have to assume reciprocal circuits with positive resistors. Weiss and Mathis developed a new approach for noise analysis of nonlinear circuits based on ideas of nonlinear nonequilibrium thermodynamics which were invented by Stratonovich [26]. However, a noise analysis of oscillator circuits including nonreciprocal devices (e.g., transistors; equivalent to negative resistors using feedback principle) from first physical principles is not possible until now. Only certain noise aspects of active devices can be studied by these thermodynamical concepts (see e.g., [32]). If we are interested in noise properties of complete oscillator circuits nonreciprocal effects of electronic devices have to be included. With respect to noise behavior of electronic oscillator circuits many research was done with respect to phase noise; see Lee and Hajimiri [15] and Goldberg [10] for an overview. Since a sophisticated basis of phase noise in nonreciprocal circuits is missing these authors use a phenomenological approach. In our paper, we study noise aspects of oscillator circuits also on the foundations of a phenomenological approach and its impact to bifurcation phenomena.

## Deterministic Circuit Description

Although the deterministic describing equations of oscillatory circuits are generally of the type of so-called differential algebraic equations (DAEs, see e.g., [16]) we will consider only those oscillator models which can be described by explicit ordinary differential equations

$$\dot{x} = F(x), \quad F: R^n \rightarrow R^n, \quad (1)$$

the *state-space equations*. In contrast to transient analysis problems we have to consider (stable) asymptotic solutions of (1) and especially limit cycles in oscillator circuits. Since in higher dimensional cases no systematic methods for calculating limit cycles are available Papalexi, Mandelstam, and Andronov developed a bifurcation approach for electrical oscillators using ideas from Poincaré's results of nonlinear differential equations (see [20] and in particular the papers of Bissell [9] and of Aubin, Dalmedico [6]). A first overview on this subject was published in 1935 and later on these results were included in the monograph of Andronov, Witt, and Chaikin that was published in 1937 (English version: 1966

[1]). The main idea of Papalexi, Mandelstam, and Andronov was the embedding of equation (1) into a  $\mu$ -parametrized family of differential equation

$$\dot{x} = F(x, \mu), \quad F : R^n \times R \rightarrow R^n \quad (2)$$

for searching a qualitative changing of the asymptotic solutions within this family. It is already known from Poincaré that there is a changing in the case of the describing equations of sinusoidal oscillators from a stable equilibrium to a stable limit cycle and therefore Mandelstam et al. [17] studied this case intensively; today this phenomenon is called *Andronov–Hopf bifurcation*. Unfortunately their fundamental results were not noticed by other researchers in electrical engineering. It lasted more than 40 years until this subject was considered again in the electrical engineering community by Mees and Chua [24] in 1979. Afterwards Andronov–Hopf bifurcation became an essential subject in the theory of electrical circuits (e.g., [17, 18]). It should be remarked that in higher order dimensional systems ( $d > 2$ ) additional methods (e.g., the center manifold theorem or Liapunov–Schmidt approach) are needed (see e.g., [12, 19]).

Whereas many aspects of deterministic networks and systems can be studied efficiently in “time-domain” differential equations (1) or (2) there is an equivalent description that emphasized the statistical point of view. It is known from classical mechanics (e.g., [11]) that differential equations of form (1) or (2) can be formulated as *Frobenius–Perron* evolution equation or as *generalized Liouville equation*. In these cases we are interested in the dynamics of a suitable class of density functions  $f : R^n \rightarrow R^n$ . The dynamics can be formulated by an associated *Frobenius–Perron–Operator*  $P^t$  in the following form:

$$f(x, t) = P^t(f(x)). \quad (3)$$

This equation is closely related to the generalized Liouville equation (see [23])

$$\frac{\partial f}{\partial t} = -\operatorname{div}(f \cdot F) = -\sum_{i=1}^n \frac{\partial (f \cdot F_i)}{\partial x_i} =: L(f), \quad (4)$$

where  $P^t$  is related to the *Liouville operator*  $L$  in the energy-preserving case. The changing from (1) or (2) to (3) or (4) can be interpreted in the following manner: instead considering the system dynamics starting from a single initial point we consider weighted whole sets of initial points where the density function  $f$  is the weighting function. An advantage of this representation is that it can be generalized to the more general class of noisy systems.

## Stochastic Circuit Description

It was already mentioned that in the case of nonreciprocal circuits a physical derivation of dynamical equations for noisy electrical networks from first principle

is not available. Therefore a heuristic approach is needed. For our considerations we use the so-called Langevin approach. For describing stochastic networks and systems we start with a deterministic description of circuits (1) and add a *white noise stochastic process*  $\xi$

$$\dot{x} = F(x) + \sigma(x) \xi, \quad (5)$$

where the coefficient  $\sigma(x)$  characterizes the coupling of the noise source and the average of the process  $\xi$  vanishes that is  $\langle \xi \rangle = 0$ . The first term of (5) can be interpreted as the *dissipation term* where as the second term corresponds to the *fluctuation term*.

Using the concept of stochastic differential equations  $\xi$  has to be interpreted as a generalized white noise process but in order to solve these equations a more generalized concept of integration (e.g., [14]) is needed. In essential there are two concepts of stochastic integration which are due to Ito and Stratonovich, respectively; see van Kampen [30] for further details with respect to their interpretation. The associated type of stochastic differential equation is

$$dx = F(x) dt + \sigma(x) dW, \quad (6)$$

where  $W$  is the *Wiener process*. Both concepts of stochastic differential equations are mathematical equivalent to a corresponding *Fokker-Planck partial differential equation* which generalizes in some sense the concept of the Liouville equation of (4) (see also [3], Sect. 4.2)

$$\frac{\partial f}{\partial t} = -\sum_{i=1}^n \frac{\partial(f \cdot F_i)}{\partial x_i} + \sum_{i,j=1}^n \frac{\partial^2(\sigma^2 f)}{\partial x_i \partial x_j}, \quad (7)$$

In the case of linear stochastic differential equations – the original subject of Langevin – there is no difference between Ito's and Stratonovich's type. Unfortunately stochastic differential equations (of Ito or Stratonovich type) are sound concepts only from a mathematical point of view if we consider nonlinear Langevin equations. The reason is that certain interpretation rules are needed for this type of differential equations; otherwise its meaning is not well defined. It is interesting to see that for nonlinear Langevin equations in contrast to linear ones the associated deterministic equation (without noise) does not correspond to the averaged equation (see van Kampen's paper for further details [28])

$$\left\langle \frac{dx}{dt} \right\rangle = \frac{d\langle x \rangle}{dt} = \langle F(x) \rangle + \langle \sigma(x) \xi \rangle. \quad (8)$$

Note that the first moment of  $x$  does not fulfill the differential equation even if  $\sigma$  is constant since the function  $F$  and the average operator  $\langle \cdot \rangle$  does not commute. Only if  $\langle F(x) \rangle = F(\langle x \rangle)$  is valid (just like in the linear case) the averaged stochastic process  $x$  – that is the first moment of the process – fulfills the deterministic equation  $\dot{x} = F(x)$ . Therefore, with van Kampen [29, 30] we come to



the conclusion that there is no good reason why the dissipation term of (5) should be identical to the vector field of the deterministic equation. However, only in the reciprocal case a sound physical concept is available (e.g., [32]).

## Bifurcation Concepts in Noisy Circuits and Systems

In the previous section we consider two related concepts for describing general stochastic or noisy circuits and systems if we have a deterministic description of a network or a system of the form  $\dot{x} = F(x)$ . As mentioned above, we have to apply the heuristic Langevin approach if nonreciprocal (nonlinear) circuits are studied where associated stochastic differential equations can be derived. From a systems theoretical point of view stochastic differential equations belong to the class of state space equations which are formulated in time-domain. An alternative concept for describing noisy circuits we use probability density functions  $f$  which satisfies a Fokker–Planck-type equation (7).

In this section, we are concerned with parametrized families of stochastic dynamical systems in the Langevin form  $\dot{x} = F(x, \mu) + G(x)\xi$  and its associated Fokker–Planck equation. Although it is known that both concepts are equivalent from a mathematical point of view it turns out that there are different concepts of stochastic bifurcation. The earlier stochastic bifurcation concept based on the Fokker–Planck-type description which was founded in physical applications; see e.g., Horsthemke and Lefever [11]. In this approach a qualitative changing of stationary solutions within the family of Fokker–Planck equations is studied. Although it is a suggestive concept which can be illustrated easily there is no time dependence included and therefore it is rather a static concept to bifurcation. In the mathematical literature it is called “*P-bifurcation*” (e.g., [5]).

Another “dynamical” concept of stochastic bifurcation is based on the stochastic differential equation itself. In contrast to the P-bifurcation concept where we are looking for qualitative changes of the asymptotic probability density function the *dynamical* (or *D-*) *bifurcation* concept is concerned with qualitative changes of certain properties within the family of stochastic differential equations. For this purpose a suitable analogue for equilibrium points of deterministic differential equations is needed. It turns out (see [5]) that so-called *invariant measures* of stochastic flows are adequate analogues for deterministic equilibrium points. In doing so we assume that like in the deterministic case a stochastic differential equation is replaced by a “*stochastic flow*” or so-called *cocycle*; the readers are left to e.g., Arnold [5].

Note that if  $x_0$  is a deterministic equilibrium point of a cocycle  $\varphi(t, \omega, x_0) = x_0$  then the *Dirac measure*  $\delta_{x_0}$  is stationary and invariant. Therefore there is a close relationship of deterministic equilibrium points and invariant measures.

Therefore the fundamental question of D-bifurcation is “Are there other invariant measures than Dirac measures?”. It turns out that a necessary condition for qualitative changing in the sense of D-bifurcation is the vanishing of a Lyapunov exponent. It should be mentioned that there is no general relation between P-bifurcation and D-bifurcation.

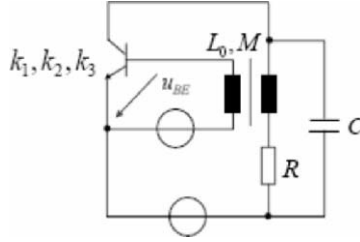


**Fig. 1.** Transistor Meissner oscillator

For illustrating these bifurcation concepts we restrict us for simplicity to 2-dimensional circuit. However, further results as well as corresponding analytical and numerical methods will be published in forthcoming papers. For higher dimensional systems stochastic concepts for normal forms and/or center manifolds are needed (see [5]). We consider a Meissner oscillator circuit in fig. 1. If  $k_2 = 0$  the following circuit equation for the voltage between basis and emitter can be derived ( $\omega_0^2 = 1/(LC)$ )

$$\ddot{u}_{BE} + \left( \frac{R}{L} - \omega_0^2 M (k_1 - 3k_3 u_{BE}^2) \right) \dot{u}_{BE} + \omega_0^2 u_{BE} = 0. \quad (9)$$

Equation (9) can be normalized in the standard van der Pol form  $\ddot{x} - (\mu - \gamma x^2)\dot{x} + x = 0$ . Now we assume with Ariaratnam [2] that we have a noisy resistor which results in an additive decomposition of

$$\ddot{x} - (\mu_0 + \sigma \xi - \gamma x^2)\dot{x} + x = 0. \quad (10)$$

If (10) is converted into first-order equations and polar coordinate transformations are applied to the system we obtain after a stochastic averaging the following stochastic differential equation for the amplitude process  $a(t)$ .

For the analysis of D-bifurcations we have to determine the stability of stationary solutions  $a_s(t)$  by means of associated Lyapunov exponents. If small variations  $r(t)$  of  $a_s(t)$  are considered the following linearized stochastic differential equation for amplitude process can derived:

$$dr = \frac{1}{2} \left( \mu_0 + \frac{5}{8} \sigma^2 - \frac{3}{4} \gamma a_s^2 \right) r dt + \left( \frac{3}{8} \right)^{\frac{1}{2}} \sigma r dW_a. \quad (12)$$

For the bifurcation analysis, the zeros of the Lyapunov exponents have to be found

$$\lambda = \frac{1}{2} \left( \mu_0 + \frac{1}{4} \sigma^2 - \frac{3}{4} \gamma \langle a_s^2 \rangle \right). \quad (13)$$

Obviously, it results a zero Lyapunov exponent for the trivial solution  $a_s = 0$  at  $\mu_0 = -\sigma^2/4$ . Furthermore, for the same value of  $\mu_0$  we have a zero Lyapunov exponent for  $a_s \neq 0$ , too, such that we have a D-bifurcation.

For studying P-bifurcation we need a solution of the stationary Fokker–Planck equation associated to the noisy van der Pol equation. It turns out that a first P-bifurcation occurs at  $\mu_0 = \sigma^2/8$ , where the peak of the probability density function shifts as  $a_p := 2((\mu_0 - \sigma^2/8)/\gamma)^{1/2}$ . Another changing occurs at  $\mu_0 = \sigma^2/2$ , where the uni-modal density centered at the origin changes to a bimodal density possessing a ring of peaks; see Ariaratnam [2]. Note that  $\mu_0$ -values for D- and P-bifurcation differ substantially.

## Conclusions

In our paper, similarities and differences of describing methods for deterministic and stochastic circuits and systems are discussed. Especially, we discussed some difficulties with respect to a sound physical interpretation of describing equations of noisy networks and systems if nonlinear and nonreciprocal circuits and systems are considered. Moreover, we considered basic ideas of two concepts of bifurcation analysis in noisy nonlinear circuits and systems. By means of a generalized noisy van der Pol equation derived from a Meissner oscillator including a transistor these bifurcation concepts are illustrated.

## References

- [1] A.A. Andronov, A.A. Witt, S.E. Khaikin, *Theory of Oscillators*, Pergamon, Oxford, 1966 (first published in Russian in 1937)
- [2] S.T. Ariaratnam, “Stochastic Bifurcation in Hereditary Systems”, *Proceedings 8th ASCE Spec. of the Conference on Probability Mech. Struct. Reliability*. Notre Dame University, 23–26 July 2000, USA
- [3] L. Arnold, “The unfoldings of dynamics in stochastic analysis”, *Comput. Appl. Math.* 16, 1997, 3–25
- [4] L. Arnold, P. Imkeller, “Normal forms for stochastic differential equations”, *Probab. Theory Relat. Fields* 110, 1998, 559–588

- 
- [5] L. Arnold, *Random Dynamical Systems*, Springer, Berlin Heidelberg, New York, 1998
- [6] D. Aubin, A.D. Dalmedico, "Writing the History of Dynamical Systems and Chaos: Longue Durée and Revolution", *Disciplines Cultures. Hist. Math.* 29, 2002, 273–339
- [7] A. Buonomo, A. Lo Schiavo, "Analyzing the Dynamic Behavior of RF Oscillators", *IEEE Trans. CAS-I* (49) 1525–1534
- [8] C. Bissell, A.A. Andronov, "the Development of Soviet Control Engineering", *IEEE Control Syst. Mag.* 18, 1998, pp. 56–62
- [9] L.O. Chua, Y.S. Tang, "Nonlinear oscillation via Volterra Series", *IEEE Trans. Circuits Syst.* CAS-29, 1982, 150–168
- [10] B.G. Goldberg, "Oscillator phase noise revisited – a Heuristic review. RF Design" January 2002, pp. 52–64
- [11] H. Goldstein, C. Poole, J Safko, *Classical Mechanics* (3rd Edition), Addison Wesley, San Francisco, 2001
- [12] J. Guckenheimer, P. Holmes, *Nonlinear Oscillations, Dynamical Systems, and Bifurcation of Vector Fields*, Springer, Berlin Heidelberg New York, 1983
- [13] W. Horsthemke, R. Lefever, *Noise-Induced Transitions*, Springer, Berlin Heidelberg New York, 1984
- [14] H. Kunita, *Stochastic Flows and Stochastic Differential Equations*, Cambridge University, 1990
- [15] T.H. Lee, A. Hajimiri, "Oscillator Phase Noise: A Tutorial", *IEEE J. Solid-State Circuits* SC-35, 2000, pp. 326–336
- [16] G.M. Maggio, O. De Feo, M.P. Kennedy, "A General Method to Predict the Amplitude of Oscillation in Nearly Sinusoidal Oscillators", *IEEE Trans. CAS-I* (51) 1586–1595
- [17] L. Mandelstam, N. Papalexi, A.A. Andronov, S. Chaikin, A. Witt, "Exposé des Recherches Récentes, sur les Oscillations Non Linéaires", *Zeitschr. Techn. Phys.* 4 (1935) 81–134
- [18] W. Mathis, *Theory of Nonlinear Circuits* (in German), Springer, Berlin-Heidelberg New York, 1987
- [19] W. Mathis, C. Keidies, "Application of Center Manifolds to Oscillator Analysis" *Proceedings 12th European Conference on Circuit Theory and Design (ECCTD'95)*, Istanbul, Türkei, 27–31. August 1995
- [20] W. Mathis, "Historical remarks to the history of electrical oscillators", (invited). In: *Proceedings MTNS-98 Symposium*, July 1998, IL POLIGRAFO, Padova 1998, 309–312.
- [21] W. Mathis, "Nonlinear stochastic circuits and systems – A geometric approach", *Proceedings 4th MATHMOD 2003*, Vienna, February 5–7, 2003
- [22] W. Mathis, *Transformation and Equivalence*, In: W.-K. Chen (Ed.): *The Circuits and Filters Handbook*, CRC Press & IEEE Press, Boca Raton, 2003
- [23] W. Mathis, M. Prochaska, "Deterministic and Stochastic Andronov–Hopf Bifurcation in Nonlinear Electronic Oscillators", *Proceedings 11th Workshop of Nonlinear Dynamics of Electronic Systems (NDES)*, May 18–22, 2003, Scuols, Schwitzerland
- [24] A.I. Mees, L.O. Chua, "The Hopf Bifurcation and its Application to Nonlinear Oscillations in Circuits and Systems", *IEEE Trans. Circuits Syst.* vol. 26, 1979, 235–254
- [25] M. Prochaska, W. Mathis, "Symbolic Analysis Methods for Harmonic Oscillators", *Proceedings 12th International Symposium on Theoretical and Electrical Engineering (ISTET03)*, Warschawa 2003, Poland

- 
- [26] R.L. Stratonovich, *Nonlinear Thermodynamics I.*, Springer, Berlin Heidelberg New York, 1992
  - [27] M.E. Tuckerman, C.J. Mundy, G.J. Martyna, “On the Classical Statistical Mechanics of Non-Hamiltonian Systems”, *Europhys. Lett.* 45, 1999, 149
  - [28] N.G. van Kampen, “Thermal fluctuations in nonlinear systems”, *J. Math. Phys.* 4, 1963, 190–194
  - [29] N.G. van Kampen, “The Validity of Nonlinear Langevin Equations”, *J. Stat. Phys.* 25, 1981, 431–442
  - [30] N.G. van Kampen, “Ito versus Stratonovich”, *J. Stat. Phys.* 24, 1981, 175–187
  - [31] L. Weiss, W. Mathis, “A Thermodynamical Approach to Noise in Nonlinear Networks”, *Int. J. Circ. Theor. Appl.* 26, 1998, 147–165
  - [32] L. Weiss, W. Mathis, “A thermodynamic noise model for nonlinear resistors”, *IEEE Trans. Electron. Dev. Lett.* 20, 1999, 402–404
  - [33] J.L. Wyatt, G.J. Coram, “Nonlinear Device Noise Models: Satisfying the Thermodynamic Requirements”, *IEEE Trans. Electron. Dev.* 46, 1999, pp. 184–193

# When is a Linear Complementarity System Controllable?

M.K. Camlibel<sup>1,2</sup>

<sup>1</sup>Department of Electronics and Communication Engineering, Dogus University, Acibadem 81010, Kadikoy-Istanbul, Turkey, [kcamlibel@dogus.edu.tr](mailto:kcamlibel@dogus.edu.tr)

<sup>2</sup>Department of Mechanical Engineering, Eindhoven University of Technology, P.O. Box 513, 5600 MB Eindhoven, The Netherlands

## Abstract

This paper deals with the controllability problem of a class of piecewise linear systems, known as linear complementarity systems. It is well-known that checking certain controllability properties of very simple piecewise linear systems are undecidable problems. In an earlier paper, however, a complete characterization of the controllability of the so-called conewise linear systems has been achieved. By employing this characterization and exploiting the special structure of linear complementarity systems, we present a set of inequality-type conditions as necessary and sufficient conditions for their controllability. Our treatment is based on the ideas and the techniques from geometric control theory together with mathematical programming.

## Introduction

Ever since Kalman's seminal work [10] introduced the notion of controllability in the state space framework, it has been one of the central notions in systems and control theory. In the early 1960s, Kalman [11] himself and many others (see e.g. [9] for historical details) studied controllability of finite-dimensional linear systems extensively and established algebraic tests for controllability. Soon after, constrained controllability problems, i.e. problems for which the inputs are constrained to assume values from a subset of the entire input space, became popular (see for instance [12]). Early work in this direction consider only constraint sets which contain the origin in their interior [12, Thm. 8, p. 92]. However, the constraint set does not contain the origin in its interior in many interesting cases, for instance, when only nonnegative controls are allowed. Saperstone and Yorke [14] were the first to consider constraint sets that do not have the origin in their interior. In particular, they considered the case for which the inputs are constrained to the set  $[0,1]$ . More general constraint sets were studied by Brammer [2]. He showed that the usual controllability condition

together with a condition on the real eigenvalues of the system matrix is necessary and sufficient for controllability of linear systems with nonnegative inputs [2, Thm. 1.4].

While the algebraic characterization of controllability of finite dimensional linear systems is among the classical results of systems theory, global controllability results for nonlinear systems have been hard to come by. When it comes to hybrid systems, the situation gets even more hopeless. In fact, Blondel and Tsitsiklis [1] proved that the reachability problem of a bimodal piecewise linear discrete-time system is an undecidable problem. However, our recent work [3–5] shows that one can come up with algebraic conditions for controllability of conewise linear. In this paper, our aim is to extend the ideas of [3–5] to a class of hybrid systems called *linear complementarity systems* (LCSs).

The following notational conventions will be in force throughout the paper. The symbol  $\mathfrak{R}$  denotes the set of real numbers,  $\mathfrak{R}^n$   $n$ -tuples of real numbers, and  $\mathfrak{R}^{n \times m}$   $n \times m$  real matrices. The set of complex numbers is denoted by  $C$ . For a matrix  $A \in \mathfrak{R}^{n \times m}$ ,  $A^T$  stands for its transpose,  $A^{-1}$  for its inverse (if exists),  $\text{im } A$  for its image, i.e. the set  $\{y \in \mathfrak{R}^n \mid y = Ax \text{ for some } x \in \mathfrak{R}^m\}$ . We write  $A_{ij}$  for the  $(i, j)$ th element of  $A$ . For  $\alpha \subseteq \{1, 2, \dots, n\}$ , and  $\beta \subseteq \{1, 2, \dots, m\}$ ,  $A_{\alpha\beta}$  denotes the submatrix  $\{A_{jk}\}_{j \in \alpha, k \in \beta}$ . If  $\alpha = \{1, 2, \dots, n\}$  ( $\beta = \{1, 2, \dots, m\}$ ), we also write  $A_{*\beta}$  ( $A_{\alpha*}$ ). Inequalities for vectors must be understood componentwise. Similarly, max operator acts on the vectors componentwise. We write  $x \perp y$  if  $x^T y = 0$ .

## Linear Complementarity Problem/System

The problem of finding a vector  $z \in \mathfrak{R}^m$  such that

$$z \geq 0, \quad (1a)$$

$$q + Mz \geq 0, \quad (1b)$$

$$z^T(q + Mz) = 0 \quad (1c)$$

for a given vector  $q \in \mathfrak{R}^m$  and a matrix  $M \in \mathfrak{R}^{m \times m}$  is known as the linear complementarity problem. We denote (1) by  $LCP(q, M)$ . It is well-known [7, Thm. 3.3.7] that the  $LCP(q, M)$  admits a unique solution for each  $q$  if, and only if,  $M$  is a  $P$ -matrix. It is also known that  $z$  depends on  $q$  in a Lipschitz continuous way in this case.

Linear complementarity systems consist of nonsmooth dynamical systems that are obtained in the following way. Take a standard linear input/output system. Select a number of input/output pairs  $(z_i, w_i)$ , and impose for each of these pairs complementarity relation of the type (1) at each

time  $t$ , i.e. both  $z_i(t)$  and  $w_i(t)$  must be non-negative, and at least one of them should be zero for each time instant  $t \geq 0$ . This results in a dynamical system of the form

$$\dot{x}(t) = Ax(t) + Bu(t) + Ez(t), \quad (2a)$$

$$w(t) = Cx(t) + Du(t) + Fz(t), \quad (2b)$$

$$0 \leq z(t) \perp w(t) \geq 0, \quad (2c)$$

where  $u \in \mathfrak{R}^m$ ,  $x \in \mathfrak{R}^n$ , and  $z, w \in \mathfrak{R}^k$ . A wealth of examples and application areas of LCSs can be found in [6,8,15,16].

A set of standing assumptions throughout this paper are the following.

**Assumption 1.** The following conditions are satisfied for the LCS (2)

1. The matrix  $F$  is a  $P$ -matrix
  2.  $k = m$
  3. The transfer matrix  $D + C(sI - A)^{-1}B$  is invertible as a rational matrix
- These assumptions are technical in nature and most of the subsequent results can be generalized in cases for which these assumptions do not hold. However, we focus on LCSs that satisfy Assumption 1 in order not to blur the main message of the paper.

It follows from Assumption 1 that  $z(t)$  is a piecewise linear function of  $Cx(t) + Du(t)$ . This means that for each initial state  $x_0$  and locally-integrable input  $u$  there exist a unique absolutely continuous state trajectory  $x^{x_0, u}$  and locally-integrable trajectories  $(z^{x_0, u}, w^{x_0, u})$  such that  $x^{x_0, u}(0) = x_0$  and the triple  $(x^{x_0, u}, z^{x_0, u}, w^{x_0, u})$  satisfies the relations (2) for almost all  $t \geq 0$ .

We say that the LCS (2) is (completely) controllable if for any pair of states  $(x_o, x_f) \in \mathfrak{R}^{n+n}$  there exists a locally integrable input  $u$  such that the trajectory  $x^{x_o, u}$  of (2) satisfies  $x^{x_o, u}(T) = x_f$  for some  $T > 0$ .

In two particular cases, one can employ the available results for the linear systems to determine whether (2) is controllable.

### Linear systems

Consider the LCS

$$\dot{x}(t) = Ax(t) + Bu(t), \quad (3a)$$

$$w(t) = u(t) + z(t), \quad (3b)$$

$$0 \leq z(t) \perp w(t) \geq 0. \quad (3c)$$

It can be verified that Assumption 1 holds. Note that this system is controllable if, and only if, the linear system (3a) is controllable. In turn, this is equivalent to the implication

$$\lambda \in C, z \in C^n, z^* A = \lambda z^*, B^T z = 0 \Rightarrow z = 0. \quad (4)$$

In this case, we say that the pair  $(A, B)$  is controllable.



### Linear systems with nonnegative inputs

Consider the LCS

$$\dot{x}(t) = Ax(t) + Bu(t) + Bz(t), \quad (5a)$$

$$w(t) = u(t) + z(t), \quad (5b)$$

$$0 \leq z(t) \perp w(t) \geq 0. \quad (5c)$$

Note that the solution to the LCP (5b) and (5c) can be given as  $z(t) = u^-(t)$  and  $w(t) = u^+(t)$  where  $\xi^+ := \max(\xi, 0)$  and  $\xi^- := \max(-\xi, 0)$  denote the positive and negative part of the real vector  $\xi = \xi^+ - \xi^-$  respectively.

Therefore, this LCS is controllable if, and only if, the linear system

$$\dot{x}(t) = Ax(t) + Bv(t)$$

with the input constraint  $v(t) \geq 0$  is controllable. It follows from [2, Cor. 3.3] that this system is controllable if, and only if, the following two conditions hold:

1. the pair  $(A, B)$  is controllable
2. the implication

$$\lambda \in \Re, z \in \Re^n, z^T A = \lambda z^T, B^T z \geq 0 \Rightarrow z = 0 \quad (6)$$

holds.

### Main results

To formulate the main results we need some nomenclature. Consider the linear system  $S(A, B, C, D)$

$$\dot{x} = Ax + Bu, \quad (7a)$$

$$y = Cx + Du, \quad (7b)$$

where  $x \in \Re^n$  is the state,  $u \in \Re^m$  is the input,  $y \in \Re^p$  is the output, and the matrices  $A, B, C, D$  are of appropriate sizes. We define the *invariant zeros* of the system (7) to be the zeros of the nonzero polynomials on the diagonal of the Smith form of

$$P_{\Sigma(s)} = \begin{bmatrix} A - sI & B \\ C & D \end{bmatrix}. \quad (8)$$

The matrix  $P_{\Sigma}(s)$  is sometimes called *the system matrix*. It is known, for instance from [17, Cor. 8.14], that the transfer matrix  $D + C(sI - A)^{-1}B$  is invertible as a rational matrix if, and only if, the system matrix  $P_{\Sigma}(\lambda)$  is of rank  $n + m$

for all but finitely many  $\lambda \in C$ . In this case, the values of  $\lambda \in C$  such that  $\text{rank } P_\Sigma(\lambda) < n + m$  coincide with the invariant zeros. Let  $\Lambda(A, B, C, D)$  denote the set of all invariant zeros of the system (7).

The following theorem presents algebraic necessary and sufficient conditions for the controllability of an LCS.

**Theorem 2.** Consider an LCS (2) satisfying Assumption 1. It is controllable if, and only if, the following two conditions hold:

1. The pair  $(A, [B \ E])$  is controllable
2. For all  $\lambda \in \Lambda(A, B, C, D) \cap \Re$ , the system of inequalities

$$\eta \geq 0, \quad (9a)$$

$$\begin{bmatrix} \xi^T & \eta^T \end{bmatrix} \begin{bmatrix} A - S\lambda I & B \\ C & D \end{bmatrix} = 0, \quad (9b)$$

$$\begin{bmatrix} \xi^T & \eta^T \end{bmatrix} \begin{bmatrix} E \\ F \end{bmatrix} \leq 0, \quad (9c)$$

admits no nonzero solution  $(\xi, \eta)$ .

#### A quick sketch of the proof

The main ingredients of the proof are conewise linear systems. A conewise linear system (CLS) is a dynamical system of the form

$$\dot{x}(t) = Ax(t) + Bu(t) + f(Cx(t) + Du(t)), \quad (10)$$

where  $x \in \Re^n$  is the state,  $u \in \Re^m$  is the input,  $A \in \Re^{n \times n}$ ,  $B \in \Re^{n \times m}$ ,  $C \in \Re^{p \times n}$ ,  $D \in \Re^{p \times m}$  and the function  $f$  is a conewise linear function, i.e., there exist an integer  $r$ , solid polyhedral cones  $y_i$  and matrices  $M^i \in \Re^{n \times p}$  for  $i = 1, 2, \dots, r$  such that  $\bigcup_{i=1}^r y_i = \Re^p$  and  $f(y) = M^i y$  if  $y \in Y_i$ .

Note that the function  $f$  is necessarily continuous since the cones  $y_i$  are closed due to polyhedrality. In turn, continuity implies Lipschitz continuity in this case. A somewhat more explicit representation for CLSs can be given by

$$\dot{x}(t) = (A + M^i C)x(t) + (B + M^i D)u(t) \text{ if } Cx(t) + Du(t) \in Y_i. \quad (11)$$

By using the fact that the solutions of an LCP with a  $P$ -matrix depend on the data in a Lipschitz continuous way, we can reformulate the LCS (2) as a CLS. This results in a CLS of the form

$$x = P^\alpha x + Q^\alpha u, \text{ whenever } R^\alpha x + S^\alpha u \geq 0. \quad (12)$$

where

$$P^\alpha := A - E_{*\alpha} F_{\alpha\alpha}^{-1} C_{\alpha*}, \quad Q^\alpha := B - E_{*\alpha} F_{\alpha\alpha}^{-1} D_{\alpha*}, \quad (13a)$$

$$R^\alpha := \begin{bmatrix} -F_{\alpha\alpha}^{-1}C_{\alpha\bullet} \\ C_{\alpha^\epsilon\bullet} - F_{\alpha^\epsilon\alpha} F_{\alpha\alpha}^{-1}C_{\alpha\bullet} \end{bmatrix} \quad S^\alpha := \begin{bmatrix} -F_{\alpha\alpha}^{-1}D_{\alpha\bullet} \\ D_{\alpha^\epsilon\bullet} - F_{\alpha^\epsilon\alpha} F_{\alpha\alpha}^{-1}D_{\alpha\bullet} \end{bmatrix}. \quad (13b)$$

At this point, we invoke the following theorem on the controllability of LCS.

**Theorem 3.** Consider the CLS (10) such that  $p = m$  and the transfer matrix  $D + C(sl - A)^{-1}B$  is invertible as a rational matrix. It is completely controllable if, and only if,

1. the relation

$$\sum_{i=1}^r \langle A + M^i C \mid \text{im}(B + M^i D) \rangle = \mathfrak{R}^n \quad (14)$$

is satisfied and

2. the implication  $\lambda \in \mathfrak{R}, z \in \mathfrak{R}^n, w_i \in \mathfrak{R}^m$

$$\begin{bmatrix} z^\top & w_i^\top \end{bmatrix} \begin{bmatrix} A + M^i C - \lambda I & B + M^i D \\ C & D \end{bmatrix} = 0, w_i \in Y_i \text{ for all } i = 1, 2, \dots, r \Rightarrow z = 0$$

holds.

Here the notation  $\langle M \mid \text{im}N \rangle$  denotes the so-called controllability subspace associated to the matrix pair  $(M, N)$ , i.e.  $\langle M \mid \text{im}N \rangle = \text{im}N + M\text{im}N + \dots + M^{p-1}\text{im}N$  where  $M \in \mathfrak{R}^{p \times p}$  and  $F^*$  denotes the dual cone associated to the non-empty set  $F$ , i.e.,  $F = \{y \mid x^\top y \geq \text{for all } x \in F\}$ .

By using (12) and Theorem 3, one can show that the two conditions of these theorems are equivalent.

### Particular cases

We can recover the two particular cases that are mentioned earlier from Theorem 2 as follows.

**Linear systems.** If we take  $C = 0, D = I, E = 0$ , and  $F = I$  as in (3), the two conditions of Theorem 2 boil down to:

1. The pair  $(A, B)$  is controllable
2. For all  $\lambda \in \Lambda(A, B, 0, I) \subset \mathfrak{R}$ , the system of inequalities

$$\eta \geq 0, \quad (15a)$$

$$\begin{bmatrix} \xi^T & \eta^T \end{bmatrix} \begin{bmatrix} A - \lambda I & B \\ C & D \end{bmatrix} = 0, \quad (15b)$$

$$\begin{bmatrix} \xi^T & \eta^T \end{bmatrix} \begin{bmatrix} 0 \\ I \end{bmatrix} \leq 0, \quad (15c)$$

admits no nonzero solution  $(\xi, \eta)$ .

Note that (15a) and (15c) imply that  $\eta = 0$ . This means that if  $(A, B)$  is controllable then (15b) the only solution (15b) is  $\xi = 0$ . Hence, we recover the case of linear systems.

**Linear systems with nonnegative inputs.** If we take  $C = 0, D = I, E = B, F = I$  as in (5), the two conditions of Theorem 2 boil down to:

1. The pair  $(A, B)$  is controllable.
2. For all  $\lambda \in \Lambda(A, B, 0, I) \cap \Re$ , the system of inequalities

$$\eta \geq 0, \quad (16a)$$

$$\begin{bmatrix} \xi^T & \eta^T \end{bmatrix} \begin{bmatrix} A - \lambda I & B \\ C & D \end{bmatrix} = 0, \quad (16b)$$

$$\begin{bmatrix} \xi^T & \eta^T \end{bmatrix} \begin{bmatrix} B \\ I \end{bmatrix} \leq 0, \quad (16c)$$

admits no nonzero solution  $(\xi, \eta)$ .

Note that (16c) is already satisfied for this case. Together with (16a), the equality (16b) implies that the second condition is equivalent to the second condition that is presented in (6).

## Computational issues

Theorem 2 requires that one needs to check whether a set of inequalities of the form (9) admits only the trivial solution. However, it might be sometimes easier to check whether a given set of inequalities admits a nontrivial solution. To do so, one can employ the following *alternative theorem* which is originally due to Tucker [13, (1.6.10)].

**Theorem 4.** Let  $W \in \Re^{p \times r}$ ,  $X \in \Re^{p \times s}$ ,  $Y \in \Re^{q \times r}$ , and  $Z \in \Re^{q \times s}$  be given matrices. Exactly one of the following statements hold:

1. There exists a nonzero  $(\rho, \zeta) \in \Re^{r+s}$  such that

$$\begin{aligned}\rho &\geq 0, \\ W\rho + X\zeta &= 0, \\ Y\rho + Z\zeta &\geq 0.\end{aligned}$$

2. There exists a nonzero  $(\xi, \eta) \in \mathfrak{R}^{p+q}$  such that

$$\begin{aligned}\eta &\geq 0, \\ W^T \xi + Y^T \zeta &\leq 0, \\ X^T \xi + Z^T \zeta &= 0.\end{aligned}$$

A direct application of the theorem to (9) gives the following alternative formulation of the second condition in Theorem 2:

2' For all  $\lambda \in \Lambda(A, B, C, D) \cap \mathfrak{R}$ , the system of inequalities

$$\rho \geq 0, \tag{17a}$$

$$E\rho + [A - \lambda B]\zeta = 0, \tag{17b}$$

$$F\rho + [CD]\zeta \geq 0. \tag{17c}$$

admits a nonzero solution  $(\rho, \zeta)$ .

## Conclusions

In this paper, we studied the controllability problem for the linear complementarity class of hybrid systems. These systems are closely related to the so-called conewise linear systems. By exploiting this connection, together with the special structure of complementarity systems, we derived algebraic necessary and sufficient conditions for the controllability. We also showed that Kalman's and Bramer's results for linear systems can be recovered from our theorem. Our treatment employed a mixture of methods from both mathematical programming and geometric control theory. Obvious question is how one can utilize these techniques in order to establish necessary and/or sufficient conditions for the (feedback) stabilizability problem.

## References

- [1] V.D. Blondel and J.N. Tsitsiklis. “Complexity of stability and controllability of elementary hybrid systems”, *Automatica*, 35(3):479–490, 1999
- [2] R.F. Brammer, “Controllability in linear autonomous systems with positive controllers”, *SIAM J. Control*, 10(2):329–353, 1972
- [3] M.K. Camlibel, W.P.M.H. Heemels, and J.M.Schumacher, “On the controllability of bimodal piecewise linear systems”, In R. Alur and G.J. Pappas, editors, *Hybrid Syst. Comput. Control*, pages 250–264. Springer, Berlin, 2004
- [4] M.K. Camlibel, W.P.M.H. Heemels, and J.M.Schumacher, “Algebraic necessary and sufficient conditions for the controllability of conewise linear systems”, 2005. submitted for publication
- [5] M.K. Camlibel, W.P.M.H. Heemels, and J.M. Schumacher, “Stability and controllability of planar bimodal complementarity systems”, In *Proc. of the 4th IEEE Conference on Decision and Control*, Hawaii (USA), 2003
- [6] M.K. Camlibel, L. Iannelli, and F. Vasca, “Modelling switching power converters as complementarity systems”, In *Proc. of the 43th IEEE Conference on Decision and Control*, Paradise Islands (Bahamas), 2004
- [7] R.W. Cottle, J.-S. Pang, and R.E. Stone, “*The Linear Complementarity Problem*”, Academic, Boston, 1992
- [8] W.P.M.H. Heemels and B. Brogliato, “The complementarity class of hybrid dynamical systems”, *Eur. J. Control*, 26(4):651–677, 2003
- [9] T. Kailath, *Linear Systems*, Prentice-Hall, Englewood Cliffs, NJ, 1980
- [10] R.E. Kalman, “On the general theory of control systems”, In *Proc. of the 1st World Congress of the International Federation of Automatic Control*, pages 481–493, 1960
- [11] R.E. Kalman, “Mathematical description of linear systems”, *SIAM J. Control*, 1:152–192, 1963
- [12] E.B. Lee and L. Markus, *Foundations of Optimal Control Theory*, Wiley New York, 1967.
- [13] O.L. Mangasarian, *Nonlinear Programming*, McGraw-Hill, New York, 1969
- [14] S.H. Saperstone and J.A. Yorke, “Controllability of linear oscillatory systems using positive controls”, *SIAM J. Control*, 9(2):253–262, 1971
- [15] A.J. van der Schaft and J.M. Schumacher, *An Introduction to Hybrid Dynamical Systems*, Springer, Berlin Heidelberg New York, London, 2000
- [16] J.M. Schumacher, “Complementarity systems in optimization”, *Math. Program. Ser. B*, 101:263–295, 2004
- [17] H.L. Trentelman, A. A. Stoorvogel, and M.L.J. Hautus, *Control Theory for Linear Systems*, Springer, Berlin Heidelberg New York, London, 2001

# A Simple Artificial Neural Network Structure for Generating Chaos

N. Serap Şengör

Faculty of Electrical Electronics Engineering, Istanbul Technical University,  
Istanbul, Turkey

## Abstract

A rather simple artificial neural network (ANN) structure capable of yielding chaotic behavior will be introduced. Even though it is similar in some aspects to some known ANN structures, difference of this chaos-generating structure from others will be pointed out. Simulation results showing chaotic behavior will be given.

## Introduction

As more the chaotic behavior of natural and physical systems observed, more interest and need arose in obtaining structures giving rise to chaotic behavior.

Unlike the old tendency, to find a way of preventing chaos, nowadays more effort is spent in different areas of engineering to observe chaos, analyze it and find a way of utilizing it [1, 2]. In most of the applications of artificial neural networks (ANN) as, designing associative memory, solving optimization problems and identifying and controlling nonlinear systems, the main concern is to find an ANN structure where the trajectories of the system end up in one of the equilibrium points stable in the sense of Lyapunov [3, 4]. Still, there has been some attempts to utilize chaotic behavior of complex ANN structures [5, 6].

Recently, it has been shown that by modifying the activation function of Elman Network (EN) and creating an autonomous dynamical system by output feedback it is possible to obtain chaotic behavior even with a single neuron [6].

In this work, an ANN structure with continuous and discrete time versions will be introduced and it will be shown that the chaotic ANN introduced in [6] can be obtained from the proposed ANN as a special case. Simulation results revealing chaotic behavior will be given.

## The Proposed Chaotic Artificial Neural Network Structure

The continuous time, autonomous, nonlinear system given by (1) is capable of providing bounded solutions that are not stable in the sense of Lyapunov, thus giving rise to a broad class of signals resembling those encountered in different natural and physical phenomena [2]

$$\begin{aligned}\dot{\mathbf{x}}(t) &= \hat{\mathbf{w}}^{hh} \mathbf{x}(t) + \hat{\mathbf{w}}^{hi} \mathbf{f}[\mathbf{w}^{ii} \mathbf{x}(t)] \\ \mathbf{y}(t) &= \mathbf{w}^{oi} \mathbf{x}(t).\end{aligned}\quad (1)$$

In this set of equations, state variables and output are denoted by  $\mathbf{x}(t)$  and  $\mathbf{y}(t)$ , respectively, and  $\mathbf{y}(t) \in \mathfrak{R}$ ,  $\mathbf{x}(t) \in \mathfrak{R}^n$ ,  $\mathbf{f}(\cdot): \mathfrak{R}^n \rightarrow \mathfrak{R}^n$ ,  $\hat{\mathbf{w}}^{hh}, \hat{\mathbf{w}}^{hi}, \mathbf{w}^{ii} \in \mathfrak{R}^{n \times n}$  and  $\mathbf{w}^{oi} \in \mathfrak{R}^n$ . The activation function  $\mathbf{f}(\cdot)$  is a bounded function.

The system given in (1) is similar to Hopfield network (HN), but for different choices of activation function and for a large set of weight parameters, its solutions are quite different than that of HN. The differences between two systems are not only the choice of activation function  $\mathbf{f}(\cdot)$  and constraints on weight matrices  $\hat{\mathbf{w}}^{hh}, \hat{\mathbf{w}}^{hi}$  but while the bias, i.e., offset term is missing in (1), there is an extra weight matrix  $\mathbf{w}^{ii}$ . As the purpose is to obtain an autonomous system capable of giving solutions other than stable equilibrium points the bias term is not considered.

In HN, the complete stability of the system, i.e., all trajectories ending at one of the stable equilibrium points, is provided by bounded, monotonic  $\mathbf{f}(\cdot)$  function and constraints on weight matrices. When these obligations are not fulfilled, it is possible to obtain unbounded solutions. It has been observed that the system given in (1), especially with nonmonotonic activation functions has bounded input bounded output stable solutions, that are unstable in the sense of Lyapunov for a large set of weight matrices.

A difference equation version of (1) is given in (2)

$$\begin{aligned}\mathbf{x}(k+1) &= \mathbf{w}^{hh} \mathbf{x}(k) + \mathbf{w}^{hi} \mathbf{f}[\mathbf{w}^{ii} \mathbf{x}(k)] \\ \mathbf{y}(k) &= \mathbf{w}^{oi} \mathbf{x}(k).\end{aligned}\quad (2)$$

The ANN structure corresponding to the first set of equations in (2) is given in Fig. 1.

In order to obtain chaotic behavior, EN, a recurrent ANN structure, has been modified in [6] by replacing the hyperbolic tangent activation function with a nonlinear function of type  $g(x) = \sqrt{e} \frac{g}{R} x e^{-\left(\frac{x^2}{2R^2}\right)}$  and by connecting the output of EN to its input. Thus in [6], an autonomous, discrete-time nonlinear system has been obtained as shown below

$$\begin{aligned}\mathbf{x}(k+1) &= \mathbf{f}(\mathbf{W}\mathbf{x}(k)) \\ \mathbf{y}(k) &= \mathbf{w}^{yT} \mathbf{x}(k)\end{aligned}\quad (3)$$



In this set of equations

$$\mathbf{y}(k) \in \mathfrak{R}, \mathbf{x}(k) \in \mathfrak{R}^n, \mathbf{f}(\cdot): \mathfrak{R}^n \rightarrow \mathfrak{R}^n,$$

$$\mathbf{W} \triangleq \mathbf{w}^x + \mathbf{w}^u \mathbf{w}^{yT} \text{ and } \mathbf{w}^x \in \mathfrak{R}^{n \times n}, \mathbf{w}^u \in \mathfrak{R}^n \text{ and } \mathbf{w}^y \in \mathfrak{R}^n$$

Here the indexes of weight matrices are kept same as in [6]. It can be easily concluded that the system given in (3) corresponds to the system given by (2), when  $\mathbf{w}^{hh}$  is a zero matrix,  $\mathbf{w}^{hi} \triangleq \mathbf{I}$ ,  $\mathbf{w}^{ii} \triangleq \mathbf{W}$ , and the activation function  $\mathbf{f}(\cdot)$  is chosen to be  $\mathbf{g}(\cdot)$  as stated earlier.

The well-known chaos yielding systems, as Chua oscillator, Lorenz equations are also special cases of the system given by (1).

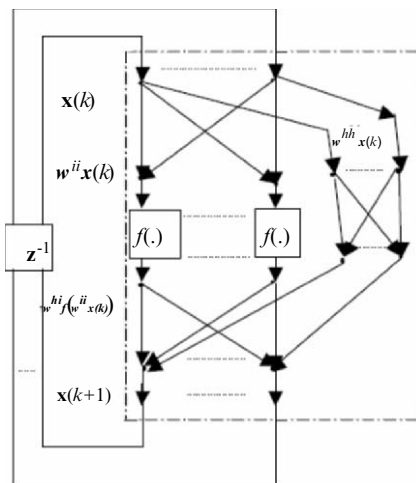
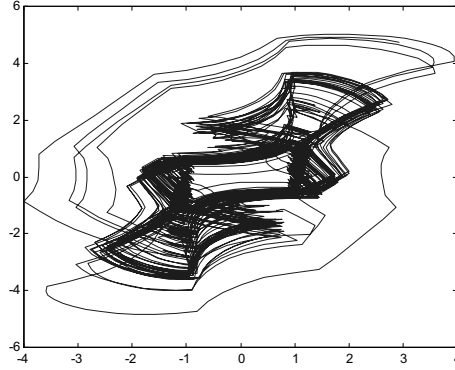


Fig. 1. The proposed ANN structure.

These systems can be obtained from the proposed structure with a suitable set of weight matrices, when the degree of the system is chosen to be three. If two of the activation functions are taken to be linear and one remaining is chosen as the nonlinear function of the system interested in, chaotic behavior of these systems can be obtained. Of course, the possibility of obtaining chaotic behavior is not restricted to these two special systems.

## Simulation Results

By setting a computer experiment with random choices of  $\hat{\mathbf{w}}^{hh}$ ,  $\hat{\mathbf{w}}^{hi}$ ,  $\mathbf{w}^{ii}$  and different activation functions, chaotic behavior has been observed as the solutions of the continuous time system given by (1) with system degree  $n \geq 3$ . The differential equation set has been solved using forward Euler method with time step 0.1.



**Fig. 2.** State portrait of continuous time system with dimension 3

One of many chaotic behaviors is the system with degree three which has the phase portrait given in Fig. 2. The activation function  $f(x)$  and weight matrices related with this example are as following:

$$f(x) = \begin{cases} 1.5 & x > 2 \\ 0.5x + 0.5 & 1 \leq x \leq 2 \\ -x & -1 < x < 1 \\ 0.5x - 0.5 & -2 \leq x \leq -1 \\ -1.5 & x < -2 \end{cases},$$

$$\hat{\mathbf{w}}^{hh} = \begin{bmatrix} 0.6145 & 0.5913 & -1.0091 \\ 0.5077 & -0.6436 & -0.0195 \\ 1.6924 & 0.3803 & -0.0482 \end{bmatrix},$$

$$\hat{\mathbf{w}}^{hi} = \begin{bmatrix} -1.0565 & 0.5287 & -2.1707 \\ 1.4151 & 0.2193 & -0.0592 \\ -0.8051 & -0.9219 & -1.0106 \end{bmatrix},$$

$$\mathbf{w}^{oi} = [0.0000 \quad -0.3179 \quad 1.0950], \quad \mathbf{w}^{ii} = \mathbf{I}.$$

The discontinuous activation function gives rise to a differential equation system with discontinuous right-hand side. A problem would be showing the existence and uniqueness of solution for this system. It can be shown that there exists a unique solution in the sense of Fillipov [7].

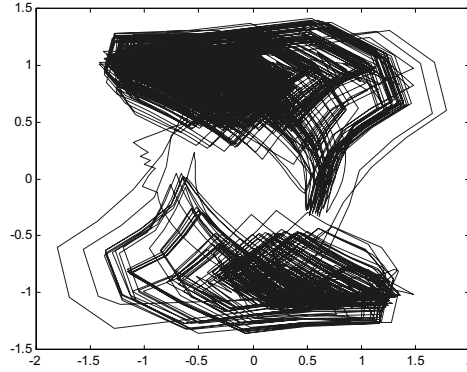


Fig. 3. State portrait of continuous time system with dimension 4

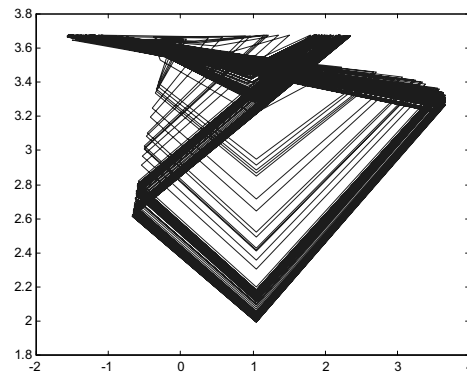


Fig. 4. State portrait of discrete time system with dimension 2

Figure 3 is another example of chaotic behavior, where the same activation function is used but the degree of the system is four. Due to lack of space, weight matrices for this case is not given.

For different choices of activation functions chaotic behavior has been also observed for the system given by (2). Phase portrait of one such example with system degree 2 is given in Fig. 4, where as an activation function  $g(x)$  given in The proposed Chaotic Artificial Neural Netuorle strucutre is considered.

The weight matrices giving rise to chaotic behavior in Fig. 4 are as follows:

$$\mathbf{w}^{hh} = \begin{bmatrix} -0.0006 & -0.0004 \\ -0.0010 & 0.0011 \end{bmatrix}, \mathbf{w}^{hi} = \begin{bmatrix} 2.1000 & 0 \\ 0 & 2.1000 \end{bmatrix},$$

$$\mathbf{w}^{ii} = \begin{bmatrix} -0.6280 & -0.0995 \\ -0.1068 & 0.1537 \end{bmatrix}$$

$$\mathbf{w}^{io} = [1.1863 \quad 0.1146].$$

During the computer experiment, the above weight matrices both for continuous time and discrete time have been obtained by selecting randomly and observing the behavior of the system. It is observed that while different nonmonotonic, piecewise linear activation functions are more capable of providing chaotic behavior for continuous time systems, continuous activation functions have to be favored for discrete time systems. Another observation is, as the dimension increases in discrete case, observing chaos is frequent. Using the activation functions of the above given examples, for example with dimension 2 ratio of observing chaotic behavior is 12/40 while with dimension 5 the ratio is 32/40. On the contrary, for the continuous time as the dimension increases, observing chaos is less. For example with dimension 3 ratio of observing chaotic behavior is 21/40 while with dimension 4 the ratio is 14/40.

Also it has to be pointed out that observing chaotic behaviour is more frequent if  $\mathbf{w}^{hh}$  matrix in discrete time has very small components and  $\hat{\mathbf{w}}^{hh}$  matrix in continuous time case has all negative components. One explanation of this, if the systems given by (1) and (2) observed, they can be thought as linear systems with nonlinear feedback terms. So, by choosing  $\mathbf{w}^{hh}$  and  $\hat{\mathbf{w}}^{hh}$  as mentioned, rendering a Lyapunov stable system into chaotic system by state feedback is more probable. For example, in continuous time case for a system of dimension 4, the ratio of chaotic behavior is 2/40 when  $\hat{\mathbf{w}}^{hh}$  is chosen from a normal distribution with mean zero and variance one. The same ratio is 14/40, when  $\hat{\mathbf{w}}^{hh}$  is chosen from a uniform distribution on the interval  $(-1.0, 0.0)$ .

## Conclusion

An ANN structure capable of generating chaotic behavior is proposed. Experimental results for different activation functions and different system dimensions are given to show the usefulness of the structure in obtaining chaos.

One application of this structure could be nonlinear system identification. Thus, the proposed structure has been used to obtain the chaotic time series of Feigenbaum system. The weights were adapted according to gradient descent method to minimize the instantaneous square of error between the chaotic time series obtained from Feigenbaum system and output of proposed neural network structure. The result was not superior to existing structures as EN, etc. but was as satisfactory as them.

## References

- [1] A. Vanecek and S. Celikovsky, *Control Systems, From Linear Analysis to Synthesis of Chaos*, Prentice Hall, London, 1996
- [2] H.D.I. Abarbanel, *Analysis of Observed Chaotic Data*, Springer Berlin Heidelberg, New York, 1996
- [3] A.N. Michel and D. Liu, *Qualitative Analysis and Synthesis of Recurrent Networks*, Marcel Dekker, New York, 2002
- [4] K. Smith, "Neural networks for combinatorial optimization: a review of more than a decade of research", *Inform Journal on Computing*, 11 (1), 1999
- [5] S.S. Kim, "Time-delay recurrent neural network for temporal correlations and prediction", *Neurocomputing*, 20, pp. 253–263, 1998
- [6] X. Li, Z. Chen, Z. Yuan and G. Chen, "Generating chaos by an Elman network", *IEEE Transactions on Circuits and Systems-I*, 48 (9), pp. 1126–1131, 2001
- [7] A.F. Filipov, *Differential Equations with Discontinuous Right-hand side*, Kluwer Dodrecht, 1988

# Advanced Signal Processing Algorithms for Wireless Communications

Erdal Panayirci<sup>1</sup> and Hakan A. Çirpan<sup>2</sup>

<sup>1</sup>Kadir Has University, Turkey, eepanay@khas.edu.tr

<sup>2</sup>Istanbul University, Turkey, hcirpan@istanbul.edu.tr

## Abstract

Traditional wireless technologies are not well suited to meet the extremely demanding requirements of providing the very high data rates with the ubiquity, mobility and portability characteristic of cellular systems. Some fundamental barriers, related to the nature of the radio channel as well as the limited bandwidth availability at the frequencies of interest, stand in the way. Unique sets of efficient advanced signal processing algorithms and techniques is the one of the primary enablers that will allow lifting these limits, primarily due to the impressive advent of low cost and low power digital signal processors. As an application of advanced signal processing techniques, we will consider the solution of blind phase noise estimation and data detection problem via a computationally efficient sequential Monte Carlo (SMC) methodology in this paper.

## Introduction

Advanced signal processing methods, such as the expectation-maximization (EM) algorithm, the SAGE algorithm, the Baum–Welch algorithm, per-survivor processing, Kalman filters and their extensions, hidden Markov modeling, SMC filters, and stochastic approximation algorithms, in collaboration with inexpensive and rapid computing power provide a promising avenue for overcoming the limitations of current wireless technologies. Applications of the advanced signal processing algorithms mentioned earlier include, but are not limited to, joint/blind/sequence detection, decoding, synchronization, equalization, as well as channel estimation techniques employed in advanced wireless communication systems, such as OFDM/OFDMA, space–time–frequency coding, MIMO, CDMA, and multiuser detection in time and frequency-selective MIMO channels. In particular, the development of suitable algorithms for wireless multiple access systems in nonstationary and interference-rich environments presents major challenges to the system designer. While considerable previous work has addressed many aspects of this problem separately, for example, single-user channel equalization, interference suppression for multiple access channels, and tracking of time-varying chan-

nels, the problem of jointly combining these impairments in wireless channels has only recently become significant. On the other hand, the optimal solutions mostly cannot be implemented in practice because of their prohibitively high computational complexity. The statistical tools implemented by the advanced signal processing techniques above provide promising new routes for the design of low-complexity signal processing techniques with performance approaching the theoretical optimum for fast and reliable communication in the highly severe and dynamic wireless environment. Although over the past decade such methods have been successfully applied in a variety of communication contexts, many technical challenges remain in emerging applications, whose solutions will provide the bridge between the theoretical potential of such techniques and their practical utility.

As an application of advanced signal processing techniques, we will address the solution of blind phase noise estimation and data detection problem via SMC methodology in the sequel.

## Phase Synchronization

Carrier phase synchronization is a critical issue in coherent digital communication systems. A considerable amount of research has been carried out for data detection in the presence of the time-varying phase noise as well as the fixed phase offset [1]. Estimating the phase offset and detecting the data jointly by maximum likelihood (ML) technique does not seem to be analytically tractable. Even if the likelihood function can be evaluated offline, however, it is invariably a nonlinear function of the parameter to be estimated, which makes the maximization step (which must be performed in real-time) computationally infeasible. A number of suboptimal algorithms have thus been proposed, most of which employ a two-stage receiver structure with a phase noise estimation stage followed by the data detection [2]. Phase synchronization is typically implemented by a decision directed (or data aided) or nondecision directed (or nondata aided). Decision directed schemes depend on availability of reliably detected symbol for obtaining the phase estimate, and therefore, they usually require transmission of pilot or training data. However, in applications where bandwidth is the most precious resource, training data can significantly reduce the overall system capacity. Thus blind or nondata-aided techniques become an attractive alternative [3, 4]. Unlike data-aided techniques, nondata-aided methods do not require knowledge of the transmitted data, and instead, they exploit statistics of digital transmitted signal. ML estimation techniques can also be used in nondecision-directed methods if the symbols transmitted are treated as random variables with known statistics so that the likelihood function can be averaged over the data sequence received. Unfortunately, except for few simple cases, this averaging process is mathematically impracticable and it can be obtained only by some approximations which are valid only either at high or low SNR values [5].

On the other hand, in order to provide an implementable solution, recently there have been a substantial amount of work on iterative formulation of the parameter

estimation problem based on the EM technique [6]. It is known that the EM algorithm derives iteratively and converges to the true ML estimation of these unknown parameters. The main drawbacks of this approach are that the algorithm is sensitive to the initial starting values chosen for the parameters, it does not necessarily converge to the global extremum and the convergence can be slow. Furthermore, in situation where the posterior distribution must be constantly updated with arrival of the new data with missing parts, EM algorithm can be highly inefficient, because the whole iteration process must be redone with additional data. The SMC methodology [7] that has emerged in the field of statistics and engineering has shown great promise to solve such problems. This technique can approximate the optimal solution directly without compromising the system model. More importantly, the SMC yields a fully blind algorithm and allows for both Gaussian and non-Gaussian ambient noise as well as high-speed parallel implementations. Furthermore, the tracking the time-varying phase noise and the data detection are naturally integrated [8].

## System Description

We consider a channel-coded communication system in the presence of random phase noise and the additive Gaussian noise. The input binary information bit  $d_t$  are encoded using some channel code, resulting in a code bit stream  $b_t$ . The code bits are passed to a symbol mapper, yielding complex data symbols  $s_t$ , which take values from a finite alphabet set  $A = \{a_1, a_2, \dots, a_{|A|}\}$ , where  $|A|$  represents the cardinality of the set  $A$ . Each data symbol is then transmitted through a channel whose input-output relationship is given by

$$y_t = s_t e^{j\theta_t} + n_t, \quad t = 0, 1, \dots \quad (1)$$

where  $y_t, s_t, \theta_t$ , are the received signal, the transmitted symbols and the phase noise, respectively, and  $n_t$  the additive complex Gaussian noise with mean zero and the variance  $\sigma_n^2 = E[|n_t|^2]$ . The phase noise process  $\theta_t$  at  $t$ th sampling instant is defined as a Wiener process determined as

$$\theta_t = \theta_{t-1} + u_t, \quad t = 1, 2, \dots \quad (2)$$

$$\theta_0 \sim \text{uniform}(-\pi, +\pi) \quad (3)$$

where  $\{u_t\}$  is a sequence of independent and identically distributed (i.i.d.) zero-mean random variables with variance equal to  $\sigma_u^2$ . Note that as Wiener phase noise is the accumulation of white noise, its variance increase linearly with  $t$ . It is assumed that  $u_t$  and  $n_t$  are independent. Our main objective is to solve the problem of online detection of the symbols  $s_t$  and estimation of the phase noise  $\theta_t$ , completely blindly, based on the received signals up to time  $t$ ,  $\{y_i\}_{i=0}^t$ . Defining the vectors,

$$S_t = [s_0, s_1, \dots, s_t]^T, \quad Y_t = [y_0, y_1, \dots, y_t]^T, \quad \theta_t = [\theta_0, \theta_1, \dots, \theta_t]^T$$



the problem may be formulated by making Bayesian inference with respect to the posterior distribution

$$p(\theta_t, S_t | Y_t) \propto p(\theta_0) p(S_t) p(y_0 | \theta_0, s_0) \prod_{j=1}^t p(\theta_j | \theta_{j-1}) p(y_j | \theta_j, s_j) \\ \propto p(\theta_0) p(S_t) \exp\left(-\frac{1}{\sigma^2} |y_0 - s_0 e^{j\theta_0}|^2\right) \prod_{j=1}^t \exp\left(-\frac{1}{\sigma_s^2} (\theta_j - \theta_{j-1})^2 - \frac{1}{\sigma^2} |y_j - s_j e^{j\theta_j}|^2\right), \quad t = 0, 1, \dots$$

Although this joint distribution can be written out explicitly up to a normalizing constant, the computation of the corresponding marginal joint distributions  $p(s_t, \theta_t | Y_t)$ , necessary for online joint symbol detection and phase noise estimation involve very high dimensional integration. Therefore, the task is mathematically infeasible in practice. The Gibbs samples [9] is a Monte Carlo method for overcoming this difficulty. However, it is not an adaptive procedure and has difficulty dealing with sequentially observed data. With new data coming the whole computation must be repeated to incorporate new information. In the following section, we present an adaptive blind algorithm for the joint symbol detection and the phase noise estimation which is based on a Bayesian formulation of the problem called SMC method first developed by [9].

## SMC Technique for Blind Detection and Estimation

We first consider the case of uncoded system, where the symbols are assumed to independent and identically distributed, i.e.,

$$P(s_t = a_t | S_{t-1}) = P(s_t = a_t), \quad a_t \in A. \quad (4)$$

For simplicity the symbols are chosen from a QPSK constellation. When no prior information about the symbols is available, the symbols are assumed to take each possible value in  $A$  with equal probability, i.e.,  $P(s_t = a_t) = 1/|A|$ . Since we are interested in jointly estimating the symbol  $s_t$  and the phase noise  $\theta_t$ , at time  $t$  based on the observation  $Y_t$ , the Bayes solution requires the posterior distribution

$$p(s_t, \theta_t | Y_t) = \int p(\theta_t | Y_t, S_t) p(S_t | Y_t) dS_{t-1}. \quad (5)$$

Note that with a given  $S_t$ , the nonlinear (Kalman filter) model (1), (2) can be converted into a linear model by linearizing the observation equation (1) as follows [10]:

$$\theta_t = \theta_{t-1} + u_t, \quad (6)$$

$$y_t = s_t H_t \theta_t + s_t Q_t + n_t, \quad (7)$$

where  $H_t = j e^{j\hat{\theta}_{t-1}}$ ,  $Q_t = (1 - j\hat{\theta}_{t-1}) e^{j\hat{\theta}_{t-1}}$  and  $\hat{\theta}_{t-1}$  denotes the estimator of  $\theta_t$  based on the observations  $Y_{t-1} = (y_0, y_1, \dots, y_{t-1})$ . Then the state-space model (3), (4) becomes a linear Gaussian system. Hence,  $p(\theta_t | S_t, Y_t) \sim N(\mu_{\theta_t}(S_t), \sigma_{\theta_t}^2(S_t))$ , where the mean  $\mu_{\theta_t}(S_t)$  and the variance  $\sigma_{\theta_t}^2(S_t)$  can be obtained as follows. Denoting

$$\mu_{\theta_t}(S_t) \triangleq \hat{\theta}_{t|t}, \quad \sigma_{\theta_t}^2(S_t) \triangleq M_{t|t} \quad (8)$$

$\hat{\theta}_{t|t}$  and  $M_{t|t}$  can be calculated recursively by using the Extended Kalman Technique [10, page 449–452] with the given  $S_t$  as

$$\hat{\theta}_{t|t} = \hat{\theta}_{t|t-1} + K_t(y_t - s_t e^{j\hat{\theta}_{t|t-1}}), \quad M_{t|t} = (1 - K_t H_t) M_{t|t-1} \quad (9)$$

where

$$K_t = \frac{M_{t|t-1} H_t^*}{(M_{t|t-1} + \sigma_n^2)}, \quad \hat{\theta}_{t|t-1} = \hat{\theta}_{t-1|t-1}, \quad M_{t|t-1} = M_{t-1|t-1} + \sigma_u^2.$$

We can now make timely estimates of  $\theta_t$  and detection of  $s_t$  based on the currently available observation  $Y_t$ , up to time  $t$ , blindly, as follows. With the Bayes theorem, we realize that the optimal solution to this problem is

$$\hat{\theta}_t = E\{\theta_t | Y_t\} = \int \theta_t p(\theta_t | Y_t) d\theta_t = \int_{S_t} \underbrace{\left[ \int_{\theta_t} \theta_t p(\theta_t | S_t, Y_t) d\theta_t \right]}_{\mu_{\theta_t}(S_t)} p(S_t | Y_t) dS_t. \quad (10)$$

It then follows that

$$\hat{\theta}_t = E\{\theta_t | Y_t\} = \int_{S_t} \mu_{\theta_t}(S_t) p(S_t | Y_t) dS_t. \quad (11)$$

Similarly, the data can be detected by the hard decisions on the symbol  $s_t$  by

$$\hat{s}_t = \arg \max_{a_i \in \mathcal{A}} P(s_t = a_i | Y_t), \quad (12)$$

where  $P(s_t = a_i | Y_t) = E\{1(s_t = a_i) | Y_t\}$ .  $1\{\cdot\}$  is an indicator function defined as

$$1(s_t = a_i) \begin{cases} 1 & \text{if } s_t = a_i \\ 0 & \text{otherwise.} \end{cases}$$

In most cases, an exact evaluations of the expectations (10) and (11) are analytically intractable. SMC technique can provide us an alternative way for the required computation. Specifically, following the notation adopted in [11], if we can draw  $m$  independent random samples  $\{S_t^{(j)}\}_{j=1}^m$  from the distribution  $p(S_t | Y_t)$ , then we can approximate the quantities of interest  $E\{\theta | Y_t\}$  and  $E\{1(s_t = a_i) | Y_t\}$  in (12) and  $P(s_t = a_i | Y_t)$ , respectively, by

$$E\{\theta | Y_t\} \cong \frac{1}{m} \sum_{j=1}^m \mu_{\theta_t}(S_t^{(j)}), \quad E\{1(s_t = a_i) | Y_t\} \cong \frac{1}{m} \sum_{j=1}^m 1(s_t^{(j)} = a_i). \quad (13)$$

But, usually drawing samples from  $p(S_t | Y_t)$  directly is usually difficult. Instead, sample generation from some trial distribution may be easier as follows:

$$E\{\theta | Y_t\} \cong \frac{1}{W_t} \sum_{j=1}^m \mu_t(S_t^{(j)}) w_t^{(j)}, \quad E\{1(s_t = a_i) | Y_t\} \cong \frac{1}{W_t} \sum_{j=1}^m 1(s_t^{(j)} = a_i) w_t^{(j)}, \quad i = 1, 2, \dots, |A| \quad (14)$$

with  $W_t = \sum w_t^{(j)}$ . The pair  $(S_t^{(j)}, w_t^{(j)})$ ,  $j = 1, 2, \dots, m$  is called a properly weighted sample with respect to distribution  $p(S_t | Y_t)$ . Note that the samples  $S_t^{(j)}$  can be drawn from the distribution  $q(S_t | Y_t)$  sequentially as follows. We can choose  $q(\cdot)$  to satisfy

$$q(S_{t-1} | Y_t) = q(S_{t-1} | Y_{t-1}).$$

Then, it can be easily shown that  $q(S_t | Y_t) = q(s_t | Y_t, S_{t-1}) q(S_{t-1} | Y_{t-1})$ , and one can draw samples  $s_t^{(j)}$  from a trial distribution  $q(s_t | Y_t, S_{t-1}^{(j)})$  and let  $S_t^{(j)} = (s_t^{(j)}, S_{t-1}^{(j)})$

for  $t=0,1,\dots$ . Specifically, it was shown in [11] that a suitable choice for the trial distribution is of the form

$$q(s_t | Y_t, S_{t-1}^{(j)}) = p(s_t | Y_t, S_{t-1}^{(j)}). \quad (15)$$

For this trial distribution, it is shown in [11] that the importance weight is updated according to

$$w_t^{(j)} = w_{t-1}^{(j)} p(y_t | Y_{t-1}, S_{t-1}^{(j)}), \quad t = 0, 1, \dots \quad (16)$$

The predictive distribution in (16) is given by

$$\begin{aligned} p(y_t | Y_{t-1}, S_{t-1}^{(j)}) &= \sum_{a_i \in \mathcal{A}} p(y_t | Y_{t-1}, S_{t-1}^{(j)}, s_t = a_i) P(s_t = a_i | Y_{t-1}, S_{t-1}^{(j)}) \\ &= \sum_{a_i \in \mathcal{A}} p(y_t | Y_{t-1}, S_{t-1}^{(j)}, s_t = a_i) P(s_t = a_i), \end{aligned} \quad (17)$$

where (17) holds because  $s_t$  is independent of  $S_{t-1}$  and  $Y_{t-1}$ . Furthermore, it can be shown from the state and observation equations in (9), respectively, that

$$p(y_t | Y_{t-1}, S_{t-1}^{(j)}, s_t = a_i) \sim N(\mu_{y_t}^{(j)}(i), \sigma_{y_t}^{2(j)}(i)) \quad (18)$$

with mean and variance given by

$$\mu_{y_t}^{(j)}(i) = E\{y_t | Y_{t-1}, S_{t-1}^{(j)}, s_t = a_i\} = a_i(H_t \mu_{\theta_{t-1}}^{(j)} + Q_t), \quad (19)$$

$$\sigma_{y_t}^{2(j)}(i) = \text{Var}\{y_t | Y_{t-1}, S_{t-1}^{(j)}, s_t = a_i\} = \sigma_{\theta_{t-1}}^{2(j)} + \sigma_n^2 + \sigma_p^2, \quad (20)$$

where the quantities  $\mu_{\theta_{t-1}}^{(j)}$  and  $\sigma_{\theta_{t-1}}^{2(j)}$  in (19) and (20) can be computed recursively for the extended Kalman equations given in (9). The trial distribution in (14) can be computed as follows:

$$p(s_t = a_i | Y_t, S_{t-1}^{(j)}) = p(y_t | Y_{t-1}, S_{t-1}^{(j)}, s_t = a_i) \times P(s_t = a_i | Y_{t-1}, S_{t-1}^{(j)}) \stackrel{\Delta}{=} \xi_{t,i}^{(j)} \quad (21)$$

where it follows from (6) and (7) that

$$\xi_{t,i}^{(j)} = \frac{1}{\pi \sigma_{y_t}^{2(j)}(i)} \exp\left(-\frac{\|y_t - \mu_{y_t}^{(j)}(i)\|^2}{\sigma_{y_t}^{2(j)}(i)}\right) P(s_t = a_i). \quad (22)$$

We now summarize the SMC blind data detection and phase noise estimation algorithm as follows:

**Step 1- Initialization:**

Initialize the extended Kalman filter: Choose the initial mean and the variance of the estimated  $\theta_j$  as the mean and the variance of a uniform distribution defined on  $-\pi, +\pi$  as

$$\begin{aligned} \mu_{\theta_{-1}}^{(j)} &= \hat{\theta}_{-1|1}^{(j)} = 0 \\ \sigma_{\theta_{-1}}^{2(j)} &= M_{-1|1}^{(j)} = \pi^2/12, j = 1, 2, \dots, m. \end{aligned} \quad (23)$$

- Initialize the importance weights: All importance weights are initialized as  $w_{-1}^{(j)} = 1, j = 1, 2, \dots, m$ . Since the data symbols are assumed to be independent, initial symbols are not needed be generated.

**Step 2- Compute  $\xi_{t,i}^{(j)}$ :** For each  $a_i \in \mathcal{A}$  compute the  $\mu_{y_t}^{(j)}(i), \sigma_{y_t}^{2(j)}(i)$  and  $\xi_{t,i}^{(j)}$  from (19), (20) and (22), respectively.

**Step 3- Draw samples  $s_t^j, j=1,2,\dots,m$ :** Draw  $s_t^{(j)}$  from the set  $\mathcal{A}$  with probabilities

$$P(s_i^{(j)} = a_i) \propto \xi_{i,i}^{(j)}, a_i \in A. \quad (24)$$

Append  $s_i^{(j)}$  to  $S_{i-1}^{(j)}$  to obtain  $S_i^{(j)}$ .

**Step 4-** Compute the importance weights

$$w_i^{(j)} = w_{i-1}^{(j)} \sum_{a_i \in A} \xi_{i,i}^{(j)}.$$

**Step 5-** *Detect the symbol  $S_i$* : Detect the symbol  $S_i$  from (12), (13) and (14).

**Step 6-** *Update the a posteriori mean and variance of the phase noise*:

If the samples drawn up to time  $t$  is  $S_i$  in Step 3, set

$$\mu_{\theta_i}(S_i^{(j)}) \stackrel{\Delta}{=} \mu_{\theta_i}^{(j)} = \hat{\theta}_{i|t}^{(j)}, \quad \sigma_{\theta_i}^{2(j)}(S_i^{(j)}) \stackrel{\Delta}{=} \sigma_{\theta_i}^{2(j)} = M_{i|t}^{(j)} \quad j = 1, 2, \dots, m.$$

and update according to the Kalman equations (9).

**Step 5-** *Do the resampling described as in [11]*.

## Numerical and Simulation Results

In this section, we provide some computer simulation examples to demonstrate the performance of the proposed SMC approach for blind phase noise estimation and data detection. The phase process is modeled by AR process driven by a white Gaussian noise with  $\sigma_u^2 = 0.0314$ . It is assumed BPSK modulation is employed. In order to demonstrate the performance of the adaptive SMC approach, we first present the performance (in terms of the phase error  $\phi(k) = \theta_i - \hat{\theta}_i$ ) during one simulation run for different initial phase errors  $\phi(k) = 0, \pi/4, \pi/2, 3\pi/4, \pi$ . The phase error for several values of  $\phi(0)$  at SNR = 10 dB is shown in Fig. 1. The performance of the proposed algorithm is further exploited by the evaluation of average BER over observed block for different SNRs and different initial phase errors. The uncoded average BER performance of this adaptive approach is plotted in Fig. 2.

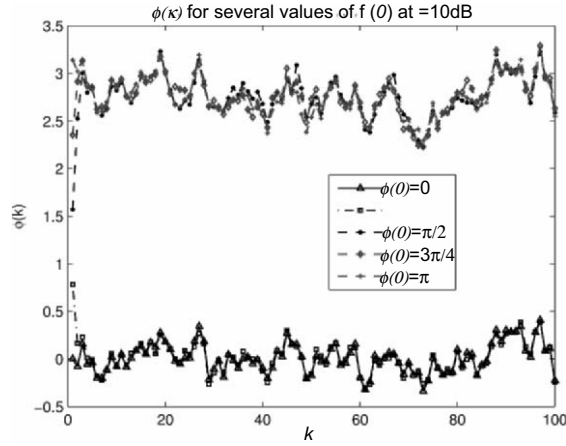


Fig. 1. Tracking performance for different initializations at SNR = 10 dB

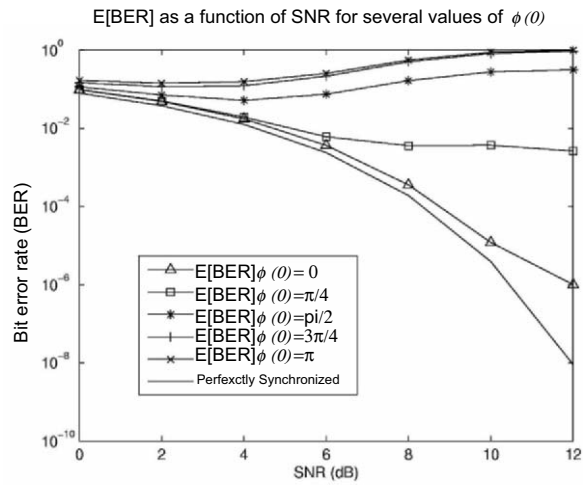


Fig. 2. BER performance

Our simulations indicate that

- as the initial phase error  $\phi(0)$  approaches  $\pi$ , the probability that the phase error converges to the dual equilibrium point becomes very high
- as the initial phase error  $\phi(0)$  approaches  $\pi$ , the BER increases, for  $\phi(0) = \pi$ , the BER is almost equal to 1 (due to ambiguity).

## Conclusions

We have developed a new adaptive Bayesian advanced signal processing approach for blind phase noise estimation and data detection based on SMC methodology. The optimal solutions to joint symbol detection and phase noise estimation problem is computationally prohibitive to implement by conventional methods. Thus the proposed advanced signal processing sequential approach offers a novel and powerful approach to tackling this problem at a reasonable computational cost.

## Acknowledgment

This work is part of the Joint Research Activities of the Network of Excellence on Wireless Communications (NEWCOM) supported by the European Commission's 6th Framework Program.

## References

- [1] H. Meyr, M. Moeneclaey and S.A. Fechtel, *Digital Communications Receivers*, Wiley, New York, 1998
- [2] C.N. Georghiades and J.C. Han, "Optimum decoding of trellis coded modulation in the presence of phase noise", *Proc. 1990 Int. Symp. Inform. Theory Appl. (ISITA '90) Hawaii*, Nov. 1990
- [3] A.T. Huq, E. Panayirci and C.N. Georghiades, "ML NDA carrier phase recovery for OFDM systems with M-PSK signaling", *Proc. IEEE Int. Conf. Commun. (ICC '99)*, June 6–10, 1999, Vancouver, Canada
- [4] E. Panayirci and C.N. Georghiades, "Non-data-aided ML carrier frequency and phase synchronization in OFDM systems", *Eur. Trans. Telecommun.*, 2000
- [5] U. Mengali and A.L. D'Andrea, *Synchronization Techniques for Digital Receivers*, Plenum Press, New York 1997
- [6] A.P. Dempster, N.M. Laird and D.B. Rubin, "Maximum likelihood from incomplete data via the EM algorithm", *Ann. R. Stat. Soc.*, pp. 1–38, December 1977
- [7] M. Pitt and N. Shephard, "Filtering via simulation: auxiliary particle filter", *J. Am. Stat. Soc. B*, no. 63, 2001
- [8] S.J. Lui and R. Chen, Sequential Monte Carlo method for dynamical systems, *J. Am. Stat. Assoc.*, vol. 93, pp. 1031, 1044, 1998
- [9] S. Geman and D. Geman, "Stochastic relaxation, Gibbs distribution and the Bayesian restoration of images", *IEEE Trans. Pattern Anal. Machine Intell.* vol. 6, pp. 721–741, 1984
- [10] S.M. Kay, *Fundamentals of Statistical Signal Processing*, Prentice Hall Upper Saddle River, NJ, 1993
- [11] Z. Yang and X. Wang, "A sequential Monte Carlo blind receiver for OFDM systems in frequency-selective fading channels", *IEEE Trans. Signal Proc.*, vol. 50, no. 2, pp. 271–280, Feb. 2003

# A Clock-Controlled Stream Cipher with Dual Mode

İ. Ergüler<sup>1,2</sup> and E. Anarim<sup>2</sup>

<sup>1</sup>Department of Electronics and Communication Engineering, Dogus University, Acibadem, 81010 Istanbul, Turkey, ierguler@dogus.edu.tr

<sup>2</sup>Department of Electrical–Electronics Engineering , Bogazici University, 34342 Bebek, Istanbul, Turkey, anarim@boun.edu.tr

## Abstract

In this paper, a new type of clock-controlled stream cipher referred as CCDM (clock-controlled stream cipher with dual mode) is proposed. This model uses five linear feedback shift registers (LFSRs) and has two different clocking mechanisms that provide security enhancements, especially against guess and determine type of attacks, compared to conventional LFSR-based stream generators. Besides its security power against some well-known attacks, the cipher also generates keystream sequences with nice statistical properties.

## Introduction

Stream ciphers are one of the most important classes of encryption algorithms used to ensure security in digital communication. The design of many stream ciphers is based on use of linear feedback shift registers (LFSRs), due to their simplicity, speed of implementation in hardware and providing sequences with good statistical properties. A stream cipher cannot be considered suitable for cryptographic applications unless its output sequences have large periods, large linear complexities and possess certain randomness properties. Moreover a stream cipher must provide high resistance against well-known cryptanalytic attacks such as time-memory trade-off attacks, guess-determine attacks and correlation attacks. The use of clock-controlled mechanism in stream generators can be a good alternative for achieving these properties.

In this study, we present a new LFSR-based stream cipher which consisted of five LFSRs and uses a 128-bit secret key  $K$  and a 287-bit initialization vector (IV). In classical clock-controlled stream generator models, usually there is a single clock-controlling mechanism; this mechanism can be controlled by a single register such as in case of LILI keystream generator, alternating step generator, ORYX

[1–3], or clock-control mechanism can take inputs from each of the registers which is also known as mutual clock-control mechanism as in the case of A5/1 [4]. For the CCDM algorithm, there are two different clocking mechanisms but operate with same LFSRs. By means of this property, information about which algorithm is used in which part of the generated keystream sequence can be hidden from a third party, although all details of the algorithm are given. As a result, increase in cryptanalysis complexity of the system has been achieved.

## Description of CCDM

The proposed algorithm is a simple LFSR-based binary stream cipher and has five LFSRs of lengths 61, 127, 107, 89 and 31 bits and denoted as R1, R2, R3, R4 and R5, respectively. The system works over two different modes as CCDM-Mode I and CCDM-Mode II that are shown in Figs. 1 and 2 respectively. The contents of R5 related to secret key  $K$  determines in which mode the cipher will operate. Since the whole responsibility of the R5 is selection of modes, it is not depicted in the figures. According to the selected mode, R1 controls the clocking of R2, R3 and R4 or it gives input bits to the clocking control mechanism. The remaining LFSRs, R2, R3 and R4, are responsible for generating the output sequence. In both the modes, R1 and R5 are regularly clocked. All of the registers have primitive polynomials for their feedback functions as follows:

$$\text{LFSR R1: } g_1(x) = x^{61} + x^{53} + x^{45} + x^{38} + x^{30} + x^{23} + x^{15} + x^7 + 1,$$

$$\text{LFSR R2: } g_2(x) = x^{127} + x^{103} + x^{96} + x^{87} + x^{66} + x^{51} + x^{41} + x^{35} + x^{23} + x^3 + 1,$$

$$\text{LFSR R3: } g_3(x) = x^{107} + x^{93} + x^{81} + x^{67} + x^{54} + x^{41} + x^{27} + x^{13} + 1,$$

$$\text{LFSR R4: } g_4(x) = x^{89} + x^{83} + x^{80} + x^{55} + x^{53} + x^{42} + x^{39} + x + 1,$$

$$\text{LFSR R5: } g_5(x) = x^{31} + x^{27} + x^{23} + x^{19} + x^{15} + x^{11} + x^7 + x^3 + 1.$$

Algorithm uses a 128-bit secret key  $K$  and a 287-bit IV which can be known. In the following subsections the detailed description of the two modes will be given.



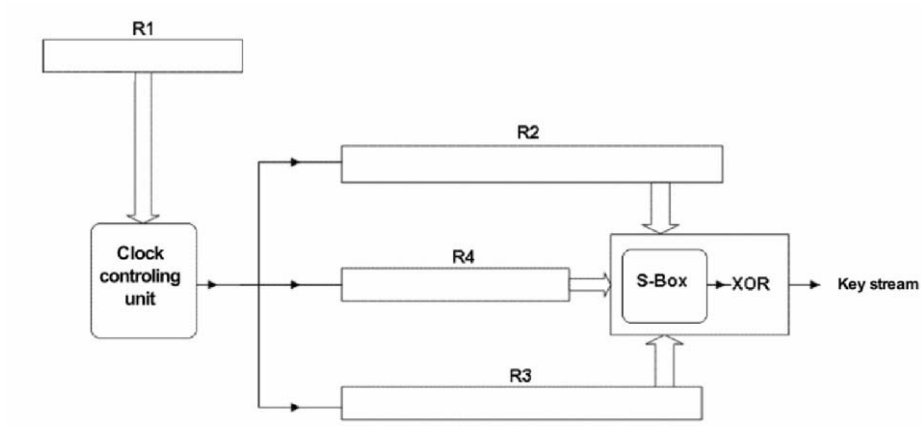


Fig. 1. The block diagram of CCDM-Mode I

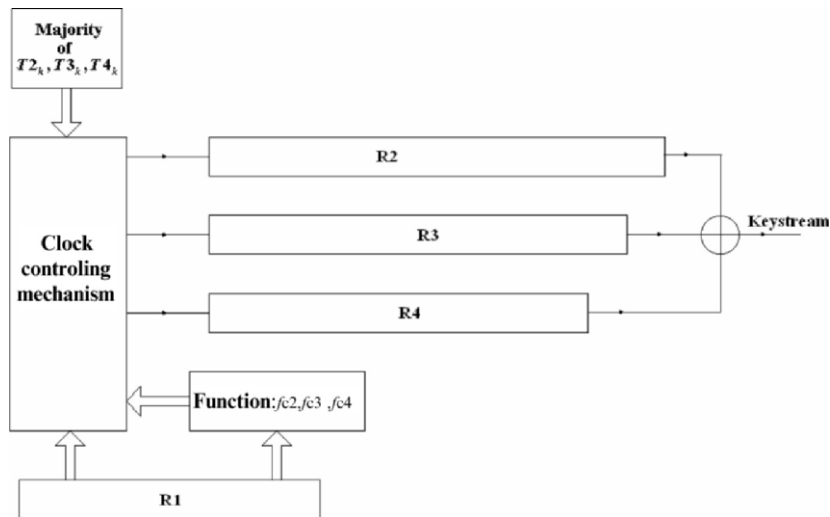


Fig. 2. The block diagram of CCDM-Mode II

**CCDM Mode-I**

As it can be seen from Fig. 1, in CCDM-Mode I four LFSRs, R1, R2, R3 and R4 can be categorized into three classes according to their functions in the algorithm; clock-controlling, S-box selection and key stream generation. R1 has a length of 61 bits and controls the clocking of the other three registers. In each clock cycle, it

computes the functions  $f_{C_2}$ ,  $f_{C_3}$  and  $f_{C_4}$ , each of these determines how many times R2, R3 and R4 are clocked, respectively, as given below:

$$f_{C_2}(\text{Rl}(8), \text{Rl}(38)) = 2\text{Rl}(8) + \text{Rl}(38) + 1, \quad (1)$$

$$f_{C_3}(\text{Rl}(22), \text{Rl}(56)) = 2\text{Rl}(22) + \text{Rl}(56) + 1, \quad (2)$$

$$f_{C_4}(\text{Rl}(16), \text{Rl}(42)) = 2\text{Rl}(16) + \text{Rl}(42) + 1. \quad (3)$$

Let  $C_i(t)$  represent the number of clocking of  $R_i$  according to  $f_{C_i}(t)$  at time  $t$  for  $i \in \{1, 2, 3, 4\}$ . As it can be seen from (1–3),  $C_i(t) \in \{1, 2, 3, 4\}$  whose distribution of elements is close to uniform. Therefore, each of R2, R3 and R4 is clocked at least once and at most four times in each clock cycle. After the clocking of the R2, R3 and R4, R1 is stepped once. CCDM-Mode I uses  $4 \times 16$  S-boxes of  $s^5\text{DES}$  [5] for the keystream generation. In each cycle, R4 decides which S-boxes are used by R2 and R3, according to the values of the functions  $f_{S_2}$  and  $f_{S_3}$ :

$$f_{S_2} = 4\text{R4}(6) + 2\text{R4}(12) + \text{R4}(24) + 1, \quad (4)$$

$$f_{S_3} = 4\text{R4}(10) + 2\text{R4}(17) + \text{R4}(29) + 1. \quad (5)$$

Equations (4) and (5) evaluate the orders of S-boxes to use among eight S-boxes for R2 and R3, respectively. For example; if  $f_{S_2}$  is 3 and  $f_{S_3}$  is 5, then R2 uses S-box S3 and R3 uses S-box S5 in generating the output sequence.

The job of R2 and R3 is producing the key stream according to the S-boxes selected by R4 as follows: Let  $S_j$  stand for the selected S-box of R2 and  $S_k$  represent the S-box for R3 where  $j$  and  $k$  denote the order of selected S-box for R2 and R3, so  $1 \leq j \leq 8$  and  $1 \leq k \leq 8$ .  $S_j$  uses six bits of R2 and  $S_k$  uses six bits of R3 as input bits with respect to the row–column method shown in Table 1. According to the table,  $S_{j\_row}$  and  $S_{k\_row}$  are the variables that keep the computed results for row decision of  $S_j$  and  $S_k$ , respectively. In a similar fashion,  $S_{j\_column}$  and  $S_{k\_column}$  save the computed values for column decision of  $S_j$  and  $S_k$ . Each of  $S_{j\_output}$  and  $S_{k\_output}$  keeps the appropriate four bits output. Another four bits of sequence is produced by concatenating the last two bits of R2 and R3. The first two bits of the sequence come from last two bits of R3 and the remained two bits of the sequence come from last two bits of R2. Then by applying XOR to the three 4-bit sequences that are produced by the S-boxes and combination of last bits of the two LFSRs, four bits of key stream is generated. In the following part, whole algorithm is summarized:

- The functions  $f_{C_2}$ ,  $f_{C_3}$  and  $f_{C_4}$  are computed according to the specified bits of R1
- R2, R3 and R4 are stepped with respect to the results of  $f_{C_2}$ ,  $f_{C_3}$  and  $f_{C_4}$
- R1 is clocked once
- $f_{S_2}$  and  $f_{S_3}$  are evaluated according to the specified bits of R4;  $S_j$  and  $S_k$  are determined
- Each of  $S_j$  and  $S_k$  contributes four bits output by using appropriate bits of R2–R3
- Four-bit sequence is generated by combining the last two bits of R2 and R3
- By XOR'ing these three 4-bit sequences, 4 bits of key stream is generated

**Table 1.** S-Box row–column method of CCDM-Mode I

$$\begin{aligned}
 S_{j\_row} &= 2R2(26) + R2(70) \\
 S_{k\_row} &= 2R3(12) + R3(32) \\
 S_{j\_column} &= 8R2(6) + 4R2(22) + 2R2(46) + R2(64) \\
 S_{k\_column} &= 8R3(21) + 4R3(40) + 2R3(53) + R3(61) \\
 S_{j\_output} &= S_j(S_{j\_row})(S_{j\_column}) \\
 S_{k\_output} &= S_k(S_{k\_row})(S_{k\_column})
 \end{aligned}$$

**CCDM Mode-II**

In this mode, instead of clock-control mechanism depending on a single register, a mutual clock control one is applied. The algorithm is depicted in Fig. 2. As can be seen all of the four registers as R1, R2, R3 and R4 give input to the clock-control mechanism. R1 gives two bit-input to the each of three clock-control functions which are denoted as  $f_{C2}$ ,  $f_{C3}$  and  $f_{C4}$ . These functions are given by:

$$f_{C2}(R1(8), R1(38)) = 2R1(8) + R1(38) + 2, \tag{6}$$

$$f_{C3}(R1(22), R1(56)) = 2R1(22) + R1(56) + 2, \tag{7}$$

$$f_{C4}(R1(16), R1(42)) = 2R1(16) + R1(42) + 2, \tag{8}$$

where  $R1(i)$  represents the  $i$ th tap bit of R1 at time instant  $t$ .  $f_{C2}$ ,  $f_{C3}$  and  $f_{C4}$  give integer numbers that are the numbers of clocking of R2, R3 and R4 at time  $t$ , respectively. If  $C_i(t)$  represents the number of clocking for  $i$ th register according to  $f_{C_i}(t)$  at time  $t$ , then  $C_i(t) \in \{2,3,4,5\}$ . If the clocking mechanism of the generator were like that, each of R2, R3 and R4 would be clocked at least twice and at most five times between the generations of two consecutive bits. However for this mode, clocking mechanism also depends on R2, R3 and R4 as follows: For each key stream bit generation majority of  $k$ th clocking tap bit of R2, R3 and R4,  $T2_k$ ,  $T3_k$  and  $T4_k$ , respectively, is calculated and only those registers whose clocking tap value is the same as majority result are clocked  $C_i(t)$  times. If there exists a register whose clocking tap value is not equal to majority, it is clocked once. So each of R2, R3 and R4 is clocked at least once and at most five times before each key stream bit is produced. The tap bit locations of the registers are shown in Fig. 3. The value of ‘ $k$ ’ is determined according the result of  $4R1(23)+2R1(34)+R1(52)$ . For example, let the  $R1(23)$ ,  $R1(34)$  and  $R1(52)$  be 1, 0 and 1, respectively. Then

' $k$ ' is evaluated as 5. Thus, for this case clocking tap bits of R2, R3 and R4 become  $T2_5$ ,  $T3_5$  and  $T4_5$ . Majority of these clocking tap bits is calculated and two or three registers whose clocking tap value is the same as majority result are clocked  $C_i(t)$  times. By using this clocking mechanism nonlinearity of the system is increased and stop and go clocking mechanism which may permit attacks is avoided.

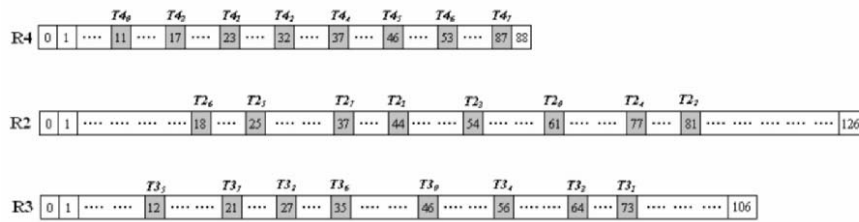


Fig. 3. Clocking tap bit locations of the generator registers R2, R3 and R4

Four bits of key stream  $z(t)$  is generated by taking 4 bits from each of R2, R3, R4 and using these input bits in four third-order nonlinear Boolean functions, each of which requires six input variables. Following the bit generation, clockings of R1, R2, R3 and R4 are done. Finally R1 is stepped once.

### Security of the Proposed Cipher

For a cipher design, the crucial point that a designer has to consider is its resistance against different attacks. Therefore, in this section we consider a number of attacks with respect to CCDM algorithm. These attacks are known-plaintext attacks conducted under the assumption that the cryptanalyst knows the whole internal structure of the generator.

#### Time Memory Trade-Off Attacks

Time-memory trade-off attack is a practical method to decrease the time for key search when plaintext is given in advance. This type of attack can be applied, if the cipher has a small state size. Usually, in time-memory trade-off attacks, attacker produces a number of output bits from certain states of the cipher and then keeps these cipher states and their corresponding outputs in pairs in a sorted list. Then he searches to find a match between a received keystream sequence and the stored output sequences. If this occurs, the corresponding cipher state is obtained and from this state the key can be successfully recovered. One can see that the state size of CCDM is  $N= 2^{415}$ ; it is too large compared to the key size  $2^{128}$ , so such an attack for CCDM is infeasible. An enhanced time memory trade-off attack presented in [6] can be applied. According to this study, state space  $N$  can be distributed between memory  $M$ , computational time  $T$  and known amount of data  $D$

with respect to the equation  $M^2TD^2 = N^2$  for  $D^2 \leq T \leq N$ . Notice that since  $N^2 = 2^{830}$ ,  $TD^2 > 2^{750}$  must be satisfied with the assumption that available memory to the attacker is about terabytes. However, such an attack is not better than exhaustive key search and it is impractical.

**Guess-and-Determine Attacks**

The basic idea of guess-and-determine type of attacks is to guess some unknown contents of the stream generator and then from the guessed values deduce the remained unknown parts. Generally, for clock-ontrrolled stream ciphers contents of the register that controls the clocking of the others is first guessed and then the information about future clockings of the other registers are revealed. After, the cryptanalyst tries to recover the whole state of the cipher using this information. To apply this attack on CCDM, one has to know in which mode the cipher operates, so he has to make assumptions about the contents of R5 and K. Also in the second mode of CCDM, all of the registers give input bits to the clocking mechanism, thus guessing the contents of R1 cannot be enough to know the clockings of the others. Furthermore, since length of R1 is 61 bits, guessing its internal state will cost  $2^{61}$  complexity. Considering clocking mechanism, use of S-boxes, length of registers and mode transitions, we have found no such attacks applicable on the proposed cipher.

**Correlation attacks**

Correlation attacks are usually the most effective attack type on certain stream ciphers. The main idea behind this attack is the cryptanalyst can attempt in some way to detect a correlation between the known output sequence and the output of one individual LFSR. Clock-controlled stream ciphers provide practical resistance against fast correlation attacks first described in [7]. However, there are different correlation attacks that can be applied on clock-controlled LFSR based stream ciphers, such as unconstrained embedding attack, constrained embedding attack, edit distance attack and edit probability attack [8].

If  $d_i(t)$  represents the number of clocking of  $i$ th generator register of CCDM at time  $t$ ,  $d_i(t) \in \{1,2,3,4,5\}$  for  $i \in \{2,3,4\}$ , then expected value of  $d_i(t)$  can be expressed as:

$$E\{d_i(t)\} = \frac{1}{2} \left\{ \frac{1}{4} + \frac{3}{16} + \frac{3}{16} + \frac{3}{16} + \frac{3}{16} + \frac{3}{16} + \frac{3}{16} + \frac{3}{16} \right\} + \frac{1}{2} \left\{ \frac{1}{4} + \frac{1}{4} + \frac{1}{4} + \frac{1}{4} + \frac{1}{4} \right\} = \frac{46}{32} + \frac{40}{32} = 2.6875. \tag{9}$$

Then the deletion rate  $P_d$  of the system can be given as:

$$P_d = 1 - \frac{1}{E\{d_i(t)\}} = 1 - \frac{1}{2.6875} = 0.63. \tag{10}$$

Since deletion rate of the system is greater than 0.5, according to [9], the unconstrained embedding attack cannot be successful. Moreover, let  $d_{\max}$  represent maximum possible number of clocking of any generator register at time  $t$  as  $d_{\max}(t) = \max(d_i(t)) = 5$ . In [9], it is shown that, the constrained embedding attack can be successful if the length of the observed output sequence is greater than a value linear in the length of the generator register and super exponential in  $d_{\max}$ . For CCDM stream cipher,  $d_{\max}$  is 5 which requires prohibitively large amount of known key stream sequence, so such an attack becomes practically impossible. Also, edit distance and edit probability type correlation attacks proposed in [10] and [11] cannot be effective, since these attacks are correlation attacks on the initial state of the generator registers implying an exhaustive search over all possible initial states. Thus, the computational complexities of the attacks remain exponential and applications of these attacks on the CCDM stream cipher are not practical.

### **Statistical Attacks**

A keystream generator which produces sequences exhibiting basic statistical biases or detectable characteristics cannot be considered as a secure cipher. Key stream sequence of the CCDM is investigated by using the statistical tests of FIPS 140-2 and NIST Statistical Test Suite to determine its randomness properties [12, 13]. The FIPS tests are based on performing a pass/fail statistical test on 10,000 sequences of 20,000 bits each produced by our proposed stream cipher. For the NIST tests, 1,000 keys for CCDM cipher are randomly chosen to generate key streams of length  $10^6$  bits. The cipher passes FIPS 140-2 in proportion of 99.49%. For the CCDM, the generated sequences pass the NIST Tests with a significance level of  $\alpha = 0.01$ . Thus, no statistical weaknesses have been detected.

### **Period and Linear Complexity**

A keystream generator cannot be suitable for cryptographic applications unless its generated sequences have large period and high linear complexity. Due to mutual clock control in the CCDM-Mode II, it does not seem possible to establish mathematical results about the period and linear complexity of the cipher. However, we can give upper bounds for the period and linear complexity of the algorithm with ignoring the mutual clock controlling and mode transition effect. All of the LFSRs used in CCDM have primitive feedback polynomials, so the individual periods of R1, R2, R3, R4 and R5 denoted as  $P_1, P_2, P_3, P_4$  and  $P_5$  become, respectively, as  $2^{61}-1, 2^{127}-1, 2^{107}-1, 2^{89}-1$  and  $2^{31}-1$ . Notice that all of these numbers are Mersenne Prime. Thus  $\gcd(P_i, S_i) = 1$  for  $i \in \{2, 3, 4\}$  where  $S_i$  represents sum of clockings of  $i$ th register in  $P_1$  duration. According to [14], since  $S_i$  cannot be a multiple of  $P_2, P_3$  and  $P_4$  and the degrees of the primitive feedback polynomials of R2, R3 and R4 are prime, the period of the key stream generator  $P_2$  can be written as:

$$P_z = \frac{P_1 P_2 P_3 P_4 P_5}{\gcd(S_2, P_2) \gcd(S_3, P_3) \gcd(S_4, P_4)}. \quad (11)$$

Also, since  $\gcd(P_i, S_i)=1$  for  $i \in \{2,3,4\}$ , (11) is simplified to:

$$P_z = P_1 P_2 P_3 P_4 P_5 \approx 2^{415}. \quad (12)$$

It can be seen that, the period of the sequence is enough high by considering the security requirements.

According to [15] since  $\gcd(P_i, S_i)=1$  for  $i \in \{2,3,4\}$ , the period of the clock control register becomes a multiplier in the upper bound on the linear complexity of the nonuniformly decimated sequence. Also in [1], it is given that if the decimating sequence is randomly chosen, then the probability that maximum linear complexity is obtained can be made arbitrarily close to one for appropriately chosen generator register lengths and the period of the clock control register. For CCDM, the clock control register is R1 whose period is  $2^{61}-1$ . Thus; if  $LC$  denotes the linear complexity of the keystream sequence generated by CCDM,  $LC$ , is very likely to lower bounded by  $2^{61}-1$ . It is clear that linear complexity of the sequence is high enough considering the fact that about  $2^{62}$  known plaintext bits must be intercepted in order to perform the Berlekamp-Massey attack [16]. Since such an amount of known keystream generated with same key and initial vector the registers seems not sensible and system should be reinitialized with a different initial vector well before this amount of data is generated, CCDM is considered to be secure for Berlekamp-Massey attack.

## Conclusion

In this paper, we proposed a new stream cipher called CCDM, which is based on irregular clocking and operating on two different modes. The description of the cipher and its security properties were given and shown that CCDM is secure considering some well known attacks. Also produced output sequences have large period, high linear complexity and good statistical properties. Some properties of CCDM have not yet been addressed, for example hardware implementation, optimized software code and investigation of CCDM against different attacks. These subjects will be concern of a future paper.

## References

- [1] L.R. Simpson, E. Dawson, J. Golic, and W. Millan, "LILI keystream generator," Proceedings of SAC 2000, *Lecture Notes in Computer Science*, vol. 2012, pp. 248–261, 2001

- [2] C.G. Gunther, “Alternating step generators controlled by De Bruijn sequences”, Proceedings of EUROCRYPT 1987, *Lecture Notes in Computer Science*, vol. 304, pp. 31–34, 1988
- [3] D. Wagner, L. Simpson, E. Dawson, J. Kelsey, W. Millan, and B. Schneier, “Cryptanalysis of ORYX”, Proceedings SAC’98, *Lecture Notes in Computer Science*, vol. 1556, pp. 296–305, 1999
- [4] A. Biryukov, A. Shamir, and D. Wagner, “Real time cryptanalysis of A5/1 on a PC”, Proceedings of FSE 2000, *Lecture Notes in Computer Science*, vol. 1978, pp. 1–18, 2001
- [5] K. Kim, S. Lee, S. Park, and D. Lee, “Securing DES S-boxes against three robust cryptanalysis”, *Proceedings of the Workshop on Selected Areas in Cryptography*, pp. 145–157, 1995
- [6] A. Biryukov and A. Shamir, “Cryptanalytic time/memory/data trade-offs for stream ciphers”, Proceedings of ASIACRYPT 2000, *Lecture Notes in Computer Science*, vol. 1976, pp.1–13, 2000
- [7] W. Meier and O. Staffelbach, “Fast correlation attacks on certain stream ciphers”, *Journal of Cryptology*, vol. 1, pp. 159–176, 1989
- [8] S. Jiang and G. Gong, “Cryptanalysis of stream cipher – A survey”, Technical Report CORR-2002-29, University of Waterloo, 2002
- [9] J. Golic and L. O’Connor, “Embedding and probabilistic correlation attacks on clock-controlled shift registers”, Proceedings of EUROCRYPT 1994, *Lecture Notes in Computer Science*, vol. 950, pp. 230–243, 1995
- [10] J. Golic and M.J. Mihaljevic, “A generalized correlation attack on a class of stream ciphers based on the Levenshtein distance”, *Journal of Cryptology*, vol. 3, pp. 201–212, 1991
- [11] J. Golic and S. Petrovic, “A generalized correlation attack with a probabilistic constrained edit distance”, Proceedings of EUROCRYPT 1992, *Lecture Notes in Computer Science*, vol. 658, pp. 472–476, 1993
- [12] FIPS PUB 140-2, Security requirements for cryptographic modules, <http://csrc.nist.gov/cryptval/140-2.htm>
- [13] Federal Information Processing Standards Publication FIPS PUB 140-2, Security requirements for cryptographic modules, NIST, <http://csrc.nist.gov/cryptval/140-2.htm>, 2001
- [14] A. Kholosha, “Clock-controlled shift registers and generalized Geffe key-stream generator”, Proceedings of INDOCRYPT 2001, *Lecture Notes in Computer Science*, vol. 2247, pp. 287–296, 2001
- [15] J. Golic and M.V. Zivkovic, “On the linear complexity of nonuniformly decimated PN-sequences”, *IEEE Transactions on Information Theory*, vol. 34, pp. 1077–1079, 1988
- [16] J.L. Massey, “Shift-register synthesis and BCH decoding”, *IEEE Transactions on Information Theory*, vol. 15, pp. 122–127, 1969



# Modeling Controller Area Networks Using Discrete Event Simulation Technique

C. Bayılmış<sup>1</sup>, İ. Ertürk<sup>1</sup>, C. Çeken<sup>1</sup>, and İ. Özçelik<sup>2</sup>

<sup>1</sup>Department of Electronics and Computer Education, Kocaeli University, Umuttepe Campus, 41380 Kocaeli, Turkey  
{bayilmis, erturk, cceken}@kou.edu.tr

<sup>2</sup>Department of Computer Engineering, Sakarya University, Esentepe Campus, Sakarya, Turkey, ozcelik@sakarya.edu.tr

## Abstract

In this study, a CAN model has been constituted using the OPNET software which is based on discrete event simulation technique. Its evaluation in reliable real-time communication environments has been realized using the obtained simulation results. Performance assessment of the network model has been carried out depending upon such parameters as end-to-end message delay, throughput, and packet loss ratio.

## Introduction

The controller area network (CAN) has been employed in many distributed real-time control applications in the industrial environments. CAN protocol is one of the most advanced and common autobus protocols in the communications industry. Initially it was intended for use in only automotive applications. It is currently also deployed in many other industrial applications due to its high performance and superior characteristics. Its common applications include intelligent motor control, robot control, intelligent sensors/counters, laboratory automation and mechanical tools [1–3].

In this paper, we present a CAN model that has been constituted using the OPNET software based on discrete event simulation technique. Its evaluation in reliable real-time communication environments has been realized using the obtained simulation results. Performance assessment of the network model has been carried out depending upon such parameters as end-to-end message delay, throughput and packet loss ratio.

Rest of the paper is organized as follows: “Modeling and Simulation of the CAN” introduces the basics of the CAN as well as the proposed CAN model and its simulation. Simulation results obtained and performance evaluation are presented next, followed by final remarks.

## Modeling and Simulation of the CAN

The CAN employs a serial communication protocol based on a CSMA/CD+CR Access mechanism with the use of priorities. It is used to support distributed real-time control and multiplexing. The maximum data rate that can be achieved depends on the bus length. For example, the maximum data rates for 30-m and 500-m buses are  $1 \text{ Mbit s}^{-1}$  and  $100 \text{ Kbit s}^{-1}$ , respectively. As CAN utilizes a priority based bus arbitration technique, the node with the highest priority continues transmitting without any interruption. Thus CAN has a very predictable behavior and in fact CAN networks can operate at near 100% bus bandwidth [1].

CAN nodes do not have addresses. Instead, each CAN message has an identifier pointing out the node it is produced. The identifier field serves two purposes: assigning a priority for transmission and allowing message filtering upon reception. Two versions of CAN are existed and they only differ in the size of identifier field (i.e., 11 and 29 bit identifiers with CAN 2.0A and CAN 2.0B, correspondingly). CAN has very efficient error detection mechanisms detecting five different error types such as bit, bit stuffing, CRC, specific delimiter and ACK errors. Also each node maintains two error counters: the transmit error counter and the receiver error counter. There are several rules governing how these counters are incremented and/or decremented [4].

The project model of the CAN network is shown in Fig. 1. It consists of eight CAN nodes, exchanging real-time data among as given in Table 1. The node model of the proposed CAN network is depicted in Fig. 2. A general CAN model consists of a three layered architecture: physical layer, data link layer (DLL) and application layer. First one provides the means for communication with CAN bus and has a bus receiver and a bus transmitter. Second one is the actual CAN controller implementing CAN protocol. The latter includes and realizes different types of application functionalities (CANopen, SDS, DeviceNet, etc.).

source node	priority	data length	destination node
1	1	8	5
2	2	8	6
3	3	8	7
4	4	8	8
5	5	8	1
6	6	8	2
7	7	8	3
8	8	8	4

Table 1. CAN messages

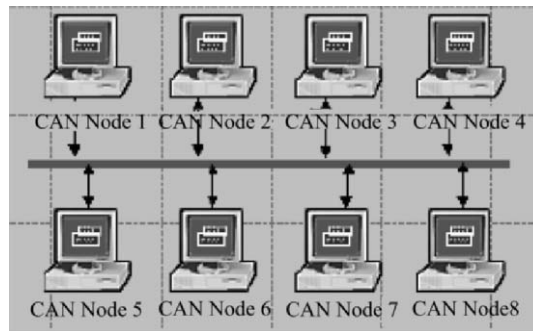


Fig. 1. CAN network project model

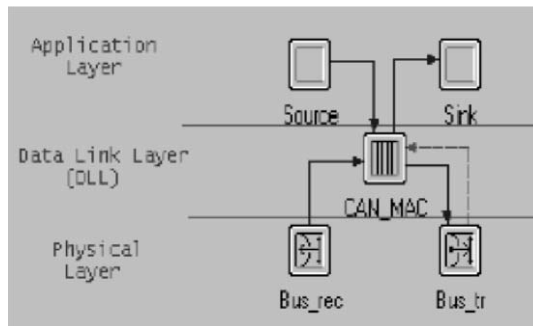


Fig. 2. CAN network node model

Process model developed for the CAN DLL functions is presented in Fig. 3. The Start state takes the initial values related to the CAN nodes. The FromBusrec state represents the CAN node starting message reception from the bus and also is used for the priority check by means of message identification numbers. The Idle state is used to handle all interrupt invocations. The Resolution state introduces predefined delays after the FromBusrec state succeeds in order to complete a CAN message transmission. The Receive state is used to begin a CAN message reception with the highest priority, which is destined to this CAN node; otherwise, the message is ignored. The FromSource state receives CAN messages from the Application layer and places them into a buffer. After, they are moved into the CAN bus by the Send state. Finally, the BusOff state suspends the CAN node according to status of fault counter.

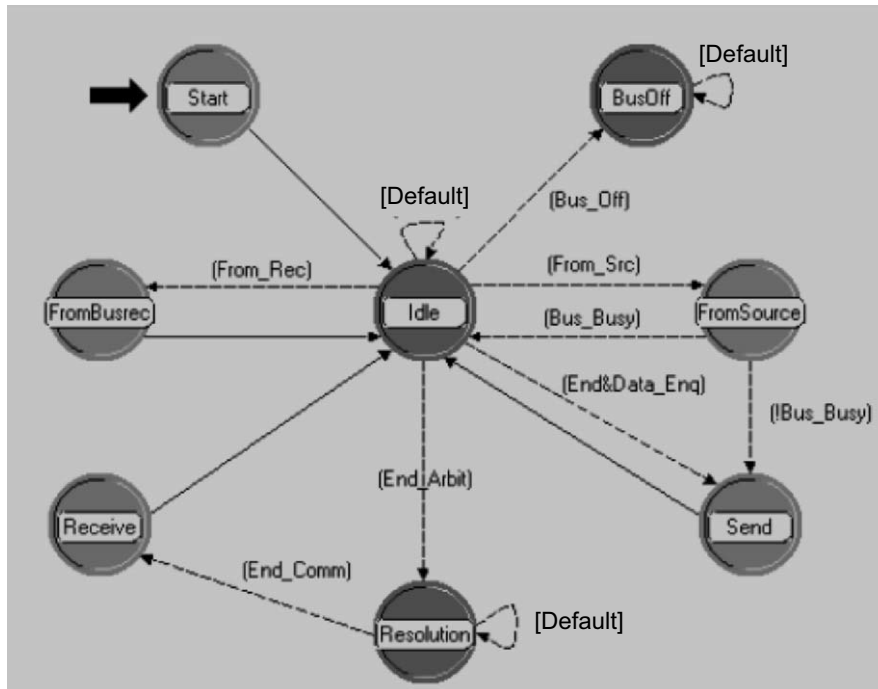


Fig. 3. CAN network process model

## Simulation Results and Performance Evaluation

In this section, the communication behavior of the CAN nodes in the developed network environment is presented, followed by a discussion about the system performance. Data rate of the CAN bus is  $100 \text{ Kbit s}^{-1}$  and all of the nodes in the bus generate CAN messages following an exponential distribution with the mean 1 s.

Each CAN node introduces a single CAN message with a certain priority to the network. Priority, data length, and destination address of the CAN messages produced in the source CAN nodes are given in Table 1.

In Fig. 4a, average end-to-end delay results of highest priority message (CAN Node 1) and lowest priority message (CAN Node 8) vs. the simulation run time are presented. As seen from the figure highest priority message experiences lower average end-to-end delays compared to the lowest priority message as expected. Figure 4b illustrates that the average throughput of CAN bus is about 15 packets per second. And finally, in Fig. 4c the average packet loss ratio of CAN bus is shown. As seen from the figure the average packet loss ratio is approximately 0.01 which is well reasonable for a CAN system.

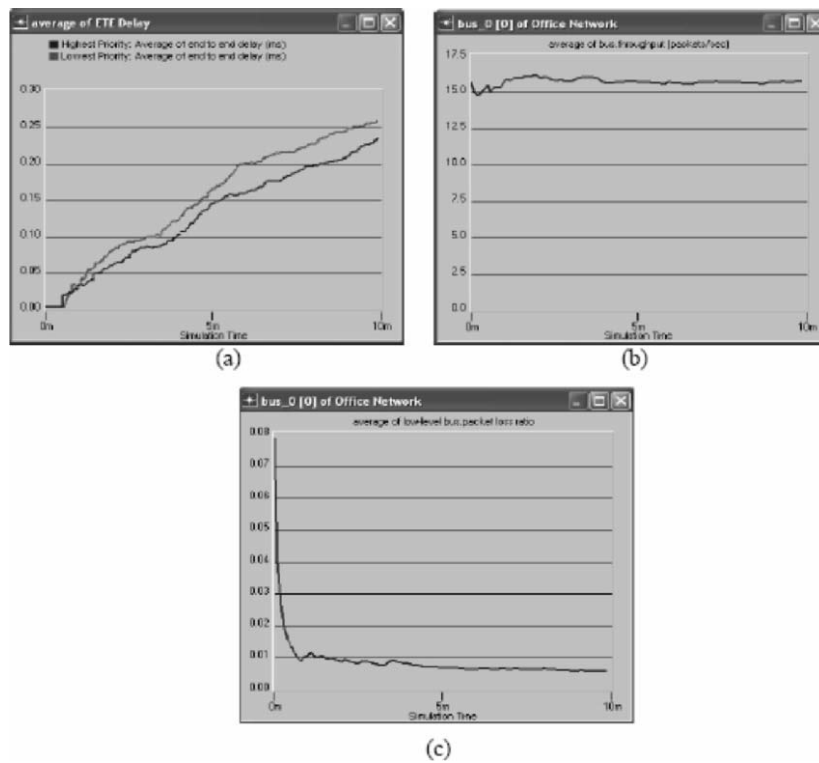


**Fig. 4.** (a) Average end to end delay of highest and lowest priority messages, (b) average throughput of CAN bus, (c) average packet loss ratio of CAN bus

## Conclusions

The main objective of this presented work has been to model and simulate a CAN network using OPNET Modeler software. Performance of the realized CAN model is examined with respect to average end-to-end message delay, throughput, and packet loss ratio parameters. According to the simulation results obtained, highest priority message has a lower average end-to-end delays compared to the lowest priority message because the highest priority lets it continue without any interruption.

## References

- [1] W. Lawrenz, *CAN System Engineering: From Theory to Practical Applications*, Springer Berlin Heidelberg, New York, 1997
- [2] M. Farsi, K. Ratckiff, M. Babosa, "An overview of controller area network", *Computing and Control Engineering Journal*, vol. 10(3), pp. 113–120, 1999
- [3] C. Bayilmis, I. Erturk, C. Ceken, "Wireless interworking independent CAN segments", *Lecture Notes in Computer Science*, LNCS 3280, pp. 299–310, 2004
- [4] N. Navet, "Validation of in-vehicle real-time applications", *Computers in Industry*, pp.107–122, 2001
- [5] OPNET, <http://www.opnet.com/support>, accessed in April 2005

---



---

Part III

Degree Award Ceremonials

## Laudatio on Professor Leopold B. Felsen

L. Sevg





ECE

Magnificent Rector,  
Distinguished guests,  
Members of Doğuş University,  
Most Renowned Colleagues and Students,

It is a great honor and a strong emotion for me to highlight the personality and scientific achievements of Professor Leopold B. Felsen.

As a former student, long-lasting colleague and collaborator, and finally close friend of him I am very happy to do this presentation.

*Istanbul, June 13, 2005*




ECE

### Short Biography

Professor Felsen was born in Munich, Germany on May 7, 1924.



He received the B.E.E., M.E.E, and D.E.E. degrees from the Polytechnic Institute of Brooklyn, Brooklyn, NY, in 1948, 1950, and 1952, respectively.



He emigrated to the United States in 1939 (after leaving Germany with a "stateless passport" given by the Nazi Government) and served in the U.S. Army from 1943 to 1946.


*Istanbul, June 13, 2005*



*ECE*



After 1952 he remained with the Polytechnic (now Polytechnic University), gaining the position of University Professor in 1978. From 1974 to 1978 he was Dean of Engineering.



In 1994 he resigned from the full-time Polytechnic faculty and was granted the status of University Professor Emeritus.

He is now Professor of Aerospace and Mechanical Engineering and Professor of Electrical and Computer Engineering at Boston University, Boston, MA.


*Istanbul, June 13, 2005*

*ECE*



Publications/Citations

Professor Felsen is the author or co-author of over 350 papers and of several books, including the classic *Radiation and Scattering of Waves* (Piscataway, NJ: IEEE Press, 1994).



His research interests encompass wave propagation and diffraction in complex environments and in various disciplines, high-frequency asymptotic and short-pulse techniques, and phase-space methods with an emphasis on wave-oriented data processing and imaging.

*Istanbul, June 13, 2005*

**Memberships/Editorial boards**

Professor Felsen is an associate editor of several professional journals and was an editor of the Wave Phenomena Series (New York: Springer-Verlag).

He is a member of Sigma Xi, a Life Fellow of the Institute of Electrical and Electronics Engineers (IEEE), and a Fellow of the Optical Society of America as well as the Acoustical Society of America.

He has held named Visiting Professorships and Fellowships at universities in the United States and abroad. His Poet's Corner appears sporadically in the IEEE/APS Magazine.



*Istanbul, June 13, 2005*




**Achievements/awards/medals**

- 1988 IEEE Life Fellow membership
- 1977 USA National Academy of Engineering Membership
- 1973 German Guggenheim Medal
- 1981 German Humboldt Foundation Medal
- 1984 IEEE Centennial Medal
- 1969, 1974, 1981 IEEE/APS Best Paper Award
- 1984, 1986, 2000 R.W.P. King Best Paper Award
- 1975 International URSI Balthasar Van Der Pol Gold Medal
- 1991 IEEE Heinrich Hertz Gold Medal
- 1998 IEEE Distinguished Achievement Award
- 2000 Third Millennium Medal
- 2003 IEEE Electromagnetics Award
- Distinguished Faculty Alumnus Awards of Brooklyn Poly

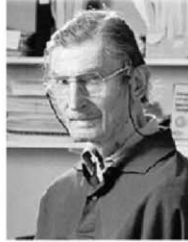
*Istanbul, June 13, 2005*





---

### Honorary Doctorate Degrees

- 1979 Denmark Technical University of Denmark
- 2002 University of Sannio, Italy
- 2004 Munich Technical University of Germany
- 2005 Brooklyn University of New York, USA



*Istanbul, June 13, 2005*





---

### PHD Advisory

Professor Felsen has had more than 30 PhD students from all around the World some of which I remember are from USA (8), Israel (8), England (3), Brasil (3), France (1), Japan (1), Korea (1) Egypt (1), Algeria (1), Turkey (2).

He has had many colleagues, collaborators and post doc researchers from various countries, e.g., USA, Germany, Italy, Israel, France, Russia, England, Japan, Korea, Egypt, China.

*Istanbul, June 13, 2005*





*ECE*

### Others

- Prof. Felsen has received many invitations from Italy, England, Germany, Denmark, Israel, France, Russia and has been conducting joint research
- He served as an IEEE/APS Distinguished Lecturer in 1974
- He has served on the APS Administrative Committee from 1963-1966,
- He was Vice Chairman and Chairman for both the United States (1966-1973) and the International (1978-1984) URSI Commission B

*Istanbul, June 13, 2005*





*ECE*

### Turkish Connection

- Professor Felsen has had a strong Turkish connections.
- He has made many visits and has given many seminars/lectures in Ankara and İstanbul for the last 30 years.
- Professors Mithat İdemem, Ercan Topuz, Edip Niver and Funda Akleman have interacted with him at various times during this period.

*Istanbul, June 13, 2005*





---

### My interaction

- In 1987, while working on my Ph.D in İTÜ I was awarded a fellowship that allowed me to work with Professor Felsen at Weber Research Institute/ Polytechnic University in New York for two years.
- My work at the Polytechnic concerned the propagation phenomena in non-homogeneous open and closed waveguides.
- Since then, we have been collaborating without a break and our joint study has produced many journal papers, tutorials, short courses, special sessions, special issues and PhD studies.



*Istanbul, June 13, 2005*



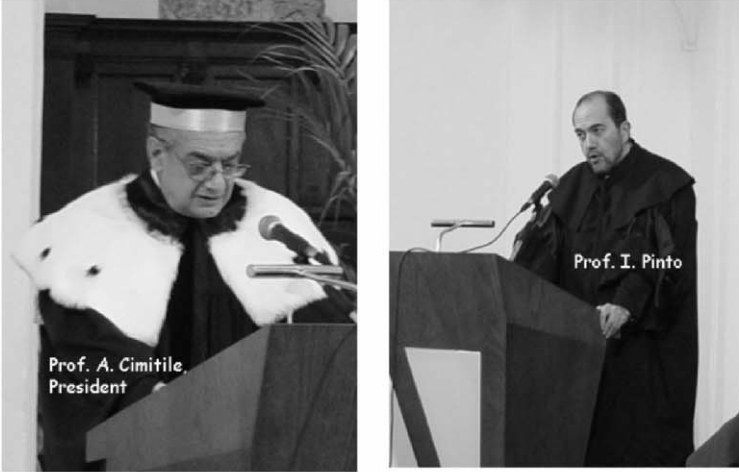
---

### Some photos from recent celebrations

*Istanbul, June 13, 2005*

 Honorary doctorate ceremony at University of Sannio, Italy 2003 

*ECE*



Prof. A. Cimitile,  
President

Prof. I. Pinto

*Istanbul, June 13, 2005*

 Honorary doctorate ceremony at University of Sannio, Italy 2003 

*ECE*



Pinto Felsen Vincenzo

Vincenzo and Pinto congratulating Felsen

*Istanbul, June 13, 2005*

 **Mini-symposium in University of Sannio, Italy 2003** 

*ECE*



**Warm atmosphere in a cold day!**

*Istanbul, June 13, 2005*

 **Honorary doctorate ceremony at Munich Technical University, 2004** 

*ECE*





Wolfgang A. Herrmann, President  
Munich University of Technology

Joerg Eberspaecher, Dean  
Department of EE and IT

Peter Russer



Felsen

*Istanbul, June 13, 2005*


 

**The last 50 years  
and quick review of some of  
Leo Felsen's studies**

*Istanbul, June 13, 2005*

 **1958** 



**Me, braveheart riding on a horse,  
while he was working on  
scattering from a conical tip  
(*"Radiation from Ring Sources  
in the Presence of a Semi-  
Infinite Cone"*, IRE Trans. AP-  
7, 168-180, 1959)**



**Akhisar, 1958**


*Istanbul, June 13, 2005*



 1980 

ECE



Me and my friend Faruk with the championship cup in the University Soccer tournament, while he was working with J.M. Arnold on evanescent waves (*"Rigorous Asymptotic Theory of Evanescent Waves for Guided Propagation"*, J. Acoust. Soc. Am., 67, 757-763, 1980), with E. Heyman on Creeping waves (*"Creeping Waves and Resonances in Transient Scattering by Smooth Convex Objects"*, IEEE Trans. AP-31, 426-437, 1983), and E. Topuz (*"High-Frequency EM Fields on Perfectly Conducting Concave Cylindrical Surfaces"*, IEEE Trans. AP-28, 819-831, 1980).



Faruk me


İTÜ, 1980

Istanbul, June 13, 2005

 1985 

ECE



Me (the one with a hat) in the army, while he was working with X.J. Gao (*"Complex Ray Analysis of Beam Transmission Through Two-Dimensional Radomes"*, IEEE Trans. AP-33, pp. 963-965, 1985).



me


Babaeski, 1985

Istanbul, June 13, 2005

 1989 



ECE

Berlin Wall falling down, while he was working with E. Heyman  
 ("Complex Source Pulsed Beam Fields",  
*J. Opt. Soc. Am. A* 6,  
 806-817 (1989).




The fall of Berlin wall, November 1989

*Istanbul, June 13, 2005*

 1990 

ECE

Me with home-made apple turnovers, and our research group  
 while he was working on my PhD thesis ("Adiabatic and Intrinsic Modes  
 for Wave Propagation in Guiding Environments with Longitudinal and  
 Transverse Variations:  
 Formulation and Canonical  
 Test", *IEEE T-AP*,  
 Vol.39 No.8, pp.1130  
 -1136, Aug, 1991)



My apple turnovers

His 66th birthday, Brooklyn Poly, Farmingdale, 1990

*Istanbul, June 13, 2005*




1996



ECE

President Clinton hugging Monica, while he was working with L. Carin and T.T. Hsu (*Wave-Oriented Processing of Scattered Field Data from a Plane-Wave-Excited Finite Array of Filaments on an Infinite Dielectric Slab*”, IEEE Trans. *AP-44*, 352-360 1996.



President Clinton and Monica, 1996  
 (was it playing piano or guitar he taught her?)

*Istanbul, June 13, 2005*

Felsen's last 50 years

ECE


He has strong and wide-spread connections within the international EM/Optical/Acoustic societies and it is almost impossible to list all of them here.

Among those, I believe I should mention


N. Marcuvitz, A. Oliner, H. Bertoni, P. Russer,  
 E. Heyman, J. M. Arnold, E. Niver, A. Kamel,  
 E. Topuz, Toraldo di Francia, L. Carin, M. İdemen,  
 E. Gago-Ribas, G. Vecchi, Tiberio, B. Anderson,  
 S. Maci, F. Capolino, V. Galdi.

(although the list is certainly incomplete).

*Istanbul, June 13, 2005*



**His Epilogue**




*ECE*


I have witnessed much  
Throughout my life,  
Been through joy and pain,  
Harmony and strife.

I have seen many countries,  
Have experienced success,  
Now enjoy my profession  
Without early-career stress.

*Istanbul, June 13, 2005*



**His Epilogue**





*ECE*

Yet I value most deeply  
The care and helping hand  
That my family, friends and colleagues  
In my times of need extend.

The ride has been bumpy  
From where it has begun.  
But in spite of it all,  
I can say, I've had fun!

*Istanbul, June 13, 2005*



*ECE*

Before concluding, I should say that almost all of his former students, colleagues and collaborators from various universities, institutes and industry in these countries who couldn't attend this ceremony today have sent their messages stating how proud they are because of being his friend, and how sorry they are since they miss this memorable event.

*Istanbul, June 13, 2005*





*ECE*

Professor Felsen has always been, and still is, involved in sustained collaborations with different universities in different countries.

I would like to thank especially Professors  
Anton Tjihuis (Netherland),  
Cevdet Akyel (Canada),  
Christos Christopoulos (UK),  
Ehud Heyman (Israel),  
Edip Niver (USA),  
Emilio Gago-Ribas (Spain)  
Stefano Maci, Vincenzo Galdi (Italy),  
who are able to make it and join us this morning.



*Istanbul, June 13, 2005*

Also many thanks to Professors  
 Mithat İdemem (Işık University),  
 Ercan Topuz (İTÜ),  
 Alinur Büyükaksoy (Gebze Institute of High Technology)  
 İrşadi Aksun (KOÇ University),  
 Ayhan Altıntaş (Bilkent),  
 Taner Şengör (Yıldız Technical University),  
 Gonca Çakır (Kocaeli University)  
 by joining us to salute and congratulate Professor Felsen.

I express my thanks to all those involved in arrangements for  
 the bestowal of the honorary doctorate degrees and  
 CCN2005 International Symposium.



*Istanbul, June 13, 2005*

I express my appreciation

- to the Chair of Electronics and Communication Dept,  
 Professor Cem Göknaç,  
 to the Dean of Engineering Faculty  
 Professor Mitat Uysal,  
 and all Faculty members  
 for taking over my proposal of bestowal of the honorary  
 doctorate degree upon Professor Felsen,
- to the Rector, Academic Senate and Board of Trustees  
 of Doğuş University for their approval,
- and last (actually first) to Professor Felsen for  
 accepting our humble recognition.

*Istanbul, June 13, 2005*



This occasion offers us a unique and happy chance to celebrate his person and achievements, for us who know and admire L. B. Felsen, for the next generations to which he shall serve as an outstanding example.

So, in front all of you  
esteemed guests, colleagues and students;


I say you Professor Felsen with great sincerity:

I'm truly proud of knowing you as a human being,  
Working with you as a PhD student, and  
Collaborating with you as a friend and scientist.

*Istanbul, June 13, 2005*

**Leopold B. Felsen**  
66th Birthday  
May 7, 1990



*"Let me tell you  
how it works."*

A tribute from those who learn from you

Yes, Professor !.  
Tell us more  
how it works ...

Thank you.  
Levent Sevgi

*Istanbul, June 13, 2005*

## Laudatio on Professor Leon O. Chua

İ. C. Gökna

### Leon Ong Chua

Born in Tarlac, Philippines of Chinese Parents



### Who is Leon Chua?

- A world famous scientist,
- A pioneer,
- A leader,
- A connaisseur of vine and food,
- A father,
- And..... a husband???





## A world famous scientist

- **Professor**
- **Fellow of IEEE**
- **Academician: European Academy of Sciences**

### Honorary Degrees:

Docteur Honoris Causa 1983: Ecole Polytechnique Federale-Lausanne, Switzerland  
 Honorary Doctor, 1984: University of Tokushima, Japan  
 Honorary Doctor, 1992: Technical University of Dresden, Germany  
 Docteur Honoris Causa 1994: Technical University of Budapest, Hungary  
 Docteur Honoris Causa 1995: University of Santiago De Compostela, Spain  
 Docteur Honoris Causa 1996: University of Frankfurt, Germany  
 Docteur Honoris Causa 1997: Technical University of Iasi, Romania  
 Docteur Honoris Causa 2000: University of Catania, Italy  
 Docteur Honoris Causa 2002: Technical University of Munich, Germany  
 Docteur Honoris Causa 2005: Doğuş University, Turkey

## A world famous scientist

### Awards and Prizes:

IEEE Browder J. Thompson Memorial Prize Award, 1973  
 IEEE W. R. G. Baker Prize Award, 1973  
 Frederick Emmons Award, 1974  
 Miller Research Professorship, 1976  
 Senior Visiting Fellowship, Cambridge University, 1982  
 Alexander von Humboldt Senior US Scientist Award, 1982  
 Visiting US Scientist Award (Japan), 1983  
 IEEE Centennial Medal, 1985  
 Professeur Invite, University of Paris, 1986  
 Professeur Invite, University of Nice, 1991  
 Mac Van Valkenburg Award, 1995  
 IEEE Circuits and Systems Society Golden Jubilee Medal, 2000  
 IEEE Third Millennium Medal, 2000  
 IEEE Neural Networks Pioneer Award, 2000  
 First IEEE Gustav Robert Kirchoff Award, 2005

\* **Patents:** 7 USA Patents

## A world famous scientist

- In the book entitled  
    **"Ad Sexaginta Annos Prospere Celebrandos"**  
    Celebrating Six Decades of Achievement  
    Published by World Scientific
- 134 eminent scientists from 28 countries wrote eulogies.

## A world famous scientist

- I often wondered in what advantageous circumstances this **gigantic existence** in our world had been educated. But the fact is that he has gained his present position as well as his great scientific achievements through his extraordinarily hard work, the circumstances of elementary education for him having been rather poor. But hard work alone will not promise one a successful career; he must be a **man of genius**

Masao Iri  
Chuo University

## A pioneer

- For his deep and profound insight into the broad field of non-linear systems,
- for his penetrating understanding of problems in distant fields where he brought the power of his methods,
- for his inspired teaching that formed generations of students,
- for his kindness to people coming into contact with him,
- Happy birthday, and a long, long life rich with scientific activity.

Pier Paolo Civalleri  
Mario Biey  
Marco Gilli  
Politecnico di Torino

## A pioneer

- .....I was nonetheless very impressed by your work in nonlinear circuit theory, chaos, neural networks and modeling theory. In each of these you were a perpetual source of original ideas, and a great motivator. When you had touched a field **it changed forever**.

Patrick Dewilde  
TU Delft

## A pioneer

Whether we were

- round the bend from Negative Resistance
- dizzy from Rotators
- forgetful of Memristors
- paranoid over Phase-planes
- confused by Chaos
- or just neurotic over Cellular Neural Networks
- Leon has offered us all something; something which created a close community from global raw material, a real network.

Anthony C. Davies  
King's College  
University of London

## A leader

- When I first started working with you in 1989, someone warned me "Prof. Chua is too creative. He'll give you so many ideas to look at that if you even tried to work on a quarter of them you'd never get anything done, much less a Ph.D." However, what I eventually did gain from working with you was much more than just my Ph.D. I learned how to explore many seemingly unrelated paths of inquiry, but following each step down those paths systematically. In the end, I was often astonished to find these paths converge.
- Thanks to your emphasis upon a balance between long term "blue sky" goals and concrete short term research efforts, you have helped lay the foundation for my future research and teaching. I hope that I can impart some of that sense of balance to my own students.

Bertram Emil Shi  
Hong Kong University of  
Science and Technology

## A leader

- Leon's legacy is not just his circuit and his writings. It is the lasting impression he leaves on each of us, ever changing our lives through his buoyant pursuit of truth and his raw, unbridled enthusiasm. Leon has contributed to Science and to Life, and my life.
- Without his faith, it would have likely been impossible for me to publish results that were so routinely out of the mainstream of what established mathematicians were doing. Leon has always been bold enough to defy existing trends with diplomacy and grace, thus opening avenues of thought that might have been lost in an academically structured scientific culture.
- .....
- Thank you, Leon, for so many of the most important gems in life.

Ray Brown  
University of California at Berkeley

## A leader

- As a young researcher, you gave me so much inspiration. With your guidance, I have been introduced to the current topics of Cellular Neural Networks and Chaos.
- Your laboratory NOEL has become the Mecca of Nonlinear Circuit Theory, I am one of the lucky ones who was there.

Cüneyt Güzeliş  
Istanbul Technical University

## A leader

- I remember you, fondly teaching EE251 from your textbook on "Introduction to Nonlinear Circuit Theory," which still occupies a prominent place on my shelf in the Director's Office at the Coordinated Science Laboratory in Illinois. Who else could remember MECCA?

Kenneth Jenkins  
University of Illinois

## A leader

- I have known you since the college days. I know you always strive for the best. You contributed so much in the field of nonlinear sciences, not only for its technical advances but also for bringing out a new generation of scientists and educators. We are all very proud of you becoming a guru in the field.

Wai-Kai Chen  
University of Illinois at Chicago

## A connaisseur of vine and food

- He succeeded in correctly answering a long questionnaire of some obscure organization with the most difficult questions regarding wine and vinification. I happened to be there when he received by mail his wine connaisseur certificate and a bottle rack for his wine cellar.

Martin Hasler  
Ecole Polytechnique Federal Lausanne

## A connaisseur of vine and food

- The last wish I would like to make is that, although I agree with you that wine is superior, you will some day be convinced that beer is not as barbarian as you thought it was when I visited your wine cellar a few years ago-at least if it is Belgian.

Patrick Thiran  
Swiss Federal Institute of Technology

## A connaisseur of vine and food

- ... I also learned with you a lot about French cheese.

René Lozi

Université de Nice-Sophia Antipolis

- ... I greatly admire your knowledge and taste on food and wine. In particular your ability to cook a french meal, comparable to the best we can find in Bay Area, is something of which you can be very proud.

Ernest S. Kuh

University of California at Berkeley

## A father

### Multiple parenthood is your main feature

- You are the father of four beautiful daughters, something of a big rarity these days,
- You are the parent of remarkable discoveries in the field of nonlinear systems, the most well-known at present being Cellular Neural Networks and Chua's Circuit,
- At last you are the initiator, coordinator and "godfather" of a unique phenomenon in the conduct of scientific studies-the creation of a worldwide "Mafia" in the field of chaotic nonlinear circuits which possesses a high scientific potential and has operated very efficiently for several years.

Dmitriev et al.

Institute of Radioengineering and Electronics  
Russian Academy of Sciences, Moscow



## A husband

- "Behind every successful man there is a woman" they say,
- I say "every successful woman creates a successful man,"
- And in this case the successful creator is Diane Chua.

İzzet Cem Gökner

## From here to....

### Inaugural lecture of the International Francqui Chair 2005 by Leon Chua

Professor André Oosterlinck,  
Rector of the Katholieke Universiteit Leuven,  
Professor Yves Willems,  
Dean of the Faculty of Engineering  
have the honor to invite you to the Inaugural lecture of  
the International Francqui Chair 2005

### **From Bernoulli Shift to Universal Computation**

On Wednesday, June 22, 2005 at 16h00 in the  
Auditorium of the Castle of Arenberg, Kasteelpark  
Arenberg 1, Leuven (Heverlee)

[www.esat.kuleuven.be/info/route.en.php](http://www.esat.kuleuven.be/info/route.en.php)

## Professor Felsen's Reply



### Prof. Felsen's Acceptance Reply ...

*ECE Dept.*

President Prof. DİNİBÜTÜN, Dean Prof. UYSAL, Prof GÖKNAR, Prof. SEVGİ, distinguished colleagues, ladies and gentlemen, students and my own family,

I am most appreciative of the honor, which has been bestowed on me today, and I am glad to be able to be here to receive it. I would like to thank you, President Dinibütün, for having approved my nomination; you, Dean Uysal, for having organized and secured the approval by the relevant faculty representatitives; and you, Prof. Sevgi, my former student and present colleague, collaborator and close friend, for having initiated the entire process and worked with your usual enthusiasm and vigor toward its realization.

*Istanbul, June 2005*



*ECE Dept.*

Receiving this recognition (which honors not only my accomplishments but also those of my collaborators) from Dogus University is especially meaningful for me because of my long-standing interaction, for almost three decades, with Turkish colleagues, students, postdocs and visitors who had joined my research group at Brooklyn Poly (now Polytechnic University), my prime affiliation until a decade ago, when I relocated to Boston University.

*Istanbul, June 2005*



ECE Dept.

During these bilateral contacts, I gained a deep appreciation of Turkish customs, cultural heritage, culinary specialties, idiosyncrasies, and above all, exceptional hospitality.

To take advantage of the multi-ethnic and multi-cultural composition of my Poly research group, I had fairly regular social gatherings, to which all participants were encouraged to bring and share a culinary specialty typical of their home environment. In fact, I had jokingly made this a "requirement" for each visiting researcher.

*Istanbul, June 2005*



ECE Dept.

In this connection, in 1989, when Prof. Sevgi was in the final stages of his doctoral dissertation, and we had some delicate discussions concerning certain tricky analytical procedures, he claimed later on that it was my enthusiastic endorsement of his Turkish-style apple turnovers at one of these social events, which brought about my approval of his thesis soon thereafter.

He may have been right!

*Istanbul, June 2005*

ECE Dept.

$$IM = \int_{C_\beta} f(\beta) e^{-j\phi(\beta)} d\beta$$

Prof. Sevgi's problem: Complex IM Integral (1988-1990) .  
Istanbul, June 2005

ECE Dept.

He studied and studied ...  
Istanbul, June 2005

 ECE Dept.



He made lots of site surveys ...

*Istanbul, June 2005*

 ECE Dept.



He even tried to measure it ...

*Istanbul, June 2005*



ECE Dept.



He thought, he might have scared it ...

*Istanbul, June 2005*

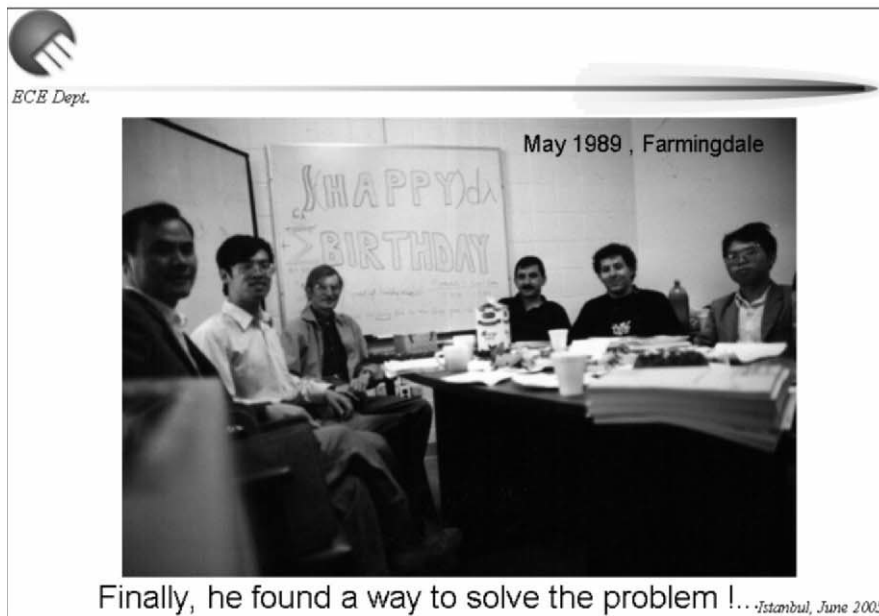
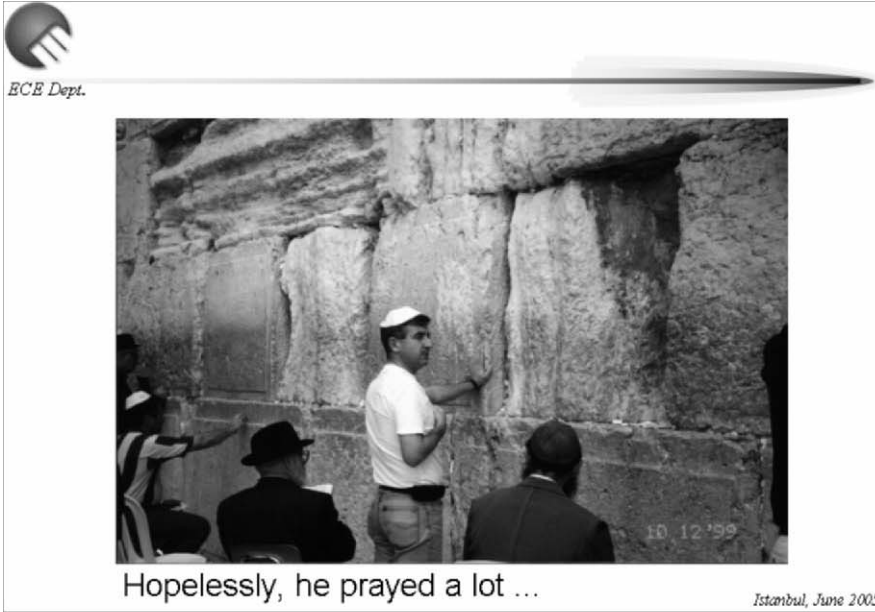


ECE Dept.



He even went to Santa ...

*Istanbul, June 2005*





ECE Dept.



Baking apple turnovers for my 65th birthday ... Istanbul, June 2005



ECE Dept.



I finally accepted his work and said "O.K. Never mind the saddle points, apple turnovers are delicious, go back to your country" ..

Istanbul, June 2005



 ECE Dept.

Sep 1990 , Istanbul



We celebrated his defense in a nice Bosphorous fish restaurant ...

Istanbul, June 2005

 ECE Dept.

Sep 1990 , Istanbul



And we said "Goodbye until next time" ...  
Thanks to Apple Turnovers !

Istanbul, June 2005



ECE Dept.

To commemorate one of my early visits to Turkey and the scientific issues current at that time, I would like to present a poem, which I wrote for that occasion (use of rhymes to comment on, and spoof, my profession has been a hobby of mine, and has been formalized through my "Poet's Corner" in the IEEE Antennas and Propagation Magazine).

Istanbul, June 2005



ECE Dept.

### An Ode to the METU [1] Symposium

At last, it has come to an end:  
Four days, hard work, and yet well spent,

\*\*\*

We've heard some old, we've heard some new,  
We have exchanged all points of view,  
Much theory, some application.  
Some theories work, some cause frustration.


\*\*\*

We've talked in generality,  
And each of his speciality.

\*\*\*

Much has been said about diffraction,  
Enough to drive you to distraction.  
High frequencies and GTD  
Are still around for all to see.

Istanbul, June 2005



ECE Dept.

There has been much to do with edges.  
 We have been given solemn pledges  
 That new results can be obtained  
 If fringe currents would be retained.


\*\*\*

The art's becoming clinical  
 When edges are umbilical.  
 But when we deal with large reflectors,  
 Then we may have to be defectors,  
 Leave GTD, and being brave,  
 Use tricky evanescent wave.

\*\*\*

Much has been said about computing.  
 It's here that there is strong disputing.  
 Do not be charmed by the machine!  
 It only yields what we feed in.

Istanbul, June 2005



ECE Dept.

We want efficiency, precision,  
 But numbers don't replace the vision  
 That comes from insight, comprehension.  
 So, hybrid methods need attention,  
 Combining numerology  
 With careful methodology.

\*\*\*

For those of us, who've come to speak  
 During this concentrated week,  
 It has been stimulus and fun.  
 We've learned how METU was begun,  
 And see what it presents today.  
 Let it continue, come what may!

Istanbul, June 2005



ECE Dept.

We sense your pride and dedication.  
 Warm student-faculty relation  
 Extends into the human sphere  
 All that you have accomplished here.

\*\*\*

We wish to work with you together,  
 To further cultivate the tether  
 That strengthens mutual interaction  
 In our quest for high perfection.

\*\*\*

This meeting has been but the first.  
 Let's hope the trend won't be reversed,  
 That METU will have more occasions  
 As host for Maxwell's field equations.

L. B. Felsen  
 June 19, 1980

Istanbul, June 2005



ECE Dept.

To conclude, I would like to present similar observations, both  
scientific and reflecting the Turkish cultural ambiance, which  
 are extracted from a poem I wrote for ICT [2] 96

### Istanbul: ICT'96

This conference was a Big affair.  
 I had received an invitation  
 To address a session organized  
Especially for Wave Propagation

Istanbul, June 2005



ECE Dept.

The wave propagationists were few  
 Among the attending totality.  
 But this cohesive spirited group  
 Fused substance with collegiality.

\*\*\*

My Turkish colleagues were present there,  
 Their students and several foreign friends.  
 This intimate reunion remains  
 Among my most memorable events.

\*\*\*

Communication is the theme.  
 For those who specialize in waves,  
 The meeting site provides a scene  
 For tracking how each wave behaves.

Istanbul, June 2005



ECE Dept.

Take target detection in noise and clutter [3].  
Istanbul's streets can be used for a test  
 That lets signal processors roam and explore  
 Which processing strategy works best.

\*\*\*

The traffic provides random clutter in motion,  
Constrained by the sidewalks on either side.  
Pedestrians trying to cross the street  
 Furnish a target with which to collide.

\*\*\*

A hit indicates that a target is there,  
 Thus raising detection probability.  
 Avoiding a hit requires some stealth  
 Via low contrast dress and evasive mobility.

Istanbul, June 2005



ECE Dept.

If this defense fails and collision occurs,  
Target ID [4] is the subsequent job.  
 ID depends on what's left on the ground  
 After target is changed into unshapely blob.

\*\*\*

Now is the time to resort to those tricks  
 That state the rules for a likely decision:  
Project the blob onto reference hit lists  
 And thus pick out the most likely collision.

\*\*\*

If you're the pedestrian, it's not a game.  
Your vested interest is to survive.  
 If you manage to cross the street intact  
 It's time to relax and enjoy new-found life.

Istanbul, June 2005



ECE Dept.

For that, Istanbul is ideal as well.  
Museums, historic sites, restaurants abound.  
 Whatever it is that you want to pursue,  
 It's certain that something can somewhere be found.


\*\*\*

The grandiose sights left by royalty past  
 Are interlaced with allies that wind  
 Around buildings and hillsides. Tiny shops on both sides  
 Offer specialty items that can blow your mind.

\*\*\*

The hustle and bustle is hard to describe.  
 You just join the flow and adapt to the mold.  
 The ambiance tells what the city is like:  
 A blending of cultures unique to behold.

Istanbul, June 2005




ECE Dept.

While these attractions work against  
 Keeping participants meeting-bound,  
Most attendees stayed on the site.  
 There was always something that kept you around.  
 \*\*\*

For this owe our gratitude  
 To those who organized this feat.  
 It all came off par excellence.  
 A pattern that others might wish to repeat.  
 \*\*\*

What stays with me most is the friendly concern,  
 The grace, the sincere hospitality,  
 Coupled with warmth, with humor and charm,  
 Because that's the Turk personality.

Istanbul, June 2005



ECE Dept.

Again, I say Thank You to my Turkish hosts.  
 This was an event I shall duly record.  
 I met former colleagues and students, dear friends.  
Friendships through science-that's the global reward.

These sentiments, voiced in 1996, remain valid for the  
 present occasion.

Many thanks again for the honor bestowed on me today.

[1] Middle East Technical University (METU), Ankara  
 [2] International Conference on Communication (ICT)  
 [3] This was then, and remains, a hot topic in electromagnetics  
 [4] Identification

Istanbul, June 2005

## Photo Gallery

This section contains a photo gallery from the Symposium and related activities.



Prof. Talha Dinib t n, President of DoĖuř University delivering his speech





Prof. Sevgi introducing Leo Felsen



Prof. Göknaar introducing Leon Chua



Prof. Dinibütün giving Leo Felsen his certificate



Prof. Dinibütün giving Leon Chua his certificate



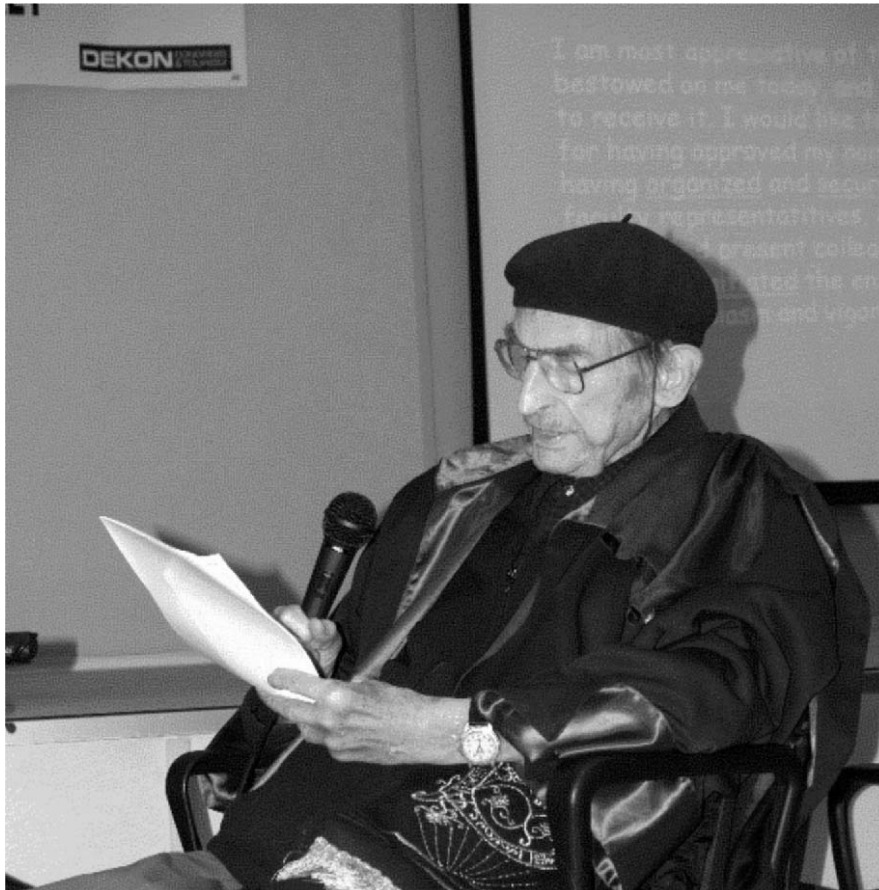
Prof. Chua delivering his acceptance speech



Prof. C. Güzeliş talking about Leon Chua



Prof. M. İdemen talking about Leo Felsen



Prof. Felsen delivering his acceptance speech of the honorary doctorate



After ceremony, (left to right) A. Dervisoğlu, L. Sevgi, L. Chua, S. Yarman, M. Idemen, and L. Felsen



After ceremony, Leo Felsen and his colleagues, (left to right) V. Galdi, E. Niver, L. Sevgi, A. Tijhuis, C. Gökner, E. Heyman, C. Christopoulos, and S. Maci on his right)



After ceremony, Leo Felsen and Family; ladies - Judith (l), daughter, Tulle (r) daughter-in-law; men (left to right) Joseph (grandson), Mike (son), Samuel (grandson), Jacob (grandson)



Leo Felsen, L. Sevgi (l) and Ç. Uluışık (r)



After ceremony, Leo Felsen and his colleagues, (left to right) F. Birbir, A. Alkumru, S. Maci, V. Galdi, E. Heyman, and Udi (on his right)



After ceremony, Leo Felsen and his colleagues, (left to right) A. Büyükaksoy, A. Alkumru, M. İdemen, Leo, and E. Niver)



CCN 2005 symposium, Prof. C. Akyel presenting his paper



Group singing Havah Nagila in the Gala dinner (left to right) L. Sevgi and his wife Esin, A. Tijhuis, Leo Felsen, E. Niver and M. İdemen, (standing) A. Alkumru



Leon Chua, his wife (on his left) with Göknar and Dervisoğlu families



Leo Felsen in his hotel suit along the Bosphorus





Cem Göknaar with Leon Chua



Dervişoğlu, Göknaar and Chua families at home with A. Savacı

# Index

## **Part I: Electromagnetic Theory**

- Antennas, 37, 45, 55, 81, 105, 113, 123, 133, 149, 157, 197
- Archimedean spirals, 123
- Arrays, 105, 123
- Beam forming, 105, 123
- Beam steering, 105, 123, 149
- Broadband filter, 141, 149
- Chebyshev filter, 141, 149
- Dielectric rod antenna, 113
- Diffraction, 27, 45, 65, 81, 87, 97
- Fast integral solutions, 55
- FDTD, 37, 45, 123, 149
- Frequency selective surface, 3, 65
- Green's function, 45, 55, 65, 97, 133
- Knife-edge diffraction- 45
- Method of Lines, 157
- Method of Moments, 3, 45, 55, 123, 133
- Microstrip filter, 141, 149
- Microwave active circuits, 167
- Millington effect, 55
- Mixed-path propagation, 55
- Ocean surface dynamics, 185
- Parabolic reflector, 105
- Printed monopole, 197
- Propagation, 3, 13, 27, 37, 45, 55, 65, 81, 113, 123, 149, 157, 185, 203
- Scattering, 3, 27, 37, 45, 55, 65, 81, 95, 97, 105, 149, 185
- Spiral antenna, 123
- SSPE, 45, 55
- Surface waves, 55
- TLM, 3, 45, 55
- Transmission line, 3, 13, 45, 65, 141, 157
- Waveguides, 113, 141, 149, 157

## **Part II: Circuit Theory**

- Andronov-Hopf bifurcation 305
- Artificial neural network 325
  
- Bifurcation 305
- Blind phase noise estimation 333
- Brouwer fixed point theorem. 225
  
- Cellular automata 221, 257
- Cellular neural network 225, 235, 243
- Chaotic ANN 325
- Chaotic circuit 297
- Chua's circuit 213, 289
- Client/server architecture 257
- Clustering 275
- Complex behaviour 297
- Conewise linear systems 315
- Controllability 315
- Controller area networks 353
- Coupled chaotic system 279, 297
- Coupling matrix 279
- CSMA/CD 353
- CSMA/CR 353
- Current follower 267
  
- Data detection problem 333
- Deterministic circuits 305
- Differential geometry 213
- Discrete event simulation technique 353
- Dynamical systems 213
  
- Elman network 325
  
- Feed-forward artificial neural network 267
- Fingerprint verification 235
  
- Gradient network 275
  
- Image compression 275
- Interval method 289
- Intermittency chaos 297
  
- Linear complementarity systems 315
  
- Meissner oscillator 305
- Method of close returns 289
- Moore type neighbourhood 221
  
- Neuron activation function 267
- Newton method 289
- Noisy nonlinear systems 305
  
- OPNET software 353
- Optimization 275
  
- Periodic orbit 289,
- Poincare map 289
  
- Roessler type attractor 289,
  
- Sequential Monte Carlo method 333
- Shift register 343
- Sigmoid PWL activation function 235
- Signal processing 333
- Slow manifold 213
- Stochastic circuits 305
- Stream cipher 343
- Stream generator 343
- Synchronization 279, 297
  
- Trapezoidal activation func. 225, 235
- Wireless Communication 333

## SPRINGER PROCEEDINGS IN PHYSICS

---

- 60 **The Physics and Chemistry of Oxide Superconductors**  
Editors: Y. Iye and H. Yasuoka
- 61 **Surface X-Ray and Neutron Scattering**  
Editors: H. Zabel and I.K. Robinson
- 62 **Surface Science**  
Lectures on Basic Concepts and Applications  
Editors: F.A. Ponce and M. Cardona
- 63 **Coherent Raman Spectroscopy**  
Recent Advances  
Editors: G. Marowsky and V.V. Smirnov
- 64 **Superconducting Devices and Their Applications**  
Editors: H. Koch and H. Lübbing
- 65 **Present and Future of High-Energy Physics**  
Editors: K.-I. Aoki and M. Kobayashi
- 66 **The Structure and Conformation of Amphiphilic Membranes**  
Editors: R. Lipowsky, D. Richter, and K. Kremer
- 67 **Nonlinearity with Disorder**  
Editors: F. Abdullaev, A.R. Bishop, and S. Pnevmatikos
- 68 **Time-Resolved Vibrational Spectroscopy V**  
Editor: H. Takahashi
- 69 **Evolution of Dynamical Structures in Complex Systems**  
Editors: R. Friedrich and A. Wunderlin
- 70 **Computational Approaches in Condensed-Matter Physics**  
Editors: S. Miyashita, M. Imada, and H. Takayama
- 71 **Amorphous and Crystalline Silicon Carbide IV**  
Editors: C.Y. Yang, M.M. Rahman, and G.L. Harris
- 72 **Computer Simulation Studies in Condensed-Matter Physics IV**  
Editors: D.P. Landau, K.K. Mon, and H.-B. Schüttler
- 73 **Surface Science**  
Principles and Applications  
Editors: R.F. Howe, R.N. Lamb, and K. Wandelt
- 74 **Time-Resolved Vibrational Spectroscopy VI**  
Editors: A. Lau, F. Siebert, and W. Werncke
- 75 **Computer Simulation Studies in Condensed-Matter Physics V**  
Editors: D.P. Landau, K.K. Mon, and H.-B. Schüttler
- 76 **Computer Simulation Studies in Condensed-Matter Physics VI**  
Editors: D.P. Landau, K.K. Mon, and H.-B. Schüttler
- 77 **Quantum Optics VI**  
Editors: D.F. Walls and J.D. Harvey
- 78 **Computer Simulation Studies in Condensed-Matter Physics VII**  
Editors: D.P. Landau, K.K. Mon, and H.-B. Schüttler
- 79 **Nonlinear Dynamics and Pattern Formation in Semiconductors and Devices**  
Editor: F.-J. Niedernostheide
- 80 **Computer Simulation Studies in Condensed-Matter Physics VIII**  
Editors: D.P. Landau, K.K. Mon, and H.-B. Schüttler
- 81 **Materials and Measurements in Molecular Electronics**  
Editors: K. Kajimura and S. Kuroda
- 82 **Computer Simulation Studies in Condensed-Matter Physics IX**  
Editors: D.P. Landau, K.K. Mon, and H.-B. Schüttler
- 83 **Computer Simulation Studies in Condensed-Matter Physics X**  
Editors: D.P. Landau, K.K. Mon, and H.-B. Schüttler
- 84 **Computer Simulation Studies in Condensed-Matter Physics XI**  
Editors: D.P. Landau and H.-B. Schüttler
- 85 **Computer Simulation Studies in Condensed-Matter Physics XII**  
Editors: D.P. Landau, S.P. Lewis, and H.-B. Schüttler
- 86 **Computer Simulation Studies in Condensed-Matter Physics XIII**  
Editors: D.P. Landau, S.P. Lewis, and H.-B. Schüttler
-